NASA/CP—2013–217479

2011 Space Cryogenics Workshop
"Poised for the Future, Reflecting on the Past"

W.L. Johnson, Co-Chair
Kennedy Space Center, Orlando, Florida

A.R. Schnell, Co-Chair
Marshall Space Flight Center, Huntsville, Alabama

L. Huget, Executive Director
Cryogenic Society of America, Inc., Oak Park, Illinois

Proceedings of the 24th Space Cryogenics Workshop
sponsored by NASA Kennedy Space Center
and NASA Marshall Space Flight Center
held in Coeur D'Alene, Idaho, June 8–10, 2011

March 2013

The NASA STI Program…in Profile

Since its founding, NASA has been dedicated to the advancement of aeronautics and space science. The NASA Scientific and Technical Information (STI) Program Office plays a key part in helping NASA maintain this important role.

The NASA STI Program Office is operated by Langley Research Center, the lead center for NASA's scientific and technical information. The NASA STI Program Office provides access to the NASA STI Database, the largest collection of aeronautical and space science STI in the world. The Program Office is also NASA's institutional mechanism for disseminating the results of its research and development activities. These results are published by NASA in the NASA STI Report Series, which includes the following report types:

- TECHNICAL PUBLICATION. Reports of completed research or a major significant phase of research that present the results of NASA programs and include extensive data or theoretical analysis. Includes compilations of significant scientific and technical data and information deemed to be of continuing reference value. NASA's counterpart of peer-reviewed formal professional papers but has less stringent limitations on manuscript length and extent of graphic presentations.

- TECHNICAL MEMORANDUM. Scientific and technical findings that are preliminary or of specialized interest, e.g., quick release reports, working papers, and bibliographies that contain minimal annotation. Does not contain extensive analysis.

- CONTRACTOR REPORT. Scientific and technical findings by NASA-sponsored contractors and grantees.

- CONFERENCE PUBLICATION. Collected papers from scientific and technical conferences, symposia, seminars, or other meetings sponsored or cosponsored by NASA.

- SPECIAL PUBLICATION. Scientific, technical, or historical information from NASA programs, projects, and mission, often concerned with subjects having substantial public interest.

- TECHNICAL TRANSLATION. English-language translations of foreign scientific and technical material pertinent to NASA's mission.

Specialized services that complement the STI Program Office's diverse offerings include creating custom thesauri, building customized databases, organizing and publishing research results…even providing videos.

For more information about the NASA STI Program Office, see the following:

- Access the NASA STI program home page at <http://www.sti.nasa.gov>

- E-mail your question via the Internet to <help@sti.nasa.gov>

- Fax your question to the NASA STI Help Desk at 443–757–5803

- Phone the NASA STI Help Desk at 443–757–5802

- Write to:
  NASA STI Help Desk
  NASA Center for AeroSpace Information
  7115 Standard Drive
  Hanover, MD 21076–1320

NASA/CP—2013–217479

2011 Space Cryogenics Workshop
"Poised for the Future, Reflecting on the Past"

W.L. Johnson, Co-Chair
Kennedy Space Center, Orlando, Florida

A.R. Schnell, Co-Chair
Marshall Space Flight Center, Huntsville, Alabama

L. Huget, Executive Director
Cryogenic Society of America, Inc., Oak Park, Illinois

Proceedings of the 24th Space Cryogenics Workshop
sponsored by NASA Kennedy Space Center
and NASA Marshall Space Flight Center
held in Coeur D'Alene, Idaho, June 8–10, 2011

National Aeronautics and
Space Administration

Marshall Space Flight Center • Huntsville, Alabama 35812

March 2013

Acknowledgments

We would like to thank the following people for significant contributions to the success of the 2011 Space Cryogenics Workshop (SCW): Laurie Huget and Theresa Boehl from the Cryogenic Society of America; former SCW chairs, especially Leon Hastings; Marshall Space Flight Center's STI Technical Publications team; Steven Van Sciver, American editor of *Cryogenics*; Kennedy Space Center; and Marshall Space Flight Center.

Wesley Johnson
NASA Kennedy Space Center, M/S: NE-F6
Kennedy Space Center, FL 32899 USA
Tel: +1 321 867 4865
E-mail: Wesley.L.Johnson@nasa.gov

Andrew Schnell
NASA Marshall Space Flight Center, M/S: ER-24
Huntsville, AL 35812 USA
Tel: +1 256 544 8913
E-mail: andrew.schnell@nasa.gov

Available from:

NASA Center for AeroSpace Information
7115 Standard Drive
Hanover, MD 21076–1320
443–757–5802

This report is also available in electronic form at
<https://www2.sti.nasa.gov/login/wt/>

TABLE OF CONTENTS

TABLE OF CONTENTS (Continued)

TABLE OF CONTENTS (Continued)

CONFERENCE PUBLICATION

2011 SPACE CRYOGENICS WORKSHOP
"POISED FOR THE FUTURE, REFLECTING ON THE PAST"

The 24th Space Cryogenics Workshop (SCW) was held at the Best Western Coeur d'Alene Inn and Conference Center, Coeur D'Alene, Idaho, June 8–10, 2011. The workshop was organized and sponsored by NASA Kennedy Space Center and NASA Marshall Space Flight Center, with a theme of "Poised for the Future, Reflecting on the Past." Over 100 scientists and engineers from around the world came together to discuss space applications for cryogenics, renew old acquaintances, and meet new practitioners in the field of space cryogenics. The workshop was held the week before the Cryogenics Engineering Conference, as has become typical.

The technical program consisted of 53 papers and posters presented at 12 oral and 1 poster session in a single-track format. New to the SCW this year was a Student Poster Competition, which was held in conjunction with the workshop poster session during the welcome reception. The first day consisted of a broad array of papers including an overview of the PIXIE, SPICA, and Astro-H missions and cryogenic cooling systems, a session containing multiple innovative components for use in various applications, a session on various thermal and fluid analyses that has been done, a session on other cryocooler developments, a session covering several novel new insulations as well as a deeper analysis of older materials, and a session discussing various experimental campaigns that have occurred over the last several years. The second day was just as broad and fast paced with sessions on the Astro-H mission, more experimental works, cryocoolers that are currently under lifetime testing around the world, analytical modeling of various aerospace cryogenic fluid systems, cryogenic long-duration propellant storage missions, and another set of component testing efforts. It was interesting to observe the combination of component testing and analysis as they fit into the bigger picture of several planned and proposed missions.

The SCW banquet was a dinner cruise on Lake Coeur D'Alene. The beautiful mountain scenery and unique social interaction provided by the cruise were enjoyed by all. The 'best paper' award for the 2009 workshop was presented to Peter Shirron and Mark Kimball, Goddard Space Flight Center, for their paper entitled, "ADR Design for the Soft X-Ray Spectrometer Instrument on the Astro-H Mission." The award for the SCW Student Competition was given to Peter Lowell, University of Colorado in Boulder, for his paper entitled, "Refrigeration of Separate, User-Supplied Payloads With Normal-Insulator-Superconductor Tunnel Junctions."

The remainder of this publication is a compilation of the individual papers presented at this conference.

SPICA SUBKELVIN CRYOGENIC CHAINS

L. Duband, JM. Duval, N. Luchier and T. Prouve*

CEA / INAC / Service des Basses Températures, Grenoble 38054 FR
* California Institute of Technology, Pasadena CA 91125 USA

ABSTRACT

SPICA, a Japanese led mission, is part of the JAXA future science program and is planned for launch in 2018. SPICA will perform imaging and spectroscopic observations in the mid- and far-IR waveband, and is exploring instrumentation spanning the 5 to 400 micron range. The SPICA payload features several candidate instruments, some of them requiring temperature down to 50 mK. This is currently the case for SAFARI, a core instrument developed by a European based consortium and BLISS proposed by CALTECH/JPL in the US.

SPICA's distinctive feature is to actively cool telescope to temperature below 6 K. In addition SPICA is a liquid cryogen free satellite and all the cooling will be provided by radiative cooling (L2 orbit) down to 30 K and by mechanical coolers for lower temperatures. The satellite will be launch warm and slowly bring to its operating temperatures once in orbit. This warm launch approach allows to eliminate a large liquid cryogen tank and to use the mass saved to launch a large diameter telescope (3.2 meters). This 4 K cooled telescope allows to significantly reduce its own thermal radiation, offering superior sensitivity in the infrared region.

The cryogenic system that enables this warm launch/cooled telescope concept is a key issue of the mission. This cryogenic chain features a number of cooling stages comprising passive radiators, Stirling coolers and several Joule Thomson loops, offering cooling powers at typically 20, 4.5, 2.5 and 1.7 K. The SAFARI and BLISS detectors require cooling to temperatures as low as 50 mK. The instrument coolers will be operated from these heat sinks. They are composed of a small demagnetization refrigerator (ADR) pre cooled by either a single or a double sorption cooler, respectively for SAFARI and BLISS. The BLISS cooler maintains continuous cooling at 300 mK and thus suppresses the thermal equilibrium time constant of the large focal plane.

These hybrid architectures allow designing low weight coolers able to reach 50 mK. Because the sorption cooler is an extremely light solution to produce sub-Kelvin temperatures, it allows the stringent mass budget to be met. These concepts are discussed in this paper.

1. INTRODUCTION

SPICA will embark several instruments, two of them, SAFARI a core European instrument, and BLISS a possible US candidate, require sub-Kelvin cooling. SAFARI – SpicA FAR-infrared Instrument - is an imaging spectrometer with both spectral and photometric capabilities covering the 33-210 μm waveband. The background-limited infrared-submillimeter spectrograph (BLISS) is a far-IR spectrograph concept which philosophy is to provide a rapid survey spectroscopy capability over the full far-IR range. Both instruments use transition-edge superconducting (TES) bolometers.

SPICA's science objectives [1] can only be achieved by increasing dramatically the sensitivity with respect to previous missions such as ISO, AKARI or HERSCHEL. The first idea is to reduce the background photon noise generated by the telescope itself, by cooling it down to 5-6 K. The second is to develop more sensitive detectors, which in general involve lower temperatures. The SAFARI and BLISS TES bolometers will be operated in the 50 mK range. When it comes to ultra low temperature coolers (< 200 mK) only two solutions are possible for a space application, the dilution cooler and the adiabatic demagnetization refrigerator. An open-cycle space compatible dilution is currently used in the ESA Planck space mission (≈ 100 nW @ 100 mK)[2], and a closed cycle version of this system is currently under development. Although temperatures

close to 50 mK have been achieved [3], several technical challenges remain to be solved and the technological maturity must be improved.
On the other hand, ADR is a proven technology, very efficient, vibration free and attractive for space missions. Several ADR can then be chained to cover an extended temperature range [4, 5, 6]. However one of the drawbacks is the mass, which becomes very large as the temperature range is raised.

2. DESCRIPTION OF THE SPICA SUBKELVIN CRYOGENIC CHAIN

The selection and design of the sub Kelvin cooling chain must be made in the light of the mission constraints. The SPICA cooling chain features Stirling and Joule Thomson coolers as depicted in Fig. 1 [7]. The use of mechanical coolers allows to extend the mission duration. One of the drawback however is that the cold stages net heat lifts are limited. In addition the JT loop cannot accept large peak powers which could dry them out. In the case of the core instrument SAFARI and for what concerns the sub-Kelvin cooler, we can rely on 5 and 10 mW respectively at 1.7 K and 4.5 K. We also have access to a 20-30 K heat sink for which the cooling power available is not clearly defined at this stage. BLISS, another candidate instrument for which the resources have not been detailed yet, is expected to have access to roughly the same allocations. These numbers may evolve in the future but they were used as the basis for the sub-Kelvin cooler design.

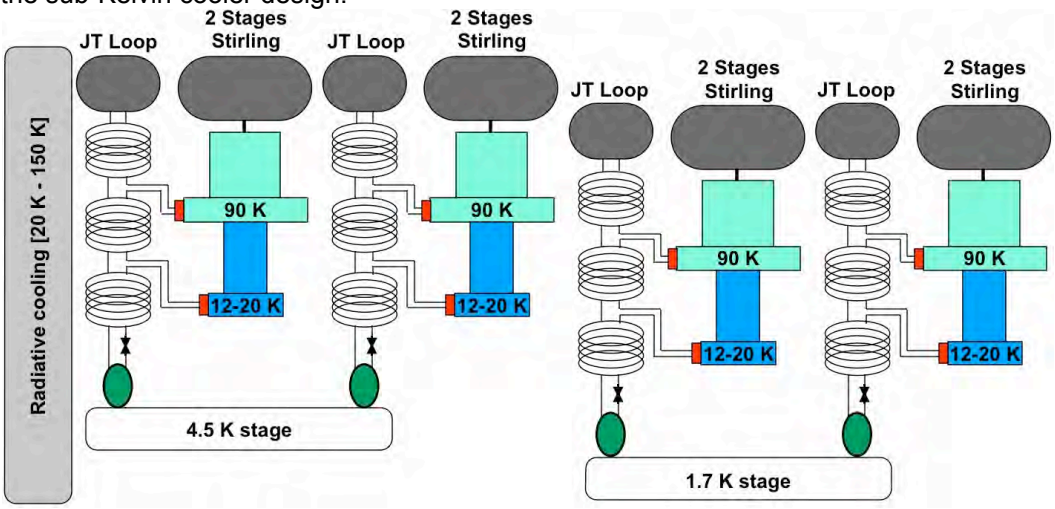

Figure 1. Schematic of the SPICA cryogenic chain

It is necessary to come up with clever thermal architectures in which all available cooling sources may be used in order to optimize the heat dissipation at each temperature stage. In addition mass has become a critical driver and a clear objective of the future space instruments is to maximize the amount of on board science within the overall mass allocation. This has a direct impact on the cryogenics for which one of the motto is now the lighter the better.

We have extended experience with the ^{3}He and ^{4}He sorption coolers, which can be made in various architectures, single or multistage, and have been successfully adapted to the space environment. HERSCHEL for instance, the largest space observatory ever flown and launched in May 2009 embarks three instruments, two of them features a ^{3}He sorption cooler developed in our laboratory [8, 9]. These coolers are compact and extremely light but are limited to temperature down to 200 mK.

For SPICA we have proposed to combine the best of both techniques, a self contained and extremely light helium sorption first stage, and a very efficient miniature ADR second stage [10]. Indeed because the ADR stage is operated from a temperature already well below 1 K (300 – 500 mK range) the field required to extract most of the

entropy remains lower than 1 Tesla. This in turn leads to a small superconducting dry coil and limited shielding for the stray field.

This system will be a one shot system: the cooler is recycled and then provides cooling powers for a given time at two temperatures, 300 mK to intercept parasitic heat loads and cool detector front end electronics and 50 mK for the detectors. Once the system is out of “cold joules” it can be recycled again and indefinitely as long as the upper heat sinks are available. For SAFARI the useful heat lift needed at 50 mK is being worked out but will be equal to or less than 1 μW with simultaneously 10 to 12 μW at 300 mK for an autonomy of 30 hours and a recycling time less than 12 hours. Currently the 4.5 K resource drives this recycling time although using an energy storage unit could significantly reduce it.

The approach for BLISS is slightly different. The current design features about 5 kilograms at 300 mK and 10 kilograms at 50 mK, with a large fraction made of Aluminum. Cooling this large mass from 1.7 K down to 300 mK is not really a problem in terms of liquid helium used. The ^{3}He latent heat is significant compared to the material heat capacities at these temperatures. As a matter of fact, assuming the whole system is made of aluminum, the cost would be about 1.1 Joules leading to 0.7 liters STP for a cooler that contains roughly 6 liters (about 10%, to be taken into account in the sizing). Note that the same calculation for copper leads to 0.26 Joules and 0.17 liters STP. The problem is related to the time constant: aluminum becomes superconducting below 1 K and thus its thermal diffusivity becomes poor leading to a prohibitively long time needed to reach thermal equilibrium. Because of the mass constraint it is not desirable to add copper straps to enhance the temperature homogenization. The solution is then to cool this part of the instrument at 300 mK once and keep it there during BLISS observations. Thus in this case we have developed a continuous double stage helium sorption cooler combined to a miniature ADR. For the present prototype the ADR stage is provided by the Jet Propulsion Laboratory (CA USA).

The SAFARI and BLISS architecture are represented in Fig. 2. For SAFARI the cooler structure is held at 4.5 K and a thermal link is provided for the 1.7 K heat sink, while for BLISS it is just the opposite, structure at 1.7 K and link to 4.5 K. These conditions have no major impact on the design, to the exception of the Kevlar suspension system, which features a heat intercept in the case of SAFARI. This aspect is discussed further in this paper.

An important challenge that needed to be solved for both systems was the peak powers dissipation. Indeed the sorption cooler recycling phase requires to thermally cycle the sorption pump between 4.5 K and 30 K [11]. This cycling implies to remove a given amount of energy: if this is done quickly, large peak powers are to be dealt with. In the case of SPICA the limited cooling powers available require that 1) the thermal architecture takes advantage of all available cooling resources and 2) the timing of the cycle is set such that the instant loads never exceed these cooling powers. In a first phase, the sorption pump is slowly raised to 30 K and if necessary maintained there until the right thermodynamic conditions are reached (mostly an evaporator temperature as close as possible to the 1.7 K heat sink). During this phase the hot gas is cooled and the corresponding energies are rejected to the heat sinks (4.5 K and 1.7 K) and finally the gas is liquefied (1.7 K). During this phase the only lever arm is through the input power to the pump. Then in a second phase the pump is cooled down to 4.5 K, and the energies related to the heat capacities and the heat of adsorption are removed at this temperature stage. During this phase the heat dissipation is controlled through the regulation of the conductance of the heat switch that links the pump to the 4.5 K interface (HS1 & HS4 in Fig.2). This is performed by operating the switch in the ballistic (or molecular) regime. In this regime the thermal conductance is directly proportional to the internal pressure of the switch. Since the temperature of the switch miniature sorption pump sets this pressure, it is possible in principle to control the conductance by temperature regulating this component.

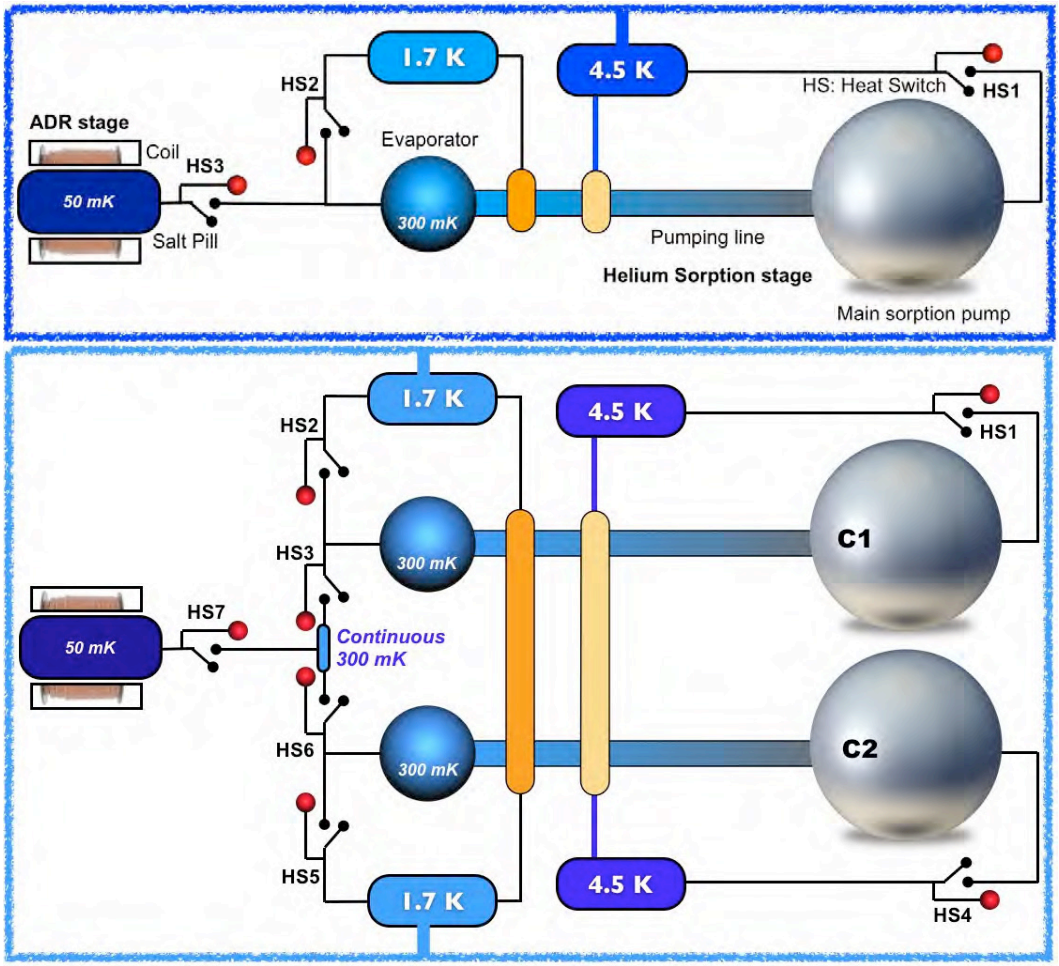

Figure 2. SAFARI (above) and BLISS (below) thermal architecture

2.1. RECYCLING PHASE AND PEAK POWER ISSUE

In order to demonstrate and validate the recycling of the helium sorption stage with limited resources, two prototypes were built respectively for SAFARI and BLISS. Since the main issue was the management of the heat flows, these systems featured only the sorption stage (2 stages for BLISS). In the meantime and as experimental results became available, the development of a complete cooler featuring an efficient ADR stage coupled to a sorption stage and its operation down to 20 mK has been investigated in the framework of an ESA TRP program focused on the IXO mission [12]. Based on these works, an engineering model has now also been designed for the SAFARI instrument while for BLISS the ADR stage has been integrated at JPL premises.

For the sorption stage prototypes, based on the required heat lift and autonomy at 300 mK, the preliminary sizing lead to cooler sizes close to that of the HERSCHEL cooler. In order to benefit from this heritage, both prototypes were thus sized as 6 liters STP unit. The SAFARI demonstrator features 3 heat switches, while the BLISS system includes 7 switches. All switches are gas gap heat switch filled with ^{3}He gas. The whole system is mounted on the cold plate of a 1.2 K pumped helium cryostat, and the 1.7 K and 4.5 K interfaces are temperature regulated. The objective of this system is to measure (and control) the flowing powers while the cooler is recycled. The principle is straightforward: each thermal interface is thermally connected to the helium cryostat cold plate by a calibrated copper link. Each link has been sized so that the heating

power required to maintain 4.5 K for instance is about twice the available cooling power specified (20 mW in this case). When there is no dissipation, the temperature controller inputs 20 mW to this interface via a heater, and as soon as heat is flowing to this interface, the temperature controller adjusts the input power accordingly. By difference it is then possible to extract exactly this flowing power.

3. SAFARI COOLER

3.1. DEMONSTRATOR

Several experiments were necessary to tune the heat switches and finally we were able to demonstrate full recycling within the specified resources. Several options were possible for this control and we selected what seems the simplest one: to adjust the conductance of the heat switch (HS1) as a function of the temperature of the main sorption pump. In other words for a given pump temperature, a given input power is sent to the miniature sorption pump. This requires calibrating the heat switch in the molecular regime, but once it is done the recycling can be performed automatically. This technique works fairly well as shown in Fig. 3. The specified limits for the dissipation are slightly overshoot but the difference remains below 10% and is just a matter of precise tuning. For comparison purpose we have reported in this figure the dissipations measured during the recycling of a HERSCHEL sorption coolers. In this case the cooler is thermally connected to only one heat sink (the superfluid tank) but features two copper links to this interface [8]. This explains why two peaks are reported on the figure. This graph shows that we are now able to reduce the peak powers by more than two orders of magnitude. Of course since the energy to be removed remains the same, the recycling time is strongly dependent on the available resources, mostly at 4.5 K and thus any increase in cooling power is most welcome. The current duty cycles are compatible with the mission scenario, but they could be substantially increased by the use of an energy storage unit, for which a development program is currently on going. Nevertheless this experiment demonstrates we can recycle the cooler while controlling the heat dissipations.

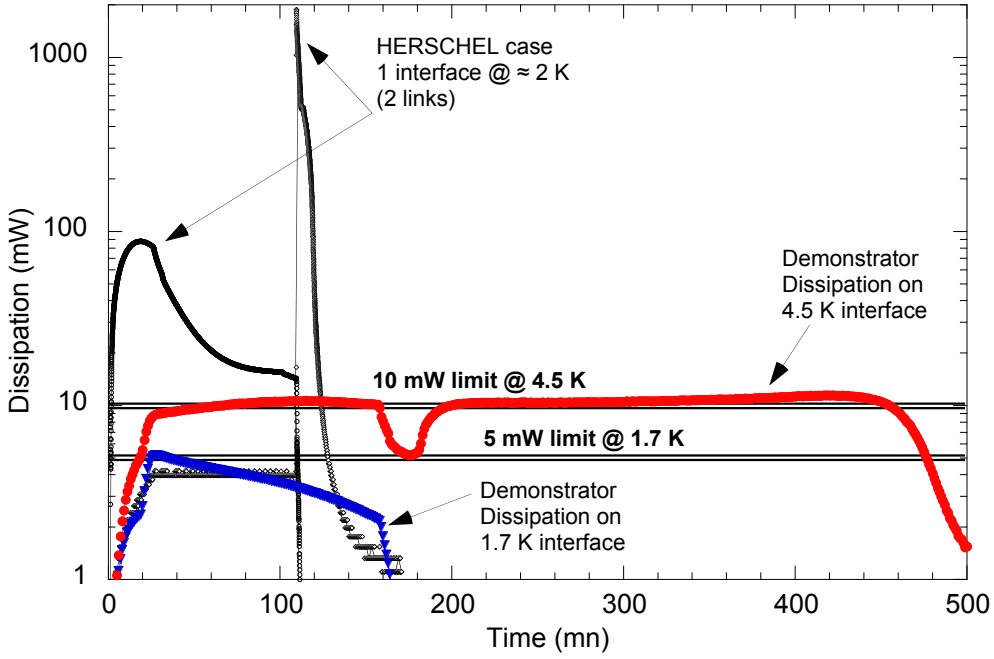

Figure 3. Typical recycling phase (Comparison with HERSCHEL cooler)

3.2. SAFARI ENGINEERING MODEL COOLER

The previous experiments allowed to validate the overall concept and the design of the first SAFARI engineering model cooler has been almost completed as shown on Fig. 4. The main specifications used to size the cooler are summarized in table 1. These specifications are not consolidated yet and several are still missing. They may evolve in the future, in particular the heat lift at 50 mK which could decrease. The overall cooler design will probably remain the same and will just be scaled down.

Safety	Structural failure mode shall be leak before burst
Thermal	• Heat lift capability: 1 µW @ 50 mK and 12 µW @ 300 mK • Gross energies: no less than 0.14 J @ 50 mK and 2.6 J @ 300 mK • Temperature stability: 5 µK rms @ 50 mK and 1 mK rms @ 300 mK, in a 0-20 Hz bandwidth • Cooler recycling time: no more than 12 hours • Heat dissipation: 5 mW peak @ 1.7 K, 15 mW peak @ 4.5 K
Geometry	• maximum envelope: 350 x 200 x 150 mm
Mass	• less than 8 kg

The cooler displays in Fig. 4 weights about 6 kg and is 300 x 190 x 135 mm in size.

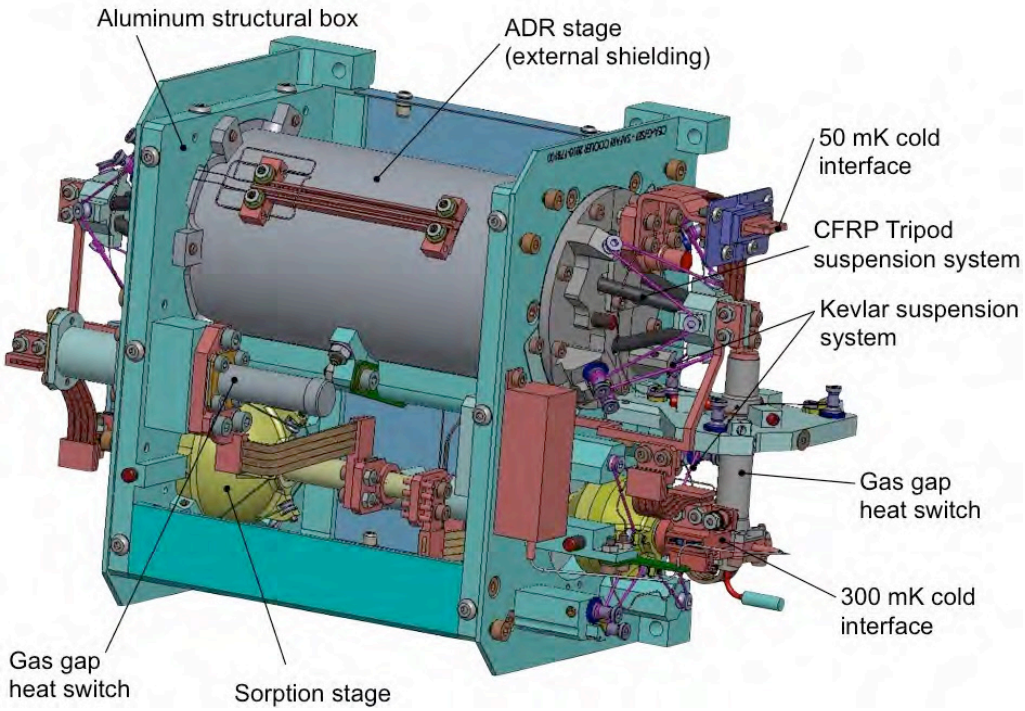

Figure 4. SAFARI Engineering model cooler

The sorption stage is similar to the HERSCHEL sorption cooler and benefit from this heritage. Yet there are several differences in particular for the Kevlar suspension system. Since the cooler structure is made of aluminum while the cooler itself is mostly made of titanium, the evaporator features Kevlar strings located in the same plane. This arrangement allows to compensate for the differential thermal contraction. The pumping line has also been adapted to match the thermal constraints of SAFARI.

The ADR stage uses a Chromium Potassium Alun (CPA) salt pill that weights about 800 grams. The parasitic heat load through the suspension system directly from the structure at 4.5 K to 50 mK would be too large, and thus two thermal intercepts are added. Between 50 mK and 300 mK we use two CFRP tripods, and from 300 mK to

4.5 K Kevlar cords. Although the mechanical analysis showed that we could use the same Kevlar cords as for HERSCHEL (0.5 mm in diameter) the experimental tests carried out on a mock up of the salt pill lead to repeated failures at 30 G sinus. We found that the problem is related to the abrasion of the Kevlar against the pulleys. Indeed due to the large mass of the pill, the tension in the cord is not enough to avoid slight displacements. The solution to this problem is straightforward: the pulley surfaces have been polished and we now use a larger diameter cord (0.8 mm) [Ian Hepburn. MSSL UK, Private communication]. With these modifications, subsequent vibration tests have been successful at level of up to 30 G. However the conductive load to the 300 mK stage through the Kevlar is now much larger and consequently a second heat intercept at 1.7 K has been introduced. It is simply made of copper wires that are rounded and glued around each section of cord at the appropriate location and then connected to the 1.7 K interface. This rather simple technique has demonstrated excellent results and in fact we also decided to use this larger cord for the evaporator, along with a 1.7 K intercept. Since the integrated thermal conductivity of Kevlar varies like $T^{2.54}$, the gain of introducing this heat intercept, taking into account the geometry, is about a factor 10.

4. BLISS PROTOTYPE COOLER

Figure 5 displays two pictures of the cooler without the lateral covers and internal thermal shields. Indeed besides the heat flow management, one of the issues for the BLISS cooler was the radiative loading from the cooler being recycled to the cooler being operated at low temperature (300 mK). The design was worked out to address this point and thermal shields were added at several locations to prevent radiation from the hot components to the cold evaporators.

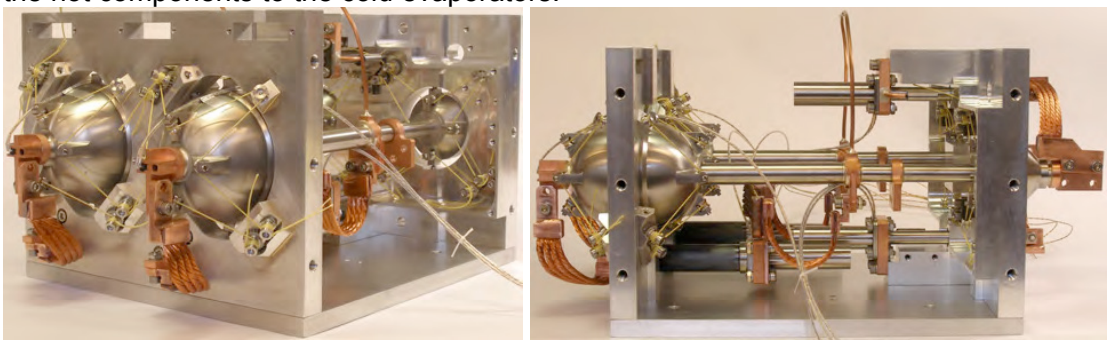

Figure 5. BLISS Prototype showing the two sorption stages and heat switches

The objective was first to demonstrate we can recycle alternatively each cooler without exceeding the limits on the power dissipation at each interfaces, ie. 5 mW @ 1.7 K and 10 mW @ 4.5 K. The curves on Fig. 6 are a typical result and show that the dissipation limits are fairly well respected and that the recycling of a cooler (component raised to 30 K) does not impact the performance of the other one. In that respect the experimental results are satisfactory and at the cooler level no problems with stray lights were spotted. In addition for BLISS it should be noted that since one cooler is always operated at 300 mK, it is possible in principle to further reduce the dissipations since the duration of the cooldown phase can be extended. In this case of course both sorption stages must have been sized accordingly.

Although we had not anticipated any problems with the low temperature switches (HS3 and HS6 on Fig. 2) that is where they did happen. We found that once they had been turned ON at 300 mK, it took several hours to obtain a full OFF position again.

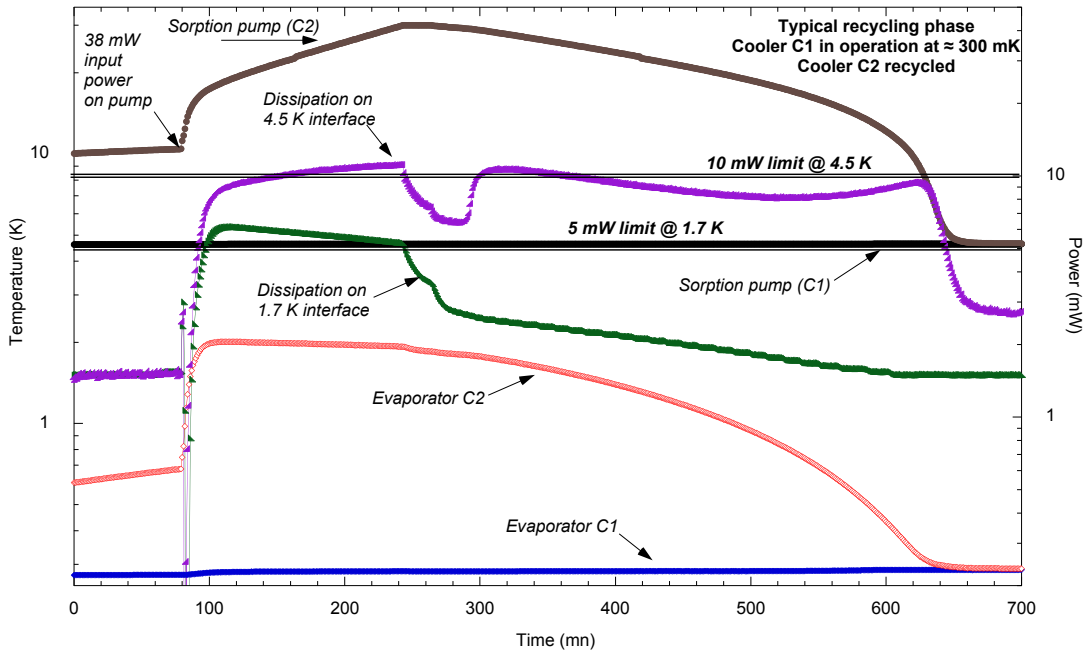

Figure 6. BLISS Prototype – Recycling phase and heat flows

We can only see two causes: either liquid condensed inside the switch or adsorbed layers of gas that eventually desorb and induce a transient conductance increase. Indeed in several experiments, temperature oscillations were seen. Several modifications were made to the design of the switch to avoid potential liquid trapping and internal holes were added to allow it to freely move. In addition the internal surfaces were polished and gold plated to limit the adsorbed gas. A new set of switch were built and tested but to date this problem has not been solved. This behavior is still under investigation but nevertheless we were able to run both stages alternatively as shown in Fig. 7. In this case and due to the residual thermal conductance of the switches, the evaporators do remain below 400 mK but show a temperature increase when the other stage is being recycled.

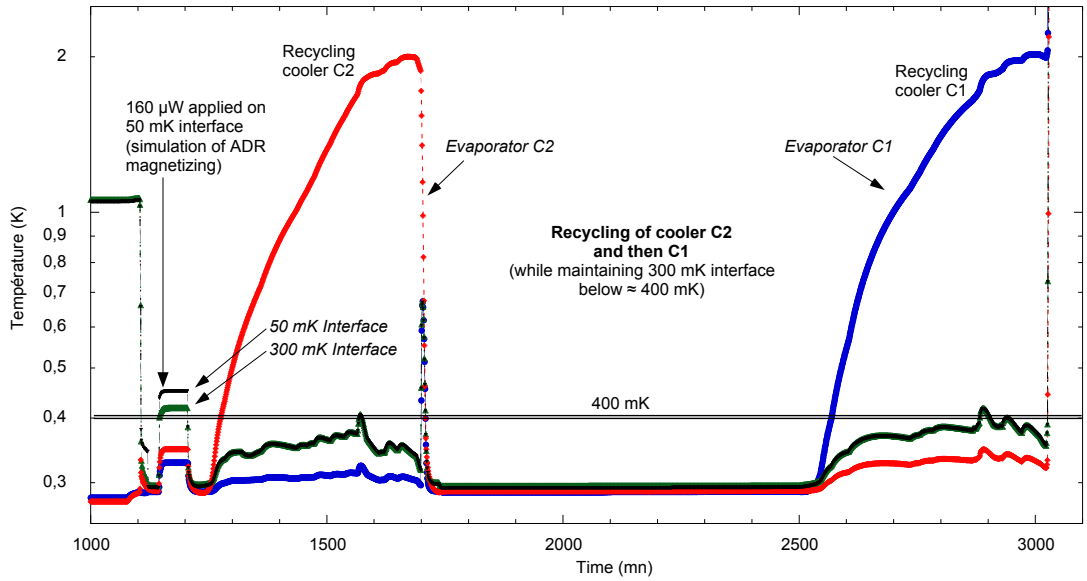

Figure 7. BLISS Prototype – Continuous operation

This unit has been delivered to JPL/Caltech where the ADR stage has been added. The full system has been integrated on a specific test cryostat featuring a Cryomech PT415 pulse tube associated to a pumped helium bath to provide temperature down to 1.7 K. A picture of the full unit is given on Fig. 8.

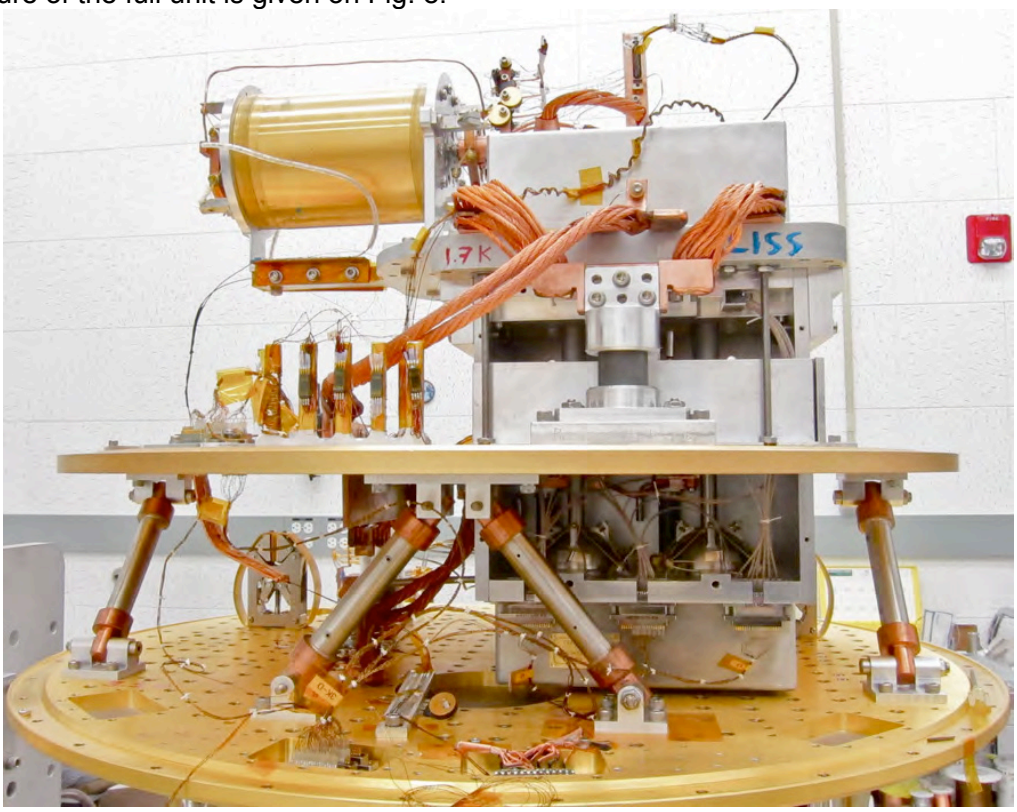

Figure 8. BLISS Prototype integrated at JPL premises

This system is currently under test and temperature down to 30 mK have been achieved. However the peculiar behavior of the 300 mK switches remains a problem and has not been solved at this time. A dedicated experiment has been set up to study this aspect. Another alternative would be to use mechanical or superconducting switches, a decision which will depend on the output of the current investigations.

5. CONCLUSION

Several future space missions will require temperature down to 50 mK for the detectors. We have proposed and validated a concept featuring the combination of a very light 300 mK sorption stage coupled to a 50 mK ADR miniature stage. Two prototypes have been manufactured and tested. The first one is devoted for SAFARI, while the second one providing continuous cooling at 300 mK has been designed for BLISS, two instruments which may be flown onboard SPICA a Japanese mission.

Operations of these systems with limited available cooling powers at the upper heat sinks have been demonstrated.

The SAFARI engineering model cooler has been designed based on these results. It will be manufactured in the coming months.

In the meantime the first fully integrated sorption / ADR cooler has been tested [12]. This unit was made in the framework of an ESA technical research program dedicated to the XMS instrument on board the IXO mission. The overall performance of this system are satisfactory and in agreement with predictions. An ultimate temperature of

22 mK has been achieved and hold time of 24 hours have been measured at 50 mK for a net heat lift of 1 µW (and simultaneously 10 µW at 300 mK).

ACKNOWLEDGMENT

We thank the French Space Agency (CNES) and the Jet Propulsion Laboratory (USA) for the funding of these works. We thank Laurent Clerc and Jean Louis Durand for their expert technical work during the assembling phase, the set-up of the test cryostats and their contribution to the test campaigns. Finally we also thank Laurent Guillemet and Florian Bancel for the 3D design of the coolers.

REFERENCES

1. ESA Assessment Study Report "SPICA Revealing the origins of planets and galaxies" *ESA/SRE [2009]6* (Dec 2009)
2. Triqueneaux, S., Sentis, L., Camus, P., Benoit, A. and Guyot, G., "Design and performance of dilution cooler system for the Planck mission" *Cryogenics*, vol. 46 (2006), pp. 288-297.
3. Martin, F., Vermeulen, G., Camus, P. and Benoit, A., "A closed cycle 3He-4He dilution refrigerator insensitive to gravity" *Cryogenics*, In Press (2010)
4. Shirron, P. et al., "Development of a cryogen-free continuous ADR for the constellation-X mission" *Cryogenics*, vol. 44 (2004), pp. 581-588.
5. Bartlett et al., "Improved performance of an engineering model cryogen free double adiabatic demagnetization refrigerator" *Cryogenics*, In Press (2010)
6. Shinozaki et al., "Development of double-stage ADR for future space missions" *Cryogenics*, In Press (2010)
7. Sugita et al., "Cryogenic system design of the next generation infrared space telescope SPICA" *Cryogenics*, In Press (2010)
8. Duband, L, Clerc, L., Ercolani, E., Guillemet, L. and Vallcorba, R., "Herschel flight models sorption coolers" *Cryogenics*, vol. 48 (2008), pp. 95-105.
9. Duband, L. et al. "In flight performance of the HERSCHEL sorption coolers – One year of operation" *Cryocoolers 16,* ICC Press Boulder Colorado (2011), pp. 689-698
10. Luchier, N., Duval, JM., Duband, L., Camus, P., Donnier-Valentin, G. and Linder, M. "50 mK cooling solution with an ADR pre cooled by a sorption cooler" *Cryogenics*, Vol 50 (2010), pp 591-596
11. Duband, L., Duval, JM., Luchier, N. and D'Escrivan, S. "SPICA SAFARI Subkelvin cryogenic chain" *Cryocoolers 16,* ICC Press Boulder Colorado (2011), pp. 699-707
12. Luchier, N., Duval, JM., Duband, L. and Tirolien, T. "Performance of the 50 mK ADR/sorption cooler" Presented at the 2011 Space Cryogenics Workshop, Coeur d'Alene, IDAHO

Development of mechanical cryocoolers for the cooling system of the Soft X-ray Spectrometer onboard Astro-H

Yoichi Sato [a] *, Keisuke Shinozaki [a], Hiroyuki Sugita [a]
Kazuhisa Mitsuda [b], Noriko Y. Yamasaki [b], Yoh Takei [b], Takao Nakagawa [b]
Ryuichi Fujimoto [c]
Masahide Murakami [d]
Shoji Tsunematsu, Kiyomi Otsuka, Seiji Yoshida, Kenichi Kanao, Katsuhiro Narasaki [e]
and ASTRO-H SXS team

[a] *Aerospace Research and Development Directorate, Japan Aerospace Exploration Agency, 2-1-1 Sengen, Tsukuba, Ibaraki 305-8505, Japan*
[b] *Institute of Space and Astronautical Science, Japan Aerospace Exploration Agency, 3-1-1 Yoshinodai, Chuo-ku, Sagamihara, Kanagawa 252-5210, Japan*
[c] *Faculty of Mathematics and Physics, Kanazawa University, Kakuma-machi, Kanazawa, Ishikawa 920-1192, Japan*
[d] *Institute of Engineering Mechanics and Systems, University of Tsukuba, 1-1-1 Tennodai, Tsukuba, Ibaraki 305-8573, Japan*
[e] *Sumitomo Heavy Industries, Ltd., Niihama Works, 5-2 Soubiraki-cho, Niihama, Ehime 792-8588, Japan*
**E-mail: satoh.yohichi@jaxa.jp, Tel: +81-50-3362-3652, Fax: +81-29-868-5969*

Abstract

Astro-H is the Japanese x-ray astronomy satellite planned for launch in 2014. The Soft X-ray Spectrometer (SXS) onboard Astro-H, is a high energy resolution spectrometer utilizing an X-ray micro-calorimeter array, which is operated at 50 mK by the ADR with the 30-liter superfluid liquid helium (LHe). The mechanical cryocoolers, 4K-class Joule Thomson (JT) cooler and 20K-class double-staged Stirling (2ST) cooler are key components to achieve a LHe lifetime for over 3 years in orbit (5 years as a goal). Based on the existing cryocoolers onboard Akari (2006) and JEM/SMILES (2009), modifications for higher cooling power and reliability had been investigated. In the present development phase, the Engineering Models (EM) of these upgraded cryocoolers are fabricated to carry out the verification tests for cooling performance, mechanical performance and lifetime. Nominal cooling power of 200 mW at 20 K for the 2ST cooler and 40 mW at 4.5 K for the JT cooler were demonstrated with temperature and power margin. Mechanical performance test for the 2ST cooler units proves a tolerability for pyro shock and vibration environment of the Astro-H criteria. Continuous running of the 4K-class JT cooler combined with the 2ST precooler for lifetime test has achieved over 5000 hours without any degradation of cooling performance.

Keywords:
Astro-H/SXS, Joule Thomson cooler, Double-staged Stirling cooler, cooling performance, lifetime

1. Introduction

Astro-H, the Japanese 6th X-ray astronomy satellite devoted to observations of celestial X-ray sources, is being developed under extensive international collaboration between Japan and the US, with European participation. It will be launched by the Japan Aerospace Exploration Agency (JAXA) with an H-IIA launch vehicle from the Tanegashima Space Center in 2014 [1], following the successful Suzaku mission (previously called Astro-E2). The Soft X-ray Spectrometer (SXS) [2], one of the scientific instruments onboard Astro-H, is a high resolution spectrometer utilizing an X-ray micro-calorimeter array, which is

operated at the 50 mK by the Adiabatic Demagnetization Refrigerator (ADR) [3] to achieve a high energy resolution of 7 eV at 0.5- 10 keV. The detector assembly and the ADR are developed by NASA, while the cooling system down to 1.3 K of the superfluid liquid helium (LHe) as a heat sink for the ADR is developed by JAXA in cooperation with several universities and academic institutes in Japan. The SXS cooling system is the critical technology to provide a 50 mK cryogenic temperature to the detector for required observatory duration of 3 years (goal : 5 years). To extend a lifetime of the 30-liter LHe for more than 3 years, the parasitic heat load to the LHe tank must be extremely suppressed to less than 1 mW by using two types of mechanical cryocoolers, the 20K-class double-staged Stirling (2ST) cooler and the 4K-class ^{4}He Joule Thomson (JT) cooler. These cryocoolers were originally developed for the Japanese infrared astronomy satellite Akari (previously called Astro-F) [4] [5] [6] and the Superconducting Submillimeter-wave Limb-emission Sounder (SMILES) [7] [8] on the Japanese Experiment Module Exposed Facility (JEM-EF) of the International Space Station (ISS), respectively. Based on heritage of these existing cryocooler, the modifications of higher cooling performance and reliability had been investigated to develop the upgraded cryocoolers for application to the Astro-H and other future missions like the next-generation infrared telescope mission SPICA (2018) [9]. This paper describes a development status of the mechanical cryocoolers for the cooling system of Astro-H/SXS with cooling performance, lifetime and mechanical environmental test.

2. Design overview of the SXS cooling system

The top requirement of the SXS cooling system is to keep the detector at 50 mK with temperature stability of < 2 μK for 3 years (5 years as a goal). Figure 1 shows the schematics for design concept of the SXS cooling system from room temperature to 50 mK. An ADR are utilized as the last 50 mK stage cooler with a LHe heat sink because it is the flight proven cooling method in the aspect of temperature, stability and recycle time. From the point of view of robustness and reliability, the SXS cooling system should configures redundancy for a failure of a single cryocooler including LHe. The LHe tank is insulated thermally by the JT shield to suppress the parasitic heat load to less than 1 mW to extend a lifetime of the 30-liter LHe for more than 3 years. The JT shield is directly cooled by the 4K-class JT cooler combined with the two units of 2ST precoolers, which are operated with half power (50 W × 2) for redundancy. If one 2ST precooler fails, a remaining one must be operated with maximum power of 90 W to cancel out the parasitic heat load through a stopped 2ST precooler. In this situation, the JT cooling power will be lost due to an insufficient cooling power of the 2ST precoolers. The JT cooler is functionally redundant with the LHe. Thus, it is required to perform as a heat sink for heat dissipation of the recycling ADR in cryogen-free operation when the LHe is consumed completely. There are three vapor-cooled shields (VCS); Inner-VCS (IVCS), Middle-VCS (MVCS) and Outer-VCS (OVCS) to block thermal radiation from the main-shell. Another two units of the 2ST cooler are installed for the IVCS and the OVCS, which are cooled down to temperature level of 20 K and 100 K, respectively. These two 2ST shield coolers are also operated with half power (50 W × 2) in nominal operation. If one 2ST shield cooler fails, the other is operated with maximum power (90 W) to compensate for lost cooling power.

In the previous design of the SXS cooling chain in 2009, the double-staged ADR with the LHe was used for the detector cooled down to 50 mK and the 1 K-class ^{3}He JT cooler was used for redundancy with the LHe. However, in progress of design investigation, it turns out that a combination of another unit of ADR (3^{rd}-ADR) and 4 K-class ^{4}He JT cooler, instead of a 1 K-class ^{3}He JT cooler, is more practical design in order to achieve the requirement of detector temperature stability of < 2 μK after the LHe is completely consumed in orbit. In the current design, the 3^{rd}-ADR unit, which is located between the LHe tank and the JT shield, is supposed to be operated to cool down the LHe tank in cryogen-free operation. This design change consequently provided a cooling power margin of the JT cooler to accommodate uncertainties of

parasitic heat load.

Figure 2 shows the cross sectional view of the SXS dewar. The He tank is mechanically suspended with CFRP straps from the IVCS. The IVCS, in turn, is suspended with GFRP straps from the main shell. The 2ST shield coolers are mounted on the girth ring of the dewar, while the JT cooler system is attached to the aft dome of the dewar. The heat dissipation from the mechanical cryocoolers is 295 W in the nominal operation (50 W × 2 at the 2ST shield coolers, 50 W × 2 at the 2ST precoolers for JT coolers and 95W at the JT compressors including the pressure gages and the solenoid valves). An average temperature of the main shell is required to be kept below 290 K to achieve the thermal performance of the cooling system. All cryocoolers must be operated below 30 degree Celsius to prevent hardware degradation. To satisfy these requirements, a part of the dewar surface is exposed to space and the main shell surface is used as a radiator. To use the dewar surface as a radiator efficiently, the dewar has a reflector around it where the dewar surface is not exposed to space [10]. The space craft provides the thermal I/F points for heat dissipation from all cryocoolers. Thermal straps of copper braid are used as thermal paths from the JT and precoolers to the thermal I/F points, while LHPs (Loop Heat Pipes) are used from the 2ST shield coolers to the thermal I/F points. The LHe lifetime with this cooling system is achieved to almost 5 years, according to the current thermal analysis.

3. Mechanical cryocoolers of the SXS cooling system

3.1. 20K-class double-staged Stirling cooler

The 20K-class double-staged Stirling cooler (2ST) is a split-type Stirling cycle cooler composed of a double-staged displacer with two expansion stages, a linear compressor and a connecting tube. It was originally developed for Akari launched on February 21, 2006 (UT) and had been operated on orbit for more than 1.5 years of design lifetime [11]. The compressor has two opposite pistons supported with the linear ball bearings. The contact seals are used for displacer seals in the cold head [12]. Based on this Akari 2ST cooler, improvements of cooling power and mechanical reliability had been investigated and evaluated with three critical modifications; 1) increasing a diameter of the second displacer up to 8 mm to enlarge a gas expansion volume at 20K stage, 2) adopting flexure bearings for displacer support to achieve a clearance seal with reduced mechanical abrasion and 3) optimization for outgassing with selection of low-outgassing materials and reduction of the glue amount to the permanent magnet fixtures [13]. These modifications can also enhance cooling performance of the JT cooler system because lower temperature at the second cold stage of the 2ST precooler is quite effective to increase a JT cooling power. At latest development phase, the upgraded 2ST cooler was fabricated as Engineering Model (EM) for verification tests. The cross-sectional view is shown in Figure 3 and the design specifications of the upgrade 2ST cooler are summarized in Table 1, respectively.

3.1.1. Cooling performance test

Cooling power of the upgraded 2ST cooler was evaluated by using a single EM unit, which was operated with gas pressure of 1.0 MPa(G) and drive frequency of 15 Hz at room temperature. Cooling power was evaluated with nominal heat inputs of 200 mW at the 2nd cold stage and 1000 mW at the 1st cold stage as shown in Figure 4. Cooling power with maximum power input (90 W) is achieved to 17.6 K with 200 mW at the 2nd cold stage and 96.1 K with 1000 mW at the 1st cold stage, while minimum temperature of 9.6 K at the 2nd cold stage and 67.0 K at the 1st cold stage is obtained without heat load input. It was also confirmed in the thermal vacuum test that nominal cooling power was obtained even at lower limit of the operation temperature of -70 degree Celsius [14].

3.1.2. Mechanical performance test

Mechanical performance test was carried out to confirm that the upgraded 2ST cooler can survive in the

launch vibration environment. The unit of compressor and cold head were separately evaluated for tolerability to pyro shock, random vibration and sine wave vibration. Test conditions was based on the QT (Qualification Test) level the environment-proof design criteria for on-board equipment of Astro-H. Especially for the sine wave test, an appropriate value of test acceleration level according to the FEM (Finite Element Method) structural analysis of the SXS dewar should be used to avoid from overloading to the resonance mechanism in the 2ST cooler. Figure 5 shows the test load levels for (a) pryo shock, (b) random vibration and (c) sine wave vibration. Note that the directions for "STC-Z" and "STH-Z" are parallel to drive-axis of the compressor and the cold head, while the directions for "STC-X,Y" and "STH-X,Y" are perpendicular to drive-axis of the compressor and cold head, respectively. It was confirmed that all test conditions are satisfied with the criteria and no degradation of cooling performance appears after these mechanical performance tests.

3.2. 4K-class ^{4}He Joule-Thomson cooler

The 4K-class Joule Thomson cooler system consists of two linear compressors, three-stage heat exchangers of co-axial tube, a needle valve in bypass line and a 4K cold stage with JT orifice. The 2ST coolers are coupled with the JT closed cycle loop at 20 K / 100 K stages for pre-cooling. Each JT compressor has a pair of suction valve and exhaust valve to provide a helium flow in the JT closed cycle. The lowest operational temperature of the JT cooler is limited by material property of these valves. At the JT orifice with 20- 27 μm in diameter, high pressure gas is expanded isenthalpicly by Joule-Thomson effect. The 4K-class JT cooler was originally developed for the SMILES launched by the H-IIB launch vehicle to the JEM/ISS and had been operated from September 2009 to June 2010 [11]. For the SMILES JT cooler, the linear ball bearings were used for piston support in the JT compressors and the 2ST cooler of Akari type was used as a precooler. For the purpose of higher cooling power and mechanical reliability, the JT compressors had been modified based on the SMILES JT cooler. The piston supporting mechanism is changed from the linear ball bearings to the flexure bearings to reduce mechanical abrasion and the low-outgassing materials are adopted to avoid degradation of cooling performance by the impurities. Furthermore, a "getter" is located upstream of the JT closed cycle loop to trap the impurity molecules. Figure 6 depicts the configuration of the 4K-class JT cooler combined with the two units of 2ST precoolers for the SXS cooling system. The EM of the upgraded JT cooler was fabricated to verify cooling performance and lifetime. The design specifications of the upgraded 4K-class JT cryocooler are summarized in Table 2.

3.2.1. Cooling performance test

Cooling performance of the 4K-class JT cooler was evaluated by using the EM units, which uses two units of the 2ST precoolers similar to the flight configuration. Test result of cooling power at the JT stage is shown in Figure 7. The JT stage temperature is fixed to 4.5 K by adjusting the suction pressure at the lower-stage JT compressor to keep around 124 kPa. Nominal cooling power of 40 mW at 4.5 K is achieved with power input of 54 W for the JT compressors and 50 W × 2 for the two 2ST precoolers. It is expected that cooling powers of 9 mW and 22 mW are required in the nominal operation with LHe and cryogen-free operation in the SXS cooling system, respectively. The gravity effect was also evaluated in this test. Test apparatus can rotate upside down to keep the JT cold stage forward and opposite direction to the gravity. Power consumption of the JT compressors had to be adjusted to keep same cooling power of 50 mW (max) because there appears difference in cold stage temperatures of the 2ST precoolers (Table 3). It is presumed that cooling power at the 2nd cold stage of the 2ST precoolers slightly changes because the neutral position of the displacer is shifted to the gravity direction.

3.2.2. Transient cooling performance test

In the SXS cryogen-free operation, thermal response of the JT cooler along with heat dissipation change

from the ADR units during its recycling is one of technical concerns. By using the JT cooler test model, transient performance along with a heat load profile simulating ADR recycling was evaluated as a preliminary test. Since it is already understood that a suction pressure of the JT closed cycle system is a sensitive parameter to control the JT stage temperature, drive voltage of the low-stage JT compressor (JT-CMP-L) was adjusted manually when the test heat load was increased from 16.3 mW to 36.3 mW to keep the JT stage temperature below 4.5 K. The test profiles of heat load, controlled power of the JT compressors and temperature response on the JT stage are shown in Figure 8. The JT stage temperature is sharply dropped corresponding to the increased power of the JT-CMP-L and kept below 4.5 K during the 800-sec of peak heat load, even though gradually increased. At the end of peak heat load, temperature is increased rapidly because the power of JT-CMP-L is put back to an initial state at that moment. This result indicates that there is possibility for the optimized JT operations to keep the JT stage temperature more stable. The JT cooler operations in the SXS cryogen-free mode is under consideration.

3.2.3. Lifetime test

To verify for lifetime of the 4K-class JT cooler combined with one 2ST precooler, the continuous running test is under operation. The 20K and 100K shields which are connected thermally to the cold stages of the 2ST cooler insulates the heat radiation to the JT stage. The laboratory refrigerator is used for cooling the outer radiation shield, surrounding the 100K shield in order to fix a test environmental temperature. A maximum cooling power of 50 mW at 4.32 K was obtained with a power input of 84 W for JT compressors and 90 W for the 2ST precooler in a preliminary test [15]. The result of the JT lifetime test in progress with accumulated operating time is shown in Figure 9. Heat load on the JT stage is set to 22 mW assumed to be that of in the SXS cryogen-free operation. Note that the heat load on the JT stage had to be reduced temporally to 10 mW from 2250 to 5150 hours due to the increased parasitic heat load for refurbishment of the laboratory refrigerator. Test conditions of temperature on the JT stage and power consumption should be kept as same level for long-term operation. During this period, it is appeared that a temperature at the 1st stage of the 2ST precooler is slightly affected by the environment temperature. Total running time is counted for over 5000 hours as of May 2011. Especially the 2ST precooler had been already running independently for 1968 hours before starting of this test. There is no degradation of cooling power in progress of continuous operation.

4. Conclusions

This paper describes design overview of the Astro-H/SXS cooling system and present development status of the mechanical cryocoolers. The ^{4}He 4K-class JT coolers combined with two units of the 2ST precoolers is used to suppress the parasitic heat load to the LHe tank. Adopting a combinations of the 4K-class JT cooler and the 3rd ADR unit for redundant with the LHe is a remarkable design change for the SXS dewar to replace a ^{3}He 1K-JT cooler. When the LHe is lost, the 4K-class JT cooler and 3rd ADR unit are supposed to be operated instead of the LHe. Another two units 2ST coolers are used to cool down the IVCS and OVCS. Each 2ST cooler is operated with half power (50 W) in nominal case for redundancy. The LHe lifetime with this cooling system is achieved to almost 5 years, according to the current thermal analysis.

Based on heritage of the existing 2ST cooler for Akari and 4K-class JT cooler for SMLIES, modifications of higher cooling performance and reliability had been investigated to develop the upgraded cryocoolers for application to the Astro-H and other future missions. The verification tests for cooling performance, mechanical performance and lifetime were carried out by using the EM cryocoolers.

Nominal cooling power of 200 mW at 20 K for the 2ST cooler and 40 mW at 4.5 K for the JT cooler were demonstrated with temperature and power margin. Result of transient performance test simulating the ADR heat dissipation in the SXS cryogen-free operation suggests that optimized operations of the JT

compressors will control the JT stage temperature along with heat load change. Mechanical performance test for the 2ST cooler units proves a tolerability for pyro shock and vibration environment of the Astro-H criteria. Continuous running of the 4K-class JT cooler combined with one 2ST precooler for lifetime test has just achieved over 5000 hours without any degradation of cooling performance.

Acknowledgements

The authors appreciate deeply all members the SXS/Astro-H project team and the cryogenic group at Niihama division of Sumitomo Heavy Industry, Ltd. for their support to this work.

Reference

[1] Takahashi, T., et al. The ASTRO-H mission. Proc. SPIE 2010; 7732: 7320Z.

[2] Mitsuda, K., et al. The high-resolution x-ray microcalorimeter spectrometer system for the SXS on ASTRO-H. Proc. SPIE 2010; 7732:773211.

[3] Shirron, P.J., et al. Thermal design and performance of a 3-stage ADR for the ASTRO-H Mission. Proc. Space Cryogenics 2011, to be published.

[4] Murakami, H., et al. The infrared astronomical mission AKARI. Publ. Astron. Soc. Japan; 59 (2007), pp. 369-376.

[5] Nakagawa, T., et al. Flight performance of the AKARI cryogenic system. Publ. Astron. Soc. Japan; 59 (2007), pp. 377-387.

[6] Hirabayashi, M., Thermal design and its on-orbit performance of the AKARI cryostat. Cryogenics, vol. 48 (2008), pp. 189-197.

[7] Seta, M., et al. Submillimeter-Wave SIS Receiver System for JEM/SMILES. Advances in Space Research, vol. 26, Issue 6 (2000), pp. 1021-1024.

[8] Narasaki, K., Development of cryogenic system for SMILES. Advances in Cryogenic Engineering, Vol. 49B (2004), Plenum Press; pp. 1785-1794.

[9] Nakagawa, T., et al. The next-generation space infrared astronomy mission SPICA. SPIE 2010; 7731: 77310O.

[10] Fujimoto, R., et al. Cooling system for the Soft X-ray Spectrometer onboard Astro-H. Cryogenics 2010;50 488-493.

[11] Narasaki, K., et al. Lifetime Test and Heritage on Orbit of Coolers for Space Use. Proc. Space Cryogenics 2011, to be published.

[12] Narasaki, K., Development of Two-Stage Stirling Cryocooler for ASTRO-F. Advances in Cryogenic Engineering: Transactions of the Cryogenic Engineering Conference – CEC, vol. 49 (2004), pp. 1428-1435.

[13] Sato, Y., et al. Development of Advanced Two-stage Stirling Cryocooler for Next Space Missions. Cryocooler Vol. 15(2008), pp.13-21

[14] Sato, Y., et al. Development of mechanical cryocoolers for Astro-H/SXS. Cryogenics 2010;50 500–506.

[15] Shinozaki K, et al. Developments of 1-4K class space mechanical coolers for new generation satellite missions in JAXA. Cryocoolers 16(2009)

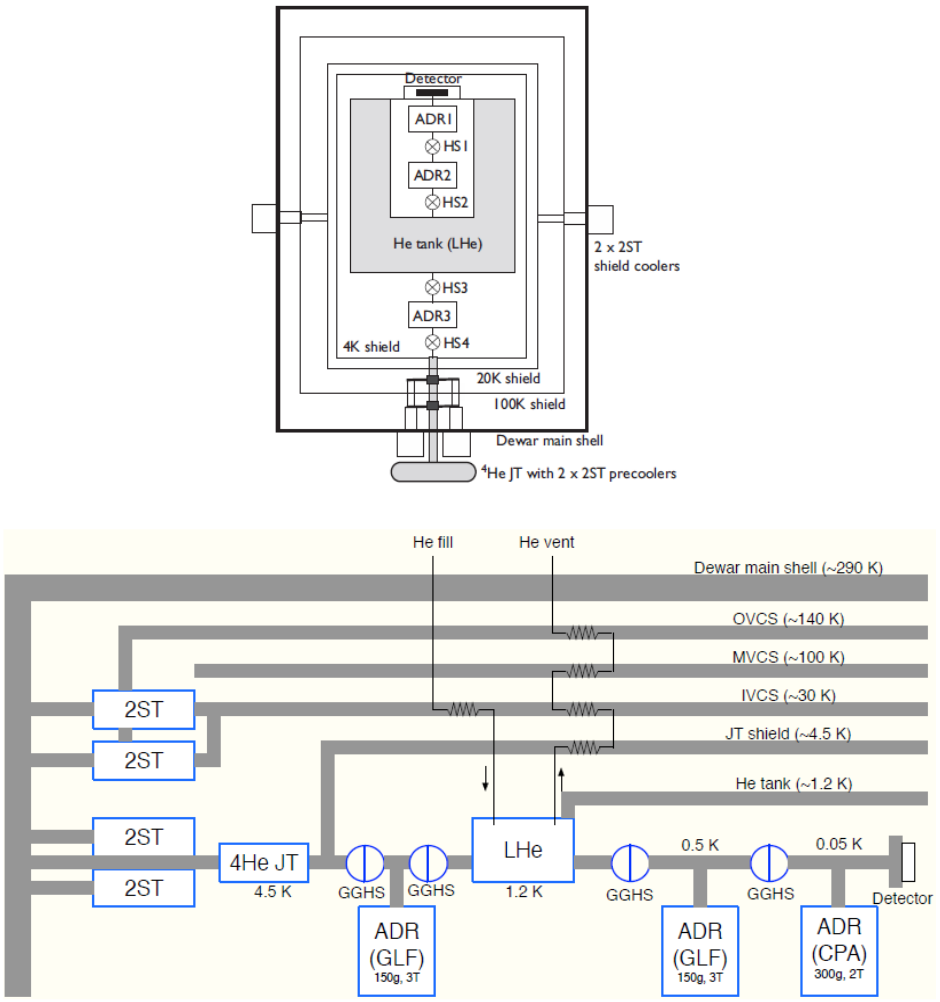

Figure 1 Schematics for design concept of the ASTRO-H/SXS cooling system

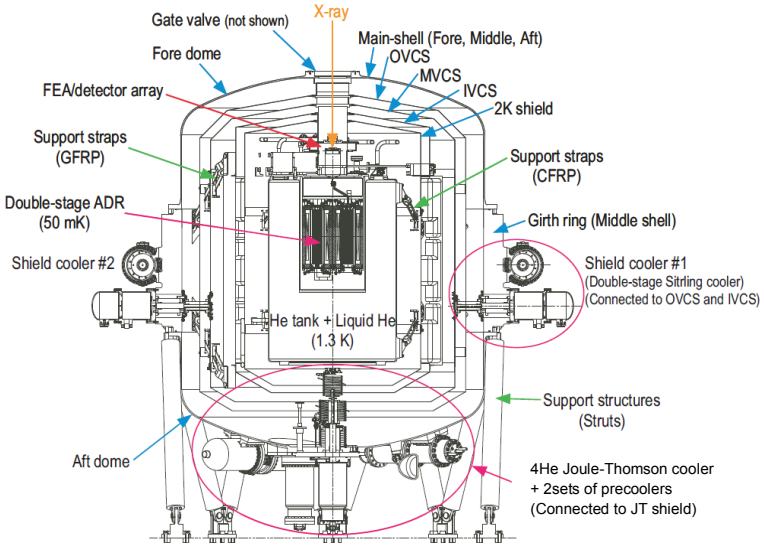

Figure 2 Cross-sectional view of the ASTRO-H/SXS dewar

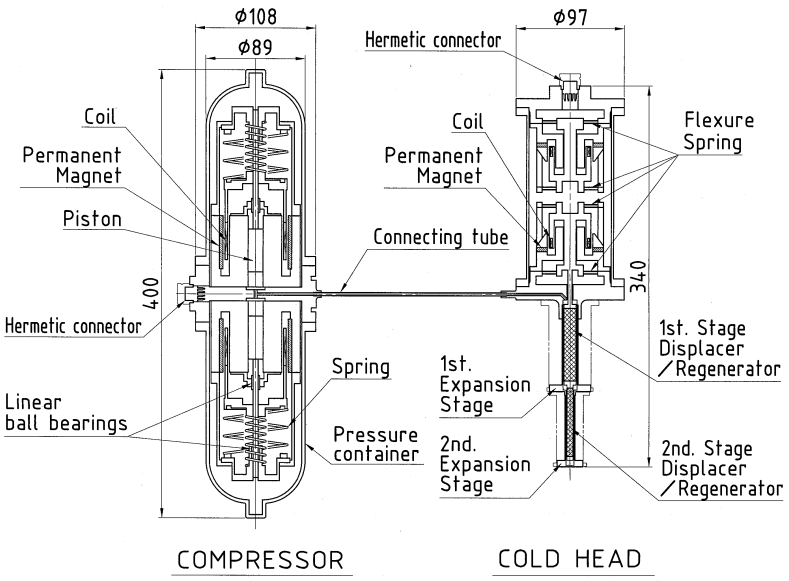

Figure 3 Cross-sectional view of the upgraded 2ST cooler

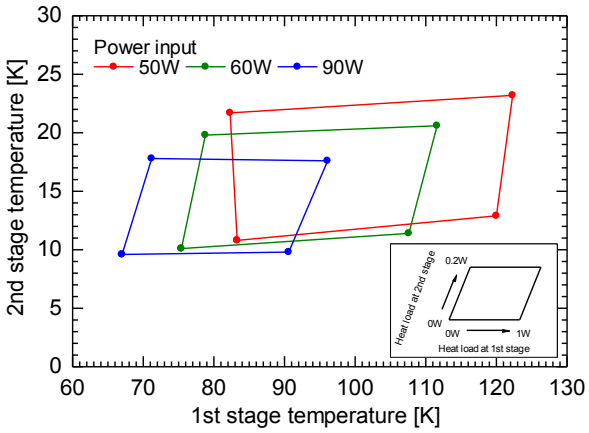

Figure 4 Cooling power diagram of the 2ST cooler.

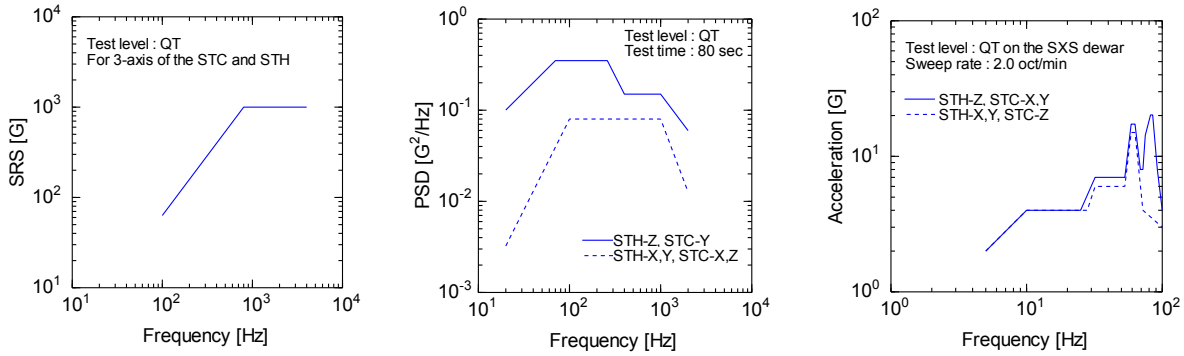

(a) Pyro shock (b) Random vibration (C) Sine wave vibration

Figure 5 Test load level of mechanical performance test for the 2ST cooler

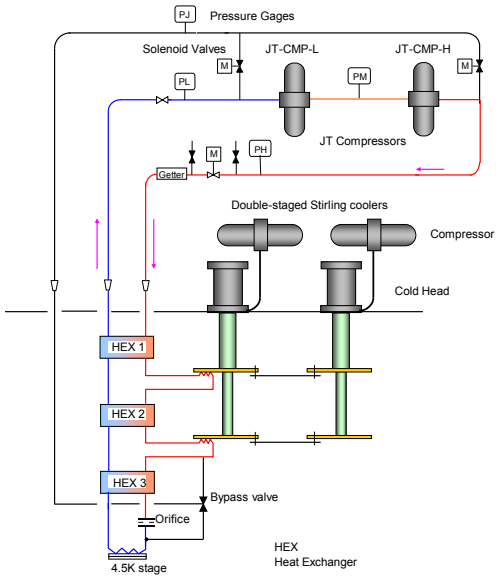

Figure 6 Configuration of the 4K-class JT cooler with two units of 2ST precoolers for Astro-H/SXS

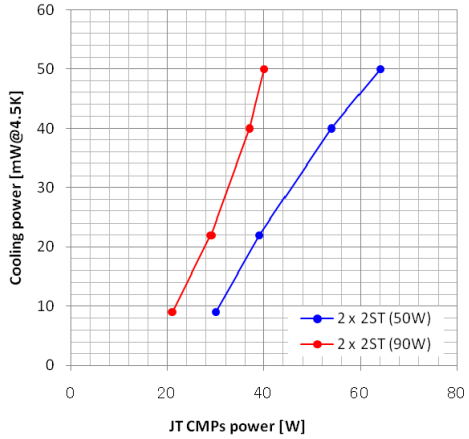

Figure 7 Cooling power at the 4K-class JT cooler with two units of 2ST precoolers

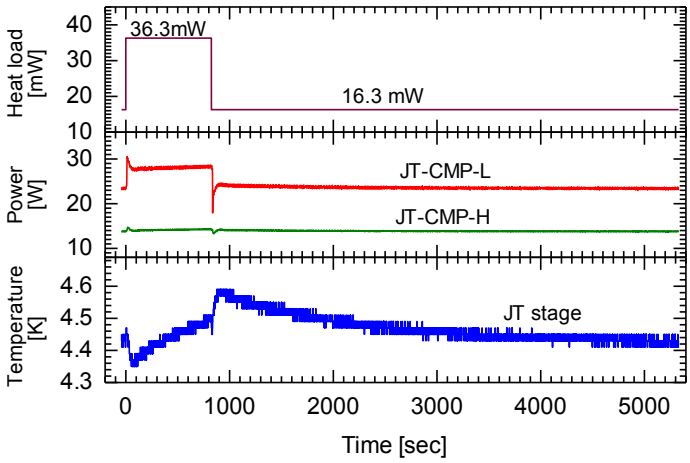

Figure 8 Test profile for transient performance of the 4K-class JT cooler

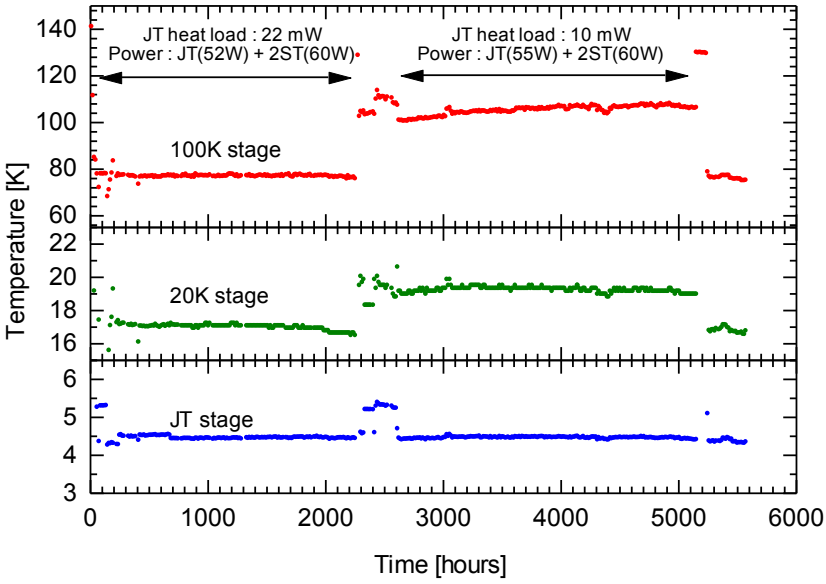

Figure 9 Result of lifetime test for the 4K-class JT cooler

Table 1 Design specifications of the upgraded 2ST cooler

Items	Specifications
Cooling power	200 mW at 20 K 1000 mW at 100 K
Life time	Requirement: 3 years Goal: 5 years
Power consumption	90 W
Environment temperature	-70～30 °C
Drive frequency	15 Hz
Mass	9.5 kg
Working gas	^{4}He
Gas pressure	1.0 MPa(G)

Table 2 Design specifications of the upgraded 4K-class JT cooler

Items	Specifications
Cooling power	40 mW at 4.5 K
Life time	Requirement: 3 years Goal: 5 years
Power	90 W
Environment temperature	0～30 °C
Drive frequency	52 Hz
Working gas	^{4}He
Gas pressure	Supply > 2.0 MPa Return < 100 kPa

Table 3 Result of upside down test for cooling performance of the 4K-class JT cooler

		Nominal	Upside down
Heat load on the JT stage		50 mW	50 mW
Temperature on the JT stage		4.5 K	4.5 K
Power consumption	2ST precoolers	50 W × 2	50 W × 2
	JT compressors	64 W	73 W
1st stage of 2ST precoolers		103 K / 104 K	102 K / 102 K
2nd stage of 2ST precoolers		18.2 K / 18.6 K	18.5 K / 19.0 K

Thermal Design and Predicted Performance of the 3-stage ADR for the Soft-X-ray Spectrometer Instrument on Astro-H

Peter J Shirron[1], Mark O Kimball[1], Bryan James[1], Donald Wegel[1], Raul Martinez[2], Dick Faulkner[3], Larry Neubauer[3], Marcelino Sansebastian[3]

[1]*Cryogenics and Fluids Group, NASA/Goddard Space Flight Center, Greenbelt, MD 20771*
[2]*Ball Aerospace & Technologies Corp., 7404 Executive Place, Suite 100, Lanham, Md 20706*
[3]*SGT, Inc., 7701 Greenbelt Road, Suite 400, Greenbelt, Maryland 20770*

ABSTRACT

The Japanese Astro-H mission will include the Soft X-ray Spectrometer (SXS) instrument provided by NASA/GSFC. The SXS will perform imaging spectroscopy in the soft x-ray band using a 6x6 array of silicon microcalorimeters operated at 50 mK. The detectors will be cooled by a 3-stage adiabatic demagnetization refrigerator (ADR). The configuration allows the ADR to operate with both a 1.3 K superfluid helium bath and a 4.5 K cryocooler as its heat sink. Initially, when liquid helium is present, the two coldest stages of the ADR will operate in a single-shot mode to cool the detectors from 1.3 K. During this phase of the mission, the 3rd stage may be used to reduce the net heat load on the liquid helium and extend its lifetime. When the liquid is depleted, the 2nd and 3rd stages will operate in a continuous mode to maintain the helium tank at about 1.3 K, allowing continued operation of the 1st stage (in a single-shot mode) and hence the SXS instrument. This paper describes the design and operating modes of the ADR, as well as details of critical components.

INTRODUCTION

The SXS instrument[1] on Astro-H contains a 6x6 array of silicon microcalorimeters read out by JFET amplifiers. The detectors are essentially the same as those flown on Astro-E2[2], except that some improvements in absorber fabrication and attachment have reduced the heat capacity and improved linearity. The latter allows the detectors to be operated over a wider dynamic range, which is partly achieved by cooling them to lower temperature: 50 mK, compared to 60 mK for Astro-E2. As a result, the Astro-H detectors will have improved energy resolution of 3-4 eV over the 200 eV to 6 keV band.

The detectors will be cooled by a multi-stage adiabatic demagnetization refrigerator (ADR), built by NASA/Goddard Space Flight Center, which interfaces to a hybrid cryogenic system, provided by the Japanese Aerospace Exploration Agency (JAXA). The JAXA cooler[3] consists of a 30 liter superfluid helium tank and a 4.5 K Joule-Thomson (JT) cooler. After launch, the JT is used to extend the lifetime of the helium by absorbing the majority of its parasitic heat loads. In this mode, the ADR uses the helium, at 1.3 K or lower, as its heat sink. After the liquid is depleted, the JT, operating at 4.5 K, becomes the ADR's heat sink. The redundancy achieved by this configuration enables the mission to achieve its science goals with loss of either the liquid helium or the JT cooler. The ADR's performance requirements are listed in Table 1.

Table 1. Performance requirements for the SXS ADR for liquid helium- and JT-based operation.

	With Liquid Helium	Cryogen-Free
Heat sink temperature	1.3 K	4.5 K
Operating temperture	0.05 K	0.05 K
Hold time	24 hours	24 hours
Recycle time	1 hour	2 hour
Detector heat load	0.25 μW	0.50 μW
Heat load on heat sink	< 0.2 mW (time average)	Peak heat flux within available cooling power of JT cooler (3-20 mW)
Stability of detector assembly	<1 mK over 10 min	<1 mK over 10 min
Failure tolerance	Failure of JT cooler Failure of shield cooler	Failure of shield cooler
Mass	<15 kg	
Volume envelope (2-stage ADR)	304 cm long x 17 cm diameter	
Magnetic field near detectors	< 10 mT	

The ADR will operate most efficiently (i.e. with the longest hold time) with liquid helium, whose lifetime is predicted to exceed 4 years. The 4+ year helium lifetime assumes only the JT cooler is operational, but the design of the ADR is such that its 3rd stage can be used to reduce the time average heat load on the liquid to less than zero. This actually cannot extend the lifetime indefinitely – because there will always be some flow out the porous plug vent system – but it is possible to extend the lifetime significantly, to 8 years or longer. When the cryogen is depleted, the ADR can continue to support science operations as long as the JT cooler is functional.

Because of the complexity of the cryogenic system, the Astro-H/SXS program includes the production of an engineering model (EM) instrument (detector assembly, ADR, helium dewar and cryocoolers) before building the flight model (FM) hardware. The EM ADR has recently been completed and is currently being integrated with the detector assembly for comprehensive performance testing. This follows extensive modeling of both on-orbit modes (cryogen-based and cryogen-free operation), and extensive component and sub-assembly level testing. This paper focuses on the design and expected performance of the ADR. A companion paper presents results of the first, recent tests of the ADR as a 3-stage unit.

3-STAGE ADR CONFIGURATION

The SXS ADR, shown schematically with the SXS cryogenic system in Figure 1, was originally designed[4] as a 2-stage unit that would operate with the superfluid helium or with a 1.8 K JT cooler. This was determined to be the most mass-efficient option for a 1.8 K heat sink. The recent switch to a 4.5 K JT cooler required the addition of a 3rd stage to span the larger temperature gap.

While it is possible for a 2-stage ADR to reach 50 mK from a 4.5 K heat sink, 3 stages are needed to meet all SXS cooling requirements. In particular, the detector assembly, from which the 50 mK stage is suspended, requires a stable base temperature in order to achieve low detector noise. Fluctuations in the detector assembly temperature can cause gain variations in the detectors. On long time scales (>10 min), gain can be tracked by an internal calibration scheme, but on shorter time scales the electronics cannot

compensate for temperature drifts, and the uncertainty in the energy scale is equivalent to noise. A stability requirement of <1 mK in any 10 minute period is derived from the detector noise budget.

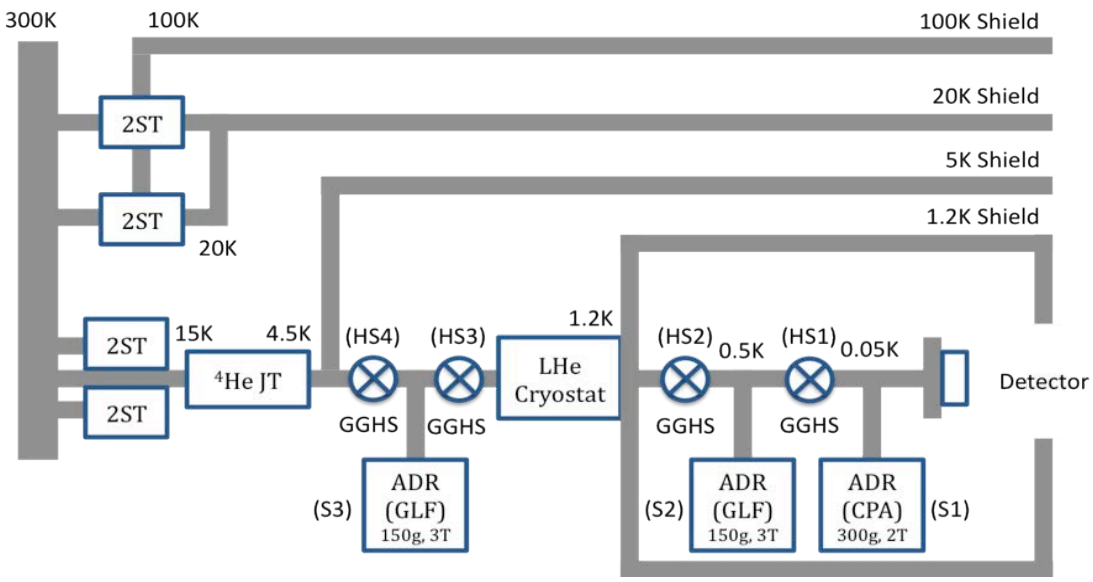

Figure 1. Thermal schematic of the Astro-H/SXS cryogenic system.

The detector assembly is thermally anchored to the helium tank. When cryogen is present, its high heat capacity passively provides a very stable temperature. In cryogen-free operation, the 3rd stage works to pump heat from the helium tank to the JT cooler. The cyclic nature of this cooling would produce significant temperature excursions given the relatively low heat capacity of the helium tank. To damp out these fluctuations, the heat switch (HS2) between the 2nd stage and the helium tank is turned on continuously, and stage 2 provides active temperature control using a thermometer at the base of the detector assembly. The 2nd and 3rd stages effectively become a 2-stage continuous ADR – cooling the helium tank to 1.3 K or lower – while the 1st stage works independently as a single-stage, single-shot cooler.

The location, and mechanical and thermal attachment of the 3rd stage within the existing design was driven several considerations. Foremost was pre-existing volume constraints, but it was also seen as vital that the ADR maintain a single mechanical interface to the dewar in order to simplify the US/Japanese interfaces and the integration of hardware into the dewar. This required the 3rd stage to be mounted on the top side of Calorimeter Spectrometer Insert (CSI) mounting plate that carries the detector assembly and the 2-stage ADR.

Thermally it is very advantageous to anchor the 3rd stage to the JT cooler. Hysteresis heat from the magnets and magnetic shields accounts for typically 1/2 of the total heat rejected by an ADR. Anchoring the 3rd stage to the helium tank would burden it with pumping its own hysteresis heat to the JT, using a significant fraction of its cooling power in the process, and limiting the base temperature it could provide. Instead, the stage is physically mounted to the helium tank by means of a low thermal conductance support, and thermally tied to the JT. The trade-off is the introduction of an ~50 μW parasitic heat leak to the helium tank in addition to the ~50 μW heat switch load.

This extra heat load can be more than offset by using the 3rd stage to transfer heat periodically from the helium tank to the JT. In this sense it is a neutral to beneficial addition. However, the cryogenic system

must be tolerant of a JT failure, in which case the boundary temperature is estimated to be 10 K. In this case, the 3rd stage cannot be operated and its presence imposes in NN μW load to the helium, and reduces its lifetime from >4 years to ~2 years.

3-STAGE ADR DESIGN

In terms of the mechanical and thermal design, the 1st and 2nd stages are largely unchanged from the original concept described in [4], and they are still configured as a 2-stage unit that is inserted into a well in the helium tank. The most notable change was the addition of structural support for heat switches HS1 and HS2, which are described in more detail below.

The 3rd stage is nearly identical to the 2nd stage, and is located on the top side of the plate that carries the detector assembly. Its heat switches thermally connect the salt pill to the helium tank and to the JT cooler. The 3rd stage assembly (salt pill, magnet, magnetic shield and suspension assemblies) is cantilevered off the mounting plate by means of a composite thrust tube. The tube is made from gamma alumina[5] pre-impregnated with resin as uniaxial fiber. The EM version uses 3 layers oriented at +30°, 0°, and -30° to the symmetry axis. The tube is slightly conic (10°) to increase strength against buckling. Pull tests were done in the lateral directions to greater than 900 N, to give confidence that the tube could support the ~3.5 kg mass under 20g accelerations.

Two views of the SXS ADR are presented in Figure 2.

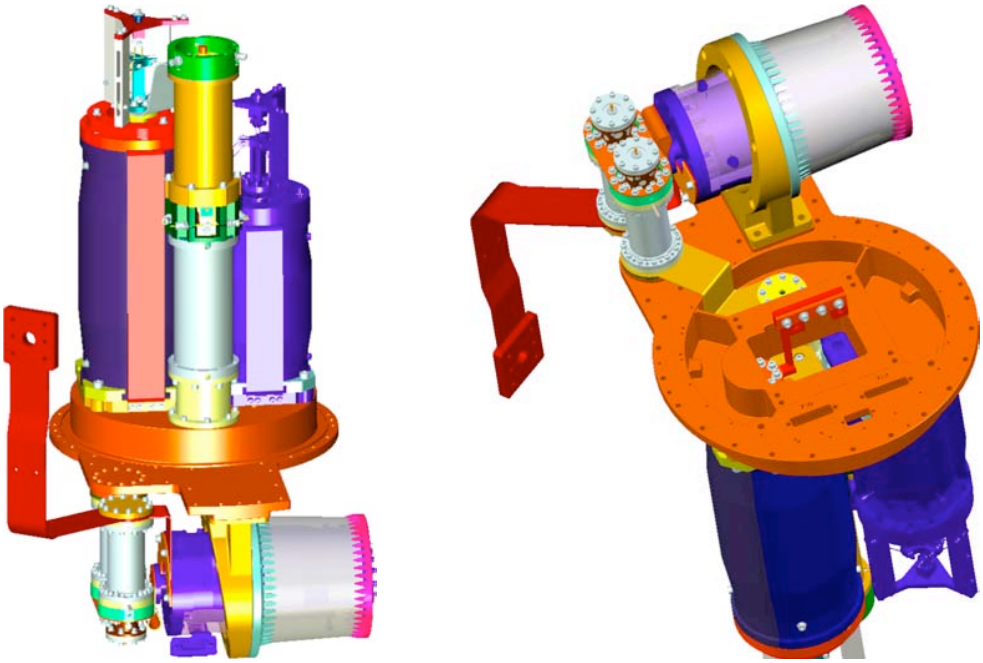

Figure 2. The Astro-H/SXS ADR is built as two separate units that are thermally connected by the CSI plate that mounts to the helium tank.

Table 2 presents a summary of the 3-stage ADR design and selected operating parameters. All 4 heat switches are active gas-gap, and are charged at room temperature with ^{3}He gas at 0.5 atmosphere. Their getters are made of bituminous charcoal, and only need to be heated to 8-9 K to achieve full conduction. The getters are very low mass (less than 5 grams) and are supported by a re-entrant tube of Ti15333.

They require less than 300 μW of input power to reach 8 K, and the switches turn on and off in less than 1 minute.

The ADR includes a number of thermal straps to provide efficient heat flow within the 2-stage ADR and to the helium tank; between the helium tank, 3rd stage and JT cooler; between the 3rd stage magnet/shield and the JT cooler; and between the 1st and 2nd stage magnets to the helium tank. The most critical straps are those that conduct heat between ADR stages; the magnet straps prevent excessive warming of the magnets and shields during lengthy (de)magnetizing periods. The straps need to be very flexible, so they are made of multiple layers of copper foil (0.125 mm) diffusion bonded at their ends.

Table N. 3-stage ADR design summary.

	Stage 1	Stage 2	Stage 3
Salt	CPA	GLF	GLF
Salt mass	270 g	150 g	150 g
Magnetic field	2 T	3 T	3 T
Magnet current	2 A	2 A	2 A
Hold temperature	*47 mK	0.5 K	1.1 K
Demagnetization temperature	0.8 K	1.3 K	4.7 K
Stage mass	6.0 kg	4.0 kg	4.0 kg
Total ADR mass	14.0 kg		

*Temperature reflects estimated 3 mK gradient between detectors and ADR stage.

Kevlar Suspension Assemblies

The most significant development effort for the SXS ADR has been the Kevlar suspensions systems that physically support the salt pills and the HS1/HS2 stack. All use bundles of unbraided Kevlar 49 put under tension by springs or spring washers that can be adjusted to give precise preloads. In each case, the Kevlar is loaded to no more than 40% of its ultimate strength to eliminate the possibility of stress rupture.

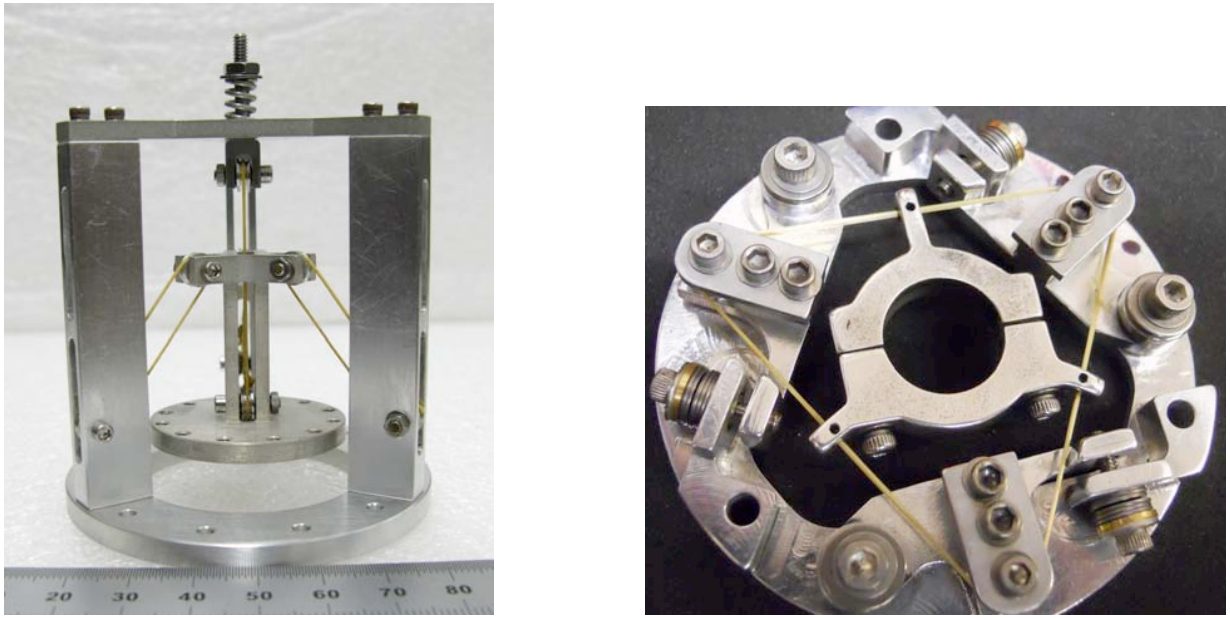

Figure 3. “Gimbal” and “lateral” suspension assemblies used to mechanically support the ADR’s salt pills.

Two Kevlar suspension assemblies, in Figure 3, are used to support the salt pills. Each is built as a stand-alone unit and then integrated with the salt pills. The "gimbal" assembly has an axial loop of 16x195 denier, with 3 counterbalancing loops of 8x195 denier at 45° to the axis. In this arrangement, all 4 loops are under the same tension, 312 N (70 lbs). This assembly is stiff in the axial direction and two lateral directions. It is relatively compliant in rotation. The "lateral" assembly uses a single loop of 8x195 denier tensioned to 178 N (40 lbs) by 3 spring-loaded arms. The central "star" has three arms that are bonded to the Kevlar with Stycast 2850 FT epoxy, and is clamped to the salt pill. This assembly is stiff in rotation and two lateral directions, but is relatively compliant in the axial direction. Consequently, the two assemblies do not over-constrain the salt pill, and the overall design is kinematic.

As seen in Figure 4 (and in the full assembly in Figure 5), the heat switches are surrounded by titanium tubes with interconnecting Kevlar suspensions. The Kevlar only needs to provide lateral support since the heat switches are very rigid along their axis and in rotation. The mid-point suspension uses 8x195 denier unbraided Kevlar 49, in three separate sections. At the ends of each section, the Kevlar is bonded into a hollow screw with Stycast 2850 FT epoxy after threading on Belleville spring washers. The Kevlar is wrapped around a bobbin attached to the thermal connection between HS1 and HS2. Once the screws are symmetrically spaced about the bobbin, the bobbin is tightened. As the Kevlar is loaded, friction prevents any slippage. With the ability to adjust tension from both sides, the Kevlar can be tensioned, to 107 N (24 lbs) without putting any side load on the heat switches. This is a critical aspect of the design since the heat switches can thermally short with displacements of as little as 0.3 mm.

The top assembly uses 4x195 denier unbraided Kevlar since the mass it supports is considerably less. Three loops are interleaved around a central pin that bolts to the free end of HS1. The Kevlar is fixed to screws in the same manner as for the mid-point suspension. Again, the Kevlar can be tensioned, to 107 N, without imparting side loads.

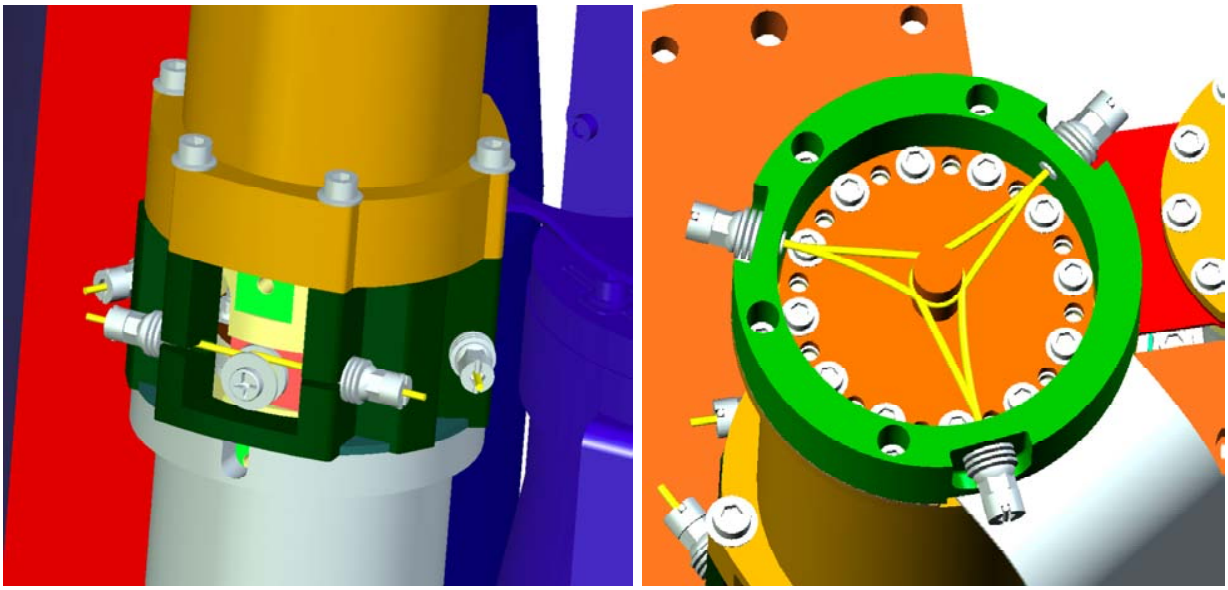

Figure 4. Kevlar suspension for the mid-point (left) and top (right) of the HS1/HS2 heat switch stack.

3-STAGE EM ADR

The complete EM ADR is shown in Figure 5. The total mass of the assembly is 14.5 kg. The two individual assemblies have undergone vibration testing at room temperature to qualify the design to 20 g sine sweeps (5-100 Hz) and random inputs (5-2000 Hz), with notching near resonant frequencies, all of which are above 140 Hz. The EM ADR, after integration with the detector assembly, will undergo cold vibration testing (at 77 K) in a specially designed vibration dewar. This is expected to occur in mid-June, 2011.

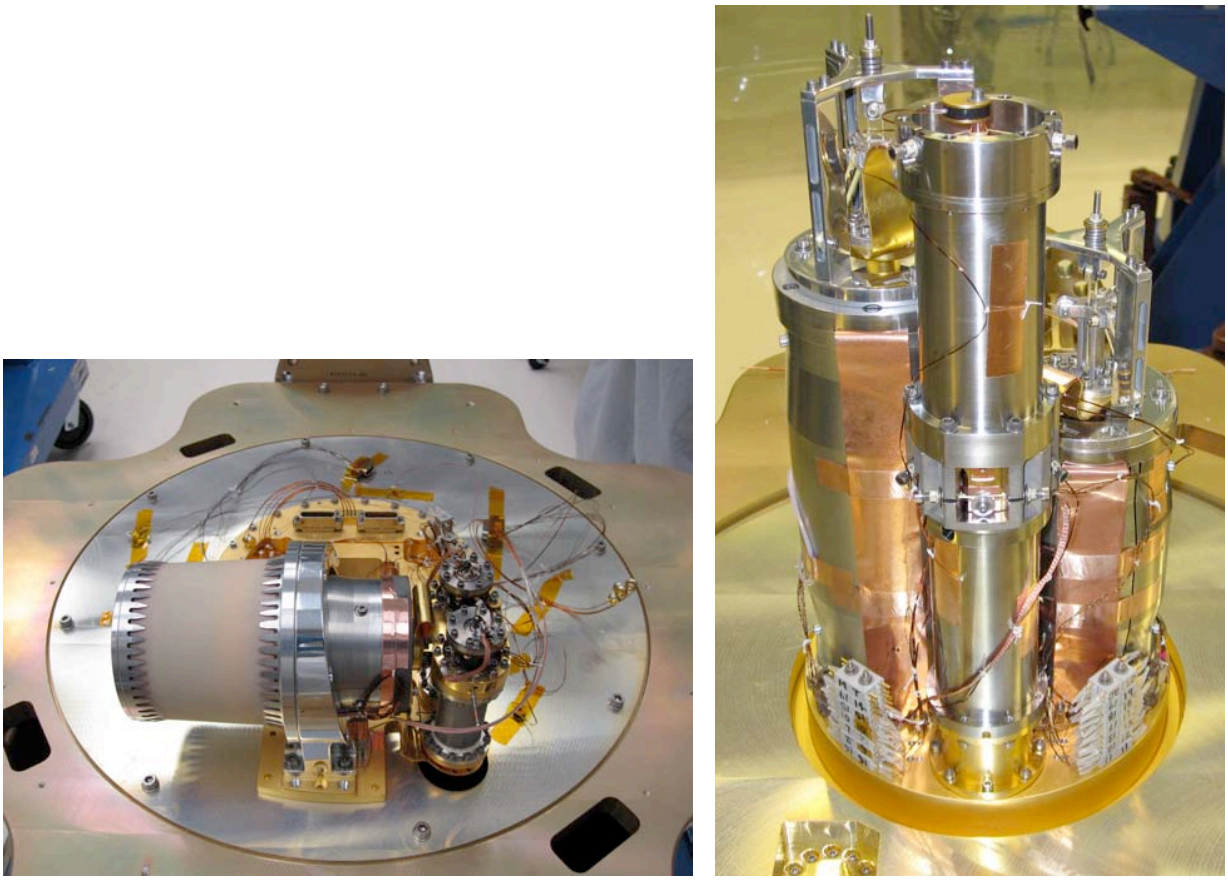

Figure 5. The 3rd stage (left) and 2-stage ADR (right) are shown just prior to performance testing. The two assemblies are mounted on opposite sides of the CSI plate.

3-STAGE ADR OPERATION AND PERFORMANCE

While the operation of each ADR stage is essentially the same whether liquid helium is present or not, the sequencing of recycling activities is quite different.

On-Orbit with Liquid Helium

When liquid helium is present, the 2-stage ADR operates independently, using the helium as its heat sink. The operating sequence is as follows. During the hold time, stage 1 holds the detectors at 50 mK and stage 2 is held at 0.5 K. When stage 1's cooling capacity is exhausted, both stages are magnetized to ~0.8

K. Heat is transferred from the 1st (at 0.8 K) to 2nd stage (at 0.72 K) through HS1. When stage 2 is fully charged (i.e. at 2 amps), HS1 is opened, and stage 2 is magnetized to ~1.5 K. Stage 2 then transfers heat to the helium tank (at <1.3 K) through HS2. When stage 2 is fully charged, HS2 is opened, then both stages are demagnetized to their hold temperatures and detector operation resumes. As modeled, the process takes less than the 1 hour requirement, allowing some time for temperatures within the detector assembly to stabilize before starting science data collection. Temperatures and magnet currents of the 1st and 2nd stages are shown in Figure 6.

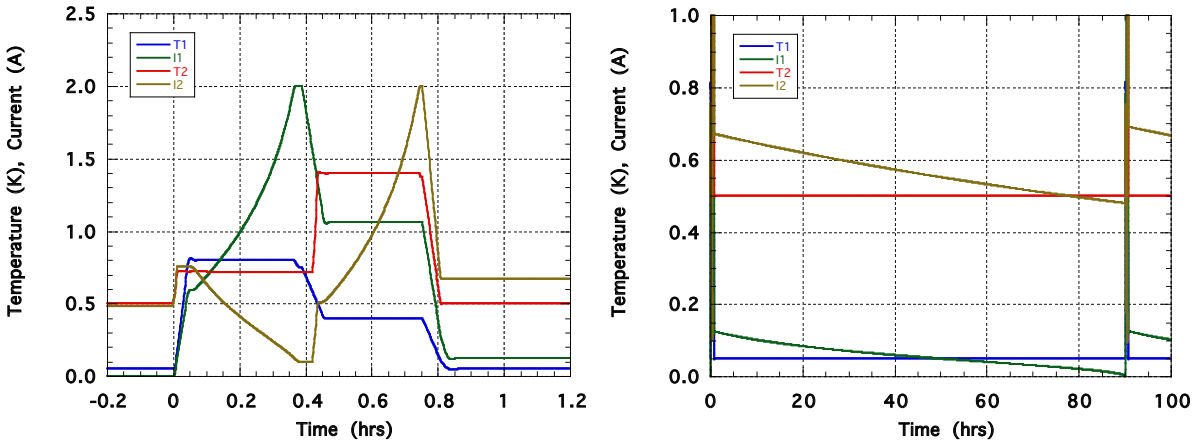

Figure 6. Currents and temperature in the 2-stage ADR during operation with liquid helium. (a) shows the recycling operation started when stage 1 runs out of current; (b) shows conditions during the subsequent hold time of ~90 hours.

All heat generated by the ADR during recycling is absorbed by the liquid helium. Three sources of heat (direct heat rejected from the 2nd stage salt pill, hysteresis heating of the magnets, and heat used to power the heat switch getters) contribute roughly equally to the total heat output, which is estimated to be approximately 11.5 J per cycle.

The hold time of the 1st stage is predicted to be about 90 hours. This follows from a measured cooling capacity of 0.13 J at 50 mK and an estimated detector heat load of 0.27 μW and parasitic loads totaling 0.15 μW. Given a total heat rejection of 11.5 J per cycle, this would impose a time average heat load of only 33 μW on the liquid helium. In the worst case, if the ADR only meets the 24-hour hold time requirement, the time average load rises to 126 μW.

At present, there is no planned use of the 3rd stage when liquid helium is present. However, it can be cycled to produce a significant reduction in the helium vent rate. The 3rd stage has demonstrated a time average heat lift in excess of 0.7 mW, cooling at 1.3 K from a ~4.3 K heat sink. This cooling power exceeds the nominal heat load on the helium tank of 0.71 mW. For the results shown in Figure 6, the helium tank temperature was assumed to be constant at 1.3 K. If the 3rd stage were used, the temperature would gradually reduce, as would the heat loads on the ADR. Figure 7 shows the cooling rate that can be achieved assuming the tank is full (30 liters of liquid).

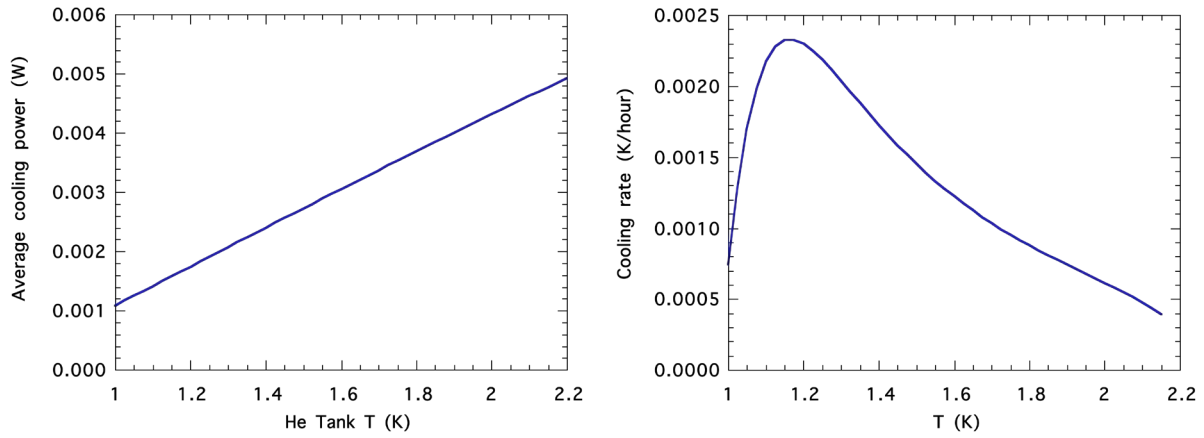

Figure 7. Gross cooling power of the 3rd stage as a function of temperature, and the cooling rate it can achieve when the helium tank contains 30 liters of liquid and its parasitic heat load is 0.71 mW.

On-Orbit Cryogen-Free Operation

When the liquid helium is depleted, ADR control is modified to operate the 2nd and 3rd stages as a continuous ADR to produce stable helium tank temperatures of 1.2-1.3 K. The 1st stage then operates independently as a single-stage ADR to cool the detectors to 50 mK. In practice, the 3rd stage must have a time average heat lift in excess of the total load on the helium, so that it can slowly build up the cooling capacity of the 2nd stage. This is used when it is necessary to recycle the first stage. This operation is shown in Figure 8. The accumulated cooling capacity of the second stage is seen as a slow increase in its magnet current superimposed on a sawtooth shape resulting from repetitive charging (as stage 3 abdsorbs heat) and discharging (as it absorbs heat while stage 3 is warm).

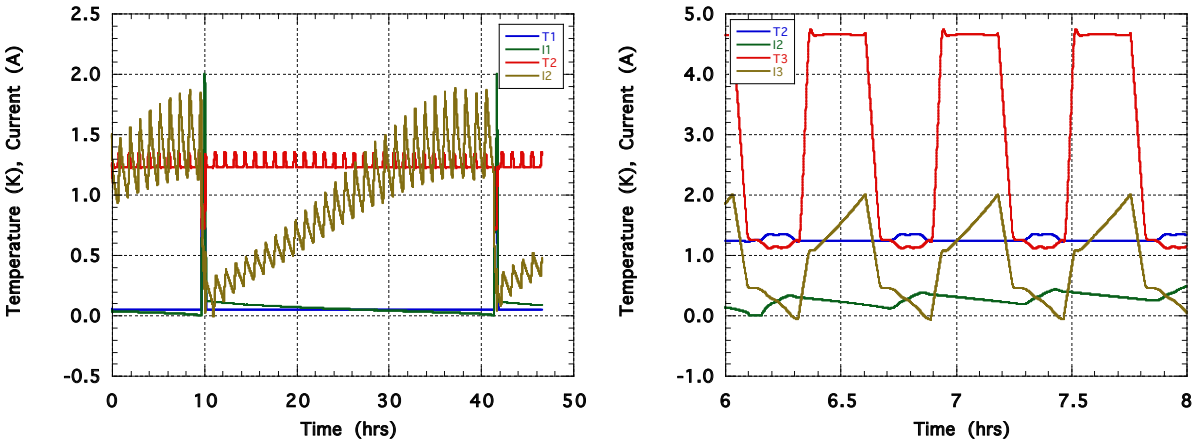

Figure 8. Currents and temperatures in the 3-stage ADR during cryogen-free operation. (a) shows the hold time of stage 1 and periodic recycling; (b) shows the cycling of the 3rd stage and interaction with the 2nd stage that results in constant tank temperature.

Since the helium tank does not need to be stable in temperature during the recycling of stage 1, the process allows the 2nd stage to decouple from the tank during this period and recycle the 1st stage at the same (or lower) temperature as for operation with liquid helium (0.8 K). Since the 2nd stage will be considerably warmer during the subsequent hold time, and the parasitic heat load through HS1 will be about 1 μW instead of 0.1 μW, it is very important to demagnetize the 1st stage from the lowest possible temperature. If demagnetized from 0.8 K, the hold time at 50 mK is predicted to be 32 hours.

For the model results shown, the 3rd stage works to maintain the helium tank at 1.25 K, assuming a constant heat load of 0.71 mW. The temperature is a selectable parameter for the ADR control system, and will be chosen in orbit based on the prevailing heat load. Figure N gives the cooling power of the 3rd stage as a function of tank temperature. The tank setpoint temperature will be chosen so that the excess cooling power of the 3rd stage is sufficient to build up the cooling capacity of the 2nd stage in time for each successive recycling of the 1st stage.

For the nominal tank load of 0.71 mW, the limiting tank temperature is about 1.10 K. In various failure modes, where the tank load rises and/or the available cooling power of the JT cooler is reduced, the tank setpoint temperature will have to be raised. However, in all modeled failure cases, temperatures less than 1.5 K can be maintained. The primary impact of raising the temperature is to raise the parasitic load on the ADR's 1st stage, and to decrease its hold time.

SUMMARY

The Astro-H/SXS ADR has the challenging requirement to operate with a redundant cryogenic system that consists of a 30 liter superfluid helium dewar (at 1.3 K) and a 4.5 K Joule-Thomson cryocooler. A 3-stage ADR has been designed to meet the cooling requirements of the SXS detectors, including a requirement for the temperature stability of the detector assembly's outer housing. The ADR is very efficient, achieving a predicted hold time of 90 hours when operating with liquid helium, and 32 hours when operating in cryogen-free mode. The lifetime of the liquid helium is predicted to exceed 4 years, although this can be significantly lengthened by the operation of the ADR. After the liquid is depleted, the SXS instrument can continue to operate as long as the JT cooler functions.

REFERENCES

[1] Mitsuda K, et al., "The X-Ray Microcalorimeter on the NeXT Mission", Proc. SPIE vol. **7011**, 701102K-1 (2008).
[2] Kelley RL, et al., "The Suzaku High Resolution X-Ray Spectrometer," *Publ. Astron. Soc. Japan* **59**, S77-112 (2007).
[3] Fujimoto R, et al., "Cooling system for the Soft X-ray Spectrometer (SXS) onboard ASTRO-H", Proc. SPIE vol. **7732** (2010).
[4] Shirron PJ, Kimball MO, Wegel DC and Miller F, "ADR design for the Soft X-ray Spectrometer instrument on the Astro-H mission", *Cryogenics* **50**, 494-499 (2010).
[5] Gamma alumina composite is produced with gamma alumina fiber produced by Sumitomo Chemical Co., Osaka, Japan, and TC-250 resin produced by TenCate Advanced Composites, Inc., 18410 Butterfield Blvd., Morgan Hill, CA 95037

Vibroacoustic Testing of Broad Area Cooling Panels

James W. Smith, ER24, Huntsville, AL
Jessica J. Wood, ER24/Yetispace, Huntsville, AL
Andrew R. Schnell, ER24, Huntsville, AL

National Aeronautics and Space Administration
Marshall Space Flight Center

1.0 EXECUTIVE SUMMARY

The development of active cryogenic storage systems that reduce or eliminate propellant boil off is required to attain NASA strategic goals for orbital propellant depots, Mars missions, and long-duration lunar missions. Broad area cooling (BAC) shields are a type of active cryogenic storage system that has been identified as a technology that could meet this need. Recent thermal design studies[1] indicate that this thermal shielding technique can be implemented to absorb orbital radiation, thereby reducing boil off to zero or near zero; however, structural aspects of this approach have not yet been addressed. The primary technical objective of this effort is to evaluate candidate BAC shield design concepts by performing acoustic testing representative of vibrational loads observed on spacecraft during launch.

Acoustic tests were performed on representative BAC shield test articles over the course of six weeks at the NASA Marshall Space Flight Center (MSFC) vibroacoustic test facility in building 4219. Fifty-eight tests were conducted, each varying some element of acoustic load level, test article attachment, test article construction, test article materials, multilayer insulation (MLI) layers, or IM7 offset and presence (where IM7 refers to the carbon fiber panels used to represent launch vehicle fairings). Data were collected from accelerometers attached to the test article frame, and visual inspections were performed after each test with written and photographic descriptions recording these inspections. The test articles generally survived the tests with no major damage, although several small tears and creases were observed in some test articles.

2.0 INTRODUCTION

2.1 Background

Active cryogenic storage systems that reduce or eliminate propellant boil off are an enabling technology for orbital depots, Mars missions, and long-duration lunar missions because they make extended-duration in-flight cryogenic storage more weight efficient. In a study of Earth departure stages for lunar missions, active cryogenic fluid management systems using BAC shields for hydrogen storage were recently shown to be more weight efficient than passive systems after 95 days in low-Earth orbit. The long transit times to and from Mars (up to 18 months) will make low-boil-off designs critical for planetary capture and descent vehicles.[1,2,3] Orbital cryogenic propulsion systems that can minimize boil off will become a viable option for missions to Mars and the lunar surface with a stay of six months or more. Operational flexibility will also increase by allowing longer loiter times in Earth orbit before departure to either destination.

Zero-boil-off passive cryogen storage systems are feasible in the relatively near term for methane/oxygen propulsion concepts. However, hydrogen/oxygen propulsion systems are limited to only reduced boil-off concepts until a working cryocooler operating in the 20 K range is available. The proposed BAC concept consists of MLI sandwiched between an additional thin metal layer. This layer is bonded to a network of metal tubes containing a circulating fluid such as helium. This shield intercepts thermal energy. A typical BAC flow schematic for a cryogenic hydrogen storage tank is shown in figure 1.

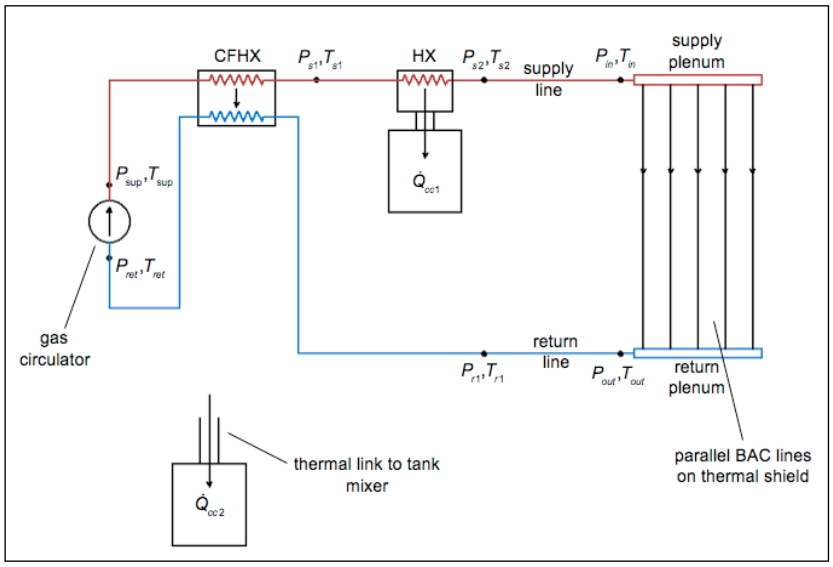

Figure 1. BAC Flow Schematic for a Hydrogen Storage Tank [1]

2.2 Objectives

Successful ground-based thermal testing of BAC system designs has been performed[1], but no structural analysis or testing has been attempted for any BAC shield concept. Structural analysis and testing are essential to ensure that a candidate design concept will be able to withstand the launch and ascent vibrational environment while remaining affordable in terms of launch mass.

The technical objectives of this effort are as follows:

1) Define concepts for the structural support of cryogenic propellant storage tank BAC shielding within MLI.
2) Assemble cooling panel segments representative of BAC shield panel concepts.
3) Perform acoustic testing.
4) Formally document recommendations for future BAC development activities based on the vibration and acoustic test results.

The effort begins at a low level of technology maturation, Technology Readiness Level (TRL) 2 (technology concept and/or application formulated).[4] Upon completion of the vibration and acoustic testing of the representative BAC shield panel segments and final documentation, it is believed this technology will be at TRL 3 (analytical and experimental critical function and/or characteristic proof of concept).

2.3 Approach

The baseline hardware configuration adopted for this effort was the hydrogen storage tank concept described in Feller and Salerno[1] and shown in figure 2. The Baseline BAC configuration is shown in table 1. This represents a flight-like test article to be used in a ground-based BAC system demonstration. Using the panel configuration shown in figure 3 as a point of departure, representative shielding panel assembly techniques were devised. Test parameters included

shield thickness, adhesive type/thickness for bonding the coolant tubing to the shielding, IM7 shield placement, shield attachment to the test frame, acoustic load level, and number of layers of MLI (ranging from approximately 30 to 60). The test panels were fabricated and subjected to acoustic testing. Associated acoustic test levels were typical of launch vehicle class environments based on structural inputs. Selected panel assembly concepts and the test setup were modified as the testing progressed. The expectation leading into testing was that this survey approach to testing would quickly and inexpensively reveal the viability of the devised assembly techniques.

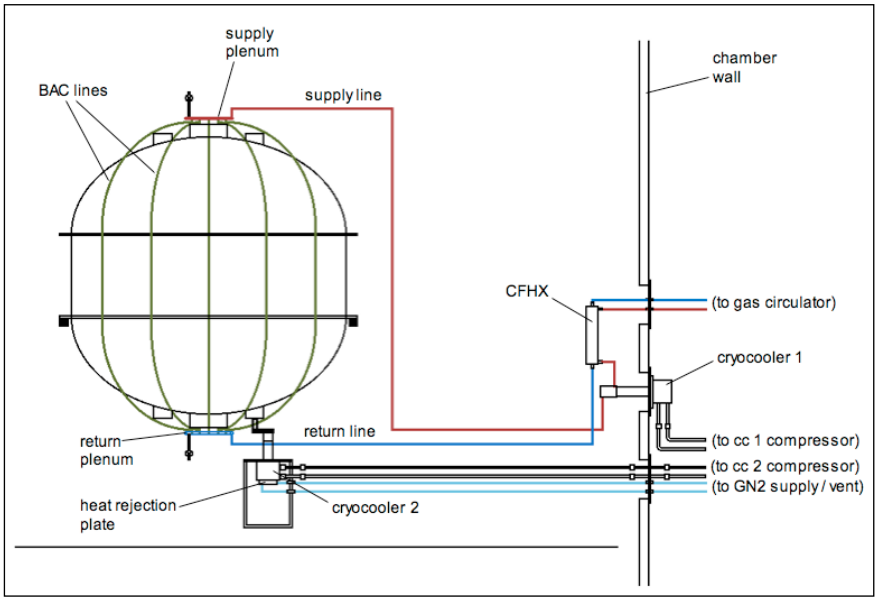

Figure 2. BAC Example Application Flow Schematic[1]

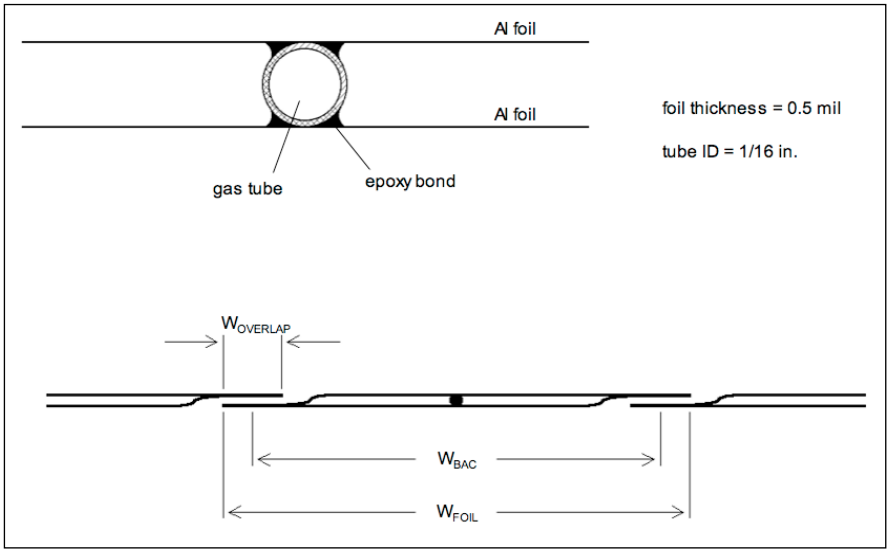

Figure 3. BAC Panel Cross Section per Ames Research Center[1]

Hydrogen Storage Tank	
Height:	6.0 ft
Diameter:	6.0 ft
Volume:	130.1 ft^3
Surface area:	125.0 ft^2
BAC Shield	
Tube size:	0.0625 in. ID
Tube pitch:	14.15 in.
Working fluid:	Helium, temperature range approximately 50–150 K
Working pressure:	218 psi
Tubes bonded with low-temperature epoxy to 2 sheets of 0.0005 in. Al 1100 foil	

Table 1. Baseline BAC Configuration[1]

3.0 TEST ARTICLE CONSTRUCTION

3.1 Multilayer Insulation Layup

Numerous MLI blankets needed to be constructed for the BAC panel tests. An effective and efficient way to manufacture these blankets was developed. The Mylar® used in MLI is 0.25 mil thick, double aluminized, and nonperforated. It is extremely delicate and presents a challenge to handling, storing, and installing the panels. The Dacron® B2A netting is also difficult to use in construction. The following system was designed for developing these 39 by 39 in. MLI blankets.

A wood stand was constructed with slots located in the top two studs. Four quarter-inch grooves were cut out of both sides of a piece of three-quarter-inch plywood such that they formed a square of 39 by 39 in. when they intersected. Brackets welded with a capped rod on their exteriors were attached to either side of the plywood, and this finished piece slid into the two slots on the top of the stand. The stand/panel combination was then placed in front of the Dacron netting and Mylar rolls, as seen in figure 4. The netting and Mylar were attached to one edge of the slotted panel and the panel was then rotated, wrapping the netting and Mylar around the panel with each turn. After achieving the desired number of layers, the netting and Mylar were cut and the panel was removed from the stand and placed on a table. The 39 by 39 in. blankets were then cut out using the grooves as a guide for the scissors. Once the blankets were cut out, they were fixed together using plastic tabs.

Figure 4. MLI Quick Layup Technique

3.2 Broad Area Cooling Panel Construction

The BAC panels were constructed in several steps. Two different thicknesses of aluminum were used. The aluminum was purchased in rolls, similar to aluminum foil purchased for consumer use. The aluminum sheets were cut into 39.5-in.-long by 18-in.-wide rectangles. Two rectangles were used per panel along with a hollow tube. Each rectangle of aluminum was creased down the center so that the tube was cupped in the grooves of the two sheets. Cryogenic-grade Loctite® E-40FL™ Hysol® epoxy adhesive was spread in the crease on each sheet and the tube was sandwiched between them. This packet was then set aside to dry. This process, shown in figure 5, was repeated for each test panel.

Figure 5. BAC Panel Layup Process

3.3 Test Article Assembly

Aluminum frames were built out of 3/16 in. material. The backside of the frame was simply a full sheet of aluminum. The sides were welded onto the base and along the corners where the frame came together. They were slotted so that the IM7 panel could be bolted to the frame and the BAC panel tubes were able to stick out. Spray-on foam insulation (SOFI) was sprayed in the cavity of the tray, with a 1.5 in. gap between the edge of the foam and the edge of the frame. As shown in figure 6a, the SOFI was sprayed on the frame with an approximate thickness of 1–2 in. The sprayed panels were sanded down to a consistent thickness of 1 in. The MLI was placed on

top of the SOFI and the IM7 panels were placed on top of the MLI, as shown in figures 6b and 6c.

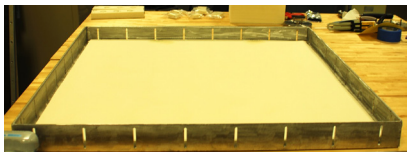

Figure 6a. SOFI in Frame

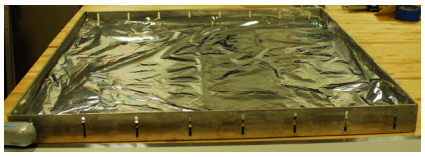

Figure 6b. MLI on SOFI

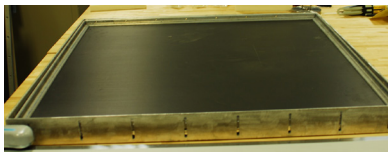

Figure 6c. IM7 Panel on MLI

The MLI was attached in the frame using two techniques. The first technique, shown in figure 7a, was to install grommets at regular intervals approximately one-quarter inch from the edge of the blanket. Cord was run through these grommets and then tied off through the slots in the frame, pulling the MLI taut in the process. The second technique, shown in figure 7b, pulled the MLI taut using a clamp-bar technique. Holes were punched at regular intervals in two opposing sides of the blanket. Two bars, one threaded and one tapped to correspond to one another were placed on either side of the MLI and screws were tightened through each hole on both ends of the blanket packet. This system was then placed inside the frame where the holes were drilled.

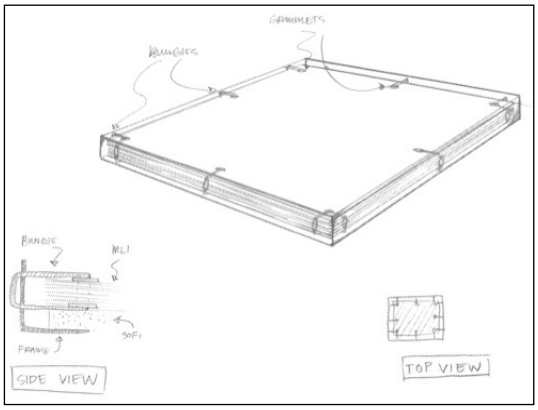

Figure 7a. MLI Attachment A

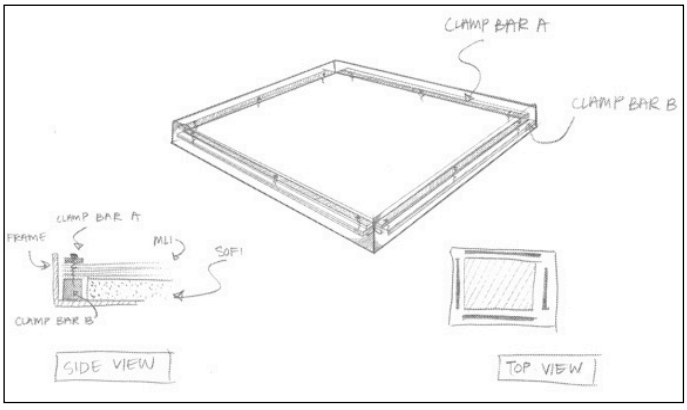

Figure 7b. MLI Attachment B

4.0 TEST INFORMATION

4.1 Facility and Test Setup

Testing was performed at the NASA MSFC Acoustic Testing Facility. Figures 8 and 9 illustrate the test setup. The aluminum frame was suspended from the ceiling of the acoustic chamber by bungee cords hooked to the corners of the frame. Accelerometers, when used, were placed on the frame and the IM7 panel. The operation was video recorded so that experimentation could be observed. After each test, the test article was visually inspected for damage.

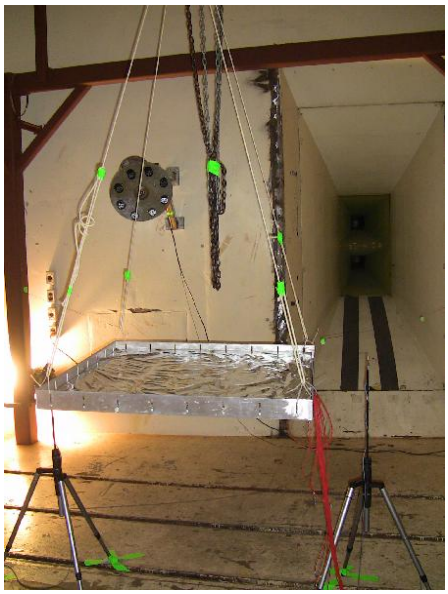

Figure 8. Test Setup

Figure 9. Test Setup with IM7 Panel

4.2 Test Matrix

The first two tests, one at half power and one at full power, were run without BAC panels or an MLI blanket to insure that the frame/IM7 assembly functioned structurally in the test environment. A preliminary test matrix was developed before the initiation of testing (table 2). As testing progressed, the test matrix was refined to explore interesting or perplexing observations that were made in early tests. A total of 58 tests were conducted.

	MLI Layers		BAC Shield Placement		BAC Attachment		MLI Attachment		IM7 Offset		Test Environment		AL Thickness		Slots		BAC Tube Ends	
	30	60	15	30	Floating	Fixed	Grommet	Clamp	1/2"	1"	Max	Max - 6dB	Thin	Thick	Open	Covered	Free	Fixed
1									X			X	X		X		X	
2									X		X		X		X		X	
3	X		X		X		X					X	X		X		X	
4	X		X		X		X				X		X			X	X	
6	X		X		X			X		X	X		X			X	X	
8	X		X		X			X	X		X		X			X	X	
10	X		X		X			X			X		X			X	X	
11	X		X		X		X			X		X	X		X		X	
12	X		X		X		X			X	X		X		X		X	
13	X		X		X		X		X			X	X		X		X	
14	X		X		X		X		X		X		X		X		X	
16		X		X	X			X		X	X		X			X	X	
39	X		X			X		X		X		X	X			X	X	
40	X		X			X		X		X	X		X			X	X	
41	X		X			X		X	X			X	X			X	X	
42	X		X			X		X	X		X		X			X	X	
43	X		X			X		X				X	X			X	X	
44	X		X			X		X			X		X			X	X	
45		X		X		X		X		X		X	X	X		X	X	
46		X		X		X		X		X	X		X	X		X	X	
47		X		X		X		X	X			X	X	X		X	X	
48	X		X		X		X		X		X		X			X	X	
49		X		X		X		X	X		X		X	X		X	X	
50		X		X		X		X				X	X	X		X	X	
51		X		X		X		X			X		X	X		X	X	
52	X		X		X			X		X		X	X			X		X
53	X		X		X			X		X	X		X			X		X
58	X		X		X			X			X			X		X		X

Table 2. Test Matrix

5.0 RESULTS

Overall, it was found that BAC panels that will withstand expected launch acoustic environments can be constructed, but preflight qualification testing will be needed. Some samples showed structural degradation of the foil at full power; these were constructed of the thinner, soft-temper foil. No tube debonding or structural tube damage was noted. Most of the MLI damage observed occurred as a result of edge tears spreading. This observation emphasizes the importance of edge preparation in the construction of BAC systems and MLI blankets. The degree of tension in the MLI blanket positioned above the BAC panels was not seen to be a major factor.

Accelerometer and facility data indicate a good match with the predicted Ares V environment. The test duration exposure of the BAC panels and MLI blanket system to 30 s of half-power and

30 s of full-power acoustic environments greatly exceeds the launch and flight duration. The actual duration of these acoustic environments at liftoff and in transonic flight near the maximum q value is only several seconds.

5.1 Visual Inspection

Visual inspections were performed after each of the tests listed in table 2. No damage was observed for any test setup in this less-severe environment. The majority of damage to the test setup was observed in the MLI. Very small cuts in the Mylar that happened during the construction of the MLI blankets spread to very large rips as a result of the acoustic testing. Similar results were observed in the aluminum used in the BAC panels but to a lesser extent. This may have been a result of less unintentional nicks in the BAC panel construction in addition to the additional thickness and sturdiness of the material. In multiple tests, the Mylar was damaged at the point where it lined up with the tube in the BAC panel. It is possible that there was a nick in the Mylar at this location, but the consistence with which the Mylar incurred structural damage at the BAC tube location leads to the opinion that the tube was the cause of this failure.

The most significant observation regarding the BAC panels themselves was a standing wave pattern that occurred in the panels in several tests. In these setups, the tubes were stabilized on the ends by placing masking tape over the slots in the aluminum frame where the tubes stuck through on either side. The standing wave marks only occurred on the thinner aluminum panels, as shown in figure 10.

Figure 10. Standing Wave Marks Appeared on the Thin AL BAC Panel at Right, But Not on the Thick Panel at Left

5.2 Post-Test Data Analysis

The tests in the MSFC Reverberant Acoustic Chamber at the 157.1 dB full-power overall sound pressure level provided a good simulation of the maximum predicted one-third-octave band spectra (table 3 and figure 11). The test article exposure to both the 30 s of half-power and the 30 s of full-power acoustic environments greatly exceed the launch and flight duration acoustic loads. These acoustic loads exist for only several seconds at liftoff for the Earth Departure Stage LH2 tank at the 280 ft station and at transonic shock passage over the payload fairing at 0.85 Mach and the maximum q value of 455 psf aeroacoustic levels for the internal payload fairing environment if a -4 dB attenuation through the payload fairing walls is assumed.

One-Third-Octave Band Freq. (Hz)	Ares V @ 280 ft (VAEPP w/ pad reflections)	Ares V Zone IIIa M = 0.85	Ares V Zone IIIb M = 0.85	Test 1 Reverberant Chamber Half Power	Test Reverberant Room Full Power	Ares V Payload Fairing Internal M=0.85 (4 dB)
1.6	125.8					
2	127.5					
2.5	129.1					
3.16	130.8					
4	132.4					
5	133.9					
6.3	135.4					
8	136.8					
10	138.1					
12.6	139.3	131.0	116.0			127.0
16	140.4	143.0	117.0			139.0
20	141.4	145.6	117.0	95.5	101.9	141.6
25	142.3	147.4	119.0	119.6	117.3	143.4
32	143.1	148.9	120.0	130.3	130.5	144.9
40	143.7	149.9	121.0	136.7	135.5	145.9
50	144.2	150.5	122.0	140.6	144.1	146.5
63	144.6	150.4	123.0	145.2	149.7	146.4
79	144.9	150.1	124.0	143.1	147.5	146.1
100	145.0	150.1	125.0	139.7	143.3	146.1
126	144.9	149.7	126.0	144.9	146.5	145.7
158	144.7	150.1	126.0	144.3	146.6	146.1
200	144.4	149.7	127.0	143.0	144.4	145.7
251	144.0	149.1	128.0	140.9	144.5	145.1
316	143.5	148.4	128.0	140.0	144.8	144.4
398	142.8	147.8	129.0	139.7	144.2	143.8
501	142.1	147.3	129.0	138.8	142.4	143.3
631	141.3	147.0	128.0	137.2	142.2	143.0
794	140.4	146.3	128.0	136.5	141.9	142.3
1,000	139.4	145.8	127.0	135.7	140.8	141.8
1,259	138.4	145.1	127.0	134.4	140.6	141.1
1,585	137.3	144.3	126.0	133.2	139.3	140.3
1,995	136.2	143.3	125.0	132.0	138.3	139.3
2,512	135.1	142.1	124.0	130.9	137.3	138.1
3,162	133.9	140.7	123.0	129.6	136.4	136.7
3,981	132.8	139.1	122.0	128.4	135.4	135.1
5,012	131.6			127.2	134.4	
6,310	130.4			126.2	133.2	
7,943	129.3			125.3	131.9	
10,000	128.2			124.6	130.8	
	156.3	**162.0**	**140.0**	**153.5**	**157.1**	**158.0**

Table 3. Accelerometer Data

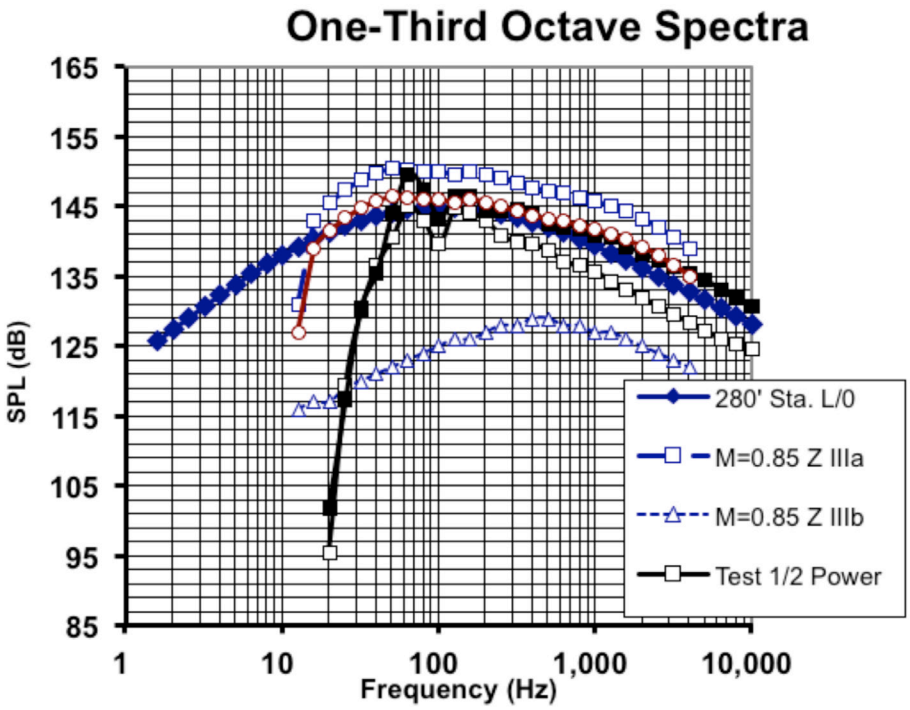

Figure 11. One-Third-Octave Spectra

6.0 FUTURE WORK

The tests conducted in this survey provide a basis from which to explore the viability of BAC systems in the launch environment. The limitations of the BAC panel testing performed in this study were primarily based on the small scale of the test articles. Additionally, the tests only dealt with acoustics and not with vibration.

The following work needs to be conducted to further understand BAC system performance during the launch environment:

1) Testing should be done with representative tank and MLI attachment schemes in both acoustic and vibration launch environmental conditions.
2) Testing should be done with span lengths similar to those on which the cooling system would be used in both acoustic and vibration launch conditions.
3) Testing should be done with liquid helium flowing through the tubes in both acoustic and vibration launch conditions.
4) Testing should be done at a frequency of less than 63 Hz. A lower-frequency excitation of less than 63 Hz may exist in launch and flight at liftoff and the transonic buffet maximum q value. This was not simulated in the acoustic tests performed in the chamber, and it should be tested in the future.

References

1. Feller, J., and Salerno, L., *Summary of Cryogenic Propellant Depot Test Bed Design Concepts*, Ames Research Center, 2006.

2. *Long Duration Earth Departure Stage (LEDS) Study*, Advanced Concepts Office (EI63), Marshall Space Flight Center, with contributions from ARC, GRC and KSC, 2006.

3. Plachta, D., and Kittel, P*., An Updated Zero Boil-Off Cryogenic Propellant Storage Analysis Applied to Upper Stages or Depots in an LEO Environment*, NASA/TM-2003-211691, 2003; also AIAA Paper 2002-3589, 2002.

4. Mankins, J. C., *Technology Readiness Levels: A White Paper*, NASA, Office of Space Access and Technology, Advanced Concepts Office, 6 April 1995; also http://www.hq.nasa.gov/office/codeq/trl/trl.pdf.

Development and Testing of an Innovative Two-Arm Focal-plane Thermal Strap (TAFTS)

E. Urquiza[1], C. Vasquez[2], J. Rodriguez[1] and B. Van Gorp[3]

[1]Cryogenic Systems Engineering, Jet Propulsion Laboratory, California Institute of Technology
[2]Dept. of Mechanical Engineering, California Polytechnic State University, San Luis Obispo
[3]Optical Technology, Jet Propulsion Laboratory, California Institute of Technology

Abstract

Maintaining temperature stability in optical focal planes comes with the intrinsic challenge of creating a pathway that is both extremely flexible mechanically and highly conductive thermally. The task is further complicated because science-caliber optical focal planes are extremely delicate, yet their mechanical resiliency is rarely tested and documented. The mechanical engineer tasked with the thermo-mechanical design must then create a highly conductive thermal link that minimizes the tensile and shear stresses transmitted to the focal plane without design parameters on an acceptable stiffness.

This paper will describe the development and testing of the thermal link developed for the Portable Remote Imaging Spectrometer (PRISM) instrument. It will provide experimentally determined mechanical stiffness plots in the three axes of interest. Analytical and experimental thermal conductance results for the two-arm focal-plane thermal strap (TAFTS), from cryogenic to room temperatures, are also presented. The paper also briefly describes some elements of the fabrication process followed in developing a novel design solution, which provides high conductance and symmetrical mechanical loading, while providing enhanced flexibility in all three dimensions.

Introduction

Air-borne and space infrared cameras require highly flexible direct cooling of mechanically-sensitive focal planes. A thermal electric cooler is often used together with a thermal strap as a means to transport the thermal energy removed from the infrared detector. In cooling focal planes, a cooling solution must be highly conductive, lightweight, and able to operate within a vacuum with no out-gassing. Furthermore, the device must also be highly flexible in all axes to accommodate adjustment of the focal plane while transmitting minimal force.

The aluminum foil-based thermal strap or link is a device that often meets the weight, conductivity, flexibility, and reliability requirements needed for thermal management of sensitive components. This type of thermal link often consists of hundreds of aluminum foils carefully stacked and swaged into terminals [1]. While effective, traditional thermal straps are only highly flexible in one axis, moderately flexible in a second axis, and relatively stiff in the third axis. Stiffness and vibration transmission on a

simpler thermal strap design was carried out by Kobayahsi and Folkman [2]. While the standard thermal strap is highly effective in cooling mechanical components, the flexibility requirements for the thermal strap are more stringent when it connects it to an adjustable focal plane, however.

Thermal Management of the PRISM Focal Plane

The Portable Remote Imaging Spectrometer (PRISM) is a push-broom airborne instrument in development at the Jet Propulsion Laboratory (JPL), California Institute of Technology, which will acquire data for the ocean science research community. The instrument will operate in the 350-1050nm spectral range and a thermoelectric coolers and flexible thermal straps are used to maintain temperature stability and to keep dark current to manageable levels [3].

A two-armed thermal strap using three swaged terminals and a twisted section offers enhanced elastic movement, significantly beyond the motion permitted by existing thermal straps. This design innovation allows for large elastic displacements in two planes and moderate elasticity in the third plane. By contrast, a more conventional strap of the same conductance offers less flexibility and asymmetrical elasticity.

Key to achieving high conductance is the fabrication process which involves the cold welds that occur between swaged or crimped surfaces. Examination of this phenomena is available in the literature [4,5]. Mrokowski and Geckle, verify the cold welding phenomena by examining the transfer of conductor material at the swaged interface using Scanning Electron Microscopy (SEM) [4].

The two-arm configuration in TAFTS reduces the bending moment of inertia for a given conductance by creating the same cross-sectional area for thermal conduction, but with only half the thickness of a conventional design. This reduction in the thickness has a significant effect on the flexibility since there is a cubic relationship between the thickness and the rigidity or bending moment of inertia in cantilever-like bending.

Mechanical Characterization

A CAD model of the two-arm focal-plane thermal strap (TAFTS) can be seen with the PRISM assembly model in Figure 1. The thermal strap must allow for translations in all three axes as depicted in Figure 2. Furthermore, a small amount of rotation in all axes must also be accommodated with minimal mechanical resistance, as the resulting load is transmitted directly to the optics mount. In Figure 1, the optical detector mount can be seen with its adjustment screws. The thermal strap is mounted onto a TEC which is then mounted onto a conductive connector. This connector then mounts onto the strap terminal's positive XY plane (just opposite of the XY-face shown in Figure 2). Also in Figure 2, the Belleville washers-mounted screws can be seen. This mounting arrangement helps maintain contact forces between the thermal strap mount and the vacuum plate as the assembly is tested by cooling to cryogenic temperatures.

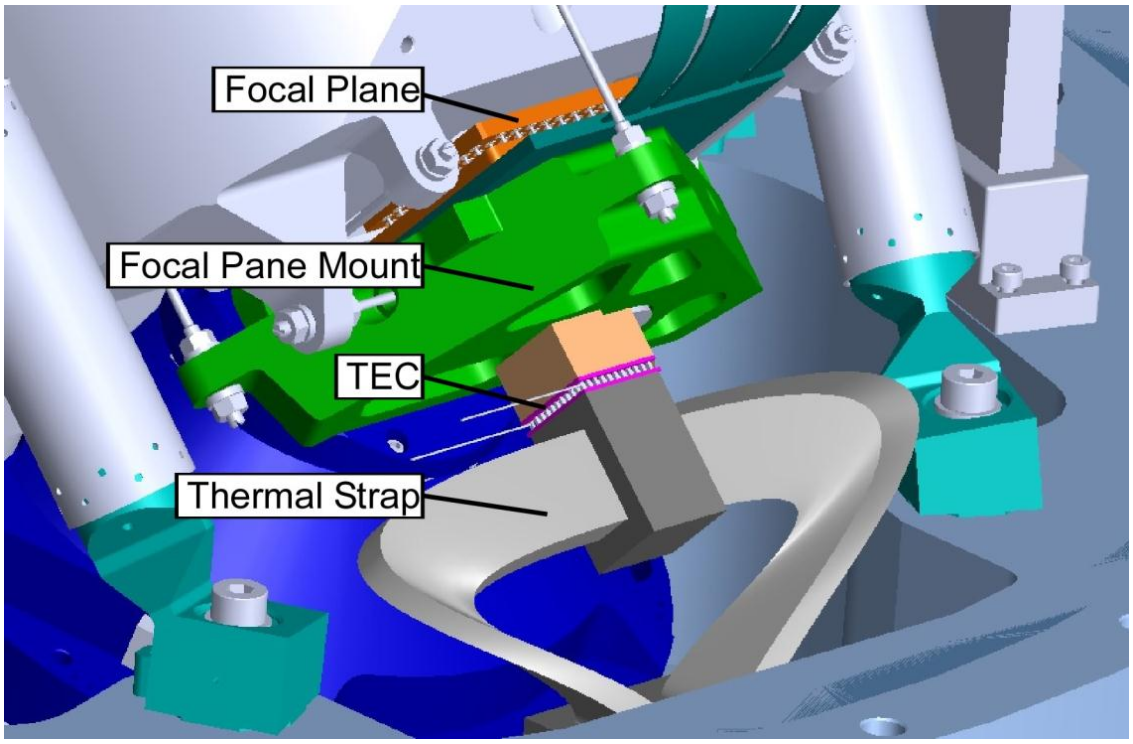

Figure 1: TAFTS and focal-plane mount assemble on a CAD molde of the PRISM instrument.

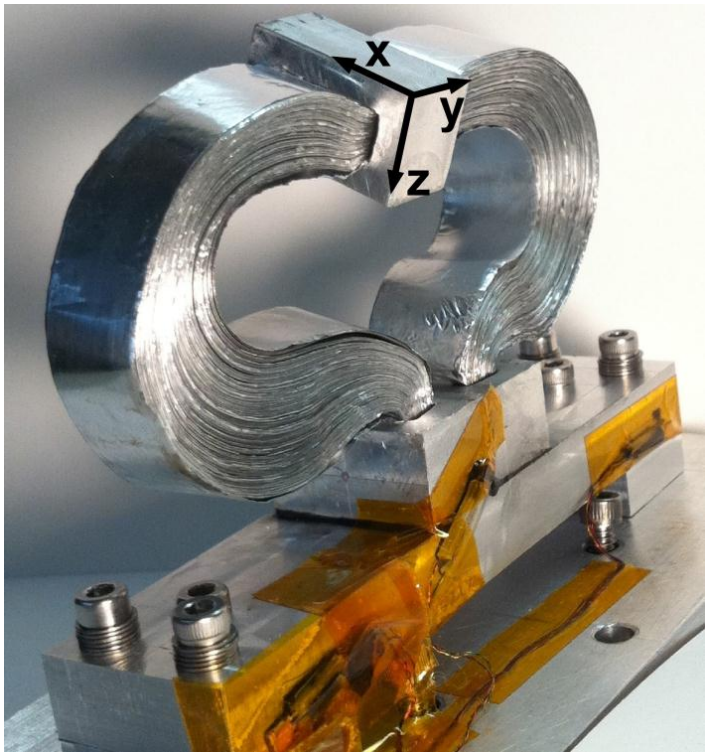

Figure 2: TAFTS co-ordinates on the center terminal showing the mounted silicon-diodes.

In order to resolve the amount of force imparted by the thermal strap onto the optical focal plane, the mechanical stiffness of the thermal strap must first be resolved to ensure that the adjustment mechanisms on the optical bench can resist the spring force in the strap. While qualitatively the TAFTS design appeared sufficiently flexible, obtaining elasticity data for the first time on the mechanical performance of a two-arm flexible thermal strap will be useful for future designs involving thermo-mechanically sensitive focal plane assemblies.

An experimental setup was devised to hold the thermal strap assembly such that a predetermined weight on a thread pulled on the strap in the coordinate axes shown in Figure 1. The displacement of the center terminal was then measured by hand using a caliper. To reduce the error associated with taking a measurement by hand, the measurement was taken three times independently an averaged. The thermal strap was then relieved of the weighted thread and allowed to return to its rest position bearing only its own weight. Finally the weight was reapplied a second and occasionally a third time; with application of the weight displacement was measured several times and averaged. The stiffness of the TAFTS was calculated and is plotted in Figure 2. The stiffness can be seen to be relatively constant in the x and y-direction (somewhat linear in the z-direction) through displacements typical for the application.

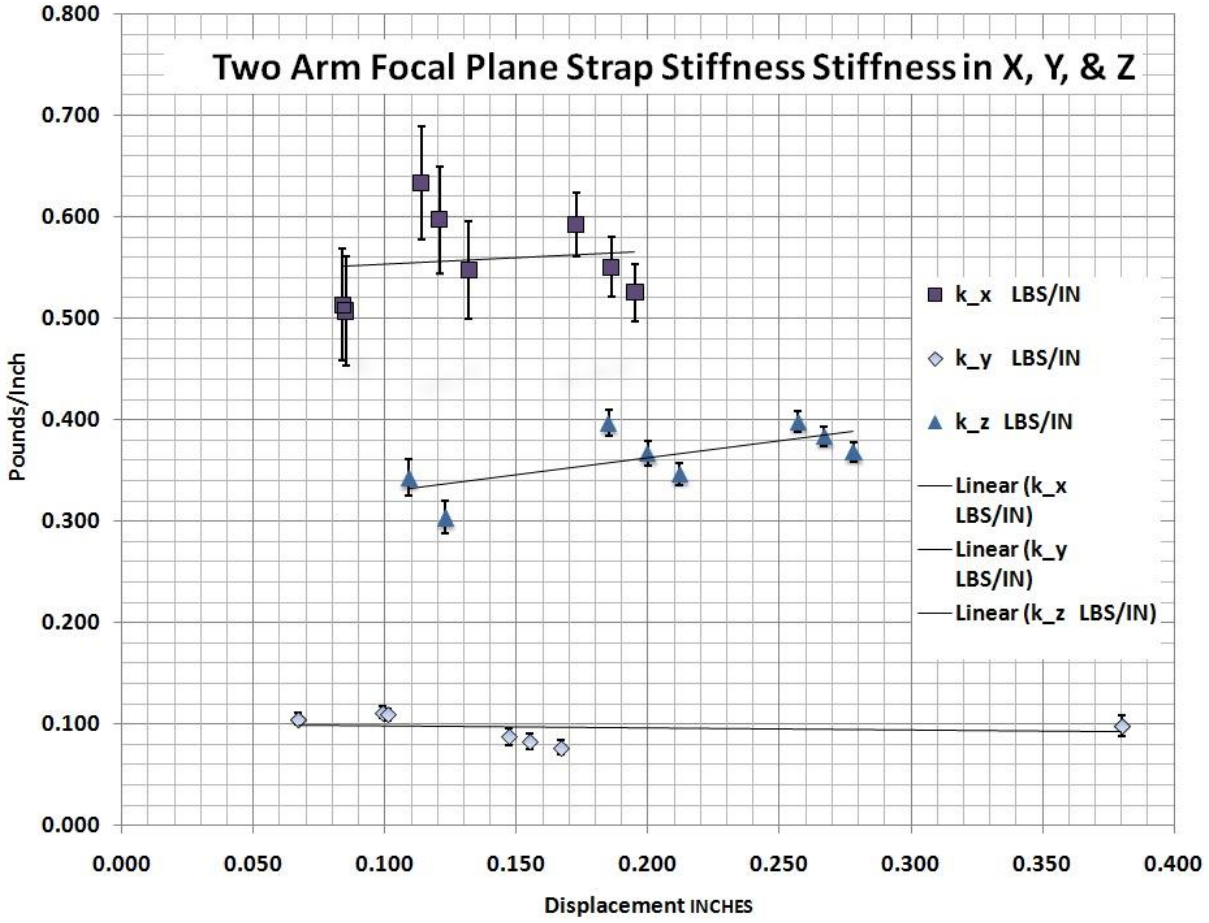

Figure 3: Experimentally determined elasticity data for the X, Y, and Z displacements for the two-arm flexible thermal strap design

The stiffness, and the relative error associated with its calculation from measured data, was calculated using both the accuracy of the scale (±0.01 grams) used to measure the test weight, and the accuracy of a hand caliper measurement, assumed to be within ± 0.020 inches. The error tolerance on the stiffness of the thermal strap is shown in the error bars in Figure 2. The relative error tolerance varied from ±2% in the most elastic direction, to ±11% in the stiffest direction. The more elastic direction measured had the largest displacement, which in turn reduced the relative error with the caliper hand measurement. While the precision could be improved with a more elaborate setup, the goal here is to provide valuable engineering data to aid in future thermo-mechanical design of focal plane mounts and thermal control systems.

Thermal Characterization

The thermal strap terminals are made of Al 1100 while the foils are Al 1245; both alloys are greater than 99.0% aluminum. The alloys are extremely maleable and little springback is exhibited when compared to thermal straps made of Al 6061. The higher purity alloy makes this thermal strap more conductive, but also makes the foils more delicate and the fabrication somewhat more challenging as well. In fabricating the thermal strap assembly, the bottom-terminals were attached to each other as well as to the strap mount using Tra-bond 2151 epoxy mixed with 1-mil glass beads, which provide a constant bond-line thickness.

In thermally characterizing the thermal strap Lakeshore silicon diodes were placed at the center and bottom-left terminal. Silicon diodes were also placed on both edges of the strap mount, which is made of Al 6061. An aluminum cryocooler adapter plate was made to mate the thermal strap assembly to a Gifford-McMahon cryocooler at Jet Propulsion Laboratory, California Institute of Technology as shown in Figure 4.

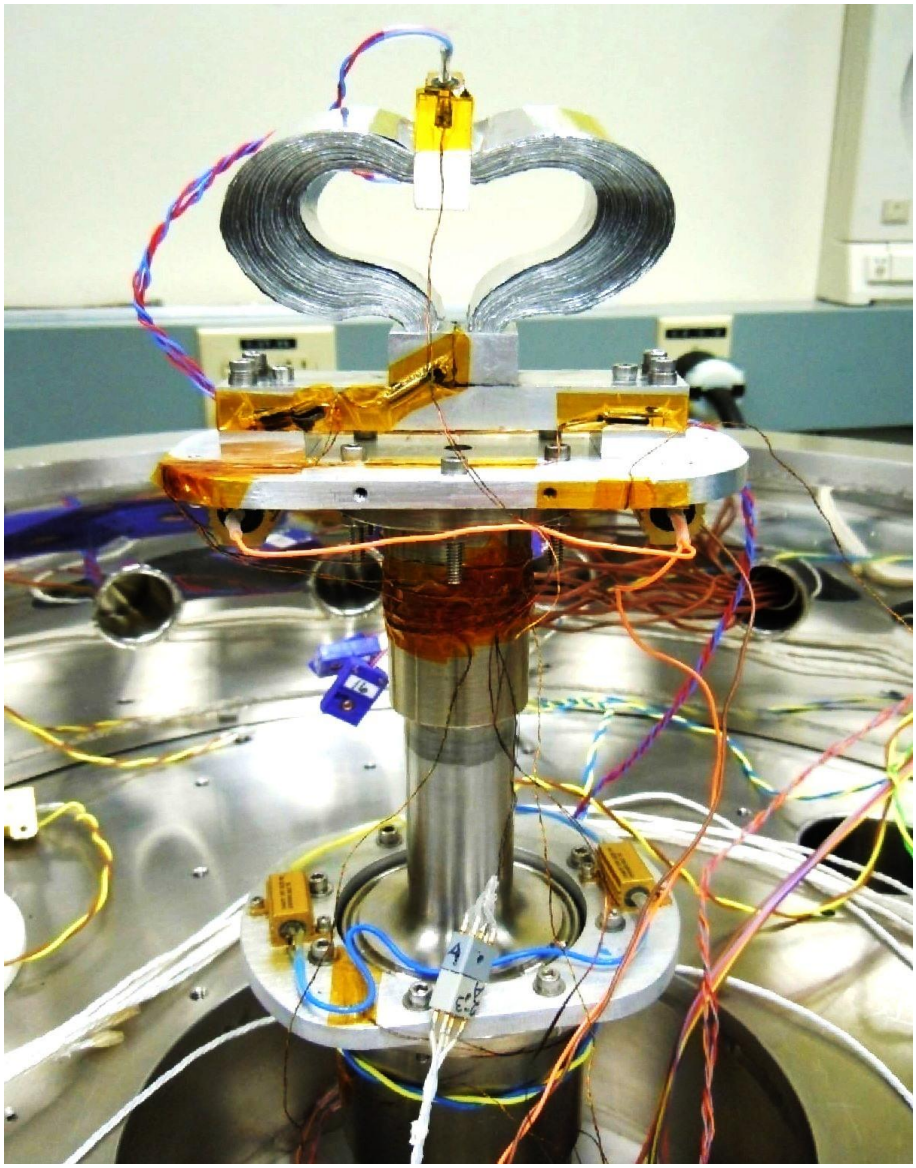

Figure 4: The TAFTS assembly mounted on a Gifford-McMahon cryocooler at Jet Propulsion Laboratory, California Institute of Technology

A resistor is the heat source and is epoxy mounted on the center TAFTS terminal. Manganin wires are used on the diodes to minimize thermal conduction and a four-wire technique is used on the resistor so to more precisely measure only the power disipated through the resistor and not the in the lead wires which extend beyond the vacuum chamber to the power supply.

Starting from at 23K, 4 Watts of heat were generated by the resistor. By controlling the temperature of both the thermal strap mount and that of the center terminal, and waiting for steady state temperatures to be reached, the conductance of the mount was calculated. This process was repeated many times until the average temperature of the strap was raised to room temperture, where thefinal measurement was taken. The thermal conductance of the TAFTS is measured and plotted in Figure 5,

using diamond icons and labeled “T. Strap Data”. The thermal conductance of the TAFTS including the horizonal bar mount whick is also part of the PRISM assembly is also plotted using squares and labeled “T. Strap + Mount Data.”

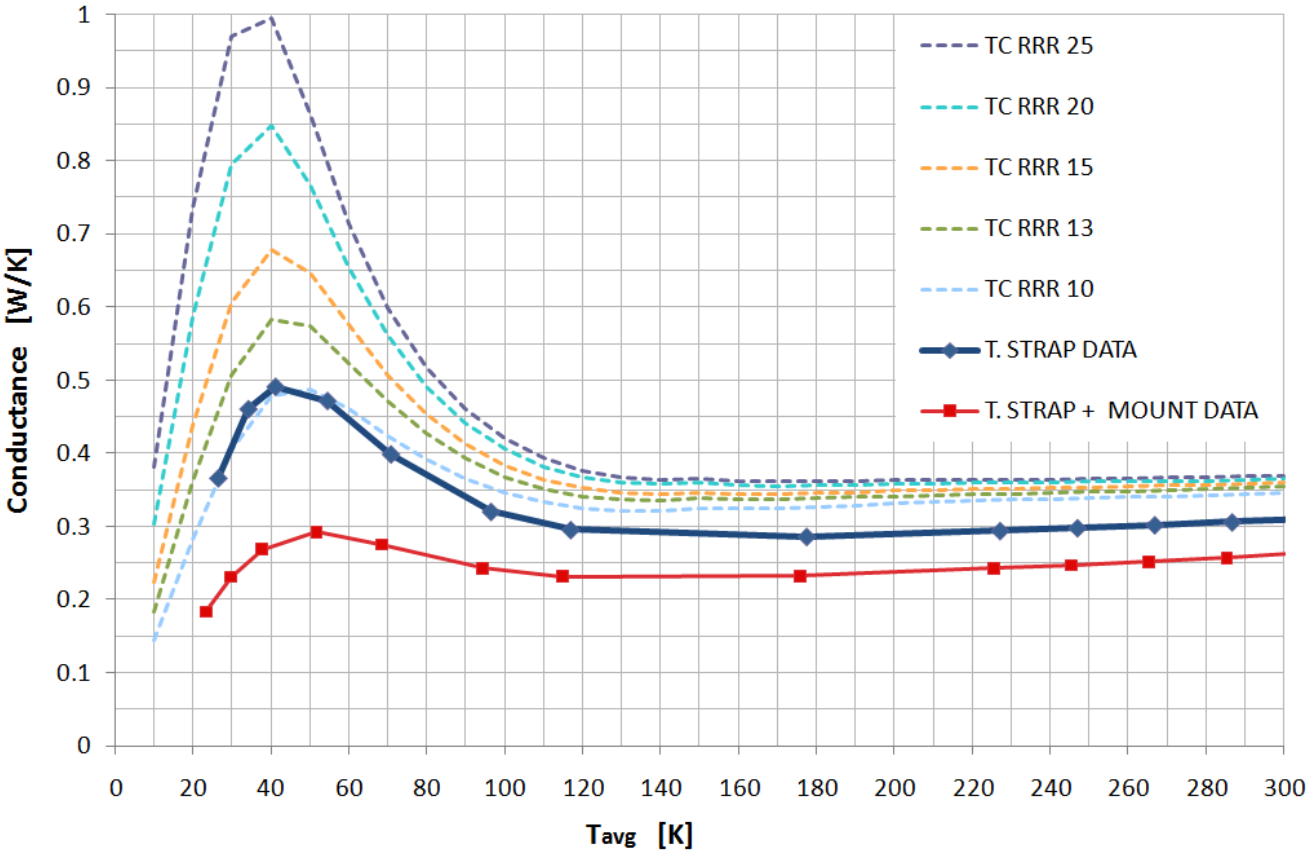

Figure 5: Experimentally determined elasticity data for the X, Y, and Z displacements for the two-arm flexible thermal strap design

The sensitivity of the thermal conductivity of aluminum is highly dependant on the purity. While the purity of the aluminum used here is not known, when the geometry is considered the theoretical conductance of the TAFTS can be calculated. Using data from CRYOCOMP [6] it seems like the effective relative resistance ratio (RRR) of the aluminum in the thermal strap assembly is somewhere in between 13 and 20, since the epoxy bonds and swaged connections all reduce the achievable conductance.

Conclusions

The novelty of the technology lies in the mechanical design and manufacturing of the thermal strap. The enhanced flexibility will facilitate cooling of mechanically sensitive components such as infrared focal plane mounts as discussed here. While the static elasticity is high, the dynamic response has not been studied and this too could be important when considering dynamic system loads. This development contributes to the field of thermal control and cooling of delicate optics. It is known to be especially important in the thermal control of optical focal planes due to their highly sensitive alignment requirements and mechanical sensitivity; however, many other applications may exist.

References

[1] B. Williams, S. Jensen, M. Chadek, J. C. Batty, "Solderless flexible thermal links," 0011-2275/96, Cryogenics 36, pp. 867-869, 1996

[2] K. Kobayahsi, S. Folkman, "Stiffness of and Vibration Transmission through Thermal Links," AIAA-98-2079. AIAA 1998.

[3] P. Mouroulis, B. van Gorp, R. O. Green, D. Cohen, D. Wilson, D. Randall, J. Rodriguez, O. Polanco, K. Balasubramanian, R. Vargas, R. Hein, H. Sobel, M. Eastwood, "Design of an Airborne Portable Remote Imaging Spectrometer (PRISM) for the Coastal Ocean," NASA Earth Science Technology Forum, Crystal City, Virginia, June 22, 2010.

[4] M. M. Yovanocich, "Four Decades of Research on Thermal Contact, Gap, and Joint Resistance in Microelectronics," IEEE, 1521-3331,2005.

[5] R. S. Mroczkowski, R. J. Geckle, "Concerning 'Cold Welding' in Crimped Connections," 0-7803-2728-4/95, IEEE 1995.

[6] CRYOCOMP, Cryogenic materials thermal properties database and thermal analysis program, Eckels Engineering Inc., Distributed by: Cryodata inc. Properties version3.05

Acknowledgments

The research was carried out at the Jet Propulsion Laboratory, California Institute of Technology, under a contract with the National Aeronautics and Space Administration.

Numerical Analysis of an OPTR: Optimization for Space Applications*

Bakhtier Farouk† and Dion Savio Antao
Department of Mechanical Engineering and Mechanics
Drexel University
Philadelphia, PA 19104, USA

ABSTRACT

A numerical study is reported here for the investigation of the flow and heat transfer processes in a co-axial type single stage orifice type pulse tube refrigerator (OPTR). The OPTR is driven by a cyclically moving piston at one end of the system with helium as the working fluid. The regenerator and the various heat exchangers are modelled as porous media and a thermal non-equilibrium model is applied in these regions. The simulations reveal interesting steady-periodic flow patterns that develop in the pulse tube due to the fluctuations caused by the piston and the presence of the inertance tube. When the secondary flow patterns are well-developed, they help isolate the cold and hot ends of the pulse tube and create a thermal buffer zone at the center of the pulse tube, enhancing the performance of the OPTR.

Keywords: Space cryocooler; acoustic streaming; pulse tube; thermal non-equilibrium; co-axial PTR

1. INTRODUCTION AND BACKGROUND

* To be presented at the Space Cryogenics Workshop, 8th – 10th June, 2011 Coeur d'Alene, ID
† Corresponding Author, FAX: 215-895-1478, E-mail: bfarouk@coe.drexel.edu

The pulse tube cryocooler is a developing technology that emerged largely in the early 1980's with a series of innovations in the broader field of thermoacoustics. In contrast with other cryocoolers (e.g. Stirling cryocooler and Gifford-McMahon cooler) this type of cryocooler can be made without moving parts in the low temperature part of the device, making the cooler suitable for a wide variety of applications. Pulse tube cryocoolers have been used in industrial applications such as semiconductor fabrication and in military applications such as for the cooling of infrared sensors [1]. However, pulse tube cryocooler are also being developed for cooling of astronomical detectors where liquid cryogens are typically used. With the added benefits of extended lifetimes and low vibrations at the cold head, pulse tube cryocoolers have found their niche application where stable operation is desired. Pulse tube cryocooler will be particularly useful in space-based telescopes where it is not possible to replenish the cryogens as they are depleted. It has also been suggested that pulse tubes could be used to liquefy oxygen on Mars [2].

The pulse tube refrigerator (PTR) is an interesting thermoacoustic device and was first discovered and reported by Gifford and Longsworth in 1964 [3, 4]. It was named a 'pulse tube refrigerator' as the displacer (found in Stirling and Gifford-McMahon type refrigerators) was replaced by a hollow tube (called the 'pulse tube'). This initial pulse tube refrigerator design is now called a Basic Pulse Tube Refrigerator (BPTR) [5]. A major breakthrough was achieved in 1984, when Mikulin [6] demonstrated that the phase and amplitude relation between velocity and temperature can be manipulated by controlling the boundary conditions at the end of the pulse tube. This was done by

placing an orifice and a reservoir (compliance/surge) volume at the end of the BPTR thus allowing a finite gas flow.

Radebaugh at NIST (Boulder, CO) worked on the OPTR as it is known today - changing the location of the orifice compared to Mikulin's system. His initial work recorded temperatures around 60 K [7]. More recent variations of the OPTR include the addition of an extra orifice and a by-pass line to connect the warm end of the pulse tube and the warm end of the regenerator, creating a double-inlet pulse tube. Another improvemet is the addition of an inertance tube between the warm end of the pulse tube and the compliance volume (in lieu of an orifice or in addition to the orifice) to control the phase relationships in the system. Marquardt and Radebaugh reported the highest efficiency for the pulse tube refrigerator when using a combination of the orifice and the inertance tube [2].

Pulse tube cryocoolers come in three basic configurations [1, 8]. These configurations are the In-line OPTR, the U-tube OPTR and the Co-axial OPTR. The In-line OPTR is the most efficient configuration due to the absence of void spaces and excess material, but the presence of a cold region in the middle of the cryocooler is not well suited for any application. The co-axial OPTR on the other hand is the most compact of the configurations and offers the best geometry for direct contact with the cold region (due to the presence of a cold head). Recently, there has been a push to build PTRs that work efficiently at higher frequencies [9-12]. The use of high frequency oscillations allows the system to be comparatively small in size. These smaller sized systems have niche applications in the space industry where localized low power (< 1 W) cooling systems with extremely fast cool-down times are required. Hence, a high

frequency co-axial cryocooler is the best choice for a pulse tube cryocooler with space applications.

1-D computational models have been widely used for modeling thermoacoustic devices. Swift *et al*. [13-15] developed a 1-D code for the entire PTR system (and other thermoacoustic engines and refrigerators) based on Rott's [16] linear acoustic equations. While, the 1-D codes provide relatively good estimations of various operating parameters of the PTR (dimensions, operating frequencies, etc.) and provide farily quick/instant results; they use idealistic assumptions and do not reflect the multi-dimensional nature of the flow and transport inside the PTR systems. In a co-axial or u-tube arrangement, it is difficult to accurately design or predict the performance using a 1-D model.

Lee [17, 18] developed a set of 2-D differential equations for use in describing the steady secondary flows generated by the periodic compression and expansion of an ideal gas in pulse tubes. The equations were used to obtain an insight into the physics of the pulse tube in a basic pulse tube (BPTR) and an orifice pulse tube refrigerator (OPTR) for what is known as the thermally strong case. Flake and Razani [19] carried out an axisymmetric analysis of a BPTR and a PTR and showed cycle-averaged flow fields in the pulse tube. Cha *et al.* [20] studied two IPTR systems based on the geometry of the pulse tube (for two values of L/D ratio). They showed the formation of instantaneous vortical structures in the pulse tube for the small L/D case which had a negative effect on the cooling performance of the IPTR due to the mixing of flow in the pulse tube. Ashwin *et al.* [12] used a thermal non-equilibrium model in the porous media (heat exchangers and regenerator) and considered a finite wall thickness for the various components of the IPTR. The effect of a finite wall thickness was found to increase the steady state

temperature at the cold end of the pulse tube due to the heat conduction along the walls of the pulse tube from the hot end to the cold end. Recetly, the authors have used CFD simulations [21, 22] to predict the performance of OPTRs for a variety of conditions. These CFD simulations reveal interesting transient and steady-periodic phenomena in the OPTR that affect its performance.

In this paper, we report time-dependent axisymmetric CFD simulations of a co-axial type OPTR (for possible space cryogenic application) for the *first* time. The transient as well as the cycle-averaged operation of an OPTR is studied for the processes occurring in a co-axial orifice type pulse tube refrigerator. The compressible form of the Navier-Stokes equations is considered for the flow simulations. For the porous media regions (i.e. the regenerator and the heat exchangers), a thermal non-equilibrium porous media model [12, 23] is used. In the non-equilibrium model, the gas and the solid temperatures are different in the porous media regions. The effect of heat transfer between the gas and the solid phases are considered in the energy equations of the gas and solid phase regions. For the purpose of the study, the OPTR is considered to operate at a frequency of 100 Hz. In this study, we investigate the effects geometry of the on the performance of the system.

2. PROBLEM GEOMETRY

Figure 1 depicts the geometry studied (i.e. a co-axial design OPTR system). The geometry was chosen for its compactness – for possible space applications. Only half the geometry shown in figure 1 is simulated (axisymmetric geometry). The OPTR consists of a compression chamber (which includes the moving piston), the transfer tube,

aftercooler (the first red hatched region), regenerator (blue cross-hatched region), pulse tube with two heat exchangers at its ends (the other two red hatched regions), an orifice (a simple obstruction to the flow), an inertance tube and the compliance volume.

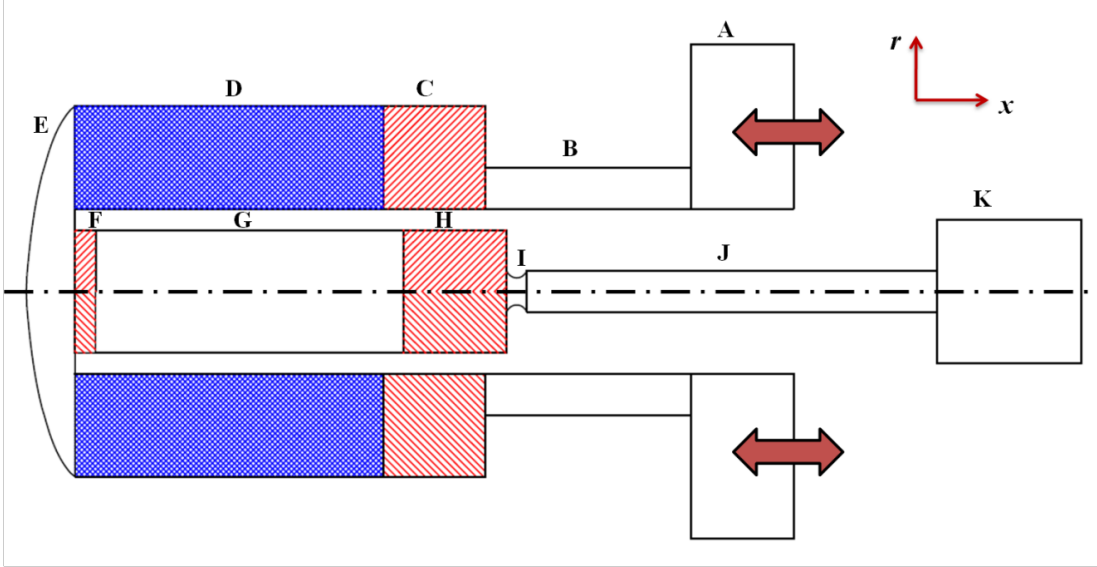

Figure 1: Schematic of the co-axial type OPTR geometry simulated

Table 1 summarizes the various dimensions of the problem geometry and the time-invariant boundary conditions in the simulations. The letters in the first column of Table 1 correspond to the components in figure 1. The mathematical boundary conditions at the various components' surfaces are explained in detail in a following section.

Table 1: Dimensions and boundary conditions of the simulated system

No.	Component	Radius (cm)	Length (cm)	Boundary condition along the outer wall
A	Compression Chamber	2.00	0.85	Adiabatic
B	Transfer Tube	0.31	10.1	h_c = 20 W/m-K
C	Aftercooler	0.80	2.00	T_w = 293 K
D	Regenerator	0.80	*	Adiabatic
E	Cold Head	-	0.50	Adiabatic
F	Cold Heat-Exchanger	0.50	0.50	Adiabatic

G	Pulse Tube	0.50	6.00	Adiabatic
H	Hot Heat-Exchanger	0.50	1.00	T_w = 293 K
I	Orifice Valve	0.0425	0.30	Adiabatic
J	Inertance Tube	0.085	25.00	Adiabatic
H	Compliance Volume	2.60	13.00	Adiabatic

* See Table 2 for values of regenerator length

3. MATHEMATICAL MODEL

The flow and heat transfer simulation model incorporates the fluid dynamic equations of conservation of mass (continuity equation), momentum (Navier-Stokes equations) and energy in the fluid domain. The various heat exchangers and the regenerator are modelled as porous media with the relevant solid properties of the regenerator and the heat exchanger materials. The current model incorporates non-equilibrium heat-transfer between the gas and the solid (porous media) phases. The mass, momentum and energy conservation equations [24-26] for the porous media regions are solved simultaneously with the gas phase equations for the OPTR as shown in figure 1.

3.1. Governing Equations

The conservation equations for the gas phase (helium) within the system undergoing periodic compression and expansion are given as follows:

$$\frac{\partial \rho}{\partial t} + \nabla \cdot (\rho \vec{u}) = 0 \tag{1}$$

$$\frac{\partial (\rho \vec{u})}{\partial t} + \nabla \cdot (\rho \vec{u}\vec{u}) = -\nabla p + \nabla \cdot \tau_{ij} \tag{2}$$

$$\frac{\partial (\varepsilon \rho h_0)}{\partial t} + \nabla \cdot (\varepsilon \rho \vec{u} h_0) = \nabla \cdot (k_f \nabla T_f) + \nabla (\varepsilon \vec{u} \tau_{ij}) + \varepsilon \frac{\partial p}{\partial t} + S_G \tag{3}$$

where ρ is the density, the vector $\boldsymbol{u}$ is the (r – z) velocity vector and the total energy h_0 is given by

$$h_0 = i + \frac{p}{\rho} + \frac{1}{2}\left(\vec{u}\right)^2 \tag{4}$$

and the gas-phase temperature is

$$T_f = \frac{1}{c}[h_0 - \frac{p}{\rho} - \frac{1}{2}\left(\vec{u}\right)^2] \tag{5}$$

The last term in the gas-phase energy equation is only applicable for the porous media zones (where the porosity ε is < 1.0):

$$S_G = \frac{h_p A(T_s - T_f)}{\varepsilon} \tag{6}$$

For the present simulations, ε is considered to be equal to 0.69 [20, 27] and in the rest of the domain (gas phase) ε has a value of 1.0. The value of the convective heat transfer coefficient h_p for the gas-solid interfaces is calculated from a heat transfer correlation for oscillating flow in regenerators developed by Tanaka *et al.* [23]. The equation is given by:

$$h_p = 0.33\frac{k_f}{4r_h}\left(\frac{8\rho_f r_h}{\mu}\frac{V_p \rho_r}{A_{sp}\varepsilon}\right)^{0.67} \tag{7}$$

where, r_h is the hydraulic diameter of the porous media material (in the case of wire mesh, it is the diameter of the wire), V_p is the volume of the solid material in the porous media, A_{sp} is the total surface area of the porous media, μ is the viscosity of the fluid and ρ_r is the ratio of the density of the fluid to the average density of the fluid in the porous media.

Helium (the operating refrigerant) is assumed to be an ideal gas and its viscosity and thermal conductivity are considered to be temperature-dependent. The temperature dependent properties were obtained from the NIST database [28]. The specific heat was kept constant since it does not vary considerably in the temperature range anticipated (i.e. 370 K – 90 K).

The mass and momentum equations for the porous media zones (Darcy-Forchheimer model) [12, 26] are given as follows:

$$\frac{\partial(\varepsilon\rho)}{\partial t}+\nabla\cdot(\varepsilon\rho\vec{u})=0 \tag{8}$$

$$\frac{\partial(\varepsilon\rho\vec{u})}{\partial t}+\nabla\cdot(\varepsilon\rho\vec{u}\vec{u})=-\varepsilon\nabla p+\nabla\cdot(\varepsilon\tau_{ij})-\frac{\varepsilon^2\mu}{\kappa}\vec{u}-\frac{\varepsilon^3 C_F\rho}{\sqrt{\kappa}}|\vec{u}|\vec{u} \tag{9}$$

The permeability κ is considered to be 1.06 $\times 10^{-10}$ m^2 [27] and the quadratic drag factor C_F has a value of 0.3917.

For the solid matrix, the energy equation is given by:

$$\frac{\partial(T_s)}{\partial t}=\nabla\cdot(\Gamma\nabla T_s)+S_P \tag{10}$$

$$S_P=\frac{h_p A(T_f-T_s)}{1-\varepsilon} \tag{11}$$

where Γ is the diffusivity of the solid porous media and A is the heat transfer area per unit volume. The value of Γ for copper (in the heat exchangers) is 1.17x10^{-4} m^2/s and that for stainless steel (in the regenerator) is 1.18x10^{-5} m^2/s.

In the heat exchangers (see figure 1) the solid phase material considered was copper. The density and specific heat of copper were assumed to be 8950 kg/m^3 and 380 J/kg-K respectively and temperature dependent thermal conductivity values were considered. Similarly for the regenerator (considered as porous media), stainless steel was considered as the solid phase material and the density and specific heat were assumed to be 7810 kg/m^3 and 460 J/kg-K respectively and the temperature dependent thermal conductivity values were considered.

3.2. Initial and Boundary Conditions

Initial Conditions: At the start of the simulation, the temperature in the system is assumed to be 300 K everywhere. The initial pressure in the system is set to 3.1 MPa.

Table 2 specifies the variable parameters in the three cases studied. In case 1, the length of the regenerator is maintained at 6.0 cm and the cold head (component E in figure 1) is assumed to be a gas filled region. In case 2, the length of the regenerator is increased to 7.5 cm. In case 3, the regenerator length is maintained at 6.0 cm, however the cold head is assumed to be a porous media region. In this porous media region, the porosity is assumed to be 0.8, the permeability 1×10^{-7} m^2 and the quadratic drag factor 0.15. The porous media material is assumed to be copper and non-equilibrium heat transfer is assumed between the gas and solid in this region too.

Table 2: List of the cases simulated

Case No.	Length of Regenerator (cm)	Cold Head Region
1.	6.00	Gas
2.	7.50	Gas
3.	6.00	Porous Media

Boundary Conditions: Table 1 (given earlier) specifies the flow and heat transfer boundary conditions used at the surface boundaries of the various components.

The piston is modeled as a reciprocating wall having an oscillatory velocity. The velocity of the piston is defined by the function, $u = A_0 \omega Cos\ (\omega t)$, where A_0 is the maximum displacement of the piston (4.511 mm) and ω is the angular frequency ($\omega = 2\pi f$) and f is the frequency of operation. For the current simulations (both cases), the frequency is set at 100 Hz. This value of frequency was chosen based on the need to study high frequency pulse tube cryocoolers for space applications.

3.3. Numerical Scheme

The numerical scheme for solving the governing equations is based on the finite volume approach. The continuity, momentum and energy equations are solved for the fluid as well as the porous media using a 2^{nd} order upwind scheme. The motion of the piston is captured by a moving grid scheme near the piston wall in the compression space (component A in figure 1). The re-meshing scheme used in the simulations is the Transfinite Interpolation scheme [26]. The various cases studied are tabulated in Table 2 below.

A 2^{nd} order Crank-Nicholson scheme (with a blending factor of 0.7) is used for the time derivatives in the continuity, momentum and energy equations. The Crank-Nicholson scheme provided a better prediction of the performance of the OPTR compared to the 1^{st} order Euler scheme [21]. The time-step size was determined by allowing 80 time-steps/cycle, which is sufficient to accurately simulate the problem. Based on the aforementioned criterion, the time-step used was found to be 1.25×10^{-4} s for the chosen frequency of 100 Hz. An overall convergence criterion is set for all the variables at 10^{-4} in the iterative implicit numerical solver. Mass conservation and energy conservation was verified in the simulations.

Grid convergence studies were performed at locations where high gradients (in velocity and temperature) were observed. A hybrid (structured-unstructured) grid system was employed in the simulations. Structured grid (non-uniform orthogonal mesh) was used in all components except the cold head region between the regenerator and the cold heat-exchanger and in the orifice valve region. Higher density un-structured triangular

mesh is used in the cold head and the orifice sections to accommodate the irregular shapes, the junction geometries and the high temperature and velocity gradients. A total of 6591 grid points were used for Case 1 and Case 3 in the simulations and a total of 7396 grid points were used for Case 2 (to account for the larger regenerator). The governing equations and the boundary conditions were solved using CFD-ACE+ [26].

4. RESULTS

Code validation studies were reported in an earlier study [21] by comparing the results to previously published data for an in-line IPTR system. In the following sub-sections, results for spatio-temporal evolution of the flow and temperature fields in the OPTR (figure 1) are presented.

4.1 Temporal Processes in the System

Figure 2 shows the temporal variation of the gas temperature at the exit of the cold heat-exchanger into the pulse tube (x = 1.0001 cm and r = 0.499 cm) for the first two cases (Table 2). The band-like trends visible in the plots are the cyclic structures of the temperature variation over the time period displayed (i.e. 0 – 22 sec). The simulations predict a better performance for case 1 (shorter regenerator section). This is indicated by the faster cool-down time and lower quasi steady-state temperature.

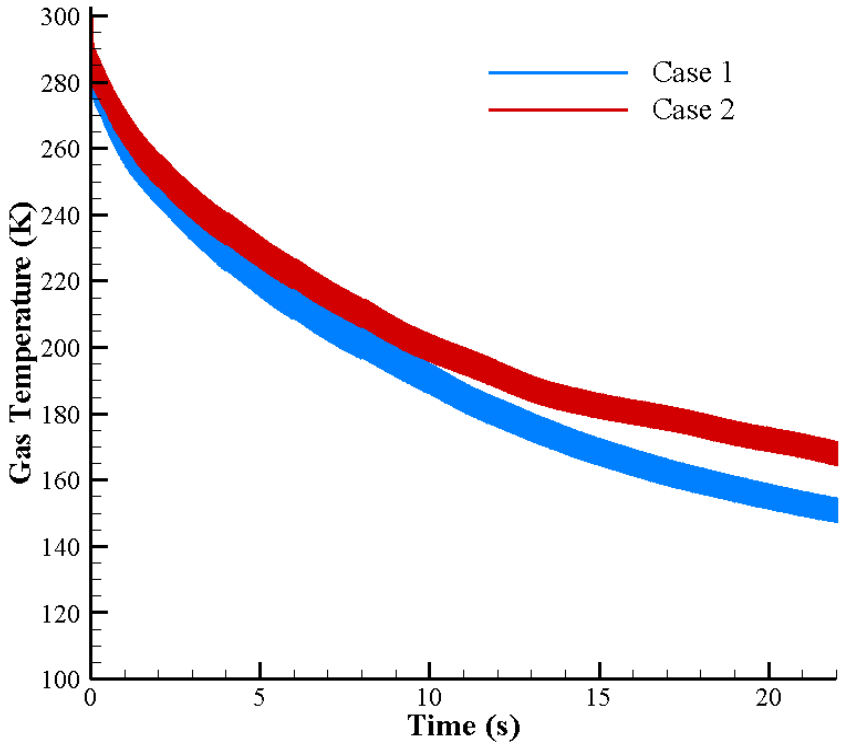

Figure 2: Comparison of the cool-down behaviour of the OPTR at the entrance to the pulse tube for cases 1 and 2

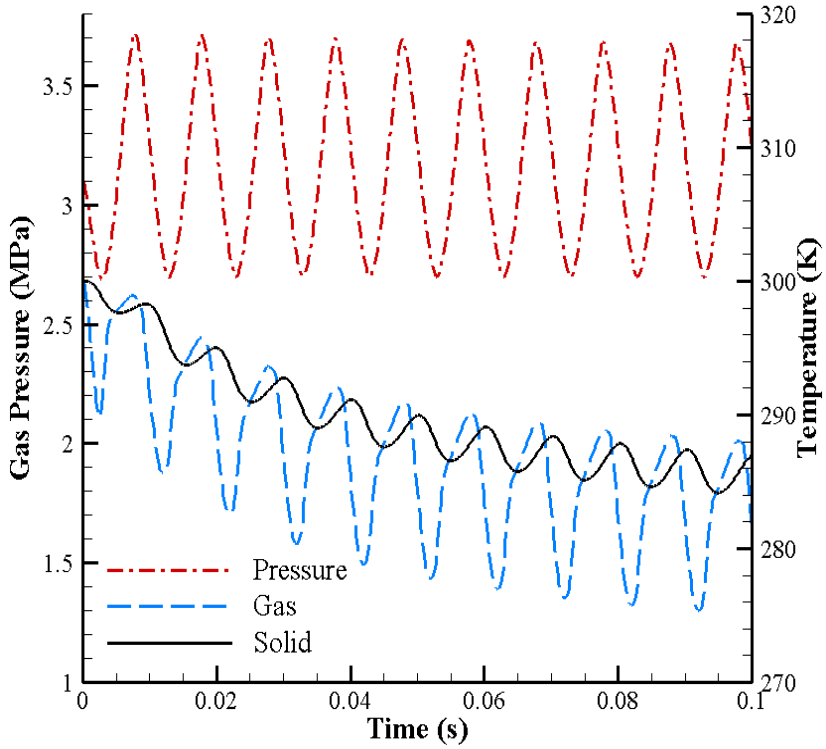

Figure 3: Pressure, gas temperature and solid temperature profiles at the start of the simulation for case 1

To illustrate and better visualise the band-like structures, the gas temperature, solid temperature and pressure are plotted in figure 3 in an expanded time scale at the start of the simulations (i.e. the first ten cycles) for case 1 (x = 10.001 mm and r = 4.99 mm). The cyclic nature of the temperature is clearly evident in figure 3. The solid (porous media) temperature follows a similar oscillatory trend as the gas temperature. The pressure exhibits a fairly sinusoidal pattern; however the gas temperature profile is distorted. The solid (porous media) temperature also appears to be near-sinusoidal. Due to the high density and thermal mass of the solid region, the solid temperature does not respond as rapidly to changes in the gas temperature profile. This results in the solid temperature that lags the gas temperature by a fixed phase angle. The authors have shown in an earlier study [21] that the phase angle difference between the gas and solid temperatures is dependent on the operating frequency of the system. At higher frequencies, the phase angle difference is much higher [21]. For case 1, the phase angle difference is 85.5^{o} and for case 2 the phase angle difference is 90^{o}.

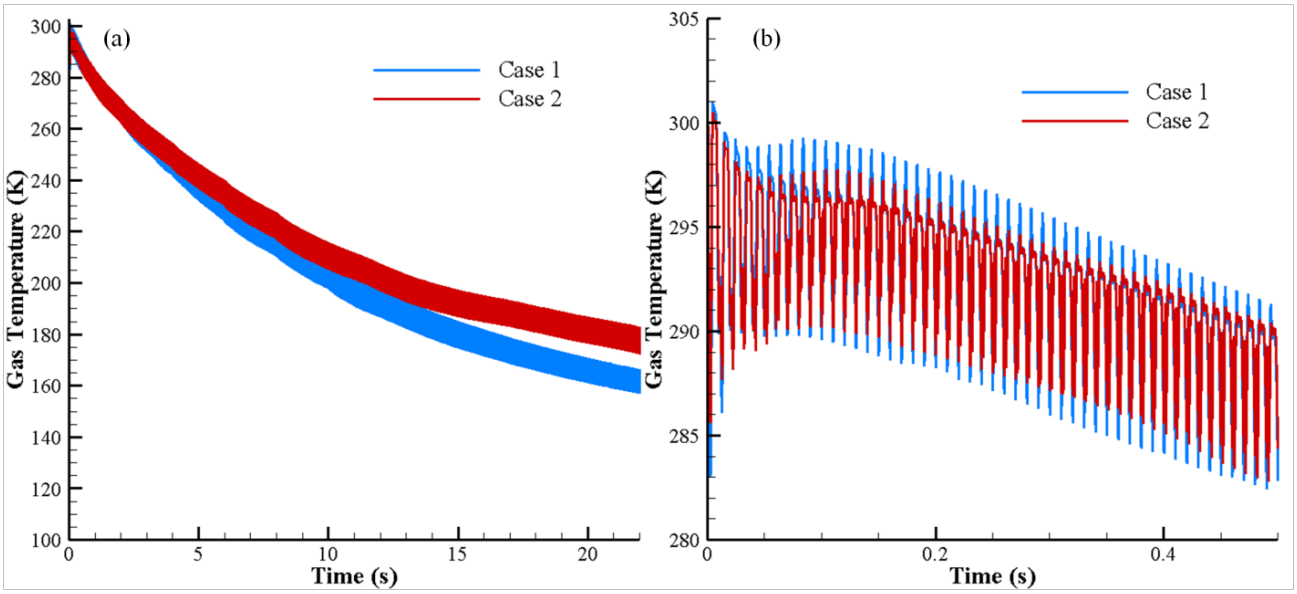

Figure 4: Temporal evolution of the gas temperature at the exit of the regenerator in case 1 and case 2 for (a) 0 - 22 sec and (b) early time (0 - 0.5 sec)

Figure 4a shows the temporal variation of the gas temperature at the exit of the regenerator (x = 0.499 cm, r = 1.200 cm) from 0 to 22 seconds of simulation time. The gas temperature at the exit of the regenerator follows a similar trend to the gas temperature evolution at the entrance to the pulse tube. However the gas temperature behaviour at the start of the simulation is interesting. Figure 4b shows the temporal evolution of the gas temperature at the start of the simulations for the first two cases at the exit of the regenerator. The gas temperature appears to rise at first before decreasing. This is an effect of the void volume/gas region in the cold head. During each cycle of the OPTR, the gas in the cold head is compressed and expanded. Thus there is a large variation in the gas temperature and this creates a temperature variation between the exit of the regenerator (cold end of the regenerator) and the cold end of the pulse tube. This large variation in gas temperature affects both the exit of the regenerator (figure 4b) and the entrance to the pulse tube. We find that this effect can be reduced by adding a porous substance in this region. Figure 5 shows the pressure variation at the exit of the regenerator (x = 0.499 cm, r = 1.200 cm) for the first two cases studied. As expected, the longer regenerator in case 2 results in a larger pressure drop as compared to case 1 (when the piston amplitude is kept constant).

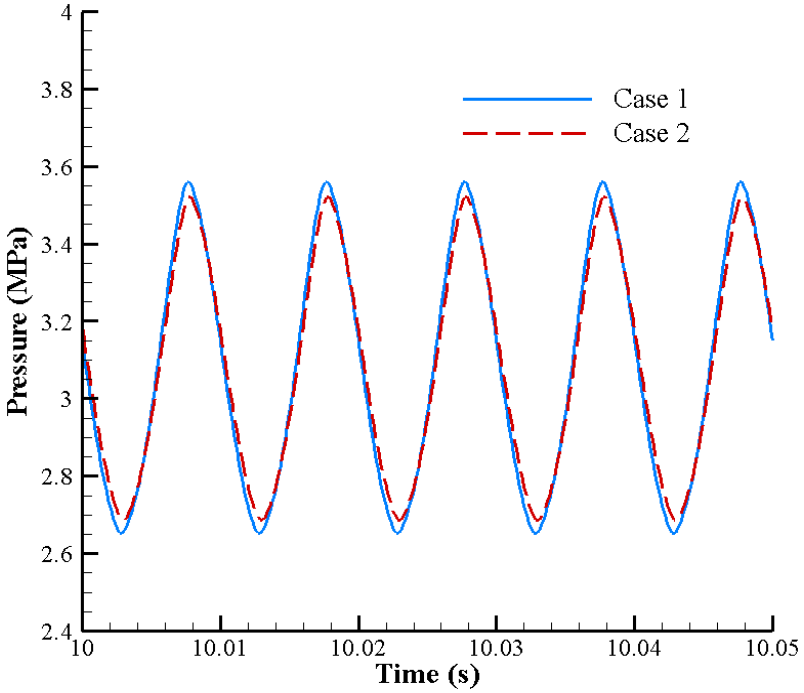

Figure 5: Comparison of the pressure variation at the exit of the regenerator for case 1 and case 2

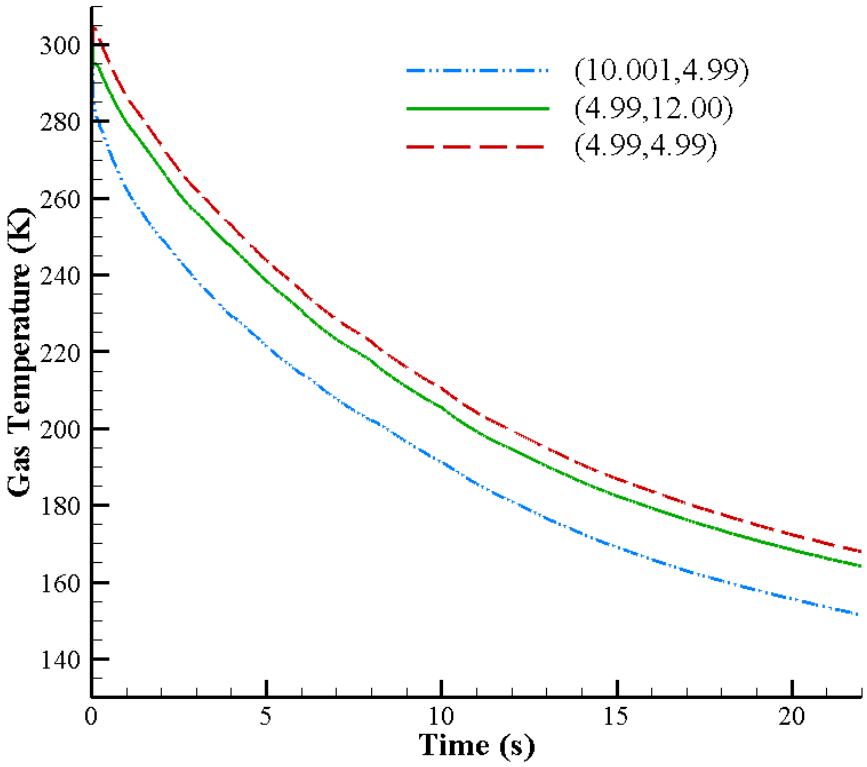

Figure 6: Comparison of temporal evolution of the cycle-averaged gas temperature at three locations in the OPTR (co-ordinates are in 'mm') for case 1

Figure 6 compares the cycle-averaged temperature at three locations in the OPTR. The three locations are the entrance to the pulse tube (x = 1.001 cm, r = 0.499 cm), the entrance to the cold heat-exchanger (x = 0.499 cm, r = 0.499 cm) and the exit of the regenerator (x = 0.499 cm, r = 1.200 cm). It is evident from the figure that the major cooling occurs at the entrance to the pulse tube and the exit of the regenerator. The void volume between the regenerator and the cold heat-exchanger (i.e. in the cold head) allows the temperature in the cold head to oscillate. The amplitude of these oscillations is on the order of ~ 15 – 20 K (see figure 7). Figure 7 compares oscillatory nature of the gas temperature in the three locations of the OPTR. The gas temperature is non-sinusoidal; however the temperature profiles at the entrance of the cold heat-exchanger (dashed red line) and the exit of the regenerator (solid green line) are distorted. This distortion can be explained by the nature of the flow in the cold head region. Due to the flow reversal (~ 180^{o}) when going from the regenerator to the pulse tube and vice versa and the fact that the cold head is a void gas filled region, the flow is highly rotational and there is mixing of cold and warm gas. This leads to the distorted cyclic temperature profiles.

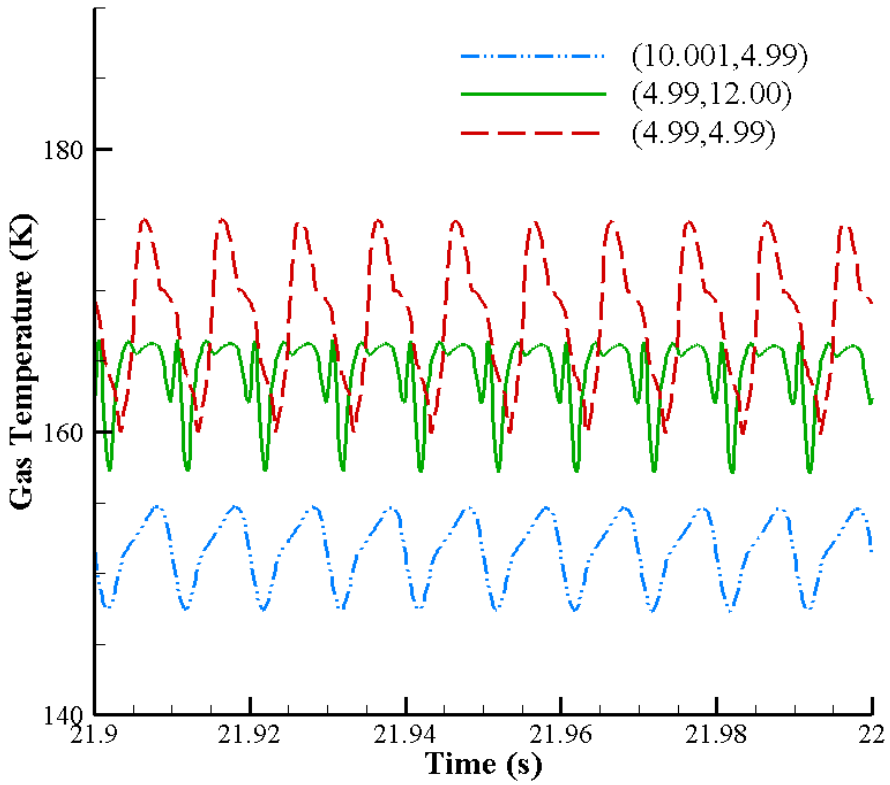

Figure 7: Cyclic variation of gas temperature at three locations in the cold end of the OPTR (co-ordinates in 'mm') for case 1

Porous-media Cold Head Region: To reduce the void volume in the cold head region of the OPTR, the cold head is filled with porous filler that is highly porous and highly permeable. The porous media conditions are described in an earlier section (see section 3.2 Initial Conditions). In addition to reducing the void volume, the porous media prevents excessive mixing of the flow in the cold head region of the OPTR. In this section we compare the transient performance of this system with a porous media cold head (case 3) with the transient performance of the OPTR system for case 1 and case 2.

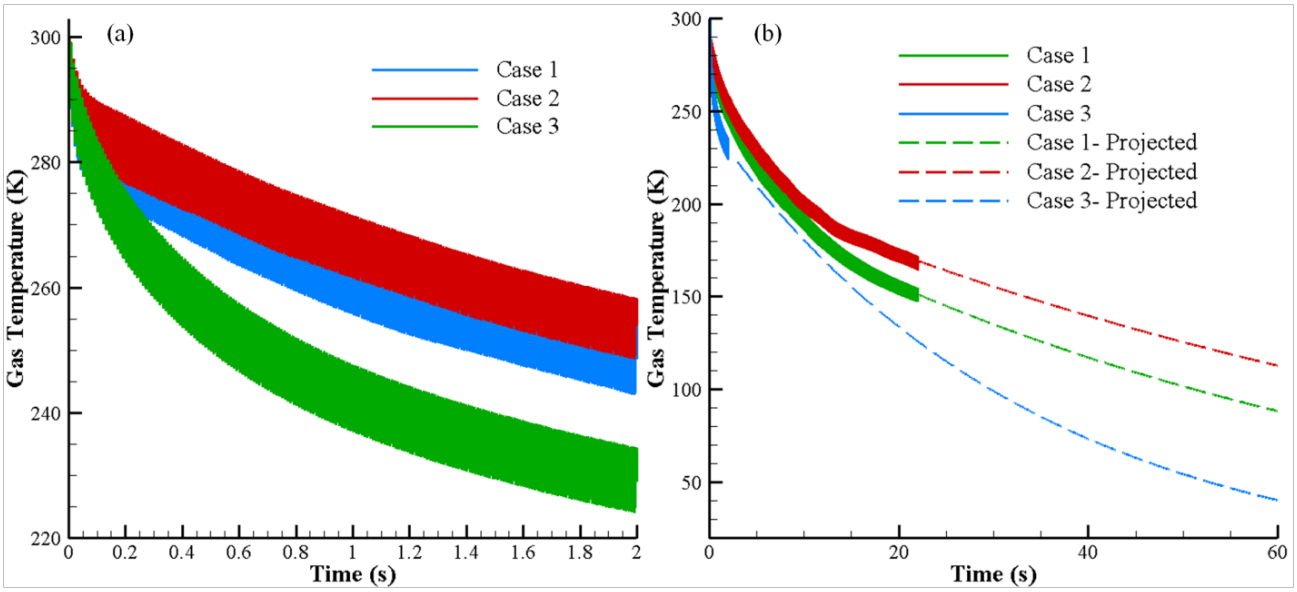

Figure 8: Comparison of the cool-down performance for the three cases studied (a) up to 2 seconds of simulated time and (b) predicted values

Figure 8a shows the cool-down behaviour (up to 2 seconds of simulation time) for the three cases studied. The performance of the OPTR system in the Case 3 configuration shows a remarkable improvement over the first two cases. The gas temperature in case 3 is lower than the gas temperature in case 1 by about 25 – 30 K. This clearly shows that the replacement of the void cold head region by a porous media region results in an improvement of the performance of the system. Figure 8b shows the predicted temperature evolution for the three cases simulated. The predictions (shown by dashed curves) are based on extrapolation of the simulated data based on an exponential decay curve.

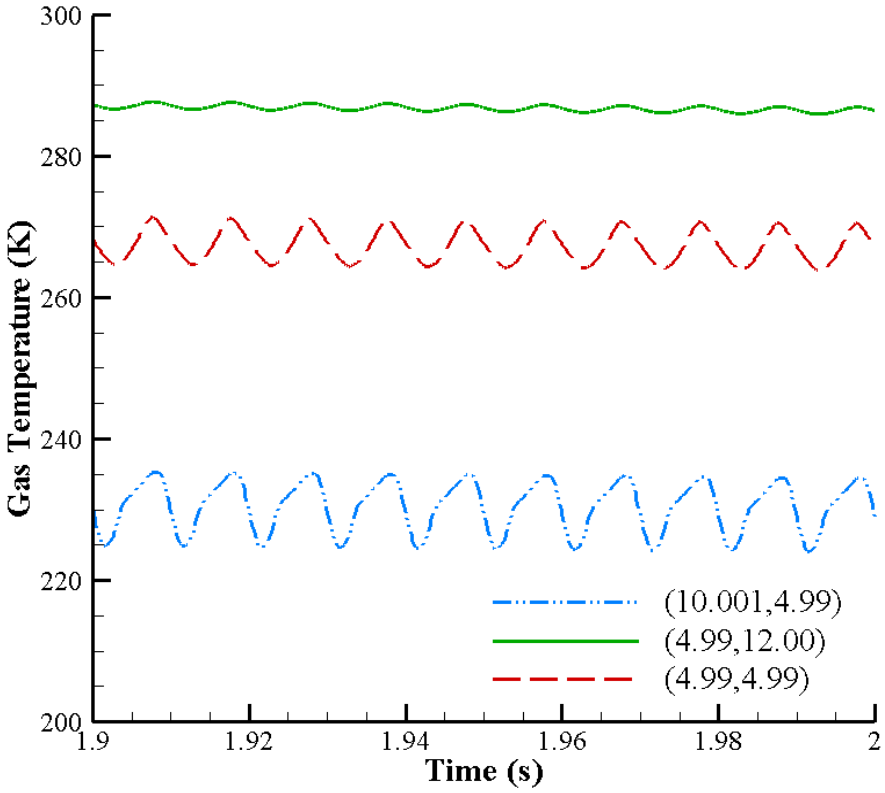

Figure 9: Comparison of gas temperature at three locations in the OPTR (co-ordinates in 'mm') for case 3

In figure 9 we compare the gas temperature profiles in three locations in the cold region of the OPTR system. These results are interesting as they show the effect that the porous media has on the gas oscillations. Firstly, the gas temperature oscillations are fairly small (~ 1 – 3 K) at the entrance to the cold heat-exchanger (dashed red line) and the exit of the regenerator (solid green line). The importance of the addition of the porous media is emphasized when comparing figures 7 and 9. The high temperature oscillations in the cold head and the exit of the regenerator (figure 7- case 1) degrade the performance of the OPTR system. The second effect of the porous media is reduction in the rotational nature of the flow in the cold head region. This is evident in the gas temperature profiles at the entrance to the cold heat-exchanger (dashed red line) and the

exit of the regenerator (solid green line). In figure 9, these lines have a fairly sinusoidal shape in addition to reduced amplitudes of oscillation. In comparison, in figure 7 the same temperature profiles are distorted and have high amplitudes of oscillation. These results (for case 3) are shown for a fairly short time (0 – 2 seconds of simulation time), but the nature and shape of the temperature profiles will not change as the simulations approach steady-periodic state.

4.2 Spatio-temporal Temperature and Velocity Variations

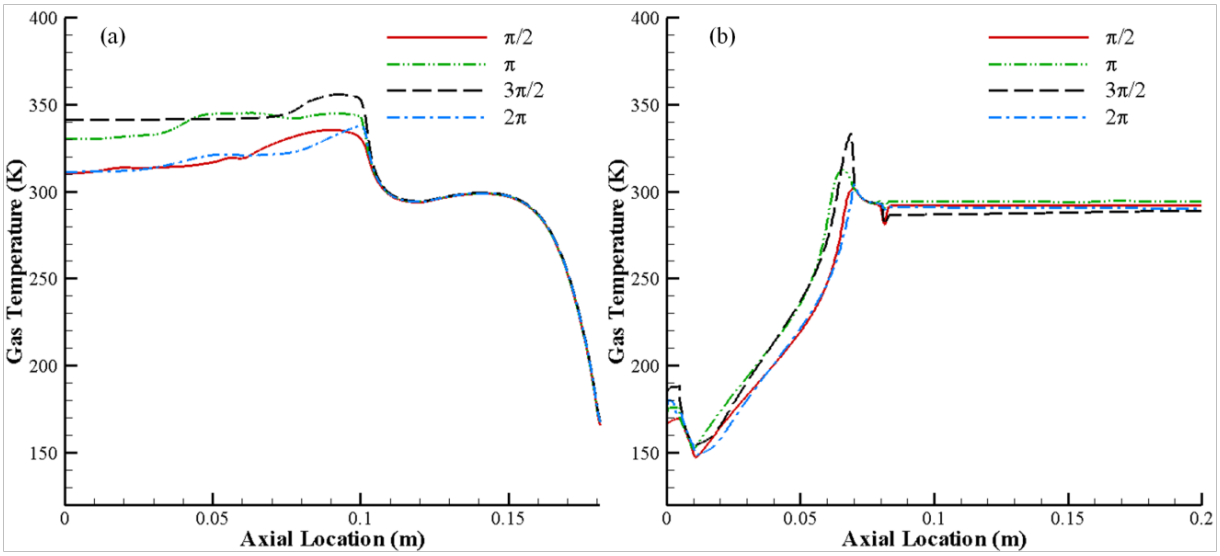

Figure 10: Gas Temperature in the various components of the OPTR at four instants in the 2201st cycle for case 1 (a) transfer tube to the regenerator (r = 0.0095 m) and (b) cold head to the inertance tube (r = 0.00 m)

In this sub-section, the spatial and temporal variations of the gas temperature and the axial velocity in the OPTR. Since the geometry is co-axial in nature, the results are shown along two different radii. In figure 10a the gas temperature is shown for the transfer tube, aftercooler and the regenerator (at r = 0.0095 m). Figure 10b shows the gas temperature variation from the cold head to the middle of the transfer tube (r = 0.00 m,

i.e. the axis of symmetry). Only part of the transfer tube is shown because the temperature variation in the entire transfer tube is small. The results are plotted at four instants in the 2201st cycle for case 1. The four plots in the figure show the temperature profiles at 0, (π/2), π and (3π/2) radians. The temperature in the transfer tube (x = 0 – 0.1 m in figure 10a) oscillates with a large amplitude due to the compression and expansion of the gas in the compression chamber. The temperature profile along the aftercooler and the regenerator (x = 0.1 – 0.181 m in figure 10a) and the two heat-exchangers in figure 10b (x = 0.005 – 0.01 m and x = 0.07 – 0.08 m) show negligible oscillation, i.e. ~ 1 – 2 K. In these regions the gas interacts with the porous media (via the non-equilibrium coupling of the energy equations) which has a high thermal mass and hence we observe a damped temperature oscillation. In the pulse tube, the temperature oscillations at the four instants (0, (π/2), π and (3π/2)) are similar and the temperature profile over the length of the pulse tube is linear. This trend in the pulse tube is encouraging as it suggests thermally stratified pulse tube and hence a lack of mixing in that region. As stated earlier, the gas temperature in the orifice, the inertance tube (x = 0.08 m onwards in figure 10b) and the compliance volume oscillates negligibly and its value lies between 285 and 295 K.

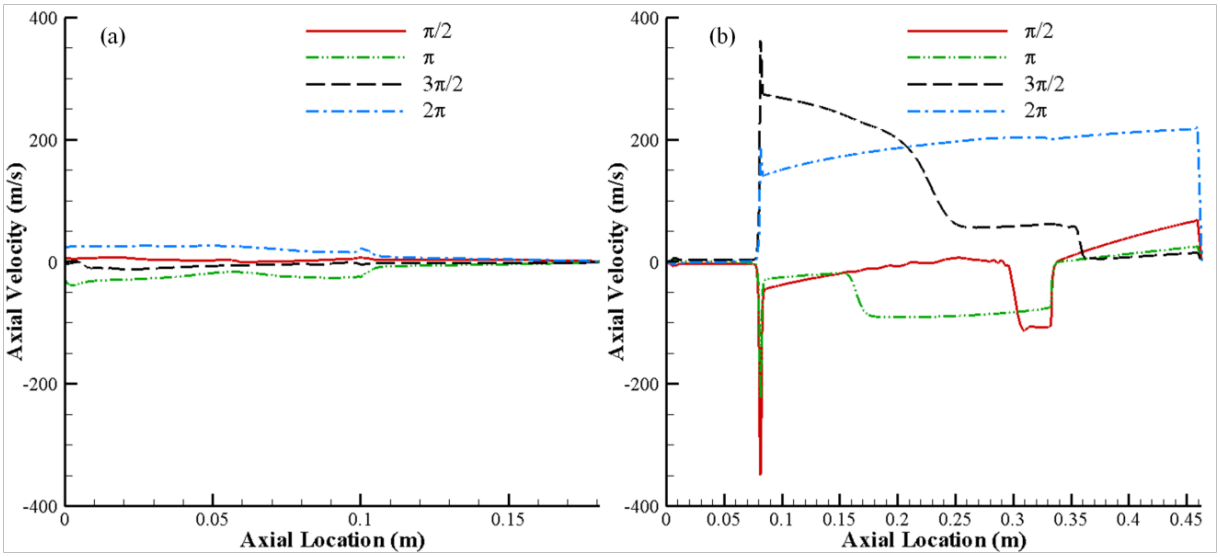

Figure 11: Axial component of velocity 'u_x' in the various components of the OPTR at four instants in the 2201st cycle for case 1 (a) transfer tube to the regenerator (r = 0.0095 m) and (b) cold head to the compliance volume (r = 0.00 m)

Figure 11a shows the variation in the axial velocity vector in the transfer tube, aftercooler and the regenerator (at r = 0.0095 m) and figure 10b shows the axial velocity variation from the cold head to the compliance volume (r = 0.00 m, i.e. the axis of symmetry). Similar to the plots for gas temperature in figures 10a and 10b, the results are plotted at four instants in the 2201st cycle for case 1. The four plots in the figure show the axial component of the velocity profiles at 0, (π/2), π and (3π/2) radians. The velocity oscillation in the middle of the cryocooler is negligible due to the presence of the porous media which restricts the flow. However, in the transfer tube (0 – 0.1 m), in the orifice (0.252 – 0.255 m) and in the inertance tube (figure 11b), the flow velocities are high due to their fairly small cross sectional area. The high velocities in the orifice region and the transfer tube can lead to jetting phenomena and non-uniformities in the flow in the pulse tube [29].

4.3 Steady-Periodic Multi-Dimensional Effects

In this section, we address the steady-periodic flow properties of the OPTR in the pulse tube region. Past studies by Antao and Farouk have shown the effects of operating frequency [21] and taper angle of the pulse tube [22] on the steady secondary streaming flow patterns in the pulse tube section of an OPTR. The generation of counter rotating bi-cellular streaming structures was proposed to aid in maintaining the buffer zone in the pulse tube region of the cryocooler [21],. Suppression of secondary streaming was demonstrated [22] by tapering the walls of the pulse tube. In this section, the results are shown for the 2201st cycle of operation for case 1. At this point in the simulation (i.e. ~ 22 sec) the system is assumed to have reached a quasi-steady periodic state and the variation of the fluid temperature from cycle to cycle is small.

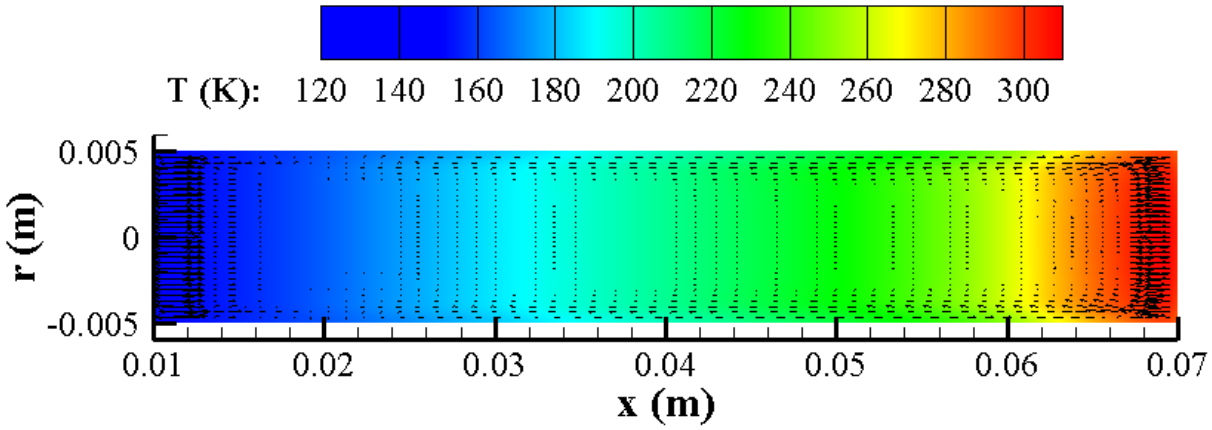

Figure 12: Cycle-averaged gas temperature and secondary streaming velocity vectors in the pulse tube region for case 1

Figure 12 shows the cycle-averaged temperature field and cycle-averaged velocity vectors in the pulse tube for case 1. The instantaneous flow field in the pulse tube is oscillatory; however the cycle-averaged flow field that is superimposed on the instantaneous flow shows remarkable organization. The maximum streaming velocity in

the axial direction is around 0.129 m/s and the minimum is also around - 0.131 m/s (the negative sign indicates flow in the negative x-direction), however the bulk of the streaming velocity is around 0.001 and -0.001 m/s. The maximum and minimum velocities in the radial direction are 0.0138 m/s and -0.0161 m/s. In figure 12, a velocity of 0.2 m/s corresponds to a vector of length 1.0 cm. It is clearly apparent from the figure that the maximum streaming velocities are at the ends of the pulse tube and along the boundaries of the boundary walls of the pulse tube. Figures 10b and 12 clearly demonstrate that the temperature gradient across the length of the pulse tube is fairly linear, thereby insulating the two ends. The radial temperature distribution in the pulse tube too is fairly uniform, except for a small region near the warm end (x = 0.058 – 0.064 m) where minor variations in the radial temperature distribution are visible. It can thus be concluded that for this case, the cycle-averaged secondary streaming velocity has no detrimental effect on the performance of the pulse tube region and the OPTR as a whole.

5. CONCLUSIONS

A computational fluid dynamic model was developed to predict the transport characteristics of a co-axial type OPTR for the first time. The co-axial OPTR simulated is the preferred configuration for space applications due to its compact nature and the high frequency of operation enables small component dimensions and fast cool-down times. A thermal non-equilibrium heat transfer model was used to simulate the temperature fields in the heat exchanger matrices. The solid temperature as predicted by the non-equilibrium heat transfer model shows a lag between the gas and solid temperatures which can be attributed to the high thermal mass of the solid media. The

simulations predict better cool-down times for the shorter regenerator due to the larger pressure drop observed in the longer regenerator. The void volume in the cold head region adversely affects the performance of the OPTR due to the large temperature oscillations in this region and the mixing of cold gas from the entrance of the pulse tube and the warm gas in the cold head. Another reason for the decreased performance is the low thermal conductivity of the gas (compared to a solid) which acts as a heat sink and further increases the cool-down time. A simple solution is the addition of a porous solid that causes low pressure drop (slots or mesh). In the simulations, this is modelled by a porous media region with high porosity and permeability and a low drag factor. At an early stage of the simulations (up to ~ 2 sec.), the addition of the porous media region in the cold head leads to a drastic improvement in the performance of the system and a faster cool-down time. The results also show the temperature and velocity distribution across the length of the OPTR. The effect of the high velocities and velocity fluctuations observed in the orifice and the inertance tube on the flow in the pulse tube region has not been investigated in this article but may provide important insights into the nature of flow in the pulse tube. Additional cycle-average gas temperature and velocity vectors in the pulse tube region indicate the presence of acoustic streaming in the pulse tube. However, the magnitude of the streaming velocity in most of the pulse tube is approximately two to three orders of magnitude smaller than the magnitude of the instantaneous velocity and hence streaming is predicted to have a small effect on the performance of the current OPTR system.

References:

[1] Radebaugh R. Pulse tube cryocoolers for cooling infrared sensors. San Diego, CA, USA: Society of Photo-Optical Instrumentation Engineers; 2000. p. 363-79.
[2] Marquardt ED, Radebaugh R. Pulse Tube Oxygen Liquefier. Adv Cryo Eng. 2000;45457-64.
[3] Gifford WE, Longsworth RC. Pulse-tube refrigeration. American Society of Mechanical Engineers -- Transactions -- Journal of Engineering for Industry Series B. 1964;86(3):264-8.
[4] Gifford WE, Longsworth RC. Pulse tube refrigeration progress. International Advances in Cryogenic Engineering: Plenum Press; 1965. p. 69-79.
[5] Radebaugh R. Review of pulse tube refrigeration. Proceedings of the 1989 Cryogenic Engineering Conference Part 2 (of 2), Jul 24 - 28 1989. Los Angeles, CA, United states: Plenum Pub. Corp.; 1990. p. 1191-205.
[6] Mikulin EI, Tarasov AA, Shkrebyonock MP. Low-Temperature Expansion Pulse Tubes. Colorado Springs, CO, USA: Plenum Press; 1984. p. 629-37.
[7] Radebaugh R, Zimmerman J, Smith DR, Louie B. A Comparison of three types of Pulse Tube Refrigerators: New methods for reaching 60 K. Cambridge, MA, Engl: Plenum Press; 1986. p. 779-89.
[8] Radebaugh R. Cryocoolers: the state of the art and recent developments. Journal of Physics: Condensed Matter. 2009;21(16):164219 (9 pp.).
[9] Radebaugh R, Garaway I, Veprik AM. Development of miniature, high frequency pulse tube cryocoolers. Infrared Technology and Applications XXXVI, 5-9 April 2010. USA: SPIE - The International Society for Optical Engineering; 2010. p. 76602J (14 pp.).
[10] Vanapalli S, Lewis M, Gan Z, Radebaugh R. 120 Hz pulse tube cryocooler for fast cooldown to 50 K. Applied Physics Letters. 2007;90(Compendex).
[11] Dang HZ, Wang LB, Wu YN, Yang KX, Shen WB. Development of a miniature coaxial pulse tube cryocooler for a space-borne infrared detector system. Infrared Technology and Applications XXXVI, 5-9 April 2010. USA: SPIE - The International Society for Optical Engineering; 2010. p. 76602Q (7 pp.).
[12] Ashwin TR, Narasimham GSVL, Jacob S. CFD analysis of high frequency miniature pulse tube refrigerators for space applications with thermal non-equilibrium model. Applied Thermal Engineering. 2010;30(2-3):152-66.
[13] Swift GW. Thermoacoustic Engines. J Acoust Soc America. 1988;84(4):1145 - 80.
[14] Swift GW. Thermoacoustics: A unifying perspective for some engines and refrigerators. Melville, NY: Acoustical Society of America; 2002.
[15] Ward B, Clark J, Swift GW. DeltaEC. 6.2 ed: Los Alamos National Labs; 2008.
[16] Rott N. Thermoacoustics. Adv Applied Mech. New York: Academic Press; 1980. p. 135.
[17] Lee JM, Kittel P, Timmerhaus KD, Radebaugh R. Steady Secondary Momentum and Enthalpy Streaming in the Pulse Tube Refrigerator. In: Ross RG, editor. International Cryocoolers Conference 8: Plenum Press; 1995.
[18] Lee JM. Steady Secondary Flows Generated by Periodic Compression and Expansion of an Ideal Gas in a Pulse Tube [Ph.D. Thesis]. Boulder: University of Colorado; 1997.
[19] Flake B, Razani A. Modeling pulse tube cryocoolers with CFD. 710 ed. USA: AIP; 2004. p. 1493-9.

[20] Cha JS, Ghiaasiaan SM, Desai PV, Harvey JP, Kirkconnell CS. Multi-dimensional flow effects in pulse tube refrigerators. Cryogenics. 2006;46(9):658-65.
[21] Antao D, Farouk B. Computational Fluid Dynamics Simulations of an Orifice type Pulse Tube Refrigerator: Effects of Operating Frequency. Cryogenics. 2011;51(4):192-201.
[22] Antao DS, Farouk B. Numerical Simulations of Transport Processes in a Pulse Tube Cryocooler: Effects of Taper Angle. International Journal of Heat and Mass Transfer. 2011;***In Press***.
[23] Tanaka M, Yamashita I, Chisaka F. Flow and heat transfer characteristics of Stirling engine regenerator in oscillating flow. Nippon Kikai Gakkai Ronbunshu, B Hen/Transactions of the Japan Society of Mechanical Engineers, Part B. 1989;55(516):2478-84.
[24] Wang CY, Gu WB, Liaw BY. Micro-macroscopic coupled modeling of batteries and fuel cells. I. Model development. Journal of the Electrochemical Society. 1998;145(Compendex):3407-17.
[25] Wang CY, Cheng P. Multiphase Flow and Heat Transfer in Porous Media. In: James P. Hartnett TFIJYIC, George AG, editors. Advances in Heat Transfer: Elsevier; 1997. p. 93-182, a, 3-96.
[26] ESI-CFD-Inc. CFD-ACE+ v2009.4 User Manual. Hunstville, AL: ESI Group; 2009.
[27] Harvey JP. Parametric study of Cryocooler Regenerator Performance [M.S. Thesis]. Atlanta, GA: Georgia Institute of Technology; 1999.
[28] NIST. NIST Standard Reference Database 12. NIST Thermodynamic and Transport Properties of Pure Fluids - NIST Pure Fluids. 5.0 ed: National Institute of Standards and Technology.
[29] Lewis MA, Taylor RP, Radebaugh R, Bradley PE. Effect of Component Geometry on Flow Nonuniformities in a Large Pulse Tube Cryocooler. In: Miller SD, Ross RG, editors. International Cryocooler Conference 16. Atlanta, GA: ICC Press; 2011. p. 227-36.

Cryogenic Helium Gas Circulation System for Advanced Characterization of Superconducting Cables and Other Devices

Sastry Pamidi*, Chul Han Kim[1], Jae-Ho Kim[2], Danny Crook[3], and Steinar Dale[4]

Center for Advanced Power Systems, Florida State University

2000 Levy Avenue

Tallahassee, FL 32310, U.S.A.

* Corresponding author, e-mail: pamidi@caps.fsu.edu, Tel: 1-850-644-1447 Fax: 1-850-644-7456
[1] email : ckim@caps.fsu.edu, Tel : 1-850-645-9179 Fax: 1-850-644-7456
[2] email : jaeho@caps.fsu.edu, Tel : 1-850-645-9179 Fax: 1-850-644-7456
[3] email : crook@caps.fsu.edu, Tel : 1-850-644-5089 Fax: 1-850-644-9462
[4] email : dale@caps.fsu.edu, Tel : 1-850-645-1183 Fax: 1-850-644-7456

* Corresponding author

ABSTRACT

A versatile cryogenic test bed, based on circulating cryogenic helium gas, has been designed, fabricated, and installed at the Florida State University Center for Advanced Power Systems (FSU-CAPS). The test bed is being used to understand the benefits of integrating the cryogenic systems of multiple superconducting power devices. The helium circulation system operates with four sets of cryocooler and heat exchanger combinations. The maximum operating pressure of the system is 2.1 MPa. The efficacy of helium circulation systems in cooling superconducting power devices is evaluated using a 30mlong simulated superconducting cable in a flexible cryostat. Experiments were conducted at various mass flow rates and a variety of heat load profiles. A 1-D thermal model was developed to understand the effect of the gas flow parameters on the thermal gradients across the cable. Experimental results closely paralleled the results from the thermal model.

Keywords: Cryogenic helium circulation system, superconductivity, power systems, 1-D thermal model.

1. Introduction

The majority of high temperature superconducting (HTS) power devices under development are cooled by liquid nitrogen [1, 2]. Liquid nitrogen offers several advantages including low cost and ease of availability. However, the operating temperature of liquid nitrogen cooled power devices is limited to the 63-77 K range. The critical current of HTS materials increases significantly as they are cooled to lower temperatures; critical current of commercial HTS increases by approximately 10% for each degree the temperatures is lowered. Hence, many HTS devices can operate at much higher currents if cooled to temperatures lower than 63 K. HTS devices get smaller in size and weight when operated at lower temperatures. Furthermore, a wider operating temperature range is ideal for devices that require large variations in operating current density because devices can be operated at the temperature most appropriate for a given current density. In some military applications, compact and lightweight power devices that offer a wide operating current density window are beneficial. Use of gaseous helium as a cryogen offers the required operational flexibility in such HTS power applications. Another benefit of helium gas is that there is no phase change in the coolant, allowing a much larger temperature gradient across the power device. There are, however, some drawbacks in using gaseous helium as the cooling medium such as lower heat capacity, inferior dielectric strength, and lower efficiency of commercial cryocoolers used for maintaining helium gas at cryogenic temperatures. One additional challenge in using

gaseous helium as the cryogenic medium is difficulty in achieving the required mass flow rates due to its low density. Even when operating temperature is not an issue, safety concerns in the event of a system breach posed by a distributed liquid cryogen circulation system render liquid nitrogen an unfavorable choice as a cryogen onboard a ship [3-5]. In order to take advantage of the flexibility in operating temperatures, compact size, and lower weight, smart power system and cryogenic designs are required to mitigate some of the challenges posed by gaseous helium as cryogen.

It has been envisioned that HTS power devices for naval and airborne applications be cooled by cryogenic gaseous helium [3-6]. Fitzpatrick et al. [3] and Kephart et al. [4] have described helium flow cryogen based HTS degaussing system for Navy ships. The optimum temperature for the degaussing system was reported to be 55 K, making it necessary to use a gaseous cryogen. The two gases suitable for the temperature range are helium and neon. Helium was chosen for the degaussing system application because it is less expensive and has higher thermal conductivity compared to neon. Haugan et al. [6] presented the benefits and analysis of compact and lightweight power transmission devices for specialized high power airborne applications operating at temperatures of 50-80 K. Circulating gaseous helium would be the cryogen of choice for the application.

Use of cryogenic gaseous helium circulation systems for cooling HTS power devices is relatively a new idea and requires some systematic investigations for system optimization and in order to understand the limitations of such systems. This paper describes the design of a versatile cryogenic helium gas circulation system designed and installed at the Florida State University Center for Advanced Power Systems (FSU-CAPS) for the purpose of understanding the helium gas based cryogenic system integration issues and to understand the benefits and limitations of using gaseous helium circulation systems in providing the cryogenic environment for HTS power devices. A 30 m flexible cryostat connected to the circulation system is used as a case study to understand the thermal management issues of power devices cooled by such a cryogenic gas circulation system. Experimental results are compared with that of a thermal model in order to gain a better understanding of the mass flow and temperature gradient issues of such a system.

2. Experimental

The helium gas circulation system installed at FSU-CAPS was designed with a nominal cooling capacity of 1.2 kW at 77 K obtained from a set of four Cryomech AL330 cryocooler units. Each cold head is attached to a heat exchanger, a Cryozone Noordenwind Cryofan, and a valve. The four individual gas flow paths form a parallel network and feed a single inlet and outlet stream. The nominal total cooling capacity of the set of four cryocoolers is approximately 700 W at 50 K. The installation of one valve for

each cold head and heat exchanger combination allows for flexible operation of the system with one, two, three or four cryocoolers at any given time. All of the cold heads, heat exchangers, cryogenic, and the plumbing system are enclosed in a vacuum vessel as shown in Figure. 1. The figure depicts a gas flow manifold designed to facilitate connecting multiple superconducting devices simultaneously. The manifold allows distribution of total gas flow among multiple devices. Each heat exchanger has multiple heaters installed on the sides to control the temperature gas stream. The Noordenwind Cryofans have controllable speeds between 8000 and 21000 rpm. The complete helium gas circulation system and the manifold are designed to operate in high pressures up to 2.1 MPa (300 psi). The mass flow rate and the gas stream temperature can be controlled by varying the cryofan speed, number of operating cryocooler and heat exchanger combinations, and heater settings. Test runs on the system under no load conditions required approximately 5 hours for the gas stream temperature to cool to 35 K from room temperature.

A 30 m Nexans Cryoflex® cryostat with inner and outer diameters of 39 mm 66 mm, respectively, was used in evaluating the performance of the circulation system. The cryostat was connected to one T-piece on each end to allow two additional ports for multiple heaters, thermal sensors, and pressure monitors. Figure 2 depicts a schematic of the flexible cryostat, end pieces, and a 30 m long simulated superconducting cable. The simulated cable consists of a flexible stainless steel former similar in size and thermal mass to that used for superconducting cables. Seven calibrated Cernox temperature sensors were mounted on the steel former along the length at 5-meter intervals. Many type-E thermocouples were also mounted on the cable former and the additional two Cernox sensors were used for reference temperature junctions for thermocouple readouts. Three sets of heaters made of Lakeshore Nichrome heater wire (NC-32) were installed in order to simulate various heat load profiles along the length of the cryostat. To simulate local point defects that mimic manufacturing or handling defects in superconducting tape material, several point heaters were installed. Similarly, several 5-meter-long sectional heaters were installed to represent joints in superconducting tape of sectional damage in the material. Two 15-meter-long heaters covered the entire length of the cryostat. Figure 2 shows the locations of the two spot heaters and three sectional heaters used in the present study. The point heaters are labeled as HPn, where n is the location number denoted in Figure 2. Each HPn has a resistance of 18 Ohms and extends 5 mm along cable length. Sectional heaters are labeled as HSn-m, where n-m shows the beginning and ending locations of the heaters. Each sectional heater extends 5 meter along the length and has a resistance of 110 Ohm. The 15-meter heater covers half of the cable length and has a resistance of 330 Ohm. In this study, thermal behavior of helium gas flow was mapped for spot heat loads of up to 20 W at 5 W intervals. Sectional heaters were used to produce a heat load of 20 W/m with 5 W/m intervals creating a total of up to 100 W for the 5-meter sectional heaters and 300 W for the 15-meter sectional heater.

3. Thermal Model

A 1-D thermal model for the cable system was developed in order to understand detailed thermal behavior of the cable cooled with cryogenic gaseous helium. The model used a cryostat identical in dimensions to the one used in the experiments. A 30-meter-long cryostat was used with inner and outer diameters of 39 mm 66 mm respectively. The cable former was modeled as a stainless steel tube with an outer diameter of 15.9 mm and covered the entire length of the cryostat. Figure 3 shows the heat flux within a finite section of the cable that was considered in this model. In this model calculation, several assumptions were made: helium flow around the cable is in a steady state with no radial temperature gradient; superconducting cable has thermal properties similar to that of stainless steel; helium gas in the cryostat at any given point inside the cryostat has the same temperature as cable; and heat leak from outside the cryostat is constant along the length of the cryostat. Both conductive and convective heat transfers for the cable were considered and the Nusselt number to estimate convective heat exchange between stainless steel former and helium gas flow was calculated using the equation for concentric annuli by Dirker and Meyer [6] which is slightly modified from the original equation of Dittus and Boelter [7].

From the heat balance in this finite section of the cable, the governing equations are;

for helium flow,

$$q_{\mathrm{O,\,j}} + q_{\mathrm{He,\,HT}} + q_{\mathrm{He,\,CV}} = \dot{m}_{\mathrm{He}} C_{\mathrm{p,He,\,j}} (T_{\mathrm{He,\,j+1}} - T_{\mathrm{He,\,j}}) \tag{1}$$

and for stainless steel cable

$$\begin{aligned} q_{\mathrm{SS,\,HT}} - q_{\mathrm{He,\,CV}} + q_{\mathrm{SS,\,CD,\,j}} - q_{\mathrm{SS,\,CD,\,j+1}} &= \rho_{\mathrm{SS}} A_{\mathrm{SS}} u_{\mathrm{He,\,j}} C_{\mathrm{p,SS,\,j}} (T_{\mathrm{SS,\,j+1}} - T_{\mathrm{SS,\,j}}) \\ &+ \rho_{\mathrm{He,\,in,\,j}} \pi D^{2}_{\mathrm{SS,\,in}} u_{\mathrm{He,\,j}} C_{\mathrm{p,He,\,in,\,j}} (T_{\mathrm{He,\,in,\,j+1}} - T_{\mathrm{He,\,in,\,j}}) \end{aligned} \tag{2}$$

where T, C_p and q are temperature, specific heat and heat conveyed in the calculation step, and $\rho, u, A, \dot{m}$ and D are density, velocity, cross-sectional area, mass flow rate and inner diameter, respectively. Subscripts of He and SS represent the properties of helium and stainless steel tube and the subscripts of CV and CD correspond to convective and conductive transfer of heat, respectively. Subscript o and HT stand for added heat leak from outside and from heater, respectively and subscripts in, j show the properties inside the stainless steel tube and j-th location in the calculation domain. Material properties of helium and stainless steel tube were assumed constant in the length of computational grid. Finally, conductive heat transfer through stainless steel cable can be based on the temperature gradient as

$$q_{\mathrm{SS,\,CD,\,j}} = -k_{\mathrm{SS}} A_{\mathrm{SS}} (T_{\mathrm{SS,\,j+1}} - T_{\mathrm{SS,\,j}}) / dx \tag{3}$$

where k is conductive heat transfer coefficient, and dx is the length of this calculation step.

For given inlet conditions, such as temperature, pressure and mass flow rate, properties of helium and stainless steel can be calculated. Equations (1)-(3) can be solved simultaneously with given heat from outside and heaters, and new temperature at downstream of dx can be found. By solving this progressively, temperature profile along a 30-m-long cable can be obtained and result will be discussed in next section.

4. Results and Discussion

The heat removing capacity of helium gas as a coolant can be characterized by the temperature increase of the flowing stream. In addition the heat capacity of helium and the temperature increase depends on several flow parameters such as pressure, velocity resulting in different flow regime, inlet temperature, etc. However, in a gas circulation system such the one used in this study mass flow rate is the most important parameter that affects the effectiveness of helium stream in cooling a superconducting device such as a cable. Mass flow rate is determined directly from pressure, velocity, cross sectional area, and temperature considered. In this study, the cooling capacity of helium was investigated at five different mass flow rates. Varying mass flow rates were achieved by changing the pressure and velocity of the flow. A detailed list of the set of experimental conditions investigated, in order of increasing mass flow rate, is listed in Table. 1.

Table 1. Conditions of helium flow at inlet of cryostat

	unit	Case A	Case B	Case C	Case D	Case E
Pressure, p	psi	154	187	177	155	177
Density, ρ	kg/m^3	10.8	12.5	11.8	10.4	11.8
Flow velocity, u	m/sec	0.17	0.21	0.33	0.50	0.50
Mass Flow rate, $\dot{m}$	**g/s**	**1.8**	**2.5**	**3.3**	**4.3**	**4.9**

Mass flow rate was evaluated using measured pressure, temperature and time delay between two locations when heat load was generated locally at an upstream location.

4.1. No Heater

With no heat load generated on the cable, the only heat load is the heat leak from outside the cryostat and from both end connectors. Figure 4 shows the temperature increment of helium gas as a function of mass flow rate. Generally, higher mass flow lowers the temperature increase due to a shorter time the gas

stays in the cryostat and the higher thermal mass circulating though the cryostat. Heat leak from outside can be estimated from the temperature increase over a 5- meter section of the cryostat. Figure 5 shows the calculated heat leak into the cryostat for various flow rates. As illustrated in Figure 5, there is a significantly larger heat load from the two ends of the cryostat. Furthermore, the inlet side of the cryostat is more influenced by the heat leak from outside the outlet side because the flow carries the heat leak into the system.

Excluding both of the ends, the center section of the cryostat experiences heat leak of about 1.0 W/m and the heat leak does not depend on the mass flow rate. This heat leak value is consistent with the product specification value of the manufacturer, Nexans, which is 1.5 W/m. The constant value of 1.7 W/m as an averaged heat leak was used for the model in calculating the temperature gradient along the cryostat. A comparison of the experimental results with that of the calculations for one mass flow rate is shown in Figure 6. A good agreement between the experimental results and those calculated from the model is observed except for the inlet section suggesting that the constant heat leak assumption along the cryostat is not valid for the initial few meters of the inlet side of the cryostat. The temperature of stainless steel cable former is slightly lower than helium stream throughout the cable because of the large thermal mass of the former and the delay in attaining thermal equilibrium with the helium gas. Temperature difference between the helium stream and the cable former gradually decreases as the mass flow rate increases.

4.2. Spot Heater (HP)

Local heat generated from a defective spot in the cable as mimicked by the point heaters is distributed to the helium gas flow as well as directly to cable. Depending on the nature of the heat source, heat distribution to helium and cable is arbitrary. In the simulated heater on stainless steel tube, temperature increase varies depending on the structure of heater wire winding. Figure 7 shows the two different temperature increments as a function of heat input for various mass flow rates. Temperature rises as more heat is added almost linearly for a given mass flow rate. As expected, the extent of temperature increase is smaller for larger mass flow rates. This is because at higher mass flow rates there is more thermal mass of helium moving through the cryostat. It is clearly illustrated in Figure 8 that the temperature increase per unit heat load generated decreases with increasing mass flow rate. As the mass flow rate increases, generated heat can be more efficiently removed by a larger thermal capacity of helium gas resulting in a smaller temperature increase.

Figure 9 presents a comparison of results from the experiment and the thermal model for a 10 W input at location 2 (HP2) with smallest mass flow rate (Case A). The discrepancy at the location of the

heater is probably due to the assumption of homogenous temperature in a radial direction. As the heater is attached to the cable former, the temperature distribution is non-uniform in the radial direction in the thin cross section of the cryostat at the location of the heater. As the homogeneity is established, the measured temperatures downstream of the heater matched well with calculations from the model.

4.3. Sectional Heater (HS)

Sectional heater generated heat load over a long section of the cryostat. Within the section, the heat load was uniform. Three different cases were studied; two with the 5- meter-long sectional heaters and one with a 15-meter section. Temperature increase at the downstream end of heater for the 5-meter sectional heaters is shown in Figure 10. Since heat is distributed uniformly and distribution of added heat to helium and cable is similar for both 5-meter sectional heaters, temperature increase varies linearly with heat load and the results of the two cases are identical. Figure 11 shows the comparison of the experimental results with those obtained from the model for the sectional heater HS3-4 at 10 W/m heat load. Discrepancy due to non-uniform radial distribution is not as large as in the case of the spot heater but is noticeable at the inlet section, probably due to the heat leak from outside the cryostat.

Temperature rise in the case of the 15-meter sectional heater is illustrated in Figure 12. Similar to 5-meter sectional heaters, temperature at the end of the heater location increases linearly as input heat increases, but decreases as mass flow rate increases. Figure 13 shows the agreement between the experimental and model calculation results for 10 W/m heat input on HS3-6.

Based on the result similarities among the three cases with sectional heaters, it would be useful to generalize the results for sectional heater cases. The extent of temperature increase per unit heat load as a function of mass flow rate is shown in Figure 14. The results suggest that as helium mass flow rate increases the extent of temperature increase of helium gas stream drops rather sharply. This result can be interpreted as a heat removal ratio of helium, r_q, which can be defined by

$$r_q = \frac{\dot{m}\, C_p\, \Delta T}{Q_{HT}} \tag{4}$$

where , C_p are mass flow rate and heat capacity of helium, respectively and Q_{HT} is total heat input added by heater. If helium carries all of the heat generated upstream, the ratio approaches 100%. For the cases considered, the heat removal ratio is plotted in Figure 15. The results suggest that at a mass flow rate of 4.4 g/s, the heat removal by helium gas flow is about 90 % of heat generated for up to 20 W/m in upstream section.

5. Conclusions

A versatile cryogenic helium gas circulation system was designed and installed to evaluate the utility of such a system in cooling HTS power devices that operate in the 50-80 K temperature range. Compact and lightweight power devices for airborne and naval applications benefit from a helium circulation system that can operate at variable temperatures. One of the advantages of a helium circulation system is the ease of system integration when multiple cryogenic devices need to be operated in close proximity, such as onboard a ship or an aircraft. The system was evaluated using a simulated cable in a 30-m-long cryostat. A 1-D thermal model was developed to measure the effect of helium gas flow parameters on the thermal gradients across the cryostat under a variety of heat load conditions. The results from the thermal model paralleled the experimental results, suggesting that the model is useful in cryogenic system design for superconducting power devices cooled by cryogenic gaseous helium flow. The results also suggest that mass flow is an important parameter that affects cooling efficacy in a helium circulation system. The cryogenic system investigated can remove heat loads up to 20 W/m without developing substantial temperature gradients. Currently available commercial gas flow systems are limited to flow rates of less than 10 g/s. Development of high capacity circulation fans and matching heat exchangers is necessary for using helium circulation systems for large superconducting devices.

Acknowledgement

The authors acknowledge financial support from The United States Office of Naval Research.

6. References

[1] Maguire J F, Yuan J, Romanosky W, Schmidt F, Soika R, Bratt S, Durand F, King C, McNamara J, Welsh TE. Progress and Status of a 2G HTS Power Cable to Be Installed in the Long Island Power Authority (LIPA) Grid. IEEE T Appl Supercon 2011; 21(3) 961–966.

[2] Honjo S, Mimura T, Kitoh Y, Noguchi Y, Masuda T, Yumura H, Watanabe M, Ikeuchi M, Yaguchi H, Hara T. Status of Superconducting Cable Demonstration Project in Japan. IEEE T Appl Supercon 2011; 21(3); 967–971.

[3] Fitzpatrick BK, Kephartl JT, Golda EM. Characterization of Gaseous Helium Flow Cryogen in a Flexible Cryostat for Naval Applications of High Temperature Superconductors. IEEE T Appl Supercon 2007; 17(2);1752–1755.

[4] Kephart J T, Fitzpatrick BK, Ferrara P, Pyryt M, Pienkos J, Golda EM. High Temperature Superconducting Degaussing From Feasibility Study to Fleet Adoption. IEEE T Appl Supercon 2011; 21(3); 2229–2232.

[5] Ferrara PJ, Uva MA, Nowlin J. Naval Ship-to-Shore High Temperature Superconducting Power Transmission Cable Feasibility. 2011; 21(3); 984 – 987.

[6] Haugan TJ, Long JD, Hampton LA, Barnes PN. Design of Compact, Lightweight Power Transmission Devices for Specialized High Power Applications. SAE Int. J. Aerosp. 2008; 1; 1088.

[7] Dirker J, Meyer JP. Convective Heat Transfer Coefficient in Concentric Annuli. Heat Transfer Eng 2005; 26(2); 38-44.

[8] Dittus FW, Boelter LMK. Publications on Engineering. 1930; 2; pp. 443.

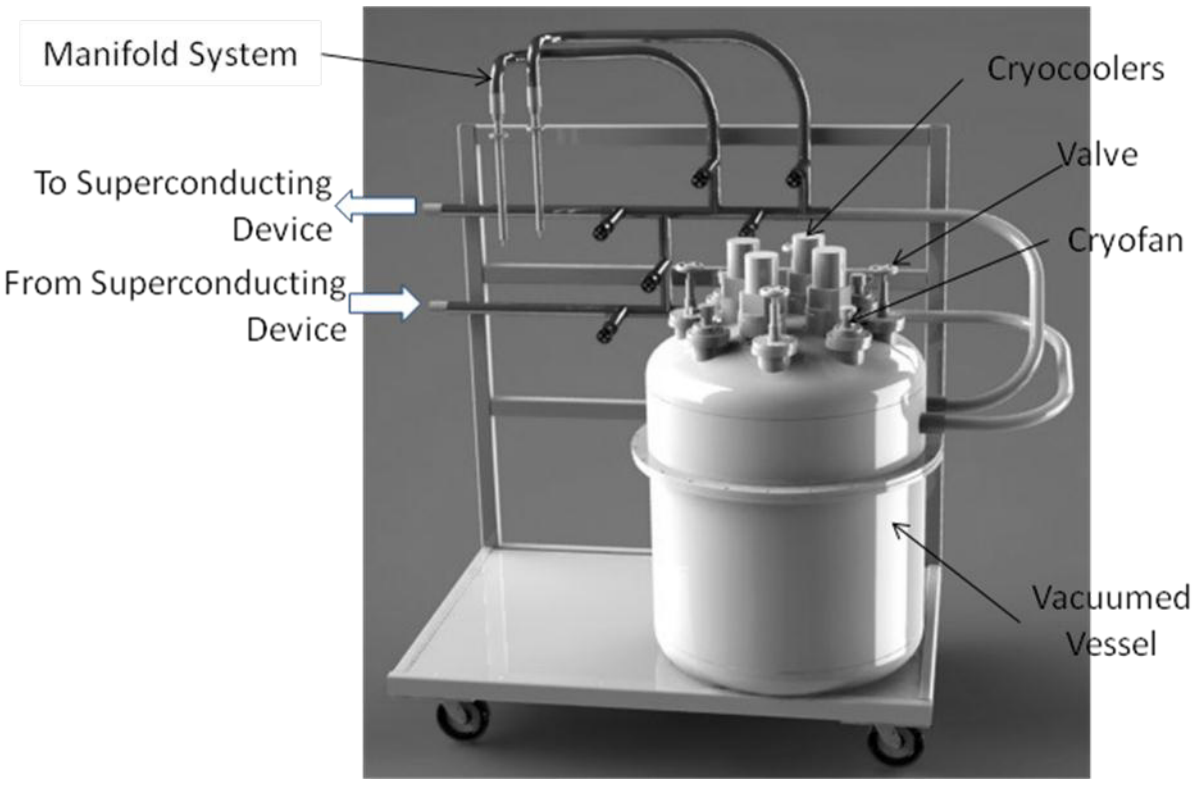

Figure 1. Schematic view of the cryogenic helium circulation system installed at the Florida State University Center for Advanced Power Systems.

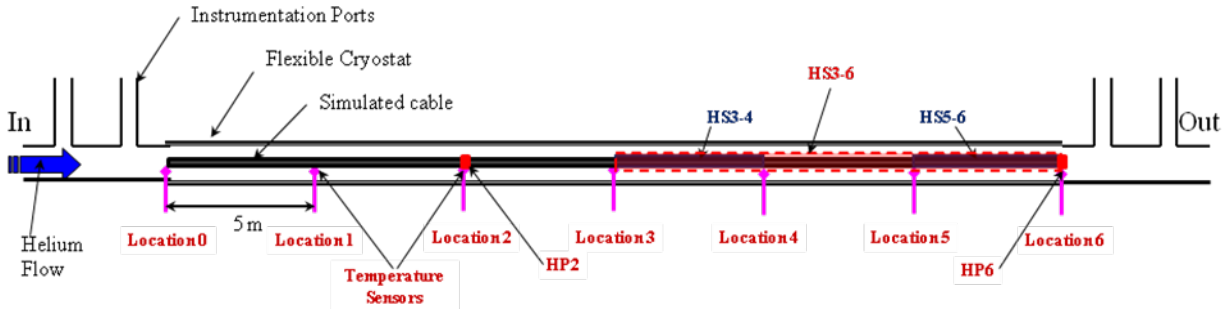

Figure 2. A schematic diagram of the 30-m flexible cryostat with simulated cable showing the location of various sensors and heaters.

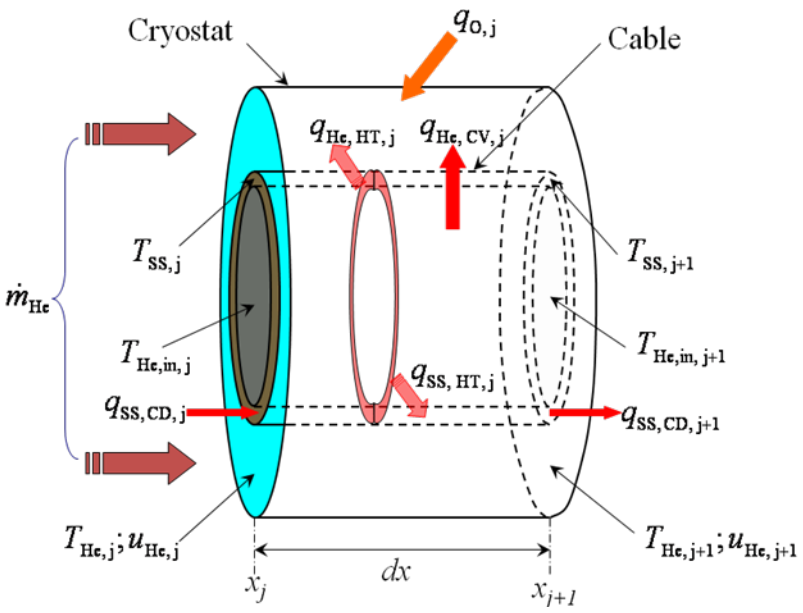

Figure 3. A representation of the thermal model of cryogenic helium gas cooled superconducting power cable.

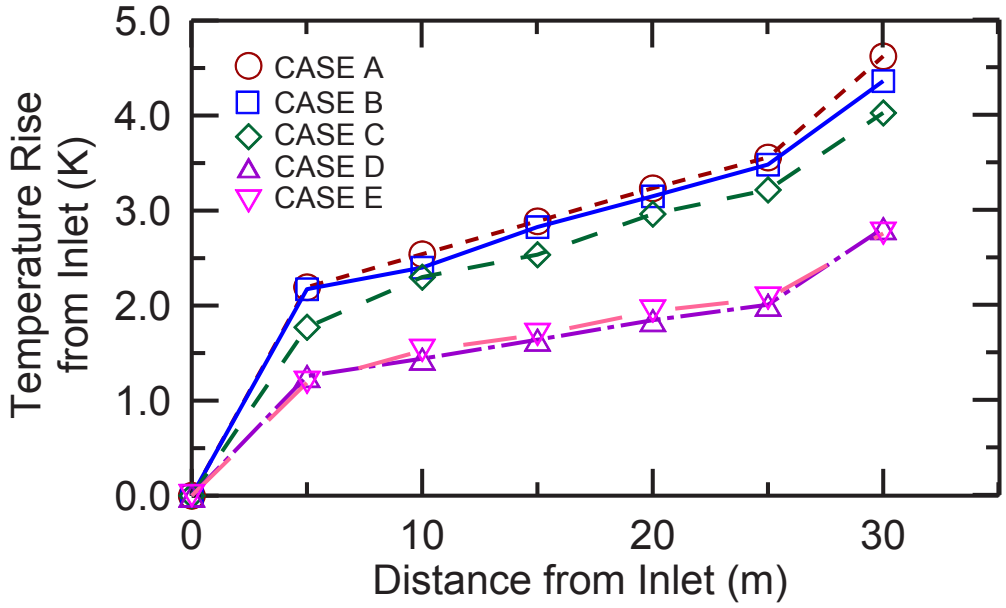

Figure 4. Temperature rise of helium gas flow along the length, for different mass flow rates, of the 30-m-long cryostat starting from the gas inlet.

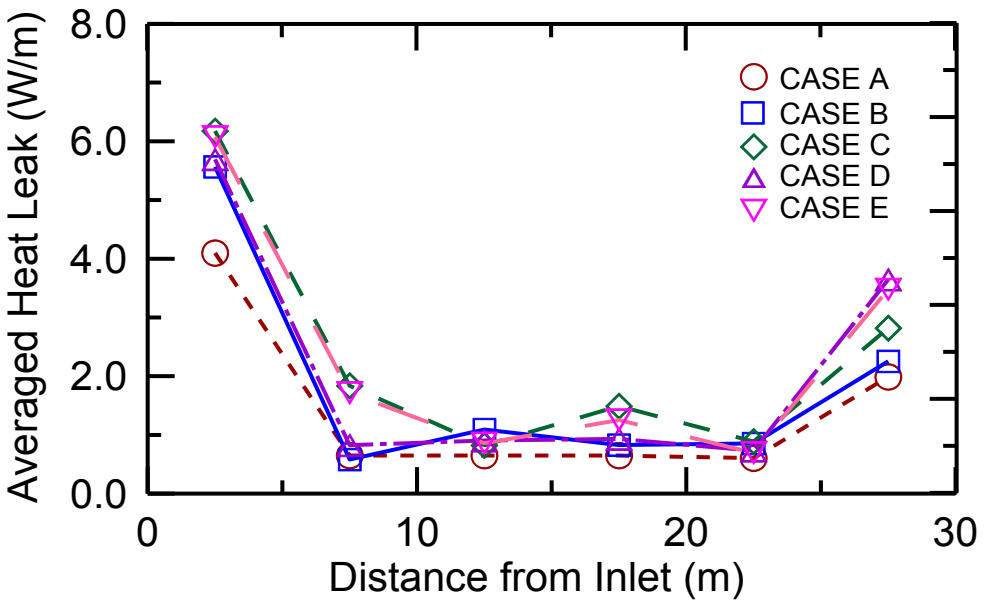

Figure. 5. Heat leak, averaged over each 5-meter section of the cable under no internal heat load.

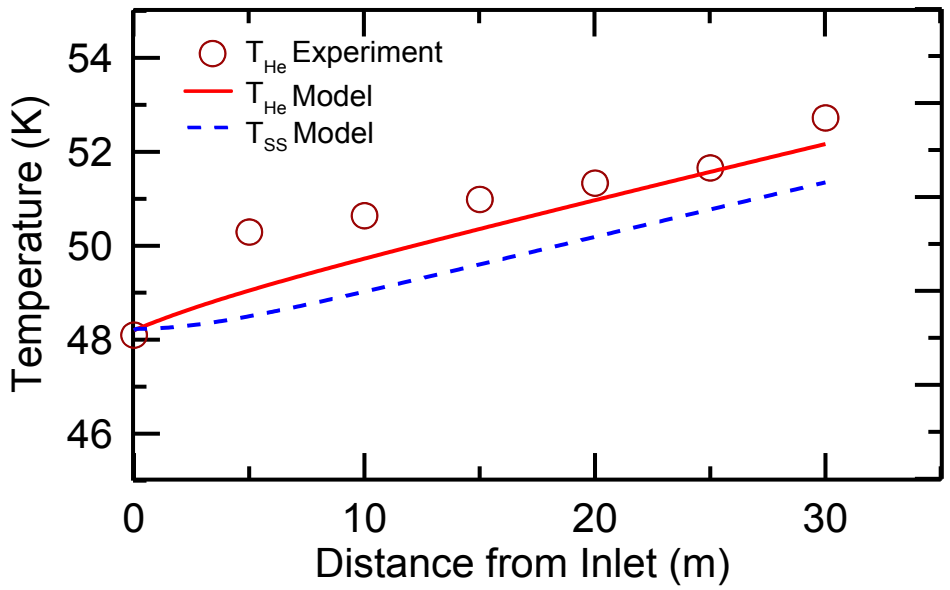

Figure 6. Comparison of the temperature profile of helium gas obtained from the model and measured experimentally under no internal heat load condition for case A.

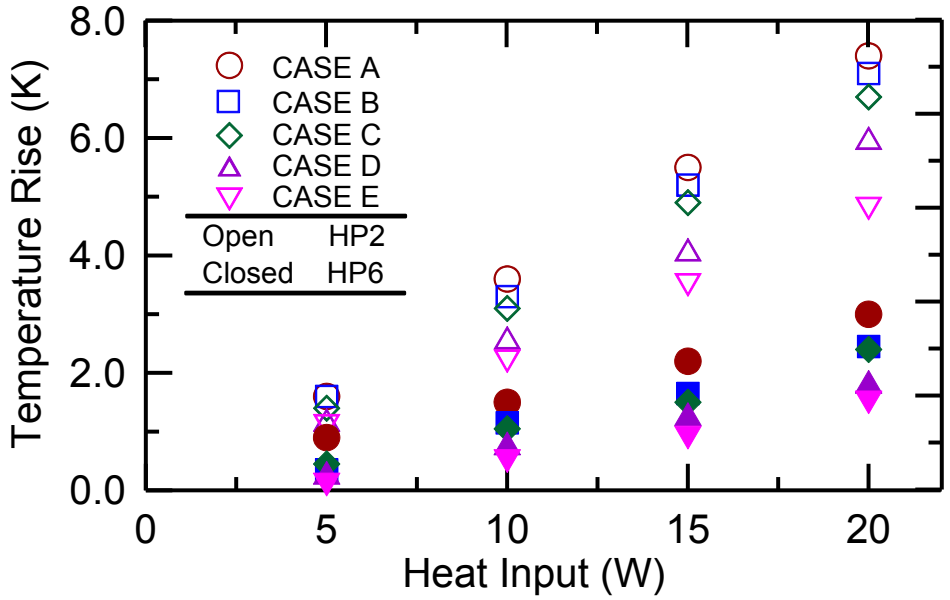

Figure 7. Temperature rise across the cryostat with varying heat load from point heater for several flow rates

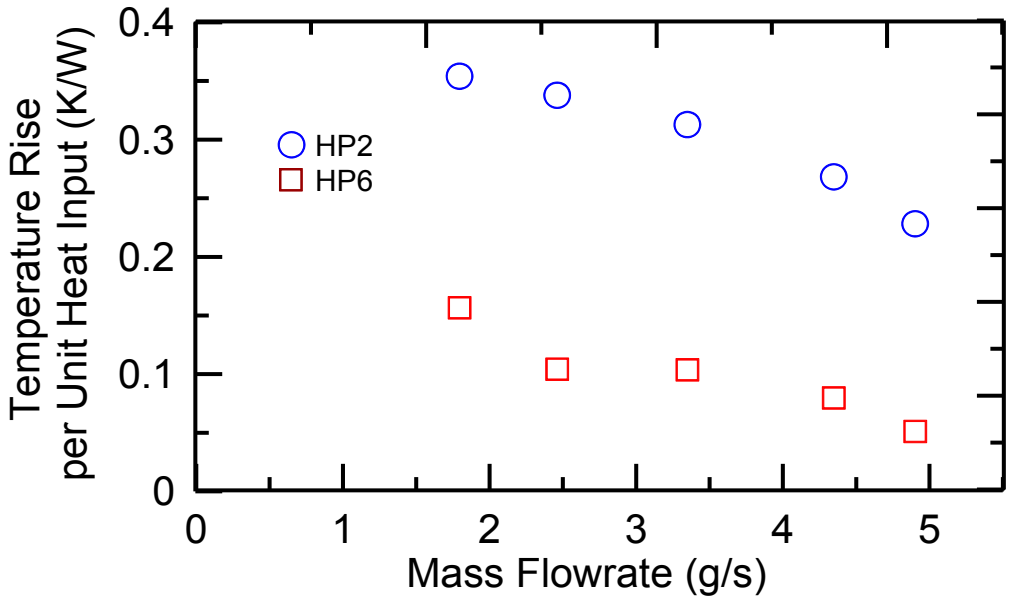

Figure 8. Temperature rise per unit heat load from point heater.

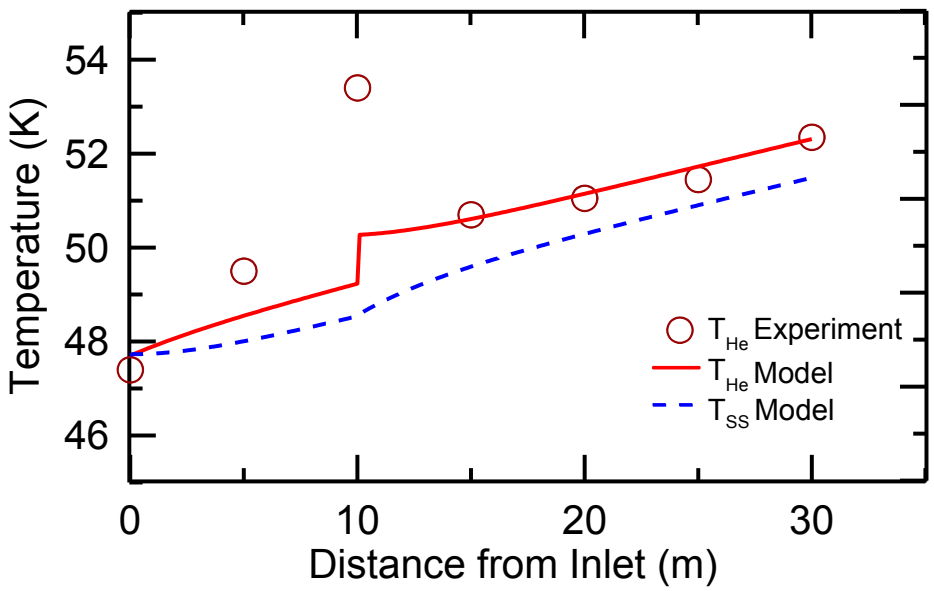

Figure 9. Comparison of experimental and thermal model results for 10 W heat load by HP2 at lowest mass flow rate (Case A).

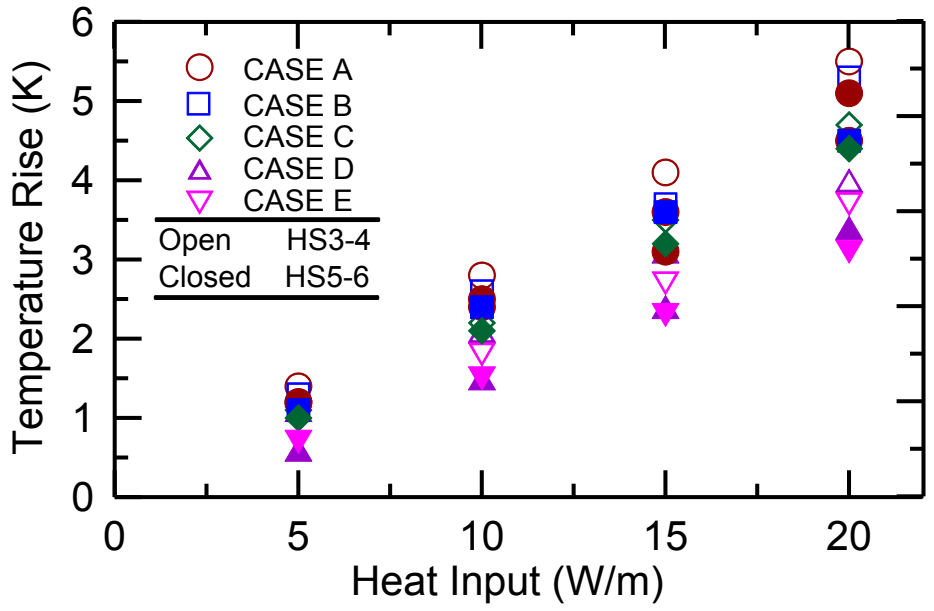

Fig.10. Temperature rise at the end of heater location with heat load from a 5-meter sectional heater.

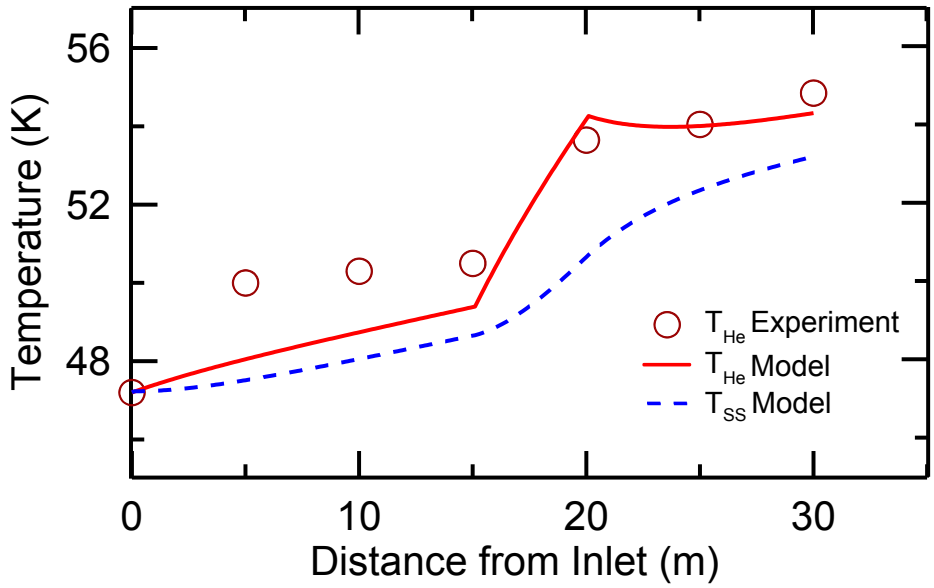

Fig. 11. Comparison of experimental and thermal model results of temperature profiles for 10 W/m heat load from HS3-4 heater for the lowest mass flow rate (Case A).

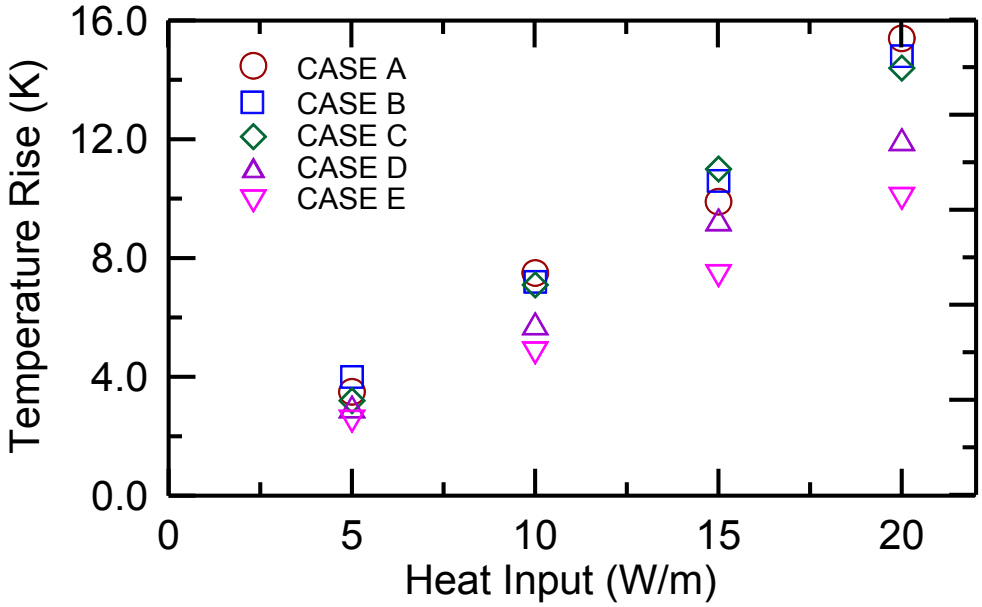

Figure 12. Temperature rise at the end of 15-meter sectional heater location as a function of heat load per meter.

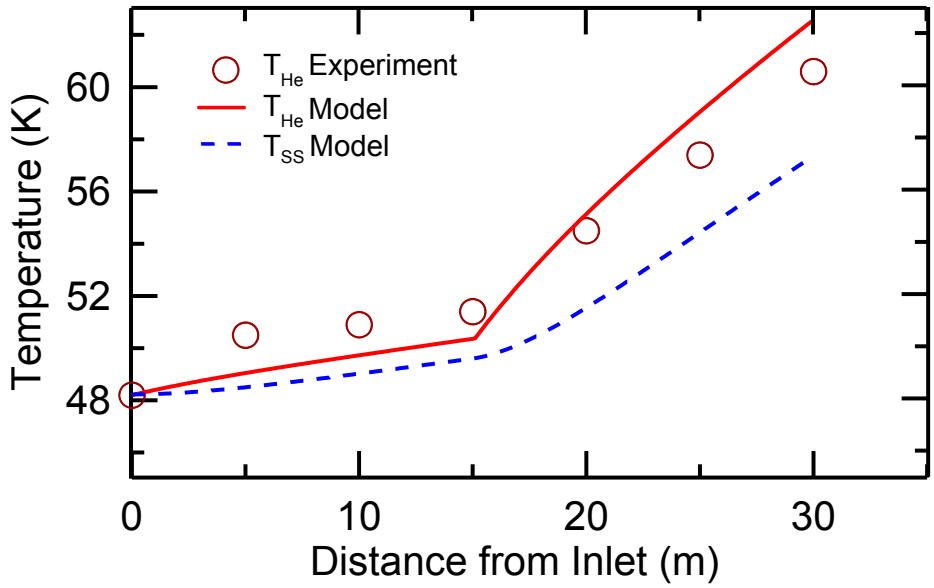

Figure 13. Comparison of experimental and thermal model results of temperature profiles for 10 W/m heat load from HS3-6 heater for the lowest mass flow rate (Case A).

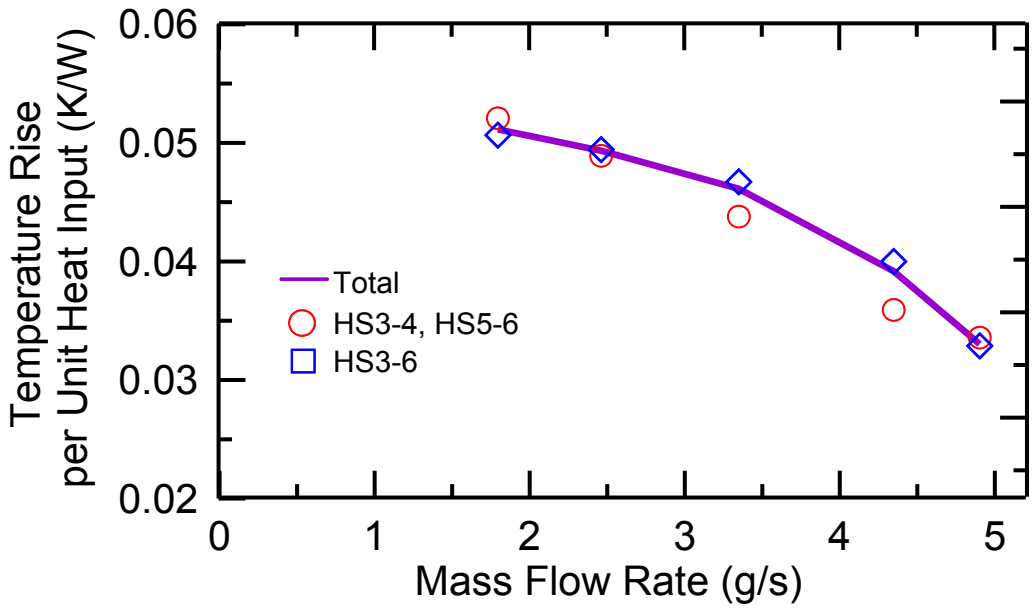

Figure 14. Temperature rise per unit heat input from the sectional heaters as a function of mass flow rate.

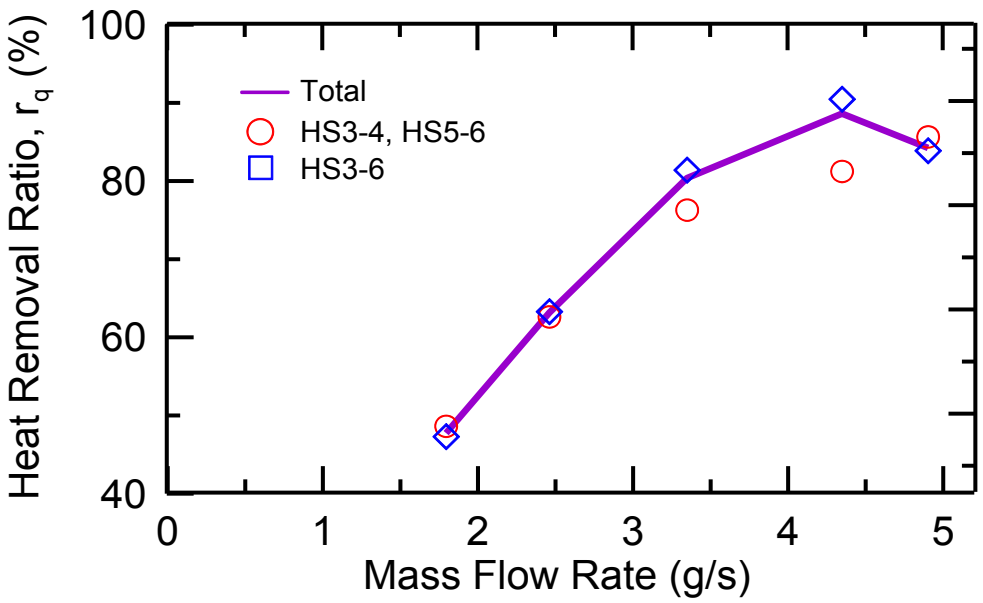

Figure 15. Heat removal ratio for helium gas circulation system as a function of mass flow rate.

Title:
A Standardized Cryogenic Temperature Sensor for Aerospace Applications

Authors:
S.S. Courts

Affiliation:
Lake Shore Cryotronics, Inc., Westerville, OH 43082, USA

Abstract:
The success of any aerospace mission depends upon the reliability of the discrete components comprising the instrument. To this end, many test standards have been developed to define test protocols and methods for the parts used in these missions. To date, no recognized MIL-type standard exists for cryogenic temperature sensors that are from room temperature to 20 K or below. The aerospace applications utilizing these sensors require the procuring entity to develop a specification which the sensor manufacturer uses to screen and qualify a single build lot for flight use. The individual applications often require only a small number of sensors with the end result being a relatively high cost and long delivery time. Over the past three decades, Lake Shore Cryotronics, Inc. has worked with numerous aerospace companies to supply cryogenic temperature sensors for various missions. The experience gained from this work has led to the development of a manufacturing and test protocol resulting in "off-the-shelf" cryogenic temperature sensors that should meet the requirements for many aerospace applications. Sensors will be available at the base part level with the ability to configure the delivered part with regard to package adapter, lead wire extensions, tolerance band, and calibration as appropriate or necessary for the application. The details of this manufacturing and test protocol are presented.

Keywords:
thermometer, cryogenic temperature sensor, Cernox^{TM} temperature sensor, diode temperature sensor, aerospace temperature sensor

1. Introduction

Space is a challenging environment for any electronic component. The component must operate in extreme cold, vacuum, and radiation. Just getting to space presents another set of obstacles with the component required to survive the mechanical shock, vibration, and acceleration of launch. In most cases, replacement of a failed component is virtually impossible once launched. Depending upon the criticality, failure of a single component can cause failure of a portion of, or an entire mission. For these reasons, any component chosen for use in space must meet rigorous screening and qualification requirements. For many types of components, the screening and qualification test protocol as well as the specific test method details have been developed and accepted by both by NASA and its subcontractors [1-5]. Given the cold temperatures of space, one glaring omission in the accepted standards is one for cryogenic temperature sensors. In the absence of an accepted test standard, every aerospace procurement for a cryogenic temperature sensor leads to an inefficient process resulting in an expensive, long lead time part. This article addresses the development of a standardized aerospace screening and qualification test protocol for the Lake Shore Cryotronics' model DT-670-SD diode temperature sensor (DTS) with the end goal of making available a commercial off-the-shelf sensor (COTS) suitable for aerospace use [6].

2. Background

Lake Shore Cryotronics has supplied cryogenic temperature sensors for aerospace applications for over thirty years. During this history, no recognized DoD or NASA standard has existed that addresses the required screening and qualification test protocols when the sensors are intended for flight applications. While the sensor types may sound generic such as "resistive" temperature detectors (RTDs) or "diode" temperature sensors, they do not fit neatly into the general categories as defined by MIL standards or by NASA standards. Complications arise when procurement of these sensors is based upon the general term of resistor or diode. As an example, for semiconductor devices, different tests are called for in the DoD MIL-PRF-19500 and NASA EEE-INST-002 depending upon whether the device is a diode or transistor. However, "diode" temperature sensors are often small signal transistors operated in a diode manner with the junction measured from base to collector or base-emitter to collector making it unclear as to which, if either, test sequence should be followed. Assuming the diode test sequence is chosen, the DTS is not really being used as a diode per se, so many of the MIL-PRF-19500 specified tests such as intermittent life are likely unwarranted. The maximum current for DTSs is limited by the manufacturer and is typically smaller than would be expected for a true diode rendering other tests useless (e.g. Burn-In when performed at 10 μA is unlikely to stress the device as intended) or impossible (e.g. Thermal Impedance where the necessary ΔT cannot be achieved to determine proper attachment).

Lacking a proper standard to reference, every cryogenic temperature sensor procurement for aerospace application results in the customer development of a unique source control document (SCD). The process is entirely inefficient as it requires time on the customer's part to create the SCD, and time on the manufacturer's part to review the SCD. If the test specifications are confusing (i.e. they don't readily apply to the part in question) then long conferences are required between the customer and manufacturer. Typically multiple drafts of the SCD are created during the customer-manufacturer review before the final version is agreed upon. For a given part, quite often the points of discussion and disagreement are the same points for every SCD. From a manufacturing perspective, reviewing a unique SCD for each customer for the same physical part is inefficient and undesirable. It's often the case that the number of needed temperature sensors for an application is relatively small. Many of the screening steps are performed in-process which requires starting a new production lot specific to that order which dramatically increases the delivery time. Beyond a lead time issue, the process is engineering-time intensive as it also requires customer specific documentation in the form of a process identification document (PID) or traveler, as well as a final report detailing the manufacturing and testing results. This leads to very expensive parts manufactured in small quantities with long lead times. The process is disruptive to standard manufacturing as the aerospace orders routinely have DO or DX ratings moving them ahead of commercial orders already in process. Compounding the inefficiency of the process is the confidential treatment of each customer's SCD. This means that any extra sensors remaining for one customer's procurement are precluded from delivery to a different customer (including NASA) even if two separate customer's specifications for the part are nearly identical. The ideal solution to address these issues is the development of a screening and qualification protocol that is acceptable to NASA and its subcontractors.

3. Choosing a Sensor for Standardization

While many properties can be used for measuring cryogenic temperature, by far the two most common types of cryogenic thermometers used in space applications are based on resistance or on the voltage drop across a p-n (diode) junction. Diode temperature sensors have many advantages over most resistive temperature sensors and are often the best choice for an aerospace application. Compared to most resistance temperature detectors (RTDs), diodes offer a wider temperature range of use, better interchangeability, reduced instrumentation requirements, and greater flexibility in packaging. For a DTS the forward voltage drop at constant current is a strong function of temperature with the signal increasing as temperature decreases. The typical voltage and sensitivity response curves for the Lake Shore Model DT-670-SD silicon diode temperature sensor are shown in Figures 1 and 2 [7]. Silicon based DTSs in particular are quite uniform and a single model can be interchangeable to within a few kelvins over their

1.4 K to 500 K operating temperature range. Even silicon based DTSs across models and manufacturers have a similar response curve, which allows a single instrumentation design to be used across many DTS models with little to no revision. Since the measurement is performed at constant current, only a single valued constant current source and a voltmeter are needed for instrumentation. This instrumentation is much simpler than for negative temperature coefficient (NTC) resistors or thermistors where the extreme increase in resistance requires scaling current to maintain a reasonable excitation level to avoid self-heating. These advantages of diodes over NTC resistors led to the decision to target a screening and qualification protocol for the Lake Shore Model DT-670-SD DTS. A second motivation for the sensor choice is that both the Model DT-670-SD and its predecessor, the Model DT-470-SD, have been used on numerous aerospace missions dating back over twenty years.

The Model DT-670-SD DTS characteristics and package make it well suited for aerospace applications. While Figures 1 and 2 give the voltage response and sensitivity as a function of temperature for the Model DT-670-SD, Figure 3 shows a schematic of the DT-670-SD package with dimensions, and Figure 4 shows a cutaway side view of the sensor package. The package is a flat, hermetically sealed package consisting of a sapphire base with alumina body and top. The overall dimensions are 1.9 mm wide × 3.2 mm long × 1.0 mm high with a small total mass of 37 mg. The diode chip is eutectically (gold-silicon) bonded to a metallized pad within the cavity of the package directly on top of the sapphire substrate base. A gold wire bond is made from the top of the die chip to a bond pad on the internal of the package to finish the electrical connection and the lid is soldered into place using gold-germanium solder to form a hermetic seal. Feedthrough traces connect the interior cavity to the exterior of the package where Kovar® leads are spot welded. This package was specially designed for cryogenic diode thermometry to provide excellent thermal connection between the diode and outside world and provides a wide temperature range robust package with low outgassing. The package top and bottom are metallized and the serial number is scribed into the metallization eliminating the need for a Resistance to Solvents test. From a functional standpoint, the metallurgical bonds in the sensor fabrication provide high mechanical strength interfaces and eliminate the need for intermittent contact tests (FIST and BIST).

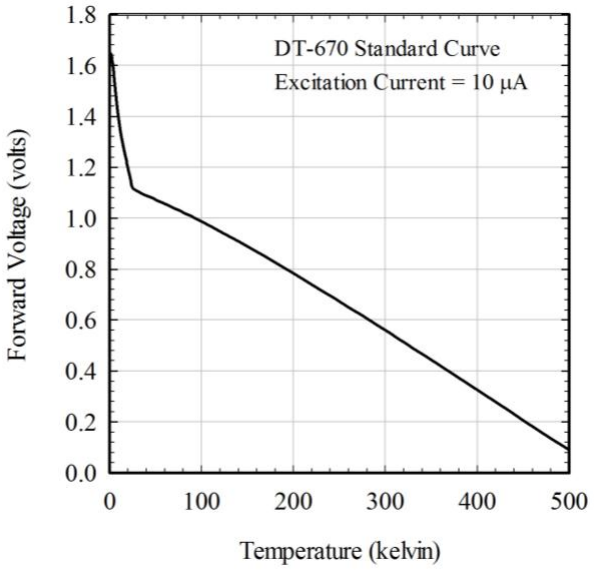

FIGURE 1. Voltage as a function of temperature for a Lake Shore Model DT-670-SD diode temperature sensor.

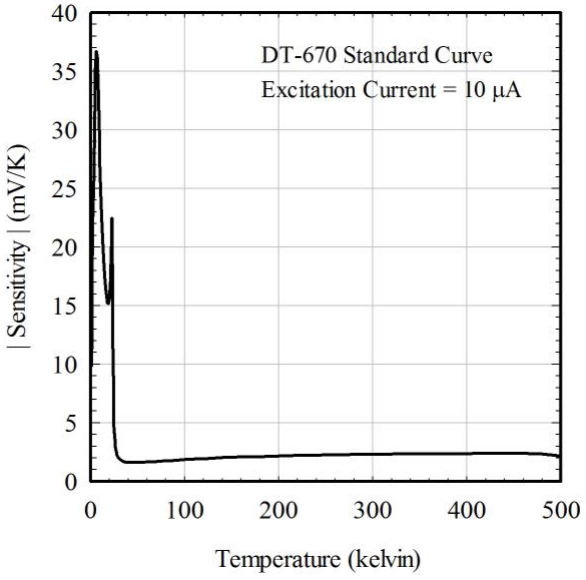

FIGURE 2. Sensitivity (absolute value) as a function of temperature for a Lake Shore Model DT-670-SD diode temperature sensor.

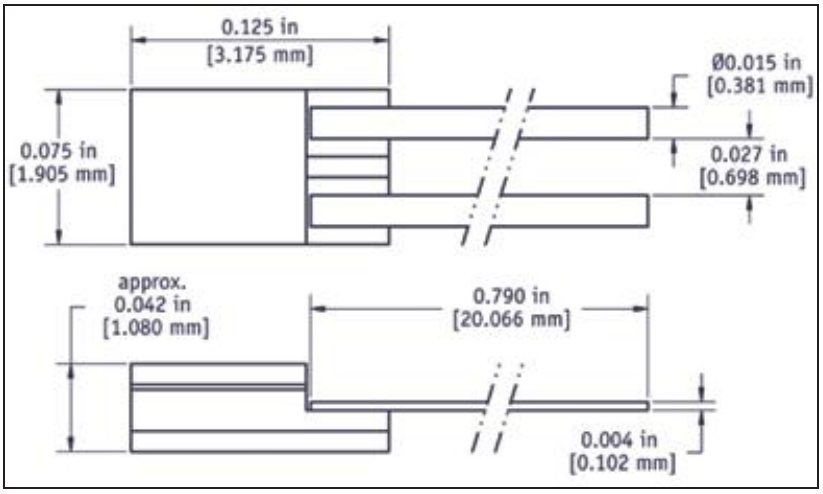

FIGURE 3. Schematic and dimensions of the Model DT-670-SD DTS package.

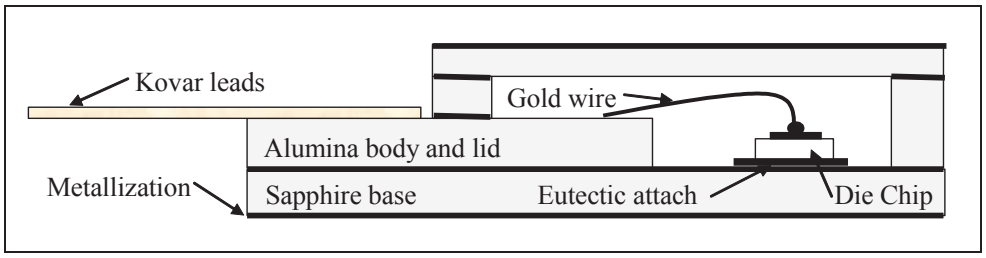

FIGURE 4. Side view of the Model DT-670-SD DTS package.

4. SCD Development Progress

As a first step to create an SCD for the Model DT-670-SD DTS, Lake Shore approached the Defense Logistics Agency Defense Supply Center Columbus (DSCC) in 2010 for assistance in defining the necessary course of action. The intent was to develop a performance specification (i.e. MIL-PRF drawing) that could be used for procurement by any private contractor or government entity. Lake Shore has supplied cryogenic temperature sensors for aerospace applications for over thirty years. During this 30 year period, the Lake Shore sensor engineering group has interacted with design engineers from virtually every prime contractor and through these interactions has developed an understanding of the testing that should be performed particular to these sensors when they are used in aerospace applications. As a result of these past customer-vendor collaborations, Lake Shore proposed to provide the screening and qualification test protocols, but DSCC would create and own the MIL-PRF document.

By chance, NASA Goddard Space Flight Center was in the process of updating document EEE-INST-002, "Instructions for EEE Parts Selection, Screening, Qualification, and Derating." The person charged with revising the document, Bruce Eyrich, wanted to include a section on cryogenic thermometry. Through conversations with DSCC, Mr. Eyrich discovered our common goal and in 2011 contacted Lake Shore for our assistance in determining and documenting the proper test sequences for various cryogenic temperature sensor types. As of this writing, the EEE-INST-002 is still undergoing revision, but a section on cryogenic thermometry detailing test protocols has been proposed covering diode, platinum, Cernox™, germanium, and ruthenium oxide, and rhodium-iron temperature sensors. The proposed screening test sequence for cryogenic diode temperature sensors is given in Table 1 while the proposed qualification test sequence is given in Tables 2A through 2F. Table 3 lists the minimal electrical characterization data necessary for the screening and qualification testing.

Table 1. EEE-INST-002 proposed screening test sequence for cryogenic diode temperature sensors.

Inspection/Test	MIL-STD-750		Level		
	Method	Conditions	1	2	3
1. a) Die Visual b) Internal Visual **1/**	2072 2073 2074	Transistor Diode Diode	X	X	
2. Stabilization Bake		8 h at maximum rated temperature	X	X	X
3. Temperature Cycling	1051	20 thermal cycles, liquid to air, 77.3±0.5 K to 300±10 K, minimum 3 min per cycle	X	X	X
4. Initial electrical measurements		Per Table 1C herein, minimum, or per SCD	X Read/ Record	X	X
5. Serialization			X	X	X
6. Constant Acceleration	2006	20,000Gs in Y1 direction	X		
7. PIND **2/**	2052	Condition A	X	X	X
8. HTRB **3/**	1038	Test condition A, 80% of rated VR, 48 h minimum, TA=125±5ºC	X	X	X
9. Interim electrical measurements		Per Table 1C herein, minimum, or per SCD	X Read/ Record **4/**	X	X
10. Calculate Deltas			X		
11. Calculate PDA **5/**			5%	10%	20%
12. Hermetic seal a. Fine Leak b. Gross Leak	1071	G or H C or K	X	X	
13. Radiographic	2076	2 views, top and one side	X	X	
14. External Visual **6/**	2071		X	X	X
15. Final electrical measurements or calibration **7/**		Per Table 1C herein, minimum, or per SCD	X Read/ Record **4/**	X	X

Notes:

1/ Metallurgical bond preferred. MIL-STD-750 method chosen as appropriate for the device being inspected.

2/ All cavity devices shall require PIND testing, Condition A, Method 2052, of MIL-STD-750 shall be used.

3/ Limit HTRB temperature to the maximum operating temperature of the diode as specified by the manufacturer. This temperature may be lower than 125º C for commercial or manufacturer's in house HI-REL parts.

4/ Read and Record (as a minimum) delta parameters listed in Table 1C. The non-delta parameters may be tested as "go/no-go."

5/ PDA applies to cumulative failures during all burn-in steps. The cumulative failures for all levels shall include functional/DC parametrics (excluding deltas) for the lot to be accepted.

6/ Pure tin plating is prohibited as a final finish on EEE parts. Solder with tin content exceeding 95% is prohibited.

7/ Electrical characterization over temperature range of intended use may be required. Specific tolerances for device interchangeability may be required.

Table 2A. EEE-INST-002 proposed Subgroup 1 qualification test sequence for cryogenic diode temperature sensors.

Inspection/Test	MIL-STD-750		Quantity (Accept number) or LTPD		
	Method	Conditions	Level 1	Level 2	Level 3
Subgroup 1 **1/**		Separate samples may be used for each test.	6 (0)	4 (0)	Not required
Physical Dimensions	2066	Dimensions in accordance with specified case outline.	X	X	
Solderability	2026		X	X	
Resistance to Solvents **2/**	1022		X	X	
Outgassing **3/**		Per ASTM E 595.	X	X	

Notes:
1/ Electrical failures may be used if endpoint electrical measurements are not required.
2/ Not applicable for scribed or etched markings.
3/ Perform test or provide historical data if process and parts have not changed.

Table 2B. EEE-INST-002 proposed Subgroup 2 qualification test sequence for cryogenic diode temperature sensors.

Inspection/Test	MIL-STD-750		Quantity (Accept number) or LTPD		
	Method	Conditions	Level 1	Level 2	Level 3
Subgroup 2			6 (0)	4 (0)	Not required
Thermal Shock (liquid to air)		100 thermal shocks from 77.3±2 K (liquid) to 300±10 K (air).	X	X	
Electrical measurement		Per Table 3 herein, minimum or per SCD	X	X	
Hermetic Seal, Fine	1071	Condition G or H	X	X	
Decap-Internal Visual	2075		X	X	
SEM	2077	Die with expanded metallization or metallization interconnects	X	X	
Bond Strength	2037	All wire bonds	X	X	
Die Shear	2017		X	X	

Table 2C. EEE-INST-002 proposed Subgroup 3 qualification test sequence for cryogenic diode temperature sensors.

Inspection/Test	MIL-STD-750		Quantity (Accept number) or LTPD		
	Method	Conditions	Level 1	Level 2	Level 3
Subgroup 3			6 (0)	4 (0)	Not required
Moisture Resistance	1021		X	X	
Electrical measurement		Per Table 3 herein, minimum or per SCD	X	X	

Table 2D. EEE-INST-002 proposed Subgroup 4 qualification test sequence for cryogenic diode temperature sensors.

Inspection/Test	MIL-STD-750		Quantity (Accept number) or LTPD		
	Method	Conditions	Level 1	Level 2	Level 3
Subgroup 4 1/			6 (0)	6 (0)	6 (0)
Radiation resistance	1019	Condition B	X	X	X
Electrical measurement		Per Table 3 herein, minimum, or per SCD	X	X	X

Notes:

1/ Perform test or provide historical data if devices are from a previously tested wafer lot. Special note: radiation testing of semiconductor devices performed at room temperature may not be representative of cryogenic irradiation where charge trapping and/or subsequent thermal annealing may occur.

Table 2E. EEE-INST-002 proposed Subgroup 5 qualification test sequence for cryogenic diode temperature sensors.

Inspection/Test	MIL-STD-750		Quantity (Accept number) or LTPD		
	Method	Conditions	Level 1	Level 2	Level 3
Subgroup 5			6 (0)	4 (0)	Not required
Steady State Life test **1/**	1026	1000 hours minimum at TA=225±10ºC with 10 µA forward excitation or as specified by SCD	X	X	
Electrical Measurement		Per Table 3 herein, minimum, or per SCD	X	X	

Notes:

1/ Limit life testing to the maximum operating temperature of the diode as specified by the manufacturer. This temperature may be lower than 225ºC for commercial or manufacturer's in-house HI-REL parts. Kirkendall voiding is expected to occur for devices with Al-Au interfaces after extended exposure at temperatures above +125ºC.

Table 2F. EEE-INST-002 proposed Subgroup 6 qualification test sequence for cryogenic diode temperature sensors.

Inspection/Test	MIL-STD-750		Quantity (accept number) or LTPD		
	Method	Conditions	Level 1	Level 2	Level 3
Subgroup 6			6 (0)	6 (0)	Not required
Shock	2016	Non-operating, 1,500 Gs, 0.5 ms, 5 blows in each orientation: X1, Y1, Z1 or per SCD	X	X	
Vibration, Variable Frequency	2056		X	X	
Constant Acceleration	2006	1 minute minimum in each orientation. X1, Y1, and Z1 at 20,000 Gs minimum.	X	X	
Electrical measurements		Per Table 3 herein, minimum or per SCD	X	X	

Table 3. EEE-INST-002 proposed electrical measurement requirements during screening and qualification test sequences for cryogenic diode temperature sensors

Test	Symbol	MIL-STD-750 Method	Condition	Units
DC (static) test	V(f)	N/A	Forward voltage at I_{exc} = 10 μA and T=4.2±0.5K	Volts
	V(f)	N/A	Forward voltage at I_{exc} = 10 μA and T=77.3±2K	Volts
	V(f)	N/A	Forward voltage at I_{exc} = 10 μA and T=300±10K	Volts

The EEE-INST-002 document is purposely written as a general document and does not detail specific manufacturers or numbers. While the proposed cryogenic temperature sensor for diodes goes a long way in simplifying their procurement for aerospace applications, a manufacturer/model-specific performance specification document would allow further customization of the test sequences as appropriate. Acceptance of revised EEE-INST-002 document will simplify the future development of a performance specification (MIL-PRF) drawing for the Model DT-670-SD DTS. When accepted, the sensor can be built and stocked at the DT-670-SD level, but final configuration including lead extensions, tolerance band selection, adapter, and calibration are still available and yield even greater flexibility than just the one base part.

5. Conclusions

In order to reduce cost and delivery time for cryogenic temperature sensors used in aerospace applications, Lake Shore Cryotronics, Inc. has proposed a screening and qualification test protocol for its Model DT-670-SD diode temperature sensor. The test screening and sequences shown in Tables 1 and 2 are proposed, and feedback is welcome from interested parties. Acceptance of this test protocol by aerospace customers will allow the sensor to be manufactured in larger numbers with proper testing and documentation to deliver an "off-the-shelf" aerospace temperature sensor with shorter delivery time and decreased cost to the customer.

Acknowledgements

The authors wish to acknowledge Bruce Eyrich of NASA GSFC and Michael Radecki of Defense Logistics Agency Defense Supply Center Columbus for their help in the current work.

References

[1] NASA EEE-INST-002, Instructions for EEE Parts Selection, Screening, Qualification, and Derating, available at "http://nepp.nasa.gov/DocUploads/FFB52B88-36AE-4378-A05B2C084B5EE2CC/EEE-INST-002_add1.pdf".

[2] MIL-PRF-19500, Rev P, Performance Specification, Semiconductor Devices, Test Specifications For, 20 Oct 2010, available at https://assist.daps.dla.mil/quicksearch/.

[3] MIL-STD-750 Rev E, Test Method Standard, Test Methods for Semiconductor devices, 20 Nov 2006, available at https://assist.daps.dla.mil/quicksearch/.

[4] MIL-STD-883, Rev H, Test Method Standard, Microcircuits, 2/26/2010, available at https://assist.daps.dla.mil/quicksearch/.

[5] MIL-STD-202, Rev G, Test Method Standard, Electronic and Electrical Component Parts, 2/8/2002, available at https://assist.daps.dla.mil/quicksearch/.

[6] Lake Shore Cryotronics, Inc. Westerville, OH, USA.

[7] Lake Shore Cryotronics Temperature Product Catalog or www.lakeshore.com.

Design of the PIXIE Adiabatic Demagnetization Refrigerators

P. Shirron[1], M. Kimball[1], D. Fixsen[2], A. Kogut[1], X. Li[1], and M. DiPirro[1]

[1] NASA/Goddard Space Flight Center, Greenbelt MD 20771 USA
[2] University of Maryland, College Park MD 20740 USA

Abstract

The Primordial Inflation Explorer (PIXIE) is a proposed mission to densely map the polarization of the cosmic microwave background. It will operate in a scanning mode from a sun-synchronous orbit, using low temperature detectors (at 0.1 K) and located inside a telescope that is cooled to approximately 2.73 K – to match the background temperature. A mechanical cryocooler operating at 4.5 K establishes a low base temperature from which two adiabatic demagnetization refrigerator (ADR) assemblies will cool the telescope and detectors. To achieve continuous scanning capability, the ADRs must operate continuously. Complicating the design are two factors: 1) the need to systematically vary the temperature of various telescope components in order to separate the small polarization signal variations from those that may arise from temperature drifts and changing gradients within the telescope, and 2) the orbital and monthly variations in lunar irradiance into the telescope barrels. These factors require the telescope ADR to reject quasi-continuous heat loads of 2-3 mW, while maintaining a peak heat reject rate of less than 12 mW. The detector heat load at 0.1 K is comparatively small at 1-2 μW. This paper will describe the 3-stage and 2-stage continuous ADRs that will be used to meet the cooling power and temperature stability requirements of the PIXIE detectors and telescope.

1.0 INTRODUCTION

The Primordial Inflation Explorer (PIXIE)[1] in Figure 1 is a proposed mission to produce full-sky maps of the cosmic microwave background (CMB) polarization. The instrument will use a polarizing Michelson interferometer and optics cooled to the CMB temperature (2.73 K) to measure the difference spectrum between two orthogonal linear polarizations of light collected from two co-aligned telescope barrels. The weak polarization signals are read out with harp-string bolometers cooled to 0.1 K. A calibrator can be moved to uncover one or both of the telescope barrels, so that the instrument can sample the difference between sky signals, or between sky signals and a calibrated ~2.73 K black body.

The instrument achieves a high degree of systematic error rejection by its highly-symmetric, nulled design, and by nearly continuous calibration of the polarization signal. In addition, errors caused by to temperature gradients within telescope and optical components will be reduced by reduced by independently varying the temperature of these components by small (5-20 mK) amounts relative to the CMB, at unique frequencies. The impact is that the instrument's cooling system must not only lift heat conducted and

radiated onto the instrument, but a significant amount of heat (~1 mW) associated with these fluctuations.

PIXIE will be in a sun-synchronous, 575 km orbit, so that it can continuously map the sky to obtain full coverage every 6 months. As such, the instrument will experience some radiative input from the Moon during a portion of nearly every orbit. The input is relatively small when the Moon is full or new, but peaks when it is half full. The lunar irradiance into each open telescope barrel is a half-sinusoid with a maximum of 1 mW. The orbit average is 0.5 mW, and since this will occur each orbit for many days, the instrument cooling system must be designed as if this is a continuous heat load.

The PIXIE cryogenic system will use a set of radiation shields and a 4.5 K cryocooler to minimize heat flow into the instrument from the room temperature spacecraft and from the Sun and Earth. Two ADR assemblies will cool continuously from 4.5 K to ~2.6 K for the telescope, and to 0.1 K for the detectors. This paper discusses the requirements, design and performance of the ADR system.

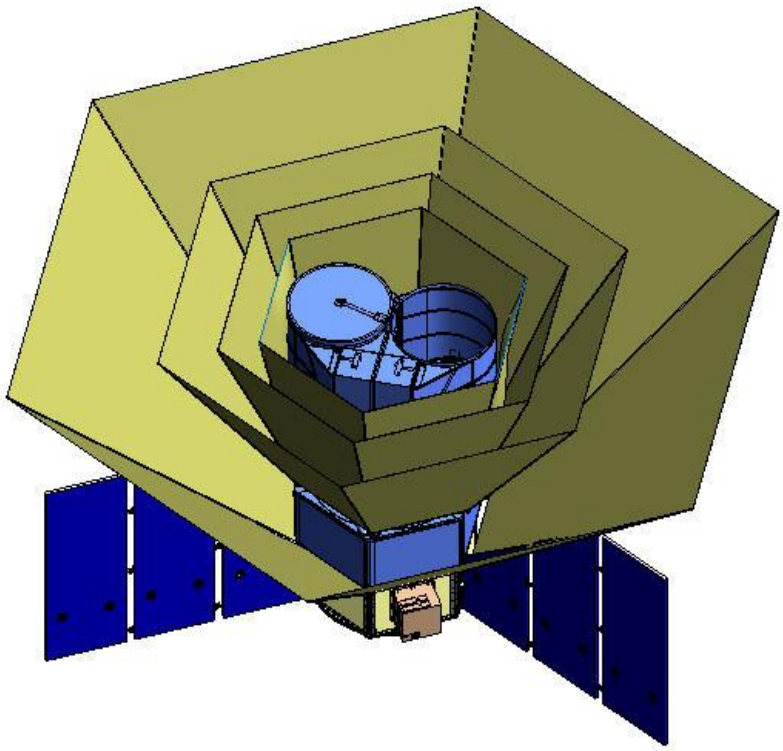

Figure 1. The PIXIE instrument (center) and 4 thermal shields. The outermost shield is approximately 3.5 m across when deployed.

2.0 ADR SYSTEM REQUIREMENTS

Figure 2 is a heat map of the PIXIE instrument. The ADR is shown as a lumped unit, but consists of two separate assemblies: the iADR which cools the telescope and optical components, and the dADR which cools the detectors. A breakdown of heat loads for each is given in Table 1. The detector heat load is a relatively minor factor in the design, since the high efficiency of the dADR results in a heat output at ~2.7 K of only about 0.2 mW (including parasitic heat loads and hysteretic heat generation). This represents only 3% of the unmargined capability of the iADR. At this early stage of mission design, it was deemed prudent to allocate 1 mW of the iADR's cooling power budget to heat rejection from the dADR.

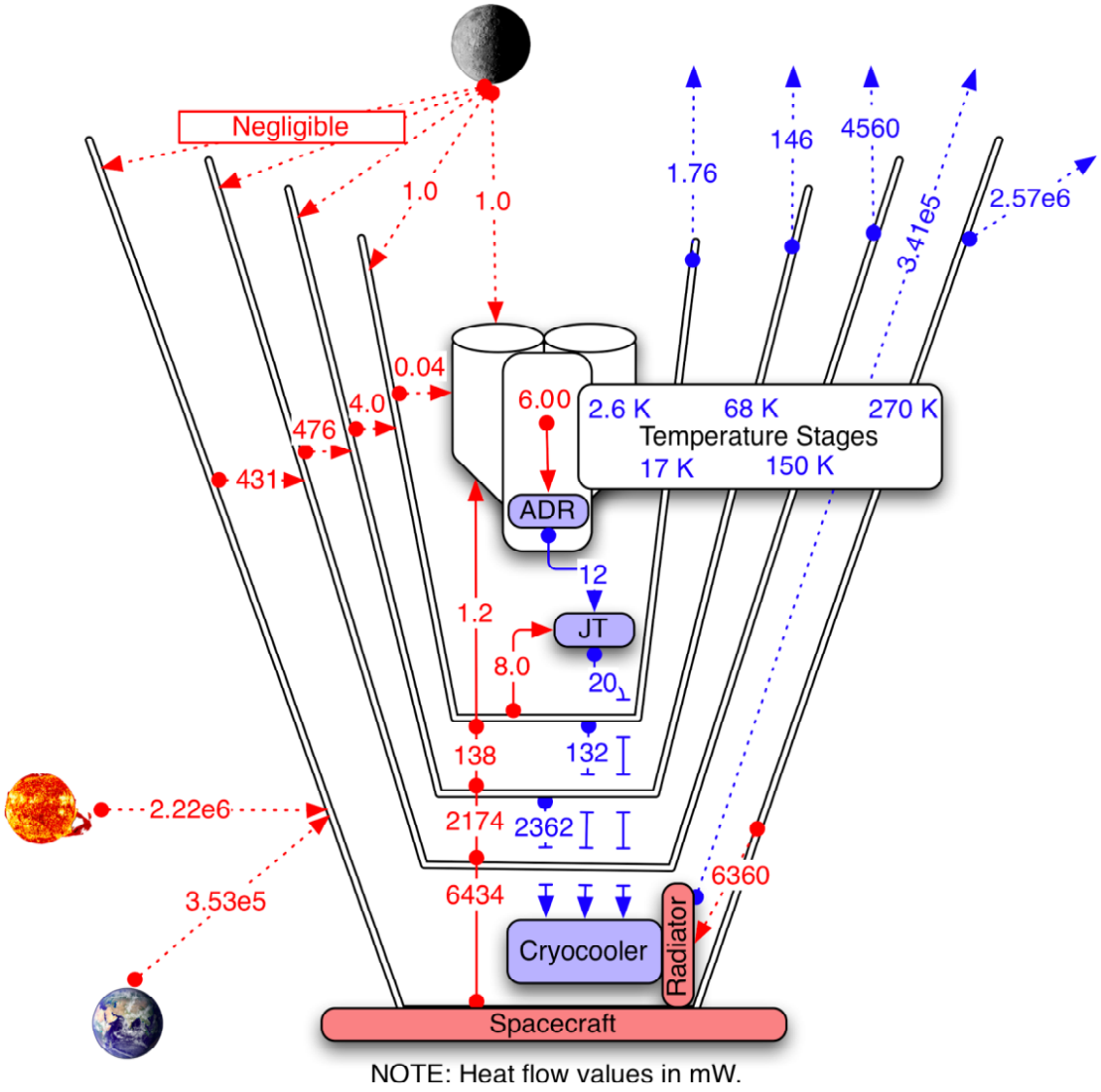

Figure 2. Heat Map of the PIXIE Cryogenic System. Red indicates heat inputs and blue shows heat outputs either radiated or absorbed by coolers. Dotted lines indicate radiative heat and solid lines indicate conducted heat flow.

Table 1. Heat budgets for the dADR and iADR.

dADR	
Operating temperature	0.100 K
Duty cycle	100%
Temperature stability	1 μK rms
Detector heat load	2 μW
Heat sink temperature	2.66 K
Heat load on heat sink	< 1.0 mW (time average)
iADR	
Operating temperature (see Section 2.4)	2.66 K
Duty cycle	100%
Heat load	6.00 mW
Input from dADR	1.0 mW
Conduction from 17 K	1.2 mW
Thermal control of optics	2.85 mW
Lunar irradiance (peak orbit average)	1.0 mW
Heat sink temperature	4.5 K
Peak heat load to sink	12 mW

2.1 iADR Configuration

The driving requirement for the iADR is the peak heat reject rate of 12 mW[2]. This results from power constraints imposed by the PIXIE's spin (which reduces the time average output of the solar arrays) and the goal of operating during the eclipse season. According to mandatory design rules for this stage of mission development, the cryogenic system must be designed for 100% margin on all heat loads, therefore the iADR must actually be capable of 12 mW of heat lift at 2.66 K, and the cryocooler capable of accepting a peak load of 24 mW from the iADR.

To see how this constrains the design, we note that a cooler operating between 2.66 K and 4.5 K with a cooling power of 6.0 mW at 100% (Carnot) efficiency (for the cold components only) would have a continuous heat reject rate of just over 10 mW. This would seem to imply that the iADR must achieve an unrealistic efficiency of 85%. However, this calculation is based doubly margined heat loads. The current best estimate for the heat output of the iADR is 0.2 mW, and the dissipation needed for control of the optics is 1.85 mW. Thus the unmargined cooling power requirement is 4.2 mW at 2.66 K. Moreover, the optics dissipation can be reduced during periods of peak lunar input to further reduce the maximum heat load on the iADR. Consequently, the required efficiency of the iADR is less than 60%, for which the entire cryogenic system still carries a margin of 100%.

This has a significant impact on the architecture of the iADR. Continuous operation of an ADR can be achieved with 2 stages in either a series or parallel configuration. These are shown schematically in Figure 3. In the series configuration, one stage is held at constant

temperature while the other shuttles back and forth in temperature, spending about half the time offloading heat at the cold end and half the time rejecting heat to the sink. At best, this can result in about 50% duty cycle for heat rejection, and a maximum efficiency of less than 50%. In the parallel configuration, one stage absorbs heat from the load and controls its temperature while the other is rejecting heat, then the roles reverse. In this mode, the load is always being cooled, while heat is being rejected nearly continuously – realistically ~80% of the time. The iADR can achieve 60% overall efficiency if each of the two stages can achieve 80% efficiency for heat absorption and rejection. At temperatures in the 2.6-4.5 K range, these kinds of efficiencies have already been achieved with laboratory ADR stages.

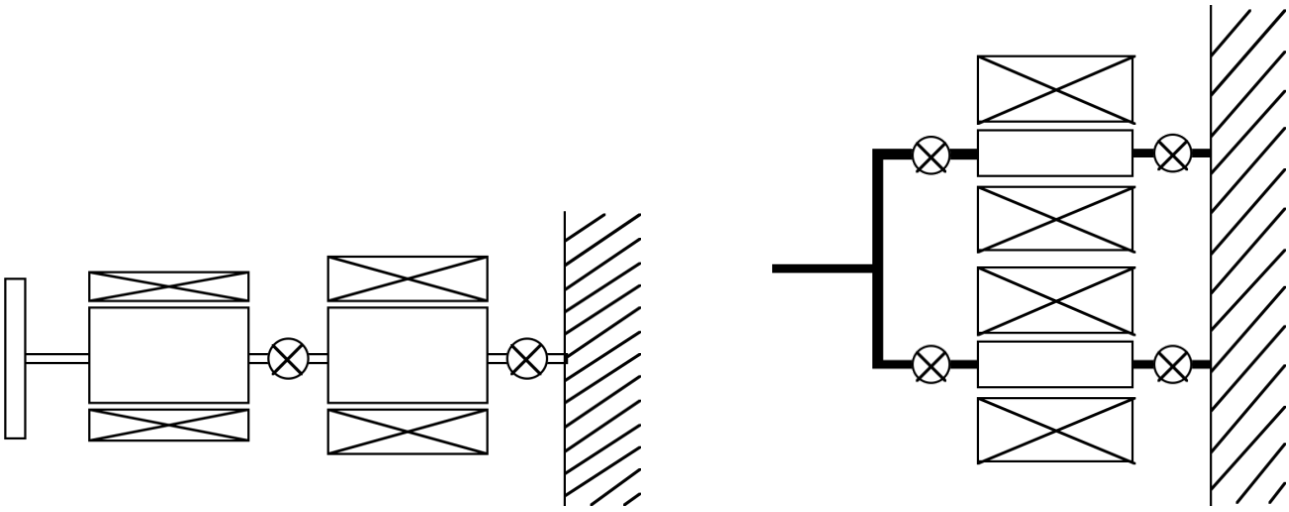

Figure 3. Series and parallel configurations for an ADR capable of continuous cooling.

The drawback to the parallel configuration is the need for 4 heat switches instead of 2. The control system is also more complex as there is a handoff in temperature control each half cycle. However, there are benefits: the mass of each stage is half of what would be necessary in the series configuration, as are the heat fluxes. The latter contributes significantly to being able to meet the necessary efficiency for heat inflow/outflow.

For the refrigerant, gadolinium lithium fluoride (GLF)[3] has the highest entropy density of any material that has been used in space and/or laboratory ADRs in the temperature range from 2-5 K. Its high density (5.6 g/cm^3) enables relatively high magnetic field (3 T) to be used, yet maintain low overall mass. The heat switches will all be gas-gap. The two switches connecting the salt pills to the heat sink will be passive[4], while those connecting the salt pills to the telescope thermal bus must be active.[5]

2.2 dADR Configuration

The cooling power requirement and presumed efficiency for the dADR are low compared to what has already been demonstrated in a developmental continuous ADR (CADR) [6] developed at NASA/Goddard Space Flight Center. This was a 4-stage assembly, using a

linear thermal arrangement, that cooled to temperatures below 50 mK using a 4.2 K heat sink. Using design rules that have been validated by the CADR, the PIXIE cooler requires only 3 stages to span 100 mK to 2.66 K. The lower cooling requirement means that the PIXIE stages can be scaled smaller, though less than proportional with cooling power required because the 3 coldest stages of the CADR operate over a wider temperature range. In practice, this just requires larger refrigerant mass and magnetic field for the 2 upper stages.

For stages 1 and 2, operating in the 100 mK regime requires the use of a low density refrigerant like chrome potassium alum (CPA) or ferric ammonium alum (FAA). Entropy considerations favor FAA, but the long history within NASA/GSFC of using CPA for low temperature ADR stages and its compatibility with copper thermal buses provide a strong rationale for its use. As in the 4-stage CADR, stages 2 and 3 will use passive gas-gap heat switches, and to connect stage 1 to 2, a superconducting heat switch using high-purity Pb wire will be used.

Design parameters for the dADR and iADR are given in Table 2.

Table 2. Summary of design parameters for the dADR and iADR.

Stage	Refrigerant	B (T)	Upper T (K)	Lower T (K)	Mass (kg)
1	20 g CPA	0.1		0.1	0.26
2	20 g CPA	0.5	0.5	0.09	0.49
3	30 g CPA	2	2.8	0.45	1.88
4a	100 g GLF	3	4.8	2.66	2.69
4b	100 g GLF	3	4.6	2.66	2.69
Total					8.00

2.3 ADR System Configuration

While the PIXIE cooler uses 5 ADR stages, shown schematically in Figure 4, the continuous cooling produced by the iADR allows the two ADR assemblies to operate completely independently. Thus the “complexity” of the ADR and its control system is significantly reduced. Moreover, the two ADR systems can be independently developed and tested prior to integration with the telescope.

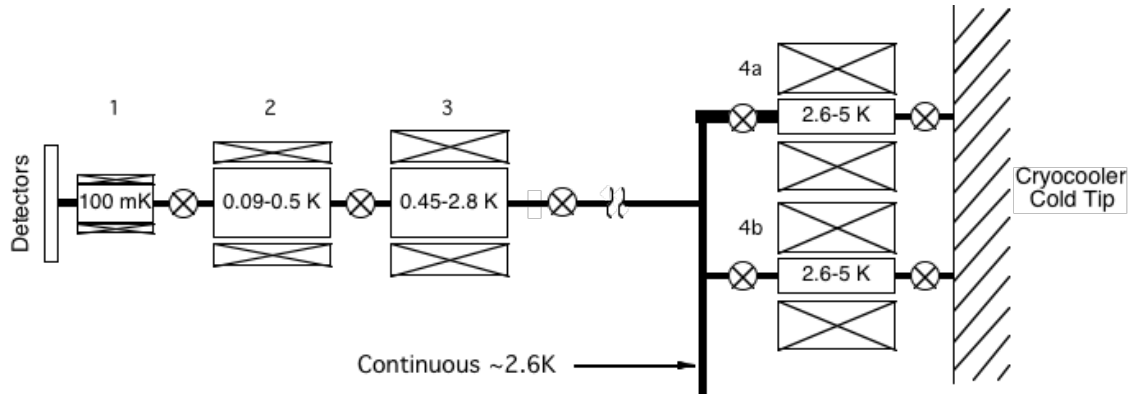

Figure 4. Schematic of the dADR (stages 1-3) and iADR (stages 4a-4b).

2.4 Temperature Control of the Telescope and Optical Components

The polarization signals from the CMB are extremely small. It is for this reason that the PIXIE telescope is cooled to the CMB temperature of 2.725 K. Even so, gradients within the telescope and optics may contribute spurious signals. To separate these errors from the polarization signals, the telescope and major optical components (20 in all) will be dithered about the CMB temperature at unique frequencies. The typical excursion, Δ, positive and negative, will be 5-10 mK, at time scales of tens of minutes, but not commensurate with the orbit period.

For the optical components to be warmed above and cooled below the CMB temperature, the iADR must establish a low enough base temperature. Based on the final temperature selected, the thermal conductance of each component to the thermal bus will be tailored to yield a suitably short cooling time from +Δ to -Δ. From the thermal conductance and the difference between the CMB and thermal bus temperatures, the average control heater input for each optical component can be calculated. More important than the total heater dissipation, $\dot{Q}$, which is simply the sum for all optical components, is entropy usage ($\dot{Q}$ /T_{bus}) in the iADR to absorb this heat.

For thermal bus temperatures close to the CMB temperature, the thermal conductance of each optics link must be large in order to cool the component through a small temperature gradient. This yields large total heat flow at the average (CMB) temperature. As the thermal bus is lowered, total heat flow and entropy usage drop. Below an optimum temperature, where the heat flow stabilizes, the entropy usage will rise.

The optimal thermal bus temperature was determined to be 2.66 K, for which the time average heater dissipation will be 1.85 mW. The thermal budget for the iADR carries 2.85 mW for temperature control to provide margin against the inability to achieve very low thermal conductance for some very low mass components. Strictly speaking, this is not necessary since the 100% margin on ADR cooling power/heat rejection provides margin

for such realities. However, the criticality of the temperature control scheme for removing instrument errors suggests the need for additional margin.

3.0 iADR MODELING

Operation of the iADR was modeled using control software and ADR simulators developed for the CADR R&D program. The software has been validated through the design and build of several ADRs, including the CADR and Astro-H ADR. The model captures all aspects of the operation relevant to the thermodynamic performance, including internal thermal boundary resistance in the salt pills, heat switch transition times, and magnet/magnetic shield hysteresis.

Figure 5 shows the modeled operation of the iADR with a constant heat load of 5 mW (the total heat load without the additional margin on telescope/optics temperature control). Shown are the temperatures of stages 4a and 4b through several cycles. The cycle period is 1600 seconds, during which each stage spends half the time absorbing heat from the thermal bus and half the time rejecting heat to the JT cooler. Each stage absorbs only a fraction of its total cooling capacity (~5 J out of 7 J) before recycling. This maintains some cooling reserve in the event of off-nominal (i.e. temporary) heat loads. It also allows the iADR to absorb larger heat loads during operation (i.e. the margined thermal control heat load).

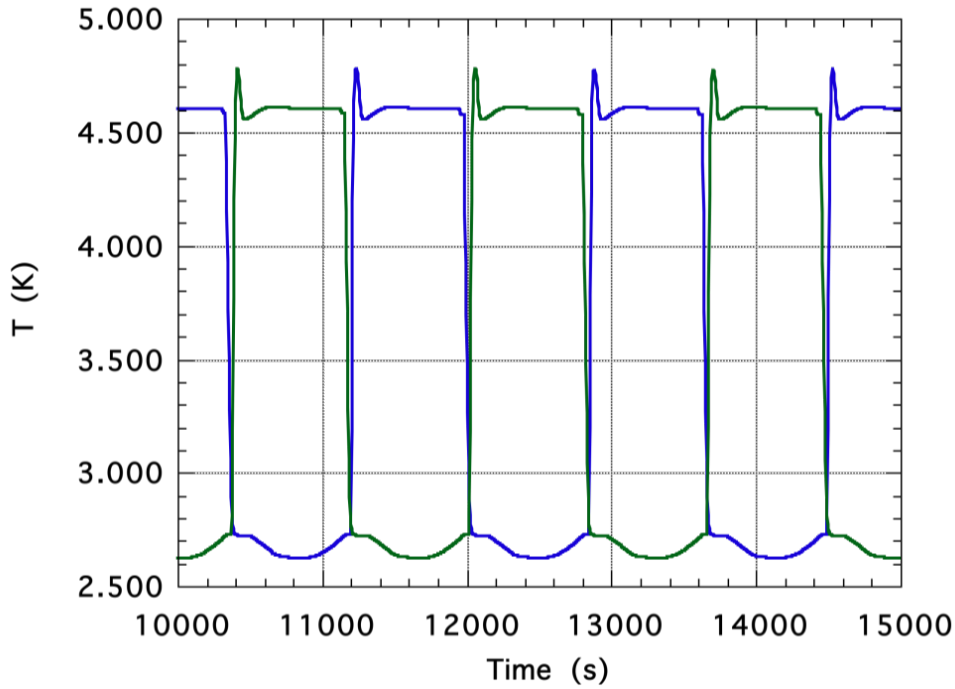

Figure 5. Modeled temperatures of the iADR stages through several cycles with a constant 5 mW heat load imposed.

Figure 6 shows the instantaneous heat load to the JT cooler from the iADR. The time average is 9.8 mW, while the peak momentarily exceeds 12 mW. The difference between the two is due to the overhead operations of magnetizing each stage from 2.66 K to 4.5 K, and subsequently demagnetizing over the same range. From the plot, it is obvious that the gap can be narrowed by fine-tuning the control parameters to achieve constant 12 mW heat rejection for the entire recycling operation. Less obvious is the ability to reduce the fraction of time taken up by overhead operation by extending the heat absorption and heat rejection phases. This can be accomplished by more deeply discharging each stage before it is recycled, or (worst case) adding refrigerant mass. Additional modeling is needed to test these cases.

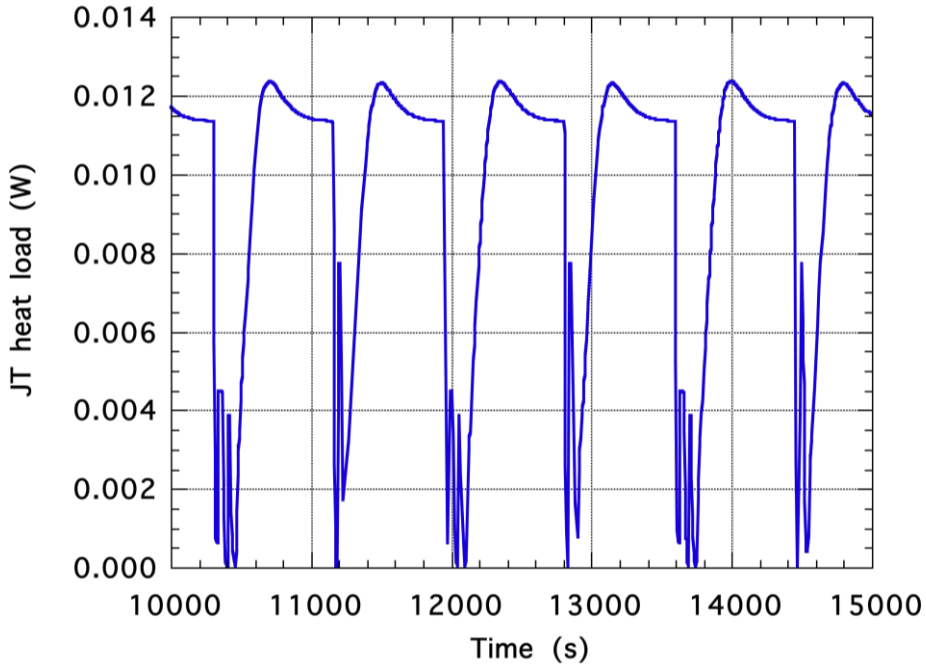

Figure 6. Modeled heat rejection rates of the iADR stages through several cycles with a constant 5 mW heat load imposed.

In summary, the model results show that the PIXIE ADRs can meet the current best estimate for instrument heat loads with 100% margin on cooling power and heat rejection, but at present cannot show 100% system-level margin with the additional margin on telescope/optics thermal control heater dissipation. It is expected that if PIXIE is selected from Phase A study under NASA's 2011 Mid-Ex AO, additional modeling and breadboard development will be done to demonstrate a system capable of meeting the more conservative requirements.

4.0 SUMMARY

The PIXIE mission presents a challenging set of cooling requirements: continuous cooling of detectors to 100 mK and continuous cooling of its telescope and optics to near the CMB temperature of 2.725 K. A low base temperature of 4.5 K, from which the instrument cooler will operate, is provided by a set of nested thermal shields and a Stirling/JT cryocooler. Limited power resources require the instrument cooler to achieve very high efficiency, on the order of 60% of Carnot between 2.66 K and 4.5 K.

The PIXIE instrument will use two ADR assemblies. Using two stages in a parallel configuration connected to the JT cooler, the iADR establishes a constant base temperature for the telescope and optics, and serves as a heat sink for the dADR. The dADR uses 3 stages in a linear configuration to operate continuously at 100 mK. The ADRs have been sized according to worst case, margined heat loads. Modeling shows that the PIXIE ADRs are close to meeting the heat lift requirements within the capability of the JT, after derating its cooling power by a factor of 2.

During Phase A studies, additional modeling will be done to determine optimal control parameters for the ADRs, better estimates for heat loads, and the ability to phase various heat loads to reduce peak and time average values.

5.0 REFERENCES

[1] Kogut AJ, Chuss DT, Dotson JL, Fixsen DJ, Halpern M, Hinshaw GF, Meyer SM, Moseley SH, Seiffert MD, Spergel DN, and Wollack EJ, "The Primordial Inflation Explorer (PIXIE) Mission", Proc. SPIE 7731, 77311S (2010).

[2] DiPirro MJ, Fixsen D, Kogut A, Li X, Marquardt J, and Shirron PJ, "Design of the PIXIE Cryogenic System", submitted for publication in the proceedings of the 2011 Space Cryogenics Workshop, Coeur d'Alene, ID.

[3] Numazawa T, Kamiya K, Shirron PJ, DiPirro MJ, Matsumoto K, "Magnetocaloric Effect of Polycrystal $GdLiF_4$ for Adiabatic Demagnetization Refrigeration", *AIP Conference Proceedings,* 850 (2006) 1579-1580.

[4] DiPirro, MJ, Shirron PJ, Tuttle JG, Canavan ER, "Design and Test of Passively Operated Heat Switches for 0.2 to 15 K", *Adv. Cryo. Eng.* 49 (2004) 436-442.

[5] Kimball MO and Shirron PJ, "Heat switches providing low activation power and quick switching time", submitted for publication in the proceedings of the 2011 CEC/ICMC, Spokane, WA.

[6] Shirron, P.J., Canavan, E.R., DiPirro, M.J., Tuttle, J.G., and Yeager, C.J., "A Multi-Stage Continuous Duty Adiabatic Demagnetization Refrigerator," in *Adv. Cryo. Eng.* 45B, edited by Q.-S. Shu et al., Plenum, New York, 2000, pp. 1629-1638.

Performances of the 50 mK ADR/sorption cooler

N. Luchier[(1)], J.M. Duval[(1)], L. Duband[(1)], T. Tirolien[(2)]

(1): SBT, UMR-E CEA / UJF-Grenoble 1, INAC, Grenoble, F-38054, France

(2): ESA/ESTEC, Noordwijk, The Netherlands

Abstract

CEA/SBT is currently testing a 50 mK cooler developed in the framework of an ESA Technical Research Program (TRP) targeted for the IXO space mission. This cooler is composed of a small demagnetization refrigerator (ADR) pre cooled by a sorption stage. This Engineering Model is able to produce 1 µW of net heat lift at 50 mK and an additional 10 µW at 300 mK provided by the sorption stage. The autonomy of the cooler is 24 hours, and once the low temperature phase at 50 mK is over, it can be recycled in about 8 hours with 10 µW and 100 µW available at respectively the 2.5 and 15 K heat sinks. These performances are in agreement with the ESA requirements.

In this paper, we present the detailed thermal performances of the cooler in nominal conditions as well as sensitivity measurements of the variation of the heat sink and the cold end temperatures.

This work is conducted under a European Space Agency funding.

Keywords

Adiabatic demagnetization; 3He systems; Magnetic refrigeration; Sorption coolers; Space cryogenics

1. Introduction

IXO and SPICA, two satellites candidate for the 2015-2025 ESA Cosmic Vision program, will feature detectors that need to be cooled down to temperatures as low as 50 mK. One of the main features of these missions is that the liquid reservoirs previously used to provide temperature down to 1.5 K will be replaced by a set of mechanical coolers producing cooling powers at various temperatures. This solution allows extending the mission duration to 5 years with a target at 10 years.

One of the most stringent requirements in the definition of these future missions is the limited mass budget. In this framework, we propose to associate a sorption cooler with a low temperature Adiabatic Demagnetization Refrigerator (ADR) stage [1]. Indeed, with space-adapted dilution refrigerators [2], ADR is the only technology able to produce 50 mK range temperatures [3,4,5]. It is a reliable, high efficient technology, with no moving part and insensitive to gravity. A full multi stage ADR is able to cover an extended temperature range from 6-8 K down to about 20 mK.

Our combination takes advantage of the low weight of a sorption cooler. Indeed, an Herschel type cooler weights about 300 g and is able to cover the temperature range 3-0.3 K. The sorption role is twofold: providing cooling power at 300 mK and pre cooling the ADR stage. Thus, it allows limiting the needed field below 1 Tesla and thus keeping the need in coil, current and magnetic shield low.

Figure 1 shows the principle in the IXO thermal environment for which two heat sources are available at 2.5 K and 15 K with respective cooling powers of 10 mW and 100 mW dedicated to the sub-Kelvin stage.

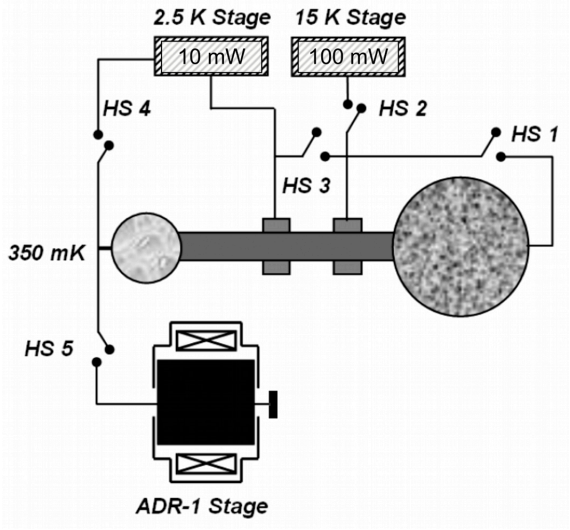

Fig. 1. Association of a sorption cooler and ADR (IXO thermal environment)

During recycling of our system, the heat rejected is distributed to these sources as depicted in Fig. 1. The details of its operation is detailed in [7] and [8].

In the framework of an ESA contract, we designed, manufactured and tested a 50 mK Engineering Model (EM) based on this concept. The EM is designed to provide a net heat lift of 1 and 10 µW at respectively 50 and 300 mK during at least 24 hours and with a recycling time of less than 8 hours.

This paper discusses the measured performance of the system.

2. ESA Engineering Model

A picture of the EM is shown without the covers in fig. 2. It features the sorption cooler and the ADR stage in parallel given the two cold ends at the front of the model. The structure is made of aluminum and has mechanical and thermal functions. All heat switches are gas-gap type using miniature sorption pumps that are heat-sinked on the structure regulated at 2.5 K (except for HS2). HS2 is heat-sinked at 15 K and is filled with hydrogen since helium is not well trapped at this temperature.

The salt pill contains 460 grams of Chromium Potassium Alum (CPA) grown on the 780 copper wires of the thermal bus. It is suspended inside the coil by 16 Kevlar cords.

The magnetic shield is 4 mm thick. It is made of a Fe-Co alloy (AFK1 from Arcelor-Mittal) and has been designed to shield the magnetic field up to 3 mT at 10 cm perpendicularly to the shield when the coil produces 0.8 T. It also participates to the system stiffness

The system weights 5800 grams, including the covers.

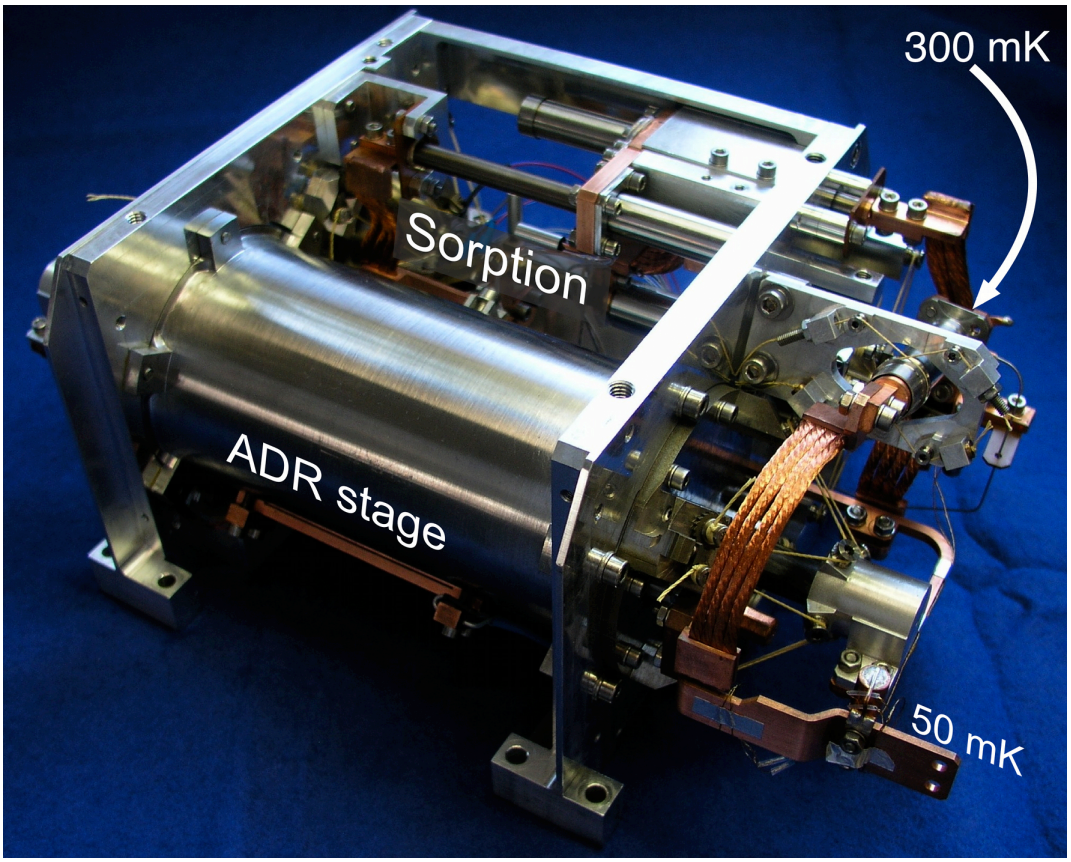

Fig. 2. Picture of the Engineering Model as tested

3. Low temperature characterizations

An ultimate temperature of 22 mK and a parasitic heat load of about 0.3 μW have been measured, in agreement with the calculations.

Fig. 3 shows the typical measurements conducted at low temperatures. They allowed us to determine the specific heat of the pill as well as its thermal conductance. Depending on the temperature, power ranging from 20 to 200 μW have been applied during a known time (from 300 up to 540 seconds). This results in a step in the ADR stage temperature, from which both the specific heat and the thermal resistance can be extracted.

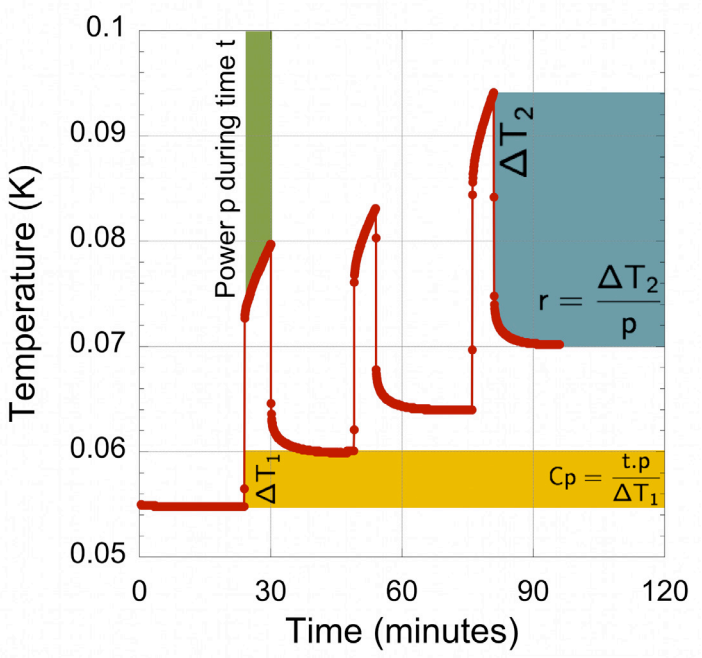

Fig. 3. Measurements method of specific heat and thermal conductance of the salt pill

3.1. Specific heat

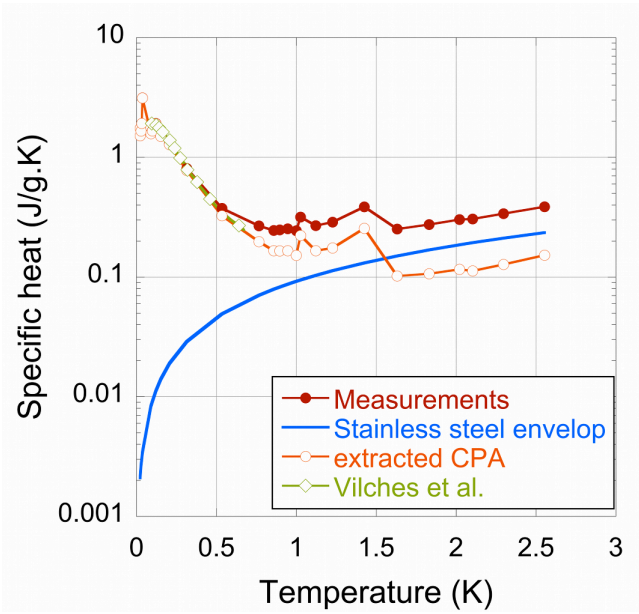

Fig. 4. Salt pill specific heat measurements

The amount of energy deposited on the pill is well determined since both the applied power and the duration are precisely set. Thus the pill specific heat can be extracted. It consists in the specific heat of the salts, the stainless steel envelope and the copper thermal bus. The two latter contributions can be subtracted to our measurements, as their weights are well known. The results are shown in fig.4.

It appears that the copper specific heat is negligible on the whole temperature range. On the contrary, the stainless steel envelope contribution is of the same order of magnitude as the salts' above 1 K. This causes an excess of mass to be cooled down by the sorption cooler and the salt pill envelope could be optimized in future systems.

Once the envelope contribution has been subtracted, our measurements agree well with the data of Vilches *et al.* [9] on the whole range of temperature.

3.2. Thermal resistance

The thermal resistance r has been measured: the temperature gradient (ΔT_2 in fig.3) for a given power (between 20 and 200 µW) is measured. The thermal resistance is given by:

$$r = \frac{\Delta T_2}{P_{applied} + P_{parasitics}}$$

The temperature of the measurements is the mean temperature of the measured gradient.

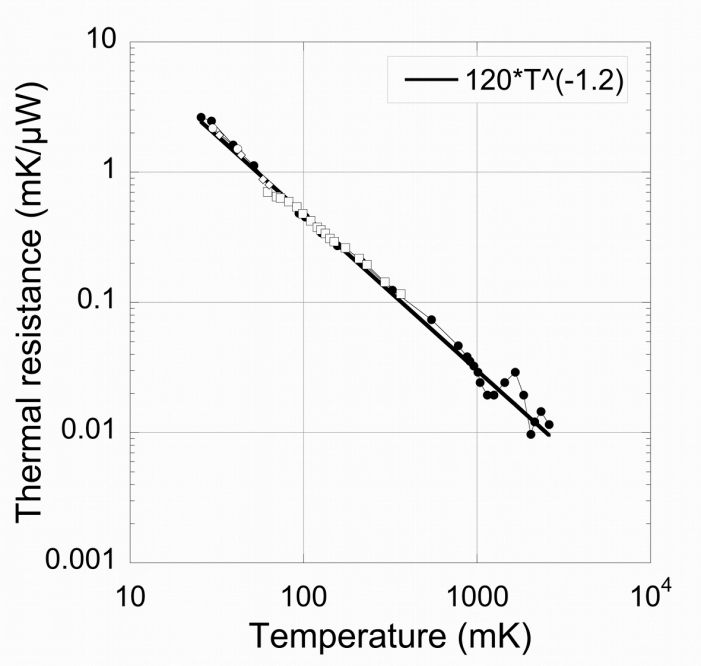

Fig. 5.a. Measured salt pill thermal resistance

Fig. 5 shows the results of the pill thermal conductance. Typical result is a thermal resistance of about 1.1 mK/µW at 50 mK. Precise results study shows that half of the thermal resistance comes from the copper bar between the ADR end and the EM 50 mK cold end. Ensuring the copper presents a very good thermal conductivity is an important point for the cooler performances.

3.3. Available energy

The available energy has been measured at 45, 50, 100 and 320 mK. The results are gathered in table 1. The table gives the total power ($P_{applied}$ + $P_{parasitics}$) and the autonomy measured at each temperature.

The available energy increased by a factor 3.8 between 50 and 100 mK. This point is very important in the requirements put on the cooler during the design phase of a mission: the higher the set point, the smaller the salt needed, the lighter the cooler.

ADR Temperature (mK)	Total power (µW)	Measured autonomy	Energy (J/mole)
45	1.3	22h31mn	0.11
50	1.3	24h	0.12
100	5.4	21h51	0.46
320	50.3	10h42	2.1

Table 1. Effect of ADR temperature of the autonomy

4. Autonomy and recycling

The autonomy measurements using the full cooler depend greatly on a balance between ADR and sorption autonomy. By changing the ADR final state of magnetization, both ADR and sorption autonomies are modified: the higher the field and/or the lower the temperature, the higher the ADR autonomy at the cost of additional energy dumped on the sorption, thus lowering its autonomy. At first order, a change of 1 hour in the ADR autonomy results in a change of 18 minutes in the sorption autonomy.

The recycling scheme involves a succession of phases that have to be carefully controlled. Several schemes have been considered which included different magnetization period for the ADR in respect to the sorption recycling. The study of these different schemes has been presented in [8]. Our test campaign has been mostly done using the cycle that gave the best duty cycle in our simulation, which we will call the “nominal cycle”. However, at the end of the campaign, a simpler algorithm has been used, the so-called “simplified cycle”. For this cycle, the magnetization at 15 K has been suppressed. Our calculation indicated that this cycle would be more efficient (longer autonomy), but with a longer recycling time resulting at the end in a slightly shorter duty cycle. However, the simpler cycle has been tested, showing a comparable duty cycle.

The different phases for the two cycles mentioned are described in fig. 6. All the regulations are set using a PID as a main control and sometimes with additional refinement to deal with the beginning and end of the phases. The information of the power flowing to the heat sink is therefore used in real time to offer the best transfer possible. During the recycling, the power at the interface has been kept within the 10 and 100 mW specification at each heat sink.

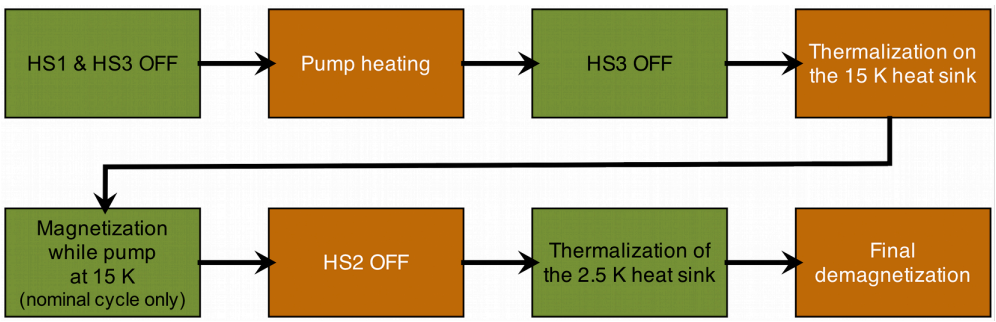

Fig. 6. Cycle phases description

A cycle representative of the nominal cycle is presented on fig. 7. An autonomy of 23h and 57 minutes has been measured with a recycling time of 8 hours. The duty cycle is 75 %. Considering the measurements uncertainties, these results are fulfilling the requirements. A simplified cycle presents an autonomy of 25h05 for a recycling time of 8h37. The duty cycle is 74 %.

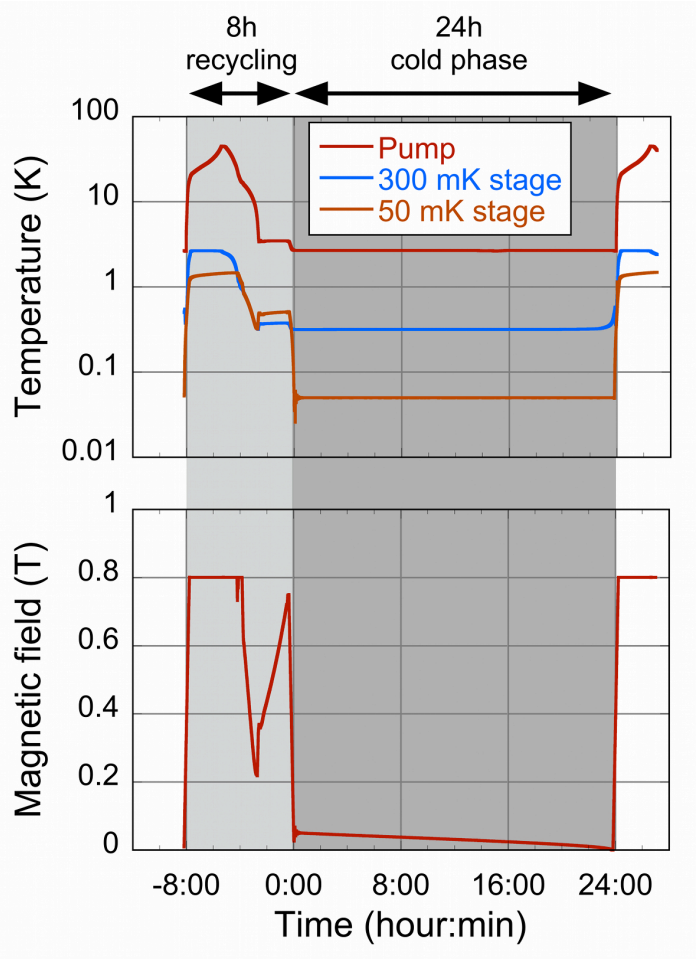

Fig. 7. Nominal cycle operation

The power dissipations at the 2.5 and 15 K heat sinks are shown in fig. 8. They remain below the requirements. One can see that in the first phase, there is a short spike in the power deposited on the 2.5 K heat sink. This peak corresponds to the closing of the evaporator heat switch when its temperature is higher than 2.5 K. It is not possible to completely suppress it but it is so short, it would be filtered in a real setup. The second spike seen on the figure has been eliminated by carefully tuning the PID control in the following experiments.

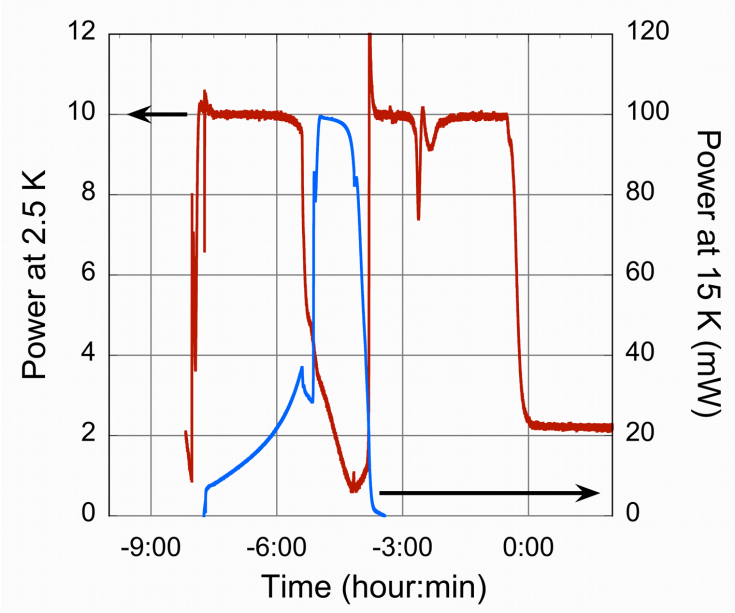

Fig. 8. Power dissipated to heat sinks (nominal cycle)

4.3 Cold heat sink temperature

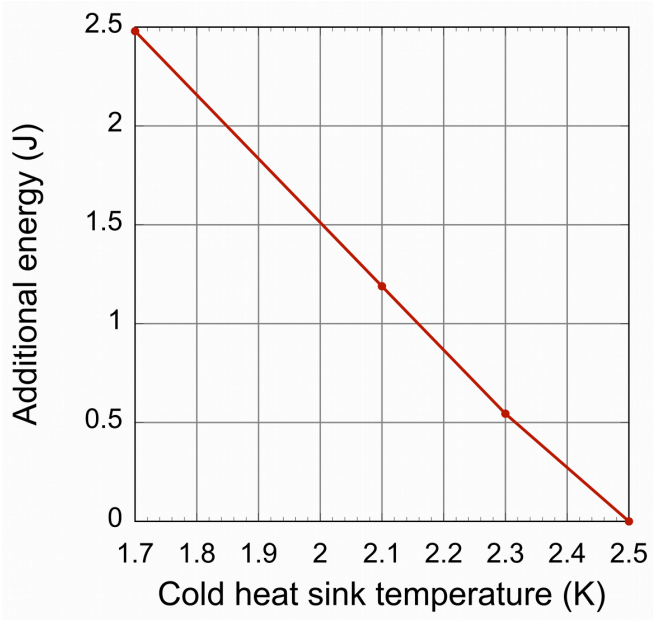

Fig. 9. Margin in energy relative to the 2.5 K case

The impact of the heat sink temperature has been tested for several cases between 1.7 and 2.5 K. The heat sink temperature has an influence on the condensation temperature and on the losses on the evaporator during the cold phase. The direct influence is therefore mostly restricted to the autonomy of the sorption cooler. A real optimization of the full cooler would involve adapting the magnetization state of the ADR to provide a similar cold time for the sorption and for the ADR. In our case, to restrict the number of changed parameters during this study, we measured only the additional cooling energy available at the sorption stage as function of the heat sink temperature. With the reduced cold heat sink temperature, the autonomy of the sorption cooler will increase and we expected autonomy of more than 40 hours. These long autonomies would have been complicated to measure because of the finite hold time of the test cryostat. Therefore, the available energy has been measured by integrating the energy and the losses on the evaporator after a standard 24 hours cold phase. Depending on the specification, this additional energy is equivalent either to additional power on the sorption or on the ADR, or longer hold times.

As our simulation predicted, the influence of the heat sink temperature on the recycling time is small: for all the experiments, the recycling time ranges from about 7h43 to 8h47. The variations measured are within the accuracy of the measurements considering all sources of uncertainties. The ADR parameters and mainly the magnetizing conditions have been kept the same during each of these experiments. Because the change on the heat sink temperature has only a marginal impact on the losses on the ADR, its autonomy is also practically independent of the heat sink temperature. Most of the influence of the heat sink temperature is on the autonomy of the sorption cooler. The margin in energy relative to 24 hours with 10 µW is measured. The results are presented in fig. 9. The results showed that a gain of about 3 additional Joules at 300 mK are obtained by reducing the temperature from 2.5 to 1.7 K. This demonstrates that the cold heat sink temperature is of crucial importance on the duty cycle of this cooler.

4.4 Temperature stability

The temperature stability on the cold interface is of importance to guarantee stability of the detectors. For this work, the evaporator temperature has not been regulated because the temperature stability is sufficiently stable by design, with a drift usually acceptable. The ADR temperature on the other hand has to be regulated. Also, for thermodynamic reasons, it is much more efficient (about twice the autonomy) to regulate the temperature at 50 mK by controlling the ramp rate of the coil rather than to fully demagnetize and let the temperature drift. For this work, the frequency of the temperature acquisition and regulation has been set to 1 Hz. This is a good optimum between the temperature readout and the necessary sensitivity of the power supply.

The RMS noise measured is of 5 to 7 µK RMS with a power spectral amplitude below 10 µK/√Hz. The limitation is the temperature readout of the thermometers. Several possibilities to improve this sensitivity have been identified and will be implemented as part of our implication in SAFARI (see [10]).

5. Residual magnetic field

The residual magnetic field has been measured at three locations: at 5 and 10 cm from the magnetic shield perpendicularly to the ADR axis and 8 cm from the magnetic shield along the axis, see fig. 10, respectively point 1,2 and 3. The Hall probe used is a calibrated THS118 probe from Toshiba. Its sensibility is 220 Ω/T with an error of 10 %. It has been supplied with a current I of 2 mA (with a precision far inferior to 10 %) and the tension has been measured.

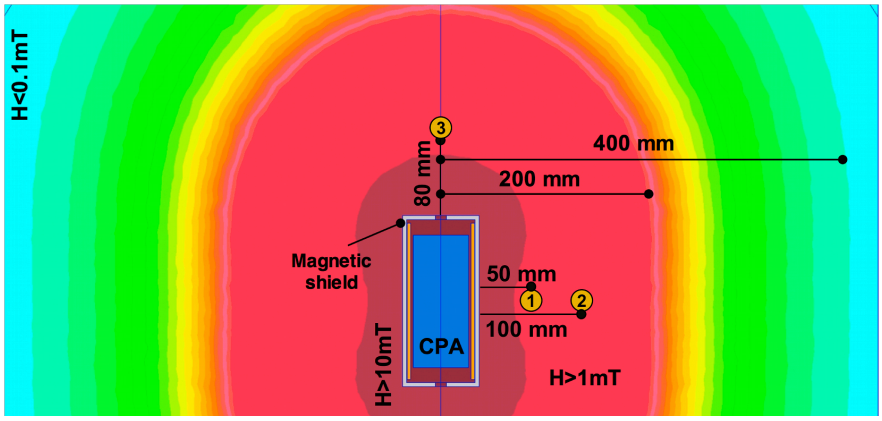

Fig. 10. Magnetic field measurement points

The results are shown in fig. 11, with the 10 % error bars. The 50 mm point has been measured twice in a row to have a view of the scattering of the measurements. Both measurements are within 3 percents. For the 80 mm measurement point, the calculations have been performed for a distance of 80 and 90 mm to have a view of the sensibility of the probe position.

The calculations are performed with the same EM shield geometry and are based on the AFK1 saturation curve measured at 77 K. In the perpendicular direction, the calculations produce 40 % higher than the measurements; the shield performances are better than predicted. Results are in better agreement with calculation along the coil axis (results and calculation are within 10 %).

The measurements show that the residual magnetic field produced by the EM during the cold phase remains well below 0.1 mT, our requirement.

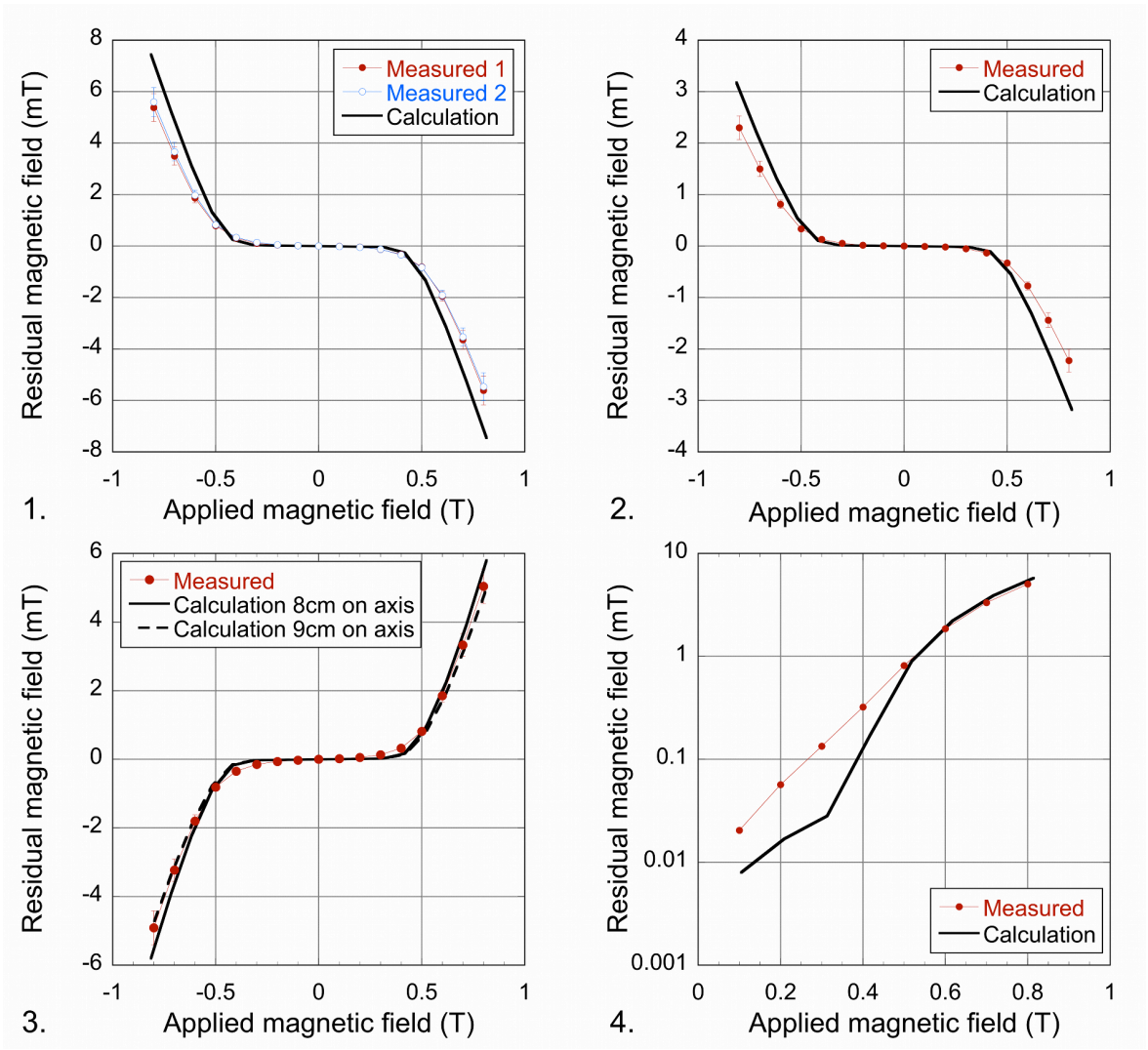

Fig. 11. Residual magnetic field measurement. 5 cm and 10 cm from the magnetic shield perpendicular to the ADR axis (1 and 2) and 8 cm from the magnetic shield along the axis (point 3). 4: Close-up of the results at the 8 cm point.

6. Mechanical tests

Resonant frequencies have been measured at the structure, the sorption pump and evaporator and ADR level. The results are shown in table 2, the X-axis and Y-axis are respectively the longitudinal and perpendicular to the sorption/ADR, the Z-axis is the vertical axis.

	X (Hz)	Y (Hz)	Z (Hz)
Structure	825	1204	-
Sorption pump	353	482	515
Evaporator	353	323	410
ADR	294	160	881

Table 2. First resonance frequencies at subsystem level

The lowest resonant frequency measured is 160 Hz for the salt pill in the Y direction (perpendicular to its axis). The calculation predicted a resonance frequency in the same direction at about 130 Hz. The requirement specified that all resonance frequencies have to be higher than 100 Hz. The EM fulfills this objective.

7. Conclusions

The first complete hybrid cooler featuring a sorption stage coupled to a miniature ADR stage has been designed, manufactured and tested. This engineering cooler development has been carried out in the framework of an ESA Technical Research Program. The overall performance are satisfactory and in agreement with predictions. An ultimate temperature of 22 mK has been achieved and hold time of 24 hours have been measured at 50 mK for a net heat lift of 1 µW (and simultaneously 10 µW at 300 mK). Low temperature characterizations of the salt pill show a thermal resistance of about 1.1 mK/µW at 50 mK and measured salts specific heat in agreement with literature. A strong effect of the ADR stage regulation temperature on the available energy has been measured. A recycling time of 8 hours and an autonomy of 24 hours under 1 µW have been measured as stated in our objectives. The influence of the heat sink temperature has been experimentally measured and indicates a strong link between duty cycle and temperature of the cold sink.

8. Acknowledgements

We thank the European Space Agency for funding this work. We thank JL. Durand and L. Clerc for their work in the EM manufacture and assembling and the test campaign. We thank Guillaume Donnier-Valentin of CNRS Institut Néel for the measurement of the AFK1 saturation curve.

9. References

[1] Luchier N.; Duband L., Small Adiabatic Demagnetization Refrigerator for space missions, *Cryocoolers 13, Proceedings of the 13th International cryocooler conference, March 29th-April 1st 2004, p561-566*

[2] Martin F., Vermeulen G., Camus P., Benoit A., “A closed cycle ^{3}He–^{4}He dilution refrigerator insensitive to gravity », *Cryogenics*, *Volume 50, Issue 9*, *September 2010*, *Pages 623-627*

[3] Shirron P. *et al.*, “Development of a cryogen-free continuous ADR for the constellation-X mission” *Cryogenics*, vol. 44 (2004), pp. 581-588.
[4] Bartlett J. *et al.*, Improved performance of an engineering model cryogen free double adiabatic demagnetization refrigerator, *Cryogenics*, *Volume 50, Issue 9*, *September 2010*, *Pages 582-590*
[5] Shinozaki K. *et al.*, “Development of double-stage ADR for future space missions”, *Cryogenics*, *Volume 50, Issue 9*, *September 2010*, *Pages 597-602*
[6] Duband L. *et al.*, “Herschel flight models sorption coolers”, *Cryogenics*, vol. 48 (2008), pp. 95-105
[7] Luchier N. *et al.*, “50 mK cooling solution with an ADR precooled by a sorption cooler”, *Cryogenics, Volume 50, Issue 9, September 2010, pages 591-596*
[8] Duval J.M. *et al.*, “Progress in the development of the IXO 50 mK Sorption-ADR stage”, *16th International Cryocoolers Conference, 17-20 May 2010*
[9] O. E. Vilches, J. C. Wheatley, “Measurements of the Specific Heats of Three Magnetic Salts at Low Temperatures”, *Physical Review, vol.148, 1966, page 509*
[10] L. Duband *et al.*, “SPICA Subkelvin Cryogenic Chains”, presented at the 2011 Space Cryogenics Workshop, Coeur d’Alene, IDAHO.

40 K Single-stage coaxial pulse tube cryocoolers

Haizheng Dang*

* Corresponding author. Shanghai Institute of Technical Physics, Chinese Academy of Sciences, 500 Yutian Road, 200083, Shanghai, P.R. China
Tel.: +86-21-25051191
Fax: +86-21-65441819
haizheng.dang@mail.sitp.ac.cn

Abstract

Several 40 K single-stage coaxial high frequency pulse tube cryocooler (PTCs) have been developed to provide reliable and low-noise cooling for GaAs/AlGaAs Quantum-Well infrared photodetectors (QWIPs). The inertance tubes together with the gas reservoir become the only the phase shifter to guarantee the required long-term stability. The mixed regenerator consisting of three segments has been developed to enhance the overall regenerator performance. At present, the cooler prototype has achieved a no-load temperature of 29.7 K and can typically provide 860 mW at 40 K with 200 W of electric input power rejecting at 300 K. The performance characteristics such as the temperature stability and ambient temperature adaptability are also presented.

Key words: 40 K; single stage; coaxial; E. pulse tube cryocooler; QWIPs

Highlights

> Single stage coaxial pulse tube cryocoolers without the double-inlet reach a no-load temperature of 29.7 K. > The mixed regenerator consisting of three segments has been developed to enhance the overall regenerator performance. > The inertance tubes together with the gas reservoir as the only the phase shifter guarantee the stability. > They provide 860 mW at 40 K with 200 W of electric input power rejecting at 300 K. > They have the potential to cool GaAs/AlGaAs QWIPs.

1. Introduction

In recent years, more and more space applications such as weather monitoring, Earth observation systems, astronomy, etc. require high performance large format long wavelength infrared (LWIR) detector arrays in the range of 13-16 μm [1]. Traditionally, longer wavelengths could be accessed by narrowing the band-gap of the most common photon detectors such as $Hg_{1-x}Cd_xTe$ by changing its alloy composition x. However, very narrow bandgap materials are difficult to grow and process into devices, which often reduce the yield and also increase the cost of the arrays [1]. These difficulties motivate the exploration of low effective material systems such as GaAs/AlGaAs. As a result, the significant efforts have been devoted in developing GaAs-based Quantum Well Infrared Photodetectors (QWIPs) and rapid advances have been achieved in the past decade. Such a GaAs-based QWIP benefits from the highly mature GaAs growth and processing technologies, which becomes critical at the very long wavelengths where narrow band-gap materials become very difficult to work with. Besides the high production yield, low cost, and very long wavelength capability, the GaAs/AlGaAs QWIPs also have other important advantages in large uniform FPAs, mature III–V technology, high speed, and radiation hardness, etc.

Recently, the GaAs/AlGaAs QWIPs with the response wavelength of longer than 15 μm have been worked out [2], and the practical applications are underway. They require about 0.5-1.0 W of cooling power at around 40 K. The conventional cooling method using the cryogens brings some intrinsic inconvenience in transportation, maintenances, the impact of orientations, etc, and thus a turnkey mechanical cryocooler is desirable. However, while a cryocooler is employed instead of a cryogen cryostat, the low vibration and EMI have to be especially emphasized in order to bring the minimum additional interferences. The absence of any moving mechanical component at the cold end of the pulse tube cryocooler (PTC) endows it the intrinsic advantages such as minimum vibration and EMI, which have a strong appeal to GaAs/AlGaAs QWIPs application.

2. Development goals

Several single-stage coaxial PTC prototypes have been developed in our group to meet abovementioned requirements. In general, the multi-stage arrangement is often employed to realize the applications below 40 K [3,4]. However, obviously, the single-stage arrangement will definitely minimize the complexity of the cooler system and also reduce the research cost. Furthermore, although the in-line PTCs working at 30-40 K have already achieved remarkable performance in some other groups [5-7], owe to the practical applications, the coaxial arrangement is chosen in our group to ease the integration between the cold head and the detectors. The double-inlet mechanism is also often employed as an effective means to evidently enhance the thermodynamic performance of the abovementioned developed PTCs [6-7]. However, owing to the potential instability induced by the possible DC effect, for the

developing PTCs, the double-inlet mechanism will not be considered, while the phase shifting mechanism at the warm end only uses the inertance tubes together with the corresponding gas reservoir instead to guarantee the required long-term stability.

Considering the necessary irreversible losses, the refrigeration requirement is to provide around 0.8 W of cooling power at 40 K. The bus power source and the reject environment require that the electric input power is less than 200 W and the warm end is at a 300 K of reject temperature. The overall weight including cooler control electronics will be kept below 8.0 kg. Table 1 gives a summary of key development goals, of which the parameters such as the ambient temperature adaptability, temperature stability, vibration output of the cold head and expected lifetime are very important for the practical applications.

3. Design and optimizations

The schematic of the developed single-stage coaxial inertance PTC is shown in Figure 1. The cooler system is addressed as the split arrangement because the cold finger is connected the linear compressor with a 25 cm flexible metallic connecting tube. The linear compressor adopts the dual-opposed piston configuration to minimize the generated vibration. The inertance tubes, which consist of two sections with different inner diameter and length (as the Inertance tube I and II shown in figure 1), are optimized at 40 K to obtain desirable phase relationship since a single inertance tube with a constant diameter has great difficulty in obtaining the desired phase relationships. The double-segmented inertance tube, together with a gas reservoir, serves as the only phase-shifting components in order to guarantee the reliable performance of the system. The two straighteners at the warm and cold ends try to keep the laminar working gas in the pulse tube.

An important feature of the 40 K PTC different from other types developed in the same group for providing coolings above 50 K [8] is that the former employs a mixed regenerator, which consists of three segments with the same diameters (as the Regenerator I, II and III shown in figure 1). The three-segmented regenerator is filled into the stacked stainless steel screens made of the same material while with the different meshes, respectively. Table 2 gives the key dimensional parameters of the mixed regenerator.

The optimization of the three-segmented regenerator is based on the principle of minimizing the flow resistances while keep the necessary thermal penetration depths of the regenerator matrix at the same time along the whole regenerator. The development of the mixed regenerator is an important optimization to enhance the refrigeration performance in the range of 30-40 K. In the comparison experiments, compared with a single regenerator filled with the constant 400-mesh SS, provided that the other components are kept the same except that the inertance tubes have been optimized for the corresponding regenerator geometry, the no-load temperature goes down from 34 K to 29.7 K, while the cooling capacity at 40 K increases evidently from 0.52 W to 0.86 W with the same electric input power of 200 W at 300 K reject

temperature.

The typical cool-down curve of the developed 40 K PTC is shown in figure 2. It takes about 37 minutes for the cold tip to cool down from 298 K to the no-load temperature of 29.7 K. The more detailed cool-down process below 40 K is shown in figure 3 as a supplement. The cooling performance at several typical temperatures is shown in figure 4, while the performance of the PTC with a single constant regenerator is also shown as comparisons.

The fine slit exchanger has become the conventional optimization means in designing a coaxial PTC operating at lower temperatures, as described in our developed 60 K high frequency single-stage coaxial PTCs [9]. As the operating working temperature goes down to 40 K or below, there will be much more demanding requirements on the high efficiency of the cold and warm-end heat exchangers to exchange the heats as soon. Therefore, for both exchangers, each slit is fabricated by the EDM technology into with the gap width as narrow as 0.15 mm, in stead of the 0.2 mm used in the 60 K PTCs. The much finer slits further increase the effective heat exchange area for the given dimensions, and also become additional straighteners at both ends to suppress the turbulence introduced by the flow reversal.

4. Ambient temperature adaptability

The investigation on the temperature adaptability of the developed 40 K PTC is emphasized. In contrast to designing one PTC for operation over 50 K, the reversible losses introduced by the thermal conduction in a 40 K cooler system will play an important role, because of the smaller gross refrigeration power, and also owe to the even larger temperature difference between the cold and warm ends. Here an experiment is conducted to examine the cooler's sensitivity to the heat sink with the constant heat load of 860 mW, as shown in figure 5. It shows that with a 213 K of reject temperature, the aimed cooling capacity is achieved with only a 165 W of input electric power. However, a 230 W of input electric power has to be applied in order to keep the same cooling performance when the reject temperature increases up to 313 K. The dramatic change of the input power with the reject temperature will bring adverse effect on the PTC operating in a fluctuating source temperature environment.

At present, two measures are under consideration to enhance the performance of the heat exchangers, especially at the warm end. They are: 1) to fabricate the slit exchangers with further more narrow gap width to increase the effective exchange area, and 2) to try to optimize the interface between the warm end of the pulse tube and the warm heat exchanger, which is also regarded as one of the sources accumulating the heat.

5. Temperature stability

The developed 40 K single-stage PTC system only adopts the inertance tube together with a reservoir to realize the stable performance. Before the acceptance tests are conducted, the cold head temperatures have been monitored over a relatively longer period to examine the temperature stability at 40 K. Figure 6 shows the experimental results during 150 minutes. The fluctuations are far below the required ± 0.1 K.

6. Discussions and conclusions

The 40 K single-stage coaxial high frequency pulse tube cryocooler (PTCs) have been developed to provide reliable and low-noise cooling for GaAs/AlGaAs QWIPs, which have a potential space application to replace some $Hg_{1-x}Cd_xTe$ based IR detector arrays in the range of very long wavelength (such as >15 μm).

The single-stage arrangement is employed instead of the two-stage to minimize the complexity of the cooler system. Furthermore, in order to avoid the potential instability induced by the possible DC effect, the double-inlet mechanism is excluded while the phase shifting mechanism only uses the inertance tubes together with the corresponding gas reservoir. The coaxial arrangement is chosen instead of the in-line type to ease the integration between the cold head and the cooled detectors.

A mixed regenerator, which consists of three segments filled into with the different meshes stainless steel screens, respectively, has been developed to enhance the regenerator performance at the coldest end and also to minimize the overall flowing resistance along the tube.

At present, the developed cooler prototypes, which weights 7.5 kg including the cooler control electronics, has achieved a no-load temperature of 29.7 K, and can typically provide 860 mW at 40 K with 200 W of electric input power at 300 K reject temperature. The preliminary shows that the long-term temperature stability (<250 minutes) of the cold head is also within the required limit.

In the practical experiments, it is found that the developed QWIPs shows better performance when the cold head temperature is lowered 2 K or around. Therefore, the performance of the developed PTC will be further optimized correspondingly at the temperatures of 38 K or even lower ones in the next step.

Acknowledgements

The work is financially supported by The Knowledge Innovation Project of The Chinese Academy of Sciences (No. KGCX1-YW-23) and also sponsored by Shanghai Pujiang Program (No. 10PJ1410800).

References

[1] Kukkonenb CA, Sirangelo MN, Chehayeb R, et al. Commercialization of quantum well infrared photodetector focal plane arrays. Infrared Physics & Technology 2001; 42 (3-5):397-405.

[2] Li N, Guo FM, Zhen H, et al. Detection wavelengths and photocurrents of very long wavelength quantum-well infrared photodetectors. Infrared Physics & Technology 2005; 47 (1):29-36.

[3] Nast TC, Olson J, Evtimov B, et al. Development of a two-stage pulse tube cryocooler for 35 K cooling. Cryocoolers 2003; 12:213-8.

[4] [Chan CK, Nguyen T, Jacob C, et al. High capacity two-stage pulse tube cooler. Cryocoolers 2003; 12:219-24.

[5] Burt WW and Chan CK. New mid-size high efficiency pulse tube coolers. Cryocooler 1997; 9:173-82.

[6] Yang LW, Xun YY, Thummes G, et al. Single-stage high frequency coaxial pulse tube cryocooler with base temperature below 30 K. Cryogenics 2010; 50 (4):281-6

[7] Ren J, Dai W, Luo E. Experimental investigation on a single-stage Stirling-type pulse tube cryocooler working below 30 K. Cryocoolers 2011; 16:51-5.

[8] Dang HZ. High frequency coaxial pulse tube cryocoolers for cooling infrared focal plane arrays. In: Proceedings of SPIE 7854, 2010

[9] Dang HZ, Wang LB, Wu YN, et al. Performance investigation on SITP's 60 K high frequency single-stage coaxial pulse tube cryocoolers. Cryocoolers 2011; 16:149-56

Table list

Figure list

Table 1. A summary of key development goals of the SITP's 40 K PTC

Parameters	Design goal
Stage arrangement	Single-stage
Geometrical arrangement	Coaxial
Phase shifting mechanism	Without double-inlet
Cooling capacity	≥ 0.8 W@40K (at 300K reject)
Power consumption	≤ 200 W (electric input power)
No-load temperature	≤ 30 K
Mass	≤ 8.0 kg (including control electronics)
Ambient temperature adaptability	243 K to 323 K
Temperature stability	± 0.1 K
Vibration output of the cold head	≤ 0.1 Nrms
Expected lifetime	≥ 50,000 hours

Table 2. The key parameters of the mixed regenerator

	Inner diameter	Length	Regenerator matrix
Regenerator I	21 mm	15 mm	250-mesh SS
Regenerator II		45 mm	400-mesh SS
Regenerator III		15 mm	500-mesh SS

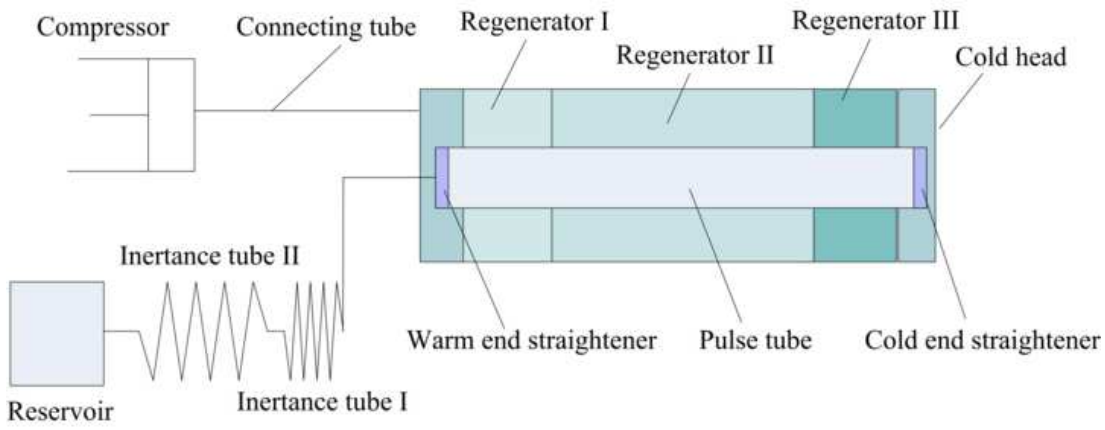
Compressor
Connecting tube
Regenerator I
Regenerator II
Regenerator III
Cold head
Inertance tube II
Warm end straightener
Pulse tube
Cold end straightener
Reservoir
Inertance tube I

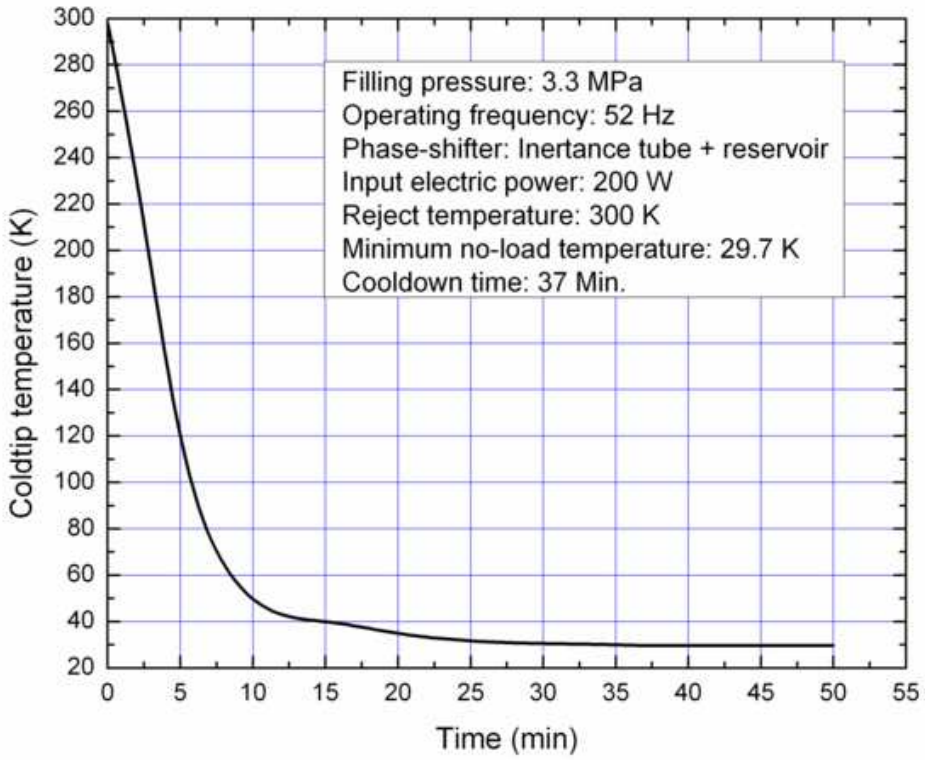
Filling pressure: 3.3 MPa
Operating frequency: 52 Hz
Phase-shifter: Inertance tube + reservoir
Input electric power: 200 W
Reject temperature: 300 K
Minimum no-load temperature: 29.7 K
Cooldown time: 37 Min.
Coldtip temperature (K)
Time (min)
300
280
260
240
220
200
180
160
140
120
100
80
60
40
20
0
5
10
15
20
25
30
35
40
45
50
55

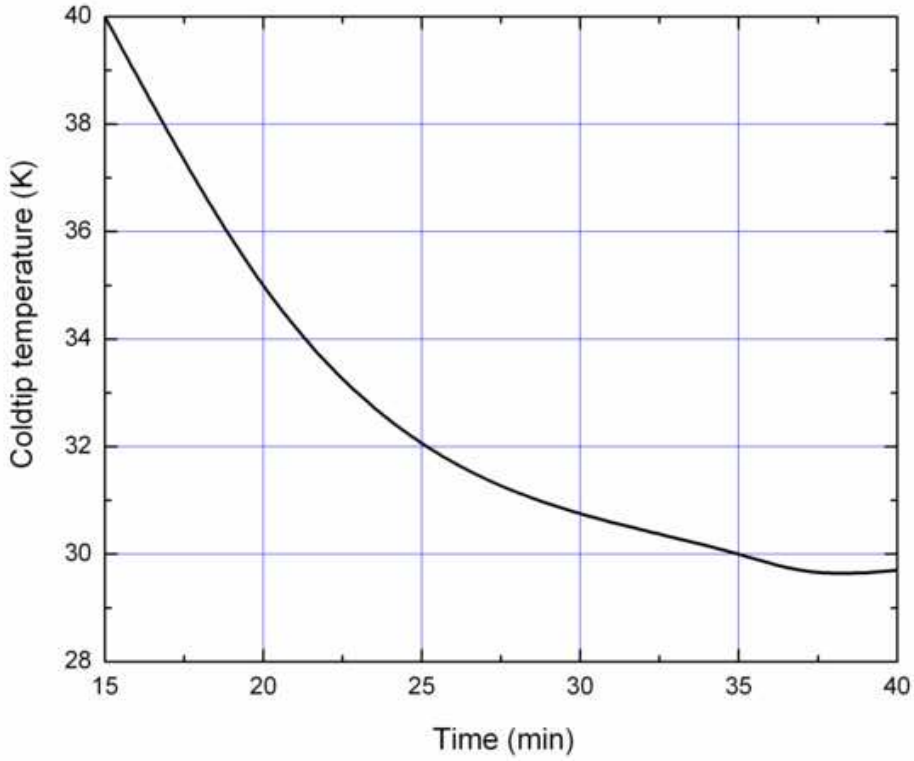
Coldtip temperature (K)
Time (min)
40
38
36
34
32
30
28
15
20
25
30
35
40

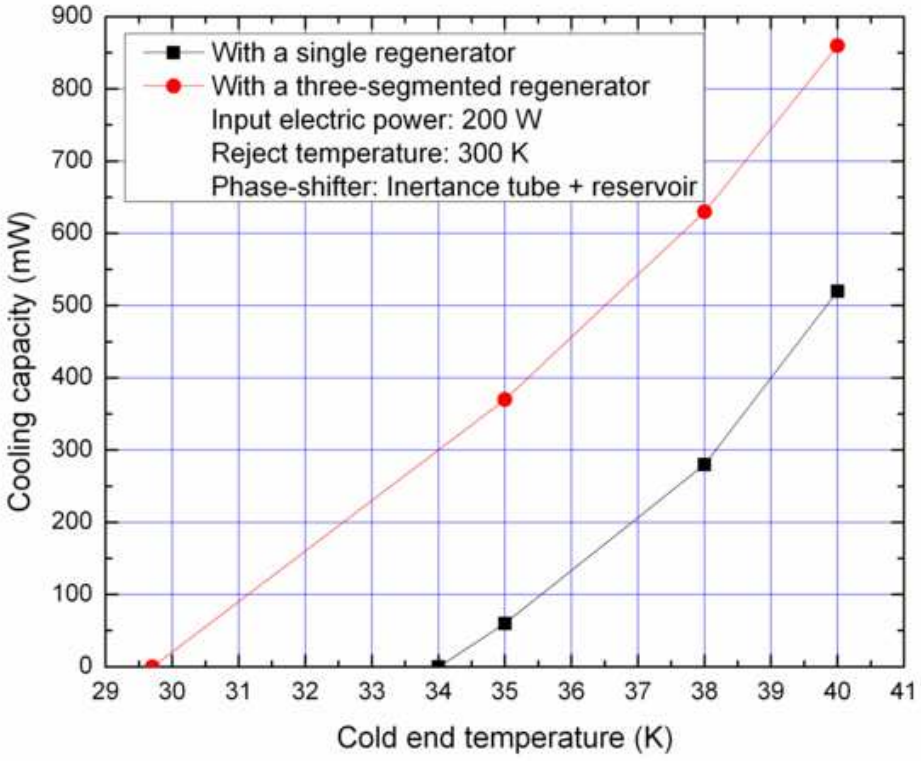
With a single regenerator
With a three-segmented regenerator
Input electric power: 200 W
Reject temperature: 300 K
Phase-shifter: Inertance tube + reservoir
Cooling capacity (mW)
Cold end temperature (K)
900
800
700
600
500
400
300
200
100
0
29
30
31
32
33
34
35
36
37
38
39
40
41

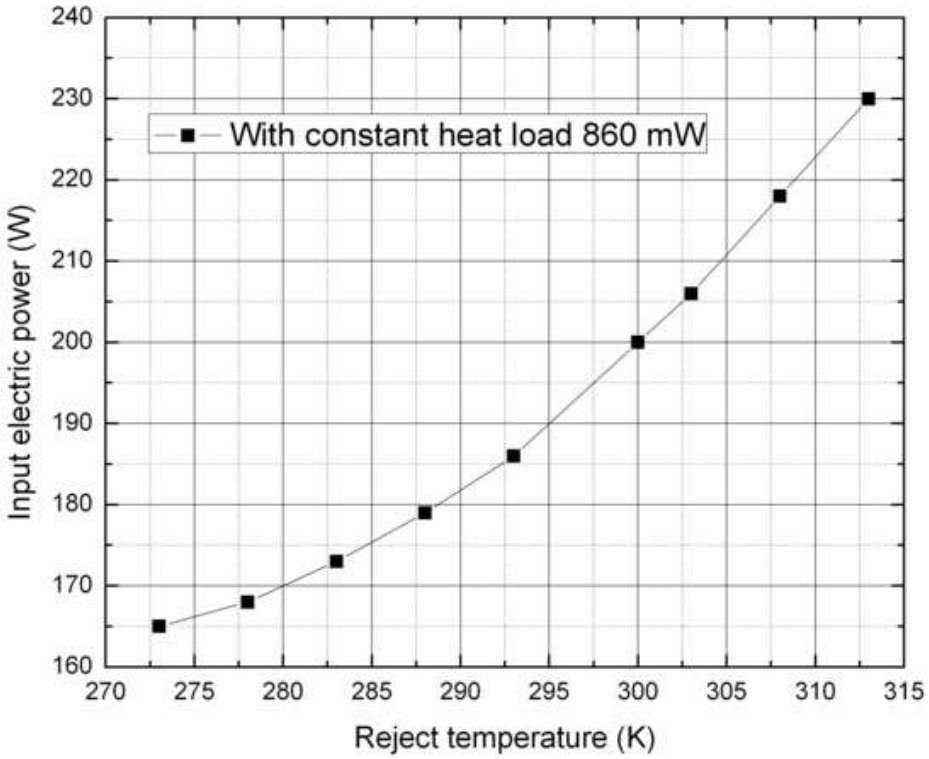
With constant heat load 860 mW
Input electric power (W)
Reject temperature (K)
240
230
220
210
200
190
180
170
160
270
275
280
285
290
295
300
305
310
315

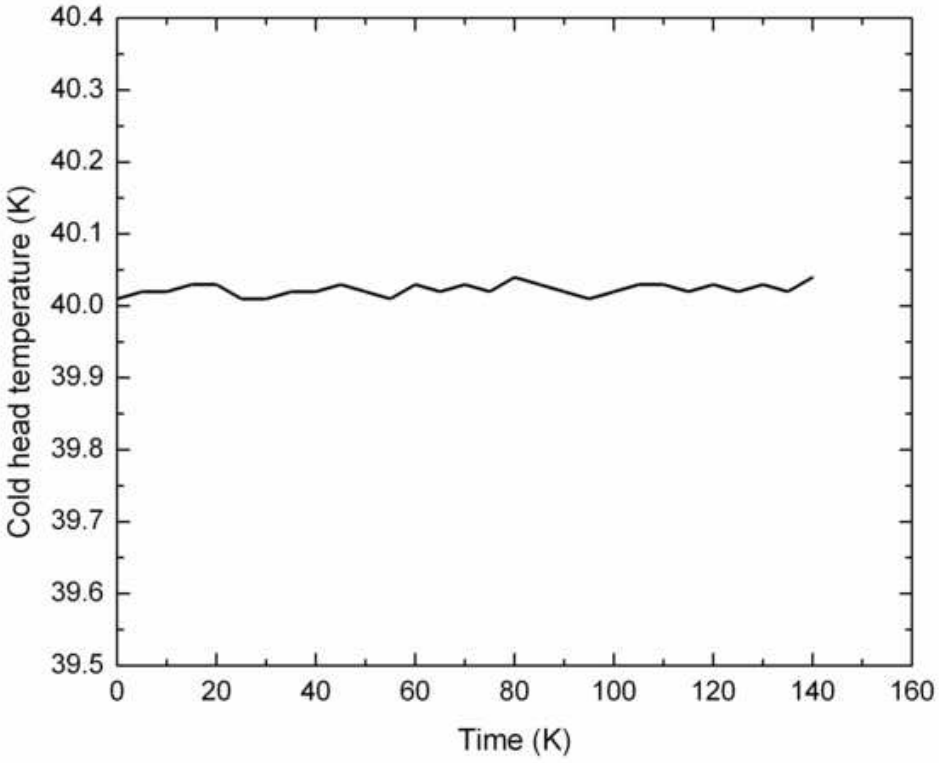
Cold head temperature (K)
Time (K)
40.4
40.3
40.2
40.1
40.0
39.9
39.8
39.7
39.6
39.5
0
20
40
60
80
100
120
140
160

Novel Load Responsive Multilayer Insulation with high in-atmosphere and on-orbit thermal performance

S. Dye [a], A. Kopelove [a ‡] , G. L. Mills [b]

[a] Quest Product Development Corp
6833 Joyce Street
Arvada, CO 80007
303.670.5088 Ph
303.674.1020 Fax
sdye@quest-corp.com
alank@quest-corp.com

[b] Ball Aerospace & Technologies Corp
1600 Commerce Street
Boulder, CO 80301
303.939.4700
gmills@ball.com

[‡] Corresponding Author

Abstract

Aerospace cryogenic systems require lightweight, high performance thermal insulation to preserve cryopropellants both pre-launch and on-orbit. Current technologies have difficulty meeting all requirements, and advances in insulation would benefit cryogenic upper stage launch vehicles, LH_2 fueled aircraft and ground vehicles, and provide capabilities for sub-cooled cryogens for space-borne instruments and orbital fuel depots. This paper reports the further development of Load Responsive MultiLayer Insulation (LRMLI) that has a lightweight integrated vacuum shell and provides high thermal performance both in-air and on-orbit.

LRMLI is being developed by Quest Product Development and Ball Aerospace under NASA contract, with prototypes designed, built, installed and successfully tested. A 3-layer LRMLI blanket (0.63cm thick, 77°K cold, 295°K hot) had a measured heat leak of 6.6 W/m^2 in vacuum and 40.6 W/m^2 in air. In-air LRMLI has an 18X advantage over Spray On Foam Insulation (SOFI) in heat leak per thickness and a 16X advantage over aerogel. On-orbit LRMLI has a 78X lower heat leak than SOFI per thickness and 6X lower heat leak than aerogel.

The Phase II development of LRMLI is reported with a modular, flexible, thin vacuum shell and improved on-orbit performance. Structural and thermal analysis and testing results are presented. LRMLI mass and thermal performance is compared to SOFI and aerogel.

Highlights

- Load Responsive MLI dynamically compresses a spacer under atmospheric load, supporting an integrated, thin, lightweight vacuum shell, then disconnects spacers under vacuum for reduced heat leak and higher performance on-orbit.
- A 3-layer LRMLI prototype was built, installed and tested with a measured in vacuum performance of 6.6 W/m^2, equal thickness SOFI has a heat leak of 515 W/m^2, equal thickness aerogel heat leak is 42 W/m^2 (77°K to 295°K, 0.63cm).
- In air 3-layer LRMLI has heat leak of 40.6 W/m^2, equal thickness SOFI heat leak is 730 W/m^2, aerogel equal thickness heat leak is 657 W/m^2 (77°K to 295°K, 0.63cm).
- On orbit LRMLI performance shows a 78X lower heat leak than an equal thickness of SOFI, with an 8X mass advantage for equal heat leak. In-air LRMLI has 18X lower heat leak than SOFI per thickness, and 1.6X lower mass for equal heat leak.
- LRMLI has inherent construction benefits with reliability & robustness, provides excellent thermal performance both in-atmosphere and on-orbit, and offers advantages over SOFI and aerogels for insulating cryogens.

Keywords

Multilayer insulation, Load Responsive multilayer insulation, thermal insulation, integrated multilayer insulation

Abbreviations

Multilayer insulation	MLI
Load Responsive Multilayer insulation	LRMLI
Integrated Multilayer insulation	IMLI
Spray On Foam Insulation	SOFI

1. Introduction

Lightweight, high performance thermal insulation is critical to NASA's next generation spacecraft and missions - which will increasingly use cryogenic propellants. Zero or low cryogenic propellant boiloff is required during extended missions and lengthy on-orbit times. Heat flow through multilayer insulation is usually the largest heat leak in cryogenic systems, so improved insulation is desirable. Insulation meeting requirements for low heat leak, low mass, no cryopumping and robustness is especially challenging when the system must operate both within the atmosphere and on orbit.

Multilayer insulation (MLI) in a vacuum can usually provide the thermal performance required but requires a prohibitively heavy vacuum shell for use in air. Spray On Foam Insulation (SOFI) is typically used to insulate cryogenic propellant tanks pre-launch because of its light weight and insulating ability in air, but it has higher thermal conductivity than MLI and has a lack of robustness.

Quest Product Development Corp, working with Ball Aerospace, has developed a next generation MLI product called "Integrated MLI" (IMLI) (Dye et.al. 2009), which uses discrete ultra-low thermal conductance polymer micromolded spacers between radiation shield layers. This proprietary discrete spacer technology provides precise, controlled layer spacing and blanket density, reduces the conductance from layer to layer, and forms a bonded up, very robust and repeatable structure. IMLI prototypes produced for NASA and independently tested by NASA's Cryogenics Test Laboratory show a measured heat leak of 0.56 W/m^2 (20 layers, 3.6cm, 77°K to 295°K) (Johnson, 2010), about 37% lower heat leak per layer than typical conventional netting-based MLI.

Load Responsive Multi-Layer Insulation (LRMLI) is an innovative new technology designed to provide high performance insulation both in-atmosphere and on-orbit. LRMLI uses a dynamic beam polymer spacer that provides both low thermal conductance and support of a lightweight integrated vacuum shell.

LRMLI consists of layers of metalized polymer thermal radiation shields that are separated and supported by proprietary micro-molded spacer posts with low thermal conductance. In-air, the posts support a thin, lightweight hermetic vacuum shell that allows high vacuum to be maintained within the insulation. The spacers dynamically respond to load, compressing to support the external load of atmosphere acting on the thin wall vacuum shell, and disconnecting under reduced atmospheric pressure for lower heat leak at high altitudes or on-orbit. The dynamic spacer supports a vacuum shell under external atmospheric pressure, allowing a very thin, lightweight, flexible vacuum shell to be used. As external pressure is reduced at high altitudes or on-orbit, spacers dynamically disconnect to provide lower solid conduction resulting in lower heat leak.

IMLI is designed as a next generation MLI replacement with higher thermal performance, robust structures and a lower installed cost. LRMLI is designed as an insulation layer for use where both in-atmosphere and on-orbit performance is important. LRMLI could be a SOFI replacement for use in ground hold and pre-launch insulation to reduce ice formation and to enable use of sub-cooled cryogens. A mixed LRMLI/IMLI insulation system could provide ultra high thermal performance for cryopropellant tanks, spacecraft, space-borne instruments and orbital fuel depots.

Possible NASA applications include:

- Cryopropellant thermal insulation for launch vehicles, commercial crew vehicles and orbital fuel depots
- Replacement for SOFI insulation
- Space cryogenic instrument thermal insulation
- Orbital fuel depots

Possible Non-NASA applications include:

- Liquid hydrogen fueled aircraft fuel tank insulation
- Terrestrial applications requiring high performance thermal insulation
- Cryogenic dewar insulation for research, medical & industrial uses
- Appliances including refrigerators, freezers and water heaters
- Liquid hydrogen fueled ground vehicles

- Insulating superconducting devices such as MRI & superconducting power systems
- Insulated and refrigerated shipping & storage containers
- Thin insulation panels for high efficiency buildings

2. Results and Discussion

2.1 Phase I work

LRMLI development was performed under a NASA Phase I contract that was completed in 2009 demonstrating the feasibility of the LRMLI insulation system. A small scale LRMLI prototype was designed, fabricated and installed on a 20L test tank. The vacuum shell was a thin semi-rigid shell supported by the LRMLI blanket. The mass of the shell was approximately 4.4 kg/m^2. Thermal performance was measured via LN_2 boil-off calorimetry. LRMLI exhibited good performance with a 3-layer, 0.63cm thick blanket with a measured heat leak of 7.1 W/m^2 (0.19 mW/m-K) heat leak for in vacuum operation and 14.3 W/m^2 (0.34 mW/m-K) for one atmosphere operation. Predicted performance for a three layer LRMLI system was 6.9 W/m^2 for in vacuum operation and 31 W/m^2 for in-atmosphere, using a detailed thermal model created by Quest and Ball. LRMLI was successfully proven feasible in Phase I work, thereby reaching TRL4.

2.2 Phase II work

A NASA Phase II contract is in progress to advance system design, build and test larger scale prototypes, and progress the technology to TRL5. The LRMLI Phase II program has identified primary applications, optimized dynamic post design, designed modular vacuum shells for ease of application, built and tested small scale LRMLI prototypes. Tasks underway are to evaluate mixed LRMLI/Integrated MLI insulation systems, and insulate and measure LRMLI performance in the relevant environment of mid-scale cryotanks.

The dynamic beam post spacer is a key component of LRMLI and has been redesigned to provide higher structural strength and a higher safety margin, and more easily micromolded in the preferred low conductivity, low outgassing polymer material. A trade study of strength, moldability and heat leak through the part was completed, and indicates that larger cross-sections and center beam supports would be acceptable with a change in polymer.

A 3rd generation Tripod Post was designed, heat flow through the part analyzed, structural strength analyzed via FEA, and should achieve the desired safety margin of 2 under external atmospheric loading of 14.7psi, with lower conducted heat leak. The latest design dynamic post (with a mass of 32mg) can support over 29 pounds with a safety margin of 2 for 1 atm loading. Posts can support this force, and still dynamically rebound in the absence of compressive loading to reduce thermal conduction. Thermal solid conductance through the spacer decreases six fold after rebound.

A second major focus of Phase II work is to develop improved thin, lightweight vacuum shell designs to reduce mass, increase structural integrity, and ease design, manufacture and installation burdens. A modular vacuum shell design would allow less expensive application to varying tank geometries. Design of a thin, flexible vacuum shell has been a technical challenge. Analysis of the vacuum shell flexibility required with cryotank temperature changes and external pressure changes was completed. Shell FEA was performed analyzing vacuum shell stresses, thickness and mass. A trade study was performed for seven possible vacuum shell designs comparing their technical risks, performance and handling/manufacturing characteristics. The system was designed, prototyped and tested, showing good thermal performance.

An image of the LRMLI concept as applied to a cryogenic tank is shown in the figure below. The spacers are bonded to each Mylar layer and are aligned to transmit the load from the vacuum shell to the tank wall.

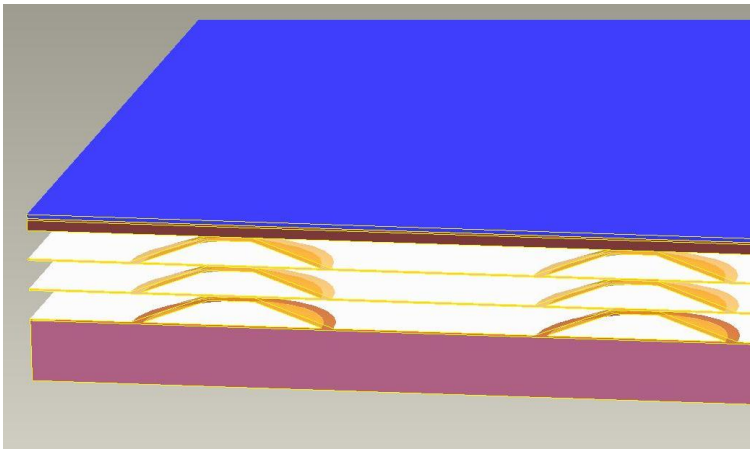

Figure 1. LRMLI and integrated vacuum shell concept.

Through careful design and innovative ideas the mass of the vacuum shell has been reduced by 57% to 1.87 kg/m^2. The new design is modular for application across a broader range of tank sizes and geometries, based on a flexible and thin vacuum shell supported by the LRMLI spacers which support a hermetic outer layer. The vacuum shell panels have shown good structural integrity through thermal cycling and repeated atmospheric pressure/high vacuum cycles.

The LRMLI thin wall self-supported vacuum shell offers significant mass advantages over vacuum shells required for conventional MLI. Traditional vacuum shells required to provide internal high vacuum for MLI weigh approximately 10 kg/m^2 for a 0.15" thick 5083 Al shell, whereas the LRMLI semi-rigid shell is approximately 1.9 kg/m^2 (17.5% the mass of a traditional shell). This mass savings is due to the strength of the LRMLI dynamic spacer.

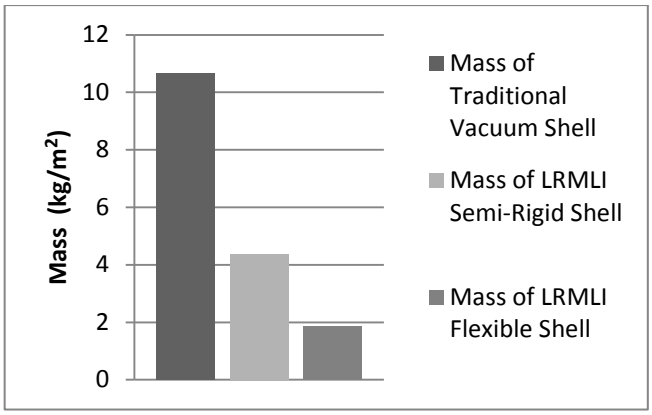

Figure 2. Vacuum shell mass comparisons

Liquid nitrogen boiloff testing has shown results of 6.6 W/m^2 in vacuum and 41 W/m^2 in atmospheric conditions. The on-orbit performance of the LRMLI system has a slightly lower heat leak than predicted from our thermal model, while the in-air heat leak is substantially higher than modeled. It is believed the in-atmosphere performance can be improved by achieving lower permeation of the hermetic layer and improvements in the spacer post to reduce loading and heat leak via solid conduction through the dynamic beam. Improvements over earlier LRMLI builds have already demonstrated a 40% reduction in overall in-atmosphere system heat leak.

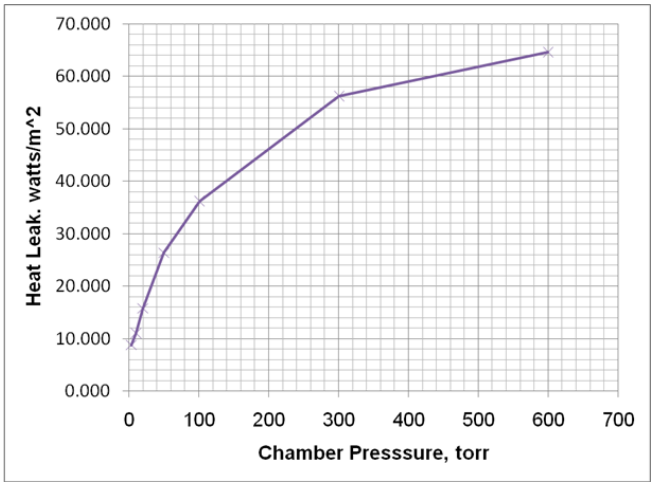

Figure 3. LRMLI heat leak from 295°K to 77°K as a function of external atmospheric pressures.

LRMLI thermal performance was measured at various external pressures, from high vacuum to one atmosphere, to evaluate the change in LRMLI heat leak and validate dynamic post performance with external load. Full compression of the dynamic beam results in a sharp increase in heat leak as the posts connect, rebound and disconnection causes a sharp decrease. See in Figure 3 the steep slope of heat leak at chamber pressures around 50 torr. The LRMLI polymer spacer posts were tested for structural load capacity, and began to compress at one pound force per post, which in the LRMLI blanket corresponds to an external load of 52 torr, where compression should occur.

3. LRMLI Performance Comparisons

3.1 Thermal performance, mass and thickness comparisons between LRMLI, SOFI and aerogel

In a comparison of LRMLI to SOFI and aerogel, LRMLI shows significant advantages (Fesmire, 2006; NIST, 1978). The three types of insulation systems were compared on a thickness and mass basis.

TABLE 1. Insulation performance in-air with one atmosphere pressure (pre-launch environment) (77°K cold, 295°K hot).

In-atmosphere thermal performance							
LRMLI Layers	LRMLI Heat Leak W/m^2	LRMLI Thickness (cm)	SOFI Same Heat Leak Thickness (cm)	Aerogel Same Heat Leak Thickness (cm)	LRMLI Mass (kg/m^2)	SOFI Same Heat Leak Mass (kg/m^2)	Aerogel Same Heat Leak Mass (kg/m^2)
3	41	0.63	11.3	10.1	2.44	4.7	12.6
4	31	0.82	14.8	13.4	2.63	6.2	16.7
5	25	1.00	18.4	16.6	2.82	7.7	20.7

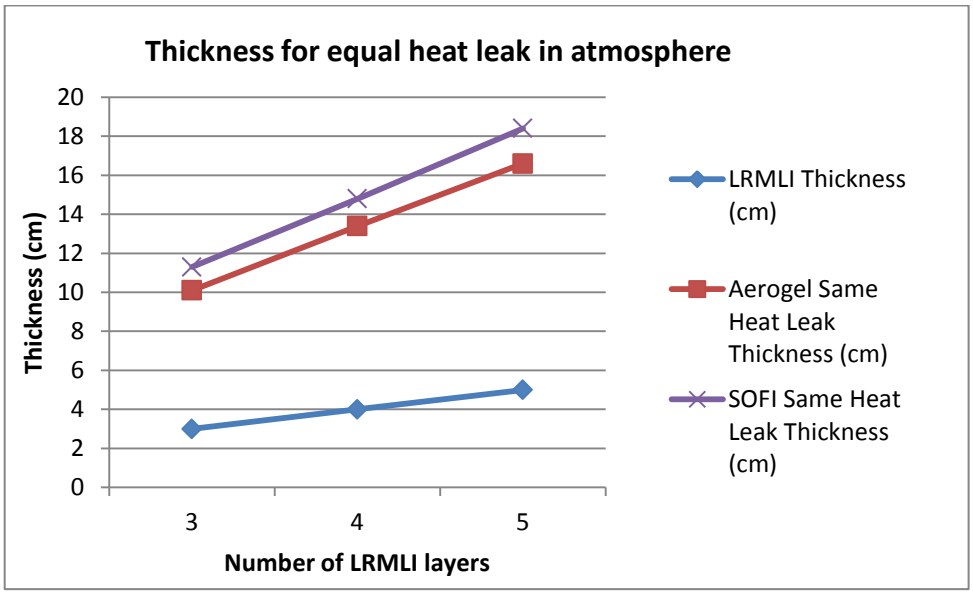

Figure 4. Insulation thickness required for equal heat leak to 3, 4 and 5-layer LRMLI.

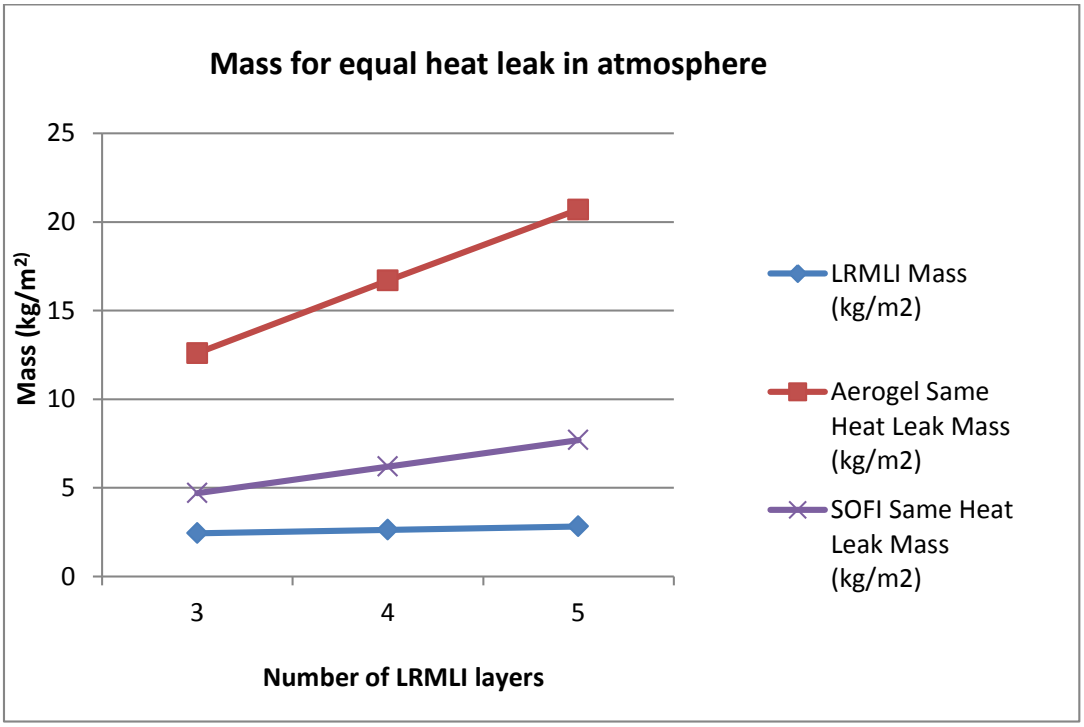

Figure 5. Insulation mass required for equal heat leak to 3, 4 and 5-layer LRMLI.

TABLE 2. Insulation performance in vacuum (77°K cold, 295°K hot)

In Vacuum thermal performance								
LRMLI Layers	LRMLI Heat Leak W/m^2	LRMLI Thickness (cm)	SOFI Same Heat Leak Thickness (cm)	Aerogel Same Heat Leak Thickness (cm)	LRMLI Mass (kg/m^2)	SOFI Same Heat Leak Mass (kg/m^2)	Aerogel Same Heat Leak Mass (kg/m^2)
3	6.6	0.63	49.2	4.0	2.44	20.7	5.0
4	5.0	0.82	65.6	5.3	2.63	27.5	6.6
5	4.0	1.00	82.0	6.6	2.82	34.4	8.3

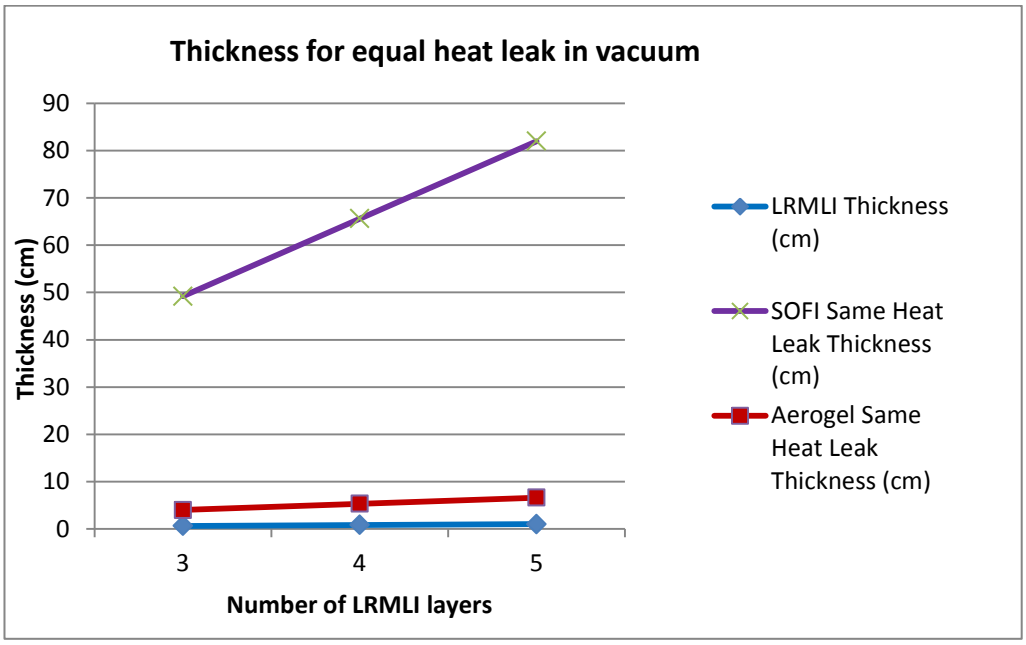

Figure 6. Insulation thickness required for equal heat leak to 3, 4 and 5-layer LRMLI.

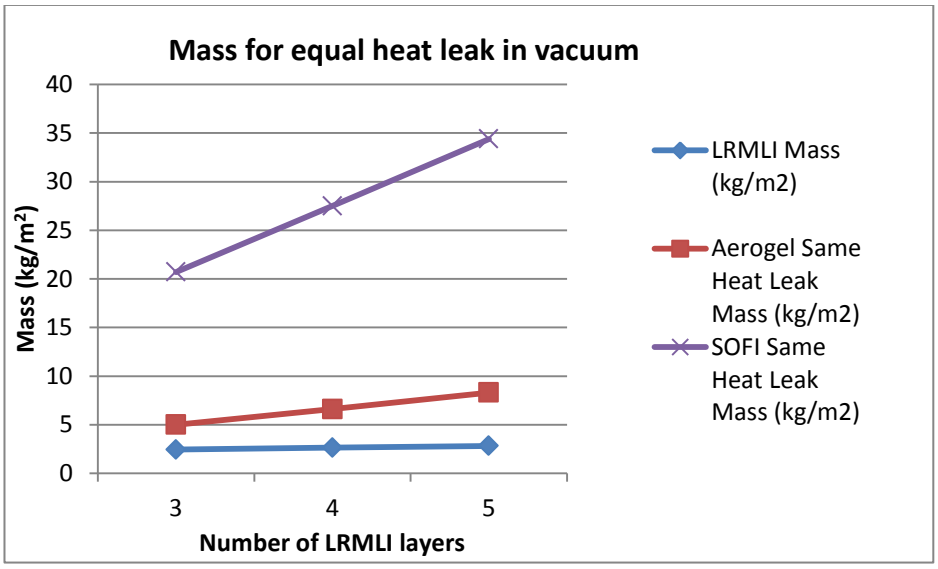

Figure 7. Insulation mass required for equal heat leak to 3, 4 and 5-layer LRMLI.

3.2 LRMLI compared to SOFI

LRMLI Advantages over SOFI

- To achieve equal heat leak in vacuum of a 3-layer LRMLI blanket (0.63cm thick, 2.44 kg/m^2) would require 49.2cm of SOFI at 20.7 kg/m^2

- LRMLI has 78X lower heat leak per thickness than SOFI and a 8x mass advantage for on-orbit operation
- To achieve equal heat leak in-air of a 3-layer LRMLI blanket (0.63cm thick, 2.44 kg/m^2) would require 11.3cm of SOFI at 4.7 kg/m^2
- LRMLI has 18X lower heat leak per thickness than SOFI and a 2x mass advantage for in-air operation
- LRMLI has inherent construction benefits with controlled layer spacing, can provide reliability & robustness, and provides excellent thermal performance both in-atmosphere and on-orbit
- Robust LRMLI can replace SOFI, which has significant problems and a lack of robustness with cracking and cryopumping

3.3 LRMLI compared to aerogel

Aerogels have an apparent thermal conductivity of 1.2 mW/m-K at high vacuum, and 19 mW/m-K at 1 atm (Reference: Fesmire), for 77°K to 295°K.

This correlates to a thermal performance advantage of a 3 layer LRMLI blanket being 10 times better in atmospheric conditions and three times better in high vacuum (on-orbit) conditions for a blanket of similar thickness.

- To achieve equal heat leak on-orbit of a 3-layer LRMLI blanket (0.63cm thick, 2.44 kg/m^2) would require 4.0 cm of aerogel blanket at 5.0 kg/m^2
- LRMLI has 6X lower heat leak per thickness than aerogel for on-orbit operation, and 2X lower mass than equal heat leak aerogel blanket
- To achieve equal heat leak in-air of a 3-layer LRMLI blanket (0.63cm thick, 2.44 kg/m^2) would require 10.1cm of aerogel at 12.6 kg/m^2
- LRMLI has 16X lower heat leak per thickness than aerogel and a 5x mass advantage for in-air operation
- LRMLI provides substantially better thermal performance in-air than aerogel blankets on both a thickness and mass basis

4. Conclusions

Load Responsive Multi-layer Insulation (LRMLI) offers a unique insulation product that is lightweight, high performing, and supports its own thin wall vacuum shell enabling both in-air and on-orbit operation. LRMLI prototypes have been built, installed on small tanks, and actual heat leak measured. LRMLI has demonstrated significant improvements over conventional insulations such as SOFI and aerogel. The LRMLI performs well for both in-atmosphere and in-vacuum (equivalent to on-orbit conditions).

LRMLI in-air thermal performance is achieved by an innovative approach using low thermally conductive micromolded polymer spacers that dynamically respond to external atmospheric pressure (load) to support a thin, lightweight vacuum shell, and disconnect in on-orbit condition to provide even higher thermal performance on orbit.

Continuing R&D includes building and testing mixed LRMLI/IMLI insulation systems, and designing, fabricating, installing and testing an LRMLI system on a larger 400L cylindrical with spherical ends cryotank. Goals are to continue to reduce overall system mass, increase structural integrity, reduce manufacturing and installation cost, and provide a versatile insulation system suitable for various tank geometries.

LRMLI is proving to be a new innovative product for both aerospace and commercial applications.

An excellent non-NASA aerospace application has already been selected, that of cryotanks for LH_2 powered aircraft, as operational requirements cannot be met by SOFI and can be readily met by LRMLI. First prototypes of such aircraft are currently being built. The best application for NASA application is under study, including launch vehicle cryogenic upper stages and cryogenic fueled landers, and requires consideration of NASA's mission and direction. LRMLI may provide extremely high performance thermal insulation for a variety of terrestrial applications, such as cryogenic dewars, refrigerator-freezers and water heaters.

Acknowledgements

The authors gratefully acknowledge the support of NASA via contracts NNX09CD77P and NNX10CA70C and the support of NASA Technical Monitors Shuvo Mustafi and David Plachta.

References

1. S. Dye, A. Kopelove and G. Mills, Integrated and Load Responsive Multilayer Insulation, CEC 2009.
2. Private test communications, Wesley Johnson and James Fesmire, NASA KSC, January 2010.
3. Fesmire, J.E." Aerogel insulation systems for space launch applications", Cryogenics Volume 46, Issues 2-3, February-March 2006, Pages 111-117, 2005 Space Cryogenics Workshop
4. NIST data, "National Bureau of Standards, Cryogenics Division, Institute for Basic Standards, LNG MATERIALS AND FLUIDS--A USER'S MANUAL OF PROPERTY DATA IN GRAPHIC FORMAT", 1978, chart 1221

Foam Insulation for a Liquid Oxygen Densifier

G. E. McIntosh[1] and R. Stuckenschmidt[2]

[1]Cryogenic Technical Services, Frederick. CO 80516
[2]Systems Undercover, Inc. Greeley, CO 80631

Abstract:

Analyses indicated that it would not be cost effective to vacuum insulate a 7 foot diameter by 30 foot long liquid nitrogen vessel for a launch facility liquid oxygen densifier. Foam insulation appeared to be the logical choice for this infrequently used ground support equipment but the history of foam problems due to cracking, adhesive failure and internal shearing weighed against the use of commercial spray-on material. These problems were solved with a system consisting of alternate sealing and flexible foam layers: (1) An inner membrane sealed to itself but not attached to the cold shell or pipe; (2) A flexible foam insulation layer; (3) A vapor-tight sealing membrane; (4) A second flexible foam insulation layer and (5) An outer aluminized sealing membrane. The second and subsequent layers are sealed to each underlying layer by flexible foam contact adhesive. The inner sealing membrane is particularly vital in that it allows the first foam layer to expand and contract as the tank temperature changes and it also protects the tank from chloride corrosion from the foam. This paper describes preliminary testing to prove out the system and the steps taken to install flexible foam insulation on the oxygen densifier vessel.

Background:

In 1955, Beech Aircraft of Wichita, Kansas was awarded a U. S. Air Force contract to draw on their experience as an aircraft drop tank manufacturer to develop a light weight liquid hydrogen external store. Their first move was to open an office and fabrication facility in Boulder, Colorado to gain access to liquid hydrogen and appropriate test facilities at the National Bureau of Standards Cryogenic Engineering Laboratory (now NIST) which had received a support contract from the Air Force.

Several years of educational but disappointing work followed. All of the conventional problems of cryogenic foam were encountered first hand. A variety of commercial foam products and spray-on foams were tested. None were really successful and the final solution[(1)] was to take advantage of the weight bearing characteristics of foam by attaching a vacuum tight external membrane which could be (very slowly) evacuated.

In a coordinated parallel program, Paul Ordin and his associates at the NACA (later NASA) built an external liquid hydrogen tank with Styrofoam insulation wrapped with four layers of resin-impregnated Fiberglas which was maintained with a positive pressure of gaseous helium[(2)]. This tank was suspended from the wing of an RB-57 aircraft and made several flights with one engine running on liquid hydrogen for a portion of each flight. Paul Ordin himself was on board the aircraft on these flights to operate the hydrogen system.

More Recent Developments:

A spray-on foam composition and method of application was developed for the Space Shuttle and has been generally successful. This application involves mechanical rotation of the tank

being insulated with robotic spray operation followed by machining to achieve a smooth surface. This process was utilized on the Multipurpose Hydrogen Test Bed[3] by Martin Marietta and, more recently, by Ball Aerospace on a liquid hydrogen aircraft fuel tank. High quality insulation was achieved in each case but it is not particularly lightweight, it is expensive, the tank must be rotatable and, for practical purposes, the work must be done at the source.

Insulating the Oxygen Densifier:

This heat exchanger assembly is approximately 32 ft long and 7 ft in diameter (9.75 x 2.13 m). The active liquid nitrogen bath is 27 ft (8.23 m) long. The insulation requirements are:

1. Provide sufficient insulation to prevent frost from forming on the exterior surface during an extended cooldown of the densifier assembly.
2. Seal the inner tank surface so that air cannot condense on it.
3. Robust structure that does not deteriorate after extended use cycles.
4. Readily available material that is easy to install.

In our 2010 investigation, none of the commercial spray-on vendors were willing to guarantee extended performance of their foam at liquid nitrogen temperature. One brand of rigid poly vinyl chloride (PVC) foam was determined satisfactory but was rejected for time reasons because individual sheets required heat forming prior to installation. At this point, our insulating vendor suggested testing flexible foam. Some simple tests were performed as shown on photos 1, 2, and 3. The following conclusions were reached:

1. The foam and an adhesive joint were unaffected by direct contact with liquid nitrogen.
2. The observed thermal conductivity was low.
3. The foam sheared next to the bond line when bonded to stainless steel and cooled to liquid nitrogen temperature.
4. Physical properties of the foam and adhesive joint recovered completely after exposure to liquid nitrogen.

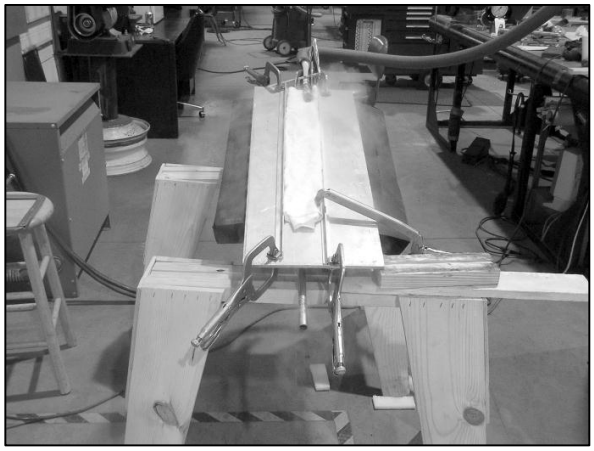

1. Test of Aerocel foam and adhesive joint exposed to LN2 surface.

2. Test of foam bonded to stainless steel.

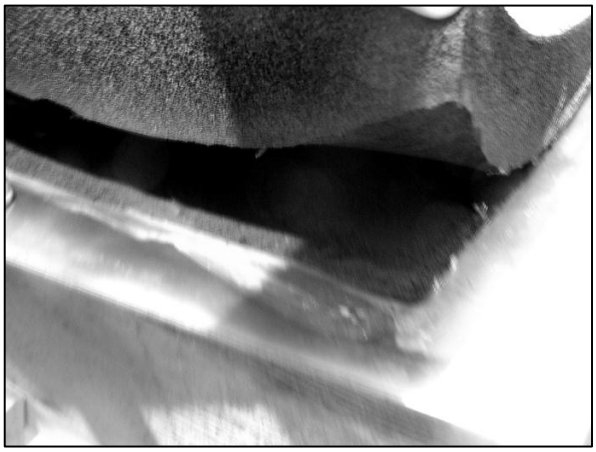

3. Shearing failure of foam bonded to stainless steel.

4. Liquid oxygen sub-cooler prior to insulation.

A five element insulation system was selected for the oxygen subcooler based on our tests and recommendations from the manufacturer:

1. A vapor barrier membrane was wrapped around the vessel. It was bonded to itself to make a tight enclosure but was not bonded to the vessel.
2. The selected foam was Aerocel No. ACSR20 EPDM (Ethylene Propylene Diene Monomar) having an ambient thermal conductivity of 0.0353 W/m-K and density of 2.58 lb/ft^3 (41.3 kg/m^3). A two inch (2.54 cm) thick layer was carefully fitted and bonded to the inner vapor barrier using Armaflex 520 adhesive. The Armaflex adhesive was also used to bond the edges of the foam sheets together.
3. A second vapor barrier was applied over and bonded to the Aerocel foam.
4. A second foam layer was installed as in (2) above.
5. A final covering of zero permeability 5-ply outdoor service membrane was bonded to the second foam layer.

The inner vapor barrier is an important part of this system. It allows the insulation to flex relative to the stainless steel liquid nitrogen vessel without any destructive shearing force. Also, the membrane provides an inert surface next to the stainless steel which eliminates possible corrosion of the stainless steel from the foam.

5. Inner vapor barrier plus first layer of foam.

6. Final pass of middle vapor barrier with outer foam layer.

7. Cold shock test of final assembly.

8. Final assembly being loaded on shipping trailer.

Results:

The selected insulation system was installed on the liquid oxygen sub-cooler in less than 10 working days. A liquid nitrogen cold shock/chilldown test was successfully performed. Residual liquid nitrogen remained in the reservoir three days after the cold shock test despite relatively high heat leak from the tank supports. The sub-cooler is being installed at the Wallops Island NASA facility and a preliminary system test is scheduled for late July 2011.

Acknowledgements:

The liquid oxygen sub-cooler was designed and fabricated for Orbital Sciences, Inc. as part of their Taurus II launch facility.

References:

1. L. R. Stoecker, On the evacuation of plastic foams to reduce their thermal conductivity, in: “Advances in Cryogenic Engineering,” Vol. 5, (1960), Plenum Press, New York, page 273.
2. P. M. Ordin, S. Weiss and H. Christenson, Pressure-Temperature histories of liquid hydrogen under pressurization and venting conditions, in: Ibid., page 431.
3. J.J. Martin and L. Hastings, Large scale liquid hydrogen testing of a variable density multilayer insulation with a foam substrate, in: “NASA/M-2001-211089,” June 2001.

Spray-On Foam Insulations for Launch Vehicle Cryogenic Tanks

J. E. Fesmire[1], B.E. Coffman[1], B.J. Meneghelli[2], K.W. Heckle[2]

[1]Cryogenics Test Laboratory, NASA, Kennedy Space Center, FL USA
[2]Cryogenics Test Laboratory, ASRC Aerospace, Kennedy Space Center, FL USA

Abstract

Spray-on foam insulation (SOFI) has been developed for use on the cryogenic tanks of space launch vehicles beginning in the 1960s with the Apollo program. The use of SOFI was further developed for the Space Shuttle program. The External Tank (ET) of the Space Shuttle, consisting of a forward liquid oxygen tank in line with an aft liquid hydrogen tank, requires thermal insulation over its outer surface to prevent ice formation and avoid in-flight damage to the ceramic tile thermal protection system on the adjacent Orbiter. The insulation also provides system control and stability throughout the lengthy process of cooldown, loading, and replenishing the tank. There are two main types of SOFI used on the ET: acreage (with the rind) and closeout (machined surface). The thermal performance of the seemingly simple SOFI system is a complex array of many variables starting with the large temperature difference of 200 to 260 K through the typical 25-mm thickness. Environmental factors include air temperature and humidity, wind speed, solar exposure, and aging or weathering history. Additional factors include manufacturing details, launch processing operations, and number of cryogenic thermal cycles. The study of the cryogenic thermal performance of SOFI under large temperature differentials is the subject of this article. The amount of moisture taken into the foam during the cold soak phase, termed Cryogenic Moisture Uptake, must also be considered. The heat leakage rates through these foams were measured under representative conditions using laboratory standard liquid nitrogen boiloff apparatus. Test articles included baseline, aged, and weathered specimens. Testing was performed over the entire pressure range from high vacuum to ambient pressure. Values for apparent thermal conductivity and heat flux were calculated and compared with prior data. As the prior data of record was obtained for small temperature differentials on non-weathered foams, analysis of the different methods is provided. Recent advancements and applications of SOFI systems on future launch vehicles and spacecraft are also addressed.

KEYWORDS: foam insulation; cryogenic tanks; thermal conductivity; environmental exposures; space launch

1. Background

Spray-on foam insulation (SOFI) materials were first developed in the 1960s and included applications for the Saturn V moon rockets and subsequently the Space Shuttle.[1,2] From a volumetric viewpoint, all space launch vehicles consist primarily of large tanks to contain the propellants. For example, the Space Shuttle's External Tank (ET) is comprised of a forward liquid oxygen (90 K) tank of 141,000 gallons capacity and an aft liquid hydrogen (20 K) tank of 383,000 gallons capacity (see Figure 1). These cryogenic propellant tanks and feed-lines must be thermally insulated to prevent or minimize, according to specific requirements, the condensation of air or the formation of ice and otherwise provide sufficient isolation from the ambient environment. The thermal insulation system is designed to meet three conjoined areas of requirements: safety, control, and flight performance. Safety aspects include the prevention of excessive ice formation or liquid air condensate that could present a debris hazard or an enhanced flammability problem. Control during pre-launch loading operations is of course vital for successful cooldown, tanking, stabilization, and replenishment within the time constraints of the mission. The insulation system provides the added benefit of reducing the continuous boiloff losses of the cryogenic propellants. Flight performance requirements include thermal protection of the vehicle tanks from radiant heating or aerodynamic effects.

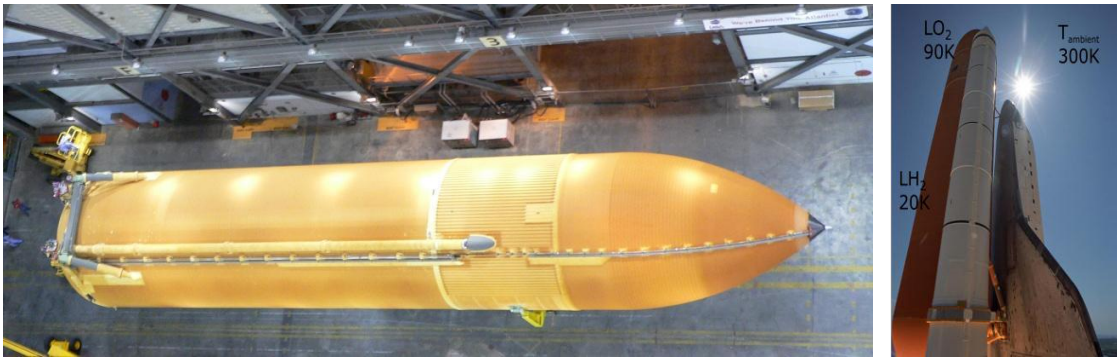

Figure 1. A view of the Space Shuttle External Tank in the Vehicle Assembly Building (left) and in flight (right).

Other cryogenic tank insulation materials used in the past include rigid foams and cork. For some vehicles, the liquid oxygen tanks have been left bare; the insulation in this case is layers of frost from the humid air surrounding the vehicle on the launch pad. Cryogenic propellant loading operations can take from several hours up to around 12 hours. Provision must also be made for unloading the vehicle due to a scrub and repeat loading at some later date. This thermal cycling is an important design parameter for the mechanical behavior of the insulation and must be carefully considered to avoid adverse consequences such as cracking or delamination from the tank wall.

The objective of the tank insulation system is to reduce heat flux to acceptable levels while providing consistent performance at the least total system mass. Apparent thermal conductivity [k-value, mW/m-K] is the overall measure of the thermal performance per unit thickness of insulation material. The variations of apparent thermal conductivity (k-value) with cold vacuum pressure for different cryogenic insulation materials are shown in Figure 2.[3,4] The boundary conditions are approximately 293 K and 77 K and the residual gas is nitrogen. There are two

main regions of interest for space launch and exploration applications: ambient pressure (non-vacuum) and high vacuum. Although the non-vacuum application is of primary interest, SOFI applications for in-space cryogenic storage are also of interest. In such cases where the cryogenic tanks are loaded on the launch pad, a composite system of materials that offers both non-vacuum and high-vacuum performance must be devised. Figure 2 illustrates the extreme thermal performance difference between these two cases. Even though aerogel blankets may be twice as good as SOFI at the ambient pressure, the performance of a typical multilayer insulation (MLI) system is 100 times better.[5] However, MLI is not practical for use in an open ambient, humid-air environment while the aerogel blanket is fully hydrophobic and well-suited for such exposures.[6] Therefore, the proper design and selection of insulation materials depends strongly on the environmental parameters.

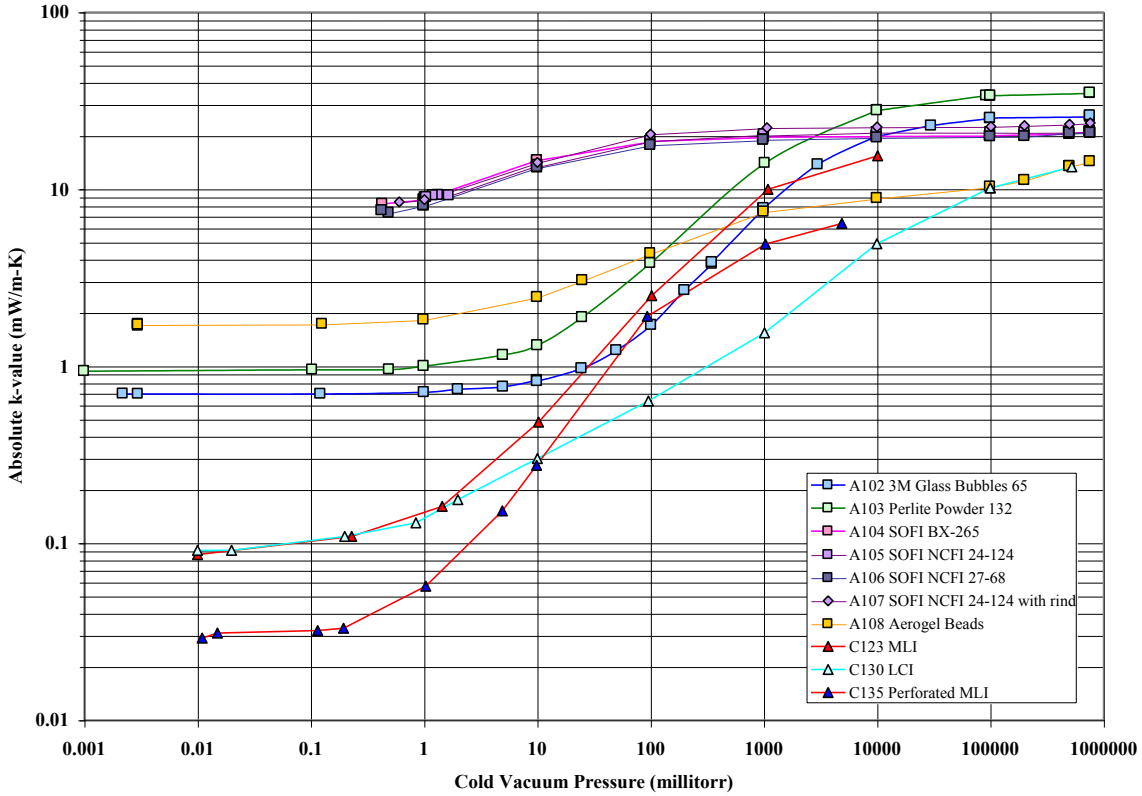

Figure 2. Variation of apparent thermal conductivity (k-value) with cold vacuum pressure for different cryogenic insulation materials at the boundary conditions of approximately 293 K and 77 K (the residual gas is nitrogen).

2. Introduction

The well-developed, modern SOFI materials have an extraordinary combination of mechanical and thermal properties in addition to being light in weight. The main limitations are those of weathering exposure and repeated thermal cycling. Therefore, the uses are generally for one-time-use vehicle tanks. Reusable space launch vehicles will likely require an insulation and thermal protection approach that is not based on SOFI technology.

These foam systems are complex chemical formulations with a host of complicating factors requiring extensive physical and chemical testing as well as characterization through analysis and modeling. Most of the data produced are based on baseline (not aged or weathered) foams. Data from tests that do include some aging or weathering exposure are generally done without imposing a large temperature difference from cryogenic to ambient.

A comprehensive experimental study, *Long-Term Moisture/Aging Study of SOFI under Actual-Use Cryogenic-Vacuum Conditions*, was conducted to investigate the thermal performance of SOFI under simulated actual-use conditions.[7] The study included the following elements: environmental exposure testing (aging and weathering), thermal conductivity testing under both cryogenic-vacuum and ambient conditions, physical characterization of materials, cryogenic moisture uptake testing under actual-use conditions, and fire chemistry testing. This study was part of a larger project entitled *Technologies to Increase Reliability of Thermal Insulation Systems* for space launch and exploration applications.[8] The testing described in this report is focused primarily on the thermal performance of SOFI under the representative operational conditions of a large temperature difference. Materials are tested after both aging and weathering exposures. Experimental results on cryogenic moisture uptake and fire chemistry have been previously reported.[9]

3. Materials

Foam materials were sprayed at NASA's Marshall Space Flight Center in accordance with nominal Space Shuttle External Tank flight specifications.[10,11] Baseline (new condition) specimens were allowed to cure for approximately one month. Several 610 mm x 610 mm samples of the three types of foam, NCFI 24-124 (acreage foam used on External Tanks), NCFI 27-68 (formerly proposed alternative acreage foam), and BX-265 (closeout foam), were packaged and shipped to KSC. The 610 mm x 610 mm samples of foam were then machined into 203 mm diameter test specimens of 25 or 32 mm thickness. The measured densities of all specimens were comparable, ranging from 37 to 40 kg/m^3 prior to testing.

Environmental exposure of the SOFI materials was an integral part of the performance testing. The aging and weathering simulations were performed at two exposure sites. The KSC Vehicle Assembly Building (VAB) was used for the aging test (see Figure 3). The aging site simulates the area where the External Tank is stored before the vehicle stacking and launch preparations begin. The conditions in this area are mild with ambient humidity levels and no direct sunlight. The Corrosion Beach Site at KSC was used for the weathering test as shown in Figure 4. The weathering site simulates the conditions that a mated External Tank is exposed to while it is on the pad awaiting launch. The aging time for an External Tank can be several years whereas the typical weathering exposure is about one month. The maximum weathering exposure, as recorded in the Shuttle flight history, is about six months.[12] The test specimen mounting enclosure, shown in Figure 3 (right), was designed to expose only the center portion of the top face of the material. Figure 4 (right) shows a SOFI test specimen type NCFI 24-124 after only one month of weathering. Exposure time durations are as follows: baseline, 2 weeks, 1 month, 3 months, 6 months, 12 months, 18 months, and 2 years.

In addition, a total of five 1-m long cylindrical clam shell test articles were produced for testing by means of a cylindrical thermal conductivity test instrument (Cryostat-100). The specifications for these cylindrical test articles of approximately 25-mm thickness are given in Table 1. Photographs of one of the BX-265 test articles are shown in Figure 5. The test articles composed of SOFI material NCFI 24-124 include a specimen that is machined (shaved) and one that is in the net spray condition (rind).

Figure 3. Aging of SOFI test specimens inside the Vehicle Assembly Building at Kennedy Space Center (left). The mounting enclosure is shown on the right.

Figure 4. Weathering of SOFI test specimens exposure testing at the Corrosion Beach Site of the Kennedy Space Center (left). A one-month weathered specimen is shown on the right.

Table 1. Specifications of 1-m long cylindrical clam shell test articles.

Ref. No.	Material	Outer surface	Date Sprayed	T_{final} mm	Density g/cc
N/A	BX-265	Shaved	3/31/2005	24.1	0.044
A104	BX-265	Shaved	4/6/2005	26.70	0.042
A107	NCFI 24-124	Rind (Partial)	5/11/2005	23.90	0.038
A105	NCFI 24-124	Shaved	6/9/2005	25.60	0.038
A106	NCFI 27-68	Shaved	7/6/2006	24.40	0.037

Figure 5. One of five 1-m long cylindrical clam shell test articles were produced for testing using a cylindrical thermal conductivity test instrument (Cryostat-100). Machined thickness of approximately 25-mm is shown in the top view while the precise longitudinal fit-up is shown in the bottom view.

4. Experimental Test Methods

4.1 Cryogenic-Vacuum Testing

The Cryostat-100 instrument uses the steady-state liquid nitrogen boiloff (evaporation rate) calorimeter method to determine apparent thermal conductivity (k-value) and heat flux.[13] Preparations of the test article included installing temperature sensors through the thickness of the insulation at approximate 6.4 mm intervals. The two halves of the SOFI test article were secured tightly in place by using a series of four stainless steel band clamps as shown in Figure 6. Thin PVC plastic foils were positioned underneath the band clamps to prevent damage to the foam. Finally, three temperature sensors were affixed to the outer surface of the test article. Fit-up to the cold mass was precise in the first case with the BX-265 test article; there were no visible gaps or deformities at the two longitudinal seams. The remaining test articles each had gaps less than about 4 mm which were filled with fiberglass insulation material to complete the installation. Photographs of the two NCFI 24-124 test articles (one shaved and one with rind) installed and ready for testing are shown in Figure 7.

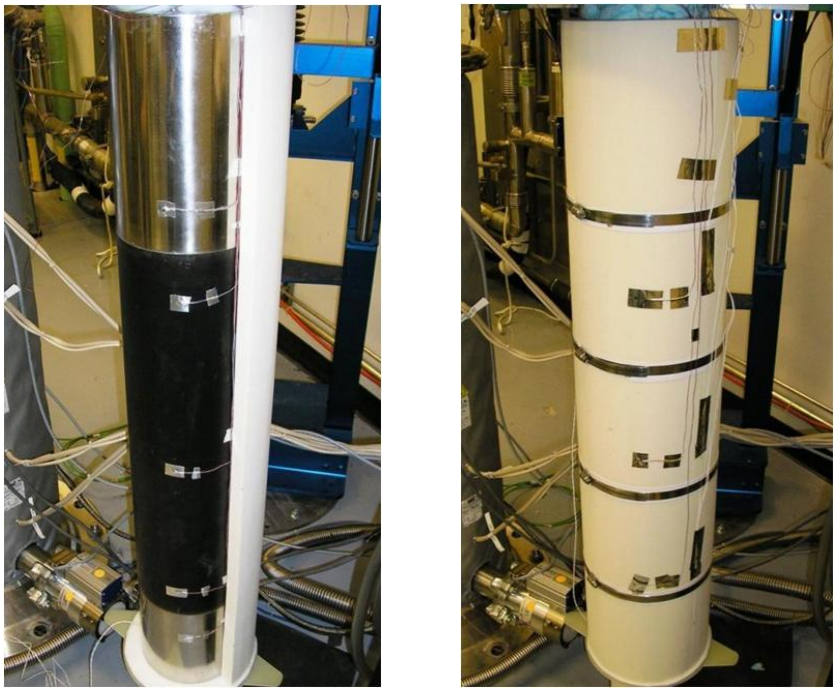

Figure 6. Installation of a SOFI clam-shell test article on the cold mass assembly of thermal conductivity instrument Cryostat-100.

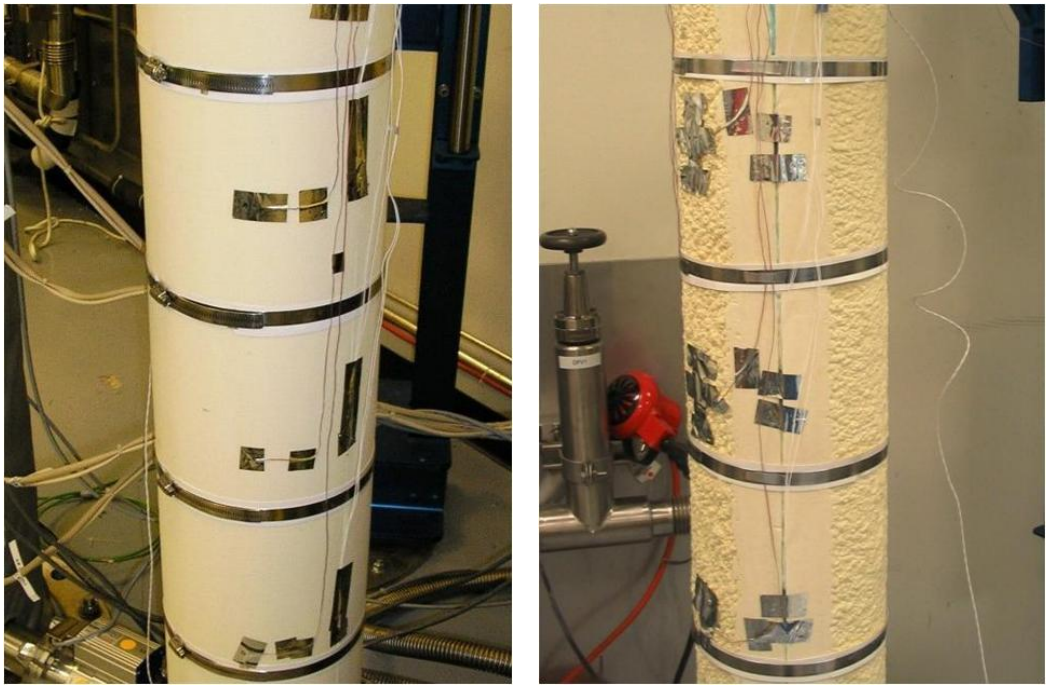

Figure 7. Installed Cryostat-100 insulation test articles: NCFI 24-124 shaved (left) and NCFI 24-124 with rind (right).

A satisfactory cryostat test is defined as the steady-state heat leak rate (watts) through the specimen at a prescribed set of environmental conditions, including a stable warm-boundary temperature (WBT), a stable cold-boundary temperature (CBT), and a cold vacuum pressure (CVP). A minimum of eight CVP test points are obtained for each test article. A liquid nitrogen cold mass maintains the CBT at approximately 78 K. The WBT is maintained at approximately 293 K using an external heater with an electronic controller. The delta and mean temperatures are therefore 215 K and 185 K, respectively. Vacuum levels cover the full range from high vacuum (HV) (below 1×10-4 torr) to soft vacuum (SV) (~1 torr) to no vacuum (NV) (760 torr). The residual gas is nitrogen and testing proceeded in a step-wise progression from NV to HV.

The rate of the heat transfer, Q, through the insulation system into the cold-mass tank is directly proportional to the flow rate of liquid nitrogen boiloff as shown by equation (1). The flow rate is measured by a mass flow meter connected to a data acquisition system. The average boiloff flow rate is taken as the average over a calculated test chamber liquid level from 92 to 88 percent full. In measuring the flow rate, the back-pressure from the flow meter and connecting tube is approximately 0.1 psig. This pressure, taken as the saturation pressure of the cryogen, corresponds to a heat of vaporization of 198.6 J/g for liquid nitrogen. The k-value (λ_k) is determined from Fourier's law for heat conduction through a cylindrical wall as given in equation (2). The symbols used in these equations are given in Table 2.

$$Q = V_{STP}\rho_{STP}h_{fg}\left(\frac{\rho_f}{\rho_{fg}}\right) \qquad (1)$$

$$\lambda_k = \frac{Q \ln\left(\frac{R_o}{R_i}\right)}{2\pi L_{eff} \Delta T} \qquad (2)$$

Table 2. Symbols Used for Calculation of Thermal Properties from Boiloff Testing

Symbol	Description	Unit
V	Volumetric Flow Rate	cm^3/s
ρ	Density of Gaseous or Liquid Nitrogen	g/cm^3
h_{fg}	Heat of Vaporization	J/g
R_o and R_i	Radius of Insulation, outer and inner	m
L_{eff}	Length, effective heat transfer (cylindrical)	m
A_{eff}	Area, effective heat transfer area	m^2
ΔT	WBT – CBT	K

The mean heat flux is calculated by dividing the total heat transfer rate (Q) by the effective heat transfer area (A_{eff}). Further details on the heat transfer calculations as well as uncertainty analyses for the apparatus have been previously reported.[14] A total error of 3.2 percent has been calculated for this test apparatus. Figure 8 gives a simplified schematic of the Cryostat-100 instrument as well as a photograph of a completed SOFI test article ready for placement into the vacuum can assembly.

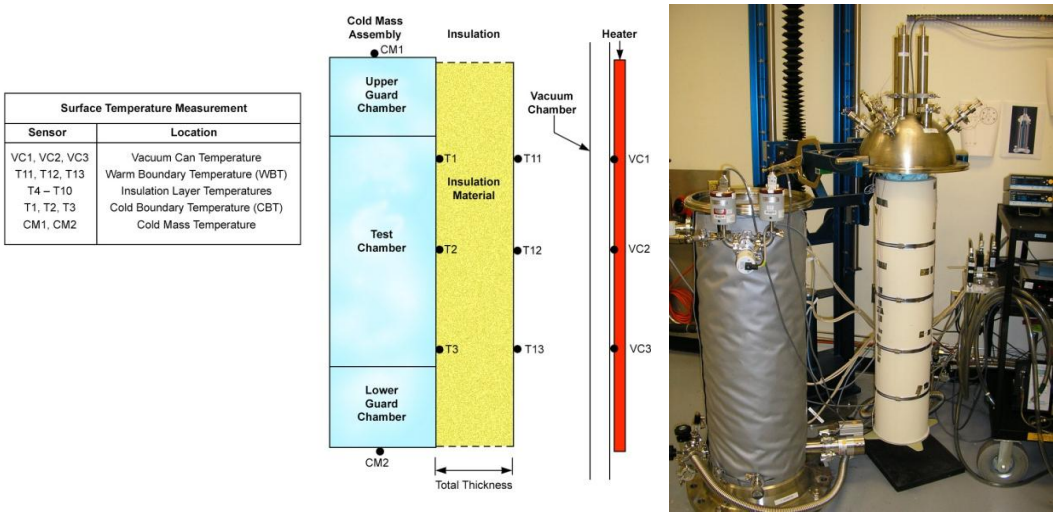

Figure 8. Simplified schematic of Cryostat-100, left, showing typical locations of temperature sensors. Photo on right shows completed test article and cold-mass assembly adjacent to the vacuum can assembly.

4.2 Ambient Temperature Testing

Thermal performance testing under ambient room temperature and pressure conditions provides both a baseline and a reference for comparison with other materials. Thermal conductivity (λ) testing under ambient conditions of both new and aged specimens (26 specimens and a total of 30 tests) was performed in accordance with standard test method ASTM C518.[15] The instrument used was a Netzsch Lambda 2300F heat flux meter. The average boundary temperatures are 307K (upper plate) and 286 K (lower plate) for a mean temperature (T_m) of 297 K. A specimen holder was built to accommodate the 203-mm diameter round specimens. The holder consisted of a 305-mm by 305-mm frame constructed of a SOFI foam material (BX-265) and featuring a cut-out as shown in Figure 9. Preparation of the test specimens included removal of the approximate 6-mm thick rind for both the NCFI 24-124 and NCFI 27-68 materials or removal of any indentations for the BX-265 material. That is, all specimens were machined to a smooth surface finish with a thickness of approximately 25-mm or less.

Figure 9. Specimen holding frame for heat flux meter testing (left); test specimen being installed for testing (right).

4.3 Physical Characterization Testing

Physical characterization tests included percent open-cell content and surface area (and pore size). Testing for open cell content was performed in accordance with ASTM D-6226 using a Quantachrome Instruments UltraFoam™ pycnometer.[16] These tests were performed at ambient temperature. Surface area testing was performed using a Quantachrome Instruments Nova™ surface area analyzer. These tests were performed under vacuum in sequence with LN2 bath immersion and in accordance with standard laboratory methods.

5. Results

5.1 Cryogenic Thermal Performance

Cryogenic thermal performance testing included a total of over 100 tests of four baseline (new condition) test articles using Cryostat-100 (absolute apparent thermal conductivity, k-value). Graphical summaries of the results for three machined test articles are presented in

Figures 10 and 11 for k-value and heat flux, respectively. The k-values for the baseline foam materials ranged from 21.1 mW/m-K at ambient pressure to approximately 7.5 mW/m-K at high vacuum. The alternate acreage foam NCFI 27-68 showed the lowest thermal conductivity overall with a k-value of 20.7 mW/m-K at 760 torr and 7.3 mW/m-K at 0.5 millitorr cold vacuum pressure. Thermal conductivities for the three foams at ambient pressure were found to be in a close range from 20.9 to 21.1 mW/m-K. Heat flux values were in the range from approximately 70 to 170 W/m^2 for the vacuum and no vacuum conditions, respectively, for the typical 25-mm thickness test articles. A simplified summary of the cryostat data is given in Table 3.

There are multiple test points at each cold vacuum pressure for all materials. The multiple points are not shown for clarity as the variation was typically less than 1 percent. The multiple test points are shown in Figure 12 for the 760 torr (no vacuum) cases as this test condition is generally the most important for space launch vehicle applications.

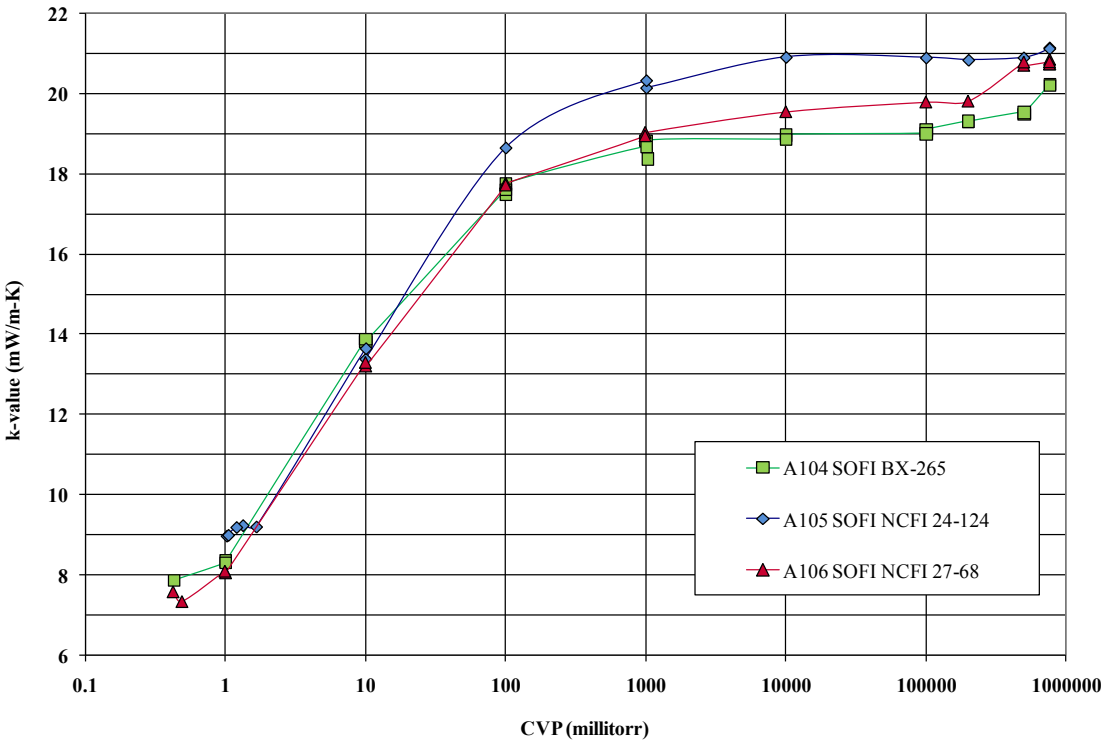

Figure 10. Variation of apparent thermal conductivity (k-value) with cold vacuum pressure for three different SOFI materials. Boundary temperatures are approximately 293 K and 78 K. The residual gas in nitrogen.

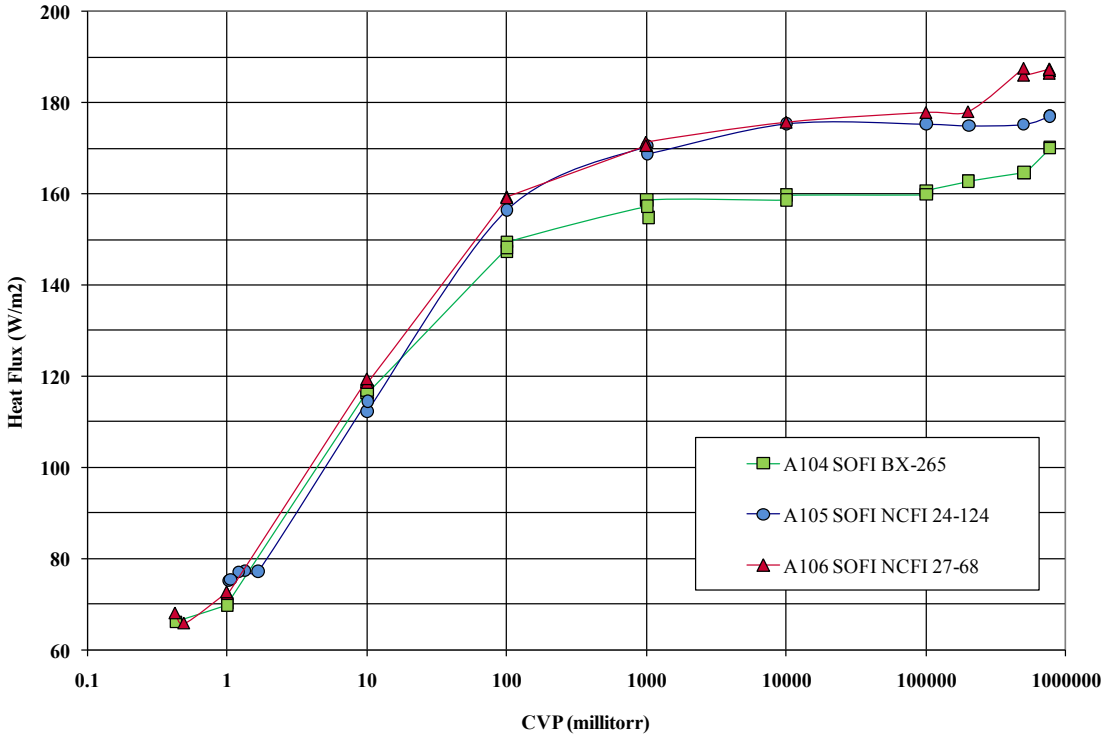

Figure 11. Variation of heat flux with cold vacuum pressure for three different SOFI materials. Boundary temperatures are approximately 293 K and 78 K. The residual gas in nitrogen.

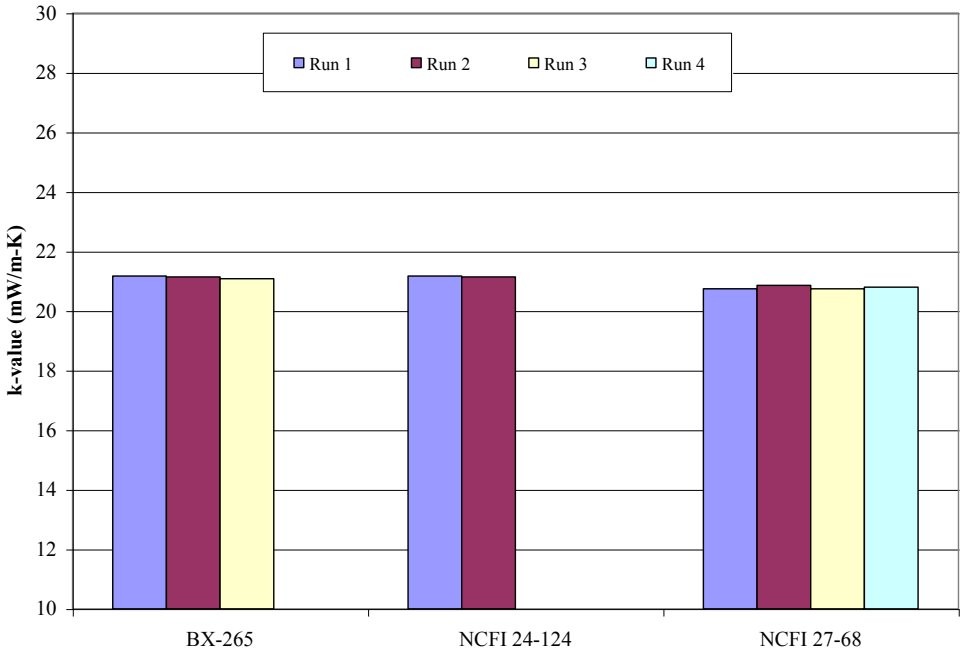

Figure 12. Apparent thermal conductivity (k-value) of SOFI materials at a cold vacuum pressure of 760 torr (no vacuum) gaseous nitrogen. Boundary temperatures are approximately 293 K and 78 K.

Table 3. Summary of Cryostat-100 thermal performance data for three SOFI materials.

No.	Description	CVP millitorr	*k-value mW/m-K	*Heat Flux kg/m3
A104	SOFI, BX-265, shaved	0.5	7.9	66
	34 kg/m3	1	8.3	70
	26.7 mm	10	13.9	117
		100	17.6	148
		1000	18.6	157
		10000	18.9	159
		100000	19.1	160
		760000	20.2	170
A105	SOFI, NCFI 24-124, shaved	0.1	**7.5	**51
	39 kg/m3	1	9.0	76
	25.6 mm	10	13.5	113
		100	18.7	157
		1000	20.3	171
		10000	20.9	175
		100000	20.9	175
		760000	21.2	177
A106	SOFI, NCFI 27-68, shaved	0.5	7.5	67
	39 kg/m3	1	8.1	73
	23.9 mm	10	13.3	119
		100	17.7	159
		1000	19.0	171
		10000	19.6	176
		100000	19.8	178
		760000	20.8	187

*Boundary temperatures 293 K and 78 K; residual gas nitrogen.
**Reduced warm boundary temperature of 253 K.

The temperature profiles for each Cryostat-100 test article were measured using thermocouples located at 6-mm intervals through the thickness of the foam. The variations of temperature with cold vacuum pressure for three different SOFI materials are presented in Figure 13. The temperature sensor location is approximately 6-mm from the cold mass. Test articles A105 and A106 are seen to correspond quite closely at temperatures around 285 K for vacuum conditions and 263 K for ambient pressure conditions. The same temperature sensor location for test article A104 was measured to be from 5 to 10 K lower, but this difference could be due to a slight additional displacement of the sensor toward the cold mass. The temperature sensor locations were not positively measured but estimated through recording the penetration depth of the lead wires. These results show that the temperature gradient is steep next to the cold mass and that the bulk of the material is fairly close to the warm boundary temperature of 293 K. This information is helpful for analytical comparisons of thermal conductivity data taken under the different test conditions of ambient temperature, cryogenic temperature (small delta temperatures), and Cryostat-100 (large delta temperature).

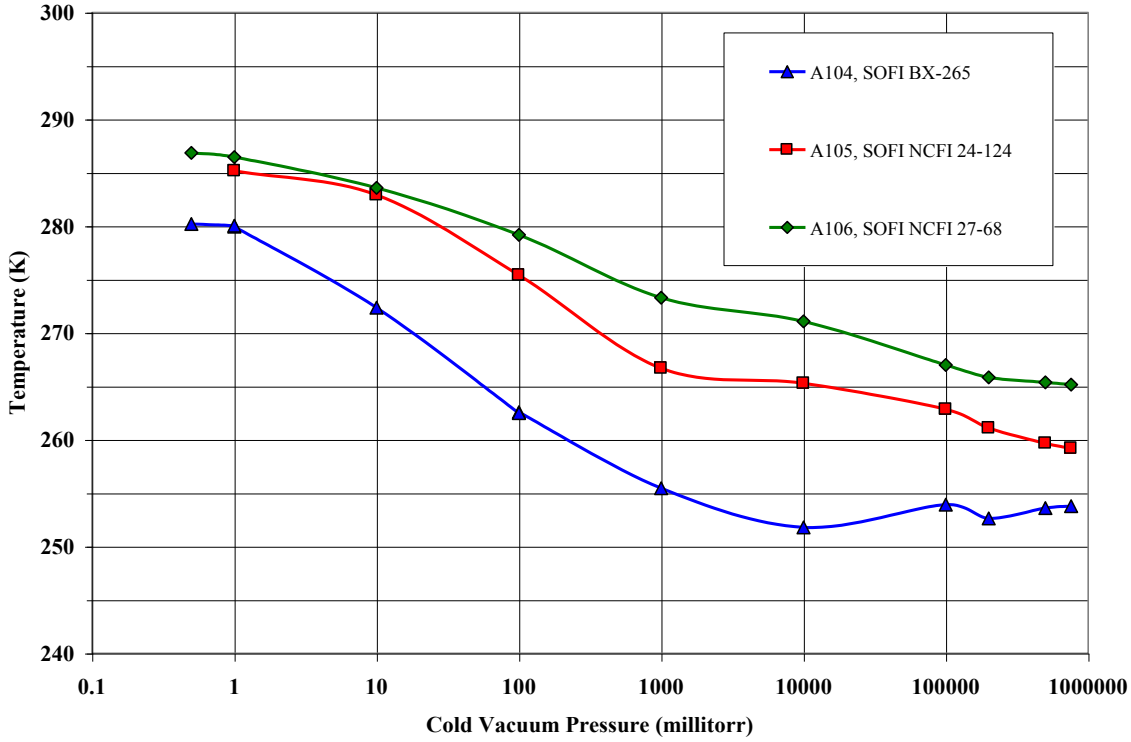

Figure 13. Variation of temperature with cold vacuum pressure for three different SOFI materials. Boundary temperatures are 293 K and 78 K. Temperature sensor location is approximately 6-mm from cold mass.

To better understand thermal performance differences between shaved (machined) and rinded (net spray) foam materials, an additional Cryostat-100 test article composed of NCFI 24-124 with rind was tested. The results of this test series, in comparison with the shaved test article of the same material, are given in Figure 14. The k-value for the rinded specimen was calculated to be approximately 13% higher at ambient pressure. Although the average thicknesses were about the same, the thickness was not entirely uniform for the rinded test article as it was for the machined test article. In addition, portions of rinded test article were necessarily machined to enable fit-up and proper installation of the two halves (see Figure 7).

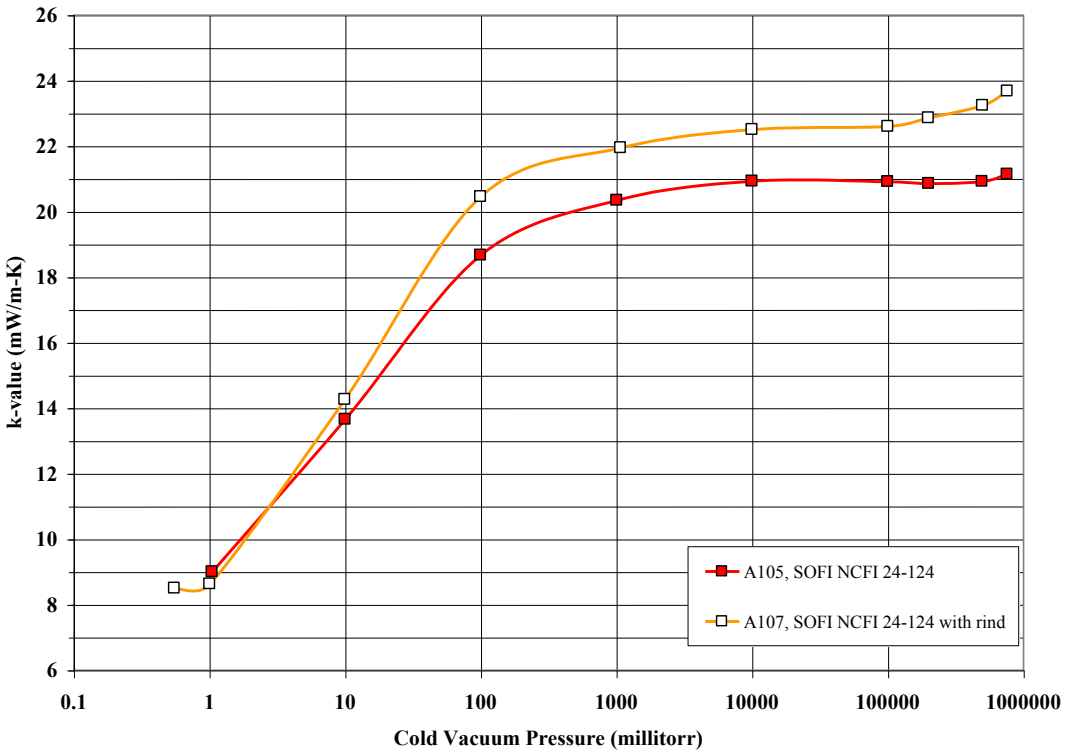

Figure 14. Variation of apparent thermal conductivity (k-value) with cold vacuum pressure for SOFI material 24-124 shaved and with rind. Boundary temperatures are approximately 293 K and 78 K. The residual gas in nitrogen.

Because these foam materials include a blowing agent and are approximately 95 percent closed cell, the order of testing in vacuum was considered. A special series of tests was performed to understand if evacuation and subsequent re-pressurization of the foam with nitrogen (or air) would have a noticeable effect on the thermal conductivity under cryogenic-vacuum conditions. The test article was SOFI BX-265 and the results are given in Figure 15. No significant effect was found which allowed a more flexible test methodology for obtaining the multiple data points through the Cryostat-100 test program.

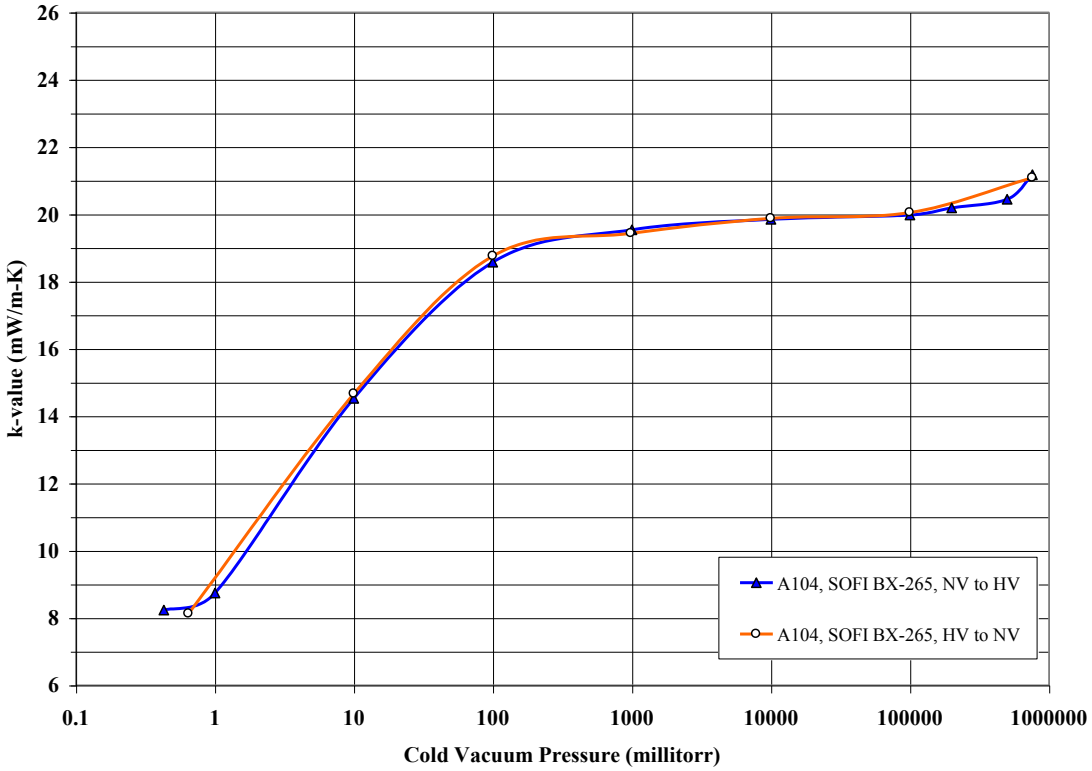

Figure 15. Variation of apparent thermal conductivity (k-value) with cold vacuum pressure for SOFI material BX-265 tested from no vacuum to high vacuum and from high vacuum to no vacuum. Boundary temperatures are approximately 293 K and 78 K. The residual gas in nitrogen.

5.2 Ambient Thermal Conductivity

The ambient thermal conductivities (λ) ranged from 19 mW/m-K (baseline) to 32 mW/m-K (aged). The results for aging of BX-265 and NCFI 24-124 are given in Figure 16 while the results for weathering are summarized in Figure 17. Only the BX-265 material has data for zero months aging or weathering as this was the only one that not fully cured before testing. This data point shows the dramatic difference that the nominal one-month curing time can make. Results show that the actual thermal performance is significantly degraded from exposure durations of up to 24 months with the sharpest change occurring within the first six months of aging or weathering. Compared to the aged specimens, the weathered specimens showed higher thermal conductivities as expected. However, much of the effect is presumably lessened by the fact that the rind is necessarily shaved off in preparation for performing the test.

The thermal conductivity is widely variable based on many factors such as test method, test conditions, aging, weathering, density, closed cell content, surface area, pore size, foam chemistry, and spraying conditions. The baseline results are therefore an important and necessary starting point for thermal performance comparison among foam materials.

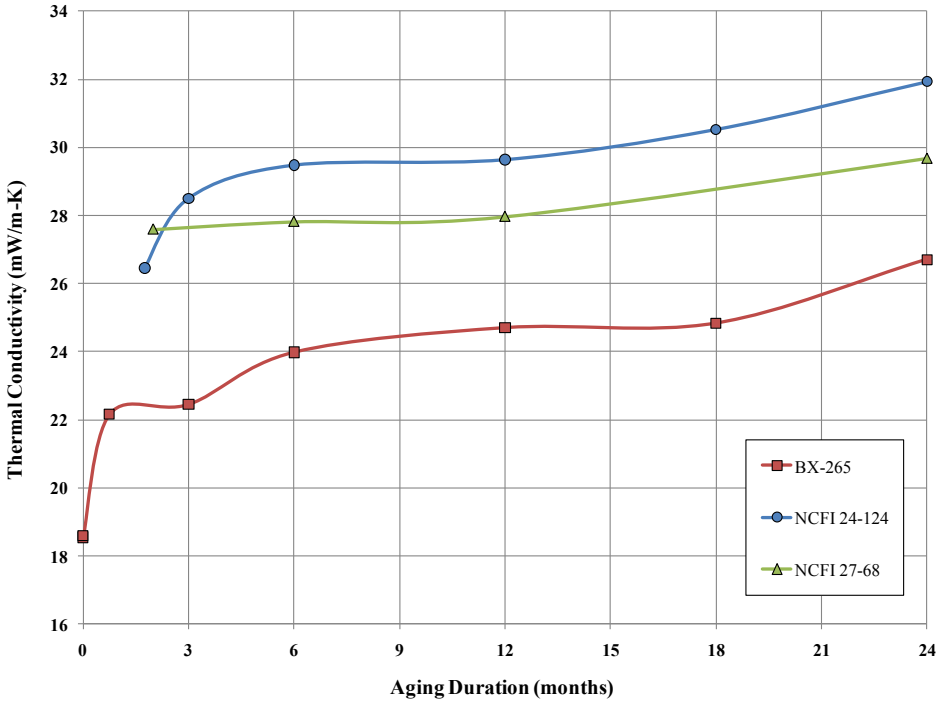

Figure 16. Variation in thermal conductivity with aging duration for SOFI materials.

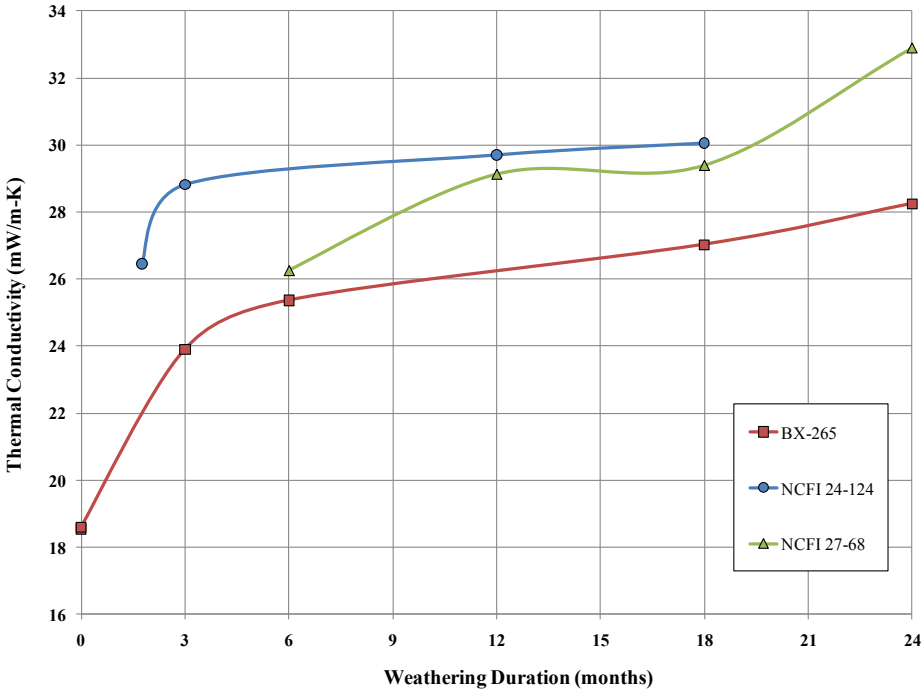

Figure 17. Variation in thermal conductivity with weathering duration for SOFI materials.

5.3 Physical Characterization

The physical characterization tests are used to support the thermal conductivity results and provide a basis for future thermal modeling and analysis efforts. The open cell content testing included 43 specimens and a total of 237 tests; the results are summarized in Figures 18 and 19. The open cell content was found to be approximately 6% for the baseline foam specimens. The average measured open cell contents for the aged and weathered specimens were 10% and 12%, respectively. The surface area testing included 13 specimens and a total of 112 tests; the results are summarized in Figures 20 and 21. The average surface areas for the baseline specimens were measured to be approximately 130 m^2/g for the BX-265, 170 m^2/g for the NCFI 24-124, and 180 m^2/g for the NCFI 27-68. The surface area was found to increase by approximately 35% after three-months of aging or weathering. The surface area then diminished somewhat with further aging but continued to increase with further weathering exposure.

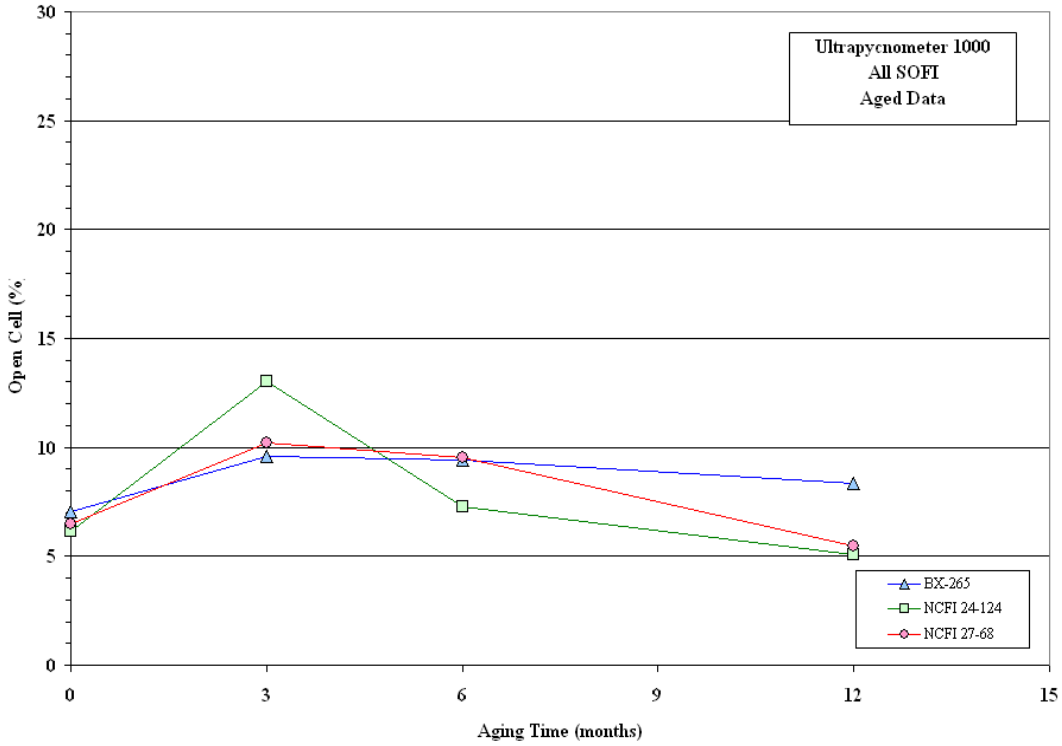

Figure 18. Variation of open cell percentage with aging times for three SOFI materials.

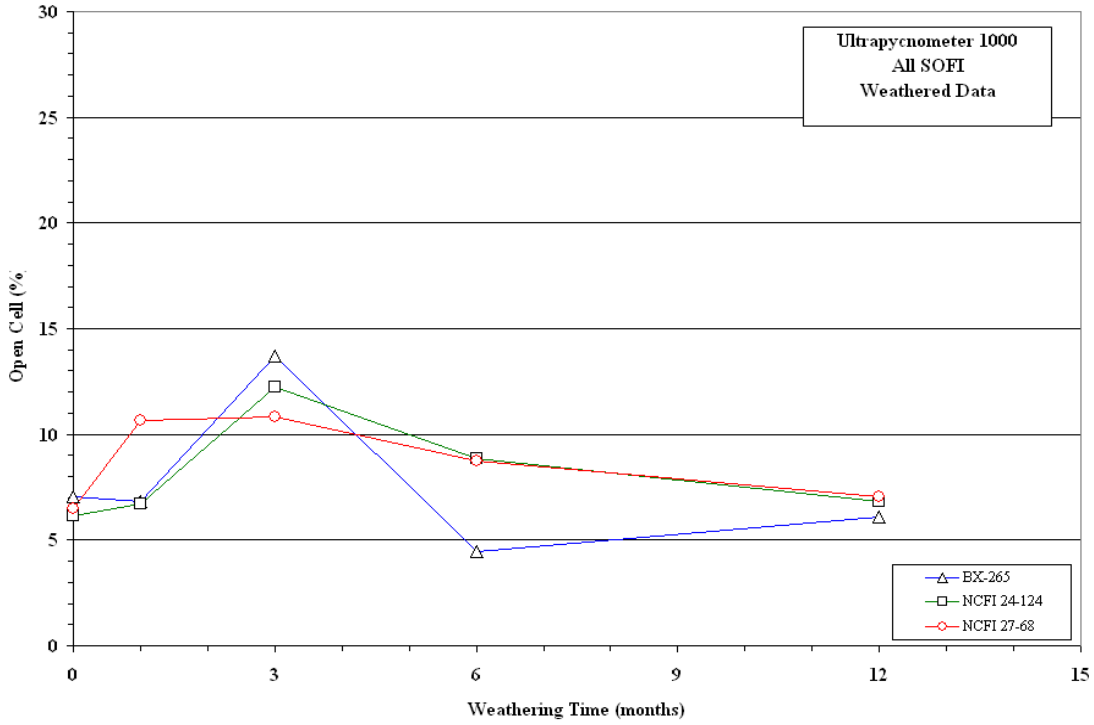

Figure 19. Variation of open cell percentage with weathering times for three SOFI materials.

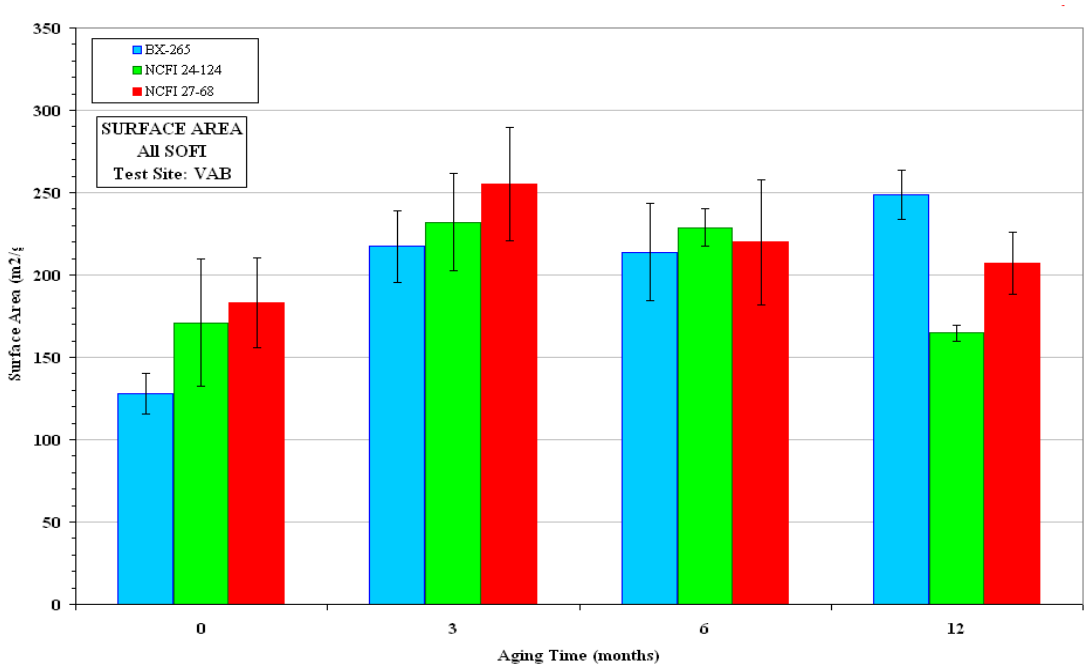

Figure 20. Variation of surface area (m^2/g) with aging times for three SOFI materials.

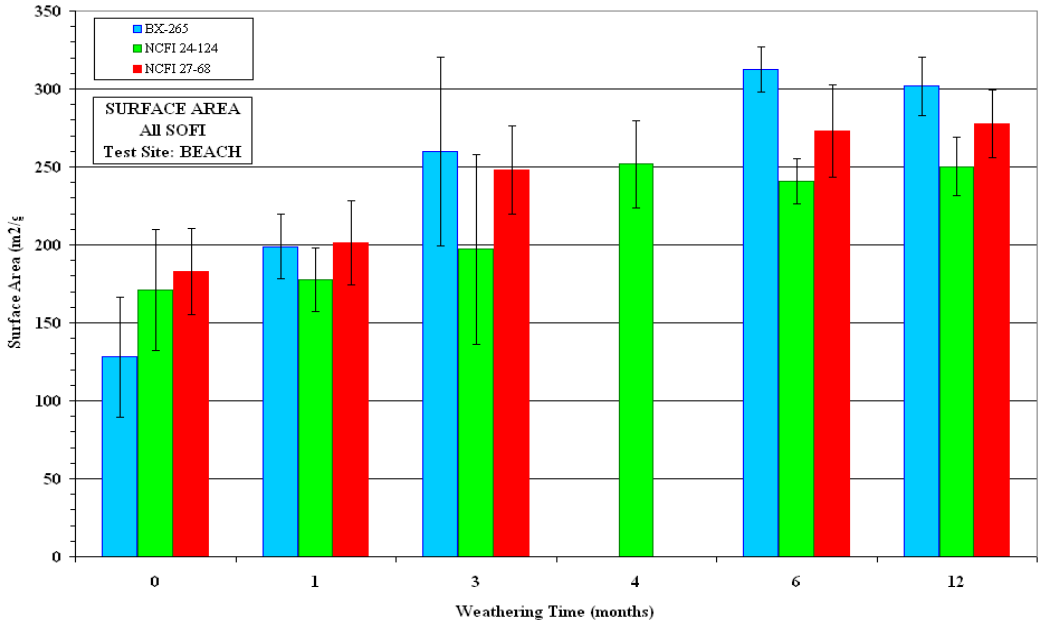

Figure 21. Variation of surface area (m^2/g) with weathering times for three SOFI materials.

6. Discussion and Analysis

The results from the cryogenic testing part of this thermal performance study of SOFI materials shows that the k-value rises sharply from high vacuum to 10 millitorr as gas conduction begins to dominate the rate of heat transfer. The k-value increased only slightly in the soft vacuum range of 100 millitorr up to 100 torr. The k-value increases significantly from 100 torr to 760 torr, as convection becomes the dominant factor. The alternate acreage foam NCFI 27-68 was the overall best performer in terms of lowest heat transfer. The order of testing, either from no vacuum to high vacuum, or vice versa, was not found to be a factor in cryostat thermal performance testing.

Prior cryostat thermal performance testing on a similar one-meter-long SOFI specimen of BX-250 material (51-mm thickness and a density of 38 kg/m^3) shows a generally similar result to the data presented in this work.[17] In this case, the k-value was determined to range from 4.1 mW/m-K at 0.1 millitorr to 21.4 mW/m-K at 760 torr. It should be noted that this specimen was sprayed, machined, and installed on the cryostat as a single piece rather than two clam-shell halves. Reference data for a similar polyurethane foam tested by the guarded hot plate (under relatively small differential temperatures) is found in the publication by Sparks and Arvidson.[18] The thermal conductivity is reported as 21.7 mW/m-K at conditions of near ambient pressure and a mean temperature of 186 K. The density of the specimen is 0.032 kg/m^3 which is lower but comparable to the specimens described here. Good agreement for this data point is found for this particular test condition as the cryostat test boundary temperatures provide the same mean temperature. However, experimental test data for the polyurethane foam type of material under the combined conditions of full temperature difference and full vacuum pressure range is not readily found in the literature.

The international standard for rigid polyisocyanurate foams, ASTM C591, provides specifications for both HCFC (Grade 2) and non-HCFC (Grade A2) blown foams over a wide range of densities.[19] For densities of either 32 or 40 kg/m^3, the maximum thermal conductivity is listed as 22 mW/m-K at 172 K and 25 mW/m-K at 200 K. The same foams at an ambient temperature of 297 K are listed as 26 mW/m-K for the HCFC-blown grade and 29 mW/m-K for the non-HCFC-blown grade. The minimum closed cell content is listed at 90 percent (maximum open cell content of 10 percent). These standard specifications provide a point of reference for further analytical comparisons with both ambient test data and cryostat data obtained under large-temperature-differential cryogenic conditions.

The results from the ambient testing part of the study show somewhat higher thermal conductivities, as expected, but a marked difference between the close-out foam (BX-265) and the acreage foams (NCFI 24-124 and NCFI 27-68). The BX-265 is the best performer from baseline to any aging or weathering duration. The aged BX-265 increases from roughly 20 to 27 mW/m-K over 24 months while the NCFI 24-124 increases from roughly 24 to 29 mW/m-K over that same period. (The starting thermal conductivity for newly sprayed foams is highly variable in the first 30 days as the curing is fully completed and the excess blowing agent is diffused out of the material.) The three-months weathered thermal conductivities for BX-265 and NCFI 24-124 are 24 and 29 mW/m-K, respectively.

New information on the intrusion of moisture into SOFI under large temperature gradients was also produced through a related study. Experimental data for a significant number of test specimens were produced and the overall trends are clear. The details of the cryogenic moisture uptake apparatus and complete test results are reported elsewhere.[9,20] The SOFI materials were found to gain an extraordinary amount of water weight during a cryogenic propellant loading (cold soak) period. Moisture uptake for the NCFI 24-124 specimens (acreage foam) averaged 30% for the baseline condition and 78% after 3 months of weathering. Cryogenic moisture uptake continued to increase for both aging and weathering. The weight increase of SOFI was also found to be additive for three consecutive cryogenic thermal cycles, or simulated tanking operations, resulting in as much 167% weight gain for the one-month weathered acreage foam as shown by the example in Figure 22. The boundary conditions are 295 K and 78 K with a 90% humid environment on warm side. The moisture uptake results are expressed in terms of percentage weight gain for foam materials of similar density. However, much more intensive investigation and analysis is warranted to understand the moisture uptake phenomenon, determine the distribution and morphology of the moisture through the thickness of the foam, and enable suitable engineering analysis of the propulsion performance of space launch vehicles.

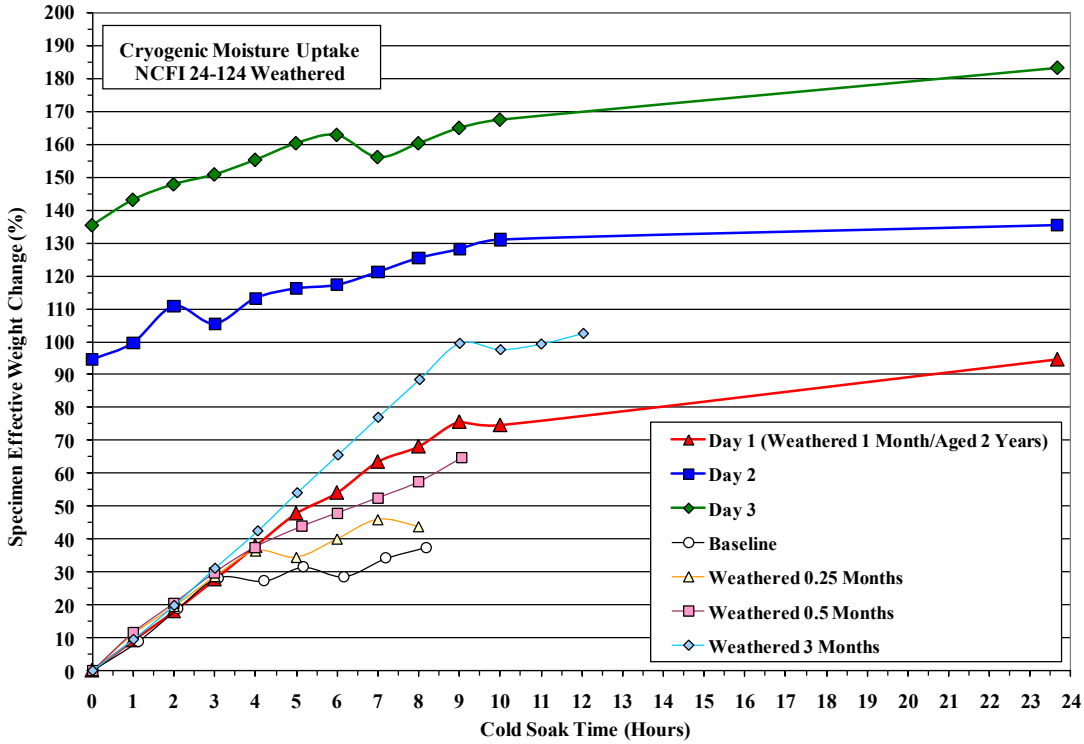

Figure 22. Example of weight gain due to cryogenic moisture uptake in SOFI. Days 1-3 simulate consecutive days of launch vehicle cryogenic tank loading and draining operations.

7. Conclusions

Spray-on foam insulation (SOFI), originally developed for use on the cryogenic tanks of space launch vehicles beginning in the 1960s with the Apollo program, has been futher developed through the course of the Space Shuttle program. The Space Shuttle's External Tank uses a number of different insulation materials in a complex system of thermal insulation during cryogenic propellant loading and thermal protection during flight. Thermal conductivity data for three such SOFI materials under both cryogenic and ambient temperature conditions were presented. New laboratory standard equipment and methods including the Cryostat-100 insulation test instrument were used to produce thermal performance data for actual-use cryogenic-vacuum conditions.[21] The effect of a rinded (net spray) versus machined outer surface were also examined. Trends for aging and weathering environments were included as part of the ambient test series.

The cryogenic test conditions were representative of the actual-use conditions for most cryogenic insulation systems including those used on the cryogenic tanks and propellant feedlines of space launch vehicles. The test measurements were made at the full temperature difference (approximate boundary temperatures of 78 K and 293 K) and included the full vacuum pressure range. The results are reported in terms of the apparent thermal conductivity (k-value) and the mean heat flux.

This study of the cryogenic thermal performance of SOFI under large temperature differentials provides data and basic new information to apply in the design and optimization of

future launch vehicles and other cryogenic insulation systems. Many environmental effects and manufacturing details, and operational factors must also be considered in the design and performance analysis for foam insulation systems in dynamic and extreme conditions. The physical characterizations including thermal conductivity, surface area, and open cell content must be put together with the actual-use cryogenic thermal performance data and mechanical data to obtain a complete picture of the insulation system performance and design margins.

Work continues to develop modeling techniques based on these new thermal performance data and enable more robust, lighter weight, and higher efficiency foam insulation systems. Future launch vehicles with cryogenic stages will likely use SOFI due to its combination of lightweight, mechanical strength, and low thermal conductivity. Insulation systems for any reusable vehicle still remain a challenge due to the continual breakdown of SOFI with weathering exposure. Spacecraft providing long-duration storage of cryogens in the vacuum of space will likely employ a type of MLI as the primary insulation system. However, these tanks also require a level of thermal insulating performance in the ambient environment during launch preparations and initial flight.

ACKNOWLEDGEMENT

This work was funded in part by the Space Operations Mission Directorate through the NASA Internal Research and Development (IR&D) project, *Technologies to Increase Reliability of Thermal Insulation Systems*. The authors thank Jim Rice and Gweneth Smithers of NASA Marshall Space Flight Center for their support in producing the test articles and Nancy Zeitlin of NASA Kennedy Space Center for guiding this project.

REFERENCES

1. Anon., "Design of thermal protection systems for liquid hydrogen tanks," Technical report to NASA, Arthur D Little Inc., Cambridge, MA 1963, pp. 14-15.
2. Glaser, P.E., et al., "Thermal insulation systems," Technical report NASA SP-5027, 1967, pp. 82-83.
3. Scholtens, B.E., Fesmire, J.E., Sass, J.P., and Augustynowicz, S.D., "Cryogenic thermal performance testing of bulk-fill and aerogel insulation materials," in Advances in Cryogenic Engineering, Vol. 53A, American Institute of Physics, New York, 2008, pp. 152-159.
4. Fesmire, J.E., Augustynowicz, S.D., and Scholtens, B.E., "Robust multilayer insulation for cryogenic systems," in Advances in Cryogenic Engineering, Vol. 53B, American Institute of Physics, New York, 2008, pp. 1359-1366.
5. Coffman, B.E., Fesmire, J.E., Augustynowicz, S.D., Gould, G., White, S., "Aerogel blanket insulation materials for cryogenic applications," Advances in Cryogenic Engineering, AIP Conference Proceedings, Vol. 1218, pp. 913-920 (2010).
6. Fesmire, J.E., "Aerogel insulation systems for space launch applications," Cryogenics, 46, issue 2-3, February 2006, pp. 111-117.
7. Fesmire, J., "Moisture/Aging Study of Spray-On Foam Insulation (SOFI) Under Actual-Use Cryogenic Conditions," executive summary report to NASA Space Operations Mission Directorate, September 2006.
8. Smithers, G., "Technology Development for Thermal Insulation Systems (TIS)," executive summary report to NASA Space Operations Mission Directorate, September 2006.
9. Fesmire, J.E., et al, "Cryogenic Moisture Uptake in Foam Insulation for Space Launch Vehicles," AIAA Space 2008, September 2008. (submitted for publication in *Journal of Spacecraft & Rockets*).

10. Anon., Space Shuttle External Tank System Definition Handbook SLWT, Volume 1 – Configuration and Operation, Lockheed Martin Michoud Space Systems, Report No. LMC-ET-SE61-1, December 1997.
11. Rice, J., Certificate of Traceability, DIRR00047, "Moisture/Aging Study of SOFI under Cryogenic Conditions," Marshall Space Flight Center, 2005.
12. Anon., "Space Shuttle Production Control, Vertical Products, ET/SRB Matrix History," United Space Alliance Ground Operations.
13. Fesmire, J.E. and S.D. Augustynowicz, "Methods of Testing Thermal Insulation and Associated Test Apparatus," U.S. Patent 6,742,926, issued June 1, 2004.
14. Fesmire, J. E., Augustynowicz, S. D., Scholtens, B. E., and Heckle, K. W., "Thermal Performance Testing of Cryogenic Insulation Systems," Thermal Conductivity, Vol. 29, 2008, pp. 387-396.
15. ASTM C518, "Standard Test Method for Steady-State Thermal Transmission Properties by Means of the Heat Flow Meter Apparatus," ASTM International, West Conshohocken, PA, USA.
16. ASTM D6226, "Standard Test Method for Open Cell Content of Rigid Cellular Plastics," ASTM International, West Conshohocken, PA, USA.
17. Fesmire, J., Augustynowicz, S., and Heckle, W., "Testing of space shuttle spray-on foam insulation under cryogenic vacuum conditions," NASA-TM-2003-211190, pp. 78-79.
18. Sparks and Arvidson, "Thermal and Mechanical Properties of Polyurethane Foams and a Survey of Insulating Concretes at Cryogenic Temperatures," from the Chemical Engineering Science Division of the National Bureau of Standards (NBS) in Boulder, Colorado.
19. ASTM C591, "Standard Specification for Unfaced Preformed Rigid Cellular Polyisocyanurate Thermal Insulation," ASTM International, West Conshohocken, PA, USA.
20. Fesmire, J., et al., "Cryogenic Moisture Apparatus," NASA Tech Briefs, May 2010, pp. 5-6.
21. ASTM WK29609, "Guide for Thermal Performance Testing of Cryogenic Insulation Systems," ASTM International, West Conshohocken, PA, USA.

Cryogenic Shockwave Abatement

Charl E Janeke (PE)

Kartago Inc, 1330 Ingraham Street #114, Los Angeles CA 90017, www.kartagoinc.com

Abstract

Subsequent to benign beginnings in Auburn Massachusetts March 1926 when Robert Goddard tested the 1st liquid rocket system, the world has been in awe as to the power of the rocket engine and achievements thereto that peaked with man conquering the moon. However the Apollo myth soon faded into the realities of global disorder and deficit funding that could not sustain the Shuttle and Apollo derivatives beyond strategic security needs. Although SpaceX, Orbital Sciences, XCOR et al reincarnated the rocket as we know it, the ultimate orbital solution vests in air breathing launch systems to unshackle the bondage of staged launching systems. In order to spawn the art of SSTO (single-stage-to-orbit) orbital systems to sustain space commerce, it will be necessary to master the art of propulsion in the hypersonic domain. The explosive discharge and consequential thermal stress of shockwaves however imposes severe limitations on the viability of SCRAM (supersonic combustion) driven aerospace planes in the abstract. In order to manage OR obliterate the shock wave impediment in viscous fluids, the speed of sound must be elevated OR means created to dissipate the heat of compression at formation. As shockwaves are the consequence of rampart adiabatic compression, the project focused on the power of cryogenic propellants as means to isothermal compression and liquefaction of atmospheric oxygen as a propulsion byproduct.

The consequential finding that oxygen and nitrogen functions as independent <disjoint> substances in the cryogenic zone (with oxygen the weaker link), become the principal focus of the project.

Key words: Cryogenic, shockwave, abatement, stagnation, and liquefaction.

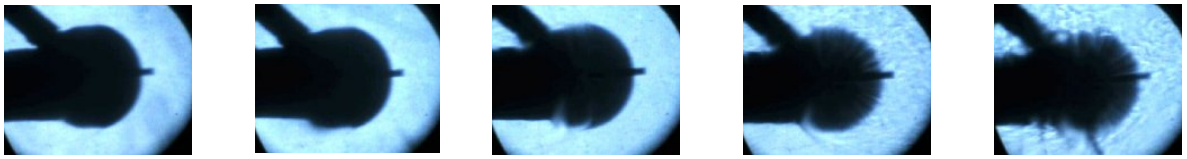

1. INTRODUCTION

Shockwaves are the consequence of the inability of atmospheric air to absorb the heat of (rapid) compression at supersonic and hypersonic speed that results in a sudden/explosive shockwave discharge. The discharge of shockwaves imposes severe drag and thermal stress on hypersonic aircraft and projectiles. Scram engines also functions only marginally effectively in the hostile shock environment. In order to manage OR obliterate the shock wave impediment in viscous

fluid, the speed of sound must be elevated OR means created to dissipate the heat of compression at formation.

2. BACKGROUND

Aspiration of atmospheric air is a necessity to SSTO means. Shockwaves form as a consequence of the inability of air to absorb heat of compression at high speeds. Viscosity in real fluids results in friction losses with consequential heat and entropy gain. The inability of atmospheric air to absorb heat of compression at high speed results in an explosive (shock) discharge. The explosive discharge of shockwaves imposes severe drag and thermal stress on supersonic aircraft and projectiles. SCRAM (supersonic combustion) engines function only marginally effectively in the hypersonic environment due to the extreme thermal environment.

3. SUPERCOOLING ANALYSIS

In order to manage or obliterate the shockwave impediment in viscous fluids, the speed of sound must be suppressed, or means created to dissipate the heat of compression at formation. A rational analysis of dissipating the heat of compression led to the notion of *supercooling* (i.e. an extreme high rate of heat transfer) in the cryogenic zone as a means to (1) sustain *isothermal* compression and (2) *piercing* the hypersonic front by liquefaction of the oxygen component of the ambient air. Because of the unique makeup of atmospheric air (19% oxygen), liquefaction of ambient oxygen will lead to 34% abatement of the kinetic potential (the resistance vector). Liquefaction (100%) atmospheric air however exceeds the chilling power of liquid hydrogen and liquid methane as cryogenic propellants. A piecewise testing program was therefore conceived to approach the problem adaptively. Testing facilitation was acquired at the *Virginia Tech* hypersonic lab at Blacksburg, VA.

4. SUPERCOOLING PARADOX

The answer to the (shockwave) piercing enigma was found in a two-step methodology by teaming the power of *cryogenic* chilling and *supercooling* as means to (1) isothermally compressing the incipient hypersonic air stream into the saturation zone and (2) liquefaction of the oxygen component of the ambient air via the power of cryogenic chilling. Liquefaction of the oxygen component of the ambient air stream depresses the Mach number by a factor of 19% (the volume of the oxygen fraction of the ambient air). Because the kinetic pressure is a squared function of the Mach number, liquefaction depresses the kinetic pressure by a factor of 0.81^2 =34%. The combination of Mach number depression and supercooling in the cryogenic zone spawns the formation of isothermal pressure surges in lieu of adiabatic shockwaves. However because *liquefaction* and *supercooling* are germane in the abstract (the paradox), the application must be viewed within the domain of infiniteness, i.e. that of an infinitely constrained boundary layer, and the power of *supercooling*.

5. PIERCING APPARATUS

In order to demonstrate *supercooling* and consequential piercing, an elemental shockwave experiment was devised whereby a cryogenically chilled copper ball was subjected to a hypersonic blast in a blow-down wind tunnel. The project was devised into three stages, viz. Phase-1 (Mach 4) as to cryogenic particularities that was performed July 27/30; Phase-2 (Mach 5) as to liquefaction dynamics that was performed September 2/3; and Phase-3 (Mach 6) as to stagnation regression that was performed December 9/10 2010. Piercing was successfully achieved on BOTH the initial runs July 29/30 at –148C and -158C (a *first-time* universal accolade). Liquid helium was introduced via the Phase-2 program at -180C to -230C. Phase-3 hence focused on stagnation dynamics and refining of the saturation charts. The refined tests were executed concurrent with the May/2011 Phase-4 testing program. *The Phase-4 work however is not part of the presentation*.

6. SELECTED PICTURES (phase-3 apparatus) …*See footer!!*

7. TEST RESULTS (1)

Phase-1 Tests

Phase-1 tests were directed at devising means as to cryogenic augmentation and piercing of the hypersonic front. Although liquid Helium was considered the means to the end, the initial (Phase-1) program was limited to liquid Nitrogen. The apparatus comprised a base plate and and "quick-fit" adapter plate, an aluminum strut, titanium rod and a 1¾" copper ball (see picx). Liquid nitrogen was fed into an aperture within the copper ball and the vapor exhausted via ancillary vents. The apparatus was chilled outside the lab. The copper ball was encapsulated in a foam rubber cocoon that was designed to split and disintegrate at Mach-1 (the critical *supercooling* juncture). Only two tests were conducted, viz. Thursday *July/29* 2010 and Friday *July/30* 2010. Although the max atmospheric chilling potential of –190C of liquid Nitrogen was achieved each time, icing and transfer handling limited the initial (July/29) test to -150C. Ice abatement measures lead to a –160C threshold July/30 2010.

8. **TEST RESULTS (2)**

Phase-2/3 Tests

As a consequence of the phase-1 learning curve a new testing platform was devised with a Teflon mounting jack, vacuum jacketed feeding and insertion apparatus and expanded supply and ventilation ports. A pneumatically driven vacuum exhausting system as also added with the Phase-3 tests (see picx). Liquid Nitrogen as well as liquid Helium was used with (both) the Phase-2 and Phase-3 tests. A custom made cryo-chilling box was employed with the Phase-2 tests that accelerated chilling and precluded ice formation. As a consequence of the learning curve that was refined to plug-and-play art via pneumatic ventilation and functional refinements, *Phase-3 chilling was consequently affected inside the lab*. Phase-3 testing was consistently conducted at –160C to -230C. Whereas it became apparent during the Phase-2 program that liquefaction and *supercooling* are germane events, means of pressure sensing was devised and successfully implemented with the Phase-3 program. *As a consequence of post analysis the Phase-3 tests were rerun during the Phase-4 program that lead to the abatement symbiosis that is being presented with the Coeur D'Alene meeting*.

9. STAGNATION PRESSURE MEASUREMENTS (May/2011) …*See footer!!*

10. STAGNATION PRESSURE SPREAD (1)
See footer!!

11. STAGNATION PRESSURE SPREAD (2)
See footer!!

12. STAGNATION PRESSURE SPREAD (3)
See footer!!

13. STAGNATION PRESSURE SPREAD (4)
See footer!!

14. STAGNATION REACTION VECTOR (M5) …*See footer!!*

15. STAGNATION HYPERBOLE

Shockwaves are the consequence of the inability of atmospheric air to absorb trapped heat of rapid adiabatic compression. The premise of elevating the speed of sound *OR dissipating the heat of compression at formation* hence lead to the notion of *supercooling* to negate shockwave formation via cryogenic means. Initial testing identified liquefaction of atmospheric oxygen in the saturation zone as the key to shockwave abatement means. However it soon became apparent via retesting of the phase-3 stagnation platform during the phase-4 program that additional forces are entrained in the equation system that lead to the prevalence of *isothermal compression* as a *default augmentation means*. Shockwave abatement in the cryogenic zone is hence the consequence of superposition (viz. summation) of liquefaction and isothermal compression in the abstract. *Liquefaction (the hyperbole) however simply equates to Mach number and consequential stagnation suppression (viz. 34% in totality) in the cryogenic zone!*

16. STAGNATION VECTOR ANALYSIS (1)
See footer!!

17. STAGNATION VECTOR ANALYSIS (2)
See footer!!

18. THERMAL RESPONSE (RECORDED) (HQ23/M6) …*See footer!!*

19. ISOTHERMAL SURGING (RECORDED) …*See footer!!*

20. ACKNOWLEDGEMENTS

Author wishes to express recognition to the following entities;

- Office of Sponsored Programs, Virginia Tech, Blacksburg, VA 24060
- American Precision Tool Company, Pacoima, CA
- International Cryogenics, Indianapolis, ID
- Superior Spinning, Santa Fe Springs, CA
- Scarrott Metallurgical, Culver City, CA
- Cutting Edge, Newbury Park, CA
- Julian and Diana Gurrola, LA/CA.

Figures and Inserts;

Item #6 illustrates the makeup of the test rig and supporting equipment.
Item #9 illustrates the stagnation pressure measurements over the span of the blow-down blast.
Item #10 illustrates the linearalized stagnation recordings.
Item #11 illustrates the linearalized stagnation recordings with the Dec/2010 saturation recording.
Item #12 illustrates the linearalized stagnation recordings with the Mach 5 reference head.
Item #13 illustrates a stack version of the Mach 5 reference head.
Item #14 illustrates the stagnation vector (drag index) analysis.

6. SELECTED PICTURES (phase-3 apparatus)



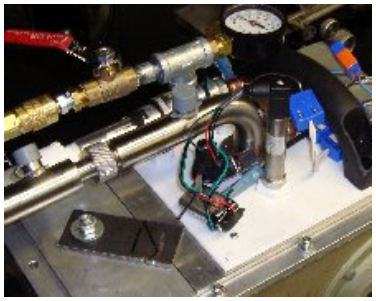

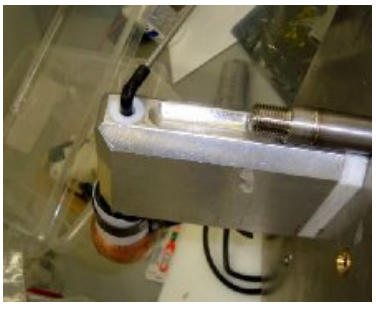


9. STAGNATION PRESSURE MEASUREMENTS (May/2011)

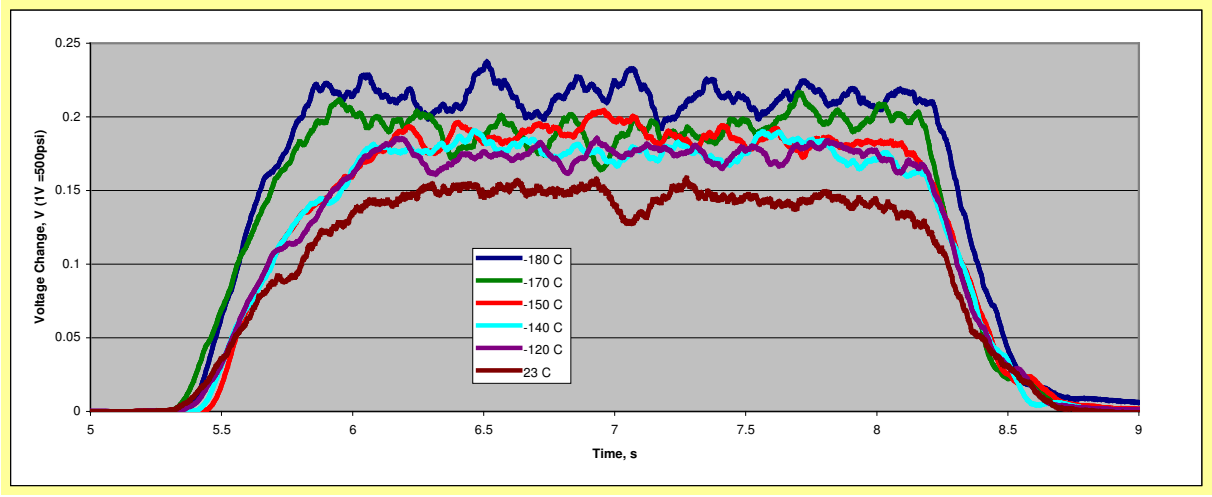

10. STAGNATION PRESSURE SPREAD (1)

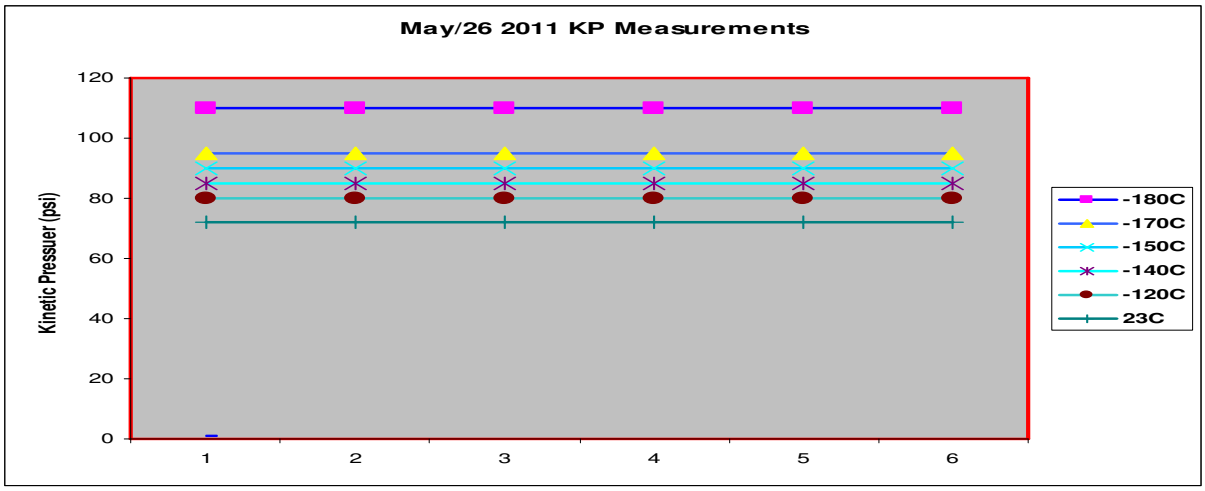

11. STAGNATION PRESSURE SPREAD (2)

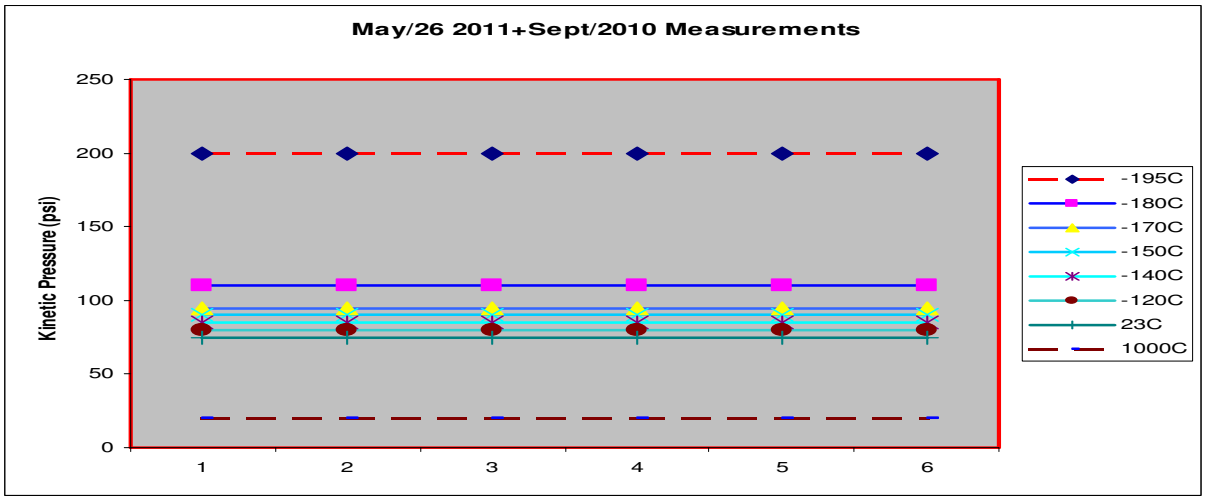

12. STAGNATION PRESSURE SPREAD (3)

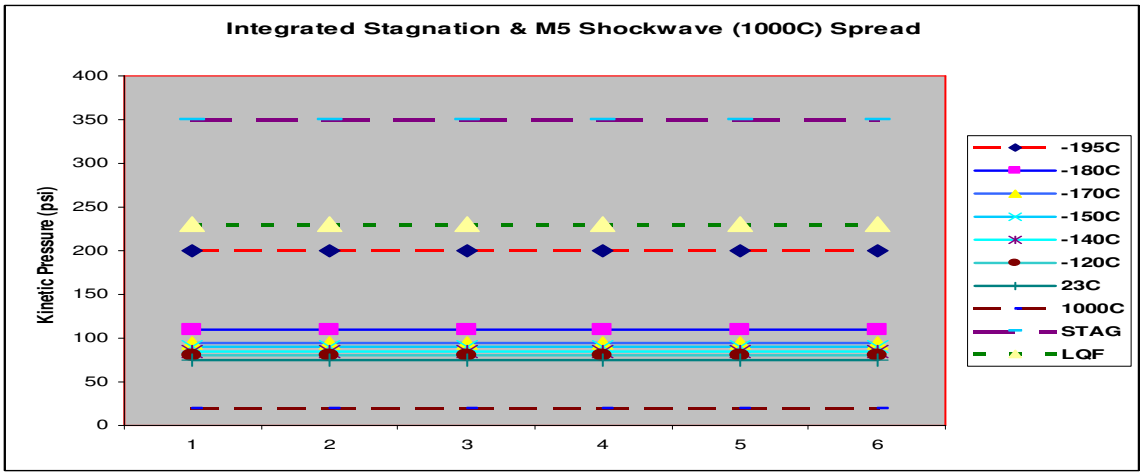

13. STAGNATION PRESSURE SPREAD (4)

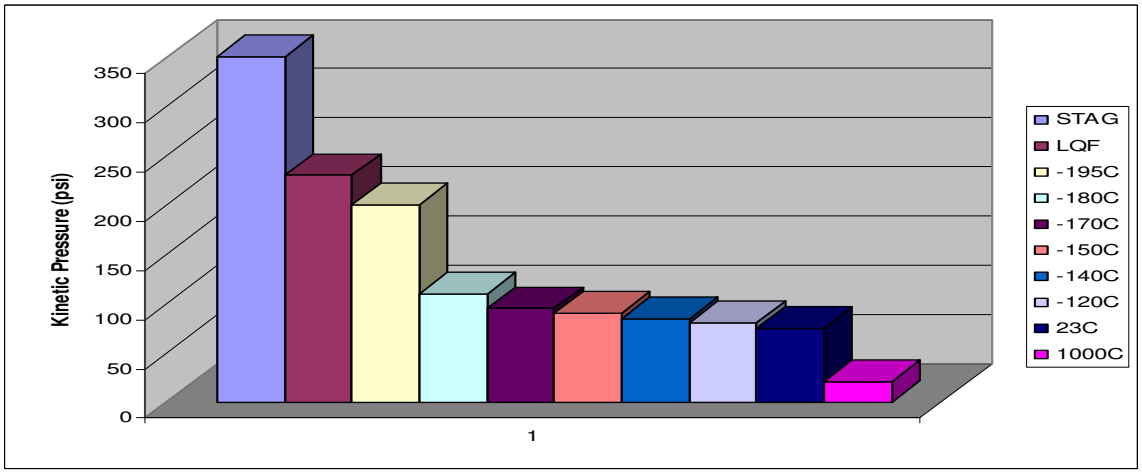

14. STAGNATION REACTION VECTOR (M5)

- **Adiabatic M5 shock** (<[[[[]]]]>)))))) **….KP <350-20 =330psi>**
- **Isothermal +23C** ….((<[[[[]]]]>)))))) **…..KP <350-75 =275psi>**
- **Isothermal -120C** …(((<[[[[]]]]>)))))) **…..KP <350-80 =270psi>**
- **Isothermal -140C…** ((((<[[[[]]]]>)))))) **…..KP <350-85 =265psi>**
- **Isothermal -150C….** (((((<[[[[]]]]>)))))) **…..KP <350-90 =260psi>**
- **Isothermal -170C…..** (((((<[[[[]]]]>)))))) **…..KP <300-95 =205psi>**
- **Isothermal -180C…** (((((<[[[[]]]]>)))))) ….**KP <260-110 =150psi>**
- **Isothermal -195C……..** (((((<[[[[]]]]>)))))) ……**KP <230-200 =30psi>**

- **Piercing Hyperbole =hypo when the Kinetic/Stagnation Pressure =230psi**
- **((((= Reaction vector;)))))) = Kinetic pressure vector**

16. STAGNATION VECTOR ANALYSIS (1)

In accordance with the premise of isothermal compression, the impact of stagnation suppression in the cryogenic zone (at Mach 5) may be presented as follows;

1. Stagnation potential at Mach 5 (q=0.004 lb/ft3) = *350psi*
2. Stagnation pressure after a normal shock (1,000C default state) = *21psi*
3. Stagnation potential with liquefaction in the cryogenic zone = *230psi*
4. Stagnation pressure with isothermal compression at 23C (measured) = *75psi*
5. Stagnation pressure with isothermal compression at -120C (measured) = *80psi*
6. Stagnation pressure with isothermal compression at -140C (measured) = *85psi*
7. Stagnation pressure with isothermal compression at -150C (measured) = *90psi*
8. Stagnation pressure with isothermal compression at -170C (measured) = 9*5psi*
9. Stagnation pressure with isothermal compression at -180C (measured) = *110psi*
10. Stagnation pressure with isothermal compression at -195C (measured) = *200psi*

STAG	350	350	350	350	350	350	350	n/a
LQF	230	230	230	230	230	230	n/a	230
-195	200	200	200	200	200	200	150	30
-180	110	110	110	110	110	110	240	120
-170	95	95	95	95	95	95	255	135
-150	90	90	90	90	90	90	260	140
-140	85	85	85	85	85	85	265	145
-120	80	80	80	80	80	80	270	150
23	75	75	75	75	75	75	275	155
1000	20	20	20	20	20	20	330	n/a

17. STAGNATION VECTOR ANALYSIS (2)

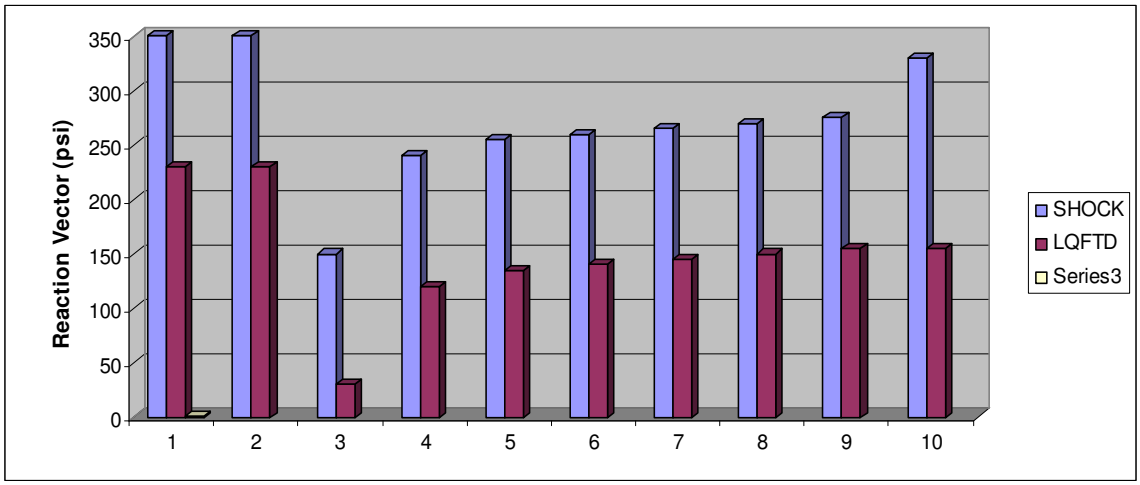

STAG	350	350	350	350	350	350	350	n/a
LQF	230	230	230	230	230	230	n/a	230
-195	200	200	200	200	200	200	150	30
-180	110	110	110	110	110	110	240	120
-170	95	95	95	95	95	95	255	135
-150	90	90	90	90	90	90	260	140
-140	85	85	85	85	85	85	265	145
-120	80	80	80	80	80	80	270	150
23	75	75	75	75	75	75	275	155
1000	20	20	20	20	20	20	330	n/a

18. THERMAL RESPONSE (RECORDED) (HQ23/M6)

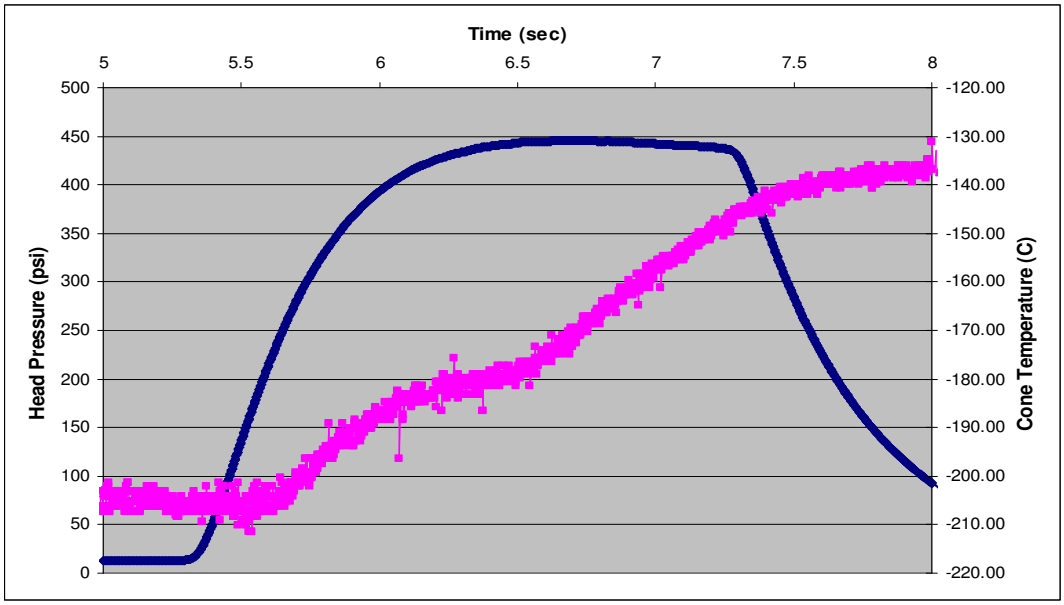

19. ISOTHERMAL SURGING (RECORDED)

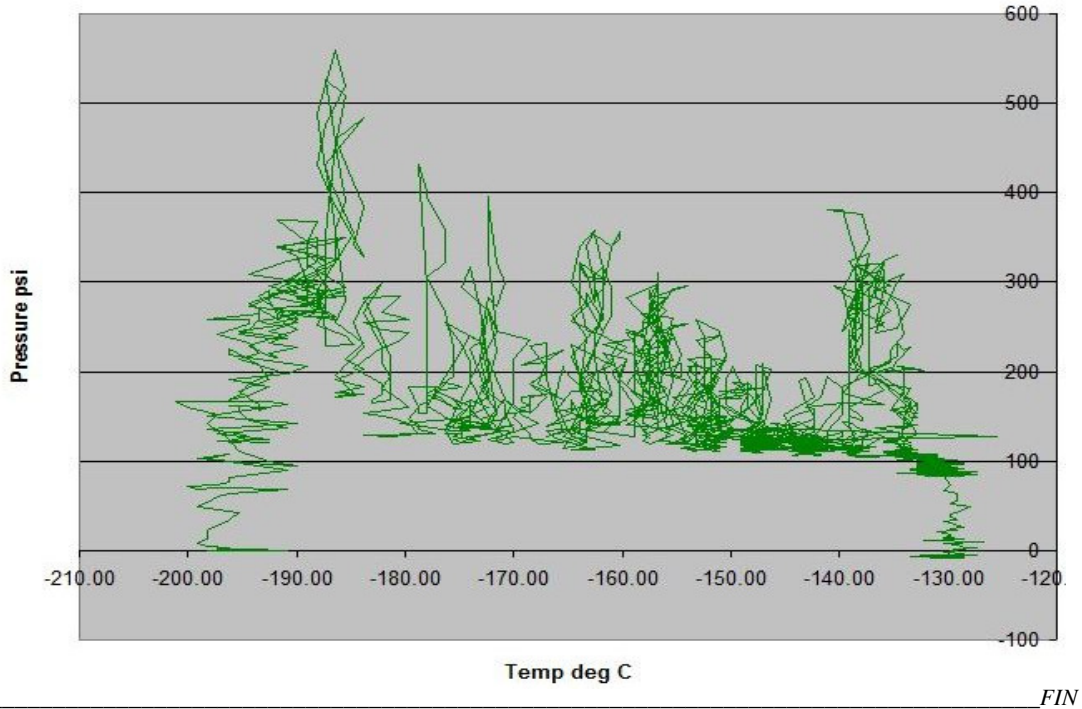

FIN

Experimental study on flow patterns and heat transfer characteristics during cryogenic chilldown in a vertical pipe

Hong Hu[1], J. N. Chung[1], and Sam Amber[2]

[1]Department of Mechanical and Aerospace Engineering, University of Florida
[2]Department of Physics and Nuclear Engineering, U.S. Military Academy

Abstract

In the present paper, we report the experimental results for a chilldown process that is involved with the unsteady two-phase vapor-liquid flow and intense boiling heat transfer of the cryogenic fluid coupled with the transient heat conduction inside pipe walls. The objective for the present study is to compare the chilldown rates and flow patterns between the upward flow and downward flow in a vertical pipe. Liquid nitrogen is employed as the working fluid and the test section is a vertical segment of Pyrex glass pipe with inner diameter of 8mm. The effects of mass flow rate on flow patterns, heat transfer characteristics and interface movement can be determined through experiments performed under several different mass flow rates. Through visualization, measurement and analysis on the flow patterns and temperatures, a physical explanation of vertical chilldown is given. By observing and analyzing these changes, it is concluded that chilldown in a vertical flow is similar to that in microgravity to some extent.

Key words: cryogenics, quenching, flow boiling, heat transfer

Nomenclature

q	Heat flux(W/m^2)
G	Mass flow rate(kg/m^2s)
T	Temperature(K)
h	Heat transfer coefficient(W/m^2K)
k	Thermal conductivity(mW/mK)
d	Tube diameter(mm)
P	Pressure(kPa）
L	Latent heat(kJ/kg)
c	Specific heat(J/kgK)
r	Tube radius(mm)
t	Time(s)

Greek symbols

α	Thermal diffusivity(m^2/s)
ρ	Density(kg/m^3)
σ	Surface tension(mN/m)
μ	Viscosity(Ns/m^2)

Subscripts

o	Outer wall
l	Liquid
sat	saturated
i	Inner wall
sub	Subcooling
w	Tube wall
v	vapor
rew	Rewetting

1. Introduction

Cryogenic fluids are involved in power and propulsion, life support, and thermal management aboard a spacecraft. Moreover, cryogenic propellants, such as liquid hydrogen, liquid oxygen and liquid helium, and their management on orbit are an area of important space technology that will be common to all future space missions [1]. In many of these applications the cryogenic fluid is initially introduced into piping systems that are in excess of 200K that is higher than the boiling point, which leads to intense evaporation of the fluid and significant temperature and heat flux fluctuations. This process is known as the line chilldown.

The chilldown process is the inevitable initial stage during cryogenic fluid transport. Due to their low boiling points, boiling and two-phase flows are encountered in most of the cryogenic operations. The complexity of the problem results from the intricate interaction of the fluid dynamics and heat transfer, especially when phase-change and flow pattern evolution are taken into consideration. The phenomenon of chilldown is of interest since it directly impacts the design of transport systems for the cryogenics as well as the whole applications. The flow pattern development and heat transfer characteristics of the chilldown process are not well understood even under earth gravity.

This experiment investigates the vertical pipe chilldown process in terrestrial condition. The analysis based on the data collected will be given on the heat transfer aspects and flow pattern development during the chilldown process.

1.1. flow regimes of boiling and chilldown

There has been a large amount of research on the boiling of normal fluid such as water, FC-72 and R-113. However, with respect to special physical property and wide use of cryogenics, the flow boiling experiments on cryogenics have gradually receives more attention in recent years.

By experimental research on vertically upward 0.5 and 1.0 mm microtones, Zhang et al[2] has have studied the flow patterns in vertical micro tubes and five different flow patterns have been observed respectively, when heat flux increased. In order to catch and analyze the bubble dynamic and flow pattern evolution during flow boiling in a mini tube more carefully, a 3-D visualization method [3] have been developed especially for mini and micro tubes. X.Fu et al [4] found that the tube size effect on the flow boiling mainly lies in the flow patterns evolution following the bubble departure. Mass flow rate and heat flux were found to be two major factors affecting the bubble departure from the nucleation site.

From the typical boiling curve, the path of the chilldown defers significantly from that observed for boiling due to the completely reverse processes. The differences between

two conditions may arise in the transition boiling regime and at the transition between nucleate coiling and natural convection, which causes the change both on flow patterns as well as the heat transfer characteristic.

Subcooled water has been used as working fluid for chilldown test by Y. Barnea et al [5]. They have studied the quenching front movement and the volumetric void fraction as a function of distance from the quench front. With respect to the research of Osamu Kawanami et al [6], a unique flow pattern, called filamentary flow was observed only under downward flow in large tube diameter with high mass flow velocity. This kind of flow used to be seen only in microgravity condition. They also pointed out that the gravity effects on heat transfer of forced convective boiling decrease with an increase in the mass velocity.

1.2. Effect of gravity and flow direction on chilldown

Chilldown has relationship not only on mass flow rate, wall temperature, liquid subcooling, but the gravity and orientation of the tube also have large effects on the flow pattern and corresponding heat transfer characteristic. Experiments have done on parabolic flight and drop tower worldwide in past several decades and both horizontal and vertical pipes are used. Quenching of a horizontal hot stainless steel tube by injection of R-113 was investigated by C.J.Westbye et al [7]. The same tests were conducted both under normal gravity condition as well as microgravity condition. They concluded that heat transfer coefficient in microgravity ere only 20-50% of the value obtained in normal gravity and rewetting temperature were also found to be 15K-20K lower in microgravity.

Comparing to the horizontal flow, it is believed that chilldown in vertical pipe is less affected by gravity and easier to capture the movement of quenching front than in the horizontal pipe. Brian Verthier et al [8] have carried out some experiments on vertical quenching process with use of FC-72 and pointed out that microgravity flow pattern is closer to upward vertical flow pattern in 1-g than down flow, due to the rising of vapor bubbles. Also some experiments on FC-72 were conducted by G.P. Celata et al [9] during parabolic flight. They stated that mass flow-rate has a significant influence on the structure and the behavior of the liquid core during the inverted annular flow regime.

Because of the difficulties in designing and conducting the experiments, there are limited chilldown data for cryogenics fluid compared to normal fluid. Liquid nitrogen was used as a working fluid in tests of Osamu Kawanami et al [21] to investigate the heat transfer characteristics and flow pattern during the quenching of a vertical tube. The tests were finished at both terrestrial condition and 10s microgravity condition with the help of drop tower in Japan Microgravity Center (JAMIC). They claimed that the heat transfer and quenching front velocity under microgravity condition increase up to 20% compared to normal gravity condition.

Furthermore, Kun et al [10] have done a series of profound job on the cryogenics chilldown in horizontal pipe in both microgravity and terrestrial conditions using a drop tower. According to their research, as the temperature decreases, the liquid droplets tended to form filaments and settled down on the bottom of the test section in terrestrial gravity condition. At this time, heat transfer characteristic at upper part and bottom were totally different because gravity effect leaded to the separation of vapor and liquid. While in drop tower test, a lower heat transfer rate was observed due to vapor film sounding the liquid core which flow in the center of the pipe.

With the goal of improving the knowledge of chilldown process of the cryogenics in the tubes, the present paper is mainly focus on the heat transfer characteristic based on the experimental data at normal gravity in vertical pipes. The effect of the gravity is analyzed though a comparison between upward and downward flow. The research also aims to clarify the effect of mass flow rate and flow orientation during the chilldown in terrestrial gravity.

2. Experiment

2.1 Experimental apparatus

For the safety consideration, liquid nitrogen is selected as the test fluid in the present study, and in addition, liquid nitrogen is a suitable model fluid because its surface tension, boiling point and evaporative latent heat are similar to liquid hydrogen and liquid oxygen The initial temperature of the test section was kept at the normal room temperature.

Table 1.
Principle physical properties of liquid nitrogen (77.35K) [11]

P	101.3
T_{sat}	77.35
ρ_l	807.10
ρ_v	4.621
L	198.38
μ_l	163
μ_v	5.41
σ	8.85

The test apparatus, as Fig 1 shows is meanly constructed from 80/20 and the major components include a pressurized liquid nitrogen tank (Airgas 180Lts 22PSI), the stainless steel tube casing (MDC), thermocouples and DAQ (Measurement Computing PCI-DAS-TC), mass flow rate meter (Sensirion EM1) a vacuum pump and a high speed camera (Redlake MotionScope PCI 8000s).

In Fig 1, the liquid nitrogen is driven to flow through a valve into a transparent tube

housed inside a stainless steel shell. The shell will be kept a vacuum environment to insulate the tube. There are two glass ports in the shell for the high speed camera and background light. Here high speed camera will catch the video of chilldown and flow pattern change. The tubing will then vent gas phase nitrogen out of the venting port. After that, the two phase flow will enter a heat exchanger to fully evaporate, at the end of which a mass flow rate meter will be placed to measure the gas flow rate.

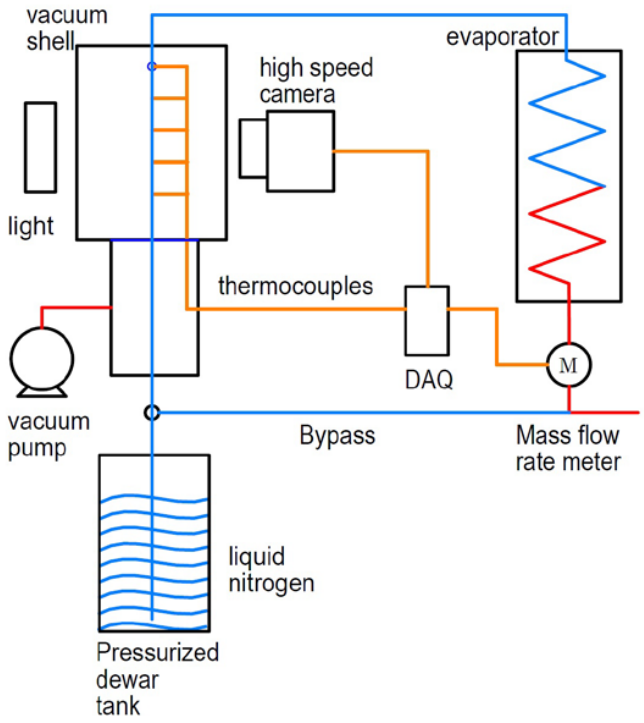

Fig1. Schematic of the experimental apparatus

One of the most important issues in the experiment is the total time required for chilldown as well as the temperature and heat flux profiles. Therefore, the test will employ several different mass flow rates to quench a Pyrex tube initially at room temperature with a certain length and diameter. The change of temperature of the tube will be acquired through 15 T-type thermal couples. They are glued to the external surface tube with special epoxy resin. The thermocouples are located at five different sections with interval of 20mm, as Fig 2 shows. At each cross-section, three thermocouples are located circumferentially at equal separation distance.

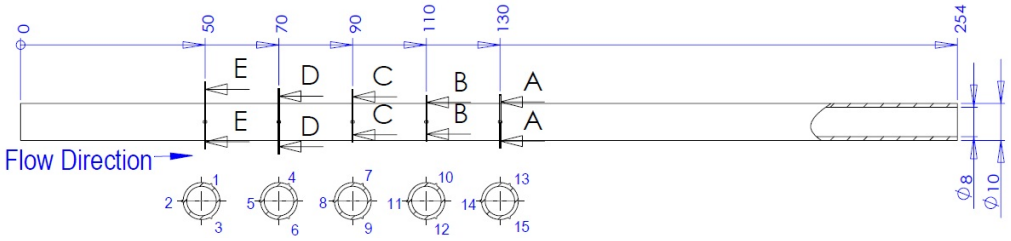

Fig 2. locations of thermocouples

3 Uncertainty Analyses

In current experiments, the inverse heat conduction problem needs to be solved in order to get the surface heat flux from temperature measurements introduced by Ozisik et al [12,13]. Both the uncertainty from experimental apparatus and from parameters derived from equations will be given.

The type T thermocouples used for temperature measurement have the uncertainty of ± 0.50K declared by the manufacturer. In order to get quick response for highly transient process like chilldown, the wire diameter is set for 0.25 mm. The responding time is less than 0.2 second at this condition according to the datasheet from the manufacturer.

Another uncertainty source of temperature measurement comes from the data acquisition (DAQ) system. The accuracy of the measurement depends on the gain, the sample rate and the thermocouple type. For current experiment, the gain is set at 400 the sample rate is about 60 Hz and type T thermocouples are used. It is found that the uncertainty for current settings is about ±0.30K.

The mass flow rate is measured by gas flow meter which combines a sensor element with the amplification and A/D converter circuit on one single CMOS chip as well as an integrated temperature sensor. When flow range is set to 0-200L/min, the sensor return a value with 0.05% accuracy and 0.02% repeatability of full scale, 5% accuracy and 0.5% repeatability of full scale of measured value due to offset, non-linearity, hysteresis. The vacuum level is measured by a vacuum gauge that has the minimum scale of 0.02 bars, so the uncertainty of the vacuum level is approximately 0.01 bars.

Table 2.
Summary of the uncertainty

Parameter measured	uncertainty
D (mm)	0.001
T_o (K)	0.8
G (%)	0.5
Vacuum level (bar)	0.01
Parameter derived	uncertainty
T_i (K)	0.8
q_i (%)	6.8
h_i (%)	6.8

4. Result and discussion

The chilldown process is a transit process which involves complicated flow pattern

development, rapid temperature and dramatic heat flux change. This paper will present detailed analysis on these aspects. The test was carried out with reference to thermal hydraulic conditions as reported in the following table

Table 3.
The range of the main experimental parameters

D	8.00
G	20-80
T_{sub}	0
T_w	293
Flow orientation	Upward, downward
P	101.3

4.1 Heat transfer characteristic

Heat transfer characteristic analysis is the mean part of the research and includes various kinds of thermal parameter. In this research, the temperature profile and heat flux change are two highlights. Temperature changing with time indicates an intuitive view on how liquid nitrogen quenches the tube and how fast the tube is cooled. The careful analysis on heat flux and temperature will help to determine the heat transfer mechanisms during the chilldown process and serves for the comparison between chilldown of different directions.

When at high mass flow rate and subcooling, as showed in middle images in Fig 3, two different flow patterns, inverted annular flow and bubbly flow have been observed during the chilldown tests. This sequence of flow patterns was observed by Kawaji et al. [14]. Inverted annular flow occurs at the beginning of the chilldown test when the wall temperature is higher than the rewetting temperature. Bubbly flow will be seen when the wall is cooled down to rewetting temperature and the liquid has a direct contact with the wall, which leads to the bubble nucleation. On the other hands, Kawaji et al [14] has also recorded flow patterns for saturated flow at low mass flow rate, as the right images in Fig 3 shows. They claimed that this flow pattern is typical for cryogenic liquid.

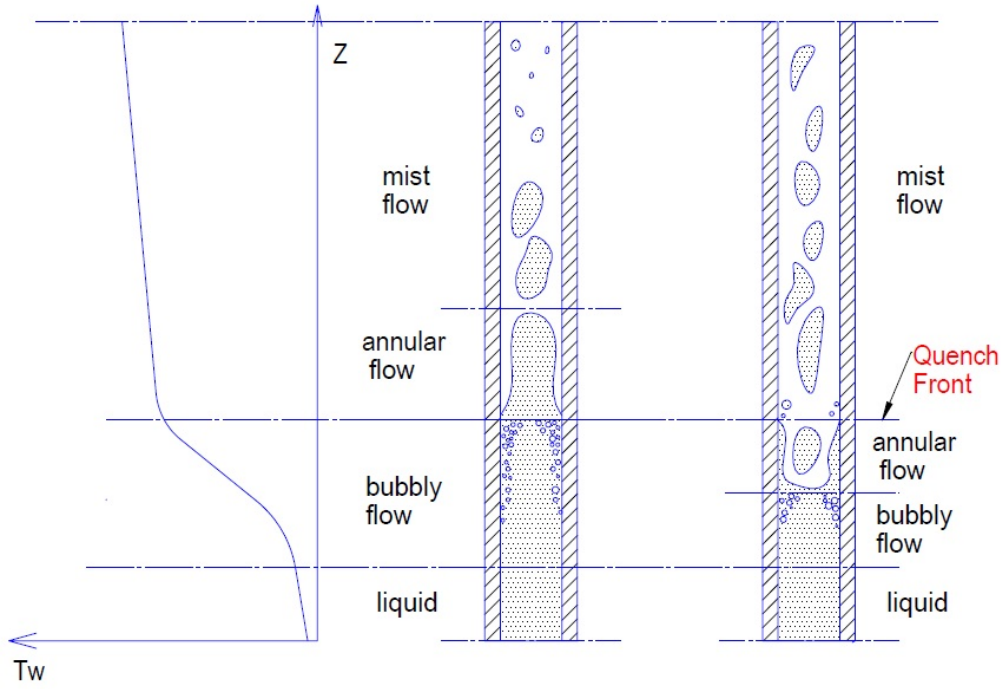

Fig 3. Heat transfer regimes and flow patterns during quenching in a vertical pipe

Because all of the thermocouples are placed at the outside surface, the inner wall temperature needs to be derived from the temperature acquired. Burggraf [15] developed a method to obtain the temperatures and heat fluxes at the inside tube wall from the temperature history data of the thermocouple welded on the outside of the test section:

$$T_i = T_o + (\frac{r_0^2}{4\alpha}((\frac{r_i}{r_0})2 - 1 - 2\ln(\frac{r_i}{r_0}))\frac{dT_o}{dt}$$
$$+(\frac{1}{64\alpha^2}(r_i^5 - 5r_0^4) - \frac{r_0^2 r_i^2}{8\alpha^2}\ln(\frac{r_i}{r_0}) - \frac{r_0^4}{16\alpha^2}\ln(\frac{r^i}{r_0}) + \frac{r_0^2 r_i^2}{16\alpha^2})\frac{d^2T_o}{dt^2} \quad (1)$$
$$+\cdots$$

This method has been used by Kun et al [10] to acquire the inner wall temperature

The temperature profiles measured from the embedded thermocouples at five different cross-sections with different mass fluxes are showed in the following figures, Fig 4 to Fig 6, to evaluate the how temperature changes.

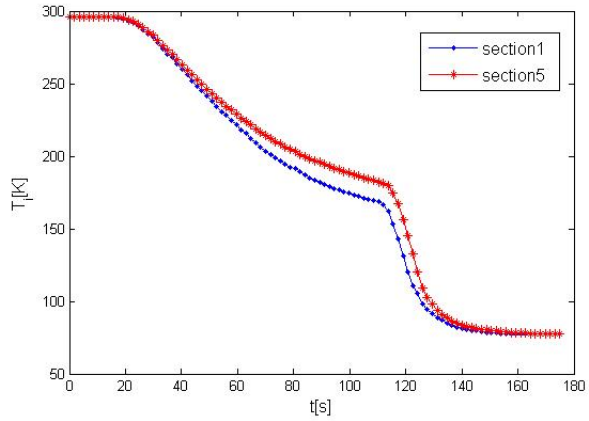

Fig 4. Typical wall temperature profile upward flow for G=66kg/m^{2}s

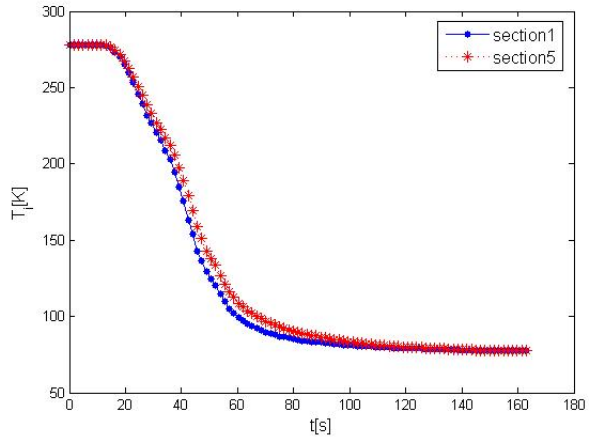

Fig 5. Typical wall temperature profile downward flow for G=66kg/m^{2}s

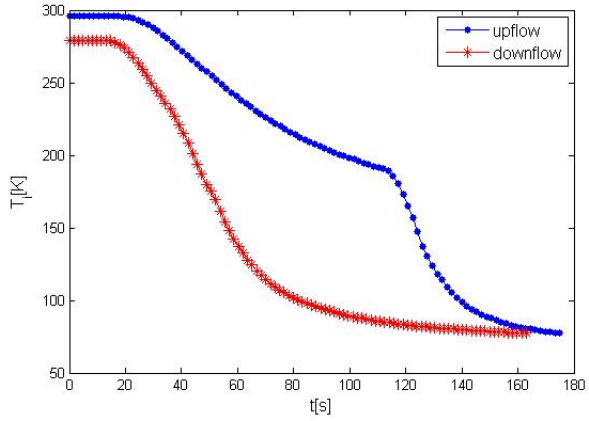

Fig 6. Comparison of upward and downward flow for G=66kg/m^{2}s

The entire temperature profile has been divided into two segments. One occurs at the beginning and the other appears after the mid-point. The big temperature gradient between liquid and wall drives a rapid evaporation, which attributes to the first period of decrease. For the second large drop in temperature is due to the direct contact

between liquid and wall when achieving the rewetting temperature. It can be seen from Fig 6 that for the downward flow, there is no appreciable film boiling regime and the quench front arrives at this downstream much faster than upward flow. Compared to the data C.J.Westbye et al [7] got, the downward flow performs like normal gravity horizontal pipe, while the curve for upward flow is similar to that for microgravity condition.

After the inner wall temperature is acquired, then the inside wall heat flux with the first three leading terms can be written as [10]:

$$q_w" = \rho c(\frac{r_i^2 - r_0^2}{2r_i})\frac{dT_o}{dt} + (\frac{(\rho c)^2}{k}(\frac{r_i^3}{16} - \frac{r_0^4}{16r_i} - \frac{r_0^2 r_i}{4}\ln(\frac{r_i}{r_0})))\frac{d^2T_o}{dt^2}$$
$$+\frac{(\rho c)^3}{k^2}(\frac{r_i^5}{384} - \frac{3r_0^4 r_i}{128} + \frac{3r_0^2 r_i^3}{128} - \frac{r_0^6}{384r_i} - \frac{r_0^2 r_i^3}{32}\ln(\frac{r_i}{r_0}) - \frac{r_0^4 r_i}{32}\ln(\frac{r_i}{r_0}))\frac{d^3T_o}{dt^3} \quad (2)$$

For vertical chilldown experiment, the axial-symmetrical assumption can be employed. Therefore, we can get the diagram with heat flux and temperature as well as with heat flux and time.

After the heat flux is calculated, heat transfer coefficient h_w at the inner wall of the tube are given by

$$q_w = -k\frac{\partial T}{\partial r} \quad (3)$$

$$h_w = \frac{q_w}{T_w - T_i} \quad (4)$$

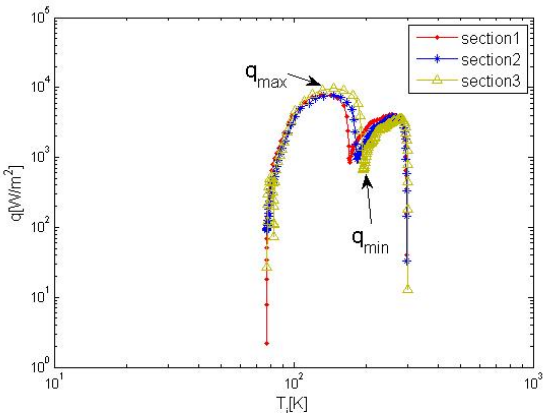

Fig 7. Typical wall heat flux profile upward flow for G=66kg/m^{2}s

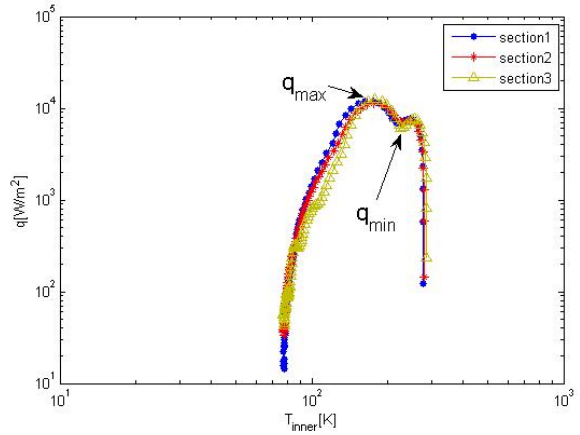

Fig 8. Typical wall heat flux profile downward flow for G=66kg/m^{2}s

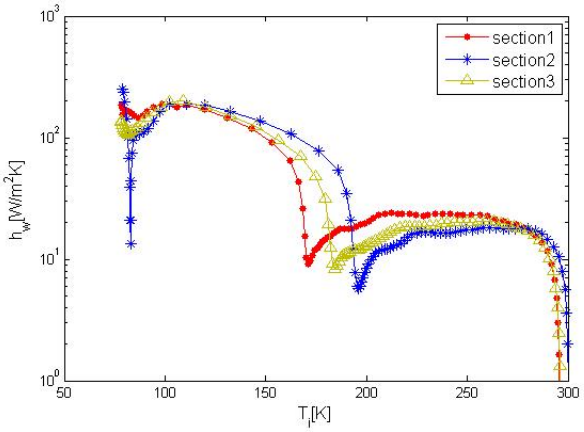

Fig 9. Typical wall heat transfer coefficient profile upward flow for G=66kg/m^{2}s

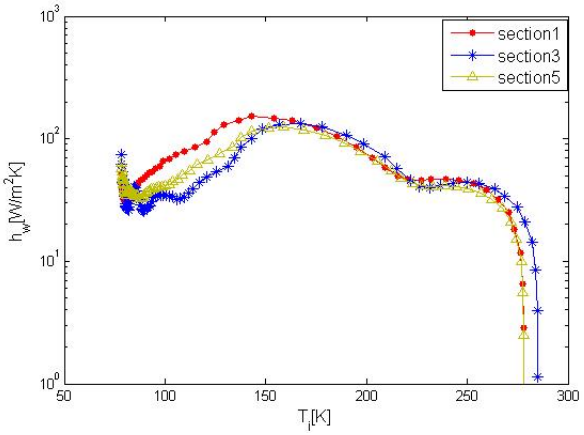

Fig 10. Typical wall heat transfer coefficient profile downward flow for G=66kg/m^{2}s

Regarding to the heat flux profiles, showed in Fig 7 and Fig 8, two peaks are found in each of the graph. Similarly, regarding to the heat transfer coefficient profile in Fig 9 and Fig 10, there are also two peaks during the whole chilldown process and the second one is larger than the first one. The first one represents the maximum heat flux

for film boiling, which appears at the beginning of the chilldown. Film boiling will be the mean heat transfer mechanism of this regime due to the large temperature difference between the wall the inlet liquid. Although the heat transfer coefficient is not high enough, yet the temperature difference will still lead a high heat flux, the same order as the second one. The second one is the critical heat flux, which is a sign of the change of boiling mechanism, from transition boiling to nucleation boiling. It is caused by quenching front movement, where liquid has direct contact with the wall, rapid phase change involved. It is believed that heat transfer coefficient is much higher for the quenching front than that for film boiling, because the phase change is involved at near the quenching front.

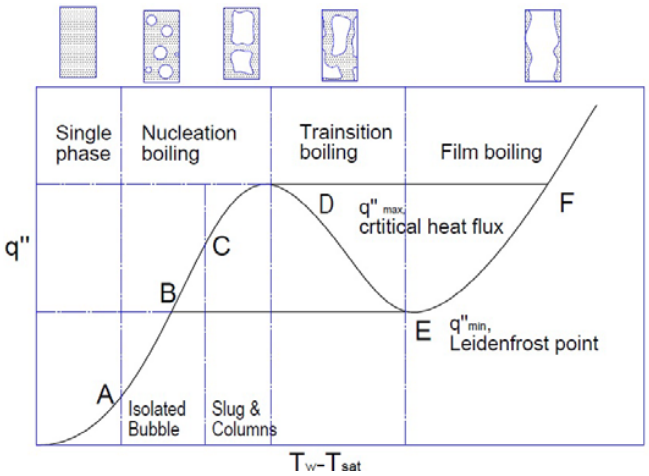

Fig 11. Typical boiling curve and flow pattern

A boiling curve drawn Fig 11 shows the relationship between the heat flux that exchange between wall and the fluid and the wall temperature clearly. As the Fig 12, the shape of the heat flux is similar to the boiling curve from the steady state pool boiling experiment. q_{min} and q_{max} can be used to divide the different regime of boiling. A cryogenic chilldown process usually starts from point F and then goes towards point E in the film boiling regime as the wall temperature decreases. Point E is usually called the Leidenfrost point which signifies the minimum wall temperature required for the film boiling. When cooling beyond the Leidenfrost point, the boiling process will proceed from E to D in the transition boiling regime, which is characterized by a decrease of temperature with an increasing heat flux. Quench front will be observed at D in the experiments. After passing the q_{max}, the CHF point, the heat transfer mechanism then changes to nucleate boiling with decrease both in heat flux and temperature.

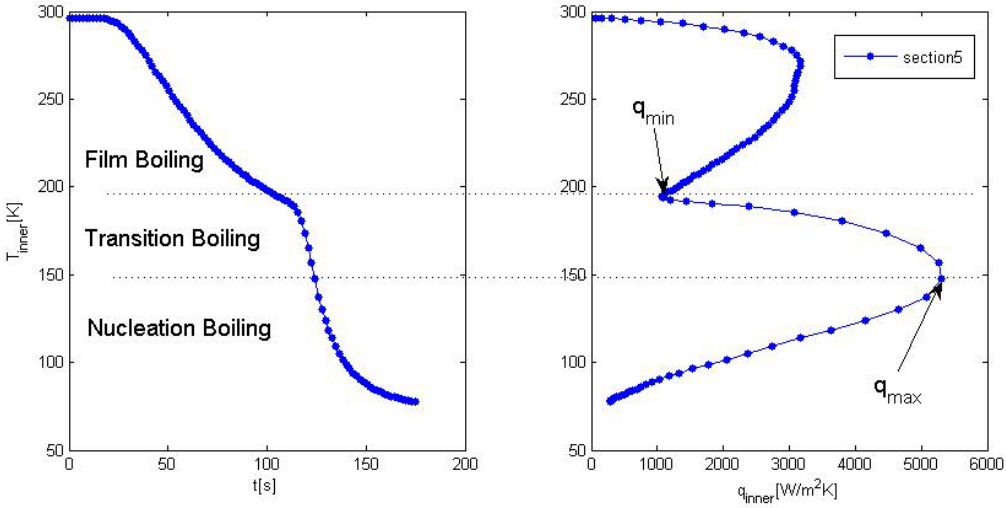

Fig 12. Typical temperature and heat flux profile for upward flow for G=66kg/m^{2}s

The orientation of the flow, the effect of gravity, not only has effect on the total time for chilldown, but the heat flux profile, critical heat flux and the heat transfer coefficient are all effected by the orientation of the flow.

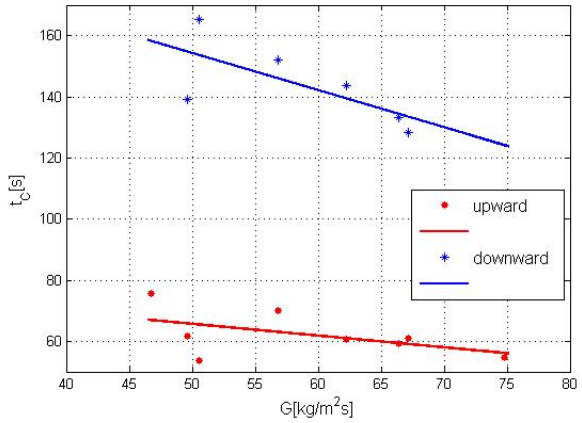

Fig 13. Variation of the total chilldown time with mass flow rate

As Fig 13 shows, longer time is needed for the flow to change at the same mass flow rate in downward flow naturally. It is also obvious that with the increase of the liquid mass flow rate, the difference in chilldown time is reduced.

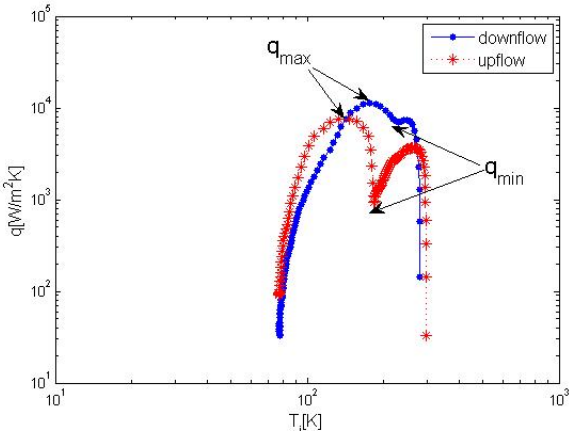

Fig 14. Comparison of heat flux between upward and downward flow for G=66kg/m^{2}s

From the Fig 14, the heat flux profiles for both orientations are of the same order. The mean difference between the profiles lies at that downward flow has lower rewetting temperature. Although the heat flux values have a greater uncertainty compared to temperature values, the heat flux profiles for nucleate boiling regime obtained for upward and downward are similar, showing that this regime is probably not affected by the orientation.

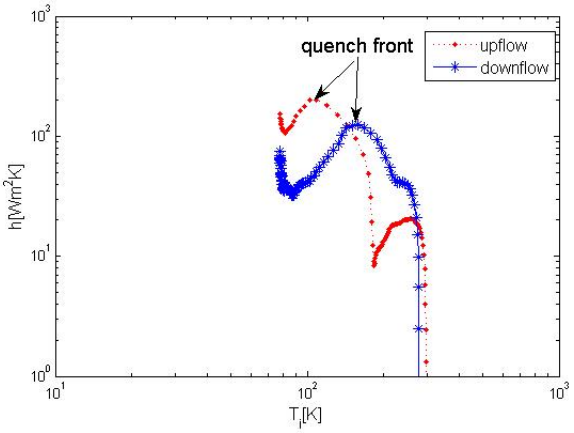

Fig 15. Comparison of heat transfer coefficient between upward and downward flow for G=66kg/m^{2}s

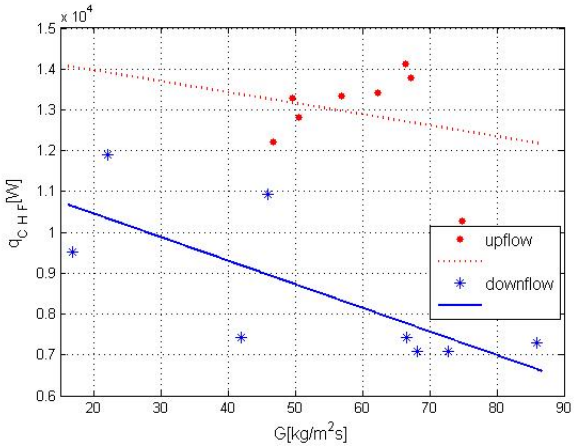

Fig 16. Variation of the critical heat flux with mass flow rate

The well-known Zuber's model for saturated pool boiling:

$$q = 0.131\rho_v L[\frac{\sigma(\rho_l - \rho_v)g}{\rho_v^{\ 2}}]^{\frac{1}{4}} \tag{5}$$

For the current experimental condition, this correlation gives a critical heat flux of 161.23kW/m^2. However, the experiment data showed in Fig 16 are far less than this value. Upward flow takes approximation 8.75% and downward takes only 6.22%.The reason for a large error partially comes from the different boiling mechanisms between chilldown and pool boiling. For the pool boiling, the heater is maintained either at constant temperature or constant heat flux. However, for the chilldown test, the energy for boiling is provided by the energy initially stored in the tubes. This means that the neither heat flux nor temperature is constant. Moreover, the boiling correlation should have some kind of relation with the tube physical property. Actually, Zuber's model only concerned with the property of fluid and vapor, which also leads to error. At low mass flow rate, CHF values for downward flow are much smaller than for upward flow. As H.Zhang et al [16] stated that CHF is very sensitive to orientation for low mass flow rate and orientation. They came to the same conclusion that the low velocity, neat-saturated data are under predicted by the Zuber's model.

It is believed that a slower speed leads to a more even temperature distribution across the section area, which means a more efficient heat transfer. Therefore critical heat flux and heat transfer coefficient are larger for up flow than for down flow. The flow accelerates in the downward flow rather than decelerates in the upward flow due to the gravity. The difference between the upward and downward flow will decrease with the increase of the mass flow rate because the acceleration and deceleration due to the gravity effect will take less and less portion of the flow velocity. Therefore, the flow velocity will become more constant along the whole tube when mass flow rate increases. It can be predicted that the effect of mass flow rate will gradually overcome that of orientation, effect of gravity when mass flow rate increases and the chilldown time will achieve the same both for upward and downward flow when mass flow rate is large enough.

4.2 Flow pattern transition

The flow pattern development is showed in Fig 17. When under present experiment condition, at the first pure gas will fill the whole tube because liquid all turned to vapor in a short time. Following this, a dispersed flow comprised of liquid drops embedded in the vapor will be observed. With further temperature decreasing, the small droplets become dense and coalesce to form a continuous liquid droplet core flowing in the center of the tube and it is generally surrounded by a thin layer of vapor film which traveled along the tube wall in this pattern. This phenomenon is called annular flow. At this time, the film is thick enough to isolate the wall and liquid core efficiently. With the decrease of the wall temperature, the vapor film becomes thinner while the liquid core will occupy more area. The vapor-liquid interface is a bit of wavy because of Kelvin-Helmholtz instability due to the big velocity (momentum) gradient at the interface. When the wall temperature is reduced to the rewetting temperature, the liquid is able to come into a direct contact with the channel walls. A rapid transition from annular flow to disperse bubbly flow will occur after the quenching front. Transient boiling, characterized by intermittent liquid-wall contact and violent bubble generation, is observed during this limited period. At this time the heat transfer rate from the hot wall to the liquid is significantly increased and a rapid variation of the wall temperature slope can be observed. The prevailing boiling regime is nucleate boiling and the flow pattern is stratified flow.

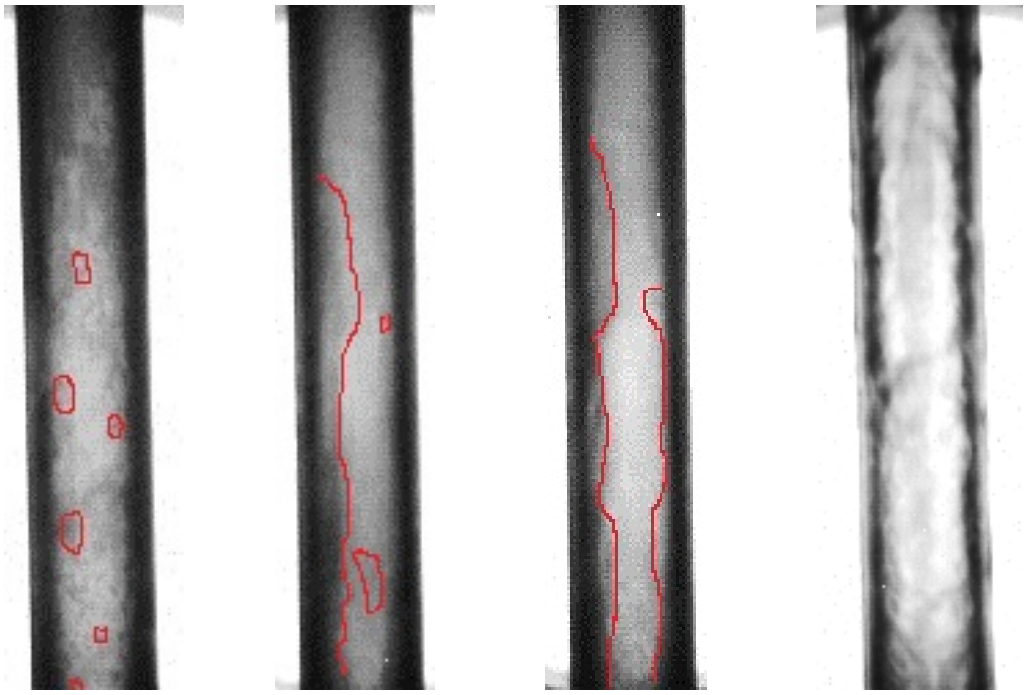

(A) Bubbly (B) transition (C) liquid

Fig 17. Flow pattern development for upward flow G=45kg/m2s,T_w=290K

According to V.P. Carey [11], the stability of a vapor – liquid interface depends on the relative velocity between the two phases and is also linked to the gravity acceleration

and to the fluid parameters such as surface tension and density of the two phases. Gravity and small values of the relative velocity of the two phases, stabilize the vapor – liquid interface. Therefore, when the liquid velocity is too small and the vapor – liquid relative velocity is high, the interface is quite unstable and the liquid core is irregular during the quench phenomenon. On the contrary, when the liquid flow-rate is high enough, and the relative velocity between the two phases is small, the interface is stable and the liquid core is characterized by a regular shape.

Based on the vertical quenching tests done both at ground and in parabolic flight using FC-72, G.P. Celata et al [9] have come across similar conclusion that for low mass flow-rates, the liquid core is irregular and continuously formed and disrupted during the cooling process, while for higher mass flow-rates the liquid core is more stable and regular.

A unique flow pattern, filaments flow, which used to be found in microgravity condition by Anter et al, was formed even in the terrestrial condition experiment by Kawanami et al [6]. This flow pattern appears under only downward flow, large tube diameter and high mass velocity conditions. From this point, it is stated that the flow velocity played an important role to the formation of this flow pattern and effect of gravity can be omitted under this condition.

4.3 Quenching front characteristic

Quenching front velocity is also a topic of this research, because quenching front velocity is concerned with the rewetting time and therefore the total time required for chilldown. Although, it is different to get clear photographs for cryogenic because of the moisture caused by strong boiling the liquid nitrogen, the movement of the quench front movement obtained though visualization is showed in Fig 18. Some researchers [21] believed that quenching front has some kinds of relationship with the mass flow rate and tube diameter. This study will connect the quench front movement with mass flow rate and flow orientations.

The extreme portion of the surface rewetted by the coolant is called quench front. The quenching front velocity indicates the speed at which the quench front moves from the inlet along the hot tube, and is the responsible of the time required for the rewetting of the whole tube.

There have been a lot of different definitions used on define the quenching front by different researchers. Celata et al [] Westbye et al [7] and Chen et al [17] prefer to use the rewetting temperature T_{rew} to define the apparent rewetting temperature obtained by drawing the tangents on the transient temperature curves in the regions where the significant change of the curve slope occurs, as schematically drawn as the following figure shows. T_{rew} marks the onset of a rapid surface cooling caused by an enhanced rate of heat transfer that does not necessitate liquid-solid contact. Some researchers [5]

have pointed out the rewetting temperature the temperature at which a triple interface, gas-liquid-solid is formed.

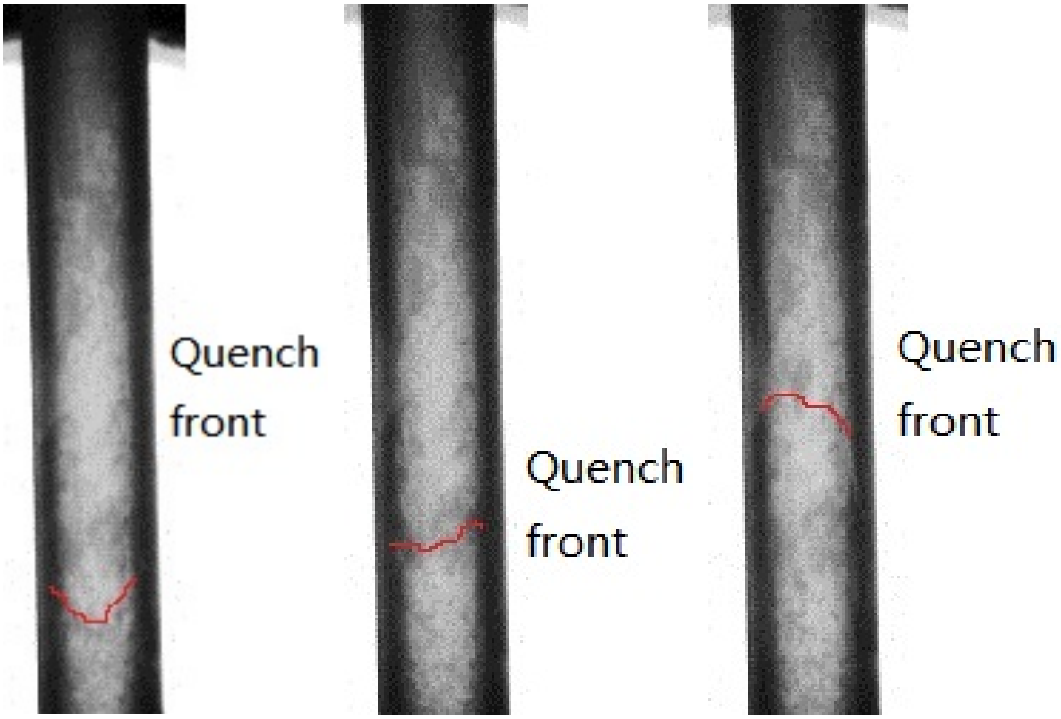

Frame 198 **Frame 208** **Frame 214**

Fig 18. Three single frames showing moving movement of upward flow, G=45kg/m^{2}s

According to the current experiment, the tangent on the transient temperature curves is used to define the quench front. The quenching front in vertical pipeline should be nearly proportional to the wall surface, which is very similar to that in the microgravity condition. However, the interface instability will cause wavy for the quench front formation at low mass flow rate, like current experiment.

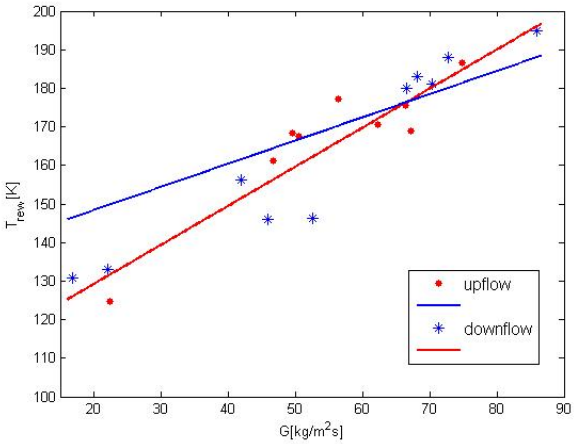

Fig 19. Variation of the rewetting temperature with mass flow rate

The rewetting temperature is observed to increase with increase mass flow rate under both conditions. From the Fig 19, it is also apparent than rewetting temperature

increases more rapidly with the mass flow rate in downward flow as compared to upward flow. According to Chan's model [18] and Westbye's analysis [7] on horizontal pipe, rewetting temperature has a close relationship between Kelvin-Helmholtz type instability. When the vapor film thickness increases, the rewetting temperature will decrease. This explains the reason for a reduction in rewetting temperature in relatively low mass flow rate region for downward flow. However, when mass flow rate is high enough, the film thickness is determined by mass flow rate to a large extent. A larger mass flow rate will push the film thinner and push it closer to the wall. For the downward flow, the flow velocity is higher. Therefore, it is reasonable that the rewetting temperature is higher for downward flow than that for upward flow in large mass flow rate.

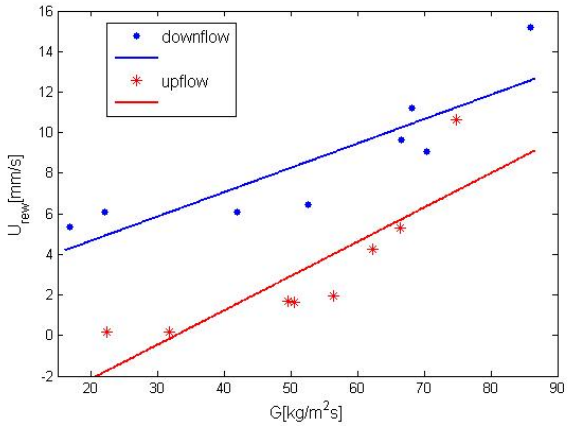

Fig 20. Variation of the quenching front velocity with mass flow rate

Quenching front velocity concerns with many factors. Some researchers [19]have pointed out that the heat transfer coefficient increases with sub-cooling which can partially explain the higher quench front velocities measured for higher flow rates and inlet sub-cooling. For current test, the inlet fluid is maintained at saturated temperature. Therefore, mass flow rate will become the mean factor. K. Adham-Khodaparast et al [20] have come to the similar conclusion on rewetting temperature using R-113. Celata et al [9] have carried out experiments on parabolic flight experiments with FC-72 quenching the 6mm tube. They conclude that the quench front is strongly affected by the mass flow-rate. With the similar experiments performed in vertical pipe in normal gravity condition, they stated that downward flow tests show rewetting velocity values always greater than corresponding upward flow tests. Kawanami et al [21] pointed out that the gravity force affects the quench front velocity under 1-g and thus the quench front velocity under 1-g becomes smaller than that under l-g. Based on explanations given by. Westbye et al [7], it is reasonable to state that under downward flow, pipe is chilled down significantly before the quench front appears as Fig 6 Shows. According to the Fig 20, once the quench front occurs, it can propagate quickly because the wall temperature is low enough to establish liquid-wall contact immediately.

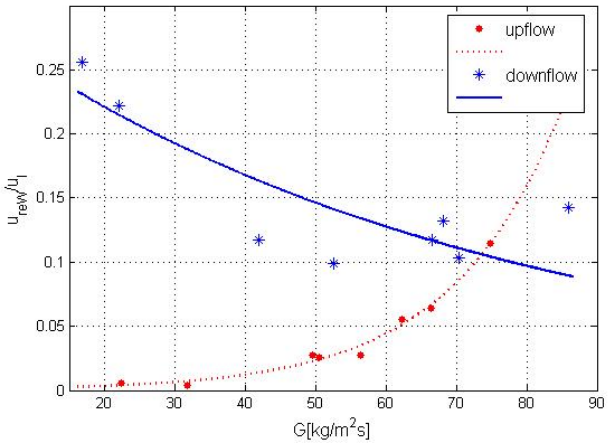

Fig 21. Dimensionless velocity with mass flow rate

Kawanami et al [21] introduced the dimensionless velocity u_{rew}/u_l to evaluate the relationship between quench front and inlet liquid velocity. From the Fig 21 based on the current experiment, it can be concluded that the dimensionless velocity for upward flow increases with the increasing of liquid velocity, while for the downward flow, dimensionless velocity is decreasing. It is also reasonable to predict that this dimensionless velocity will maintain a relatively constant value when mass flow rate is large enough.

5. Conclusion

In this paper, heat transfer during a vertical pipe chilldown process is studied. The test tube is made of Pyrex with inner diameter of 8.0mm. The tests are carried out using liquid nitrogen under terrestrial gravity. Measurements include temperatures along the pipe and mass flow rates. The results show that both mass flow rate and tube orientation affect the heat transfer characteristics.

(1). Mass flow rate has a large effect on the rewetting temperature, critical heat flux and quench front movement. Rewetting temperature and quench front movement increase with increasing mass flow rate, while critical heat flux decreases.

(2) Total chilldown time for downward flow is longer than the upward flow. Critical heat flux and heat transfer coefficient are larger for the upward flow than the downward flow. However, quench front movement velocity is smaller for the upward flow. Rewetting temperature does not show a relationship with the orientation.

It is concluded that the orientation only has some effects when the mass flow rate is low. The mass flow rate will have far larger influence than the orientation in terrestrial gravity under a high mass flow rate.

Reference

[1] Hasting, L.J., Tucker, S.P., Huggaker, C.F. CFM technology needs for future space transportation system, AIAA/NASA/OAI Conference on advanced SEI technology, AIAA 1991;91-3474

2 P. Zhang , X. Fu, Two-phase flow characteristics of liquid nitrogen in vertically upward 0.5 and 1.0 mm micro-tubes: Visualization studies, Cryogenics, 2009;49:565-575

3 X Fu, P Zhang1, H Hu, C J Huang, Y Huang and R Z Wang, J. Micromech. Microeng.2009;19:085005-085016

4 X. Fu, P. Zhang, C.J. Huang, R.Z. Wang, Bubble growth, departure and the following flow pattern evolution during flow boiling in a mini-tube, Int. J Heat Mass Transfer 2010;53:4819–4831

5 Y. Barnea, E. Ellas, I. Shai. Flow and heat transfer regimes during quenching of hot surface. Int. J Heat Mass Transfer. 1994;37:1441-1453

6 Osamu Kawanami, Teruo Nishida, Itsuro Honda, Yousuke Kawashima, Haruhiko Ohta. Flow and heat transfer on cryogenic flow boiling during tube quenching under upward and downward flow. 2nd International Topical Team Workshop on Two-phase system for ground and space applications, 2007, Oct 26-28,Kyoto, Japan

7 C.J. Westbye, M. Kawaji, B.N.Antar. Boiling heat transfer in the quenching of a hot tube under microgravity. J. Thermophys. Heat Transfer 1995;9:302-307

8 Brian Verthier, Gian Piero Celata, Giuseppe Zummo, Catherine Colin, Jérémy Follet. Effect of Gravity on Film Boiling Heat Transfer and Rewetting Temperature during Quenching. Microgravity Sci. Technol 2009;21:S185–191

9 G.P. Celata, M. Cumo, M. Gervasi, G. Zummoa. Quenching experiments inside 6.0 mm tube at reduced gravity. Int J Heat and Mass Transfer 2009;52:2807–2814

10 Kun Yuan, Yan Ji, J.N. Chung, Wei Shyy. Cryogenic Boiling and Two-Phase Flow during Pipe Chilldown in Earth and Reduced Gravity. J Low Temp Phys 2008;150: 101–122

11 Van P.Carey, Lquid vapor phase change phenomena. 1st ed, New York: Taylor&Francis;1992

12 Ozisik. M.N, Heat conduction.2nd Edition, New York: John Wiley and Sons;1993,

13 Ozisik, M.N and Orlande. H.R.B., Inverse Heat Transfer. New York: Taylor and Francis;2000

14 M. Kawaji, Y. S. Ng, S. Banerjee, G. Yadigaroglu, Reflooding With Steady and Oscillatory Injection: Part I—Flow Regimes, Void Fraction, and Heat Transfer, J. Heat Transfer 1985;107:670-679

15 Burggraf, O.R., An exact solution of inverse problem in heat condition theory and application. J. Heat Transfer 1964;86:373-382

16 H Zhang, I Mudawar, M M.Hasan, Experimental assessment of the effects of body force, surface tension force, and inertia on flow boiling CHF. Int. J Heat Mass Transfer 2002;45:4079-4095

17 W.J.Chen, Y.Lee, D.C.Groeneveld. Measurement of boiling curves during rewetting of a hot circular duct. Int. J Heat Mass Transfer1979;22:973-976

18A. M. C. Chan and S. Banerjee, Refilling and Rewetting of a Hot Horizontal Tube: Part I—Experiments, J. Heat Transfer 1981;103:281-287

19 P. Chambri, E. Elias, Boiling Heat Transfer During Rewetting, Nucl. Eng. Des. 1978;50:353-363

20 K. Adham-Khodaparast, J. J. Xu and M. Kawaji, Flow film boiling collapse and surface rewetting in normal and reduced gravity conditions, Int. J. Hear Mass Transfer.

1995;38:2749-2760
21 Osamu Kawanami, Hisao Azuma, Haruhiko Ohta. Effect of gravity on cryogenic boiling heat transferduring tube quenching. Int J Heat Mass Transfer 2007;50:3490–3497

CHARACTERISTICS OF SUBCOOLED LIQUID METHANE DURING PASSAGE THROUGH A SPRAY-BAR JOULE–THOMPSON THERMODYNAMIC VENT SYSTEM

Paper for 2011 Space Cryogenics Workshop

L. J. Hastings[a], L. G. Bolshinskiy[b], A. Hedayat[c], and A. Schnell[c]

a) Alpha Technology, Inc., Huntsville, Alabama 35801

b) The University of Alabama in Huntsville, Jacobs Engineering MSFC Group, NASA Marshall Space Flight Center, Huntsville, Alabama 35812

c) NASA Marshall Space Flight Center, Huntsville, Alabama 35812

Abstract

NASA's Marshall Space Flight Center (MSFC) conducted liquid methane (LCH4) testing in November 2006 using the multipurpose hydrogen test bed (MHTB) outfitted with a spray-bar thermodynamic vent system (TVS). The basic objective was to identify any unusual or unique thermodynamic characteristics associated with subcooled LCH4 that should be considered in the design of space-based TVSs. Thirteen days of testing were performed with total tank heat loads ranging from 720 W to 420 W at a fill level of approximately 90%. During an updated evaluation of the data, it was noted that as the fluid passed through the Joule–Thompson expansion, thermodynamic conditions consistent with the pervasive presence of metastability were indicated. This paper describes the observed thermodynamic conditions that correspond with metastability and effects on TVS performance.

I. Introduction

Maintaining propellant tank pressure control while minimizing propellant loss is a significant challenge associated with the storage of cryogens in the near zero-gravity environment of space. Thermodynamic vent systems (TVS) are frequently considered as a concept for addressing this issue. A TVS typically includes a Joule–Thompson (J-T) expansion device, a two-phase heat exchanger, and a mixing pump to destratify and extract thermal energy from the tank contents without significant liquid losses. Analytical modeling of such systems is difficult due to the complex combination of microgravity heat transfer and the thermodynamic and fluid mechanic phenomena involved.

Therefore, the primary objective of the original program was to address TVS performance with subcooled liquid methane (LCH4) pressurized with gaseous helium (GHe). Specific goals associated with this primary objective were as follows:

- Evaluate/define a control algorithm for controlling tank pressure and liquid saturation condition.

- Anchor TVS analytical modeling.
- Define operational challenges unique to LCH4.

However, in the process of addressing these goals, challenges unique to LCH4 fluid properties have been encountered. Therefore, the primary purpose of this paper is to address findings relative to that challenge. Information regarding the test facilities and other program objectives is provided only to assist in understanding the use of LCH4 as an in-space propellant. The test facilities, multipurpose hydrogen test bed (MHTB), and spray-bar TVS are described in detail in references 1 and 2, and are therefore only briefly described herein.

II. Test Hardware

The major test article elements consisted of the test tank and its supporting equipment, including an environmental shroud, the cryogenic insulation subsystem, and the test article instrumentation.

The MHTB 5083 aluminum tank is cylindrical in shape with a height of 3.05 m (10 ft), a diameter of 3.05 m (10 ft), and 2:1 elliptical domes. It has an internal volume of 18.09 m^3 (639 ft^3) and a surface area of 35.74 m^2 (379 ft^2), with a resultant surface-area-to-volume ratio of 1.92 1/m (0.58 1/ft) that is reasonably representative of full-scale vehicle tanks.

Testing was performed at the MSFC East test area thermal vacuum facility, Test Stand 300. The vacuum chamber is cylindrical in shape and has usable internal dimensions of 5.5 m (18 ft) in diameter and 7.9 m (26 ft) in height. The facility systems in combination with the test article shroud enable the simulation of orbit environmental conditions by providing vacuum levels of 10–8 torr and a temperature range of 80–320 K (140–576 °R).

Although the MHTB spray-bar TVS design (fig. 1) was optimized for LH2, the “already existing” test hardware offered a low-cost, near-term means for evaluating TVS operations with LCH4 propellant. However, it eventually became obvious that the spray-bar system had operated in a highly degraded mode throughout the test program. The testing conducted and pertinent test results, based on the instrumentation shown in fig. 1, are presented next.

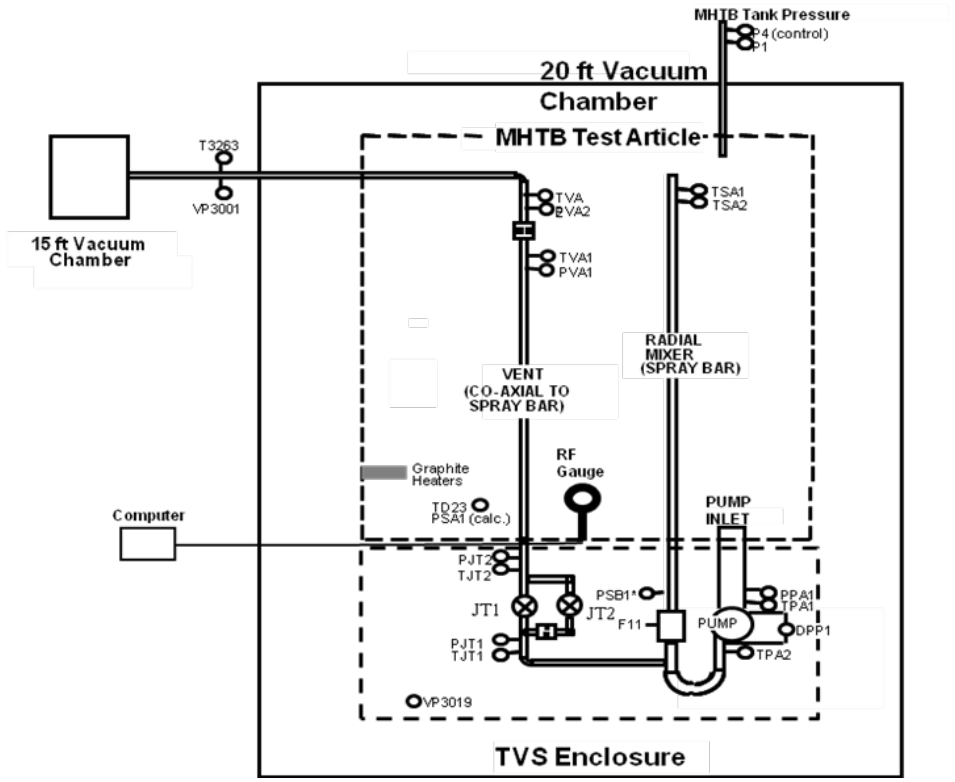

Figure 1. Spray-bar TVS instrumentation.

III. Propellant Conditioning and TVS Testing

The TVS testing with subcooled liquid methane was conducted in phases as various techniques were attempted to achieve the expected level of performance from the spray-bar system. The objectives, test conditions, hardware adjustments, and the test results associated with each of six test steps or phases are described next.

Phase I: Propellant Saturation Pressure Reduction

The LCH4 saturation conditions were reduced for two reasons: 1) to simulate densified methane in-space storage conditions, and 2) to maximize the difference between the GHe partial pressure and the methane partial or vapor pressure to thereby simulate in-flight storage conditions as closely as possible. Starting with a 90% tank fill level, the pump and J-T2 remained on to reduce the liquid saturation pressure. As shown in fig. 2, after 14 h and 40 min, the liquid saturation pressure was reduced from 110 kPa (16 psia) to 54.3 kPa (7.9 psia).

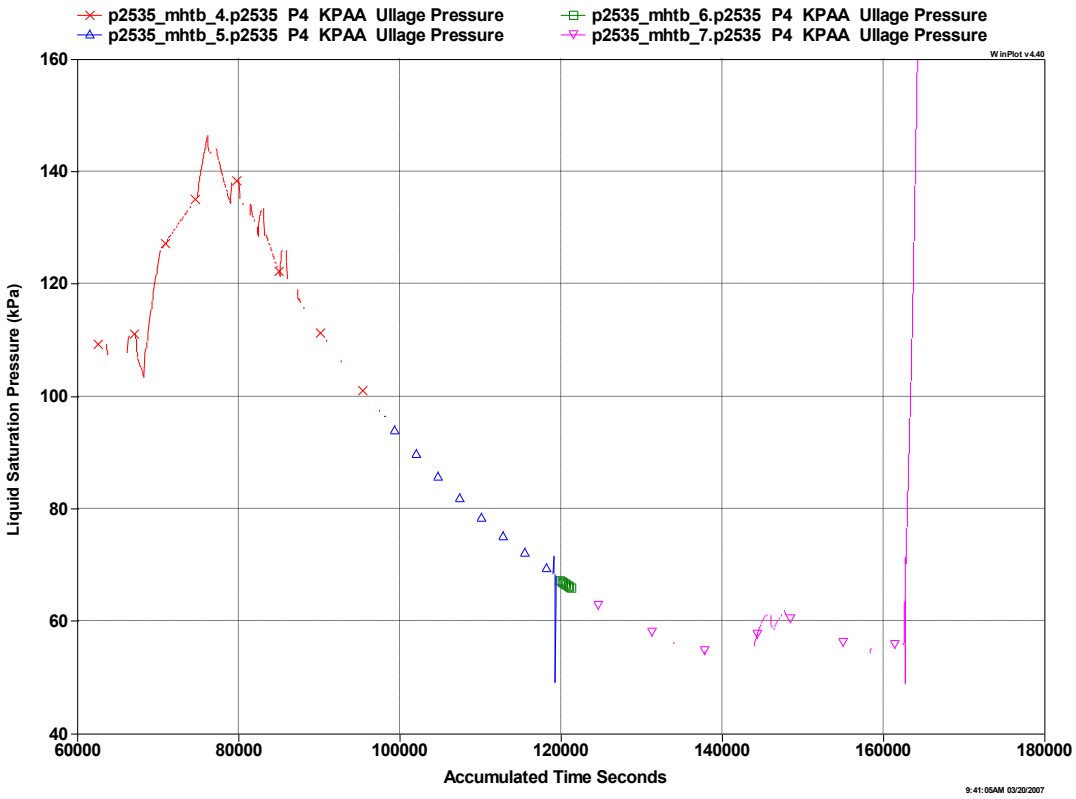

Figure 2. Liquid methane saturation pressure reduction: Phase I testing.

Phase II: Tank Lockup/Self-Pressurization

With the tank locked up, two heaters at 300 W each, and the mixer on continuously, the measured temperature rise rates for the tank contents and wall are presented in fig. 3. The tank contents and wall structure temperatures increased at a constant rate of 1.8×10^{-5} K/s throughout the self-pressurization period, which resulted in average temperature increases of 2.38×10^{-5} K/s and 1.83×10^{-5} K/s for the ullage and liquid, respectively. Because the liquid temperatures were higher than the tank wall temperatures, it was evident that not all of the heater power remained in the liquid. Thermal modeling indicated energy additions of 0.251 W (less than 1%) by the TVS operation, 438.5 W (60.9%) into the liquid, and 281 W (39%) to the tank structure for a gross energy input of 720 W.

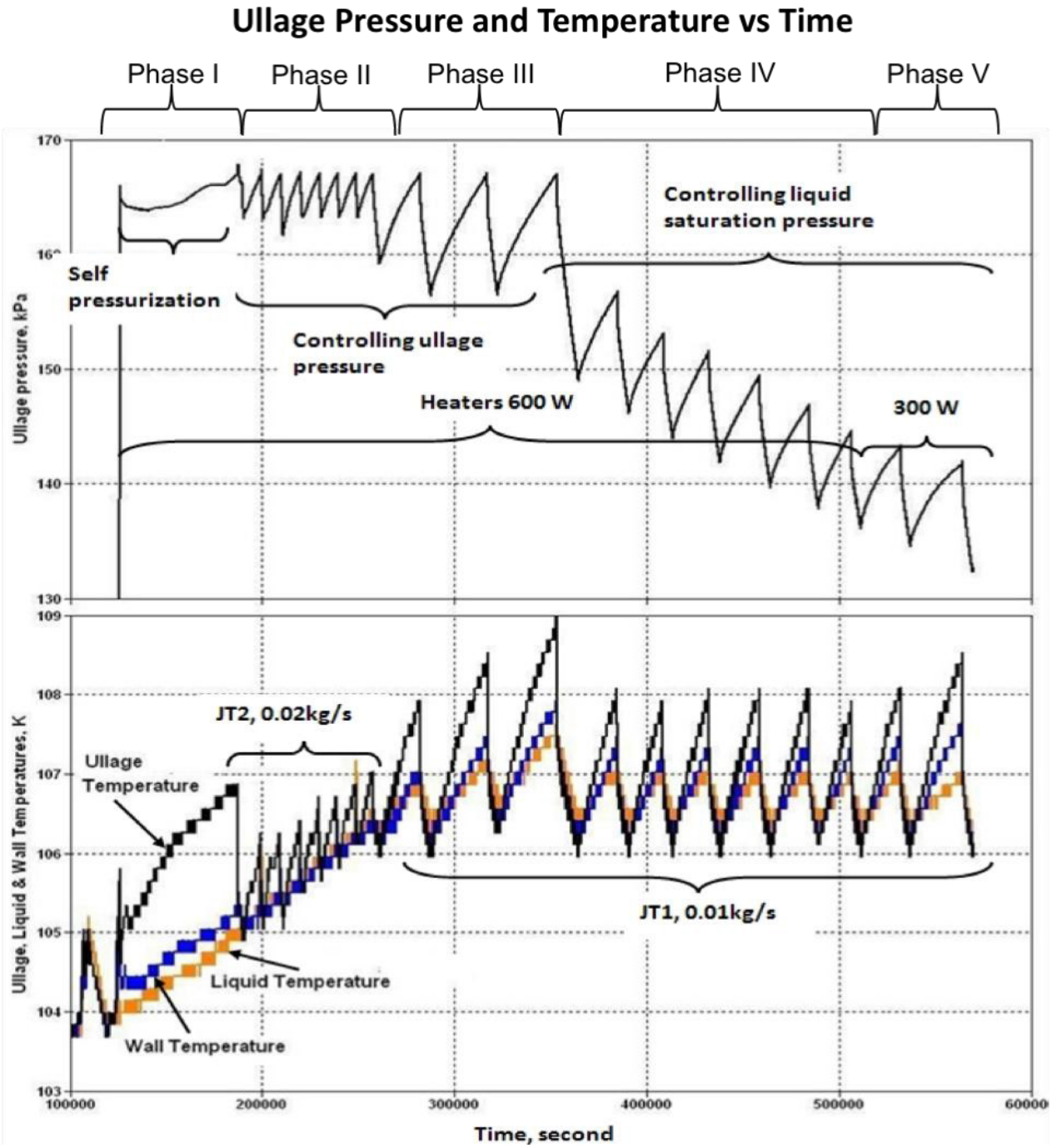

Figure 3. Methane TVS test sequence: Phases II – V.

After tank topping to 90% was complete, with the pump and J-T valve still operating and the liquid saturated at 53.4 kPa (7.9 psia), GHe was injected into the ullage until the pressure reached 166 kPa (24 psia) [GCH4 and GHe partial pressures were 56 kPa (8 psia) and 110 kPa (16 psia), respectively], the value selected for the ullage pressure control band minimum (P_{min}).

Then the pump and J-T valve were turned off, and the ullage pressure was allowed to rise to 172.4 kPa (25 psia), the pressure control band control band maximum (P_{max}). Therefore, the initial conditions established for beginning the TVS testing (Phase III) were as follows:

- Ullage pressure of 166 kPa (24 psia), the control band minimum set point.
- Two graphite heaters adjusted to 300 W each for a gross heat input from all sources of 720 W.
- J-T2, the larger valve with a flow rate of 0.02 kg/s, equals 72 kg/h.

Phase III: TVS Keyed to Ullage Pressure Control (J-T2), Heat Input = 600 W

Seven mixing/vent cycles occurred with the ullage pressure held within a ±3.45 kPa (±0.5 psia) control band for about 17 h. The TVS maintained the tank ullage pressure within the prescribed control band, but the liquid saturation pressure continued to rise throughout operation. This result was unexpected because, during previous MHTB tests with LH2 and LN2, with and without GHe in the ullage, the same spray-bar TVS controlled the ullage pressure while maintaining the liquid saturation pressure at a constant value.[2, 3, 4] However, an evaluation of the methane test data revealed several significant factors which are discussed in the section entitles Data Evaluation.

Phase IV: Extended Vent Cycles with Reduced Flow Rate (J-T1), Heater Input = 600 W

J-T1 was then used to determine if tank pressure could be controlled using a lower flow rate J-T valve, to reduce total propellant loss. J-T1 was successful in reducing the ullage pressure and was used for the remainder of the test. On the ninth vent cycle, J-T1 remained open until the liquid saturation pressure was reduced to its original value, just after the previous vent cycle, which resulted in an ullage pressure decrease of ≈10.3 kPa. The ullage pressure was allowed to rise to 10.3 kPa after the vent cycle was complete, and during this time, the liquid saturation pressure rose to a new maximum level. The conditions of the ninth TVS cycle were repeated during the tenth cycle to observe a trend. The liquid saturation continued to rise in a saw-tooth fashion. Because of the unexpected performance of the TVS, during cycle 11 the test team elected to continue testing at 90% fill instead of proceeding to the 50% level. This decision was made for two reasons: 1) the 90% fill case is the most difficult case to match analytically, and 2) the team preferred to have extensive data at one test condition rather than sparse data at multiple test conditions.

Phase V: TVS Keyed to Saturation Pressure Control (J-T1), Heater Input = 300 W

During cycles 12–17, the TVS was controlled to liquid saturation pressure. The intent of this mode of operation was to keep the liquid temperature under control, thus demonstrating the capability of providing a desired inlet temperature to an engine. The ullage pressure decreased in a saw-tooth fashion with each cycle.

Phase VI: TVS Keyed to Saturation Pressure Control, Heater Input = 300 W

The graphite heater power was reduced during TVS cycles 18–23 to determine if the ullage pressure cycles would reach a steady-state band. However, the ullage pressure cycles continued to drop until the conclusion of the test.

IV. Data Evaluation

Saturation Reduction

Examination of the J-T2 thermodynamic characteristics begins to reveal why there was limited energy removal. In fig. 4, the liquid saturation reduction data are plotted in terms of liquid temperatures upstream and downstream of the J-T valve as opposed to the bulk liquid saturation pressure presented in fig.1. The data revealed that there was no temperature drop across the J-T valve, but instead there was a temperature rise of about 0.25 K. The pressure drop across the J-T was very slight, less than 0.2 kPa (0.03 psia). Based on J-T testing of subcooled methane by Jurns, it is apparent the testing was conducted with the subcooled methane in a "metastable" state. [5] The J-T expansion coefficient was negative; that is, the change in temperature or delta temperature was negative relative to the positive change in pressure or delta pressure.

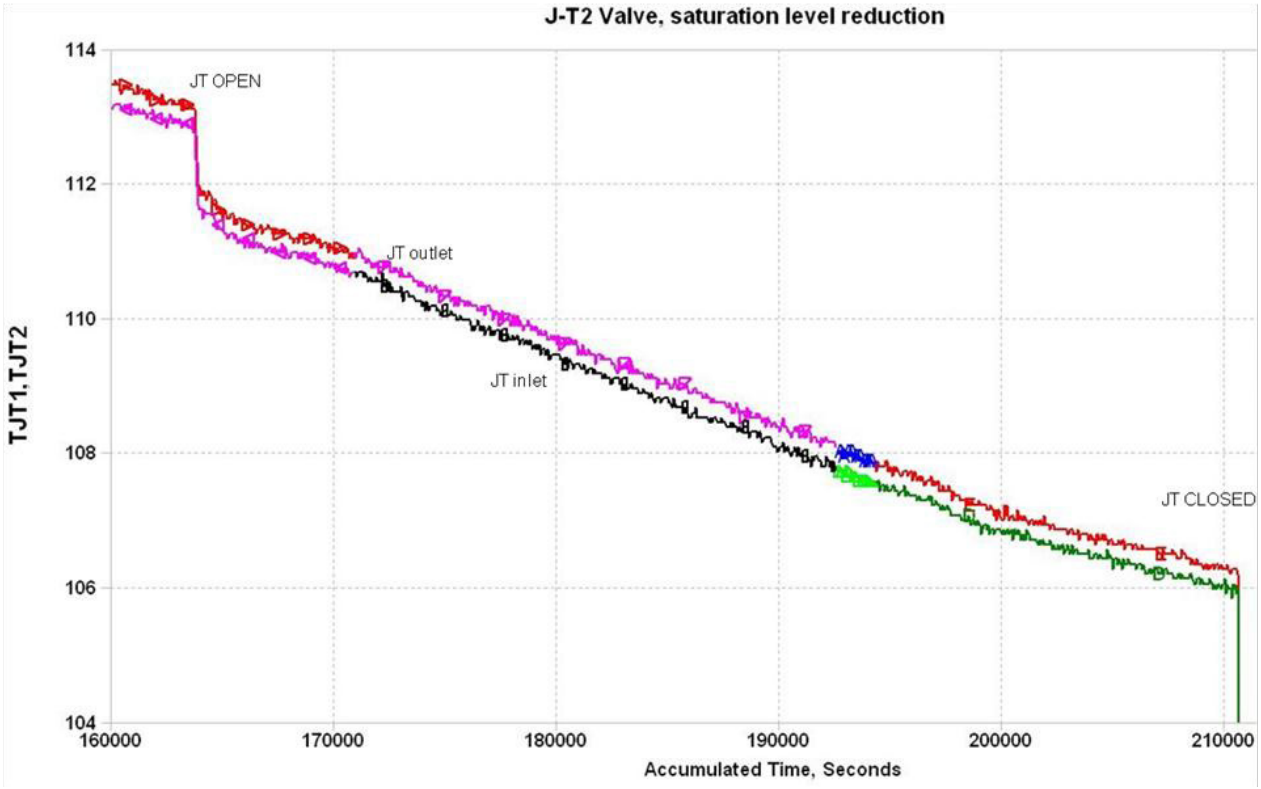

Figure 4. Liquid methane saturation temperature reduction: Phase I testing.

However, the process was successful in reducing the bulk liquid saturation level because the liquid upstream and downstream of the J-T valve were always subcooled relative to the bulk liquid and ullage saturation condition. Further, the ullage volume increased by about 2.5 m^3

(34%) based on a 1,053-kg propellant loss during the 14.7-h test period and with an average density of 427 kg/m^3. Assuming a constant average temperature, the pressure reduction would be about 34% or 35 kPa (5 psi), which is almost 70% of the total reduction of 56 kPa (8 psi). However, the primary issue or cause for concern was that of operating within the metastable regime of methane. The characteristics and implications of metastable conditions during TVS operations are discussed in the following sections.

V. Metastable Conditions

A common example of metastable conditions is demonstrated in the laboratory by gradually heating a glass tube of liquid, such as water, above its saturation level or super-heating the liquid without boiling or two-phase conditions. Similarly, as shown in fig. 5, super-heated conditions can be created by reducing pressure until the saturation line is crossed without boiling. In either case, the superheated liquid is in an unstable or metastable state, and the onset of boiling or two-phase liquid can erupt violently.

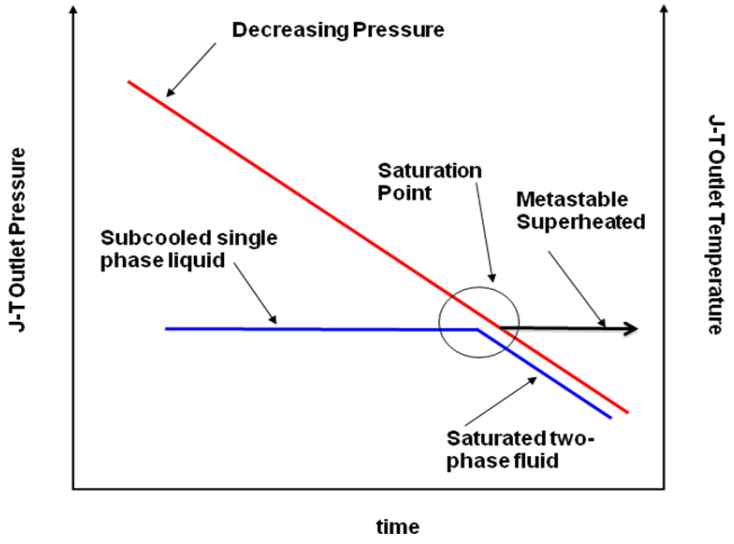

Figure 5. Recognizing presence of metastable liquid.

The same process can be visualized with a “pressure-specific volume” diagram for a pure fluid, as shown in fig. 6. Again, pressure is reduced until the saturation line is crossed and the liquid becomes superheated. However, the lower stability limit can be estimated using techniques described in Jurns.[5]

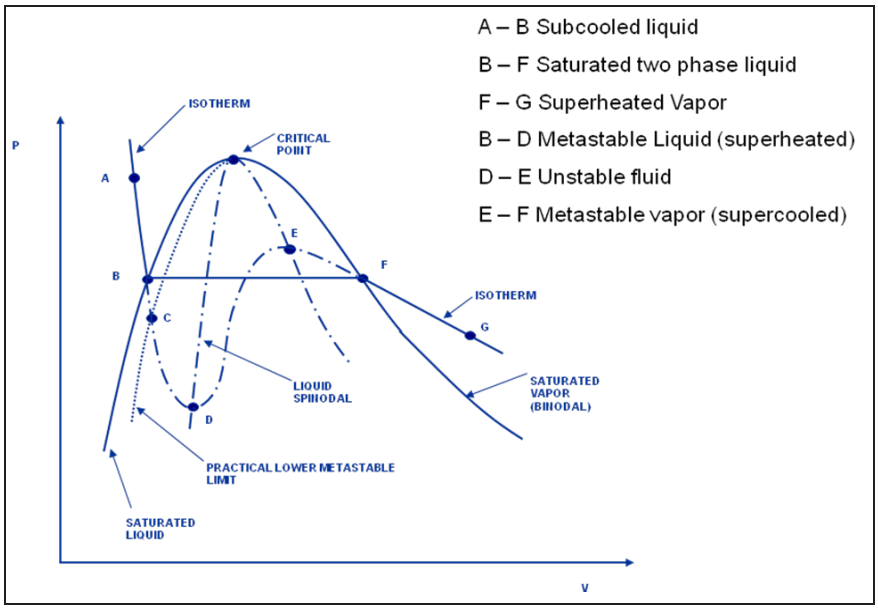

Figure 6. Schematic depicting saturation line and practical lower metastable limit.

Self-Pressurization and TVS Operation with J-T2

As mentioned earlier, once the metastable condition was identified, the TVS operation was better understood. Referring to fig. 3, it was noted that the temperature rise rate of the tank and its contents actually increased after the TVS operation with J-T2 began, whereas the TVS should have removed, rather than added, energy.

A closer look at the pressure and temperature data upstream and downstream of J-T2 (fig. 7) indicates that there was virtually no temperature change across the valve even though a pressure reduction of about 20 to 10 kPa (3 to1.5 psi) occurred. Basically, saturated liquid existed on both sides of the valve. Referring to fig. 7, it becomes clear that the metastable conditions prevented any energy reduction within the tank contents. Therefore, although the ullage temperature and pressure was reduced during each mixer operation (by the relatively cool liquid at the J-T valve entrance), thermal energy was being added instead of reduced. Consequently, the tank contents saturation level increased with each cycle.

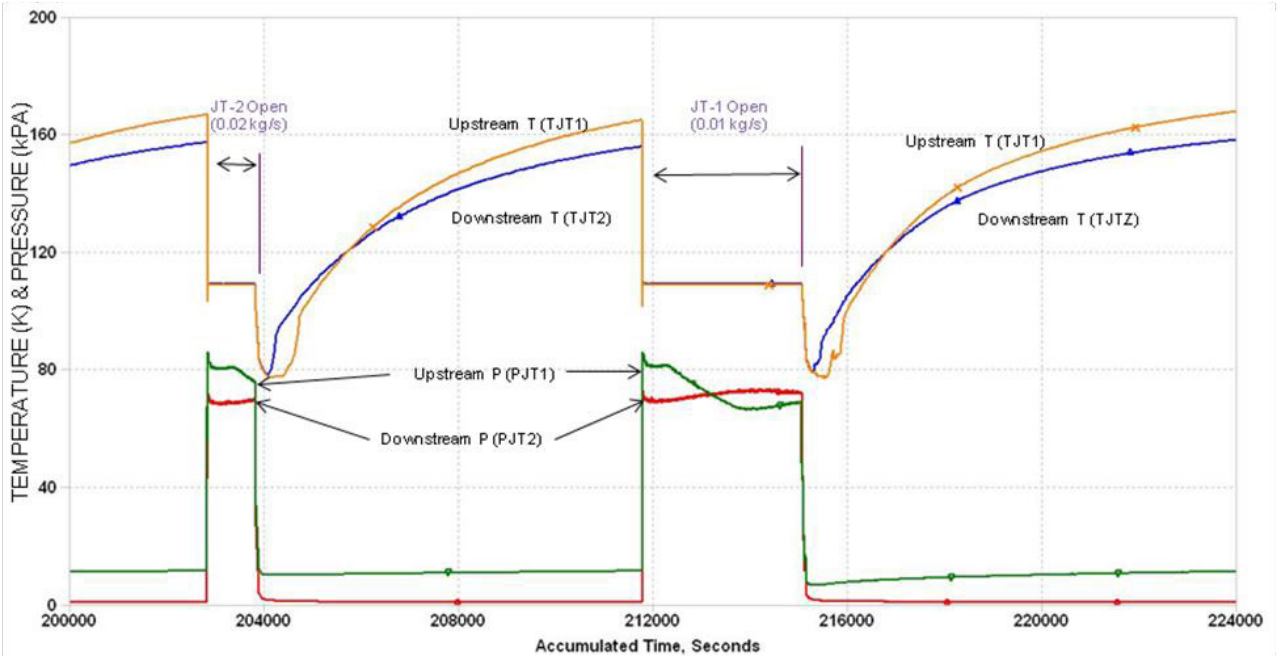

Figure 7. Pressure and temperature upstream and downstream of J-T1 and J-T2, Heater Input = 600 W

TVS Operation with J-T1

The lack of success in Phase III motivated Phase IV testing with J-T1 at a predicted flow rate of 0.01 kg/s, that is, one-half that with J-T2. Although the ullage pressure was reduced on a cycle-by-cycle basis, the bulk liquid saturation level increased with each of the first 11cycles. Therefore, Phase V testing was based on controlling liquid saturation temperature instead of ullage pressure; however, the ullage pressure decreased with each vent cycle. Finally, the Phase V testing was repeated in Phase VI with 300 W heater input, a 50% heater power reduction; however, the ullage pressure decrease continued. Examination of thermodynamic conditions on each side of the J-T valve indicates why liquid saturation temperature and ullage pressure could not be controlled simultaneously. As seen in the Phase V testing (fig. 7), there was a slight temperature rise, as opposed to a drop, across the J-T. And the ΔP was positive but became slightly negative about halfway through the cycle. An expanded version of J-T1 inlet and outlet temperatures for the 300 W heater output conditions (see fig. 8) indicate a slight temperature rise across the J-T valve. The temperature rise across the JT valve is a definite indicator of a metastable condition. Further, the vent flow could not have existed after the downstream pressure exceeded the upstream pressure. Therefore, without a doubt, the TVS performance was severely compromised by the metastable characteristics.

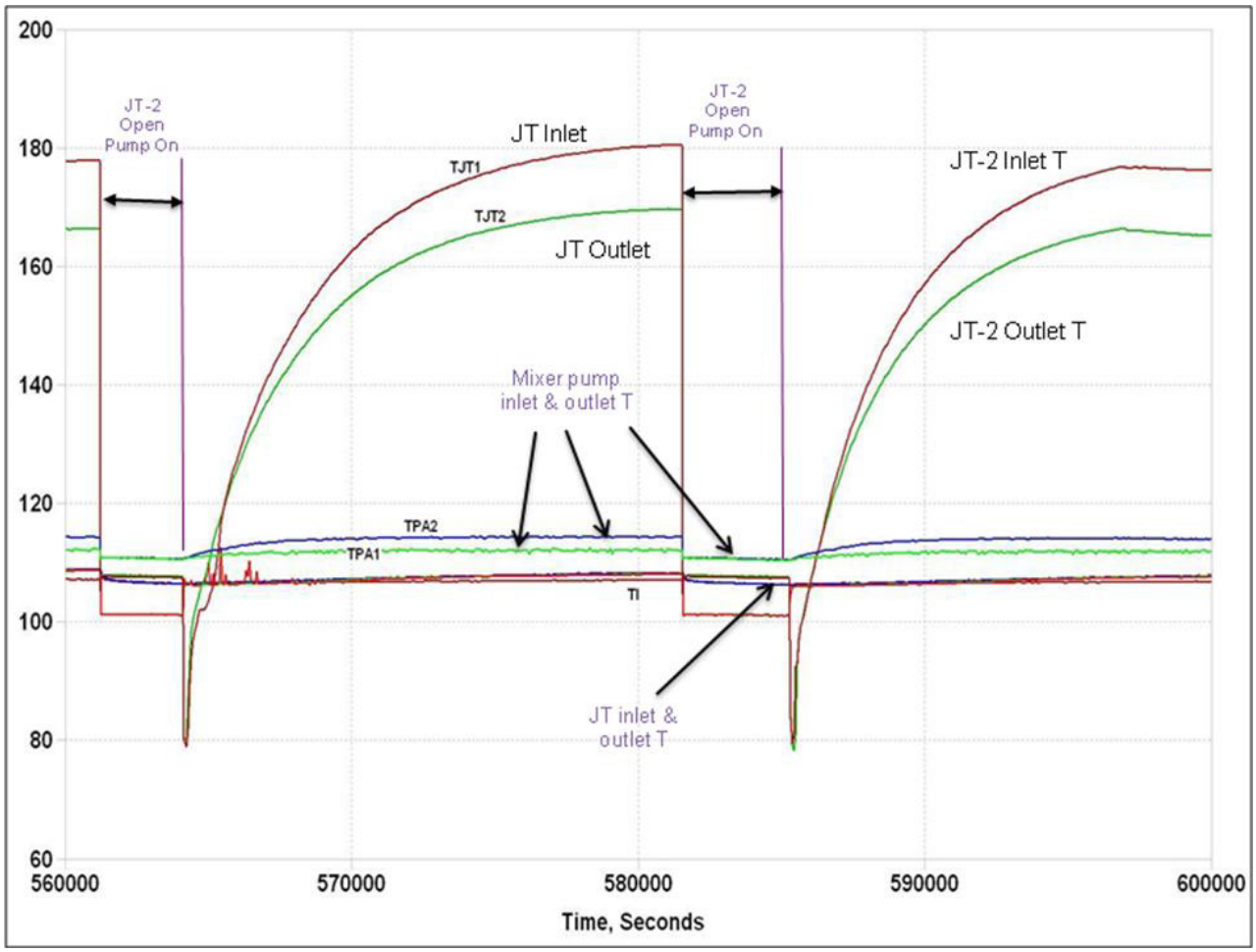

Figure 8. TVS temperatures with J-T1, Heater Input 2 = 300 W

Furthermore, regarding the "valve open" conditions measured at the J-T valve entrance and exit, it was noted that neither the temperature profile nor the magnitude varied with test condition or valve size. The same observation held regarding inlet pressures, except that the profile had longer to evolve with the smaller valve. Next it was noted that "valve open" conditions upstream and downstream of the backpressure control orifice were, for all practical purposes, also were unaffected by the J-T used or by the tank heater load variation of 600 W or 300 W. This was a substantial conclusion. Once the commonality of temperatures for a given position was established, it became convenient to group all the data for a particular measurement position onto a single graph. For example, as shown in fig. 9, the saturation temperature corresponding to the "valve open" measured pressure at a valve entrance was constant at 108 K, which closely matched the measured temperature, thereby indicating a saturated liquid condition throughout the testing. Similarly, at the position immediately downstream of the J-T valve (fig. 10), the measured temperatures also indicated the presence of a saturated liquid.

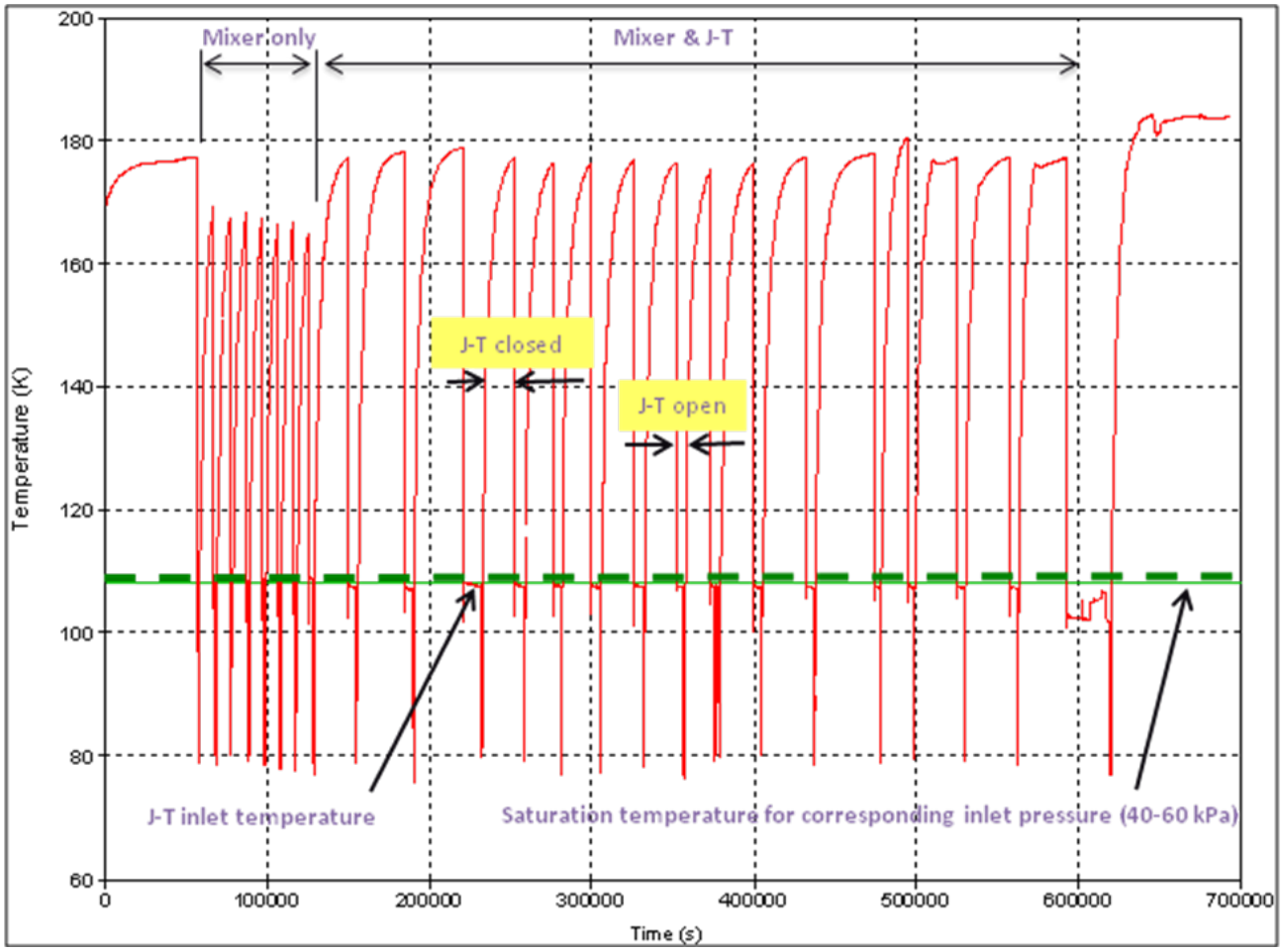

Figure 9. Comparison of J-T inlet temperature with saturation temperatures corresponding to measured inlet pressure. Conclusion: saturated fluid at J-T entrance.

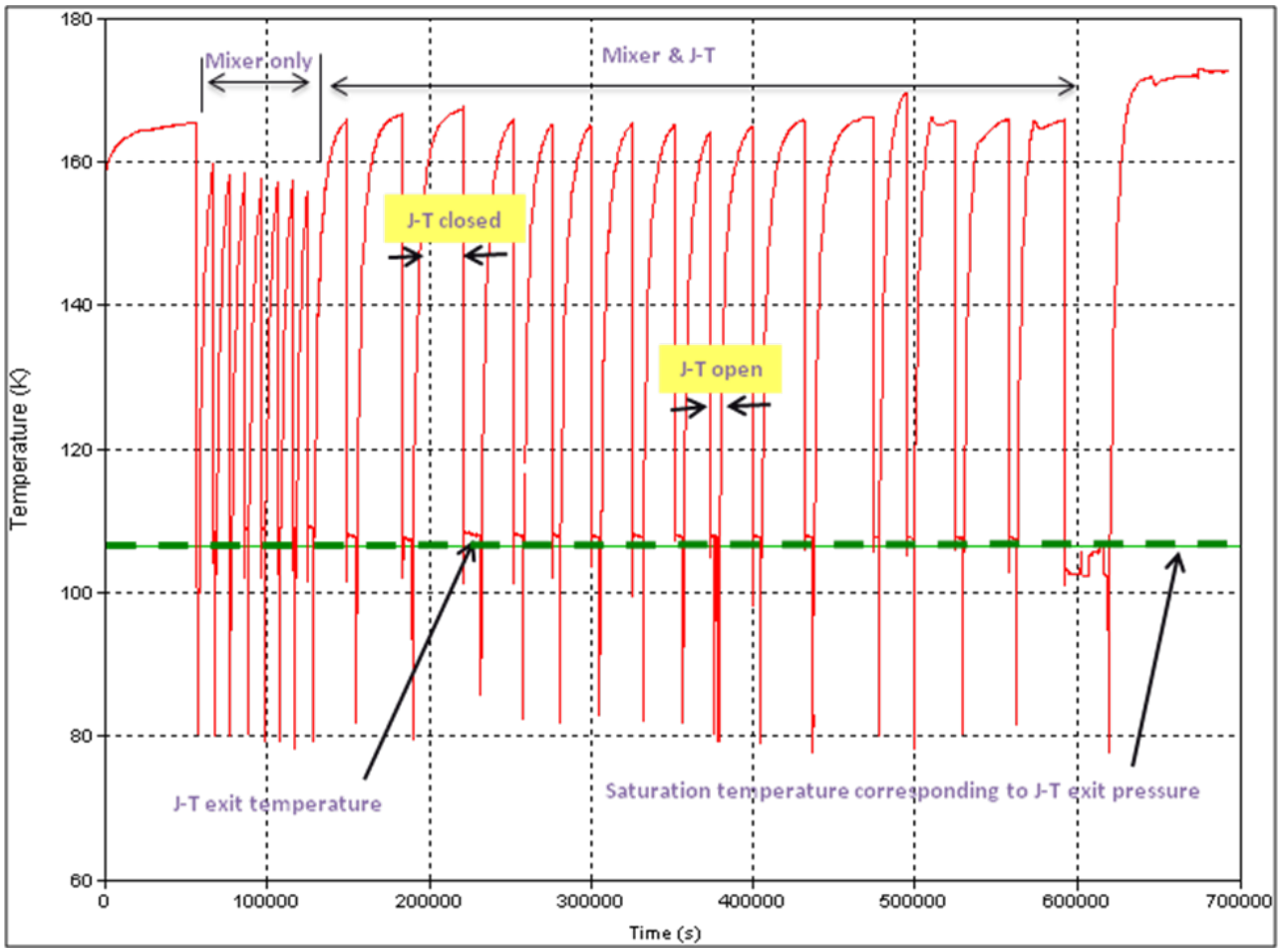

Figure 10 Comparison of J-T exit temperature (TJT2) with saturation temperature corresponding to exit pressure (PJT2). Conclusion: fluid at J-T exit slightly above saturation.

The pressures and temperatures measured upstream and downstream of the back-pressure orifice, which was positioned in the vent line external to the test article but within the vacuum chamber as shown in fig. 1, are presented in figs. 11 and 12, respectively. The temperatures measured during the vent periods on both sides of the orifice were consistently lower than the saturation temperature corresponding to measured pressures, indicating the presence of subcooled liquid throughout the testing. Additionally, the orifice inlet temperatures were about 2 K lower than at the spray-bar entrance. If the TVS had been operating in a normal manner the vented fluid temperatures would have increased, rather than decreased, as it passed through the spray-bar heat exchanger. Finally, another indication of liquid being vented was the sudden pressure spikes that occurred whenever the diffusion pumps were overwhelmed by liquid being vented into the 15-ft chamber. However, since the vent-side liquid was cooler than the bulk liquid circulated through the spray side of the TVS and the longer vent duration, some bulk liquid cooling with the smaller JT valve was obtained.

Figure 11. Comparison of venting orifice inlet temperature (TVA1) with saturation temperature corresponding to inlet pressure (PVA1). Conclusion: subcooled liquid at spray-bar exit/back-pressure orifice entrance.

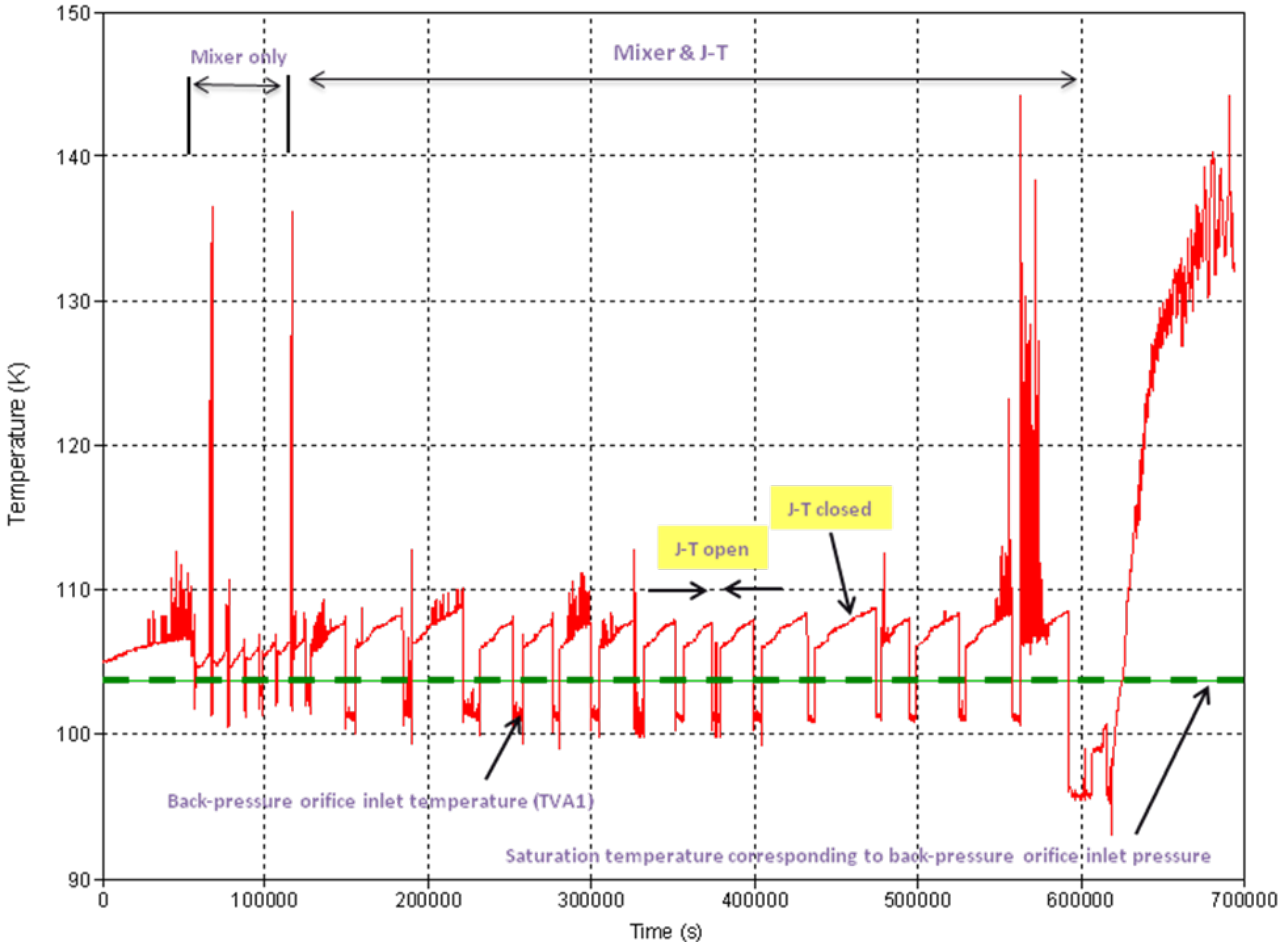

Figure 12. Comparison of venting orifice exit temperature (TVA2) with saturation temperature corresponding to exit pressure (PVA2). Conclusion: subcooled liquid at back-pressure orifice exit/15-ft vacuum chamber entrance.

Therefore, even though the data evaluation is incomplete, the major finding is evident. Without a doubt, the TVS performance was severely compromised throughout the test program by the presence of metastable conditions. This finding and other conclusions are discussed in the next section.

VI. Summary and Conclusions

MSFC conducted liquid methane testing in November 2006 using the multipurpose hydrogen test bed outfitted with a spray-bar TVS. The basic objective was to identify any unusual or unique thermodynamic characteristics associated with subcooled LCH4 that should be considered in the design of space-based TVSs. Thirteen days of testing were performed with total tank heat

loads ranging from 720 W to 420 W at a fill level of approximately 90%. During an updated evaluation of the data, it was noted that as the fluid passed through the J–T expansion, thermodynamic conditions consistent with the pervasive presence of metastability were indicated. Specific observations and implications of metastable methane on TVS performance and recommendations are discussed below.

1. Spray-bar TVS seriously compromised by metastable methane

The J-T cooling with either of two valves, one with a predicted flow rate of 0.02 kg/s and another rated at 0.01 kg/s, was seriously compromised. In both cases the downstream temperature was higher than the upstream or inlet temperature, even though the downstream pressure was lower. In other words the J-T expansion coefficient was negative (negative ΔT over positive ΔP), a characteristic of metastability. Additionally, it was noted that subcooled liquid at 102 K was consistently present at the upstream side of the back-pressure orifice. Therefore, Some cooling was obtained with the smaller valve, apparently because the liquid within the vent side of the spray bar was cooler than the bulk liquid and the longer vent duration allowed some energy exchange with the bulk liquid.

2. TVS applications to reduced gravity methane storage constrained.

Although testing was conducted with a spray bar TVS, it is believed that the metastable condition is primarily a function of degree of subcooling and or helium pressurization above the saturation level. Until further testing demonstrates other-wise, it is recommended that it be assumed that the metastable methane conditions observed herein are also applicable to other TVS concepts. Therefore, usefulness of concepts involving TVS's in combination with densified methane (below normal boiling point) to achieve long-term in-space storage are likely to either be seriously compromised or not viable. Similarly, the application of TVS's to concepts with high partial pressure helium will be constrained (since liquid below the liquid-vapor interface behaves as though it was subcooled). Therefore, in future applications of J-T cooling to methane storage, assurance must be provided that metastable effects have either been mitigated or circumvented. A strong bench test program is recommended for any and all TVS applications to space-based liquid methane storage.

3. Propellant settling to accommodate reduced gravity venting more likely

In view of the above, propellant settling to support venting during reduced gravity methane storage is now more probable.

4. Thermal modeling required to support use of heaters to expedite ground-based pressure control testing

Ground-based testing of pressure control concepts for reduced gravity storage of high density cryogens (such as liquid methane, oxygen, and nitrogen) often necessitate heaters to expedite pressure control cycle rates. However experience with the subject methane testing demonstrated the need for thermal modeling sufficient to determine the energy distribution to the tank contents

vs the tank walls and other heat leak sources. Furthermore, it is recommended future testing include at least a partial test cycle with the actual anticipated heat load.

References

1. Martin, J., and Hastings L., ”Large-Scale Liquid Hydrogen Testing of a Variable Density Multilayer Insulation With a Foam Substrate”, NASA/TM-2001-211089, MSFC, AL, June 2001.
2. Hastings, L. et al, “Spray Bar Zero-Gravity Vent System for On-Orbit Liquid Hydrogen Storage’, NASA/TM-2003-212926, MSFC, October 2003.
3. R.H. Flachbart , L.J. Hastings, A. Hedayat, S.L. Nelson, S. Tucker, pp. 1483-1490, “Testing the Effects of Helium Pressurant on Thermodynamic Vent System Performance with Liquid Hydrogen,” pp. 1483-1490, Advances in Cryogenic Engineering, Vol. 53B, American Institute of Physics, 2008.
4. R. Flachbart, L. Hastings, A. Hedayat, S. Nelson, S. Tucker, pp. 1483-1490, “Testing of a Spray-Bar Thermodynamic Vent System in Liquid Nitrogen”, pp. 240-247, Advances in Cryogenic Engineering, Volume 51A, American Institute of Physics, 2006.
5. Jurns, J. M., “Flow of Sub-Cooled Cryogens Through a Joule-Thomson Device – Investigation of Metastability Conditions,” Master’s Thesis, Cleveland State University, December 2007.

Launch Ascent Testing of a Representative Altair Ascent Stage Methane Tank

W.L. Johnson[1], J.M. Jurns[2], H.H. Bamberger[3] and D.W. Plachta[4]

[1]Cryogenics Test Laboratory, Kennedy Space Center
[2]ASRC Aerospace, Glenn Research Center
[3]Jacobs Technology, Glenn Research Center
[4]Propulsion and Propellants Branch, Glenn Research Center

Abstract:

In order to support long duration cryogenic propellant storage, the NASA is investigating the long duration storage properties of liquid methane. The Methane Lunar Surface Thermal Control (MLSTC) testing is using a tank of the approximate dimensions of the Altair lunar ascent propellant tanks. The tank was insulated with multilayer insulation and placed inside of a vacuum chamber to simulate the various environments that would be encountered during launch and travel from the earth to the lunar surface, including long duration stays on the lunar surface. One of these environments to be studied is the launch and ascent environment; while all the effects of this mission phase cannot be simulated at the same time, an effort was made to simulate as many as possible. Boil-off testing included ambient pressure ground hold testing followed by a rapid depressurization of the vacuum chamber during which the liquid methane tank was allowed to come to steady state condition in the high vacuum environment. The data gathered from the series of tests fit with-in pre-test predictions and yielded much needed test data for rapid depressurization using liquid methane.

Keywords: Multilayer Insulation, Launch Ascent Testing, Liquid Methane

1. Introduction

As NASA began to design vehicles to return to the moon, cryogenic propulsion stages were proposed to enable mass efficient transportation of hardware and astronauts to the lunar surface. One of the unique portions of the proposed architecture was the liquid methane and liquid oxygen ascent stage on the Altair lunar lander. The stage is comprised of two spherical liquid oxygen tanks and two spherical liquid methane tanks that are each approximately 1.2 m in diameter (see Figure 1). In order to show that such a small tank could be used for storing propellant for up to a six month stay on the lunar surface, an extensive modeling and testing effort was performed. A small portion of this testing effort focused on determining the heat load between the launch pad and achieving steady state in low earth orbit.

Long duration storage of cryogenic propellants in the high vacuum environments associated with earth orbit and the lunar surface have been thoroughly investigated over the past 50 years. Large vacuum chambers have been developed to allow for ground based space environmental testing of storage methods. Many tests have been run to determine the performance of small and large cryogenic propellant tanks at steady state in some simulated orbit [1-3]. Comparatively few tests have been run at any environmental pressure other than high vacuum [4]. A majority of these tests have been focused on atmospheric pressure testing for the brief stay on the launch pad. Both on the launch pad and in orbit are generally considered to be steady state

environments and have been tested as such. Minimal testing has been performed for the transient period between these two steady state conditions.

There are two major components to the heat load to a cryogenic storage tank. The first is the heat load through the structural support system. Given a known geometry (cross-sectional area and length), the conduction heat load through the support system can be calculated relatively easily, as conduction heat transfer is not a function of pressure. The second portion is the heat load through the broad area insulation. Multilayer Insulation (MLI) is generally regarded as the best performing insulation system in high vacuum; however, its performance at ambient pressure is often 3 orders of magnitude worse. Additionally, the heat load through MLI is highly sensitive to the environmental pressure. Thus the heat load to the cryogenic propellant tank will be largely a function of environmental pressure. In order to analyze any mission that begins on the ground, the heat load from the ground hold through the ascent portion of flight must be accounted for in addition to the steady state on-orbit heat loads.

2. Test Setup, Facility, and Procedure

In order to simulate an Altair ascent stage liquid methane tank, a 1.2 m diameter tank was outfitted with 60 layers of MLI and suspended in the Small Multipurpose Research Facility (SMiRF) at the Glenn Research Center (GRC) Creek Road Cryogenics Complex (CRCC) as shown in Figure 2 [5]. The MLI was designed to have a low layer density of roughly 1.0 layer/mm (conventional MLI is 2-3 layer/mm), however the final installation averaged closer to 0.7 layer/mm. 70 thermocouples were placed in the MLI at various locations through the thickness of the layers to determine the temperature profile of the MLI, 40 silicon diodes were located at know locations inside the tank, and many more thermocouples were placed on the structural and fluid lines to determine the structural heat load.

To simulate a purged launch pad environment, the vacuum chamber was filled with gaseous nitrogen to 760 torr while the thermal shroud was set to 305 K (roughly atmospheric pressure and temperature at Kennedy Space Center). The tank was then topped off with liquid methane and allowed to come to equilibrium, which took roughly 10 hours. From the 10 hour cold soak and then 6 hour test period, the liquid level dropped from 95% full to 85% full. After refill to 95% full and a few hours to come back to equilibrium, both vacuum pumps were turned on, however only one of the vacuum gate valves was opened at first. For this testing, equilibrium (steady state) was defined as: Insulation temperatures transients less than 0.55 K in 6 hours, a positive temperature gradient in the ullage (temperature increasing as height increased), and ullage pressure maintained within a +/-0.001 psi band.

Roughly 60 seconds into pumpdown the second vacuum gate valve was opened to accelerate the pumpdown. This was done to approximate the expected launch ascent depressurization profile. The pumps were then allowed to pump freely for 5 days; Figure 3 shows the vacuum chamber pressure as a function of time compared to historical testing and the shuttle cargo bay.

During the entire test, the boil-off flow rate was being measured by flow meters outside the test chamber. Also, all of the temperature sensors were being monitored within the tank, along the structural and fluid lines and within the MLI.

3. Pre Test Predictions

Pre-test heat load predictions were calculated for the ground hold testing and the ascent testing. The purpose was to validate thermal analysis codes which are needed for future design efforts.

The ground hold testing used the TISTool [6]. The Thermal Insulation System analysis Tool (TISTool) uses a nodal approach to thermal analysis and allows the use of many different types of insulations in combination with each other. The data fed into the model is test data from Cryostat-100 [7]. The MLSTC ground hold test was modeled using previous MLI testing performed at Kennedy Space Center.

The ascent heat load predictions used the Launch and Ascent Tool [8]. The Launch Ascent Tool performs a lumped parameter analysis (three lumps: liquid, vapor, and liquid/vapor interface) consistent with the Multizone code developed by Barsi, Moder, and Kassemi [9]. A variable heat load is applied to the externals of the tank as a function of time using historical data to generate the heat loads. Three different cases were analyzed, a conservative case (i.e. the pump down took longer than expected), an aggressive case (i.e. the pumpdown was much quicker than expected), and an expected case (based on the SMiRF historical and pretest pumpdown rates).

4. Results and Discussion

The ground hold heat load was 322 W, which is a mean heat flux of 51.7 W/m^2 and an overall thermal conductivity (k-oafi) of 23.7 mW/m-K. The TISTool predicted a heat load of 248 W, the difference most likely being due to the lower than expected performance of the MLI as actually tested on a calorimeter by Johnson [10].

Figures 4 and 5 show the heat load during the pump down boil-off test as a function of time and cold vacuum pressure respectively. In addition, Figure 4 shows the heat load as a function of time compared to the pre-test predictions. The expected performance curve used a very similar depressurization profile as the actual test, yet much of the test data in the early portion of the test (first 30 hours) was further from the nominal prediction than the rest of the test. This implies that there were certain physical phenomena driving the heat loads that were not necessarily a part of the insulation heat load.

Figure 5 shows the heat load as a function of cold vacuum pressure compared to several historical test points and steady state MLI [3, 11]. The large cluster of data in the high vacuum region of the data is due to the daily oscillations of the pressure and boil-off as they respond to the typical day/night temperature and tidal cycles respectively. The transient heat load does not decrease as rapidly as one would expect it to by following the steady state curve. One of the main reasons for performing the test was to determine what caused this offset to occur and if it was a phenomena directly associated with depressurization (i.e. pressure gradients within the MLI). Riesco, et.al determined that this was not due to the mass of the MLI, the mass of the gas being evacuated or by the MLI out-gassing [11]. However, during the MLSTC testing, it was noted that the top of the tank started out at a much warmer temperature than the rest of the tank (over 50 K in temperature difference), similarly temperature sensors placed halfway between the top of the tank and the liquid level recorded temperatures in excess of 30 K above the liquid temperature. Figure 6 shows the temperature at the top of the tank and halfway between the top and the liquid level as a function of time. The specific energy of the portion of the tank (166 kg and made out of SA-240 304 stainless steel) in direct contact with the ullage is also shown as a function in time. Figure 7 includes a shifted curve to account for the tank mass; it shows that by

accounting for the energy to change the temperature of the tank mass, the transient heat load is shifted between 5-10 hours to the right causing the heat load curve to more closely resemble the pressure curve as a function of time. This makes sense when comparing with KSC A125 (Cryostat-100) data that does not show a large divergence from the steady state curve (see Figure 5) and also does not have a large heat load on the top of the chamber because it has a liquid guard chamber. Thus the large divergences from the steady state performance can be mainly attributed to the cooling of the rather large thermal mass of the tank that starts in the much warmer ullage. The pressure gradients within the MLI are shown to be a much lesser cause.

The heat load break down for the integrated heat load over time is shown in Table 1. Thus the heat load during the depressurization can be estimated to be roughly 3.2 days of steady state heat load.

Table 1: Energy Breakdown for the MLSTC ascent test, first 120 hours

Integrated Heat Loads (power * time)	Test	Predicted (nominal)
Total Measured	5200 kJ	2810 kJ
Penetrations	1450 kJ (roughly 3W)	2480 kJ
MLI HV steady state load	1350 kJ	
Tank cooldown	1450 kJ	N/A
MLI Transients	950 kJ (154 kJ/m^2)	330 kJ

5. Conclusions

Steady state thermal performance testing of a liquid methane tank insulated with multilayer insulation, but in a purged nitrogen atmosphere was performed. The pretest predictions were 23% low, which can be attributed to not understanding the effects of low layer density on thermal performance of MLI systems and uncertainties associated with the relatively thick MLI blanket that was tested.

Transient thermal performance testing of a liquid methane tank was also performed. The transient pressure profile that was achieved by pumping on the system was relatively close to a launch vehicle pressure profile over the first few minutes. The heat load took 30 hours to come to steady state and the temperatures within the MLI layers took over 120 hours to come to steady state. The tank thermal mass was determined to be the main source of parasitic heat load above and beyond the MLI heat load as a function of pressure. Pre-test predictions banded the experimental data and showed that the general physics associated with the transient environment are captured in the model. The testing performed fills in a gap in the existing data for transient environments using liquid methane as the cryogenic heat sink.

6. References

[1] Fredrickson, G.O., Investigation of High-Performance Insulation Application Problems, Final Report, NASA CR-124400, 1973.

[2] Stochl, R.J., Knoll, R.H. Thermal Performance of a Liquid Hydrogen Tank Multilayer Insulation System at Warm Boundary Temperatures of 630, 530, and 152 R, AIAA-91-2400, 1991.

[3] Martin, J.J., Hastings, L.J., Large Scale Liquid Hydrogen Testing of a Variable Density Multilayer Insulation with a Foam Substrate, NASA TM-2001-211089, 2001.

[4] Augustynowicz, S.D., Fesmire, J.E., Cryogenic Insulation System for Soft Vacuum, in: Shu, Q., editor , Advances in Cryogenic Engineering, Vol. 45, Kluwer Academic/Plenum Publishers, NY, 2000, pp. 1445-1451.

[5] Bamberger, H.H., Liquid Methane Conditioning Capabilities Developed at NASA GRC's Small Multi-Purpose Research Facility (SMiRF) for Accelerated Lunar Surface Storage Thermal Testing, NASA CR-2010-216745, 2010.

[6] Demko, J.A., Fesmire, J.E., et al., Design Tool for Cryogenic Thermal Insulation Systems, in: Weisend, J.G., Editor, Advances in Cryogenic Engineering Vol 53A, American Institute of Physics, Melville, NY, 2008, pp. 145-151.

[7] Fesmire, J.E., Augustynowicz, S.D., et al., Thermal Performance Testing of Cryogenic Insulation Systems, in: Koenig, J.R., Ban, H. editors, Thermal Conductivity 29, DEStech Publications, Lancaster, PA, 2008, pp. 387-396.

[8] Johnson, W.L., Launch Hold and Ascent Effects of Cryogenic Propellants: Level Ib Model Development Report., Internal Report, (2009).

[9] Barsi, S., Moder, J., et al., Numerical Investigations of LO2 and LCH4 Storage Tanks on the Lunar Surface, 38th AIAA/ASME/SAE/ASEE Joint Propulsion Conference and Exhibit, 2008.

[10] Johnson, W.L., Thermal Performance of Cryogenic Multilayer Insulation at Various Layer Spacings, University of Central Florida, Master's Thesis, 2010.

[11] Riesco, M.E., McLean, C.H., et al., Venting and High Vacuum Performance of Low Density Multilayer Insulation, in: Weisend, J.G., Editor, Advances in Cryogenic Engineering Vol 55A, American Institute of Physics, Melville, NY, 2010, pp. 796-803.

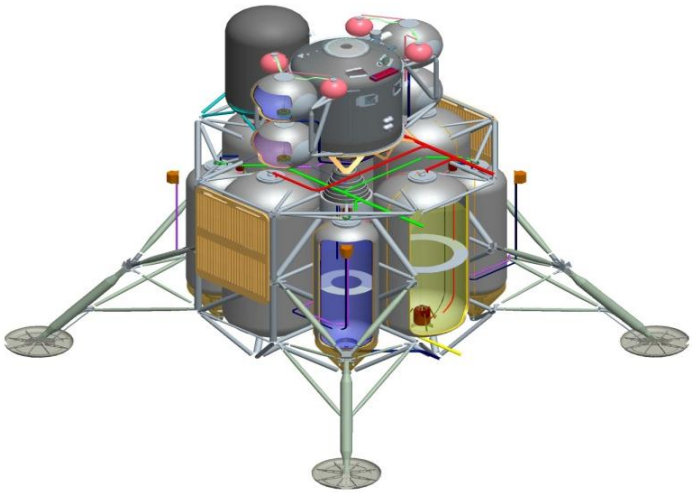

Figure 1: Altair configuration with two liquid methane tanks (purple tank & symmetrical)

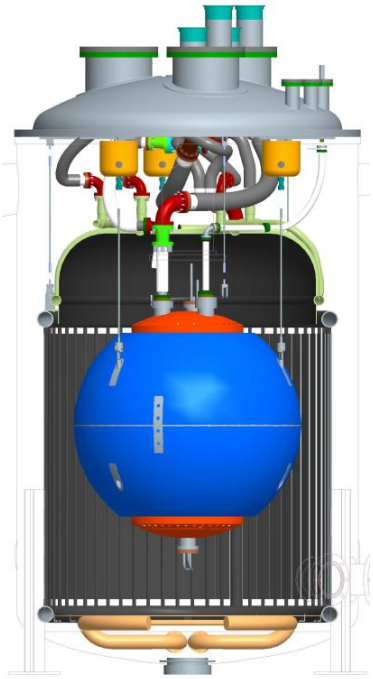

Figure 2: Graphic of the MLSTC test tank inside the environmental shroud at the SMiRF facility

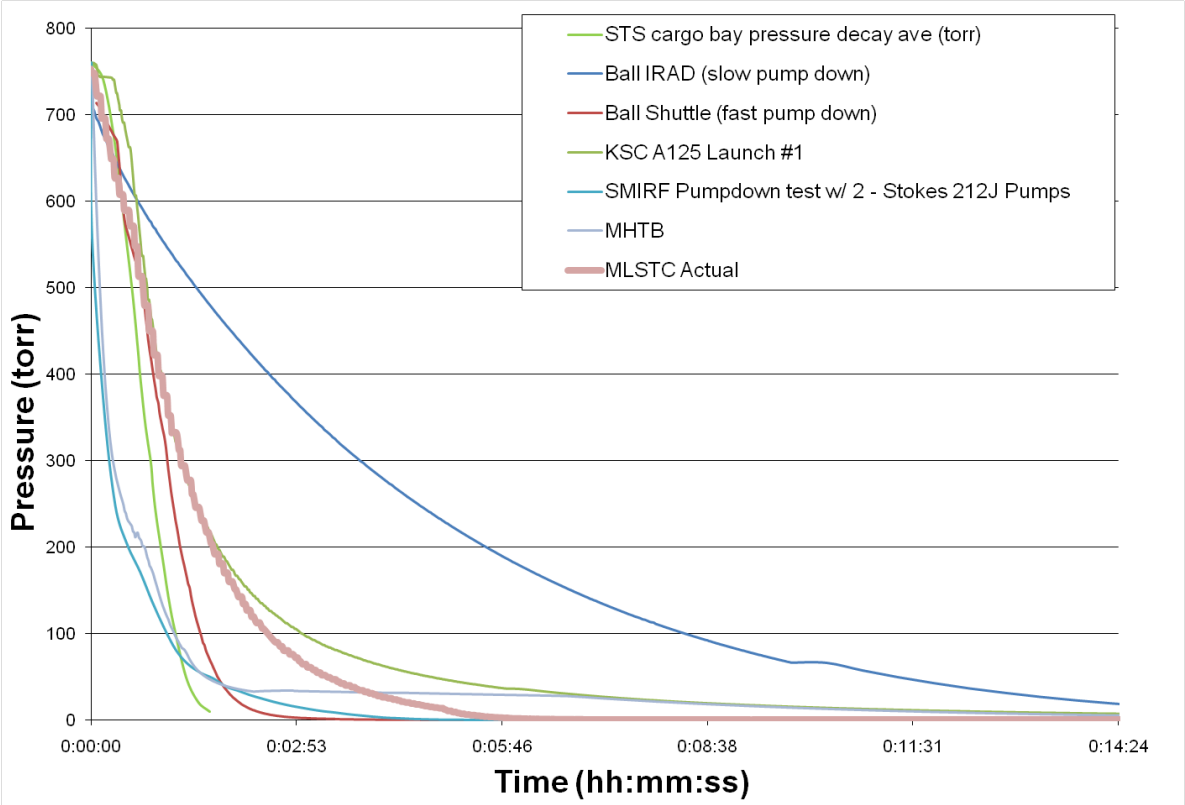

Figure 3: Pressure as a function of time for several historical tests and the shuttle flight profile

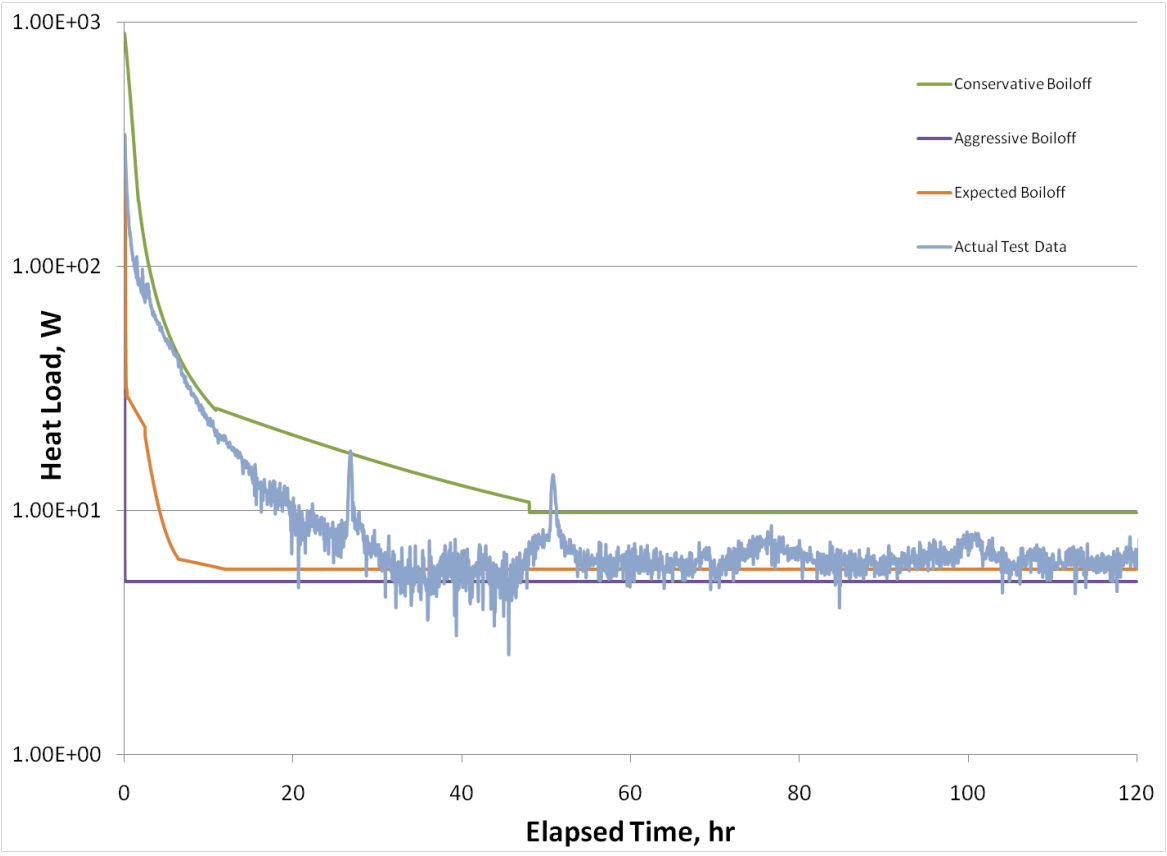

Figure 4: Heat load as a function of test time, starting when the vacuum pumps were turned on

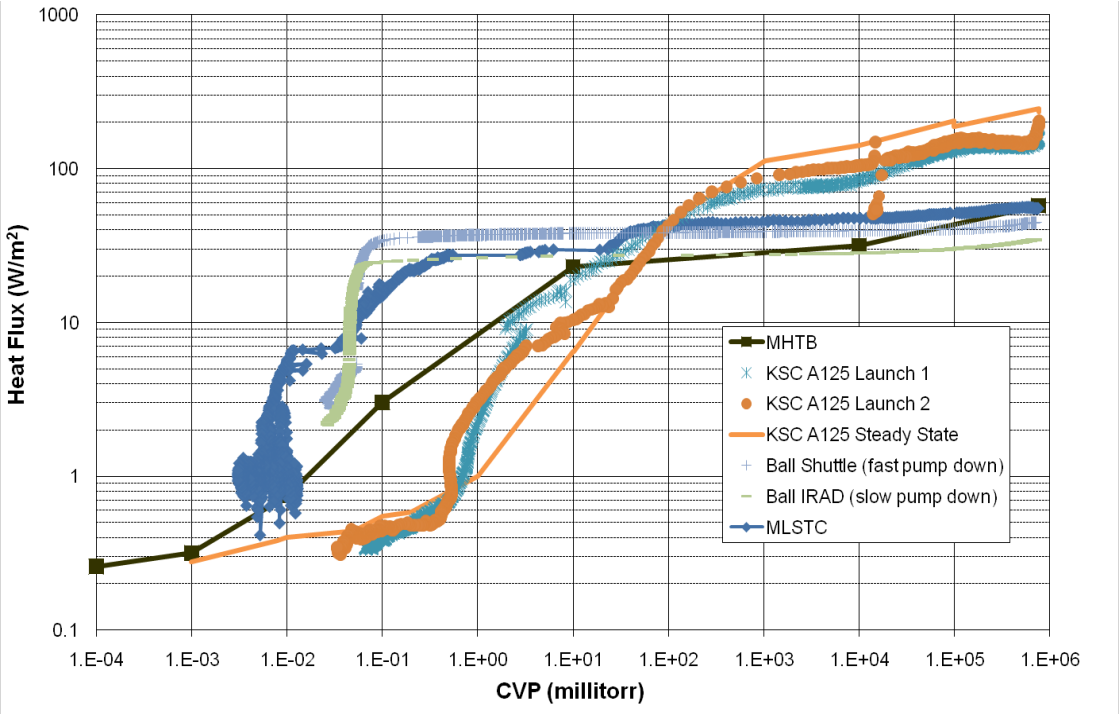

Figure 5: Heat load as a function of Cold Vacuum Pressure

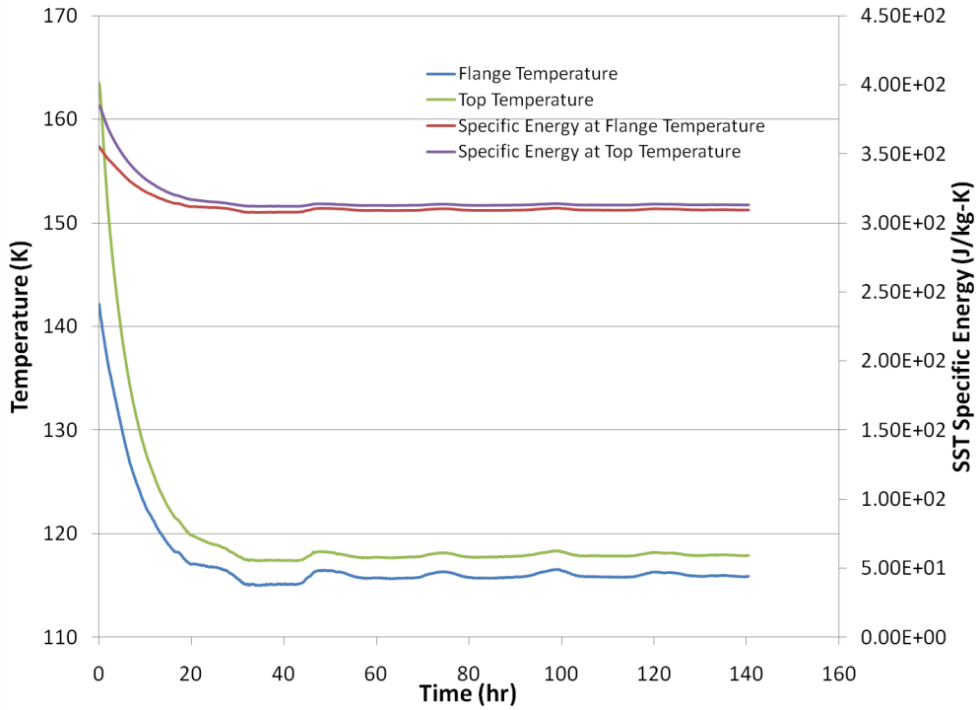

Figure 6: Temperature of the tank lid and flange as a function of time with the associated specific energy of the tank.

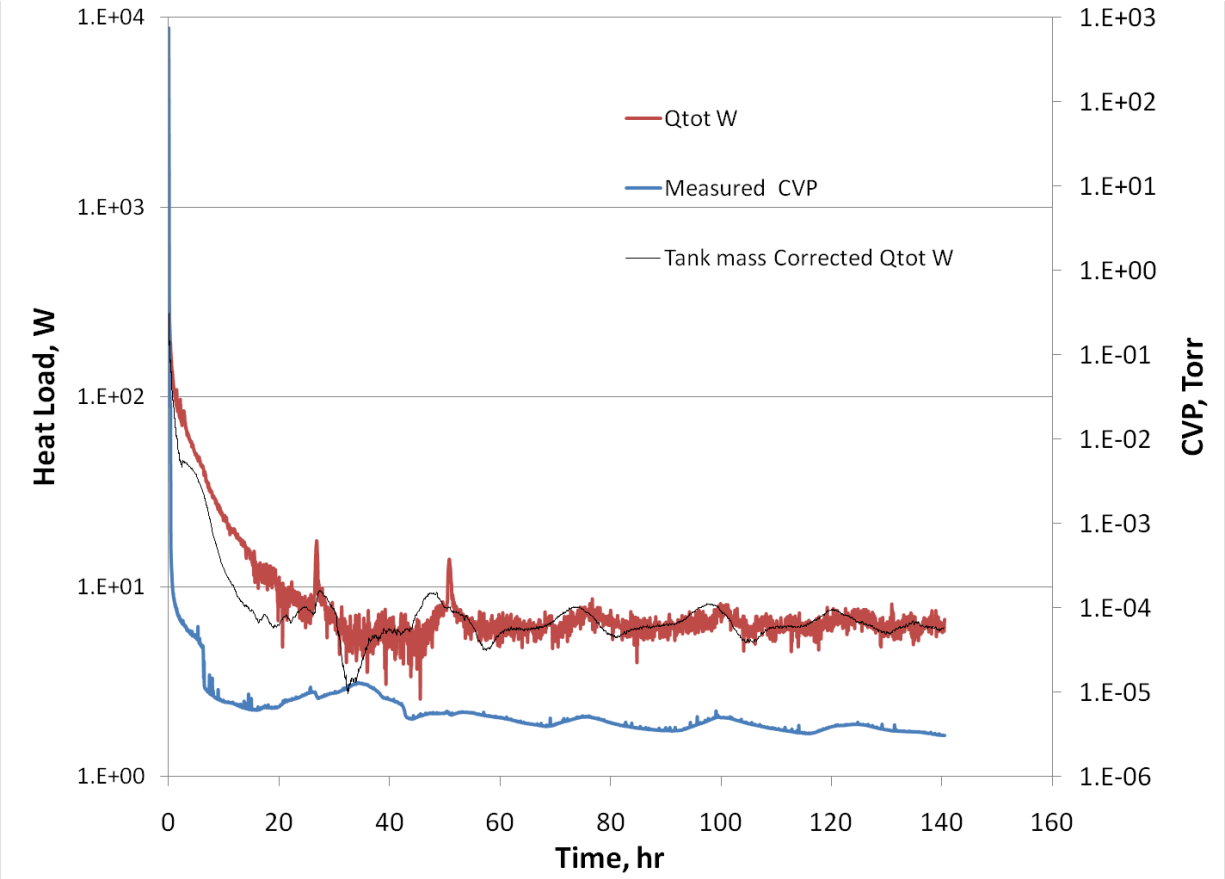

Figure 7: MLSTC heat load and vacuum pressure as a function of time, with averaged data line showing heat load corrected for removing the energy from the tank wall.

Mechanical Design of a 3-Stage ADR for the Astro-H Mission

Bryan L. James[1], Raul M. Martinez[1], Peter Shirron[1], Jim Tuttle[1], John J. Francis[1], Marcelino Sansebastian[1], Donald C. Wegel[1], Nicholas M. Galassi[2], Daniel S. McGuinness[2], David Puckett[3], Yury Flom[3]

[1]Cryogenics and Fluids Branch, Goddard Space Flight Center
[2]Mechanical Systems and Analysis Branch, Goddard Space Flight Center
[3]Materials Engineering Branch, Goddard Space Flight Center

Abstract:

The x-ray micro calorimeter array in the Soft X-ray Spectrometer (SXS) instrument on Astro-H will be cooled by a 3-stage adiabatic demagnetization refrigerator (ADR). The ADR consists of two mechanically independent assemblies. When integrated with a mounting structure and the detector assembly, they form a self-contained unit that will be inserted into the top end of a liquid helium tank. The unique configuration requires many components and sub-assemblies to be thermally isolated from their structural mount. Normally in an ADR this is limited to suspending cold salt pills within their (much warmer) magnets, but in the case of SXS, it also involves one ADR stage being supported by, but thermally isolated from, the helium tank. This paper will describe the complex thermal and mechanical design of the SXS ADR, and summarize vibration and mechanical properties tests that have been performed to validate the design.

KEYWORDS: thermal conductivity, adiabatic demagnetization refrigerator (ADR)

INTRODUCTION

The 3-stage adiabatic demagnetization refrigerator (ADR) will be the first multi stage ADR to fly in space. For this reason, the ADR was mechanically designed to optimize structural ability and to minimize thermal conductivity between components. All three stages of the ADR consist of salt pills properly suspended for minimal heat transfer from their surrounding shielding and structure. Two of the four heat switches are vertically stacked aside the first two ADR stages and are structurally supported by the surrounding stack up of tubes and rings along with similar suspension systems to minimize heat transfer. All four heat switches consist of specially designed fins for thermal and structural ability. Furthermore, materials with high strength and low thermal conductivity have been used to provide the structural support throughout the ADR. Among those materials are Kevlar 49 195 Denier and titanium 15-3-3-3. The launch temperature of the ADR will be approximately 1.3 K, and these two materials were mechanically tensile tested at cryogenic temperature to obtain their tensile properties in the launch environment. The entire ADR model has been mechanically analyzed using FEMAP software in addition to being vibration tested at the NASA Goddard Space Flight center. More in depth discussion of the ADR design in addition to the results of analysis, environmental testing and materials testing will be discussed later.

MECHANICAL DESIGN

All three stages of the ADR, heat switch 3, and the heat switch 1 and 2 stack up are connected to a calorimeter spectrometer insert (CSI) plate that interfaces with the flight hardware on the Astro-H spacecraft. This component was designed by a member of the NASA/GSFC's mechanical engineering branch.

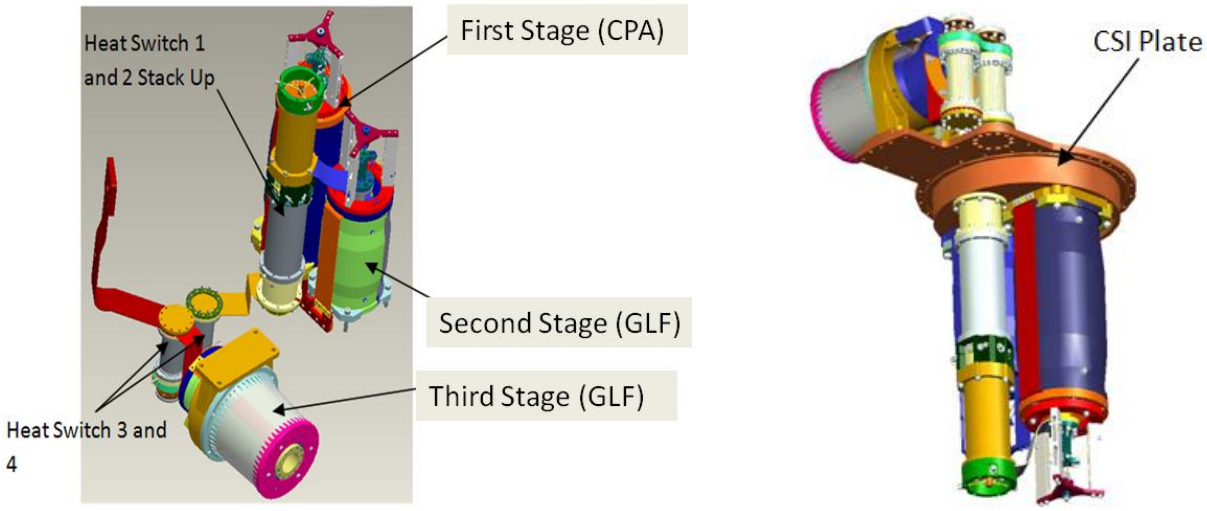

FIGURE 1: Adiabatic Demagnetization Refrigerator (ADR) (with and without CSI plate)

First and Second Stage ADR

The first and second stage of the ADR consists of magnets surrounding suspended salt pills of chrome potassium alum (CPA) and gadolinium lithium fluoride (GLF) respectively. They are mechanically designed very similarly in terms of their structural suspensions at both ends and attachment to the CSI plate. The first stage has more mass. Because of their similar design, only the first stage design is explained in full detail.

A cross section of the first stage ADR is provided in figure 2. The CPA salt pill is made of copper and it is surrounded by a copper magnet consisting of the magnet mandrel and its accompanying copper wire windings. The magnet and salt pill is shielded by a top, bottom, and surrounding shield (the surrounding shield consists of two halves which form a round shield), each made of vanadium permendur. The magnet mandrel is fastened at four places 90 degrees apart on both flanges to the surrounding shield by screws entering through the surrounding shield. To limit the transfer of heat between the salt pill and the surrounding shielding, Kevlar suspension assemblies were designed to provide the structural support. These two assemblies are the Gimbal suspension assembly (GSA) and the lateral suspension design (LSD). The specific Kevlar used in the suspension assemblies is Kevlar 49 195 Denier for its low thermal conductivity at low temperatures. The suspension assemblies will dump an estimated 0.05 μW to the salt pills which will still allow the first and second stage ADR to operate at 0.047 K and 0.500 K respectively.

The LSD is provided in detail in figure 3. The purpose of the LSD is to provide structural support to and restrict the bottom end of the CPA salt pill from any motion in the x and y direction (coordinates provided in figure 3). The assembly is fastened into the magnet mandrel by screws entering through the top ring of the LSD. The LSD consists of three tension arms equally space 120 degrees apart. The angular separation is significant in the fact that Kevlar only works in tension, and any assembly it is used in to

provide static equilibrium must be oriented this way. Also spaced 120 degrees apart and located at the end of each pivot arm is fastener where a bellville stack is sandwiched between the two. The bellville stacks act as springs and are meant to maintain the preload in the Kevlar loop that wraps around each pulley around the fasteners that connect the LSD top ring and tension arms. The Kevlar loop consists of 8 strands. The loop is grabbed at three places 120 degrees apart by the ninja star, which grabs the bottom of the CPA salt pill. The Kevlar is preloaded to 30 lbs and figure 3 provides the direction of the tension at each of the three pulleys where the Kevlar wraps around. The preload is measured based on the bellville stack's distance of compression. As long as the preload in the Kevlar loop is maintained, the bottom of the CPA salt pill will be structurally suspended while maintaining the proper thermal isolation.

The GSA is provided in figure 4. The purpose of this assembly is to provide structural support to and restrict the top end of the CPA salt pill from moving in the x and y direction (coordinates provided in figure 3). Furthermore, the GSA restricts the entire salt pill from movement in the z direction. The GSA fastens to the top shield of the second stage by screws entering through its bottom ring. Three posts are fastened to this bottom ring (equally spaced 120 degrees apart) and they support the top triangle of the GSA, also fastened together with screws. The flange fitting is inserted through the top hole of the triangle and mates with the counter bore surface of the hole. The tension screw is inserted through this flange fitting and fastened at the top of the GSA with a nut. The special tension screw has an end that holds the pulley that has wrapped around it a Kevlar preload loop (16 loops). This Kevlar loop provides the connection in the z direction between the Gimbal and the top of the GSA. The Gimbal is connected to each post of the GSA through three Kevlar loops (8 loops each) spaced 120 degrees apart. As before, this angular spacing is the orientation needed to provide static equilibrium in all directions. The Kevlar preload loop is given a preload of 70 lbs (50 lbs for the second stage). This preload forces a preload of 32 lbs in each of the other Kevlar loops (23 lbs for the second stage). The calculation is worked out below figure 4. Materials tests discussed later will validate the Kevlar loop preloads. As long as the preload is maintained in the Kevlar preload loop, the top of the CPA salt pill will be structurally suspended while maintaining the proper thermal isolation. The CPA salt pill will also maintain its suspension in the z direction.

Analysis and environmental testing was completed to validate the design of these two stages and will be discussed later.

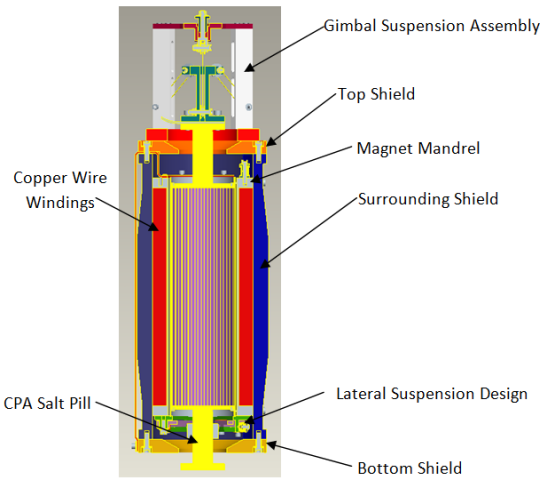

FIGURE 2: Second Stage (CPA Stage) Cross Section

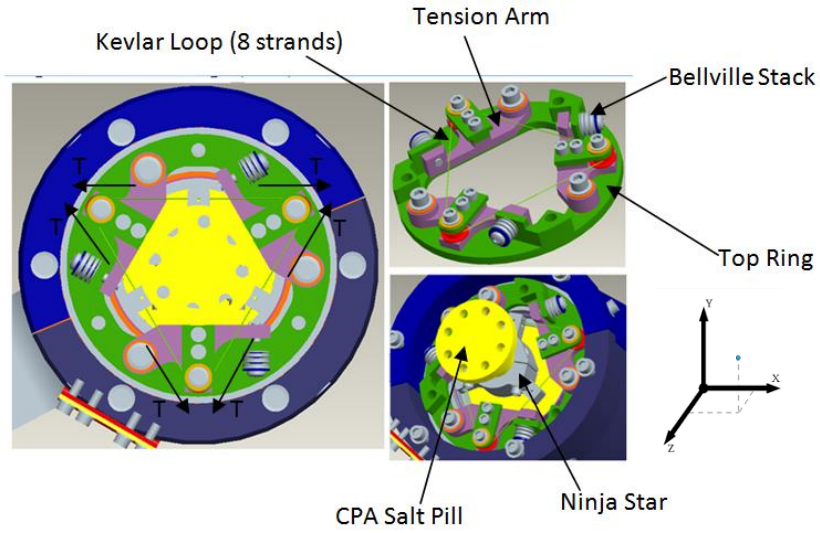

FIGURE 3: Second Stage (CPA) Lateral Suspension Design (LSD). A coordinate system is provided (right).

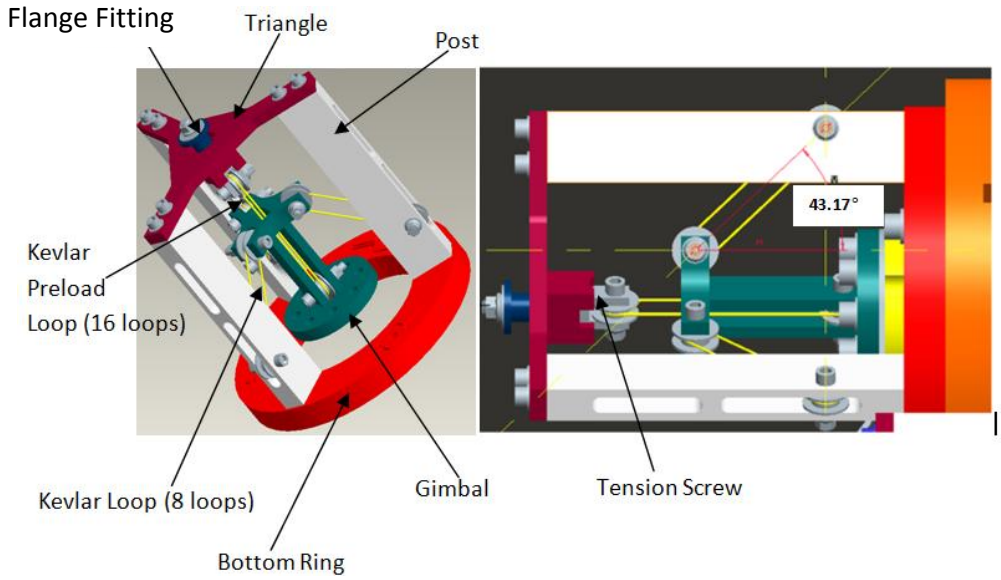

FIGURE 4: Second Stage (CPA) Gimbal Suspension Assembly (GSA)

$$Preload\ Eight\ Loop = \left(\frac{Preload\ Sixteen\ Loop}{3\cos\left(\theta\right)}\right)$$

$$Preload\ Eight\ Loop_{CPA} = \left(\frac{70\ lbs}{3\cos(43.17)}\right) = \mathbf{32\ lbs}$$

$$Preload\ Eight\ Loop_{GLF} = \left(\frac{50\ lbs}{3\cos(43.17)}\right) = \mathbf{23\ lbs}$$

Third Stage ADR

The third stage ADR is designed similarly to the first and second stages. It is provided in figure 5 and has the least mass of the three stages. An LSD assembly is used to structurally support and constrain

movement of the bottom of the salt pill in the same fashion as the first two stages. The main difference with the third stage is the top suspension of the salt pill. Kevlar is not used, but rather a thrust tube assembly to provide the third stage salt pill its structural support. A thrust tube is used for the gimbal assembly to thermally isolate the entire third stage ADR from the CSI plate. The thermal isolation comes from the use of a thin gamma alumina thrust tube (low thermal conductivity material). The thrust tube assembly consists of a top flange attached with scotch weld epoxy to the thrust tube and a bottom flange attached in the same manner. #6-32 screws run through the holes of the thrust tube bracket and fasten into the bottom flange. The thrust tube bracket is attached to the CSI plate. The top flange of the thrust tube assembly is fastened onto the top shield of the third stage by screws. Both the top flange and bottom flange consist of 48 equally spaced fingers 7.5 degrees apart. Analysis and testing performed on this thrust tube assembly to validate the design will be discussed later.

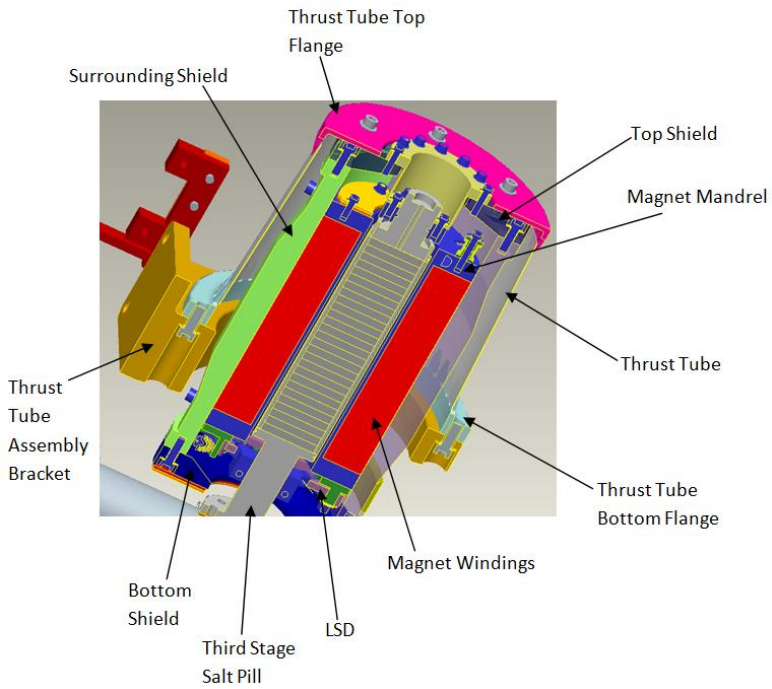

FIGURE 5: Third Stage Cross Section

Heat Switch 1 and 2 Stack Up

The first and second stage ADR are each thermally connected to a heat switch. Due to the area constraints of the CSI plate, these heat switches had to be assembled vertically. The cross section of the heat switch 1 and 2 stack up (HSS) is provided in figure 6. One of the two fins in each heat switch is shown in figure 7. Each individual fin is triangular for increased stiffness from straight rectangular fins. Initially the HSS consisted of the two copper standoffs and the two heat switches. However, early vibe tests indicated that additional structure was needed for design validation. The bottom tube was designed and fastens to the model via screws entering through the bottom copper standoff. The bottom ring fastens to the bottom tube via screws enter through the bottom surface of the bottom ring. Both the bottom ring and bottom tube are made with titanium 6Al-4V. Figure 8 shows the structural design of the bottom support in more detail. Three square cutouts were machined into the middle copper standoff 120 degrees apart about the z axis (coordinates shown in figure 8). Threaded holes for flathead screws were drilled in

the middle of each of the three flats. A pulley was also place at each of the three flats and fastened to the middle copper standoff via the flathead screws through the pulley through holes. The bottom ring was designed with walls 120 degrees apart about the z axis with through holes for #2-56 screws. As shown figure 8, a Kevlar suspension was implemented. A nut and bellville stack (six bellvilles) inserted a special #2-56 screw that had a through hole cut out of it for Kevlar strand clearance. As shown in figure 8, the Kevlar ran around the pulleys in each location and was pulled at either end of the bottom ring walls where the bellville stack, nut, pin, and screw assembly provided the preloading. The Kevlar is wrapped around the small pin and epoxy is applied at each location to securely grab and pull the Kevlar at each location. The Kevlar at each location was preloaded to 24 lbs. Again, Kevlar was used for structural support to provide the necessary thermal isolation from the heat switches to the other ADR components. The preload was measured based on the deflection of the bellville stack at each location.

The second part of the HSS is the top support shown in figure 8. The bottom ring was designed with 5 holes with threading for #2-56 screws. The top tube was designed and fastened onto the bottom ring via screws entering through holes in the top tube flange. The top ring was designed and fastened to the top flange of the top tube. Both the top tube and top ring were also made with titanium 6Al-4V. The support flange was made of copper and was designed with a post with a groove for Kevlar loops to rest. The top ring was designed with flats where through holes were drilled for #2-56 screws. At each of these locations (also 120 degrees apart), the same bellville stack, nut, pin and special screw method was designed to preload the Kevlar. With the support flange fastened to the top heat switch and grabbed at three places by 24 lb preloaded Kevlar, the structural support was complete.

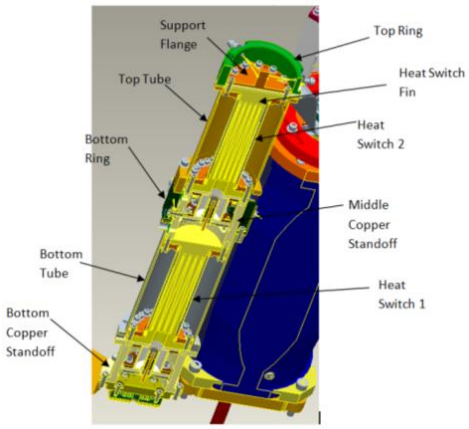

FIGURE 6: Heat Switch 1 and 2 stack up Cross Section

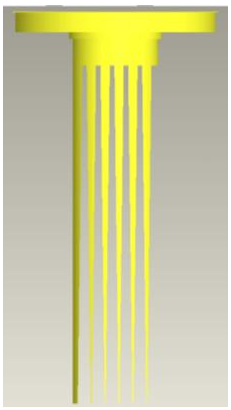

FIGURE 7: Heat Switch Fin

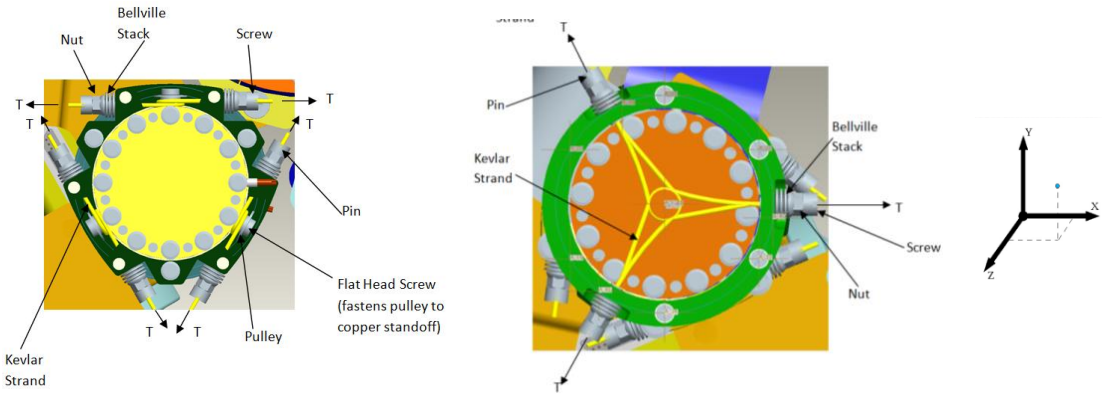

FIGURE 8: Heat switch stack bottom support (right), top support (middle), with coordinate system (left).

Heat Switch 3 and 4

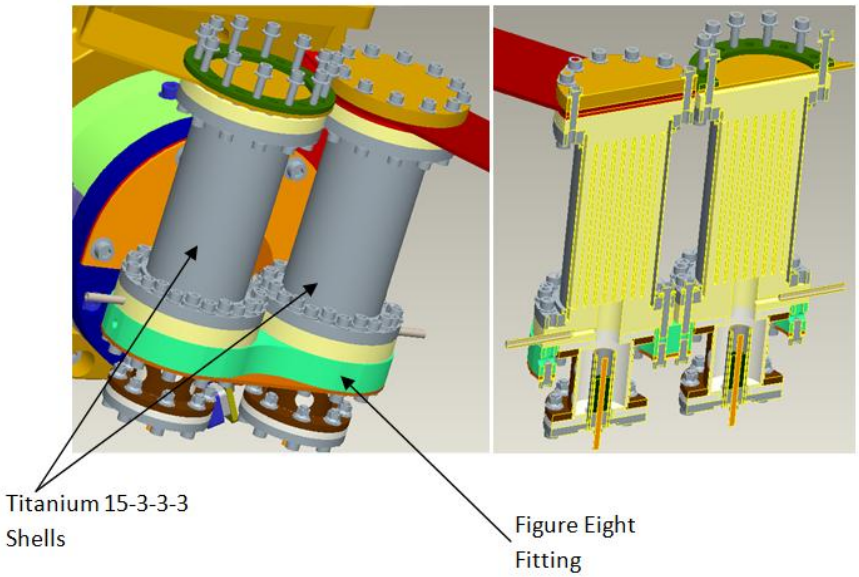

FIGURE 9: Heat Switch 3 and 4 (full picture and cross section)

MECHANICAL AND MATERIALS TESTING

Mechanical Testing

To gain structural confidence in the thrust tube assembly, consisting of the thin gamma alumina thrust tube, the actual assembly was pulled with a force of 200 lbs. The thrust tube neither buckled nor permanently deformed. The test setup is provided in figure 10. In figure 11 is a setup for the heat switches 3 and 4 assembly that were also pull tested. They were pulled to 8 lbs and the deflections ranged from 0.0201 in – 0.0215 in. There was no permanent deformation. As shown in the model, this thrust tube assembly is holding the third stage in a cantilever position, which is why the assembly was pulled laterally.

The 3-stage ADR went through and passed two room temperature vibe tests: full level sine sweep and random vibe test of third stage ADR and heat switch 3 and 4, and full level sine sweep and random vibe test of first stage ADR, second stage ADR, and HSS. Full level vibration test means a 20G.

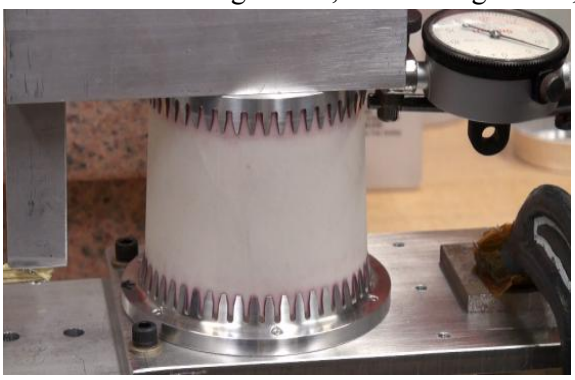

FIGURE 10: Lateral pull test thrust tube assembly

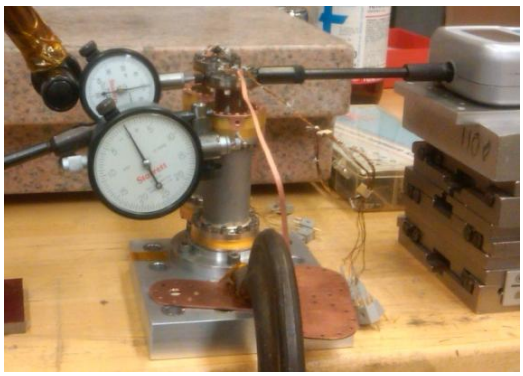

FIGURE 11: Lateral pull test heat switch 3 and 4

Materials Testing

The primary structural support for heat switch 3 and 4 comes from 1.03 inch diameter shells that are 0.005 inches thick (the shells are thin for thermal isolation). The shells are made of titanium 15-3-3-3 for its high tensile strength and low thermal conductivity at low temperatures. The tensile properties of the titanium 15-3-3-3 billet used to fabricate these structural shells were obtained at room temperature and 5.15 K. The room temperature and cryogenic temperature results are provided in detail elsewhere [1]. Results from mechanical simulation analysis verified that the tensile loads the shells will receive during launch are about 20% of the ultimate tensile strength (UTS) at room temperature. The UTS and break strength increased significantly at 5.15 K. Therefore, the titanium shells were approved statically for launch. The majority of the Kevlar 49 195 Denier structural support members are loops consisting of eight strands of the yarn. The mechanical tensile properties of this material were also unknown at cryogenic temperatures. These loops were tested at room temperature and liquid nitrogen temperature (77 K). This was especially important because information from DuPont confirmed that preloading Kevlar 49 to anything above 40% of its ultimate tensile load (UTL) is in danger of stress rupturing [2]. The mechanical tensile properties found through the testing at room temperature and 77 K are explained in detail elsewhere [1]. On average, the UTL at room temperature was 96.1 lbs. Furthermore, it was found that the UTL and young's modulus of the Kevlar loop specimens increased significantly at 77 K. Therefore, it was concluded that as long as the Kevlar structural members were preloaded to less than 40% of the UTL found, the Kevlar would survive the dynamic loads and vibration of launch granted that the those loads were significantly less than the average UTL found.

CONCLUSION

The mechanical design of the Astro-H multi-stage ADR provided the necessary structural ability needed for surviving low temperature launch in addition to limiting any thermal shorting that would hinder the ADR's performance. Mechanical and materials testing further validated the design. In the future, the ADR will be vibe tested at the low launch temperature (approximately 1.3 K) for further design validation. There is confidence in passing the vibe test especially after discovering the mechanical properties of two of the main structural materials/components. This mechanical design has qualified ADR's for space flight projects and will now be considered for future missions.

ACKNOWLEDGEMENTS

This work was part of the NASA Astro-H Small X-Ray Spectrometer (SXS) astronomy mission.

REFERENCES

1) Flom, Yury and Francis, John and Galassi, Nicholas and James, Bryan L. and Martinez, Raul M. and Mcguinness, Daniel S. and Puckett, David and Shirron, Peter and Tuttle, James, "Mechanical Tensile Testing of Titanium 15-3-3-3 and Kevlar 49 at Cryogenic Temperatures."
2) DuPont, *Kevlar Technical Guide*, Section 2 pp 1, Richmond, Virginia
3) Canavan, Edgar R. and DiPirro, Michael J. and Kimball, Mark O. and Shirron, Peter J. and Wegel, Donald C. "Design of 3-Stage ADR for the Soft X-Ray Spectrometer Instrument on the Astro-H Mission."

Development of Porous Plug Phase Separator and Superfluid Film Flow Suppression System for the Soft X-ray Spectrometer onboard ASTRO-H

Yuichiro Ezoe[a], Kumi Ishikawa[a], Takaya Ohashi[a], Hiroya Yamaguchi[b], Kazuhisa Mitsuda[c], Ryuichi Fujimoto[d], Masahide Murakami[e], Kenichi Kanao[f], Seiji Yoshida[f], Soji Tsunematsu[f], Mike DiPirro[g], Peter Shirron[g], and the SXS team

[a] *Tokyo Metropolitan University, 1-1 Minami-Osawa, Hachioji, Tokyo, 192-0397, Japan*
[b] *RIKEN, 2-1 Hirosawa, Wako, Saitama 351-0198, Japan*
[c] *Institute of Space and Astronautical Science (ISAS), Japan Aerospace and eXpoloration Agency (JAXA), 3-1-1 Yoshinodai, Sagamihara, Kanagawa 229-8510, Japan*
[d] *Kanazawa University, Kakuma-machi, Kanazawa, Ishikawa 920-1192, Japan*
[e] *University of Tsukuba, 1-1-1 Tennodai, Tsukuba, Ibaraki 305-8573 Japan*
[f] *Sumitomo Heavy Industries, Ltd., 5-2 Soubiraki-cho, Niihama, Ehime 792-8588, Japan*
[g] *NASA/Goddard Space Flight Center, Greenbelt, MD 20771, USA*

Abstract

ASTRO-H is the sixth Japanese astronomy satellite scheduled for launch in 2014. The Soft X-ray Spectrometer instrument is onboard ASTRO-H. This is a 6×6 array of x-ray microcalorimeters with an energy resolution of <7 eV at 0.5–10 keV. Superfluid liquid helium is utilized as a part of the cooling system. To retain the liquid helium in the tank under zero-gravity, a porous plug phase separator made of sintered stainless is used. Since the vapor mass flow rate is only 29 μg/s, an additional superfluid film loss influences the lifetime of the liquid helium. Therefore, a film flow suppression system consisting of an orifice, a heat exchanger, and knife edge devices is adopted based on the design used for the X-Ray Spectrometer on board Suzaku. The film flow will be suppressed to <2 μg/s, sufficiently smaller than the vapor

flow rate. In the present investigation, the design and ground experiments of a helium vent system composed of the porous plug and film flow suppression system are presented. The results show that the phase separation and the film flow suppression are satisfactorily achieved.
Keywords: Space cryogenics, X-ray microcalorimeter, porous plug phase separator, superfluid film flow

---

1. Introduction

ASTRO-H is the sixth Japanese X-ray astronomy satellite planned to be launched in 2014 [1]. The Soft X-ray Spectrometer (SXS) is an X-ray microcalorimeter onboard ASTRO-H with an extremely high energy resolution of < 7 eV in 0.5–10 keV [2]. The SXS is being developed under the Japan-US collaboration with European participation. Operated at 50 mK, it detects a subtle temperature rise ($\sim$ 1 mK) of a tiny pixel ($\sim$ 800 μm square) due to an absorption of single X-ray photon by using an semiconductor thermometer.

The cooling system of the SXS consists of four 2-stage Stirling (2ST) cryocoolers and one ^{4}He Joule-Thomson (JT) cryocooler to cool 100 K/20 K and 4 K shields, respectively, one superfluid liquid ^{4}He cryostat ($\sim$1.15 K), and an adiabatic demagnetization refrigerator (ADR, 50 mK) [2, 3, 4, 5]. To retain the superfluid liquid helium in the tank under zero gravity and to reduce a helium loss as a superfluid film flow, a porous plug and a film flow suppression system is adopted based on the experience of the X-ray microcalorimeter (XRS) onboard ASTRO-E and Suzaku [6, 7]. The principle and initial design of this SXS helium vent system are described in [8]. Ground testing results for a part of the system are presented in [9]. In this paper, we

review the design of the SXS helium vent system and ground experiments of a test system.

2. Design Overview

2.1. Requirement

Table 1 summarizes SXS requirements on the mass flow rate. The SXS helium tank is designed to contain $\sim$ 30 L liquid. In the nominal operation, an average heat load on the helium tank is estimated as 0.60 mW. Because of this heat load, the liquid helium evaporates from the tank and its latent heat balances the heat load. The expected life time from the heat load and the total volume of the liquid helium is $\sim$ 4.9 years. The expected tank temperature in the nominal operation is $\sim$1.15 K. Since the density of the liquid helium below 1.3 K is 0.145 g cm^{-3}, an average helium mass flow rate becomes 29 μg/s. This number is the smallest among the past space missions as the mass flow rate of the liquid helium.

In addition, the helium vent system have to accommodate two contingency cases. One is the single cryocooler failure case. Even if one of the five cryocoolers stops for some reason, the SXS cooling system is designed to be able to conduct astronomical observations with potential loss of observational efficiency. The heat load on the tank increases and the mass flow rate rises up to 63 μg/s. To keep the ADR performance, the tank temperature should be less than 1.3 K. The other case is the initial operation, in which all the cryocoolers are turned off. The heat load on the tank is as large as 73 mW corresponding to 3400 μg/s. The tank temperature should be kept less than $\sim$2.05 K, i.e., below the λ point of the liquid helium (2.17 K) with

margins.

Besides the mass flow rate, any additional loss due to a superfluid film flow should be minimized. Considering the mass flow rate of 29 μg/s in the nominal operation, the film flow is required to be suppressed below 2 μg/s in this case.

2.2. Design

To achieve these stringent requirements on the vapor mass flow and the superfluid film flow, we designed the SXS helium vent system as shown in figure 1. This system follows and extends the technology applied to the XRS.

The first component is a porous plug phase separator that is a traditional device to retain the liquid helium under zero gravity while releasing boiloff vapor. When the upstream side of the porous plug is attached to the superfluid helium, the helium evaporates within the micro pores of the porous plug due to a thermal input from the outside. The downstream temperature becomes lower because of the latent heat. Then, because of the thermo-mechanical force, the superfluid helium tends to move toward the high temperature side, i.e., the tank. Thus, the liquid helium can be separated from the vapor. Consequently, the temperature difference across the porous plug ΔT correlates with the mass flow rate or the amount of the evaporated liquid helium.

A candidate for the porous plug is the same type as used in the Suzaku XRS [7]. This is made of sintered stainless with a diameter of 8.9 mm and a thickness of 6.3 mm. The Suzaku XRS flight data show that ΔT of 80 mK was achieved at the tank temperature of 1.15 K. The corresponding mass flow rate estimated from the ground testing data is $\sim$ 32 μg/s and hence close to the SXS requirement for the nominal case. Moreover, an estimated

mass flow rate at 2 K of this porous plug based on the equation (1) in [8] is about 3 mg/s. Hence, this type of porous plug may be able to satisfy the requirements on the mass flow rates.

Even though the mass flow rate requirements are met, a film flow can escape from the porous plug due to the van der Waals force. Its amount is proportional to the perimeter of the porous plug and the vent line. If we use the porous plug with a diameter of 8.9 mm, the expected film flow rate from the porous plug becomes $\sim$50 μg/s that is larger than the nominal mass flow rate of $\sim$ 29 μg/s. To stop this unwanted film flow, three additional components are installed.

One is a small diameter capillary or an orifice that follows the porous plug. The narrow tube with inner and outer diameters of 1.4 and 3.0 mm restricts the film flow down to 8 μg/s. To avoid an evaporation of the stopped film by the heat from the downstream, a thermal conductance across the orifice should be low. Hence, the length and material of the orifice must be $>$ 30 mm and stainless, respectively.

Then, a heat exchanger evaporates the film out of the orifice with use of the temperature difference ΔT between the tank and the film flow. The latent heat cools down the tank. A good thermal conductance ($>$ 50 mW/K) is required for an efficient evaporation. For this purpose, the heat exchanger is made of copper and firmly bolted to the tank. Almost all the film flow is expected to evaporate inside the heat exchanger if ΔT is $>$ 50 mK.

Finally, knife edge devices made from silicon wafers stop the remaining film flow with atomically sharp edges by the surface tension. The radius of curvatures of these edges is only $<$ 10 nm. Then, the thickness of the

film flow will be negligibly small (<0.1 nm). Invar is chosen for the flange material because it has a small thermal shrinkage similar to silicon. For the same purpose as the orifice, the two mounting flanges are connected with a low thermal conductance tube with an inner diameter of 1.4 mm. The expected film flow downstream the knife edge devices is less than 2 μg/s.

To prevent a contamination material and a choke of the vent line, a bronze mesh filter with a mesh size of 30$\sim$100 μm is placed in the downstream of the knife edge devices. A contamination from the tank side can be blocked by the porous plug.

2.3. Methodology

The design methodology of the SXS helium vent system is as below. Firstly, we select a proper porous plug that can achieve the SXS requirements on the mass flow rates. Secondly, we design the film flow killer system considering ΔT across the porous plug. Thirdly, we experimentally check the mass flow rates, ΔT, and the film flow rate by building a test helium vent system. Other than these quantities, we study a saturated vapor pressure in the downstream of the porous plug in the nominal operation case and confirm that an expected pressure drop along the vent lines from the downstream of the porous plug to the outside of the tank ($\sim$32 Pa) is lower than the saturated vapor pressure. Otherwise, the helium vapor will not be able to escape to the outside of the tank. In this way, we have to design and test the SXS helium vent system so that the whole system is self-consistent.

3. Measurements of Mass Flow Rates

3.1. Experimental apparatus

Performance tests of the SXS porous plug were conducted in a specially designed helium-4 refrigerator at NASA/GSFC that had been used in those of the XRS porous plug [6]. Figure 2 shows the apparatus. The porous plug inlet was located at the top of the aluminum housing. During each test, the liquid level was raised above the inlet. In this upside down configuration, the porous plug must support the hydrostatic head of liquid which can be minimized by tuning the liquid level. To fit this SXS porous plug inlet in the housing, we introduced an angled adaptor which introduced an extra 1.5 cm hydrostatic head. The total liquid level above the porous plug was at least 2.5 cm, considering the thickness of the top plate of 1 cm.

The orifice and copper cell with a heater and a thermometer were followed by the porous plug. The copper cell was used to estimate an amount of the film flow out of the orifice by determining the necessary power to evaporate the film flow. The expected film flow rate was 8 μg/s corresponding to $\sim$ 170 μW of heat. This was verified by application of 180 μW of heat to the copper cell leading to 100 mK rise of the temperature of the cell. Below this heater power, the temperature rise was negligible.

The tank temperature was controlled by the vacuum pump and measured with a thermometer, while that in the downstream of the porous plug was by a thermometer attached to the porous plug inlet. The liquid level in the tank was estimated with thermometers separated by 1 cm in height with each other. The mass flow rate was adjusted by a control valve and measured by using a Hastings flow meter and a wet drum meter. The former was used for

the large mass flow rate, typically above ∼100 μg/s. The latter was for the small mass flow on the order of 10 μg/s that is difficult to be measured with the Hastings flow meter.

Although the heat exchanger and knife edge devices were not installed in this apparatus due to the limited space in the aluminum housing, the mass flow rate and ΔT of the porous plug will be the same as those in the SXS helium vent system because the film flow out of the orifice will be evaporated in the downstream of the vent line as if there is the heat exchanger.

3.2. Results

Figure 3 displays measurements of the porous plug temperature as a function of mass flow rate at various tank temperatures (1.06∼1.30 K). The SXS porous plug shows similar mass flow rates to those of the Suzaku XRS porous plug when the liquid level is low (3.5 cm). This is natural because both of the porous plugs are made of the same material and have the same geometry.

From the obtained curve, ΔT across the porous plug can be estimated. When the mass flow rate is 29 μg/s (SXS nominal), the downstream side of the SXS porous plug is ∼1.09 K leading to ΔT of ∼60 mK. Because mass flow rates of porous plugs are known to have a hysteresis [10], we here estimate the downstream temperature from the lower branch. This is because the tank temperature and mass flow rate will decrease in orbit by turning on the cryocoolers after the launch.

With this large ΔT, the film flow will be completely evaporated at the heat exchanger. Also the saturated vapor pressure of helium 4 at 1.09 K is ∼35 Pa and higher than the estimated pressure loss along the vent line (32 Pa). Thus, the SXS requirements in the nominal operation case will be

satisfied.

For comparison, the mass flow rates at the high liquid level of 13.5 cm are shown in figure 3. The hydrostatic pressure above the porous plug is 180 Pa. This is not negligible compared to the saturated vapor pressure of the liquid helium at 1.15 K (57 Pa) and 1.30 K (158 Pa). The mass flow rates at the liquid level of 13.5 cm are systematically higher than those at the liquid levels of 3.5 cm (SXS) and 2.5 cm (XRS). This can be understood in the context of the additional hydrostatic head. In the small mass flow rate range, the difference between the two liquid levels seems to decrease. This may be because, in the small flow rate region, the surface tension exceeds the thermo-mechanical force and the porous plug is filled with liquid. In such a situation, ΔT is determined from a balance between the evaporation rate determined by the heat input and the pressure loss at the vent line. Thus, the hydrostatic head effect becomes less significant.

Although the hydrostatic head when the liquid level is 3.5 cm is not negligible in comparison with the saturated vapor pressure of the liquid helium, ΔT will be at worst underestimated. Therefore, we consider that the SXS requirements in the nominal operation case are satisfied with this porous plug, even considering the hydrostatic head effect.

Figure 4 shows the maximum mass flow rates as a function of the tank temperature at high tank temperatures (1.29$\sim$2.11 K). The mass flow rates monotonically increase as the temperature rises because the saturated vapor pressure increases as a function of temperature. The mass flow rate is more than 100 μg/s at 1.3 K and reaches 3400 mg/s around 2.05 K. Therefore, the requirements in the single cryocooler failure and initial operation cases are

satisfied. Even if the mass flow rate in the initial operation is slightly higher than what we expect, we suppose that the tank temperature will be safely kept below the λ point, since the mass flow rate rapidly goes up (e.g., $\sim$4000 mg/s at 2.1 K).

From these results, we conclude that all the SXS requirements on the mass flow rate (table 1) and the vapor pressure (§2.3) can be satisfied by this type of porous plug.

4. Measurements of Film Flow Rates

4.1. Experimental apparatus

Having selected the porous plug, we proceeded to the film flow measurement of the full SXS helium vent system. The experiment was conducted in another helium-4 refrigerator at Sumitomo Heavy Industries, Ltd., as shown in figure 5. This had been used for ground tests of the porous plugs onboard IRTS and Akari. The porous plug and the orifice that were measured in §3 were attached at the bottom of the helium tank. In the downstream of the orifice, the copper heat exchanger, the knife edge devices, and the copper test cell followed. We estimated the amount of the film flow from the evaporation of the film flow and the resultant rise of the temperature at the copper cell, similar to the previous experiment but for the full film flow suppression system. The tank temperature was controlled by the vacuum pump and estimated from the pressure. The mass flow rate of the porous plug was adjusted by a control valve. The downstream temperature of the porous plug was monitored with the thermometer attached to the inlet. The film flow rates were measured at various tank temperatures with ΔT across

the porous plug of $\sim$ 50 mK.

In this apparatus, the liquid helium enters into the porous plug via the gate valve inside the tank. The gate valve was first closed when the liquid helium was filled in the tank and then opened for the measurements. Because of this component, the minimum liquid level above the porous plug in this setup was 5.0 cm, slightly (1.5 cm) higher than that in the mass flow measurement. Several thermometers were set inside the tank to monitor the liquid level. Due to the upside down setup and the hydrostatic head, the film flow measurements can be overestimated what will be expected in orbit.

4.2. Results

Results of the film flow measurement at the tank temperature of 1.15 K are shown in figure 6 (a). ΔT across the porous plug was kept 44$\sim$46 mK. This roughly corresponds to the nominal operation case. To observe the liquid level dependence, two liquid levels were tested. In both liquid levels, when the heater power is low, the temperature rise of the copper test cell is small. It rapidly increases when the heater power exceeds $\sim$30 μW. We fitted the linear portions of the data to estimate the amount of the film flow in the downstream of the knife edge devices. The x intercept indicates the necessary heater power to evaporate the film flow. The intercepts give the film flow rates were 26 μW or 1.2 μg/s and 30 μW or 1.4 μg/s at the liquid levels of 5 and 12 cm, respectively. We consider that the slightly larger film flow at the high liquid level is due to the hydrostatic head. In either case, the film flow is less than the SXS requirement of 2 μg/s. Because there must be the hydrostatic head and ΔT is slightly smaller than the nomical case, these numbers can be considered as upper limits.

We also conducted the similar measurement at the tank temperature of 1.30 K. The result is shown in figure 6 (b). ΔT across the porous plug was again kept $\sim$46 mK. The estimated film flow was $\sim$0.7 μg/s at the liquid levels of both 5 cm and 12 cm. Therefore, the film flow rate is again smaller than the SXS requirement. The liquid level dependence seems to be weaker at 1.3 K than that at 1.15 K because a saturated vapor pressure is higher at 1.3 K and the hydrostatic head becomes less significant.

5. Conclusion

The SXS helium vent system composed of the porous plug and film flow suppression system has been designed to accommodate to the stringent requirements on the mass flow rate, vapor pressure, and film flow. The test system has been built and tested on ground. Results of the mass flow and film flow measurements indicate that all the requirements will be satisfied with the current design.

Table 1: SXS requirements on the mass flow rate.

Case	Nominal[a]	Cryocooler failure[b]	Initial[c]
Load on the He tank (mW)	0.60	1.1∼1.3	73
He lifetime (years)	4.9	2.7∼2.2	–
Mass flow rate (μg/s)	29	52∼63	3400
He tank temp. (K)	∼1.15	<1.3	<2.05

[a] The nominal operation case where all the cyrogenic components works properly.

[b] The single cryocooler failure case where one of the five (four 2ST or one JT) cryocoolers stops. The heat load on the helium tank is slightly different depending on which cryocooler fails.

[c] The initial operation case after the launch where all the cryocoolers are turned off. Since the cryocoolers will turn on after the launch, the helium life time is not defined.

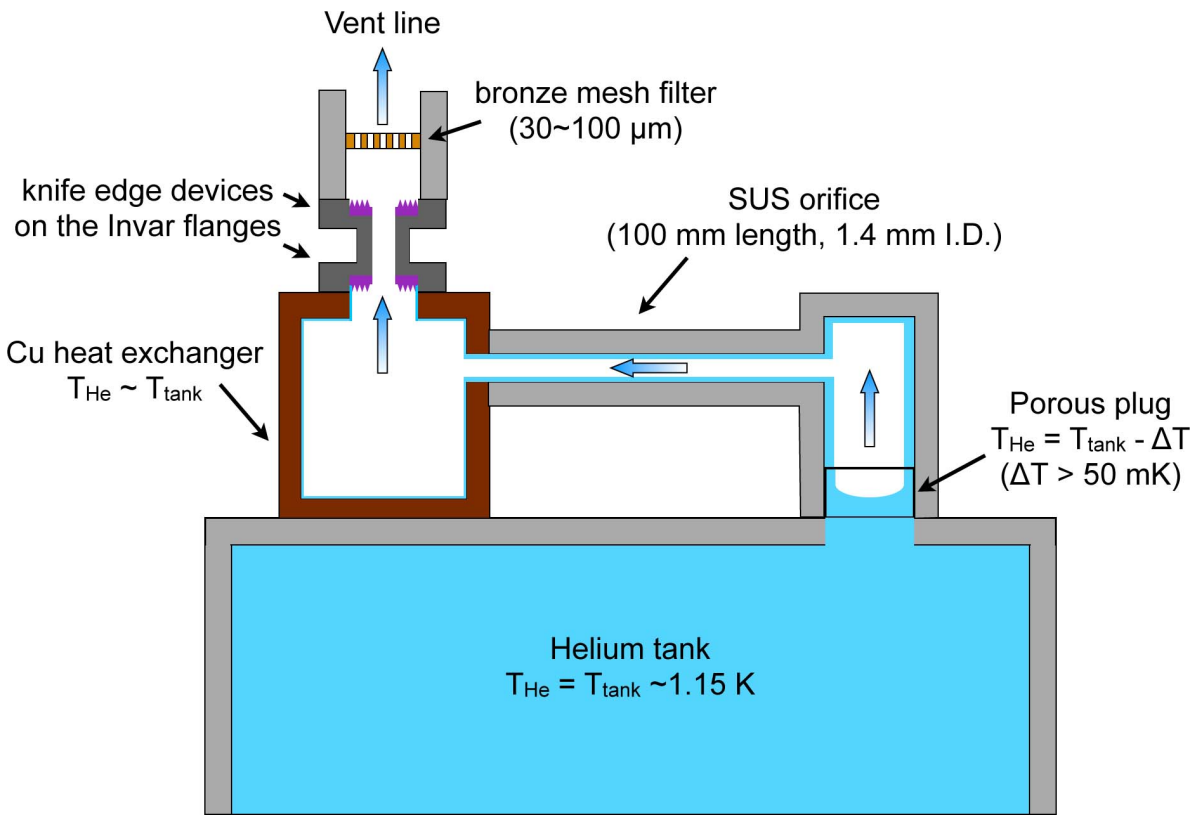

Figure 1: Schematic of the SXS He vent system. An arrow indicates the vapor flow, while blue lines along sidewalls of the vent lines represent the superfluid film flow.

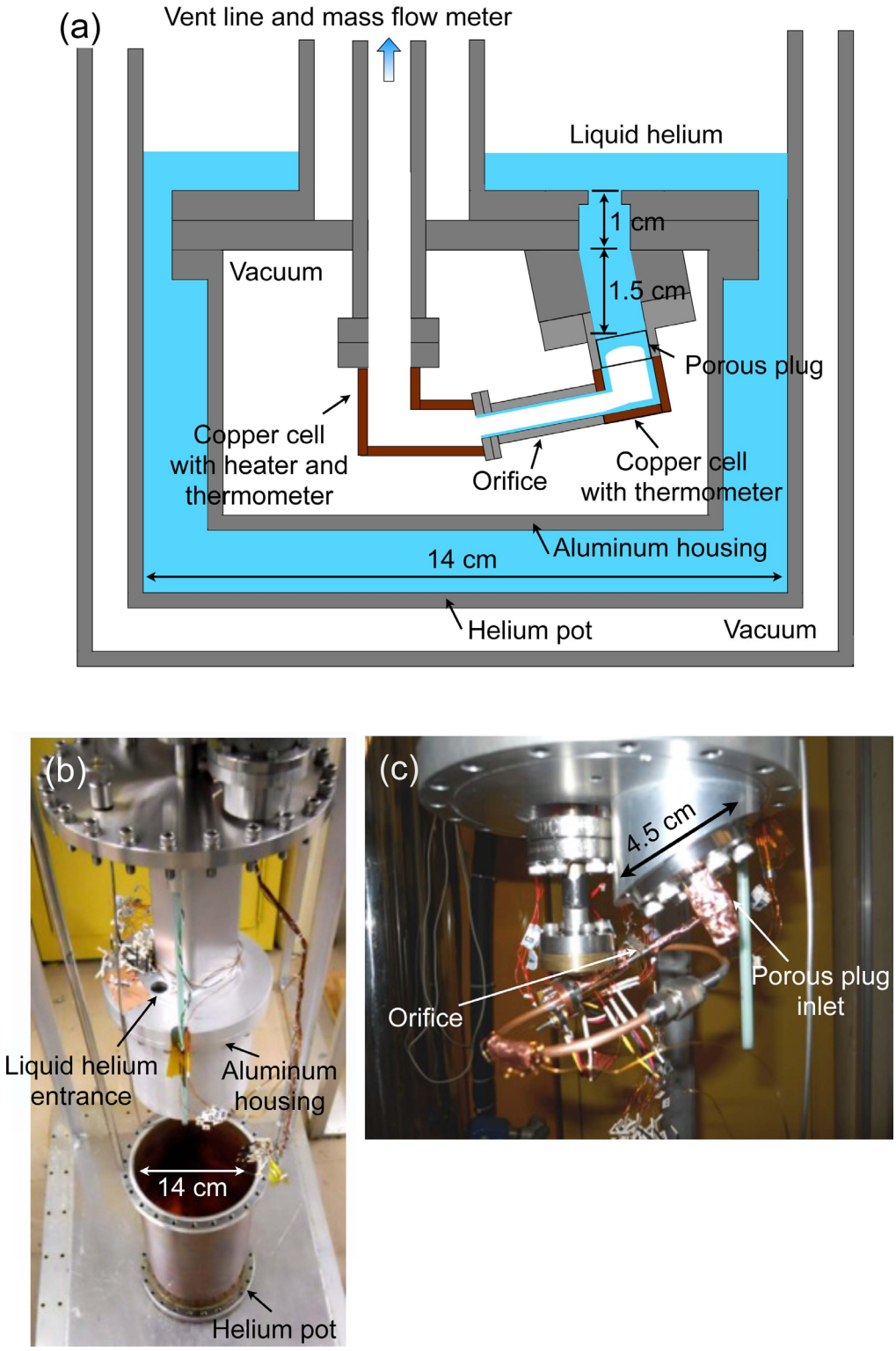

Figure 2: (a) Cut-away of a helium-4 refrigerator used for the mass flow measurement. (b and c) Photographs of the apparatus.

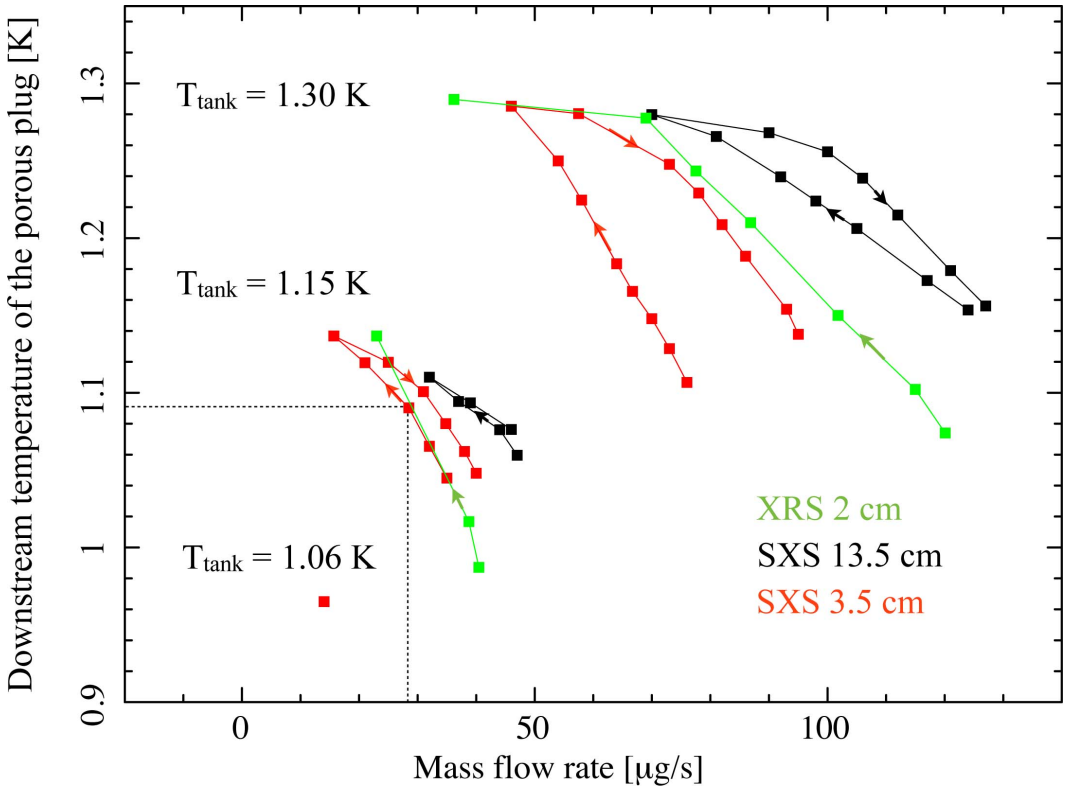

Figure 3: Downstream temperature of the porous plug as a function of mass flow rate at various tank temperatures. Different colors correspond to different porous plugs and/or liquid levels. The liquid level includes an 2.5 cm offset due to the porous plug inlet and the top plate (see figure 2). As a reference, the Suzaku XRS flight porous plug data measured with the same refrigerator are plotted. Dashed lines indicate the SXS nominal mass flow rate and the corresponding downstream temperature of the SXS porous plug. Arrows indicate directions of the measurements.

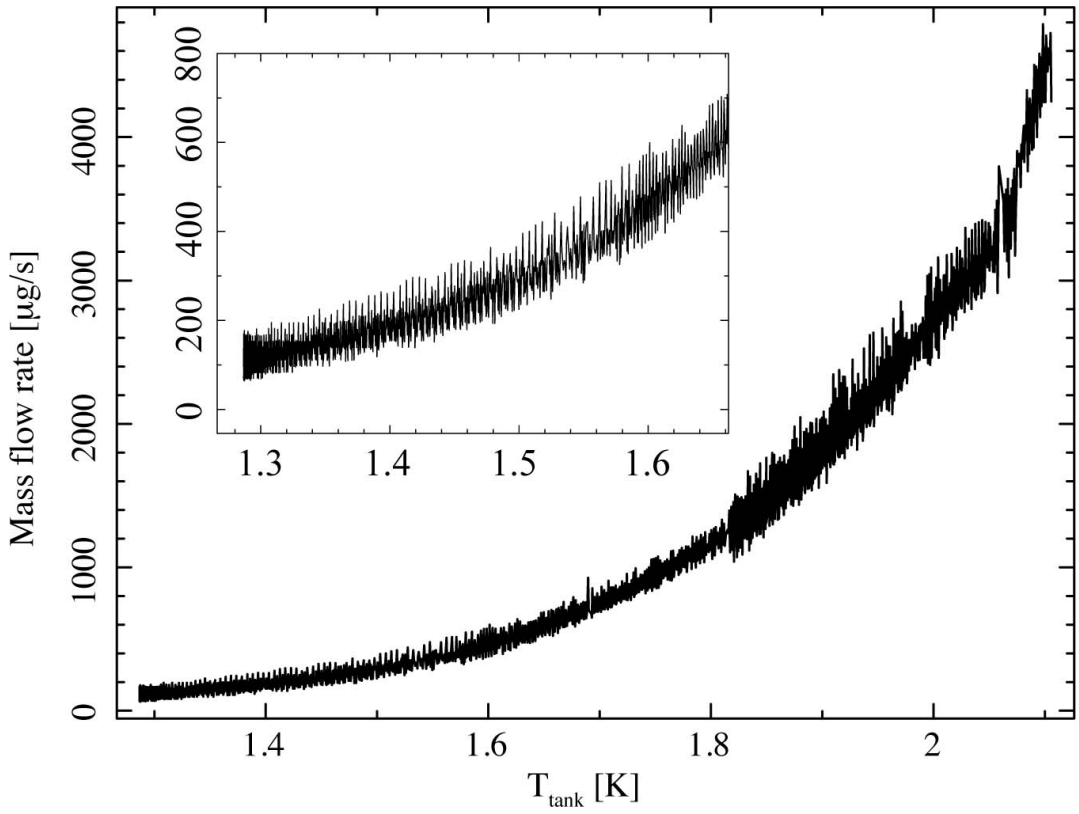

Figure 4: A mass flow rate of the porous plug as a function of the tank temperature. A small panel shows a close-up view of the low temperature region.

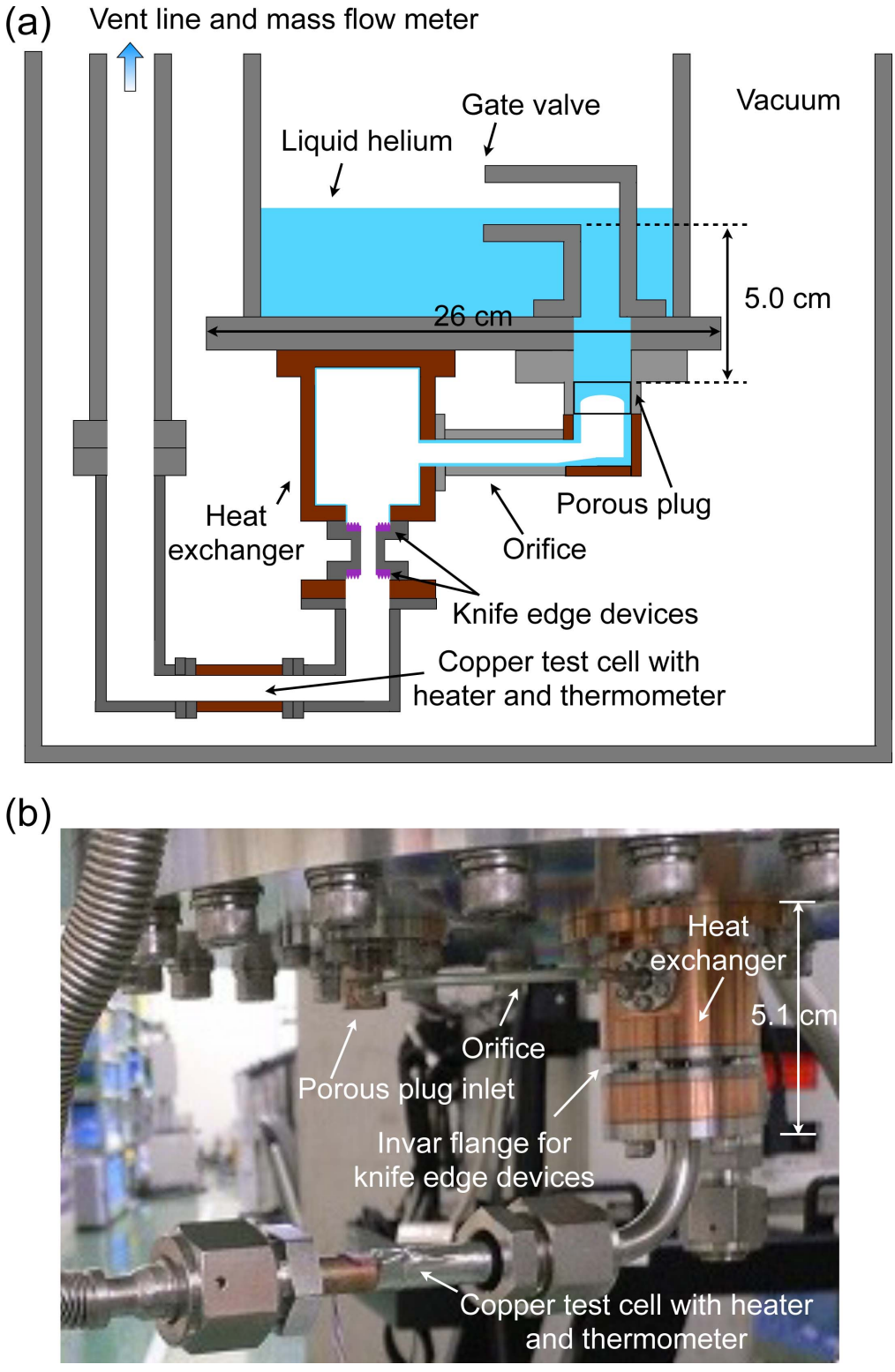

Figure 5: (a) Cut-away of a helium-4 refrigerator used for the film flow measurement. (b) Photograph of the apparatus.

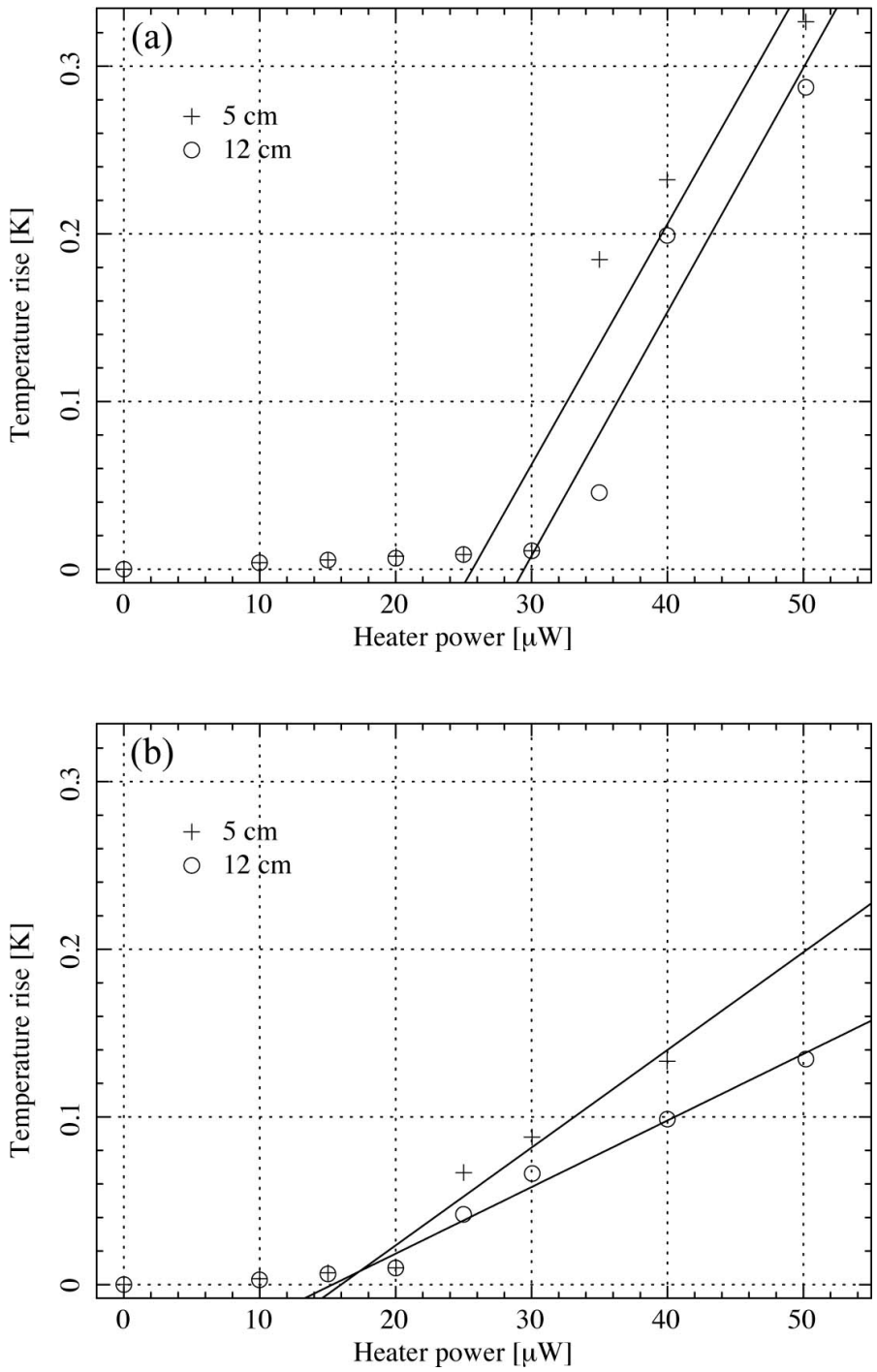

Figure 6: Temperature rise of the copper test cell as a function of heat input at the tank temperature of (a) 1.15 K and (b) 1.30 K. Solid lines are fits to the linear portions of each data set. Cross and circle symbols represent measurements at the liquid level of 5 cm and 12 cm.

References

[1] Takahashi, T., et al. The ASTRO-H Mission. Proc. SPIE 2010;7732:7320Z.

[2] Mitsuda, K., et al. The high-resolution x-ray microcalorimeter spectrometer system for the SXS on ASTRO-H. Proc. SPIE 2010;7732:773211.

[3] Fujimoto, R., et al. Cooling system for the soft X-ray spectrometer onboard Astro-H. Cryogenics 2010;50:488-493.

[4] Sato, Y., et al. Development of mechanical cryocoolers for Astro-H/SXS. Cryogenics 2010;50:500-506.

[5] Shirron, P.J., et al. ADR design for the Soft X-ray Spectrometer instrument on the Astro-H mission. Cryogenics 2010;50:494-499.

[6] Shirron, P.J., DiPirro, Suppression of Superfluid Film Flow in the XRS Helium Dewar. Adv. Cryo. Eng. 1998;43:949-956.

[7] Kelley, R.L., et al. The Suzaku High Resolution X-Ray Spectrometer. Publ. Astron. Soc. Japan 2007;59:S77-112.

[8] Ishikawa, K., et al. Porous plug and superfluid helium film flow suppressor for the soft X-ray spectrometer onboard Astro-H. Cryogenics 2010;50:507-511.

[10] Murakami, M., et al. Experimental Study on Porous-Plug Phase Separator for Superfluid HeII. ISAS Report 1984:612:1-35.

IMPROVED PRESSURE-VOLUME-TEMPERATURE METHOD FOR ESTIMATION OF CRYOGENIC LIQUID VOLUME

Mansu Seo (Corresponding Author)

Cryogenic Engineering Laboratory

Division of Mechanical Engineering, School of Mechanical, Aerospace and Systems Engineering

Korea Advanced Institute of Science and Technology

291 Daehak-ro, Yuseong-gu, Daejeon, 305-701, Korea

Fax : +82-42-869-8207, E-mail address: hipana@kaist.ac.kr

Sangkwon Jeong

Cryogenic Engineering Laboratory

Division of Mechanical Engineering, School of Mechanical, Aerospace and Systems Engineering

Korea Advanced Institute of Science and Technology

291 Daehak-ro, Yuseong-gu, Daejeon, 305-701, Korea

Fax : +82-42-869-3210, E-mail address: skjeong@kaist.ac.kr

Young-suk Jung

Department of Propulsion System,

Korea Aerospace Research Institute

Jakyung Kim

Division of Mechanical Engineering, School of Mechanical, Aerospace and Systems Engineering

Korea Advanced Institute of Science and Technology

291 Daehak-ro, Yuseong-gu, Daejeon, 305-701, Korea

E-mail address: kjkwkrud@kaist.ac.kr

Hana Park

Division of Mechanical Engineering, School of Mechanical, Aerospace and Systems Engineering

Korea Advanced Institute of Science and Technology

291 Daehak-ro, Yuseong-gu, Daejeon, 305-701, Korea

E-mail address: blackcat24@kaist.ac.kr

Mansu Seo[1], Sangkwon Jeong[1], and Young-suk Jung[2], Jakyung Kim[3], Hana Park[3]

[1]Cryogenic Engineering Laboratory, KAIST

[2]Department of Propulsion System, KARI

[3]Mechanical Engineering Department, KAIST

ABSTRACT

One of the most important issues in a liquid propellant rocket is to measure the amount of remaining liquid propellant for reignition under low gravity environment during space mission. This paper presents the results of experiment and analysis of pressure-volume-temperature (PVT) method which is simple, reliable and useful for gauging liquid quantity with uneven liquid-vapor interface. The experiment is conducted using 6.75 liter tank for liquid nitrogen with various liquid-fill level. To maximize the accuracy of PVT method with minimum hardware, the technique of helium injection with low mass flow rate is applied to maintain stable temperature profile in the ullage volume. The PVT analysis considering both pressurant and cryogen as a binary mixture is suggested. At high liquid-fill level of 72%~80%, the accuracy from the conventional PVT analysis is within 5%. At low fill level of 27%~30%, the gauging error is within 3.5% using mixture analysis of PVT with specific low mass flow rate of helium injection. It is concluded that the proper mass flow rate of helium injection and PVT analyses are crucial to enhance the accuracy of the PVT gauging with regard to various liquid-fill level conditions.

Keywords: Pressure-volume-temperature gauging; PVT gauging; Low gravity

NOMENCLATURE

A	:	Area	[m^2]
e	:	Error	[%]
L	:	Height	[m]
m	:	Mass	[kg]
$\dot{m}$	:	Mass flow rate	[kg s^{-1}]
P	:	Pressure	[Pa]
R	:	Gas constant	[J $mole^{-1}$ K^{-1}]
T	:	Temperature	[K]
V	:	Volume	[m^3]
y	:	Coordinate of height	[m]

Greek symbols

ρ	:	Density	[kg m^{-3}]
σ	:	Standard deviation	[%]

Subscript

H	:	High
He	:	Helium
l	:	Liquid
L	:	Low

lm	:	Measured by level meter
mix	:	Mixture
N_2	:	Nitrogen
PVT	:	Measured by PVT method
rep	:	Representative value
tank	:	Tank
temp	:	Temporary
tot	:	Total quantity in ullage volume
u	:	ullage

1. INTRODUCTION

A liquid propellant rocket engine is mostly adopted for modern rocket propulsion system. Liquid propellants which consist of liquid oxidizer and liquid fuel are fed from tanks into a thrust chamber at high pressure condition [1]. Since the weight of liquid oxidizer and fuel occupy approximately 90% of the total weight of vehicle, the optimization of propellant loading on a launch vehicle is the most efficient way to reduce the total weight. It is, therefore, very useful to know the gauging data of the remaining propellant after all propulsion process is finished during the space mission.

There is a sometimes coasting period with zero-thrust about a few minutes or hours for a multistage launch vehicle. In this period, the launch vehicle is placed under low gravity condition. Since the molecular force in fluid such as cohesion, adhesion and surface tension plays greater role under low gravity than under normal gravity, the liquid tends to be spread along a surface of a tank and the vapor is formed globularly in equilibrium state. In this case, it is difficult to gauge the remaining cryogenic liquid in a tank under low gravity condition unlike under normal gravity.

Although there are various gauging methods under low gravity for cryogenic fluid system, pressure-volume-temperature (PVT) method is attractive for its simplicity. In the PVT gauging method, the ullage volume is estimated from the injected mass and the density of a non-condensable pressurant gas (e.g., helium) measured by a mass flow meter (MFM), pressure and temperature sensors. Fill volume of liquid is derived when the ullage volume is subtracted from the total tank volume. PVT gauging method is suitable for space mission because it requires minimal hardware [2]. Also, it is attractive that PVT gauging method is composed of simple and reliable measuring processes.

Various experimental investigations for PVT gauging method have been studied in the

preceding works. The liquid quantity gauging in a small spherical tank with non-cryogenic propellants (e.g., N_2O_4, hydrazine) has been conducted in satellite space missions. It gives very accurate results with 0.2% error, but also sometimes gives maximum error of 1.5 kg when the tank has only 10 kg of fuel [3]. Conventional uncertainty analysis with liquid hydrogen and oxygen has been done and the experiment for liquid nitrogen in the normal gravity has been conducted. The result shows that the accurate gauging is possible within 3% by incorporating liquid nitrogen pump and spray bar to create thermal equilibrium state [2, 4]. However, such a method for cryogenic liquid requires an additional hardware and temperature uncertainty for low liquid-fill level is problematic [4].

In this research paper, the modified experimental technique and their results with no additional hardware such as pump and the results are presented to maximize the advantage of the PVT method. Instead of the pump or spray bar for thermal equilibrium, relatively low mass flow rate of helium injection is applied to stably maintain a thermally stratified temperature condition in the ullage. PVT gauging experiment is carried out using a lab-scale size tank for liquid nitrogen with various conditions of liquid-fill level. Also, PVT analysis considering both nitrogen and helium gas in the ullage as binary mixture is suggested.

2. EXPERIMENTAL APPARATUS AND PROCESS

Fig. 1(a) shows the schematic diagrams of the experiment. The dimensions of the cylindrical tank are 201 mm in diameter, 213 mm in height and 6.75 liter in internal volume. As shown in Fig. 1(b), fifteen E-type thermocouples are installed in the tank in order to measure the vertical temperature profile of vapor and liquid in the tank: six sensors from upper ceiling at intervals of 3 mm and nine sensors at intervals of 20 mm below those six sensors with ±1.0 K accuracy. Pressure sensor measures total pressure in the tank and has 0.1% accuracy of full scale, 300 kPa. Thermal mass flow meter (MFM) with full range of 10 slpm (standard liter per minute) and 0.1% accuracy of full scale is used for measuring the injected mass of helium gas during the pressurization process of PVT method. In the conventional PVT method, the mass of helium for pressurization has been estimated from the change of pressure of helium supply tank, but MFM is used in this research because it gives more accurate value [4]. The pressurized tank is thermally insulated by vacuum and superinsulation (multi-layer insulation, MLI). More information of this experimental apparatus is presented in the reference which is designed for studying self-pressurization research [5].

The experimental process is described as follows. Firstly, liquid nitrogen is charged and nitrogen gas is blown into the tank to purge residual helium or other gases in the ullage volume. After the charging and purging process, the level of liquid nitrogen is measured by a carbon resistor level meter. The level meter operates on the principle which the electrical resistance of a carbon resistor at the tip is changed rapidly when it is immersed in liquid nitrogen due to sudden temperature change. It can measure the height of liquid nitrogen in the tank with ±0.5 mm accuracy, which means ±0.2% accuracy of full volume of the tank. Because the thermal mass flow meter takes a certain period of time to reach the steady state for accurate measurement, the helium gas flow is bypassed until the steady state of the flow

before the pressurization. After confirming the steady state of the flow of helium gas, the vent valve and the bypass valve are closed and steady helium flow is injected to the tank filled with liquid nitrogen. The vertical temperature profile, the pressure in the tank and the mass flow rate of helium are monitored during the pressurization. After the forced pressurization by helium gas, self-pressurization phenomenon is observed due to boil-off gas generated by heat ingress from environment. Even though the experiment in this paper is carried out under normal gravity condition, the purpose of the experiment is to identify key factors that primarily influence the accuracy of PVT gauging method.

3. ASSUMPTIONS AND MODELING

3.1. Assumptions for PVT analysis

The following assumptions are applied to the PVT analysis in this paper.

1. During the helium gas injection, the increase of nitrogen in ullage volume by boil-off is neglected in consideration of short period of pressurization process.

2. The temperature distribution of the ullage volume is determined by conduction heat transfer only when the tank is well-insulated. Therefore, the temperature profile is linear between the liquid-vapor interface temperature, which is the saturation temperature of the liquid nitrogen, and the temperature of the top flange of tank [5].

3. The representative temperature of ullage volume to obtain the density of gas in the ullage is considered using the ideal gas equation as follows.

The temperature of the highest thermocouple in the tank is defined as the high temperature, T_{H}, the temperature of the liquid nitrogen as the low temperature, T_{L}. When the temperature profile is linear, it can be expressed as the function of the coordinate of height, y, as follows.

$$T(y) = \frac{T_{\mathrm{H}} - T_{\mathrm{L}}}{L} y + T_{\mathrm{L}} \qquad (1)$$

Then, with the idea gas equation, the density is described as Eq. (2).

$$\rho(y) = \frac{P}{RT(y)} = \frac{P}{R} \frac{1}{\frac{T_{\mathrm{H}} - T_{\mathrm{L}}}{L} y + T_{\mathrm{L}}} \qquad (2)$$

The total mass of the ullage volume can be calculated by integrating the infinitesimal mass along the height of ullage volume as Eq. (3).

$$m_{tot} = \int_0^L dm = \int_0^L \rho(y) A dy = \int_0^L \frac{P}{R} \frac{1}{\frac{T_H - T_L}{L} y + T_L} A dy = \frac{P}{R} A \frac{L}{T_H - T_L} \ln \frac{T_H}{T_L} \tag{3}$$

Finally, the density can be expressed using the total mass and volume in Eq. (4). Then, the representative temperature in the linear profile is obtained in Eq. (5).

$$\rho = \frac{m_{tot}}{V_{tot}} = \frac{m_{tot}}{AL} = \frac{P}{R} \frac{1}{T_H - T_L} \ln \frac{T_H}{T_L} = \frac{P}{R} \frac{1}{T_{rep}} \tag{4}$$

$$T_{rep} = \frac{1}{\frac{1}{T_H - T_L} \ln \frac{T_H}{T_L}} \tag{5}$$

From Eq. (1) to Eq. (5), the representative temperature in the ullage is derived with the assumption of idea gas for easy derivation, but, in the practical calculation of analysis, the gas density is obtained from $\rho_{rep} = f(T_{rep}, P)$ using REFPROP 7.0 which contains the fluid property database of NIST (National Institute of Standards and Technology). It is assumed that the derived representative temperature using the ideal gas equation is reasonable enough to be used for estimating the accurate representative density of real gas.

4. As shown in Fig. 1, liquid nitrogen and helium gas supply line and feedthrough line have an additional volume which is 2.8% of the internal volume of tank. It is assumed that the

additional volume is filled with helium and nitrogen gas which is the same composition of the ullage volume in the tank so that it is included in the total tank volume for calculation.

3.2. Procedure of modified PVT analysis

The procedure of modified PVT analysis considering the ullage gas as a binary mixture is as follows.

1. The initial representative temperature in the ullage is calculated from Eq. (5) using the measured temperature at the top of the ullage before the pressurization process.

2. Using the initial representative temperature, $T_{\mathrm{rep,i}}$, and the measured pressure before the pressurization, $P_{\mathrm{tot,\,i}}$, the density of nitrogen gas, $\rho_{\mathrm{N_2}}$, is calculated.

3. Because the ullage volume, V_{u}, is not yet known, the temporary mass of nitrogen in the ullage, $m_{\mathrm{N_2,temp}}$, is calculated as $m_{\mathrm{N_2,temp}} = \rho_{\mathrm{N_2}} / V_{\mathrm{u,temp}}$ using the temporary ullage volume, $V_{\mathrm{u,temp}}$.

4. The final representative temperature which is after the injection of helium, $T_{\mathrm{rep,f}}$, is calculated from Eq. (5) using the measured temperature at the top in the ullage after the pressurization.

5. The composition of mixture gas in ullage is obtained by $m_{\mathrm{N_2,temp}}$ and the mass of helium in the ullage, m_{He}, measured by mass flow meter. Therefore, the density of mixture gas, ρ_{mix}, is obtained from the measured $T_{\mathrm{rep,f}}$, total tank pressure, $P_{\mathrm{tot,\,f}}$, and the composition of mixture.

6. The ullage volume, V_{u}, is calculated from $V_{\mathrm{u,\,PVT\ mix}} = m_{\mathrm{tot}} / \rho_{\mathrm{mix}} = (m_{\mathrm{He}} + m_{\mathrm{N_2,temp}}) / \rho_{\mathrm{mix}}$. Hence, the liquid-fill level is obtained as $V_{\mathrm{l,\,PVT\ mix}} = V_{\mathrm{tank}} - V_{\mathrm{u,\,PVT\ mix}}$.

7. When V_{u} and $V_{\mathrm{u,temp}}$ does not satisfy the Scarborough's criterion, the process is performed iteratively from beginning with replacing $V_{\mathrm{u,temp}}$ with V_{u} [6].

8. After the calculation routine, the error of the analysis is evaluated as $e_{\text{mix}} = \left| V_{\text{l, PVT mix}} - V_{\text{l, lm}} \right| / V_{\text{tank}}$.

Additionally, since the conventional PVT analysis considering helium only is applied to analyze some experimental results in this paper, the procedure of the conventional PVT analysis is presented simply as follows. By Dalton's law, the partial pressure for helium in ullage is determined by subtracting the nitrogen partial from the measured total tank pressure. Using the measured mass of injected helium gas, m_{He} , and the helium density, ρ_{He} , obtained from the temperature and partial pressure of helium, the ullage volume is calculated as $V_{\text{u, PVT He}} = m_{\text{He}} / \rho_{\text{He}}$. Hence, the liquid-fill level is obtained as $V_{\text{l, PVT He}} = V_{\text{tank}} - V_{\text{u, PVT He}}$. The error of the conventional PVT analysis is defined as $e_{\text{He}} = \left| V_{\text{l, PVT He}} - V_{\text{l, lm}} \right| / V_{\text{tank}}$. The detailed description of the conventional PVT analysis is presented in the reference [4].

4. EXPERIMENTAL RESULTS AND DISCUSSION

4.1. Calibration of PVT method

The preliminary experiment is conducted for the empty experimental tank in the room temperature. Since there is no liquid nitrogen to cause boil-off phenomenon and low temperature condition, it is possible to calibrate and confirm the experiment set-up. The total tank volume including additional volume of the injection and the feedthrough line is measured 7.65 liter from the PVT analysis of mixture, and this is 0.16% error from the actual total tank volume, 7.64 liter. Therefore, the sensors in experimental apparatus and accuracy of PVT analysis of mixture are properly confirmed in the experimental apparatus of this research.

4.2. Results and discussion

As the first attempt, PVT test for high mass flow rate of helium injection has been conducted. As shown in Fig. 2, when the high mass flow rate of helium injection is applied at 80% and 18% liquid-fill level for each 10 and 15 slpm, the temperature profile in the ullage volume is increased significantly and becomes non-linear. Through the conventional PVT analysis considering helium gas only, the error, e_{He} is 1.28% for Fig. 2(a) of 80% liquid-fill level, and 16.3% for Fig. 2(b) of 18% liquid-fill level. The error for the low liquid-fill level is much greater than that for the high one. As the liquid-fill level gets lower, the error of PVT measurement gets larger because of the ullage temperature uncertainty [2]. During the pressurization of helium injection, the temperature in the ullage volume is increased due to the increase of pressure in the ullage and the injected helium from room temperature. After

the pressurization, the ullage becomes cold and thermally stratified again due to heat transfer with the wall of tank and liquid nitrogen. At low liquid-fill level, the increase of temperature in the ullage is caused more conspicuously than at high level, because the core region of ullage is less affected by the cold wall and the interface of liquid nitrogen. Therefore, the temperature profile of Fig. 2(b) in the ullage is grossly higher and more disturbed than the one of high liquid-fill level case, Fig. 2(a). This situation in the ullage is different from the case of the third assumption because the linear temperature profile in the ullage is not maintained. The representative temperature from Eq. (5) does not agree well, either. Since the density from this temperature is also inaccurate, the error of PVT prediction becomes significant.

As a modified method, the lower mass flow rate of helium injection is tried to maintain the temperature profile of ullage in linear and thermally stratified state during the pressurization by helium injection. Table 1 shows the experimental results for various mass flow rates of helium injection, 1, 2, 4, and 6 slpm for three liquid-fill levels; high, middle, and low. For the one liquid-fill level and one mass flow rate, four measurements are conducted, so the indicated error in Table 1 is the average and the standard deviation of the results of those four results. The final pressure after helium injection is 122 kPa for high liquid level, 116 kPa for middle one, and 110 kPa and 115 kPa for low one. Since the total injected mass of helium is too much to meet the same final pressure in the case of low liquid-fill level, the final target pressure needs to be reduced.

From Table 1, e_{He} is smaller in the high liquid-fill level than in the low liquid-fill level in the same way as previously stated. In spite of the application of low mass flow rate, the conflicting results as various liquid-fill levels are observed due to the different characteristics depending on the liquid levels. First of all, at high liquid-fill level, e_{He} is decreased as the helium injection rate is increased even though the change of temperature is larger in Fig. 3(b)

for 6 slpm than in Fig. 3(a) for 1 slpm. It is because the boil-off effect is more noticeable at high liquid level. As shown in Fig. 4, after the end of injection, the self-pressurization rate of the high liquid-fill level is much greater than that of the low one. Generally, for cryogenic liquid storage tank, the higher the liquid-fill case is, the smaller the self-pressurization rate is [7]. However, at high liquid-fill level, short and steep self-pressurization period exists in an initial period and the pressurization rate is reduced after that initial pressure-rise period as shown in Fig. 5 [5]. In the PVT gauging situation, the pressurization period by helium injection is actually overlapped with the period of initial steep self-pressurization. As the overlapped self-pressurization time is longer, it causes larger and unknown boil-off mass of nitrogen vapor in the ullage. As a result, this fact makes the PVT analysis less accurate. Additionally, because the ullage volume is small and the temperature of tank flange is low at high liquid level, the mass flow rate at high level is relatively ineffective to disturb the temperature profile in ullage volume than at low level. Accordingly, in the case of high liquid-fill level with large boil-off mass and the small ullage volume, the high mass flow rate of helium injection and the short pressurization is preferred. In our experiment, the pressurization time of helium injection of 1 slpm takes about 80 seconds and of 6 slpm takes only about 12 seconds. Therefore, for the high mass flow cases, the case of 6 slpm of helium injection produces accurate prediction as 1.14%, and of 10 slpm for Fig. 2(a) of 80% liquid-fill level also gives small e_{He} as 1.28%.

On the other hand, the application of low mass flow rate is effective to get accurate measurement at low liquid-fill levels. At low fill levels, all e_{He} become within 11% and the most accurate result is within 5%. The temperature profile before and after the low mass flow of helium injection is shown in Fig. 3(c) and (d). As opposed to Fig. 2(b), the temperature profile after the injection is stable and continuously maintaining linear shape in the ullage. It is observed that the change of temperature indicated in Fig. 3(d) for 6 slpm is greater and

more unstable than that of Fig. 3(c) for 1 slpm. Besides, the boil-off effect is negligible as shown in Fig. 4. Therefore, at the low liquid-fill level of Table 1, the lower the mass flow rate is expected to have small e_{He}. For the results of 1 slpm at low liquid level, however, the error is over 6%. As mentioned above, the boil-off effect increases as the pressurization time is extended. Since the injection time by 1 slpm, which is typically a few hundred seconds, is several times the injection time of other higher flow rate case, the boil-off mass gets increased and the error becomes large. For the middle liquid-fill level, the impact of self-pressurization and mass flow rate of helium injection is in combination, so the best result is 1.23% for 4 slpm.

Despite applying the low mass flow rate of helium injection, the maximum error is still over 10% at low liquid-fill level. Therefore, another analysis method is demanded to overcome this problem of conventional PVT gauging method. From now, it is examined by the view of e_{mix}, which is calculated from the PVT analysis considering both nitrogen and helium in ullage volume. Through this analysis for mixture, the error from mixture analysis, e_{mix} is within 3.5% in 2, 4, and 6 slpm. The mass fraction of helium in ullage at low liquid-fill level is very small as 1.9%, because the tank is pressurized from 100 kPa to 110 kPa or 115 kPa which is less than the final pressure at high liquid-fill level,. Furthermore, as shown in Fig. 4, the boil-off effect at low liquid-fill level can be neglected on contrary to the high liquid-fill level. It is confirmed that a mixture PVT analysis considering both helium and nitrogen estimates accurately because much more nitrogen mass than helium is in the ullage and nitrogen mass can be accurately obtained due to negligible boil-off effect. On the other hand, at high liquid-fill level, there is greater boil-off mass of nitrogen than the case at low level due to initial steep self-pressurization. It is difficult to predict the nitrogen mass fraction in the ullage due to the considerably increased nitrogen mass by strong boil-off phenomenon.

Consequently, the mixture analysis becomes inaccurate at high liquid-fill level. In the case of high liquid-fill level, the conventional PVT analysis considering only helium is still suitable to measure the ullage volume instead of mixture analysis, because the helium mass fraction is accurately measured by MFM.

5. CONCLUSION

In this paper, several PVT measurement experiments are conducted under normal gravity with various liquid nitrogen levels to seek more accurate PVT gauging method. Without additional devices for maintaining thermal equilibrium in ullage volume, the accuracy of PVT method can be improved with proper application of gauging technique and analysis. From the experimental results, it is observed that there is different characteristic according to liquid-fill level such as temperature uncertainty at low liquid-fill level and initial boil-off effect at high liquid-fill level.

At high liquid-fill, there are the large boil-off mass which makes unknown nitrogen mass significantly in the ullage and the small ullage volume which is hardly disturbed by high mass flow rate of helium injection. The high mass flow rate of helium injection with short pressurization and the conventional PVT analysis considering helium only is preferred for accurate gauging for high liquid-fill level. In 72% ~ 82% liquid-fill level, the accuracy from the conventional PVT analysis is within 5% in most mass flow rates of helium injection. The accuracy can be within 1.5% at high mass flow rate such as 6 slpm and 10 slpm. On the other hand, at low liquid-fill level, the low mass flow rate of helium injection which maintains the temperature profile of the ullage as thermally stratified state is suggested due to very small boil-off rate. Therefore, the partial pressure of nitrogen in the ullage is almost same as the initial condition and the mixture PVT analysis is preferred to estimate the low liquid volume. In low liquid-fill level such as 27% ~ 30%, the gauging error is within 3.5% with mixture PVT analysis in 2, 4, and 6 slpm mass flow rates. It is concluded that the proper gauging technique and analysis are needed for different liquid-fill levels.

In space, the initial rate of self-pressurization is diminished and thermal stratification under low gravity is less significant than under normal gravity due to dominant surface tension

effect. It is expected that more accurate gauging of liquid volume can be possible for remaining cryogen by the modified PVT method using the low mass flow rate of pressurant injection and mixture analysis.

REFERENCES

1. Sutton GP. Rocket propulsion elements:an introduction to the engineering of rockets. John Wiley and Sons; 1992.
2. Van Dresar NT. An uncertainty analysis of the PVT gauging method applied to sub-critical cryogenic propellant tanks. Cryogenics 2004;44(6-8):515-523.
3. Dodge FT. Propellant mass guaging: Database of vehicle applications and research and development studies. 2008. Report nr NASA/CR-2008-215281.
4. Van Dresar NT. PVT gauging with liquid nitrogen. Cryogenics 2006;46(2-3):118-125.
5. Seo M, Jeong S. Analysis of self-pressurization phenomenon of cryogenic fluid storage tank with thermal diffusion model. Cryogenics 2010;50(9):549-555.
6. Chapra SC, Canale RP. Numerical methods for engineers. New York: McGraw-Hill; 2002.
7. Li Z, Xu L, Sun H, Xiao Y, Zhang J. Investigation on performances of non-loss storage for cryogenic liquefied gas. Cryogenics 2004;44(5):357-362.

Table 1. Results of PVT analysis with various liquid-fill levels and mass flow rates of helium injection

Fig. 1. Schematic diagram of PVT experimental apparatus

(a) Assembly of whole experimental apparatus

(b) Detailed locations of temperature sensors in the tank

Figure 2. Vertical temperature profiles with high mass flow rate of helium injection (Solid square, ■: initial condition before helium injection; solid circle, ●: after helium injection)

(a) 10 slpm for 80.2% fill

(b) 15 slpm for 17.8% fill

Figure 3. Vertical temperature profiles with low mass flow rate of helium injection (Solid square, ■: initial condition before helium injection; solid circle, ●: after helium injection)

(a) 1 slpm for 81.4% fill

(b) 6 slpm for 80.2% fill

(c) 1 slpm for 28.4% fill

(d) 6 slpm for 27.2% fill

Figure 4. Pressure data for liquid-fill level with helium injection of 2 slpm (Solid square, ■: 81.1% fill; hollow circle, ○: 27.9% fill)

Figure 5. Schematic diagram of typical self-pressurization curve

	Mass flow rate (slpm)			
	1	2	4	6
High liquid-fill level (72% ~ 82%)				
e_{He} (σ_{He})	2.32 (1.49)	4.55 (1.49)	3.40 (0.52)	1.14 (0.30)
e_{mix} (σ_{mix})	4.60 (2.43)	6.78 (1.83)	6.25 (0.95)	4.36 (0.84)
Middle liquid-fill level (52% ~ 56%)				
e_{He} (σ_{He})	5.58 (1.50)	2.81 (1.39)	1.23 (1.17)	5.21 (0.52)
e_{mix} (σ_{mix})	9.53 (1.75)	6.67 (1.34)	3.56 (1.27)	0.39 (0.15)
Low liquid-fill level (27% ~ 30%)				
e_{He} (σ_{He})	6.06 (3.59)	4.62 (3.40)	8.10 (3.11)	10.7 (1.21)
e_{mix} (σ_{mix})	7.04 (3.54)	2.78 (1.20)	2.83 (1.82)	3.38 (1.13)

Fig. 1.

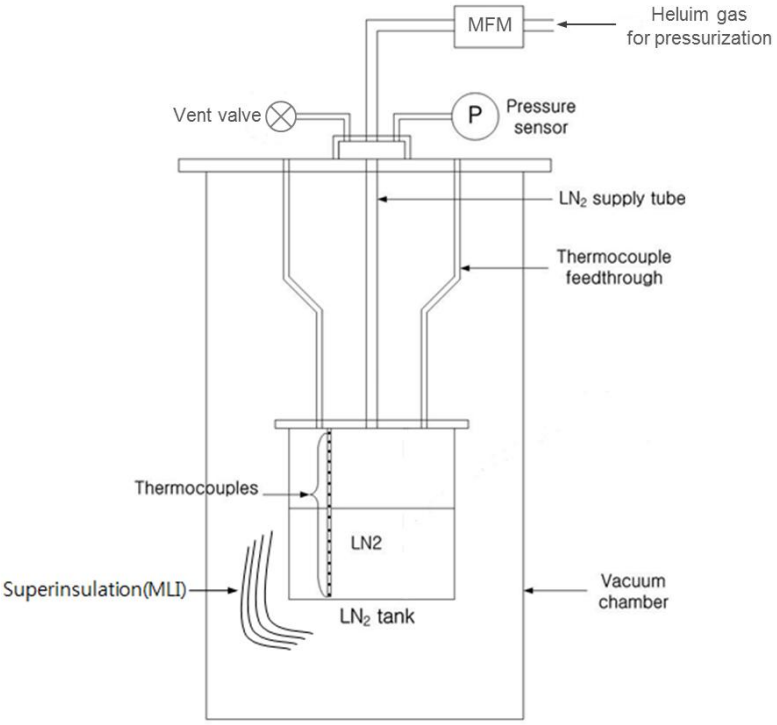
MFM
Heluim gas
for pressurization
Vent valve
P
Pressure
sensor
LN2 supply tube
Thermocouple
feedthrough
Thermocouples
LN2
Superinsulation(MLI)
LN2 tank
Vacuum
chamber

(a)

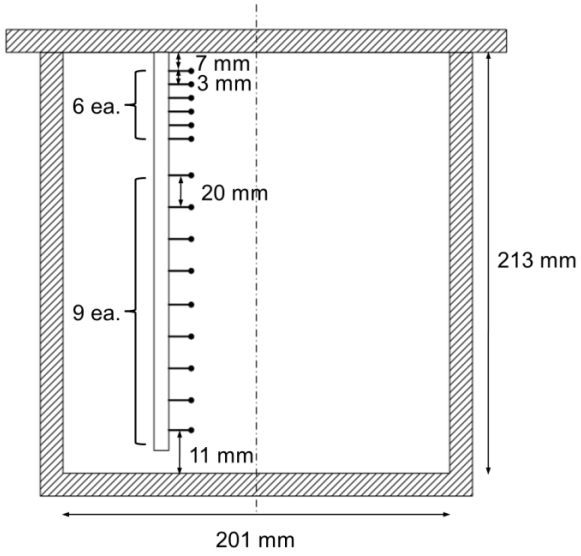
7 mm
3 mm
6 ea.
20 mm
213 mm
9 ea.
11 mm
201 mm

(b)

Fig. 2.

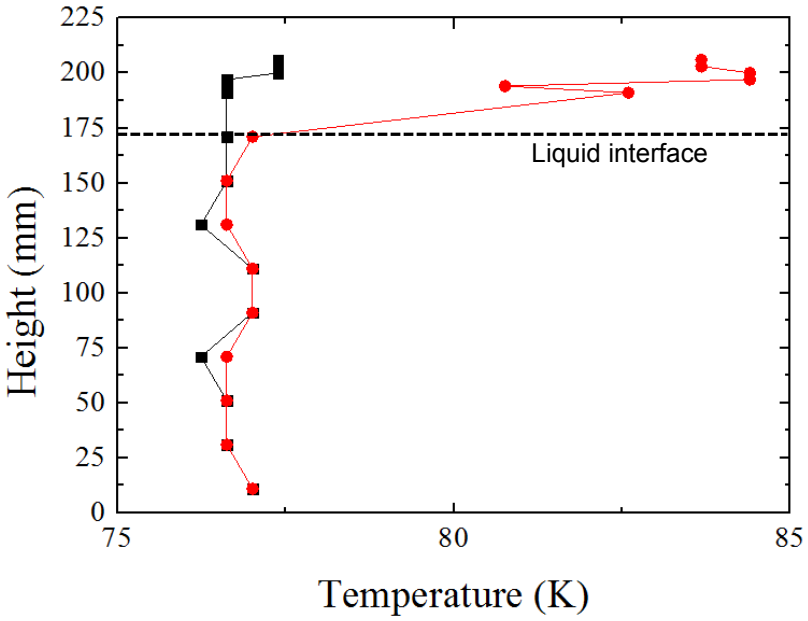
225
200
175
150
125
100
75
50
25
0
Height (mm)
Liquid interface
75
80
85
Temperature (K)

(a)

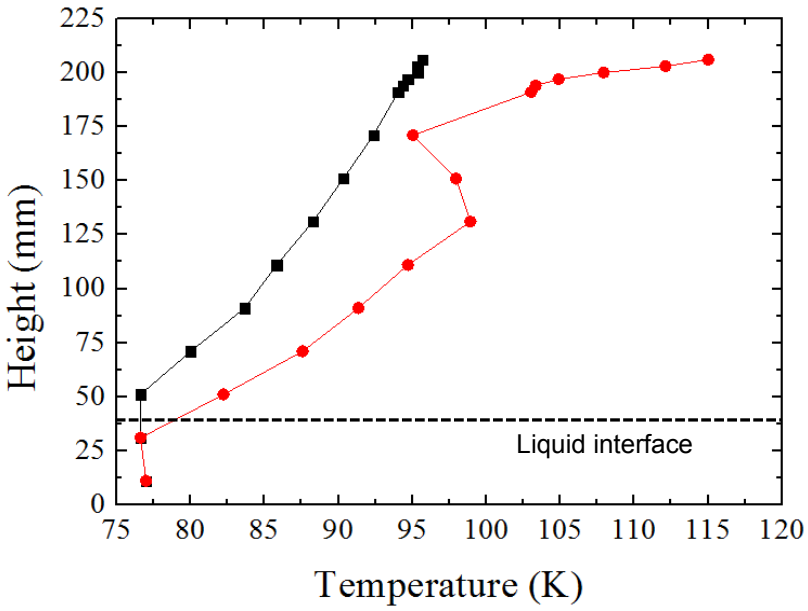
225
200
175
150
125
100
75
50
25
0
Height (mm)
Liquid interface
75
80
85
90
95
100
105
110
115
120
Temperature (K)

(b)

Fig. 3.

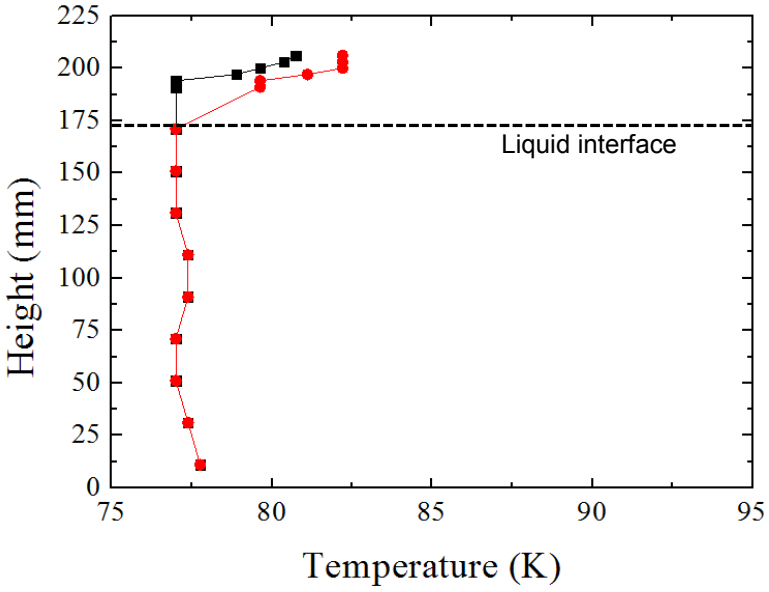
Height (mm)
Temperature (K)
Liquid interface
225
200
175
150
125
100
75
50
25
0
75
80
85
90
95

(a)

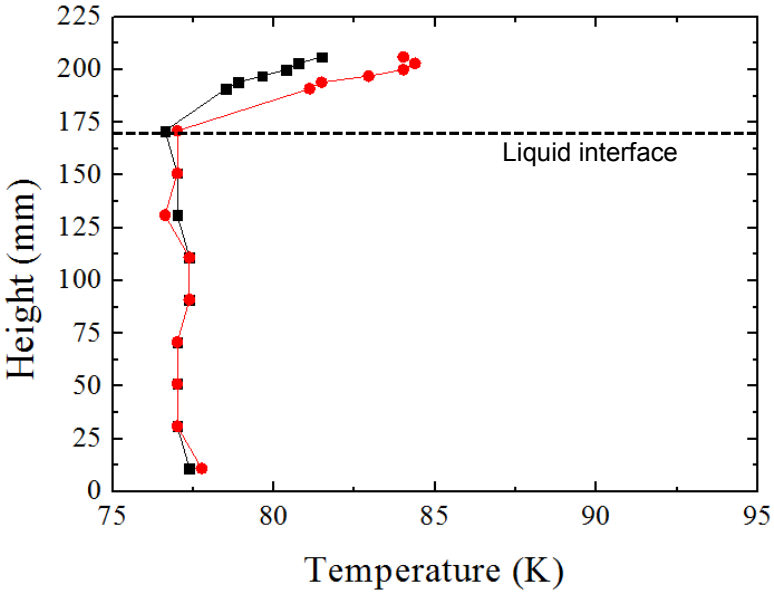
Height (mm)
Temperature (K)
Liquid interface
225
200
175
150
125
100
75
50
25
0
75
80
85
90
95

(b)

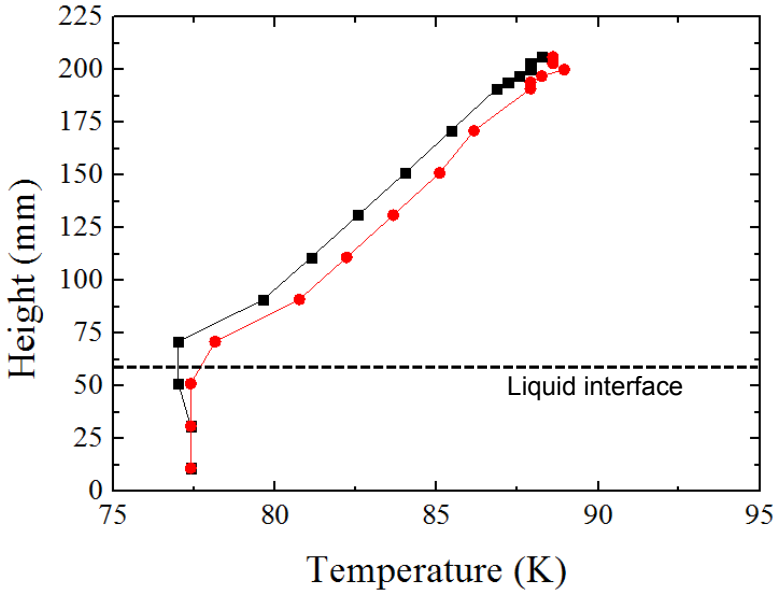
Height (mm)
Temperature (K)
Liquid interface
225
200
175
150
125
100
75
50
25
0
75
80
85
90
95

(c)

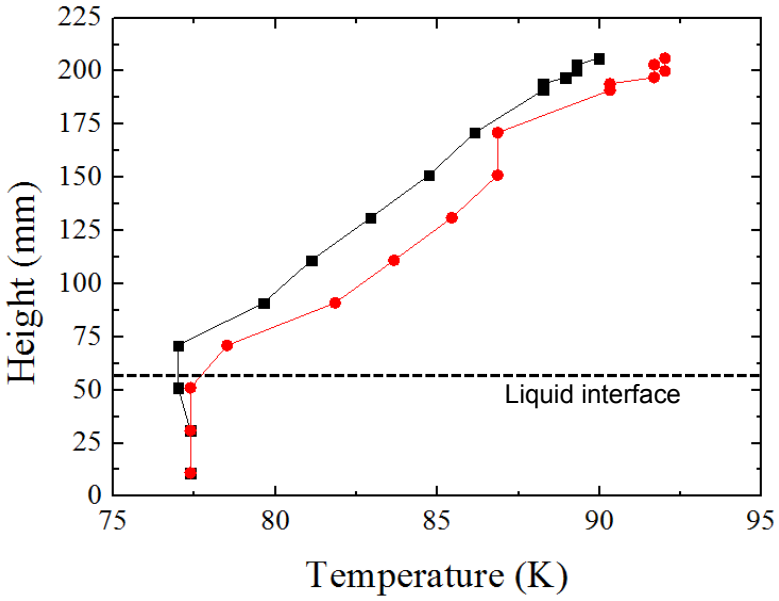
Height (mm)
Temperature (K)
Liquid interface
225
200
175
150
125
100
75
50
25
0
75
80
85
90
95

(d)

Fig. 4.

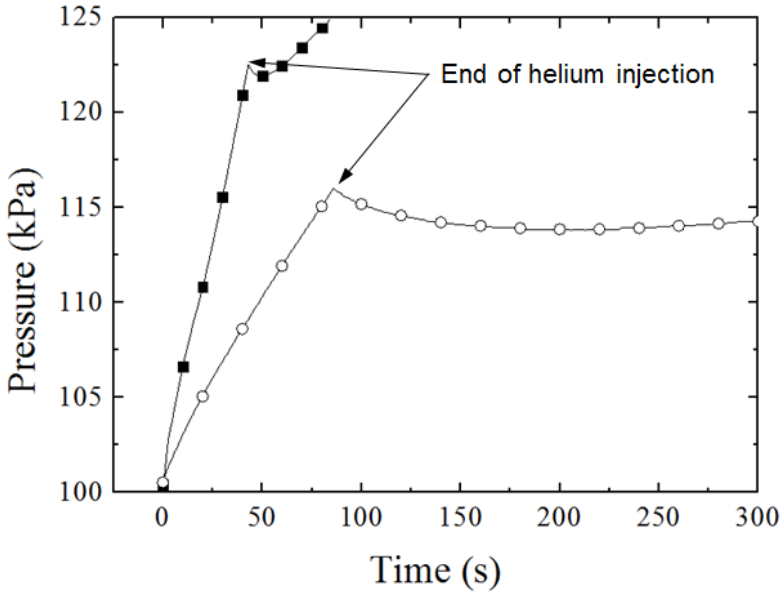
End of helium injection
Pressure (kPa)
Time (s)
125
120
115
110
105
100
0
50
100
150
200
250
300

Fig. 5.

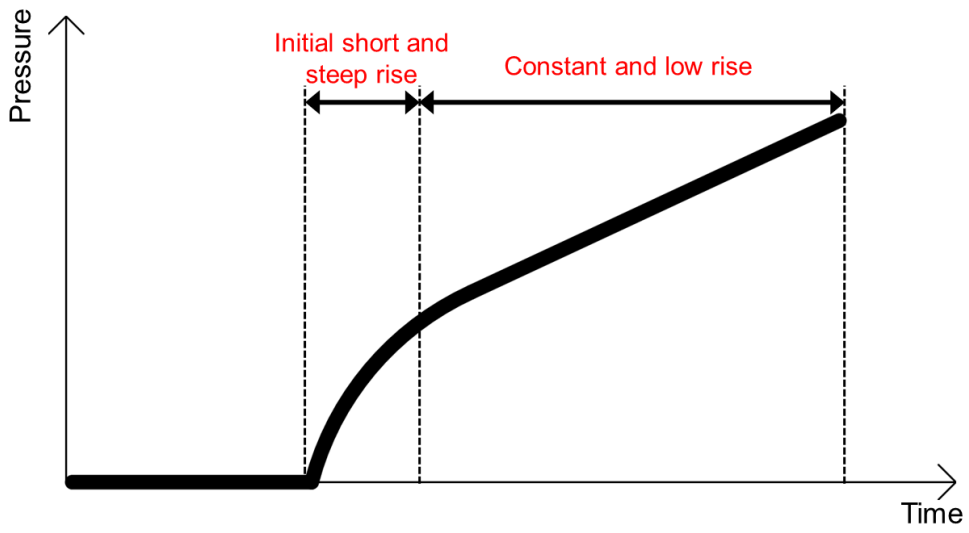
Pressure
Initial short and steep rise
Constant and low rise
Time

Demonstration of liquid nitrogen wicking using a multi-layer metallic wire cloth laminate

Tao Zhang, Ernst Wolfgang Stautner, Peter deBock, Tao Deng, Chris Immer

GE Global Research Center
1 Research Circle, EP-123
Niskayuna, NY 12309

ABSTRACT:

Cryogenic heat transport devices are the most basic and critical component for the thermal integration between the cryogenic component and its cooling source. In space environments, containment of heat transfer fluid inside a capillary structure is critical due to the absence of gravity. Cryogenic heat pipes using the capillary force for circulation may provide a solution for heat transfer in space applications due to its independence of gravity and transport distance. To achieve a high effective capillary performance, several options of wicking structures have been investigated. An efficient wicking flow of liquid nitrogen is demonstrated with a sintered, multi-layer, porous lamination of metal wire (pore size as low as 5 micro meter) in an open cryogenic chamber. The test data are presented in this paper. This technology has potential for use in development of improved cryogenic heat transfer devices and containment of cryogenic propellants under micro-gravity environment.

1. INTRODUCTION

One of the greatest challenges of spaceflights is the management of propellant in storage tanks in the absence of gravity. The propellant management device must work in all mission accelerations and operating conditions to ensure a reliable and consistent connection between the propellant and the tank outlet [1, 2]. Furthermore, it has to be carefully designed to supply the propellant in liquid form without gaseous inclusion. To achieve this goal, wicking structures are known to work. Figure 1 shows a passive surface tension device used to provide gas free propellant in micro-gravity environment. As illustrated, the wicking structures remain constantly saturated with liquid propellant. In case any drying has occurred, the capillary force generated by the wicking structures can work as a self-healing mechanism to replace liquid and restore the propellant transportation. The same wicking structures may also be used for confinement of the propellant at a designated location.

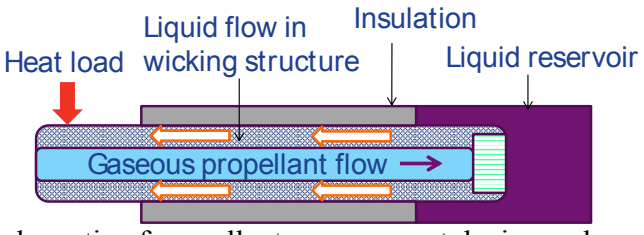

Figure 1. A schematic of propellant management device under micro-gravity.

On the other hand, thermal management is another challenge in NASA's strategic roadmaps for spaceflight and surface missions. During spaceflights, temperature can range from close to absolute zero when shaded from the sun to hundreds of degrees in full sunlight. In this

case, wicking structures can be used as active elements in thermal switches. The thermal conductivity of wicking structures may vary by several orders of magnitude imply by the presence of absence of the wicking fluid. This switching can occur very rapidly and also be well-controlled to allow precise adjustment of thermal conductivity. Cryogenic heat pipes are common for long distance heat transfer due to its superior high thermal conductivity and flexibility. In space applications, appropriate wicking structures are required due to its independence of gravity. A capillary force based cryogenic heat pipe can provide an excellent solution for the heat link between the cryocooler and distributed heat sources on a spacecraft.

For space cryogenic fluids/propellants management, liquid nitrogen, helium, hydrogen and oxygen are of prime importance. The next generation of cryogen propellants (liquid oxygen and hydrogen) is currently planned by NASA for future space missions. And both liquid helium and liquid nitrogen are the major cooling mediums for on-board scientific instruments or other superconducting devices. However, due to their low surface tension properties, cryogenic fluids are inherently challenging to contain within wicking structures. For example, liquid helium has a liquid transport capillary factor about 100 times lower than water at room temperature. Table 1 lists the capillarity constants of some cryogens. It can be seen that liquid helium has the lowest specific cohesion factor and thus is the most difficult fluid to be wicked, while liquid nitrogen and liquid oxygen have the similar specific cohesion factor. Some previous experiments have been done trying to demonstrate the wicking of liquid nitrogen using conventional metallic mesh structures [3]. Recently we at GE Global Research Center have successfully demonstrated the wicking flow of liquid nitrogen using a special Porostar® type micromesh (see Figure 2). It is a modulated porous structure having 4 stacked layers and the minimum pore size around 5 μm. The modulation should provide extra cross-sectional area for enhanced axial capillary flow and extra evaporation surface area but with only a moderate increase in wick superheat [4]. We in this paper report the experimental data and discuss the future development of nano-scale structures for wicking other cryogen such as liquid helium, oxygen and hydrogen.

Table 1. Capillarity constants of some condensed gases

Cryogen	**Temperature (K)**	**α (dyn/cm)**	**a^2 (mm^2)**	**k**
Helium	4.2	0.12	0.211	1.4
Hydrogen	20	1.98	5.75	1.4
Neon	27	4.69	0.8	1.85
Nitrogen	77	8.7	2.19	2
Oxygen	90	13.2	2.35	-

(a^2=specific cohesion=2α/s; s=specific weight of cryogen;α=surface tension; k = temperature coefficient of the molecular surface energy)

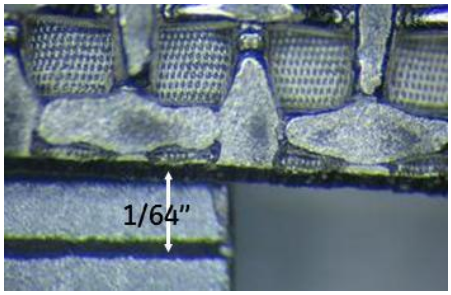

Figure 2. Microstructure of a special Porostar® metal mesh.

2. WICKING OF CRYOGENIC FLUIDS

The selection of a working fluid for two-phase heat transfer systems depends on the desired operating temperature range, maximum system pressure and fluid-structure compatibility. For systems that use a wicking structure, Chi [5] derived a figure of merit for purposes of quantitatively comparing wicking performance of different fluids. This figure of merit includes the density (ρ), surface tension (σ), latent heat of vaporization (h_{fg}) and viscosity (μ).

A fluid has particular high figure of merit due to its high surface tension, density and heat of vaporization. For desired two-phase heat transfer fluids at cryogenic temperatures, fluids such as helium, hydrogen, nitrogen and oxygen are potential working fluids.

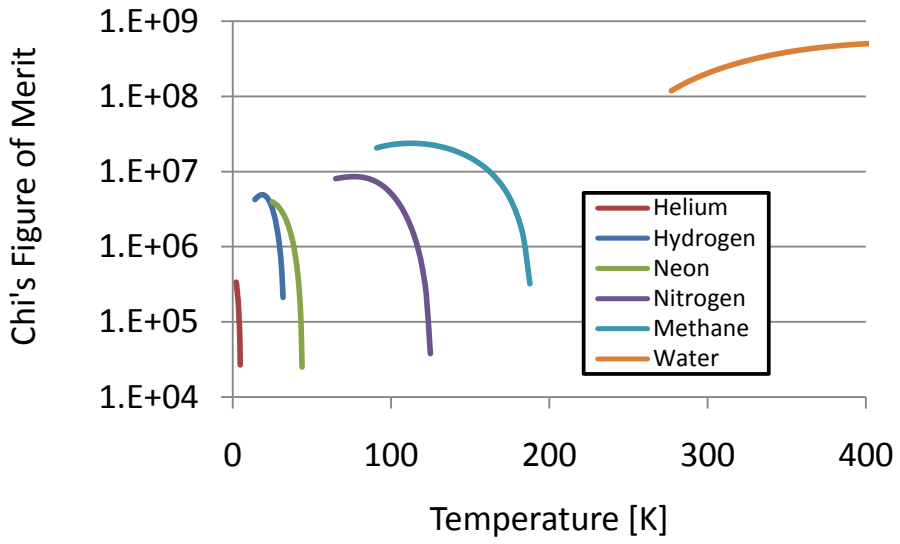

Figure 3. Comparisons of Chi's FOM of different fluids

A challenge that can be observed from Figure 3 is that cryogenic fluids in general can have FOM up to three orders of magnitude lower than water at room temperature. This indicates the difficulty of designing a two-phase heat transfer system for cryogenic applications that utilize wicking structures.

$$\Delta P_c = \frac{2\sigma \cos\theta}{r_c} \qquad (1)$$

The capillary pressure that can be exerted on a fluid by the meniscus at the liquid-vapor interface is a function of the surface tension of the fluid, effective pore radius of the wicking structure and the contact angle between fluid and structure [6]. In a configuration where a section of the wicking structure is submerged in an open reservoir, the height of the liquid column due to capillary effects is often used as a metric for wicking performance. This height (h) is a function

of the equilibrium between the capillary (ΔP_c) and the hydrostatic (ΔP_g) pressures at the liquid interface which are described by the following equations

$$\Delta P_g = \rho g h \qquad (2)$$

$$h = \frac{2\sigma \cos\theta}{\rho g r_c} \qquad (3)$$

Assuming zero contact angle, Figure 4 shows the relationship between pore radius (r_c) and liquid column height (h). It can be concluded that in order to achieve significant wicking effect and capillary rise for liquid helium, wicking structures with sub-micron or nanometer effective pore radius are required. For instance, to sustain a liquid helium column of 1.5 m high, the wick pore diameter has to be in the range of 190 nm.

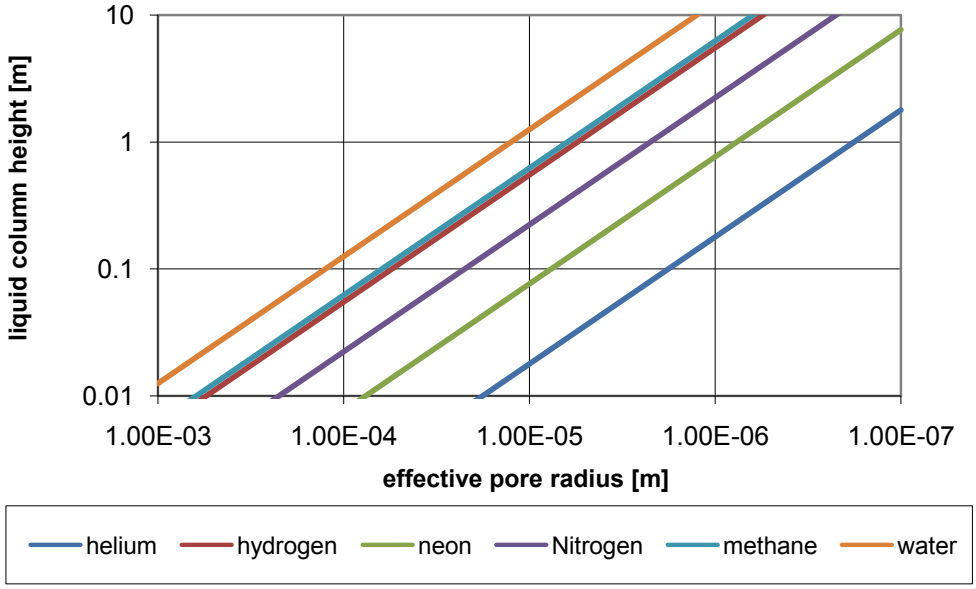

Figure 4.Liquid column height Vs. effective pore radius for different fluids.

3. EXPERIMENTAL SETUP

Although the ultimate goal is to develop nano-scale wick structures for liquid helium, we found from Figure 4 that, compared to liquid helium, wicking of liquid nitrogen is much easier and only requires the wick pore size in the range of micron-meters. We therefore first built an experiment to demonstrate liquid nitrogen wicking using the special Porostar® metallic mesh as illustrated in Figure 2.

Figure 5 shows a vacuum insulated liquid nitrogen dewar used for the demonstration. Two samples were placed inside the dewar, one has the Porostar® mesh bonded on a G-10 substrate, while the other is a dummy one with a plain stainless steel plate bonded on a G-10 substrate. The thickness of the stainless steel plate was carefully selected to match the equivalent thickness of the metallic mesh, so that the axial thermal conduction and total mass of both samples are matched with each other. On each of the samples mounted three Cernox RTD temperature sensors. All these sensors were calibrated with accuracy of ±5 mK at liquid helium temperature. On top of each sample is a custom-wound Manganin wire heater with the same

resistance of ~1 ohm. A liquid level sensor is also used to continuously monitor the liquid level inside the dewar.

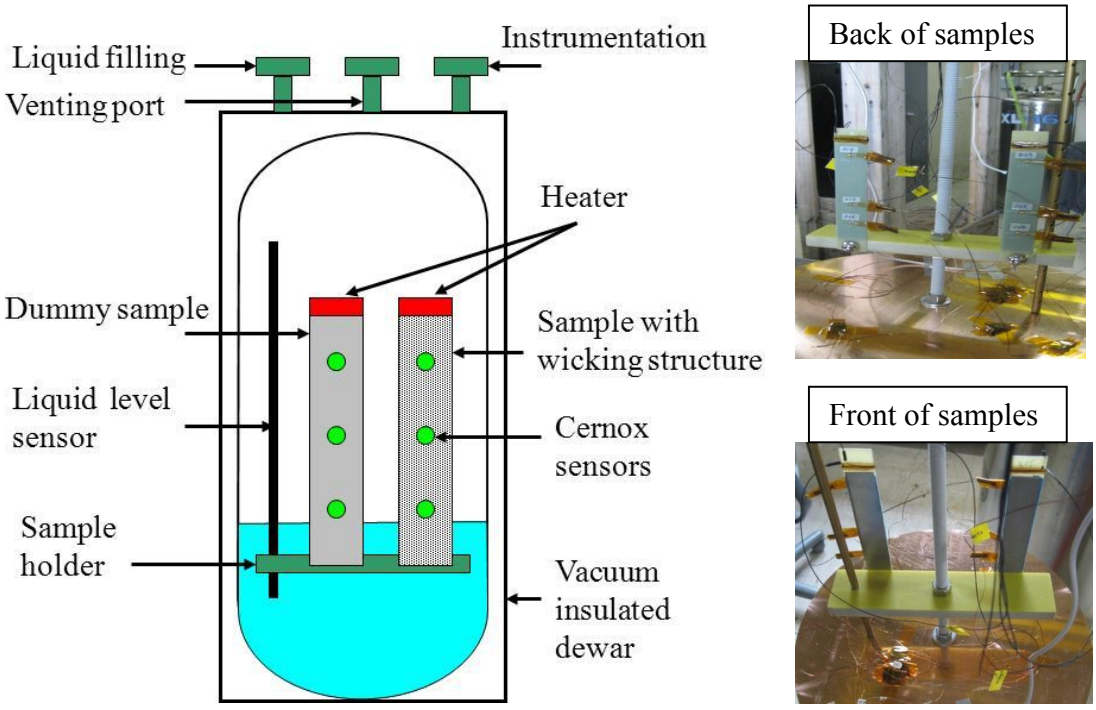

Figure 5. Experimental setup for liquid nitrogen wicking

Two different methods can be used to verify if there is significant wicking flow through the wicking structure.

1) Steady-state measurement:

The stratified vapor column above the liquid level creates a certain temperature gradient along the samples. If there is wicking flow, the temperature gradient along the wick sample will be smaller compared to that along the dummy sample due to the cooling effect from the wicked liquid nitrogen. However the difference may not be measurable in case that the wicking flow rate is low depending on the pore size and wicking characteristics of the wicking structure.

One way to enhance the difference is to use heaters on top of the samples (see Figure 5) to generate a certain heat flux along the samples. This results in a substantial temperature gradient. If there is wicking flow, the temperature gradient will be significantly reduced due to the cooling effect of liquid nitrogen. One drawback of this method is that, if the wicking flow rate is too low to overcome the applied heating power, the flow will eventually dry out. On the other hand, however, this gives a good approach to quantify the wicking flow rate by measuring the change of temperature gradient with different applied heating power.

2) Transient measurement

With high applied heating power, the temperature gradient along the samples can also be measured transiently. In this case, even the dry-out will happen, the difference between wicking and dummy samples can still be identified by carefully studying the changing of temperature profiles with time. This transient method is especially useful in case wicking flow is extremely

low. The response time constant of Cernox sensor is 15 milliseconds, sufficient for this transient measurement.

4. RESULTS AND DISCUSSIONS

The left of Figure 6 shows the liquid level relative to the temperature sensors. The distance between T1 and T2 (same as T4 and T5) is about 2.5 cm, and the distance between the T2 and T3 (same as T5 and T6) is about 5 cm. When the liquid nitrogen level was couple of cm below sensors T3 and T6, 2 W heating power was applied to both heaters H1 and H2. The temperature profile vs. time is shown on the right of Figure 6. Apparently, the temperature sensor T3 on the dummy sample started to rise soon after the heater was on. Within about 100 seconds, the temperature increased from ~ 77 K to above 87 K. The sensor T6 however didn't see the same temperature rise. This can be explained by the wicking flow of liquid nitrogen through the Porostar® mesh. After both heaters were turned off, temperature T3 returned back to ~ 77 K.

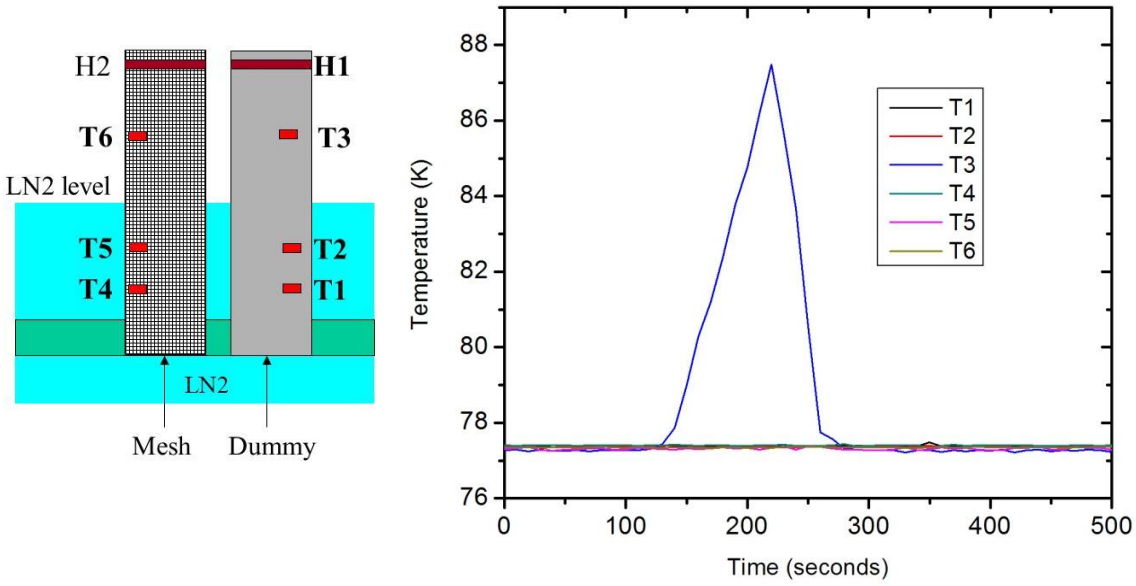

Figure 6. Temperature profile with 2 W heating power from the heaters.

A transient test was also performed by quickly lifting up the samples to make the liquid nitrogen level below sensors T2 and T5 (shown on the left of Figure 7). The samples were then set at still and there is no heating power applied from both heaters. The temperature vs. time for all six sensors were recorded and illustrated in Figure 7. Sensor T3 on the top of the dummy sample started to rise immediately. About 150 seconds later, sensor T2 at the middle of the dummy sample also started to rise, while T1 didn't change at all since it was still below the liquid nitrogen level. Therefore, a substantial temperature gradient was sequentially built along the dummy sample. As discussed previously, this is mainly due to the stratification of nitrogen vapor column. Such temperature gradient, however, was not observed along the sample with wicking structure. Even at 10 minutes after the lifting, T6, T5 and T4 on the wick sample still remained the same as the liquid nitrogen bath temperature. This result clearly demonstrates a strong wicking flow of liquid nitrogen through the mesh. Measuring from the liquid nitrogen level to the top sensor T6, a wicking height about 60 mm was achieved by the Porostar® mesh.

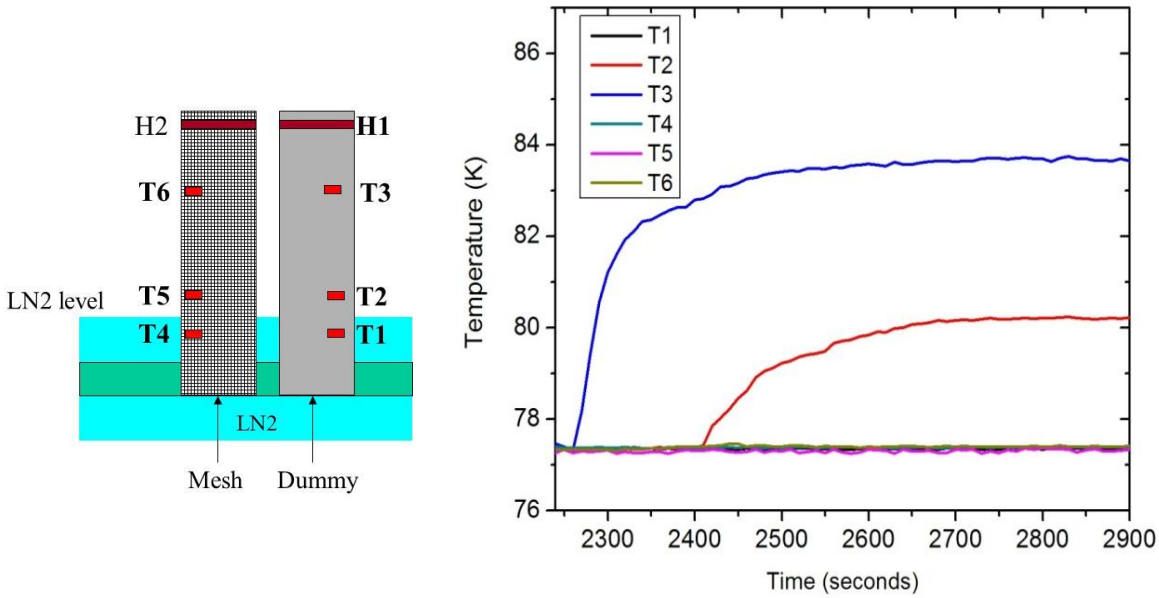

Figure 7. Temperature profile when the liquid level was above the bottom sensors.

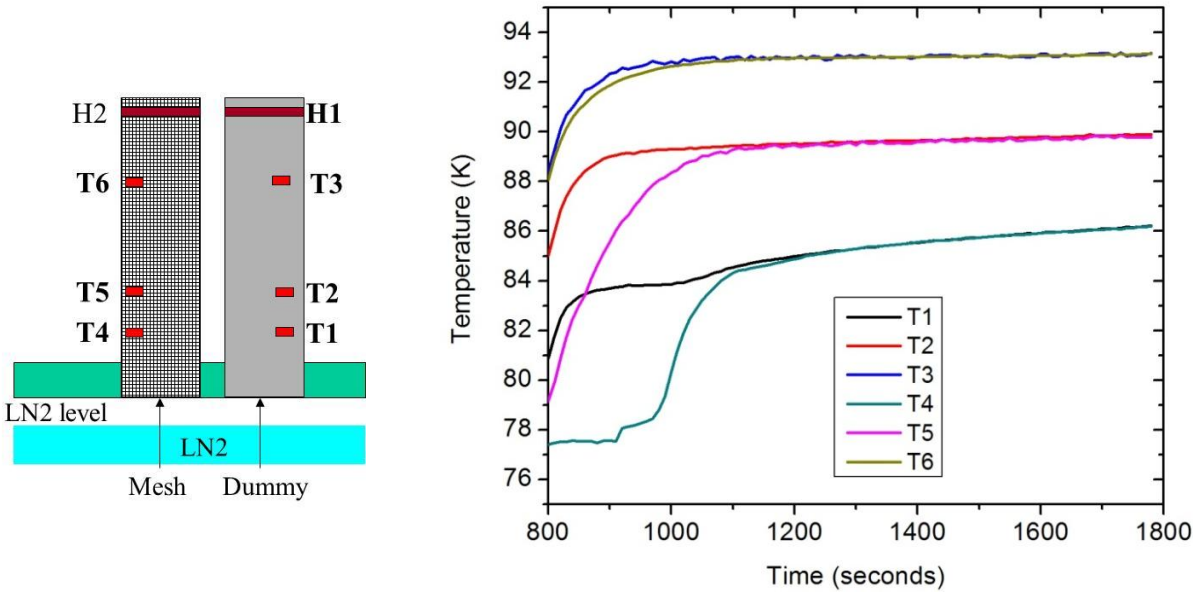

Figure 8. Temperature profile when liquid level drops below the samples

The samples were lift up again to make the liquid nitrogen level about 3 cm below the sample holder. In this case, liquid nitrogen was not in contact with either of the samples. Again, there is no any power input to both heaters. From Figure 8, exactly the same temperature gradient was built along both samples about 400 seconds after the lifting. This indicates that the two samples were almost identical in terms of axial thermal conduction, effective cross section area, and the layout of temperature sensors. And it further verified that that the difference of temperature profile as shown in Figure 7 was actually due to the wicking flow instead of the

physical difference between the samples. One interesting thing to note is the difference of temperature response between sensors T4, T5 and T6 on the wick sample and sensors T1, T2 and T3 on the dummy sample. The two top sensors T3 and T6 almost rose simultaneously, while T5 was lagging behind the temperature rise of T2. The delay of T4 was even more significant compared to T1. It took almost 200 seconds for T4 to see the temperature rise. This indicates that there was a liquid nitrogen column wicked and contained inside the metal mesh. After the lifting, although the wicking flow stopped it took some time for the contained liquid nitrogen to dry out. So, this result also demonstrated the confinement of liquid nitrogen using the wick structures.

5. CONCLUSIONS

By knowing the capillary constant and the contact angle for wicking of nitrogen in capillaries, we were able to demonstrate successfully the wicking of liquid nitrogen. A wicking height about 60 mm was achieved using a commercially available fine stainless steel mesh screen with pore size ~ 5 μm. To our knowledge this is the first reported liquid nitrogen wicking experiment in an open liquid nitrogen bath environment using a mesh type wicking structure. Based on the results we can extrapolate and refine the theoretical model of the wicking height achievable for liquid helium. Those structures really need to be in the nano pore-size range and we are working on designing and making the nano-structure to further demonstrate liquid helium wicking. This technology development will significantly enhance the capillary performance in space environment and thus enable NASA's next generation propellant management device and thermal management design.

ACKNOWLEDGMENT

The authors gratefully acknowledge the support and consultations of James Fesmire, Wesley Johnson and Louis Salerno from NASA during the course of this work.

REFERENCES

1. F. T. Dodge. *Low-gravity fluid dynamics and transport phenomena*, Vol. 130, pp. 3-14. Aeronautics and Astronautics, Washington, D.C., 1990
2. J. R. Rollins, R. K. Grove and D. E. Jaekle, *Twenty-three years of surface tension propellant management system design, development, manufacture, test and operation*. 21st Joint Propulsion Conference, pp. 1-9, AIAA, 85-1199, 1985
3. N. Fries, K. Odic and M. Dreyer, *Wicking of perfectly wetting liquids into a metallic mesh*, Proceedings of the 2nd International Conference on Porous Media and its Applications in Science and Engineering, June 17-21, Hawaii, U.S., 2007.
4. G. S. Hwang, M. Kaviany, W. G. Anderson, J. Zuo, *Modulated wick heat pipe*, International Journal of Heat and Mass Transfer, 50, pp. 1420-1434, 2007.
5. Chi, S. W., 1976, *"Heat pipe Theory and Practice",* McGraw-Hill, New York, USA
6. H. Peter J. de Bock, Kripa Varanasi, Pramod Chamarthy and etc., *Experimental investigation of micro/nano heat pipe wick structures*, Proceedings of the ASME International Mechanical Engineering Congress and Exposition, Oct. 31-Nov. 6, Boston, U.S., 2008.

LIQUID OXYGEN LIQUID ACQUISITION DEVICE BUBBLE POINT TESTS WITH HIGH PRESSURE LOX AT ELEVATED TEMPERATURES

J. M. Jurns
J.W. Hartwig
ASRC Aerospace Corp.
Cleveland, OH, 44135, USA

Corresponding author: John M. Jurns
ASRC Aerospace Corp.
NASA Glenn Research Center, M.S. 500-ASRC
21000 Brookpark Rd
Cleveland, OH 44135
John.M.Jurns@nasa.gov
00.1.216.977.7416

ABSTRACT

When transferring propellant in space, it is most efficient to transfer single phase liquid from a propellant tank to an engine. In earth's gravity field or under acceleration, propellant transfer is fairly simple. However, in low gravity, withdrawing single-phase fluid becomes a challenge. A variety of propellant management devices (PMD) are used to ensure single-phase flow. One type of PMD, a liquid acquisition device (LAD) takes advantage of capillary flow and surface tension to acquire liquid. The present work reports on testing with liquid oxygen (LOX) at elevated pressures (and thus temperatures) (maximum pressure 1724 kPa and maximum temperature 122K) as part of NASA's continuing cryogenic LAD development program. These tests evaluate LAD performance for LOX stored in higher pressure vessels that may be used in propellant systems using pressure fed engines. Test data shows a significant drop in LAD bubble point values at higher liquid temperatures, consistent with lower liquid surface tension at those temperatures. Test data also indicates that there are no first order effects of helium solubility in LOX on LAD bubble point prediction. Test results here extend the range of data for LOX fluid conditions, and provide insight into factors affecting predicting LAD bubble point pressures.

1.0 NOMENCLATURE

D_p	Pore diameter (micron)
ΔP_{BP}	Bubble point pressure (Pa)
ρ	Fluid density (Kg/m^3)
σ	Surface tension (N/m)
ν	Kinematic viscosity (centistoke)
θ_c	Fluid contact angle (degree)

2.0 KEYWORDS

Cryogenic fluid management, liquid oxygen

3.0 INTRODUCTION

Gravity affects many fluidic processes, such as the separation of liquid and vapor within a tank: the liquid (heavier fluid) settles to the bottom while the vapor (lighter fluid) rises to the top. In the reduced gravity of a space environment, surface tension becomes a controlling mechanism for this liquid/vapor separation in a tank as the liquid and vapor tend to the state of lowest potential energy. For "wetting" systems, the liquid tends to wrap the walls or interior structures within the tank often resulting in no or very little vapor contact with the walls and these structures.

When transferring propellant in space, it is necessary to transfer single phase liquid from a propellant tank to an engine to ensure efficient thermal conditioning of the engine and safe operation after ignition. In Earth's gravity field or under acceleration during "significant" thrusting, propellant transfer is fairly simple. Single-phase fluid is transferred by opening a valve at the bottom of the propellant tank and installing an anti-vortex baffle over the tank outlet to prevent vapor and gas ingestion into the outlet. In low gravity where liquid does not sufficiently cover the tank outlet, withdrawing single-phase liquid becomes a challenge. A variety of propellant management devices (PMD) are required to ensure single-phase flow, depending on the gravitational environment. One type of PMD, a liquid acquisition device (LAD) uses capillary flow and surface tension for acquiring liquid.

Trade studies were conducted to evaluate the feasibility of utilizing liquid oxygen/liquid methane (LOX/LCH_4) propellant for propulsion systems using high pressure (up to 2,400 kPa) propellant tanks to feed the engine. To date, cryogenic LAD testing has not been performed at these higher pressures, and there is a question of whether or not helium pressurant solubility in the cryogenic propellants impacts the design and operation of LADs. Tests described in this report were performed to address these questions.

LADs are designed and manufactured in a variety of sizes and geometries. Multiple types of LADs are often required to achieve sufficient vapor free liquid, especially in microgravity. One type of LAD is a screen channel device. Screen channel devices closely follow the contour of the propellant tank wall and can vary in cross-section (typically a triangular or rectangular cross section). The channel side that faces the tank wall has multiple openings that are covered with tightly woven screen. As liquid is withdrawn from the tank, surface tension forces within the screen weave create a barrier to vapor entrance into the channel but allow liquid to flow freely. Liquid is wicked into the screen pores and prevents the screen from drying out if it comes into contact with vapor. If the screen dries out, vapor is admitted into the channel.

"Bubble point" is defined as the differential pressure across the screen that overcomes the surface tension of the liquid on the screen. Mathematically, bubble point is expressed as [1]:

$$\Delta P_{BP} = \frac{4\sigma \cos\theta_c}{D_p} \tag{1}$$

The geometry of the pore and the fluid surface tension determine the bubble point of the screen. A high bubble point (fine screen mesh) is desirable to ensure single phase (liquid) fluid delivery

and good wicking of liquid into the screen pores. Fine mesh screens, however, tend to generate a large pressure loss during outflow through the screen. The total pressure loss in the system must be less than the bubble point pressure to prevent vapor ingestion into a LAD channel. Capillary flow LADs have been well characterized for storable propellants (propellants that are liquids at room temperature) for in-space propulsion needs [2]. The choice of screen for the LAD channel is governed by pore size and geometry, which is usually expressed as the screen weave. The screen weave refers to the number of wires per inch in each direction and the weave pattern, or the specific over/under pattern used during the screen manufacture. The screen weave is an important parameter affecting the choice of screen since certain weaves of wires are capable of producing much finer pore sizes than other weaves. As can be seen from equation (1), the geometry (size) of the hole and the surface tension of the fluid trapped within the screen determine the bubble point of the screen.

For hazardous storable propellants, such as nitrous tetroxide and monomethyl hydrazine (MMH), bubble points are typically determined experimentally using isopropyl alcohol (IPA) as a reference fluid to determine the screen pore diameter, and calculating the bubble point using known surface tension values for these propellants. Safety and environmental concerns over the use of storable propellants have led to the examination of non-toxic cryogenic propellants for on-orbit propulsion for the human and robotic exploration of the Moon and Mars. Developing LAD technology for cryogenic propulsion systems and depots is enabling technology for the efficient transfer of cryogenic fluids in a low gravity environment. The use of cryogenic fluids in on-orbit propulsion systems offers the advantages of higher performance. The development of the technology must be capable of providing vapor free liquid despite the continuously changing conditions in a cryogenic propellant tank including pressurization gases, liquid saturation conditions, vapor entrapment, tank pressure control/venting, and heat transfer.

Previous experimental test programs conducted at Glenn Research Center and Marshall Space Flight Center have collected LAD data for liquid nitrogen (LN_2) [3], liquid hydrogen (LH_2) [3], LOX [4,5], and LCH_4 [6,7] at saturated liquid conditions. The effects of subcooling on LAD performance were addressed at low pressure [5] Additional testing in LOX described herein continues to advance understanding of LADs.

4.0 TEST OBJECTIVES

The purpose of this experimental program was to collect additional bubble point data for a screen channel LAD by performing bubble point tests in LOX. There were three proposed objectives for this test effort:

1. Ascertain whether helium dissolution into liquid oxygen at pressures up to 1724 kPa (250 psia) significantly altered the relevant liquid oxygen properties, namely liquid oxygen surface tension, and therefore the predicted LAD bubble point pressure.
2. Verify liquid oxygen surface tension at temperatures from 90 to 122 K.
3. Assess the effect of liquid viscosity on bubble point over a broader range of test conditions than prior work.

These are discussed in detail below:

4.1 Helium Dissolution

Henry's Law is used to describe the relationship between the concentration of a dissolved gas in a liquid with the pressure of the fluid and is usually expressed as

$$c = f(P,T) \tag{2}$$

For gaseous helium (GHe) in liquid oxygen, this has been measured by Sinor and Kurata [8]

Table 1: Liquid Composition, Mole % Helium

Pressure MPa (psia)	143K (258ºR)	128K (231ºR)	113K (204ºR)	93K (168ºR)	77K (139ºR)
1.72 (250)			0.27	0.14	0.04
3.45 (500)		0.86	0.74	0.33	0.14
5.17 (750)	1.80	1.59	1.13	0.53	0.20
6.89 (1000)	3.30	2.37	1.54	0.68	0.25
8.62 (1250)	4.61	3.14	1.95	0.83	0.32
10.3 (1500)	5.98	3.84	2.32	0.99	0.36
11.9 (1750)	7.26	4.46	2.67	1.14	0.43
13.8 (2000)	8.60	5.08	3.02	1.27	0.48

Even though the proposed operating conditions for higher pressure fed engines are not likely to exceed 2.24 MPa (325 psia), there is still a significant amount of helium that can be dissolved into the liquid oxygen. While there is no data suggesting that the properties of the liquid oxygen will be significantly altered by this dissolved helium content, this remains to be verified.

4.2 Liquid Oxygen Surface Tension

By elevating the pressure of the gaseous space above the liquid volume in a tank, it is possible to suppress boiling and evaporation, even at temperatures above the normal boiling point.

While other authors give data for surface tension up to temperatures of approximately 154K, the data was extrapolated for temperatures above 95K based on similar calculations of liquid nitrogen. It should be noted though that using this correlation, the surface tension drops from 13.2 dynes/cm at the normal boiling point of 101.3 kPa (one atmosphere) and 91K to about 4 dynes/cm at the boiling point at 1724 kPa (250 psia) and 130K [9]. Thus, while there is some confidence that the predicted values of surface tensions at elevated bulk liquid temperatures are known, there has been no experimental verification of those values.

4.3 Liquid Viscosity Effect

Jurns et al [6] had previously proposed using a normalized kinematic viscosity correction term for calculating bubble point pressure as follows:

$$\Delta P_{BP} = \frac{4\sigma \cos\theta_c}{D_P}\left(\frac{\nu}{\nu_{NPB}}\right)^{1/3} \tag{3}$$

Previous tests had indicated inconclusive results regarding the suitability of this term [7]. However, the range of fluid conditions for the tests described herein was much broader than previous experiments. The suitability of this viscosity correction term should be re-evaluated in the light of this broader range of fluid conditions.

5.0 TEST PROGRAM

5.1 Description of Experiment

The experiment was conducted at GRC Creek Road Cryogenic Complex – Cryogenic Component Lab 7 (CCL-7) [10]. New research hardware was developed for this test program, and additional facility changes to accommodate the high pressure testing included the following:

- Fabrication of a new 0.6 liter volume high pressure LAD test tank
- High pressure supply system for gaseous helium and oxygen
- High pressure, high accuracy helium pressure controller
- High pressure piping for the new LAD test tank

A simplified schematic diagram of the test is shown in Figure 1.

Portable LOX supply dewars (450 liter capacity) were filled off-site and transported to CCL-7. A flexible line supplied LOX to the high pressure research test tank containing the LAD test hardware located inside the existing test facility research dewar. After LOX has been fed into the research test tank, it was isolated from the LOX supply. The test tank was then pressurized using the high pressure helium system. After testing, the test tank was vented and LOX drained and routed to a flash tank located immediately outside the test building.

Visual observation of test hardware inside the research dewar was extremely important for this test program. LAD screen bubble breakthrough was observed visually and correlated to the recorded differential screen pressure signal to determine the bubble point. Therefore, the new high pressure LAD test tank was supplied with ports to view the test hardware, and the facility had a live video feed to observe the LAD screen remotely during testing. The camera system was mounted between the CCL-7 dewar and high pressure test tank to view the LAD screen through a sight glass in the test tank. The video was recorded and time synchronized with the data system to aid in post-test data analysis.

5.2 Bubble Point Tests

For bubble point testing, the high pressure LAD test tank previously referenced is a 15.24 cm diameter vessel located inside the 0.23 m^3 volume CCL-7 dewar as shown in Figure 2. A LAD screen sample was affixed to a mounting fixture inside the test tank. Two size LAD screens were evaluated: a 325x2300 mesh screen with a D_p = 14.4μ (0.000567 inch), and a 200x1400 mesh screen with a D_p = 23.4μ (0.00092 inch). These pore diameter values were determined by performing IPA bubble point tests and calculating Dp using Equation (1) and IPA surface tension values. The volume above the LAD screen in the test tank was filled with LOX. The volume below the LAD screen was maintained at a slightly elevated pressure to prevent flooding of the test fixture during the filling process. When the entire screen surface is wetted, surface tension forces also aid in preventing flooding of the screen. Gaseous helium or oxygen pressure below the LAD screen was gradually ramped up in small pressure steps until gas bubbles broke through the screen surface. Pressure was incremented using a supply of regulated gas and precision

throttling valve. Pressure across the screen surface was measured using sensitive differential pressure transducers.

Tests were performed with LOX over a range of temperatures from normal boiling point (NBP) to approximately 122 K. For NBP tests, the LOX was transferred directly into the test dewar from the LOX supply. For pressurized LOX tests, the LOX was pressurized after the test tank had been filled. For higher temperature LOX tests, the liquid was warmed through ambient heat into the system. Tables 2 and 3 show the test matrix for the two LAD screens tested. Reported bubble breakthroughs in terms of LOX temperature and pressure are also shown graphically in Figures 3 and 4; the LOX saturation curve is also plotted for reference.

5.3 Data Acquisition

Data for this test program was acquired using the facility LabVIEW™ data collection system, and recorded data at nominally 2 Hz. As mentioned previously, video data of the LAD screen was also recorded, and bubble breakthrough times correlated with recorded pressure data.

Silicon diodes were located inside the test tank to measure bulk liquid temperature, vapor temperature, and LAD screen temperature. Additional diodes were located on the outside of the test tank and on the camera.

Differential pressures were measured using high accuracy pressure transducers. Screen differential pressure was measured using 0-7.5 kPa or 0-13.8 kPa differential pressure transducers. Liquid head was measured using a 0-7.5 kPa differential pressure transducer.

Facility instrumentation (including dewar pressure, vent system pressure, barometric pressure) was also monitored and recorded for use in data analysis.

5.4 Test Operating Parameters

- LOX test tank pressure – 1723.7 kPa (250 psia) maximum
- LOX temperature – 91-130 K (162-234 degree R)
- GHe or GOX pressurant – 2068.4 kPa (300 psia) maximum

5.5 Measured Parameters

- LOX and vapor ullage temperature – K
- Tank pressure – kPa
- LAD screen differential pressure – Pa
- LOX liquid level – Pa
- Test tank wall temperatures – K
- LAD screen temperature – K

Table 2 – 325 x 2300 Mesh LAD Tests

Liquid	Gaseous	Fluid Test Conditions	
Component	Component	Pressure [kPa]	Temperature [K]
LOX	GHe	344.7 - 689.5	105.5 - 108.3
LOX	GHe	689.5 - 1034.2	108.3 - 113.9
LOX	GHe	1034.2 - 1379.0	113.9 - 116.7
LOX	GHe	1379.0 - 1723.7	113.9 - 120
LOX	GHe	193.1 - 689.5	92.8 - 102.8
LOX	GHe	689.5 - 1034.2	100 - 105.5
LOX	GHe	1034.2 - 1379.0	105.5 - 106.7
LOX	GHe	1379.0 - 1723.7	105.5 - 108.9
LOX	GOX	1500	110.6
LOX	GHe	137.9	92.2
LOX	GHe	137.9 - 344.7	94.4
LOX	GHe	572.3 - 861.8	97.2
LOX	GHe	882.5 - 1551.3	100
LOX	GHe	1585.8 - 1723.7	104.4
LOX	GHe	517.1 - 1034.2	105.5 - 108.3
LOX	GHe	1034.2 - 1379.0	111.1 - 113.9
LOX	GHe	1379.0 - 1723.7	125 - 130.6
LOX	GOX	1379.0 - 1723.7	118.3 - 128.3
LOX	GOX	131 – 344.7	92.2 - 95
LOX	GOX	344.7 - 689.5	94.4 - 105.5
LOX	GOX	689.5 - 1034.2	100 - 113.9
LOX	GOX	1034.2 - 1379.0	105.6 - 108.9, 113.3 - 119.4
LOX	GOX	1379.0 - 1723.7	113.3, 117.8 - 122.2

Table 3 – 200 x 1400 Mesh LAD Tests

Liquid	Gaseous	Fluid Test Conditions	
Component	Component	Pressure [kPa]	Temperature [K]
LOX	GHe	676.5 - 951.4	109 - 113.7
LOX	GHe	941.9 - 980.4	116.3 - 116.5
LOX	GHe	1307.2 - 1347.6	105.7 - 119.5
LOX	GHe	415 - 532	105.7 - 108.7
LOX	GHe	213.2 - 290.3	97.8 - 101.2
LOX	GHe	746.8 - 1221.2	103.3 - 112.2
LOX	GHe	1598.4 - 1717.4	112.1 - 120.3
LOX	GHe	137.4 - 171.9	93 - 95.5
LOX	GHe	303.8 - 558.2	97.2 - 106
LOX	GHe	693.5 - 851.8	106 - 108.6
LOX	GHe	1052.7 - 1159	108.7 - 111.1
LOX	GHe	1359.4 - 1421.1	112.2 - 112.5
LOX	GHe	1607.9 - 1744.2	113.2 - 114.7
LOX	GHe	1239.1 - 1765.4	114.3 - 122.6
LOX	GHe	203.1 - 586.2	95.8 - 106.5

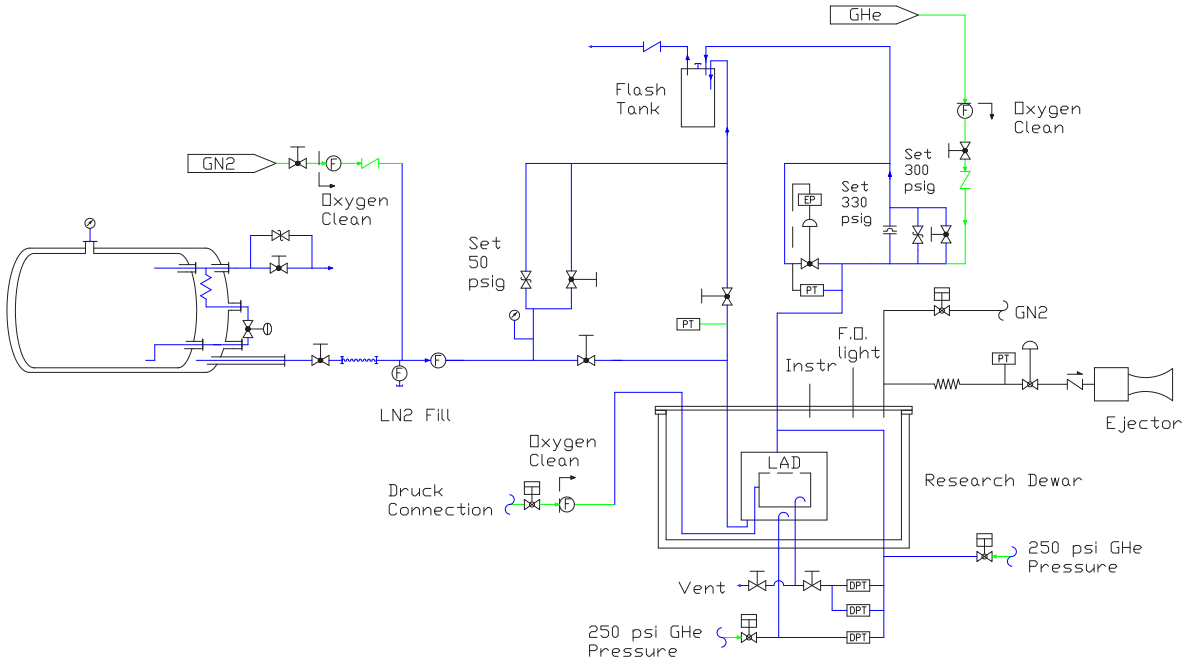

Figure 1 – Simplified System Schematic Diagram

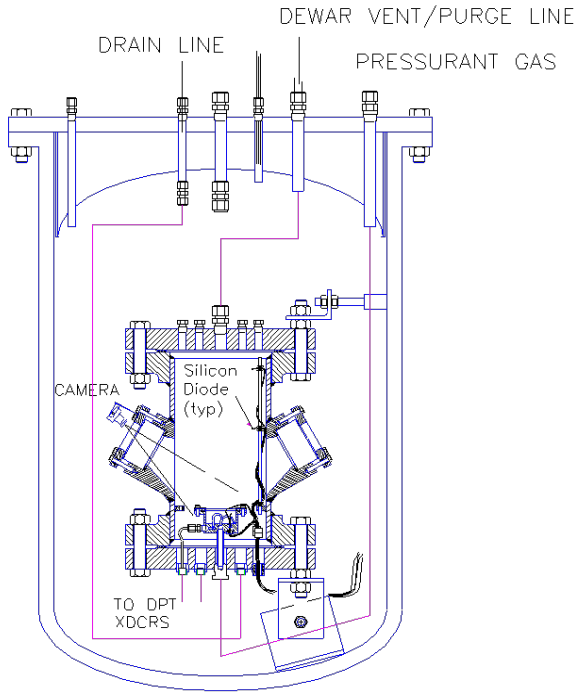

Figure 2 – Bubble Point Test Tank inside CCL-7 Receiver Dewar

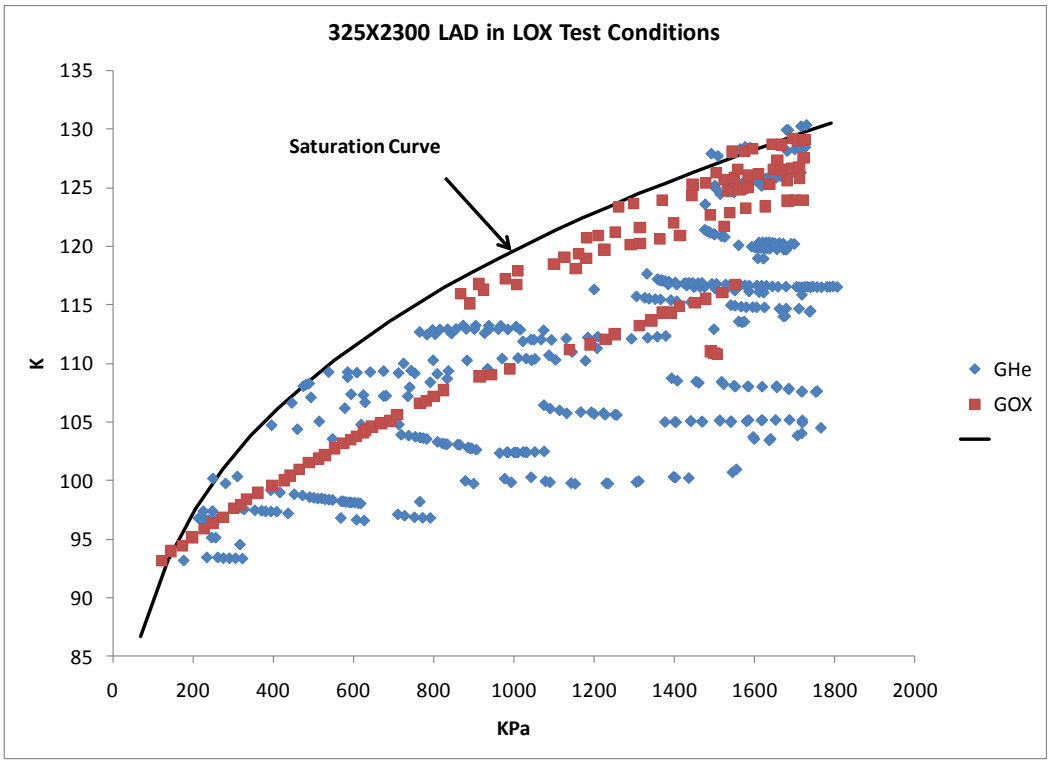

Figure 3

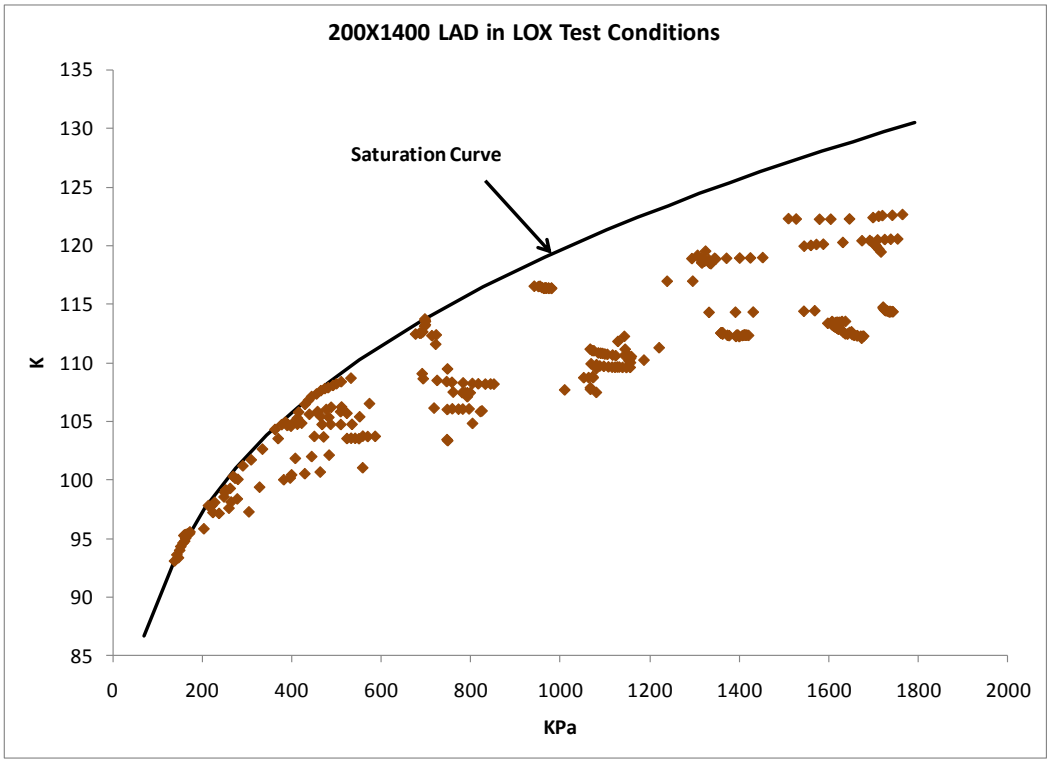

Figure 4

6.0 RESULTS

6.1 Bubble Point Predictions

Two LAD screens were tested:

- 325x2300 mesh
- 200x1400 mesh

The 200x1400 mesh LAD was tested with LOX using GHe as the pressurant gas. The 325x2300 mesh LAD was tested with LOX using both GHe and GOX as pressurant gases. GOX pressurant testing was included to provide baseline data to compare with GHe pressurant test results.

6.1.1 325x2300 LAD

For LOX with GHe pressurant tests, bubble point data was plotted as a function of bulk liquid temperature, noting that surface tension is a strong function of saturation temperature. Figure 5 shows test data and the predicted bubble point based on Equation (1). Note Equation (1) under predicts the data, slightly more so at lower fluid temperatures. As liquid temperature increases, predicted value and test data agree more.

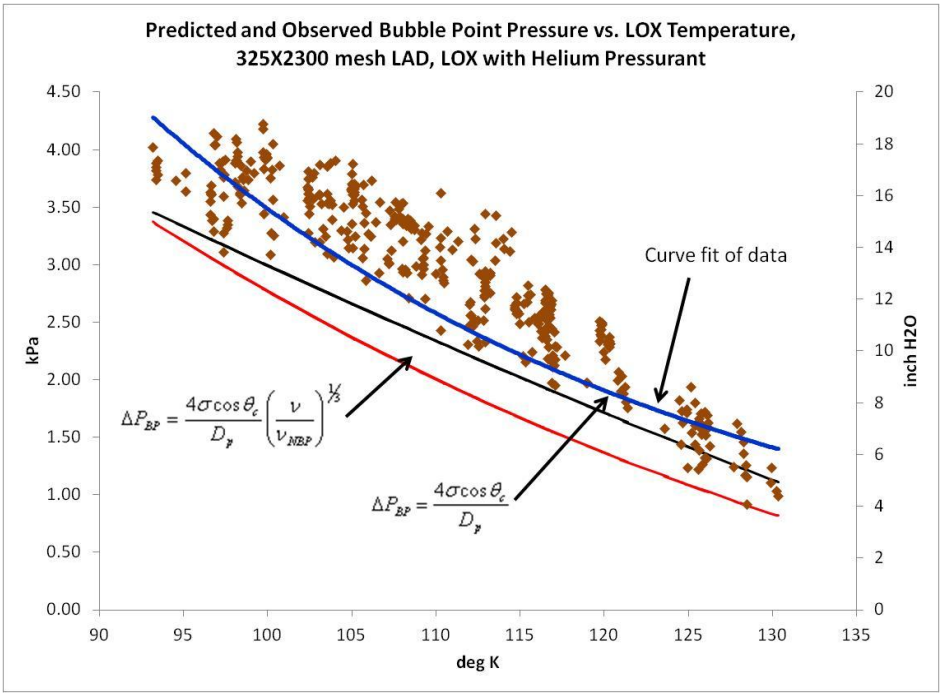

Figure 5

Comparing data and predicted bubble points using the viscosity correction term from Equation (3) [6], it appears that the when compared to a curve fit of the data, the correction provides a slightly better correlation , but with predicted bubble points still under-predicting the data. Jurns [5], and Meserole & Jones [11] both noted that for LOX and LH_2 using helium as a pressurant, bubble point data was typically higher than predicted values. This was likely due to higher surface tension values based on lower liquid temperature at the liquid/vapor (L/V) interface. A lower temperature at the L/V interface would result from the requirement that the liquid temperature at the interface must be the equilibrium temperature for the partial pressure of oxygen at the interface. Silicon diode temperatures at the LAD screen indicated that indeed the

L/V interface temperature was lower than that of the bulk liquid by approximately 3 K, as shown in Figure 6 for a typical test using GHe pressurant. By comparison, for LOX tests using GOX as a pressurant, L/V interface temperatures were typically very close to the saturation temperature based on test tank pressure, as shown in Figure 7.

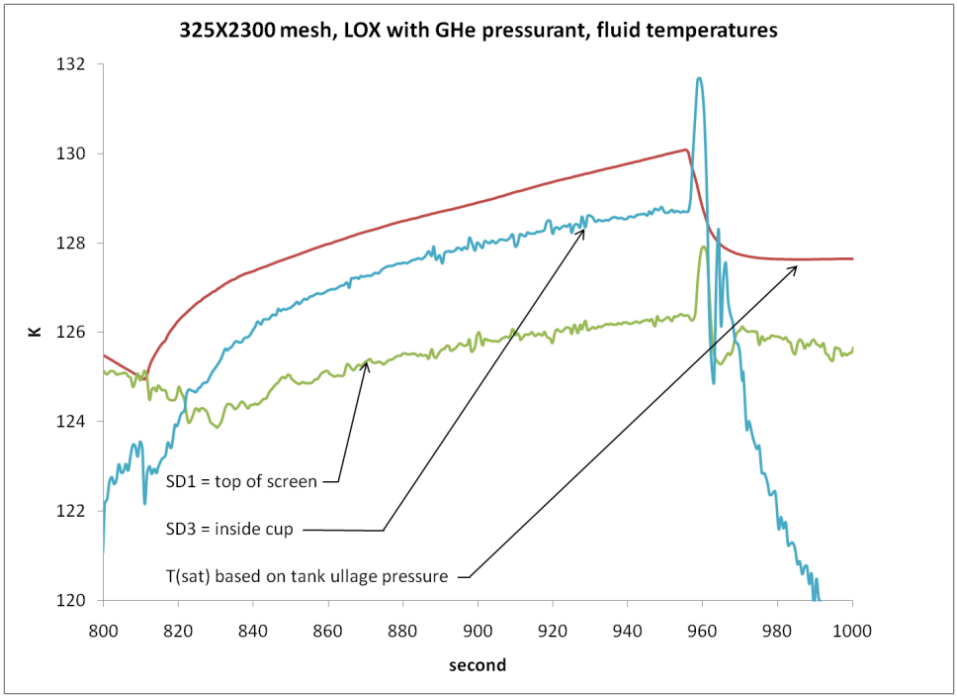

Figure 6 – LOX temperatures using GHe to determine bubble point

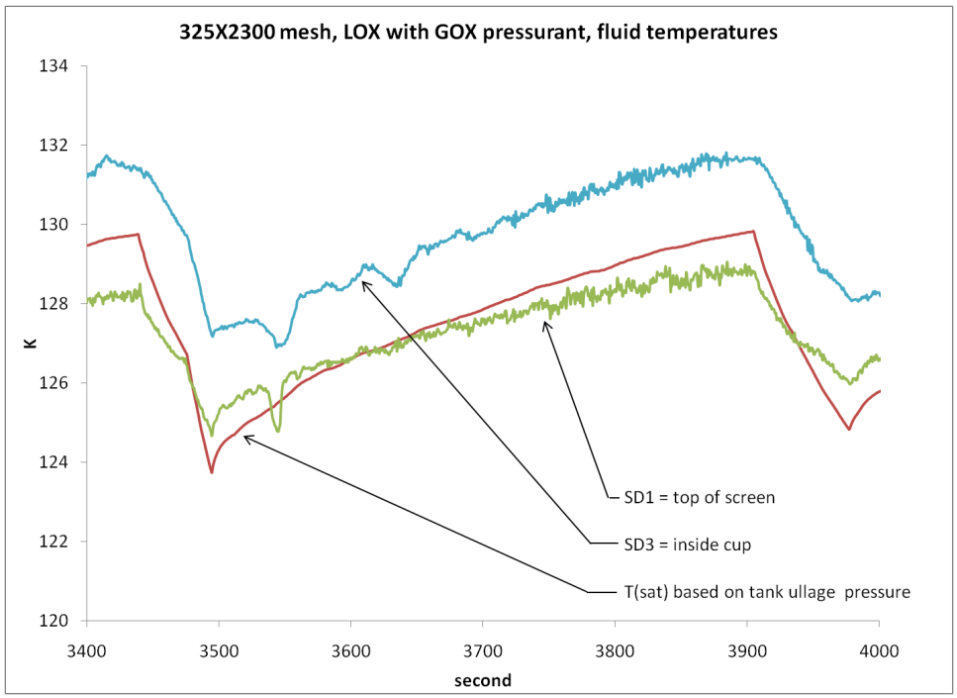

Figure 7 – LOX temperatures using GOX to determine bubble point

For subcooled LOX using GHe pressurant the measured temperature at the L/V interface was generally colder than the bulk liquid temperature. However, this may not necessarily be used to accurately determine the actual L/V interface temperature. Heat transfer from the bulk liquid to the screen would likely bias this measurement. One way to accurately determine the L/V interface temperature is to look up the saturation temperature of liquid based on the partial pressure of oxygen at the interface. However, for these tests, the partial pressure of oxygen at the interface was not directly measured. The observed lower temperature measured at the screen does give an indication of a lower oxygen partial pressure, which would result in higher surface tension values at the L/V interface, tending to shift the predicted bubble point up more towards the observed data.

Bubble point tests were also performed using GOX as the pressurant. For these tests, predicted values and test data correlated better, with predictions being slightly greater than test data. However, with corrected predictions using Equation (3), there was good agreement between data to the corrected predictions (refer to Figure 8). No correction for L/V interface temperature was required, as it was previously noted that interface temperatures were very close to the saturated temperature of the bulk liquid.

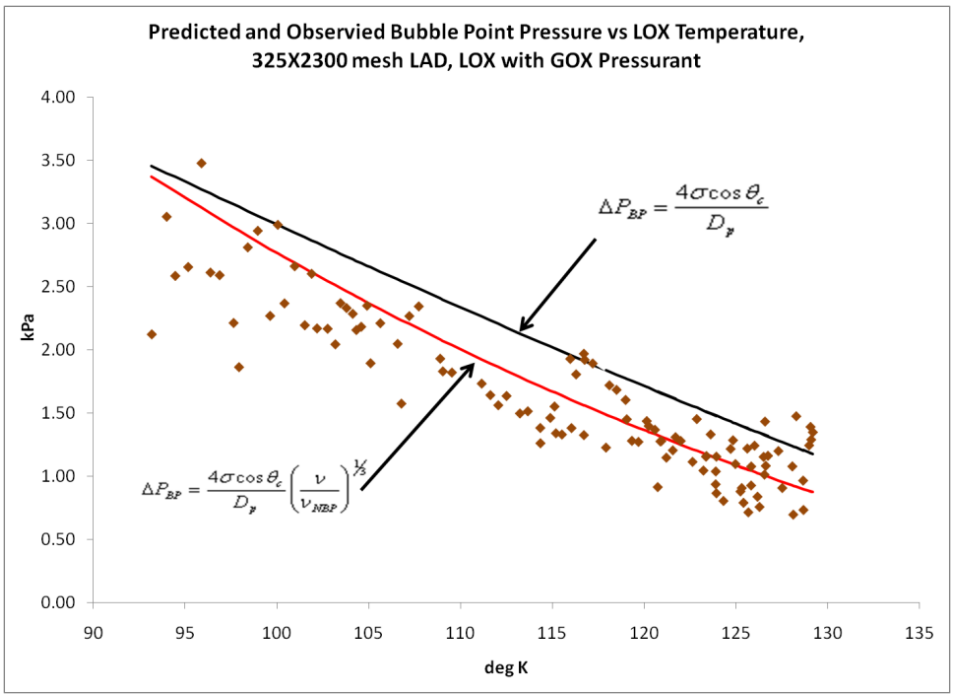

Figure 8

6.1.2 200x1400 LAD

For LOX with GHe pressurant, bubble point data was plotted as a function of bulk liquid temperature in the same manner as the 325x2300 LAD data. As with the 325x2300 mesh LAD, the prediction based on bulk liquid temperature under predicts the test data as shown in Figure 9. It is noted that comparing the 325x2300 screen with the 200x1400 screen; for LOX at similar conditions, the data correlates well with screen pore diameter. Again, as with the 325x2300 screen using GHe pressurant, a lower oxygen partial pressure would result in higher viscosity values, effectively shifting the predicted values up closer to observed data.

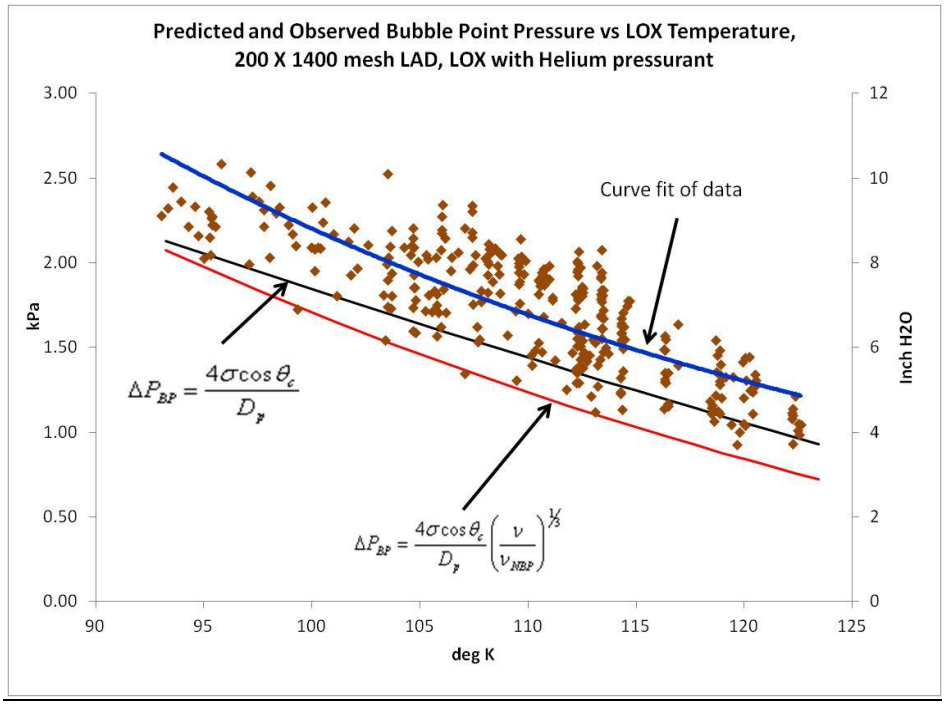

Figure 9

6.2 Helium Solubility

Test data was also analyzed to evaluate whether helium dissolving in the LOX had any appreciable effect on LOX surface tension values. To determine if helium dissolution had any effect, we examined several tests where the pressure was maintained above 1300 kPa for at least one hour, and GHe was used as the pressurant gas on the LAD, with liquid held at constant temperature and pressure.

Zimmerli [12] discussed equilibration times and diffusion rates for helium in cryogens. Equilibration time was based on straight diffusion of the solute (helium) into the solvent (cryogenic liquid), and assumed no mixing. Although there is sparse data on the diffusivity rates of helium into cryogens, some data does exist for diffusivity of helium into liquid methane [13]. Based on Zimmerli's report, it would take nearly 6 hours for helium to reach half its equilibrium concentration in liquid methane at a depth of 1 cm. Tests reported herein were on the order of several hours, and the liquid was thoroughly mixed by constant bubbling of helium through the oxygen. Therefore, if diffusivity rates were similar for helium in LOX to helium in liquid methane, it would be reasonable to assume that the amount of helium dissolved in the LOX was a noticeable fraction of its maximum solubility. That being the case, if there were an effect on surface tension, it should be evident in the data.

Several data sets that met this criteria were examined. One typical data set is shown in Figure 10. From the data examined, there was no conclusive evidence that the presence of helium had any first order effect on bubble point values.

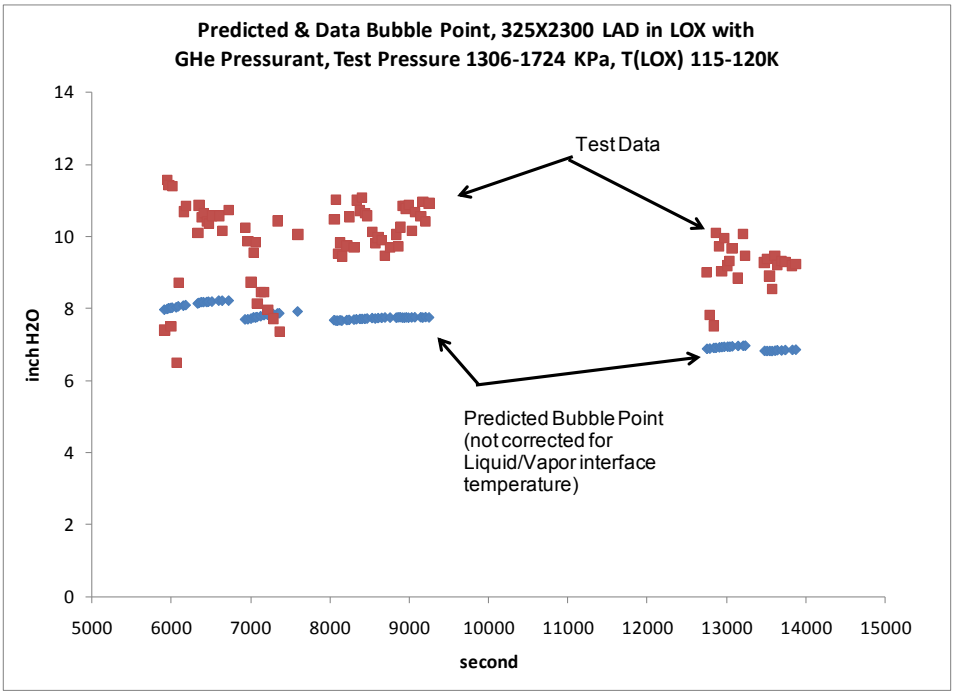

Figure 10

6.3 Liquid Oxygen Surface Tension

It was previously noted that there is published LOX surface tension values for temperatures up to approximately 154 K, and that the data is extrapolated for temperatures above 95 K. This test program evaluated bubble point data for LOX with temperatures ranging from 92 – 130 K. Using the published surface tension values, and correcting for L/V interface temperatures, bubble point data agreed well predictions. Although there was scatter in the data, one could draw the conclusion that published LOX surface tension values are consistent with this data for temperatures as high as 130 K based on this experimental data.

7.0 DISCUSSION/CONCLUSIONS

LAD bubble point tests were performed in LOX for two LAD screens – 200x1400 and 325x2300 mesh screens. The bubble point pressure was determined in LOX at liquid pressures up to 1724 kPa, and liquid temperatures as high as 130 K. Experiments conducted in this study have significantly extended the range of fluid conditions for cryogenic LAD testing. There are some general observations that can be made from these tests that are of interest to designers.

1. Tests have verified a significant drop in bubble point pressure in LOX at higher temperatures. This observation was consistent with calculations based on available LOX surface tension values in the literature. However, the significant issue that arises from this fact is that as designers consider pressure fed engines using cryogenic liquid propellants, they must also consider the possibility that cryogens stored and delivered at higher pressures may have a corresponding higher fluid temperature. This higher temperature will result in significantly lower bubble point pressures for LOX, and system design must accommodate this lower bubble point, or put controls in place to maintain LOX at lower temperatures.
2. These tests have shown that using helium as a pressurant gas results in an under-prediction of bubble point values. This was attributed to lower temperatures at the liquid/vapor interface

on the LAD screen due to the requirement that the liquid temperature be in equilibrium with the partial pressure of oxygen at the interface. The presence of helium lowers the partial pressure of oxygen, resulting in a lower temperature and higher surface tension value, effectively increasing the bubble point. Future tests may consider directly measuring the composition of the gas beneath the LAD screen to accurately determine partial pressures of helium and oxygen.

3. For autogenously pressurized LADs in LOX (gaseous oxygen pressurant), no temperature correction calculation was required, as the LOX temperature at the L/V interface was essentially the same as the saturation temperature at the system pressure.
4. Use of a normalized viscosity correction factor as shown in Equation (3) may provide an improved bubble point prediction, presuming that the surface tension at the L/V interface can be accurately ascertained based on oxygen partial pressure. The shape of the curve more closely follows the test data than does the straight line prediction from Equation (1).
5. There does not appear to be any significant first order effects of helium solubility on LOX surface tension values. This observation is valid for test durations on the order of hours. For long term missions where there may be orders of magnitude longer time, helium solubility may be an issue. However, based on known time scales for dissolution of helium in cryogens, this is unlikely a problem.

8.0 ACKNOWLEDGEMENTS

This work was sponsored by the NASA Exploration Technology Development and Demonstration Program Office, and was performed under NASA Glenn Research Center contract NNC06BA07B.

9.0 REFERENCES

1. Blatt, M.H, et al, "Low Gravity Propellant Control Using Capillary Devices in Large Scale Cryogenic Tanks", *General Dynamics Report No. GDC-DD70-006*, August 1970.
2. Fester D. A. et. al. "Surface Tension Propellant Acquisition System Technology for Space Shuttle Reaction Control Tanks", *AIAA 75-1196*, Sept. 1975.
3. Chato D.J. and Kudlac M.T., "Screen Channel Liquid Acquisition Devices for Cryogenic Propellants", *AIAA-2002-3983* 2002.
4. Kudlac M.T., Jurns J.M., "Screen Channel Liquid Acquisition Devices for Liquid Oxygen", *42nd AIAA Joint Propulsion Conference*, Sacramento, July 2005.
5. Jurns J.M., McQuillen J.B ., "Liquid Acquisition Device Testing with Subcooled Liquid Oxygen", *44th AIAA Joint Propulsion Conference, Hartford, CT, July 2008*
6. Jurns J.M. et al. "Bubble Point Measurements with Liquid Methane of a Screen Channel Capillary Liquid Acquisition Device", *54th JANNAF Propulsion Meeting, Denver, CO, May 2007.*
7. Jurns J.M., McQuillen J.B., "Bubble Point Measurements with Liquid Methane of a Screen Capillary Liquid Acquisition Device", *2007 Cryogenic Engineering Conference, Chattanooga, TN, July 2007*
8. Sinor, J. E. and Kurata, F. "Solubility of Helium in Liquid Argon, Oxygen, and Carbon Monoxide," *Journal of Chemical and Engineering Data*, Vol. 11, No. 4, 1966
9. Roder, H. M. and Weber, L. A. "ASRDI Oxygen Technology Survey. Volume 1: Thermophysical Properties," *NASA SP 3071*, 1972.
10. Jurns, J.M. and Kudlac M.T., "NASA Glenn Research Center Creek Road Complex – Cryogenic Testing Facilities", *Cryogenics 46,* 2006, pp. 98-104.
11. Meserole, J.S., Jones, O.S., "Pressurant Effects on Cryogenic Liquid Acquisition Devices," *Journal of Spacecraft and Rockets,* Vol. 30, No. 2, March-April 1993

12. Zimmerli G.A., Asipauskas M., Van Dresar N.T., “Empirical Correlations for the Solubility of Pressurant Gasses in Cryogenic Propellants”, *Cryogenics 50*, September 2010, pp. 556-560
13. Rhodes H.L., DeVaney W.E., Tully P.C., “Phase Equilibria Data for Helium-Methane in the Vapor-Liquid and Fluid-Fluid Region”, *Journal of Chemical and Engineering Data*, Vol. 16, No. 1, 1971

Thermal Vacuum Integrated System Test at B-2

M.T. Kudlac[1], H.F. Weaver[2], and M.D. Cmar[3]

[1]*NASA Glenn Research Center, Lewis Field, 21000 Brookpark Rd, Cleveland, OH 44135*
[2]*NASA Glenn Research Center, Plum Brook Station, 6100 Columbus Ave, Sandusky, OH 44870*
[3]*Sierra Lobo Inc., NASA Glenn Research Center, Plum Brook Station, 6100 Columbus Ave, Sandusky, OH 44870*

Abstract

The National Aeronautics and Space Administration (NASA) Glenn Research Center (GRC) Plum Brook Station (PBS) Space Propulsion Research Facility, commonly referred to as B-2, is NASA's third largest thermal vacuum facility. It is the largest designed to store and transfer large quantities of liquid hydrogen and liquid oxygen, and is perfectly suited to support developmental testing of chemical propulsion systems as well as fully integrated stages. The facility is also capable of providing thermal-vacuum simulation services to support testing of large lightweight structures, Cryogenic Fluid Management (CFM) systems, electric propulsion test programs, and other In-Space propulsion programs.

A recently completed integrated system test demonstrated the refurbished thermal vacuum capabilities of the facility. The test used the modernized data acquisition and control system to monitor the facility during pump down of the vacuum chamber, operation of the liquid nitrogen heat sink (or cold wall) and the infrared lamp array. A vacuum level of 1.3×10^{-4} Pa (1×10^{-6} torr) was achieved. The heat sink provided a uniform temperature environment of approximately 77 K (140°R) along the entire inner surface of the vacuum chamber. The recently rebuilt and modernized infrared lamp array produced a nominal heat flux of 1.4 kW/m^2 at a chamber diameter of 6.7 m (22 ft) and along 11 m (36 ft) of the chamber's cylindrical vertical interior. With the lamp array and heat sink operating simultaneously, the thermal systems produced a heat flux pattern simulating radiation to space on one surface and solar exposure on the other surface. The data acquired matched pretest predictions and demonstrated system functionality.

Keywords: Thermal Vacuum, Infrared lamp, Space Cryogenics, Nitrogen

Corresponding Author: Maureen.T.Kudlac@nasa.gov, Telephone: (216) 977-7476, Fax (216)433-8269

1.0 Introduction

Due to the thermal extremes in space, the hardware designer faces a unique set of challenges. Pre-flight developmental testing is essential to mission success. B-2 was designed in the 1960's to meet the challenge of testing upper-stages launch vehicles and rocket engines across their entire operational environment by simulating the pressure and thermal environment. In addition to testing upper-stages and engines, B-2 is also used as a thermal vacuum chamber. In 2006, an effort was undertaken to incrementally refurbish and modernize the facility systems. As the major facility systems are refurbished, an integrated systems test (IST) is performed. The purpose an IST is to demonstrate facility operation and performance. An IST also provides the facility staff an opportunity to gain hands on operational experience with the refurbished systems without the presence of a test article.

At the center of the B-2 complex is a large vertical vacuum chamber consisting of a cylindrical section that is 11.5 m (38 ft) diameter by 14 m (46 ft) high topped with a hemispherical head of the same diameter. The lower end of the chamber has a 3.4 m (11 ft) diameter by 11.3 m (37 ft) long exhaust duct

sealed with a high vacuum valve. Typical test article installation into the test chamber is via a hinged hatch at the top of the hemispherical dome using an 18,100 kg (20 ton) overhead crane. The hatch is 8.2 m (26.75 ft) in diameter. The nominal test article envelope is 6.7 m (22 ft) diameter by 15.8 m (52 ft) maximum vertical clearance. Personnel and small equipment access is available via 1.8 meter (6 ft) diameter circular doors located at the bottom of the chamber and at 12.5 meters (41 ft) above the bottom of the chamber. Numerous high-vacuum penetrations exist at multiple elevations for routing of fluids and electrical power, or signals internal to the chamber without compromising the vacuum environment. A cross-section elevation view of the test chamber is shown in Figure 1.

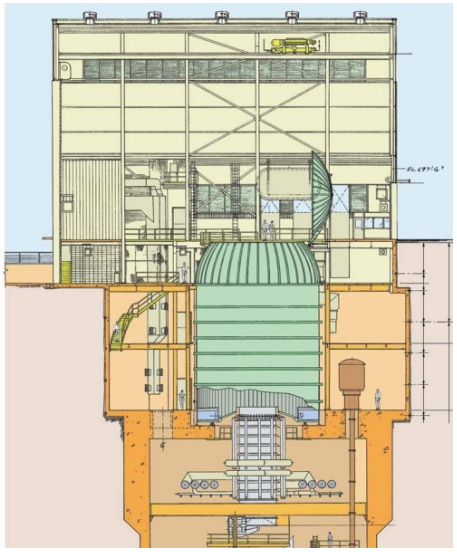

Figure 1: Artist's rendering of the B-2 test building. The vacuum chamber is shown in the center with the top access hatch open. The diffuser duct and 3.4 m valve are visible at the bottom of the chamber. A LN2 tank that supplies the cold wall is visible next to the open top access hatch.

Ultimate vacuum conditions are achieved via ten 0.89 m (2.9 ft) diameter oil diffusion pumps with integral (water) cold caps. These cold caps are cooled to approximately 280 K (504°R) by a chilled glycol system to further condense diffusion pump oil and minimize backstreaming rates.

Thermal simulation of near earth space conditions within the test chamber is accomplished via a liquid nitrogen heat sink (also called a cold wall) and an infrared lamp array.

The liquid nitrogen heat sink lines the entire interior of the test chamber, producing a final chamber interior clear diameter of 10.4 m (34 ft) and height envelope of 17 m (56 ft) on chamber centerline. Coverage includes the top access hatch, which has a separate liquid nitrogen heat sink attached. The only portion of the chamber not having integrated heat sink coverage is a 6.7 m (22 ft) diameter circle on the floor level of the chamber. Figure 2 shows a picture of the cold wall installed in the chamber.

Figure 2: View into the B-2 vacuum chamber.

The cold wall body and top cap are flooded with liquid nitrogen that is gravity-fed from a tank located above the vacuum chamber into a supply manifold located at the base. The cold wall consists of tube-in-strip panel arrangement resulting in an optically dense surface. The heat sink provides a uniform temperature environment of approximately 77 K (140°R). The cold wall is made of copper to optimize thermal conduction.

The infrared lamp array is designed to produce a heat flux pattern on the test article simulating solar exposure on one side of a test article. Currently, the array is configured with twelve (12) individually controllable "zones". Each zone consists of a vertical column of tungsten quartz infrared lamps spanning from the test chamber floor to a height of 11 m (36 ft) above floor level containing forty-eight (48) 0.75 kW lamps, for a zone power of 36 kW and a total array power of 432 kW. Lamp power is supplied by twelve zone power controllers that are rated at 50 kW and an array capacity of 600 kW.

The twelve (12) columns are distributed over a 109° arc of the test chamber circumference. The array can be controlled to provide a sinusoidal distribution of the flux pattern on the test article or other pattern as required. The radiant heat flux at the nominal test article radial envelope of 6.7 m (22 ft) diameter is 1.4 kW/m^2. Other mounting points exist for locating reflector columns at other circumferential locations within the chamber.

Test operations are conducted in a separate building, B-Control, which is located 777 m (2,550 ft) west of the test building. The state of the art controls system is a programmable logic controller (PLC) based system with a graphical user interfaces (GUI). In addition to providing facility control, the control system is used to monitor facility ancillary systems, and keep a log of key parameters. All control signals between the control room and the test facility are transmitted via a fiber optic network. The control room is shown in Figure 3.

All test data acquired is digitized in the data room located at the test facility. The resulting data is streamed immediately via fiber optics to redundant data storage arrays that are located at the B-Control building. The network does not introduce any appreciable time delay between data acquisition at the test facility and transmission to B-control. The system can acquire low speed data up to 4000 samples/sec. (The high speed channels can record data at 256,000 samples/sec.) Slower sampling rates are also achievable and set typically at 125 samples/sec. After the data has been recorded, it is then post processed where data graphs and files are generated for customer review.

Figure 3: The modernized control room for B-2. Graphical user interfaces (GUI) for the programmable logic control (PLC) based system are visible in the foreground. Along the back wall, video monitors display test site camera images.

2.0 Materials and Methods

The purpose of this integrated system test (IST) was to demonstrate the interoperability of the facility thermal vacuum systems. The facility thermal simulation systems have not been operated in a number of years. Prior to operation, the liquid nitrogen system was refurbished and the electronics for the infrared lamp array were modernized.

For the IST, three (3) zones of the solar array were installed in the chamber. A test article consisting of a rounded panel (simulating the rounded surface of a tank wall) was located 3.7 m (12 ft) above the vacuum chamber floor. (See Figure 4 and 5.) The test article was instrumented with thermocouples and heat flux sensors. Two heat flux sensors were mounted on the test article surface to measure the radiant heat flux into and out of the test article. The other two heat flux sensors were mounted above the test article to measure the flux from the lamp array. Additionally, thermocouples were placed at three (3) elevations in the vacuum chamber: 3.7 m (12 ft), 7.3 (24 ft), and 11 m (36 ft). At each elevation five (5) thermocouples were spaced equidistantly across the vacuum chamber diameter. The thermocouples were placed to obtain thermal stratification data inside the vacuum chamber.

Figure 4: The simulated test article installed in the vacuum chamber. Three (3) vertical infrared lamp arrays are visible along the back wall.

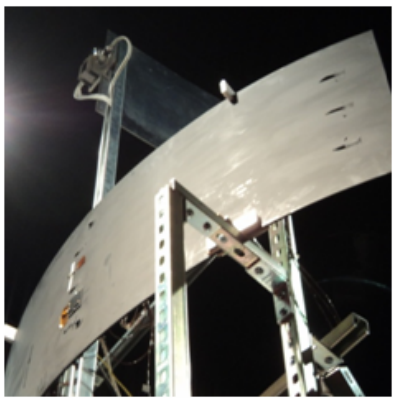

Figure 5: A close up of the simulated test article.

Following installation of the test article and instrumentation, the lamp array was powered and checked out at atmospheric pressure. The vacuum chamber was then secured and pumped down below 0.13 Pa (1 x 10-3 torr) and the lamps were activated and checked out under vacuum conditions. The lamp power was ramped from 0 to full power in four (4) steps with a power dwell of four (4) minutes at each power interval. A second test with only one infrared lamp column powered was then conducted. The array was operated in both manual and automatic mode.

Fill of the liquid nitrogen heat sink (cold wall) followed vacuum testing of the lamp array. During the fill of the cold wall body, flow was periodically terminated and the system allowed to reach equilibrium. The purpose of partially filling the cold wall was to determine the ability to provide other background temperatures in the chamber.

The lamp array was then activated with the liquid nitrogen heat sink flooded. The lamp arrays were once again ramped 0 to full power in four (4) steps with a power dwell of four (4) minutes at each power level. The liquid nitrogen heat sink was drained and the vacuum chamber re-pressurized.

3.0 Results and Discussion

Vacuum performance during the test was degraded. Pretest predictions were that levels of 7 x 10^{-6} Pa (5 x 10^{-8} torr) would be achieved with the liquid nitrogen heat sink in operation. A camera installed in the vacuum chamber for visualization of the test article was found to have a leak on the purge system. Rather than breaking vacuum to repair the leak, it was decided to continue testing with slightly degraded vacuum levels.

Performance of the infrared lamps at vacuum only conditions was controllable in both the automatic and manual modes. Four (4) different heat flux measurement were taken at the test article. The heat flux sensors mounted above the test article provided complementary data but did not precisely agree due to variation in the placement of the instrument and the instrument manufacturer. The heat flux sensors placed on the test article surface did not function as expected. One sensor was painted black and as expected the measured flux was higher than on sensors without the coating. The second sensor on the test article failed (no flux measurement) during operation with the LN2 heat sink. The infrared lamp system was designed to provide a heat flux equal to one solar constant at the test article surface. The flux equivalent to one solar constant is 1.367 kW/m^2 and varies slightly depending upon solar activity. Test results are shown in Table 1. When the cold wall is operational, the heat flux on the test article is slightly lower than when the cold wall is at ambient temperature. Reducing the number of lamp columns powered also effect the heat flux on the test article.

Table 1: Heat Flux at the Test Article

Thermal-Vacuum Condition	Columns Powered	Heat Flux kW/m^2 Lamp Power Level			
		25%	50%	75%	100%
Vacuum	3	0.16	0.73	1.6	2.5
Vacuum	1	0.10	0.48	1.1	1.6
Vacuum & Cold Wall	3	0.09	0.47	1.1	2.0

Historic facility documentation stated that cold wall fill took 24 hours to perform. Taking into account the planned flow stoppages, the wall was filled in approximately 4 hours for this test. Some optimization of technique could be performed to balance fill rate versus chilldown losses. During the test it was possible to hold liquid level in the wall and achieve relatively steady state temperature on test article surfaces. The temperature achieved during partial wall fill operations was warmer than the total fill test article steady state temperature. After the cold wall was completely filled with LN2, the test article reached steady state after approximately 5 hours. The temperatures observed at steady state on the thermocouple rakes in the chamber were consistent with the expectations. There was some thermal stratification vertically in the wall consistent with changes in saturation pressure due to the liquid head. The test article reached steady state temperature more quickly than most test articles due to the lack of insulation.

4.0 Conclusions

The IST successfully demonstrated the thermal vacuum capabilities of the B-2 facility. The infrared lamp array produced an incident heat flux in excess of a solar constant. Achieving heat flux equivalent to one solar constant can be achieved by controlling the power level supplied to the lamps or using fewer lamps. The cold wall can be completely flooded to provide approximately 77 K (140°R) background temperature for test articles. Partial fill of the cold wall can be used to achieve alternate background temperatures depending upon the test articles sensitivity to thermal gradients along the vertical axis of the chamber.

Vitae

Mr. Weaver works in the Plum Brook Management Office of NASA Glenn Research Center's Plum Brook Station in Sandusky, Ohio. He is currently serving as the Space Propulsion Research Facility (B-2) Senior Technical Lead for Vacuum Systems. He has eighteen years experience as a test engineer in NASA Glenn's Aeronautics and Space Test Facilities. He holds a BS in Mechanical Engineering from Penn State University.

Mrs. Kudlac works in the Engineering Directorate at NASA Glenn Research Center's Lewis Field in Cleveland Ohio. She is currently serving as the Space Propulsion Research Facility (B-2) Senior Technical Lead for Gas and Fluid Systems. She has over twenty years experience as a design, research, and development engineer at NASA Glenn's cryogenic facilities. She holds a BS in Chemical Engineering from the University of Detroit and a MS in Chemical Engineering from Carnegie Mellon University. She is currently a member of the AIAA and CSA.

Mr. Cmar works for the contractor Sierra Lobo, Inc. (SLI) at the NASA Glenn Research Center Plum Brook Station in Sandusky, Ohio. He is currently serving as a Facility Engineer for Cryogenic Components Laboratory (CCL), Cryogenic Research Facility (K-Site) and the Hypersonic Tunnel Facility (HTF) and as an Instrumentation Engineer at the Space Propulsion Research Facility (B-2). He has over twenty years NASA experience as an instrumentation & controls engineer, project manager and facility engineer at all of above NASA Plum Brook Facilities including the Space Power Facility (SPF). He holds a BS in Electrical Engineering from the University of Pittsburgh and is a registered Professional Engineer (PE) in the State of Ohio. He is a member of the International Society of Automation (ISA).

Lifetime Test and Heritage on Orbit of Coolers for Space Use

Katsuhiro Narasaki*, Shoji Tsunematsu, Kiyomi Ootsuka, Kenichi Kanao, Akinobu Okabayashi
Sumitomo Heavy Industries, Ltd. 5-2 Soubiraki-cho, Niihama, Ehime 792-8588, Japan
(* E-mail: Kth_Narasaki@shi.co.jp, Fax: +81-897-32-6554)
Kazuhisa Mitsuda, Hiroshi Murakami, Takao Nakagawa,
Institute of Space and Astronautical Science, Japan Aerospace Exploration Agency,
3-1-1 Yoshinodai, Chuo-ku, Sagamihara, Kanagawa 252-5210, Japan
Kenichi Kikuchi, Ryota Sato, Hiroyuki Sugita, Youichi Sato
Japan Aerospace Exploration Agency,
2-1-1 Sengen, Tsukuba, Ibaraki 305-8505, Japan
Masahide Murakami
University of Tsukuba, Tennodai 1-1-1, Tsukuba, Ibaraki 305-8573, Japan
Masanori Kobayashi
Chiba Institute of Technology, Tsudanuma 2-17-1, Narashino, Chiba 273-0016, Japan

Abstract

This paper reports results or operating statuses of ground lifetime testing and achievements on orbit of coolers for space use. The ground lifetime tests of three type coolers have carried out to demonstrate a proof of the long life and reliability. Three single stage Stirling coolers have been tested for 89016, 71871 and 68273 hours since 1998, a two-stage Stirling cooler was tested for 72906 hours and a 4K-class coolers with a two-stage Stirling cooler and a Joule-Thomson cooler was tested over 2.5 years. After the lifetime tests, few coolers were investigated the cause of the cooling performance degradation and analyzed the filled gas of the coolers. On the other hand, these coolers have been got the useful results on orbit. Three each single-stage Stirling coolers were carried on the X-ray astronomical satellite “SUZAKU” (launched in July 2005), Japanese lunar polar orbiter”KAGUYA” (launched in September 2007) and Japanese Venus Climate Orbiter “AKATSUKI” (launched in June 2010). Two units of two-stage Stirling cooler were carried on the infrared astronomical satellite “AKARI” that was launched in February 2006. A 4K-class cooler was carried on the Superconducting Submillimeter-Wave Limb-Emission Sounder (SMILES) aboard Japanese Experiment Module (JEM) of International Space Station (ISS). SMILES has launched in September 2009.

Keywords: Space use, Stirling cooler, Joule-Thomson cooler, Lifetime Test, Heritage on Orbit

1. Introduction

Sumitomo Heavy Industries, Ltd. has developed three types of small coolers with the temperature range from 80K to 4K level for space use since 1987. These coolers are single stage Stirling cooler, two-stage Stirling cooler and Joule-Thomson (JT) cooler. The single stage Stirling cooler for the cooling temperature of 80 K level has started to develop for low-noise amplifier cooling in space by modifying a commercial cooler in 1987. After that, the development has been continued for space use and three coolers were loaded on SUZAKU, KAGUYA and AKATSUKI for cooling the detectors and thermal shields etc. First, SUZAKU (former named ASTRO-EII) is the fifth in a series of Japanese astronomy satellites devoted to observations of celestial X-ray sources. It was launched into a low earth orbit with an altitude of 550km on July 10, 2005. X-Ray Spectrometer (XRS) is a system of X-ray micro-calorimeters that sit behind an imaging X-Ray Telescope. The instrument roughly covers the energy range of 0.4 - 10keV. The detectors work by monitoring the temperature of a tiny piece of silicon and measuring the temperature rise that result when it absorbs an X-ray photon. In order to detect the very small temperature rise, the detectors need to be kept extremely cold (60 mK), requiring a complex cryogenic system, which includes an Adiabatic Demagnetization Refrigerator (ADR), liquid helium, solid neon and a single stage Stirling cooler. The single stage Stirling cooler is used to

cool the outer vapor cooled shield for extending lifetime of the solid neon. Secondly, KAGUYA is the Japanese lunar polar orbiter scheduled to be launched in July 2007. Gamma-Ray Spectrometer (GRS) in Kaguya uses a high purity Ge detector cooled down to 80-90K by a single stage Stirling cooler. GRS consists of n-type Ge detector as a main detector, BGO and plastic scintillators as active shielding detectors. The 250cc Ge-detector is encapsulated in an aluminum canister with excellent energy resolution (3 keV at fwhm for ^{40}K gamma-ray line). GRS will provide the global mapping for major elements of O, Mg, Al, Si, Ti, Fe etc. and natural radioactive elements of K, Th and U with a high precision. [2] Third, AKATSUKI is a Japanese Venus Climate Orbiter and has been launched in July 2010. Mid-wave Infrared Camera (IR2) of Planet-C uses a CCD camera cooled down to around 65K by a single stage Stirling cooler.

The two-stage Stirling cooler with temperatures below 20 K for space application has been developed for AKARI (former named ASTRO-F) since 1991. AKARI is the second infrared astronomy mission of the JAXA/ISAS and it was launched into a sun-synchronous polar orbit with an altitude of 750 km for infrared sky survey in February 2006. AKARI is primarily composed of a 70 cm cryogenically cooled telescope and two focal plane instruments. One of the focal plane instruments is Far Infrared Surveyor (FIS), which will be survey the entire sky in wavelength range from 50 to 200 micron. The other focal plane instrument is equipped with Infrared Camera (IRC), which will take deep images of selected sky regions in the near and mid infrared range. The two units of the cooler were used to cool the inner vapor cooled shield for extending lifetime of the liquid helium of AKARI. [1]

The 4K-class cooler which is a combination of a two-stage Stirling cooler and a JT cooler has been developed to cool sub-millimeter detectors for a sub-millimeter atmospheric observation mission SMILES since 1993. SMILES is aimed at probing into chemical processes related to ozone depletion by means of new sub-millimeter technology such as superconductive SIS mixers and 4K-class mechanical coolers for highly sensitive observation. SMILES' sub-millimeter receiver includes two SIS mixers and four low-noise amplifiers with high-electron-mobility-transistors (HEMT), both of which are to be cooled. These components are installed in a cryostat with the cryogenic part of 4K-class cooler. [3] SMILES has launched in September 2009.

2. High-level Description of Coolers

2.1 Single stage Stirling cooler (80K-class Cooler)

The cooler for cooling temperature of 80 K level is a split type single-stage Stirling cooler, and the specification is shown in **Table 1**. A photograph of the cooler mounted on the test stand is shown in **Figure 1**. The cooler consists of a cold head unit with a single stage displacer, a compressor and a gas feed connecting tube. The dimensions of the compressor and cold head are 70 mm in diameter and 250 mm long, and 70 mm in diameter and 150 mm long respectively. The features of this cooler are moving cylinder, clearance seal by diaphragm spring, twin pole magnet system and pneumatically driven displacer. The compressor has two opposite moving cylinders for reducing the vibration level. Detail of the design and the performance test of the cooler are described in reference [9].

2.2 Two-stage Stirling cooler (20K-class Cooler)

The cooler for cooling temperature of 20 K level is a split two-stage Stirling cooler, and the specification is shown in **Table 2**. A photograph of the cooler mounted on the cryostat of AKARI is shown in **Figure 2**. The cooler consists of a cold head unit with a two-stage displacer, a compressor and a gas feed connecting tube. The dimensions of the compressor and cold head are 90 mm in diameter and 390 mm long, and 90 mm in diameter and 320 mm long respectively. The compressor has two opposite pistons mounted on a drive shaft for reducing the vibration level and the drive shaft is supported by two sets of linear ball bearings. This linear-ball-bearing supporting system achieves the piston clearance seal, the long piston stroke operation and the low frequency operation. These features have advantages for long life, compact and light weight and high efficiency of the second regenerator at low temperatures. Detail of the design and the performance test of the

cooler are described in reference [4].

2.3 4K-class Cooler for SMILES

The specification of 4 K-class cooler is shown in **Table 3** and the photograph of the whole cryogenic system for SMILES is shown in **Figure 3**. A compressor and a cold head of two-stage Stirling cooler, two JT compressors and piping of JT cycle, and a cryostat are shown in the photograph. The 4 K-class cooler is a combination of a JT cycle cooler and a two-stage Stirling cooler which is introduced in section 2.2, as former is pre-cooled by the latter. Major components of the JT cycle cooler are two JT compressors, three heat exchangers, a JT orifice and a bypass route to shorten the cooling time in the pre-cooling process. The JT compressor system consists of two units connected in tandem. The JT compressors are similar to the compressor of the two-stage Stirling cooler. Additional suction and exhaust valves mounted in each compressor are used to provide a one-way flow of helium gas. The three heat exchangers are a coaxial-double-tube heat exchanger. It is used between the room temperature and the first stage of the pre-cooler (HEX-1), between the first and the second stage of the pre-cooler (HEX-2), and between the second stage of the pre-cooler and the JT orifice (HEX-3). These three heat exchangers cool the high-pressure gas with the returning low-pressure gas. The lengths of the first, second and third heat exchangers made by thin wall stainless steel tubes are about 2.1 m, 2.0 m and 1.9 m, and the outer diameters are 5 mm, 5 mm, and 3.2 mm, respectively. The JT orifice is chosen with 24μm in diameter, and it is integrated into the 4 K stage. The valve to operate the bypass line is a kind of needle valve. A gas actuator, which is a combination of a bellows in the valve and the high pressure in the JT cycle, controls the needle to open and close the valve. Detail of the design, analysis and the performance test of the cryogenic system included the 4K-class cooler and a cryostat for SMILES are described in reference [5].

3. Lifetime Test and Operation results on Orbit

Table 4 is an attempt to summaries the number of operating hours of coolers until April 30, 2011. The Table 4 shows the operating hours on lifetime tests of coolers under development phase and the operating hours on the ground test and on orbits for launched projects. Each operation of ground lifetime test was interrupted few times per year by external reasons such as the shutdown of the plant. The operating hours mean the sum total of real operation times.

3.1 Single stage Stirling Cooler (80K-Class Cooler)

We have performed three lifetime tests of single stage Stirling coolers using an engineering model (EM) cooler and two prototype model (PM) coolers. **Figure 4** shows the lifetime test progress of the EM cooler (No. 1 in Table 4), and the two PM coolers (No. 2 and 3 in Table 4), and they have successfully passed 89016 hours, 71871 hours and 68273 hours, respectively. The **Figure 4** shows the temperatures of the cold stages and the total input power to the coolers. The test conditions are input power of 40 W (nominal), heat load of 1 W on the cold tip and normal environment temperature of 22±5 degrees Celsius. After 76000 hours later, the input power to the EM cooler needed to increase from 40W to 50W for maintaining the temperature of 80K level. Time dependent small degradation of the temperature during the lifetime test and recoverable temperature at the re-start operation after plant interrupter has been observed. As the cooler is still working with good cooling performance, we think the possibility of a mechanical fault is not likely. It seems that major source of the behavior is due to internally cooled condensation in the displacer because these units were not baked out enough and the internal gas was not enough purified. The flight model coolers have been built in a managed process at includes baking, and the charged helium-gas inside the cooler has been purified by circulating through a purifier with the temperature below 5 K at the gas exchanges for new gas after the initial running of about 1000 hours and the final system test. A time chart of operating status for a single-stage Stirling cooler of the XRS in SUZAKU (No. 4 in Table 4) is shown in **Figure 5** which shows temperatures of three vapor cooled shields and input power to the cooler with operating time. The cooler is connected to cool the outer vapor cooled shield. Initial XRS operations were excellent as follows;

(1) Estimated cryogen lifetime was well over 3 years.

(2) X-ray micro-calorimeter energy resolution performance demonstrated and a new type of

anticoincidence detector worked perfectly.

(3) ADR cooled to 60 mK with 38 hours hold time and 10 minutes recharge time.

(4) Single stage Stirling cooler is working well.

However, after 16 days in orbit, the vent valves of helium and neon tanks were opened as planned, and a few days later, liquid helium was lost due to a problem of compromised vacuum with venting of the helium and neon cryostats to space. [6] [7] [8] As the solid neon has been vaporized at 1.8 years after launch, temperatures raise of the inner and middle vapor cooled shields was observed in Figure 5. But the cooler has successfully passed 5.8 years as the outer vapor cooled shield has kept low temperature. The input power to the cooler is 35 W in nominal. The cooler operation is continuing as a kind of lifetime testing on orbit. **Figure 6** shows temperatures of Ge detector, cold tip of the cooler and radiator and input power to the cooler with operating time of GRS in KAGUYA on orbit. Kaguya was touched down on moon and completed the mission on July 30, 2009. As GRS could corrected a large number of useful data, future detail analysis of the data will provide new and more precise maps for major elements of O, Mg, Al, Si, Ti, Fe etc. and natural radioactive elements of K, Th and U on the lunar surface. [14] The real operating hours of the cooler (No. 5 in Table 4) was 21800 hours as the sum total of ground and orbit. Although the cooler was experienced on/off operations over 16 times in orbit, the cooler kept to cool the temperature of Ge detector to 80 K during the operation with input power of 35 W.

3.2 Two-stage Stirling cooler (20K-Class Cooler)

Figure 7 shows the ground lifetime test results of a two-stage Stirling cooler for AKARI from March 1999 to August 2008, the sum total of operation times was 72605 hours. The test conditions are input power of 60 W (nominal), no heat load on cold tip and normal environment temperature of 22±5 degrees Celsius. Little by little degradation of temperature during the first half of lifetime test and recoverable temperature at the re-start operation after plant interrupted were observed. The test has successfully passed 1.5 years, which is the mission life in the design of Akari with the liquid helium. Although the design goal of 30000 hours has almost achieved, big performance degradation was observed after 34000 hours passed. The cooler was investigated to analyze the reason of performance degradation after the lifetime test. Main source of the cooling performance fell off was found due to degradation of the cold head. **Figure 8** shows a summary of the investigation of the cold head. At first, we changed internal filled helium gas with a new purified one and performed a cooling test. A decline of purity of the filled helium gas was demonstrated to influence approx. 10% of the cooling capacity degradation. On the other hand, the old helium gas was analyzed by a mass spectrometer and the increase of CO, CO_2, CH_4 and H_2O was observed because the EM cooler was not baked out enough and the internal gas was not purified. The source of contamination seems to be outgases from component material like mainly adhesives and organic material. Second, seals and regenerators in the cold head of the cooler were replaced with new one and performed the cooling test one by one. The major source of the degradation is due to abrasion at seals of cold head and they were approx. 76% of the cooling capacity degradation. Next generation of two-stage Stirling cooler for future projects has been improved as follow and started a lifetime test. (No. 12 in Table 4) [12]

1) Change from contact seal to clearance seal at displacer of cold head for reducing abrasion

2) Re-selection of materials with a characteristic of lower outgas and reduction of amount of adhesives

3) Improvement for managed process of the baking and method of purification

Figure 9 shows temperatures of second stage of the two coolers and outer shell, and total input power to the two coolers with operating time of AKARI on orbit. (No. 8 and 9 in Table 4) Infrared astronomy observation of AKARI with liquid helium has been successfully completed during 1.5 years until the liquid helium was vaporized. During the period, the two coolers worked well with total input power of 100 W. [10] [11] One month later from the event, one cooler was stopped the operation due to current leak from coil to pressure container in the cold head and subsequent miss operation. However the other cooler worked for an

observation using the mid-infrared detector in original planning until February 2010. As the cooler was observed same current leak in the cold head, the cooler worked with decreasing the displacer stroke by gradually reducing the input power to the cold head. The second-stage temperature of the cooler can be observed the gradually rising from 38 K to 43 K during the one cooler operation of about 2.5 years. The sum of real operating hours included the ground operation was 15291 hours and 42448 hours respectively.

3.3 4K-Class Cooler

A first lifetime test of 4K-class cooler was conducted from September 1998 to December 1999 for SMILES. (No. 13 in Table 4) Detail is described in reference [3] and the summary is as follows:

(1) Over the whole operating hours the stage was kept at less than 4.9K within increasing 10 W of input power to JT compressor.

(2) Major source of the degradation was an enlarged gap between piston and cylinder in JT compressor due to abrasion.

(3) As for the working gas, the increase of CO (500 ppmv), CO_2 (580 ppmv), CH_4 (46 ppmv) and H_2O (42 ppmv) was observed by analyzing of a mass spectrometer. But this sort of contamination was not major cause of cooling performance degradation, at least for the period of this test.

From the above test results, JT compressor for SMILES has been improved as follows:

1) Adoption of supporting system by linear ball bearing for clearance seal

2) Modification for managed process of the baking and method of purification

Figure 10 shows temperatures of 100K, 20K and 4K- stage of the coolers and environment with operating time of SMILES on orbit. (No.11 and 15 in Table 4) The input power to the two-stage Stirling cooler was 50W and the input power to the JT compressors was 20W. After 9 months later from the operation start, SMILES stopped operation due to disorder of a water cooling system for JEM, and the cryogenic system backed to room temperature level. By that time cryogenic system for SMILES demonstrated a good enough cooling performance as shown in Figure 10 for the sub-millimeter atmospheric observation. [15] The sum of real operating hours included the ground operation was 8285 hours for two-stage Stirling cooler and 7782 hours for JT cooler. After restoration of the water cooling system, the cryogenic system for SMILES was restarted a cooling operation in July 2010, but it did not achieve a temperature of 4K level. **Figure 11** shows the cooling down process. When the temperature of 100K-stage reached around 150 K but the temperatures of lower stages were still warm, a gas flow of the JT cooler seems to stop from changing suction pressure at lower side of the JT compressor and temperature of the by-pass valve in further cooling down process. We believe the cause is due to block by internally cooled solidification of impure gas in the narrow high pressure piping around the 100K-stage. The main impure gas is CO_2 because it has a property to become solid at such temperature and its saturation pressure region, and the concentration of CO_2 contamination is estimated as about 1200 ppmv which is an unexpected amount. The cooling capability of two-stage Stirling cooler and the performance of JT compressors are not observed any degradation. Regarding SMILES, we are still trying to re-cooling down by changing various procedures of cool down process.

On the other hand, we have performed a lifetime test of a 4K-class cooler using a prototype model cooler of SMILES since May 2007. (No. 10 and 14 in Table 4) The parasitic heat and the heat from instruments are simulated to be equivalent to SMILES by heaters. Environment temperature is 20 ± 4 degrees Celsius. [13] The test result is shown in **Figure 12**. The power consumption of the two-stage Stirling cooler was 60 W. The power consumption of the JT compressor was 30 W when the lifetime test started, however 3,900 hours later, the performance of the JT compressor degraded, hence we had to increase the operating power of the JT compressor to compensate. The others, the operating condition have not been changed. When the operation time reached 12,000 hours, it was 36 W, or the total power consumption was 96 W. The operating voltage of the two-stage Stirling cooler has not changed through the test. [10] At September 2010, the lifetime test was stopped to analyze the filled gas in JT cooler for a cause investigation of SMILES on orbit. The sum of real operating hours was 22283 hours. The helium gas filled in the JT cooler was analyzed by a mass

spectrometer and the increase of CO and CO_2 was observed, but increase of H_2 and H_2O was not observed. The concentration of CO contamination was 98 ppmv, and the concentration of CO_2 contamination was 450 ppmv which is much less than the estimated amount from SMILES on orbit. At the present, an allowable concentration of CO_2 contamination is thinkable as 400 ppmv~500 ppmv during an operation period to be expected.

4. Conclusions

Ground lifetime tests of three type coolers which are single-stage Stirling cooler, two-stage Stirling cooler and JT cooler have been performed. Three single-stage Stirling coolers have been tested over 89016, 71873 and 68273 hours since 1998, a two-stage Stirling cooler was tested for 72906 hours and 4K-class coolers with a two-stage Stirling cooler and a JT cooler was tested for 22283 hours. These results demonstrated a proof of long life and reliability for space use. Three each single-stage Stirling coolers were carried on SUZAKU, KAGUYA and AKATSUKI respectively, two set of two-stage Stirling coolers were carried on AKARI and a 4K-class cooler was carried on SMILES. These coolers have been got the useful results for future projects on orbit. From the investigation results regarding degradation of cooling performance, we have learned that abrasion at seal and filled gas contamination especially CO_2 are critical. Next generation models of two-stage Stirling cooler and JT cooler for future projects have been improved for the abrasion and started a lifetime test. Development and investigation are still continuing to improve the decreasing contamination for the filled gas in JT cooler.

Acknowledgements

We wish to thank all staff of SUZAKU/XRS, KAGUYA/GRS, AKARI and SMILES project teams, and cryogenic group at SHI Niihama for their supports to this work.

References

[1] H. Murakami, Japanese Infrared Survey Mission IRIS (ASTRO-F), Proceedings of SPIE, 3356, pp.471-477, 1998

[2] N. Hasebe, E. Shibamura, T. Doke, C. D'Uston, M. Grande, T. Kashiwagi, J. Kikuchi, M. Kobayashi, et al. "Gamma-ray spectrometer for Japanese lunar polar orbiter," Advances in Space Research, 23(1999) pp. 1837-1840.

[3] J. Inatani, K. Narasaki, S. Tsunematsu, M. Kyoya, T. Manabe, M. Seta, T. Iida and R. Satoh, "Mechanical Cooler and Cryostat for Submillimeter SIS Mixer Receiver in Space," Proceedings of SPIE, Vol. 4540 September 2001

[4] K. Narasaki, S. Tsunematsu, K. Ootsuka, M. Kyoya T. Matsumoto, H. Murakami and T. Nakagawa "Development of Two-stage Small Stirling Cooler for ASTRO-F," Adv. in Cryogenic Engin., Vol. 49B pp.1428-1435, 2004

[5] K. Narasaki, S. Tsunematsu, S. Yajima, A. Okabayashi, J. Inatani, K. Kikuchi, R. Satoh, T. Manabe and M. Seta "Development of Cryogenic System for SMILES," Adv. in Cryogenic Engin., Vol. 49B pp.1785-1796, 2004

[6] R. Fujimoto, K. Mitsuda, M. Hirabayashi, K. Narasaki, S. Breon, R. Boyle, M. DiPirro, S.M. Volz and R.L. Kelley, "Neon Dewar for the X-ray Spectrometer Onboard Astro-E2 Satellite," Proceedings of the 11th International Workshop on Low Temperature Detectors, Tokyo, August 1-5, 2005

[7] P. Shirron, M. DiPirro, J. Panek, R.L. Kelley, K. Mitsuda, R. Fujimoto, M. Hirabayashi and D. McCammon, "The Astro-E2/XRS-2 Helium Insert System, "Proceedings of the 11th International Workshop on Low Temperature Detectors, Tokyo, August 1-5, 2005

[8] K. Mitsuda and R.L. Kelley, "The Suzaku X-Ray Obsevatory," Presentation of the Six Years of Science with Chandra , Boston, November 2, 2005

[9] K. Narasaki, S. Tsunematsu, K. Kanao, K. Otsuka, S. Hoshika,K. Fujioka, K. Tsurumi and M. Hirabayashi "Development of Single-stage Stirling Cooler for Space Use," Adv. in Cryogenic Engin., Vol.51B pp.1505-1512, 2006

[10] T. Nakagawa, K. Enya, M. Hirabayashi, M. Kaneda, Y. Kimura, T. Matsumoto, et al. "Flight

Performance of the AKARI Cryogenic System," Publ. Astron Soc. Japan, 59, pp.377-387, 2007
[11] M. Hirabayashi, K. Narasaki, S. Tsunematsu, Y. Kimura, S Yoshida, H. Murakami, T. Nakagawa, et al. "Thermal design and its on-orbit performance of the AKARI cryostat," Cryogenics, 48, pp.189-197, 2008
[12] Y. Sato, H. Sugita, K. Komatsu, R. Shimizu, H. Uchida, T. Nakagawa, et al. "Development of Advanced Two-stage Stirling Cryocooler for Next Space Missions," Cryocooler Vol. 15 (2008) pp.13-20
[13] K. Otsuka, K. Narasaki and S. Tsunematsu, "Test Results after Refurbish of Cryogenic System for SMILES," Cryogenics 50, pp. 512-515 (2010)
[14] S. Kobayashi, N. Hasebe, E. Shibamura, O. Okudaira, M. Kobayashi, et al. "Determining the Absolute Abundances of Natural Radioactive Elements on the Lunar Surface by the Kaguya Gamma-ray Spectrometer", Space Science Reviews, Volume 154, Issue 1-4, pp. 193-218, 2010
[15] S. Ochiai, K. Kikuchi, T. Nishibori, T. Manabe, H. Ozeki, et al. "Performance of JEM/SMILES in orbit", Proceedings of 21st International Symposium on Space Terahertz Technology, pp.179-184, 2010

Table 1 Specifications of single-stage Stirling cooler

Items	Specifications
Cooling Capacity	1 or 2W at 80 K
Environment Temp.	200 K to Room temperature
Power Consumption	30 W for 1W , 50 W for 2 W
Life Time	5 years
Mass	4.2 kg
Drive Frequency	52 Hz

Table 2 Specifications of two-stage Stirling Cooler

Items	Specifications
Cooling Capacity	200 mW at 20 K 1000 mW at 100 K
Environment Temp.	200 K～300 K
Power Consumption	90 W
Life Time	3 years
Mass	9.5 kg
Drive Frequency	15 Hz

Table 3 Specifications of 4 K-class cooler

Items	Specifications
Cooling Capacity	20 mW at 4.5 K
2-stage Stirling Cooler Cooling Capacity Power Consumption	 0.2 W at 20K, 1 W at 100 K 90 W at 15 Hz operation
JT Compressors Pressure Mass Flow Rate Power Consumption	 Supply : 1.6 MPa , Return : 0.1 MPa 2.0 NL/min (=6 mg/s) 50 W at 30 Hz operation
Heat Exchangers Efficiency Allowable Pressure Drops	 97 % 0.03 MPa in low pressure side
JT Orifice Diameter	20～30μm

Table 4 Summary of Operating hours

Test Models or Projects	Temp. Level	Operating hours			Remark
		Earth	On Orbit	Total	
Single-Stage Stirling Cooler					
1 Engineering Model	80K	89016	N/A	89016	1999 November: Operation Start
2 Prototype Model-1	80K	71871	N/A	71871	2001 November: Operation Start
3 Prototype Model-2	80K	68273	N/A	68273	2002 May: Operation Start
4 ASTRO-E 2 (SUZAKU)/XRS	150K	2000	51400	53400	2005 July : Operation Start
5 SELENE (KAGUYA)/GRS	80K	9200	12600	21800	2007 December :Operation Start 2009 June: Mission Completed
6 Planet-C (AKATSUKI)/IR2	60K	500	1200	1700	2010 July: Operation Start
Two-stage Stirling Cooler					
7 Engineering Model	20K	72906	N/A	72906	1999 March: Operation Start 2008 August: Operation Stop
8 ASTRO-F (AKARI)-A	20K	2098	40350	42448	2006 February: Operation Start 2010 May: Operation Suspension
9 ASTRO-F (AKARI)-B	20K	2121	13800	15921	2006 February: Operation Start 2007 October: Operation Stop
10 Prototype Model for SMILES	20K	22283	N/A	22283	2007 May: Operation Start 2010 September: Operation Stop
11 SMILES	20K	2250	6035	8285	2009 September: Operation Start 2010 June: Operation Suspension
12 Advanced Prototype Model	20K	5116	N/A	5116	2010 January: Operation Start
JT Cooler for 4 K level					
13 Engineering Model for SMILES	4.5K	9315	N/A	9315	1998 September: Operation Start 1999 December: Operation Stop
14 Prototype Model for SMILES	4.5K	22283	N/A	22283	2007 May: Operation Start 2010 September: Operation Stop
15 SMILES	4.5K	1172	6010	7782	2009 September: Operation Start 2010 June: Operation Suspension
16 Advanced Prototype Model	4.5K	4655	N/A	4655	2010 January: Operation Start

Figure 1 Single-stage Stirling Cooler on test bench

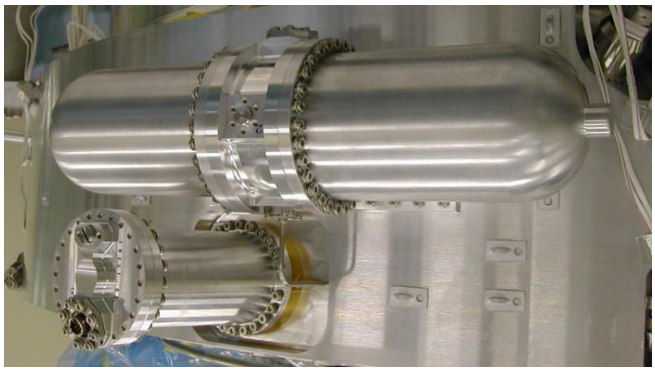

Figure 2 Two-stage Stirling Cooler on the cryostat of AKARI

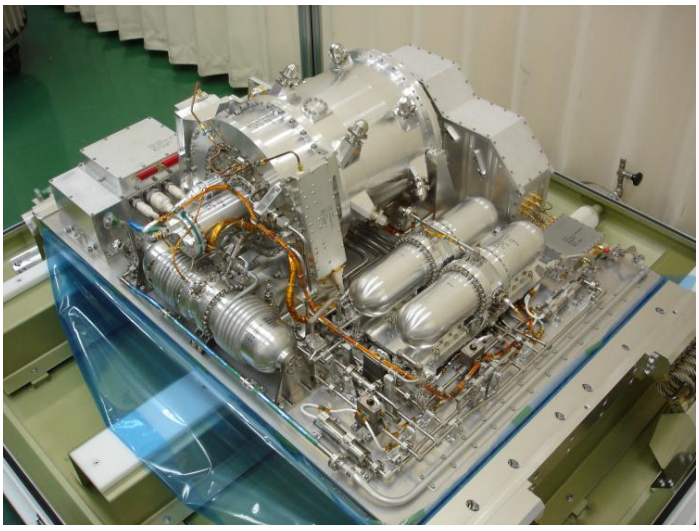

Figure 3 Whole Cryogenic Systems for SMILES

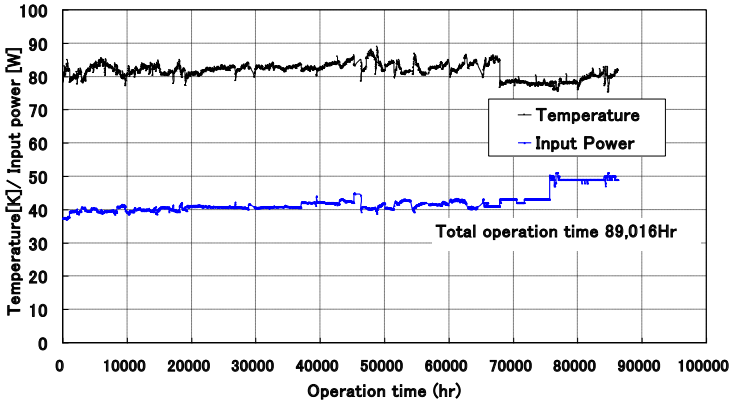

Figure 4(a) Status of ground lifetime tests of three single-stage Stirling coolers（EM）

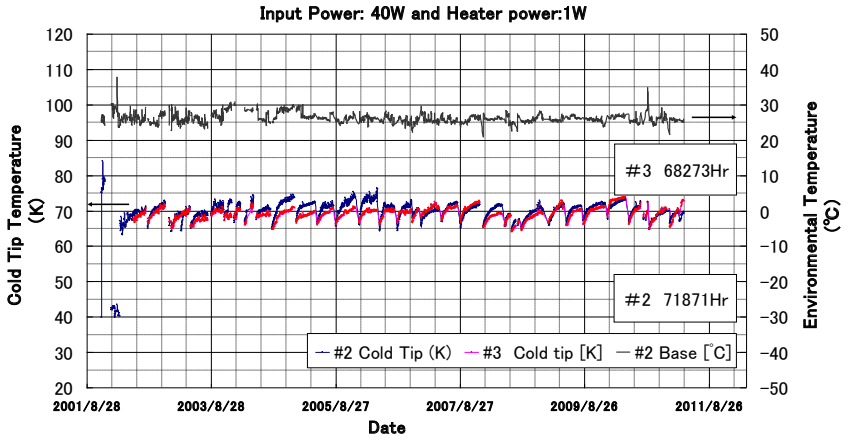

Figure 4(b) Status of ground lifetime tests of two single-stage Stirling coolers

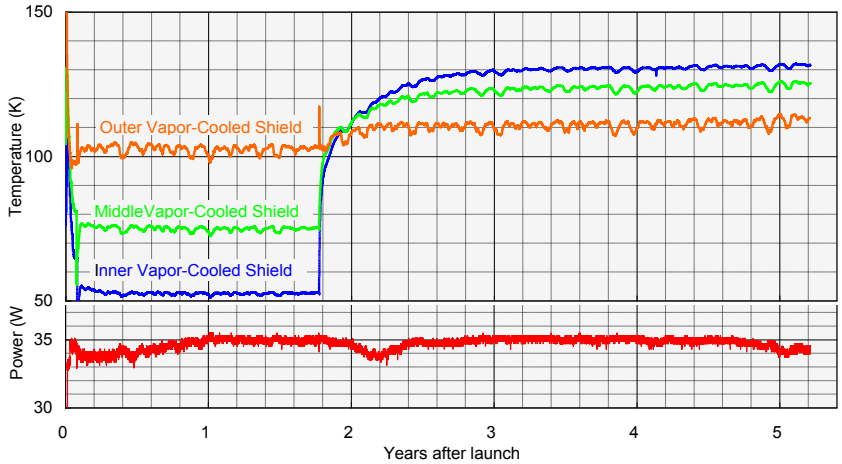

Figure 5 Operation status of single-stage Stirling cooler for SUZAKU on orbit

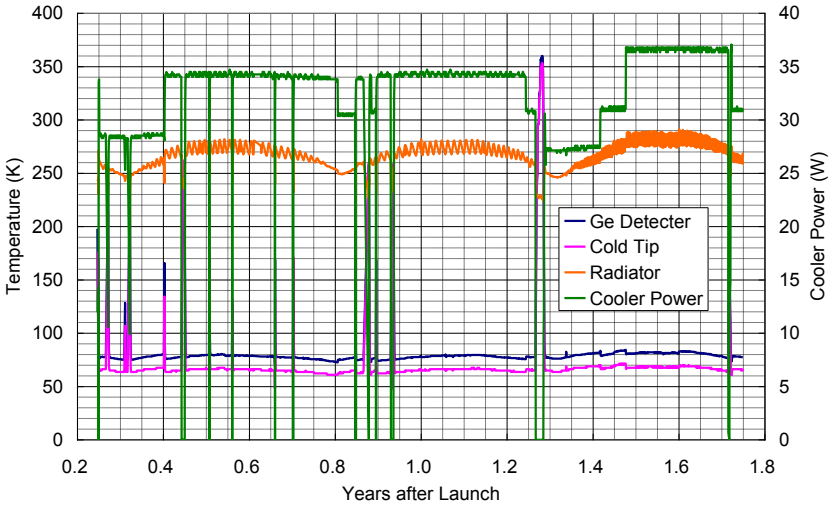

Figure 6 Operation status of single- stage Stirling cooler of GRS in KAGUYA on orbit

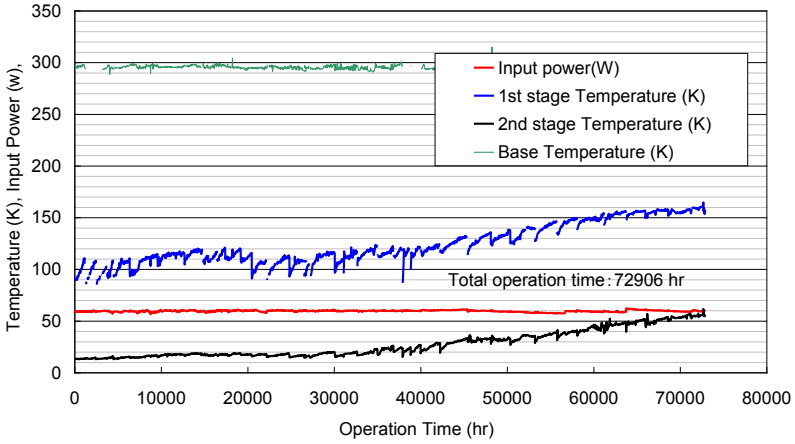

Figure 7 Results of a ground lifetime test of two-stage Stirling cooler

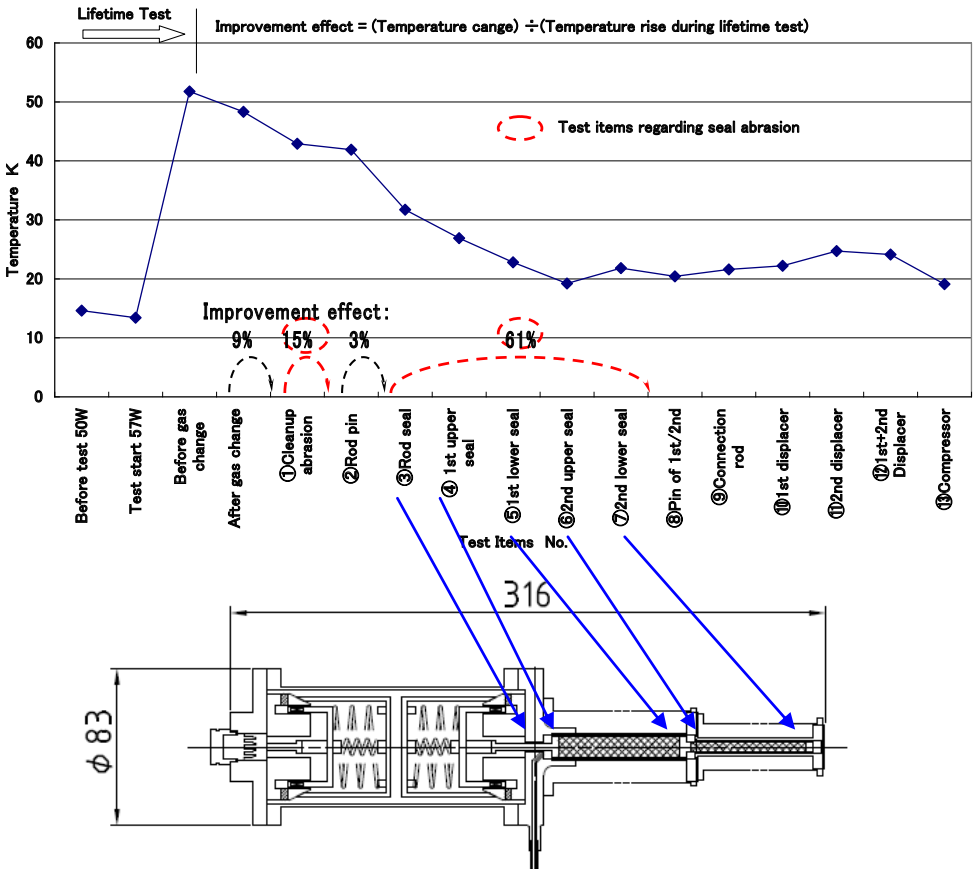

Figure 8 Investigation results for performance degradation in cold head of two-stage Stirling cooler

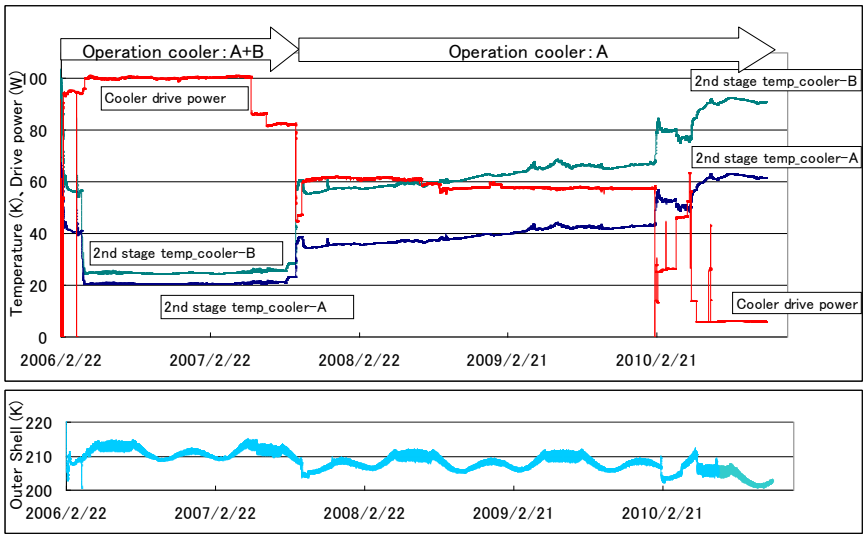

Figure 9 Operation status of Two-stage Stirling coolers of AKARI on orbit

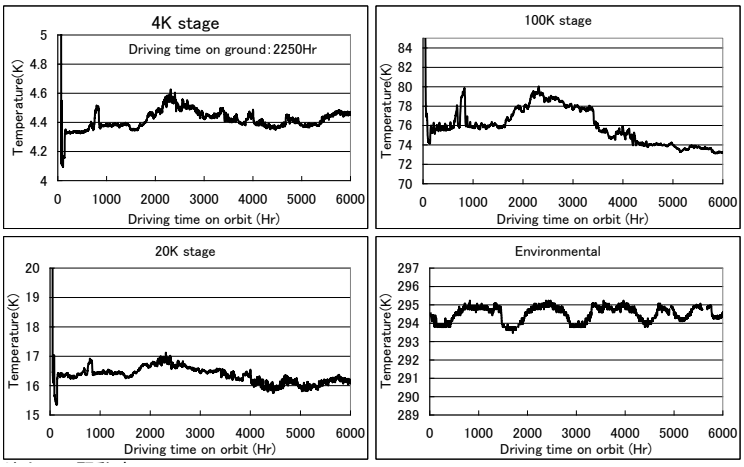

Fig.10 Operating results of 4K-class cooler for SMILES on orbit

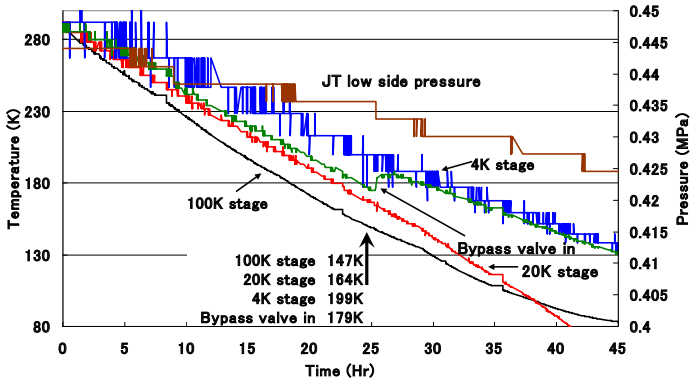

Fig.11 A cool down process with trouble of 4K-class cooler for SMILES on Orbit

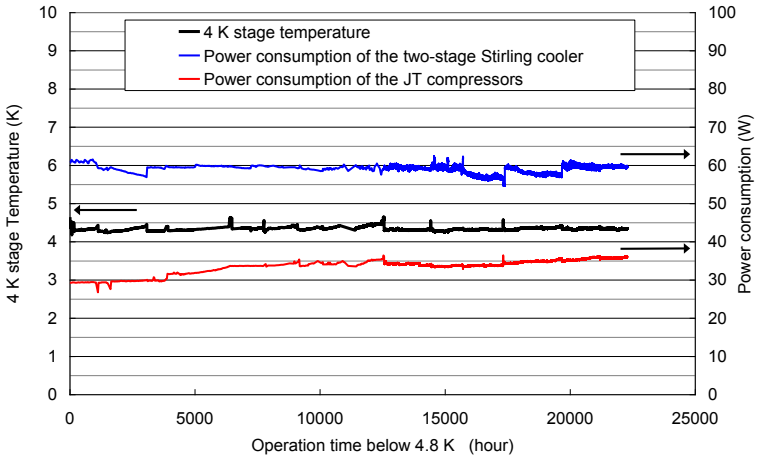

Fig.12 Results of a ground lifetime test of 4K-class cooler for SMILES

LIFE TESTING OF THE ABI CRYOCOOLER:
TWO YEARS COMPLETE

Perry G. Ramsey[a*]
Kirsten S. Swanson[b]

[a]ITT Geospatial Systems
1919 W. Cook Road
PO Box 3700
Fort Wayne, Indiana 46801
Phone: 1(260)451-1093
Fax: 1(260)451-6033
perry.ramsey@itt.com
[*]Corresponding author

[b]ITT Geospatial Systems
1919 W. Cook Road
PO Box 3700
Fort Wayne, Indiana 46801
Phone: 1(260)451-6232
Fax: 1(260)451-6033
kirsten.swanson@itt.com

The Advanced Baseline Imager (ABI) is a prime payload for the GOES-R (Geostationary Operational Environmental Spacecraft) series of meteorological satellites. Focal plane temperature control is provided by a two-stage cryocooler based on the NGAS HEC (Northrop Grumman Aerospace Systems High Efficiency Cryocooler) design. To demonstrate the long-term operation of this cooler, a dedicated life test is being performed. The life test cooler is close to the flight design, differing only in minor details of the cold head structure. The test concept simulates continuous operation the cooler at flight like conditions. Long term testing started on 12 June 2009, and has continued to this date. Test performance and anomalies are discussed.

Keywords
Cryocooler, life test, HEC

1 Introduction

The Advanced Baseline Imager (ABI) is a prime payload for the GOES-R (Geostationary Operational Environmental Spacecraft) series of meteorological satellites. This is the first use of an active cryocooler in an operational (as opposed to scientific) satellite. The mission assurance plan calls for a ten year life test on the cryocooler design, with five years being completed before first launch.

This article covers initial testing of the life test cryocooler. As of the date of preparation the cooler has been under test for 20 months.

2 Materials and Methods

2.1 Unit Under Test

The Unit Under Test (UUT) is derived from the Northrop-Grumman Aerospace Systems (NGAS) High Efficiency Cryocooler (HEC). Prototype flight units were described in Colbert et al. 2008 and Ramsey et al. 2009. A representative unit is depicted in Figure 1. The main unit, depicted on the left side of Figure 1, is composed of a compressor with an integral linear pulse tube cold head. This side of the cooler consumes the bulk of the work produced by the compressor, and is used to generate the lowest temperature. A tap on the compressor feeds a second cooler through a transfer line. This is the remote cooler, depicted on the right side of Figure 1. The remote cooler has its own expansion volume, and uses a coaxial cold head.

The compressor is driven by a dual voice coil-type linear motor. The motor is driven by a complex AC waveform, containing the fundamental frequency and higher harmonics. The basic power is set by magnitude of the fundamental; harmonics are added to provide vibration control.

Temperature control is provided at the integral cold head through a feedback control system that varies the driving waveform of the compressor to modulate the amount of cooling. The remote cooler is not directly temperature controlled. The compressor input power is modulated to control the temperature of the integral cold head, and a fraction of the work produced. This fraction is not constant; it is observed (Ramsey et al. 2008) that a colder remote draws a greater fraction of the total compressor work.

The ABI procurement specifications call for 2.27 W of cooling at 53 K at the integral cold head and 5.14 W at 183.1 K at the remote cold head. In the test setup, these fixed loads are imposed on each cold head. The control system modulates the compressor to achieve the integral temperatures, and the remote temperature floats in response.

The only significant difference between this unit and the flight units is the thickness of the remote pulse tube wall. The ABI flight units have a slightly thicker wall to withstand higher flight structural loads. This change imposes a small (< 100 mW) additional load on the flight coolers.

2.2 Test Support Equipment

Operating the life test requires 1) a vacuum environment, 2) powering and controlling the cooler, 3) test telemetry and monitoring, 4) simulated heat loads at the cold heads, and 5) waste heat removal.

The UUT is mounted in a horizontal cylinder vacuum chamber approximately 1.2 meters in diameter and 1.2 meters long. Vacuum levels below $1x10^{-6}$ torr are typical. The cooler has shared the chamber with a bearing life test since December 2010.

The cooler is mounted to a fixture that holds the cooler in "fingers up" orientation, placing the compressor below the cold heads. This produces the most flight-like loads on the linear cold head by putting the regenerator below the pulse tube. This puts the cold end of the pulse tube at the bottom, which eliminates internal heat leaks due to natural convection.

The cooler is powered through a cryocooler support rack supplied by NGAS. This unit provides the functionality of a flight cryocooler control electronics box. The control unit provides the driving waveform for the cooler, temperature control, vibration control, fault protection, and returns the full set of telemetry that is available from the flight cooler. The rack also contains power supplies and an off the shelf computer for interfacing with the control electronics and other peripheral power supplies and data loggers. Because the control electronics produces a complex AC waveform, the rack includes a Valhalla 2400 Harmonic Power Analyzer to accurately measure the power delivered to the compressor. In this paper, the power for a single motor coil is reported, as determined by the Valhalla meter. The other coil draws about the same total compressor power is approximately twice the reported value.

Heat loads are delivered to the coldheads using copper blocks with resistive heaters. Heaters are powered by an Amrel PD 120 DC power supply. A Lakeshore 218 is used to monitor eight PRTs and to control the cold head heaters, including alarms and fault protection. PRTs are located as described in Table 1. Only the first eight are read by the controller. PRT-9 is included for redundancy; wiring external to the vacuum chamber would be changed in case of a failure of PRT-8. There is also a pair of flight PRTs (primary and redundant) attached directly to the integral cold head, which is returned through the cryocooler telemetry stream. Remote cold head temperature is only measured at the attached heater block.

Cooling is provided by a Neslab ThermoScientific Thermoflex 1400 chiller/circulator. The working fluid is a 50/50 mixture of an off-the-shelf propylene glycol coolant and water. Cold plates are attached to the cryocoolers at their standard heat rejection surfaces. Flow is integral first, then remote. The bearing test also uses the circulator, downstream of the cryocooler.

2.3 Test Procedures

Prior to long term thermal testing, the UUT was put through vibration and thermal cycling tests. Before each test, a thermodynamic performance measurement was made in vacuum.

2.3.1 Initial Thermal Performance

The baseline performance test for the cooler is a load line. The compressor power required to drive the cooler to spec levels of temperature and heat load is determined. Only the integral cold head is controlled; the remote cold head temperature floats to the temperature that is in equilibrium with the loads applied. The power required to hold this condition is recorded. The set point is then changed to 32 K and the cold tip heaters are turned off. The cooler will never reach 32 K even with no load, which causes the cooler to operate at its maximum allowable power level. The maximum power level of the cooler is adjusted as required so the power consumed matches the level observed in the first part of the test. This test is used as a standard health check on the cooler. It was run as part of cooler acceptance at NGAS, and it is repeated periodically to check the baseline cooler performance.

2.3.2 Vibration Testing

The cryocooler was subjected to a random vibration test at levels reflecting predicted launch loads. At the completion of the random test the thermal performance test was repeated.

2.3.3 Thermal Cycling

The cryocooler was then put through 25 cycles over a range of -30 to +60C. The test was run in an ambient atmosphere in a Thermotron 2800 thermal test chamber with nitrogen purge to prevent condensation. The chamber ramp rate was 1.5 deg C/minute. Thermocouples were attached to the cooler at the integral cold block, integral reject surface, remote cold block, remote reject surface, and support baseplate. For the first cycle, the chamber was held at the maximum temperature, in order to determine the soak time required for the cooler to reach the test temperature. Similarly, the stabilization time at minimum was also determined. The times were used to set up the controller for automatic execution of the subsequent 24 cycles, with a two hour cold soak at each plateau.

2.3.4 Long Term Thermal Testing

The cooler was installed in the life test chamber and the thermal performance test was repeated. The long term thermal test followed immediately, beginning on June 12, 2009. The cooler was set to control to the specification temperature on the integral and loads applied to the integral and remote cold heads.

Since this is a long term test, 100% up time is not expected. In the event of cryocooler shut down the cause is evaluated. The cooler is re-started when is deemed safe to continue.

After approximately one year of operation (June 26, 2010) the baseline thermal performance test was repeated. Some additional testing at intermediate values was added to more thoroughly characterize the cooler.

The cooler was returned to normal operation after the annual test and has continued to be operated. An annual performance check is expected to be performed for the duration of the test. The test goal is to simulate 10 years (87,660 hours) of on-orbit operation.

3 Results

3.1 Thermal performance tests

Four load line thermal performance tests were run prior to initial start of the test: acceptance test at NGAS, initial test at ITT before vibration testing, pre-cycling, and when installed into the thermal chamber for long term operation. A fifth test was performed at the first annual check in June 2010. These are summarized in Table 2. In general, the thermal performance is similar at all tests. Differences in results are considered to be within the limits of repeatability of the measurement method, i.e. they show no consistent change in performance.

The notable inconsistency is the test done prior to thermal cycling ("Pre-Cycle 2009"). The compressor power is 8W lower than in the other tests. On closer examination it was found that the system was not allowed adequate time to stabilize while measuring the power at specification loads prior to moving on to the next step of the procedure. The remote cold head was still cooling down when the point was declared complete. Since a warmer remote draws a lower fraction of the total compressor work, the overall system power was lower than it would have been had the test been allowed to run to equilibrium.

Another way to show the interaction between the two sides of a two stage cooler is a "window pane" plot. This plot tests the cooler at all combinations of maximum and zero power on each of the two cold heads at constant power. Collection of these points was part of acceptance testing on this cooler at NGAS, and the measurements were repeated during the first annual check. Power was nearly the same in these two tests, 123.9W for the NGAS test and 122.6W for the ITT test. Figure 2 is a combination of ITT and NGST data collected for the active cooler at a reject temperature of 300K. The cold head temperatures are slightly higher on all counts in the ITT test. The warmer remote temperatures are possibly due to the change in sensor position. In the NGAS test there was a temperature sensing diode directly on the remote cold head, while for the ITT test the sensor is a PRT on the heater block that is attached to the cold head. The sensor measures slightly higher temperatures due to temperature drops across the block and bolted interface.

3.2 Long term operation

Side A compressor motor power as a function of time for the first 160 days of the test is shown in Figure 3. These data have been filtered to eliminate off periods and power ramp ups during re-starts. This is approximately one-half of the total compressor power. Initial Side A power was approximately 63 W, rising to approximately 67.5 W over the following forty days. During normal operation the integral cold head remained stable, within 0.050 K of its set point of 53 K. Since the remote cold head is not directly controlled it fluctuates somewhat during operation. The in-flight application uses a control heater to stabilize the components that are cooled by the remote.

The cooler safed itself three days after startup due to a vibration overload trip, resulting in both cold heads returning to room temperature. After an investigation of the event the cooler was re-started. The initial power was approximately the same as at the beginning of the test, again rising to about 67.5 W after a few weeks. This happened again several times in the following weeks, typically going through the same progression. This variation is believed to be due to water ice accumulating on the cold head or in the blankets. The ice increases the effective emittance of the insulation system, allowing more heat leak into the cold head. The control system responds by raising the power levels as required to hold the cold head temperature constant. When the cooler turns off, the frost sublimates, and the performance of the insulation system returns to its original value.

Figure 4 shows a time series of Motor A power through the date of this writing, as a function of days since test start. Compared to Figure 3 it appears quite noisy. Low power periods (i.e. restarts) have not been filtered out of this chart, so the shutdowns are more apparent. The extended periods of time without data at approximately 170 and 200 days were extended shutdown periods for the weeks of Thanksgiving and Christmas/New Years 2009. The shut down near 530 days was for installation of the bearing test in the chamber. The pattern of power increase with time seen in Figure 3 is repeated many times in Figure 4. After an extended shut down, the power starts low, then increases with the amount of time spent cold.

As of April 27, 2011, the cooler has achieved a total run time of 14,072 hours, equivalent to 1.61 years. This represents a total up time of 86%. Since June of 2010, total up time has been 94.5%. At that rate we expect to complete five years of operation late in 2014, ten years of operation in early 2020.

3.3 Anomalies

3.3.1 Trips

Since the beginning of the test on June 12, 2009, a total of 42 safing events have occurred. Forty of the forty-two trips were due to vibration overload trips. These trips are a result of the cooler sensing excessive vibration loads over a short period. These are ordinarily due to shock events; this response is a built in feature of the cooler to protect itself from potential damage. The remaining two trips were caused by a power outage and the accidental disconnection of a cable.

As shown in Figure 5, all trips have occurred on weekdays. One interesting cluster is early Wednesday mornings. Wednesday happens to be mopping day in the lab, during third shift. Once the maintenance staff was alerted to the sensitivity of the equipment, no additional trips have occurred during this period. The remaining safing events are not well explained, but the timing (almost all during normal working hours) is strongly suggestive of workers in the area.

Since the lab is next to our paint room, it was suggested that the paint shaker was causing trips. An experiment was run under worst case conditions with no anomalous vibration detected at the cooler. Pounding the floor with a hammer also did not create detectable shock loads at the cooler, but modest impacts to the chamber could create enough vibration to cause a trip.

Isolators were installed at the feet of the chamber in the summer of 2010 with no noticeable reduction in trip events. Additional isolation was installed and between the chamber and the cryocooler support plate in November 2010. Since installation of isolators there has been considerable activity in the area, including partial removal of the wall between the life test lab and the paint room. Despite this, there have been no trips since December 10, 2010. This suggests that the isolators are reducing the magnitude of shock load transmitted to the cooler.

3.3.2 Power Increase in 2011

Periodic power increases have been observed throughout the life test. Each of these power rises have been for short periods of time, usually spanning from several hours to several days. After these rises, operating power levels return to their previous levels. In January 2011, a different pattern was observed, indicated by an extended increase in the operating motor power of about 5 W above the level seen in the previous 17 months, see Figure 6. The power increase seen on Day 578 was sustained for about two weeks before a rapid decrease in power occurred. This pattern has repeated several times in the subsequent months.

It is unlikely that this variation is a result of ice or any other contaminant. Ice would cause the power to increase, but without a warm up of the cold heads there's no plausible mechanism that would cause the power level could go down. As of the date of this writing, the power level is back to the previously observed value, so it is not a permanent change in the cooler performance.

It is possible that this is an effect of cross coupling between the remote cold head and the compressor. A colder remote cooler draws a greater fraction of the total compressor power. When the remote cools down, the compressor power increases to keep the integral at the same temperature. This causes the remote to cool further. It is hypothesized that the system reaches a quasi-stable equilibrium at a higher compressor power and lower remote temperature. A random fluctuation in the system would eventually lead to a warm up of the remote, resulting in a different equilibrium point. This would not occur in a typical flight application, where the temperature of structures cooled by the remote would be stabilized with a control heater.

4 Conclusion

As of April 27, 2011 the ABI cryocooler life test has completed 1.61 years of operation, out of a goal of ten years. Total up time over the preceding nine months has been 94.5%. The cooler is performing well, with no measurable degradation in performance. Test anomalies have been observed, particular vibration overload events, but these appear to be due to conditions of the test environment rather than an indication of a problem with the cooler.

Acknowledgements

This work was funded by NASA Contract NNG04HZ07C to ITT Corporation.

References

Colbert, R, G. Pruitt, T. Nguyen, J. Raab, S. Clark, and P. Ramsey. ABI Cooler System Protoflight Performance. In: Miller, S. D., Ross, R. G, editors. Cryocoolers 15, Boulder, CO: ICC Press; 2008. p. 49-54

Ramsey, P. S. Clark, A. Chuchra, R. Boyle, D. Early, and R. Colbert. Performance Characterization of the ABI Cryocooler. In: Miller, S. D., Ross, R. G, editors. Cryocoolers 15, Boulder, CO: ICC Press; 2008. p. 49-54

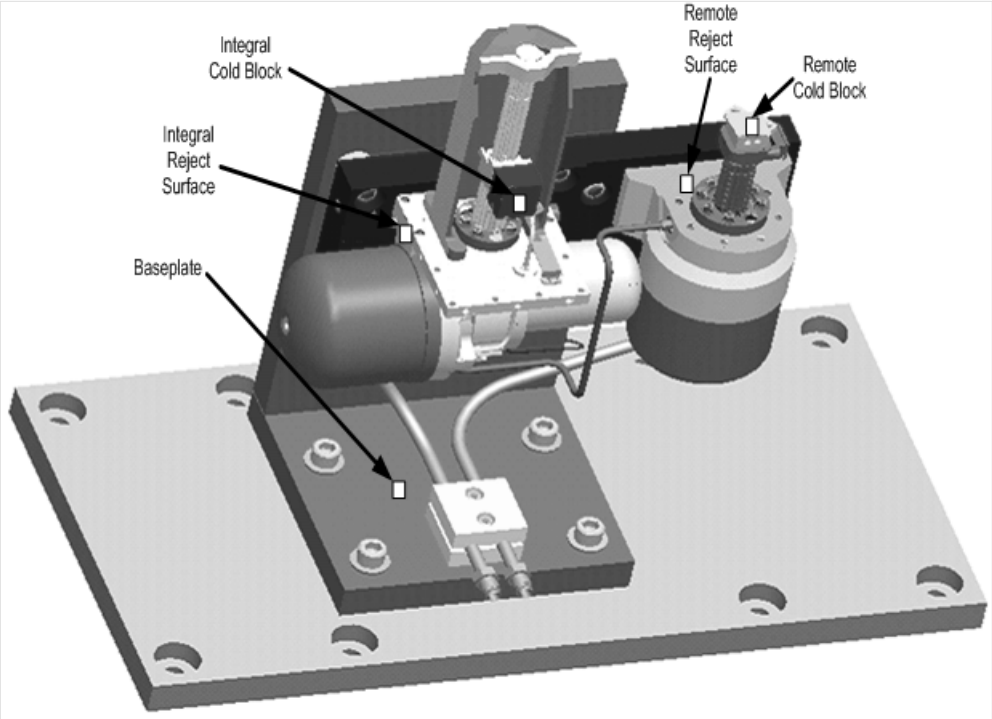

Figure 1. Unit under test, plus support equipment installed in vacuum chamber

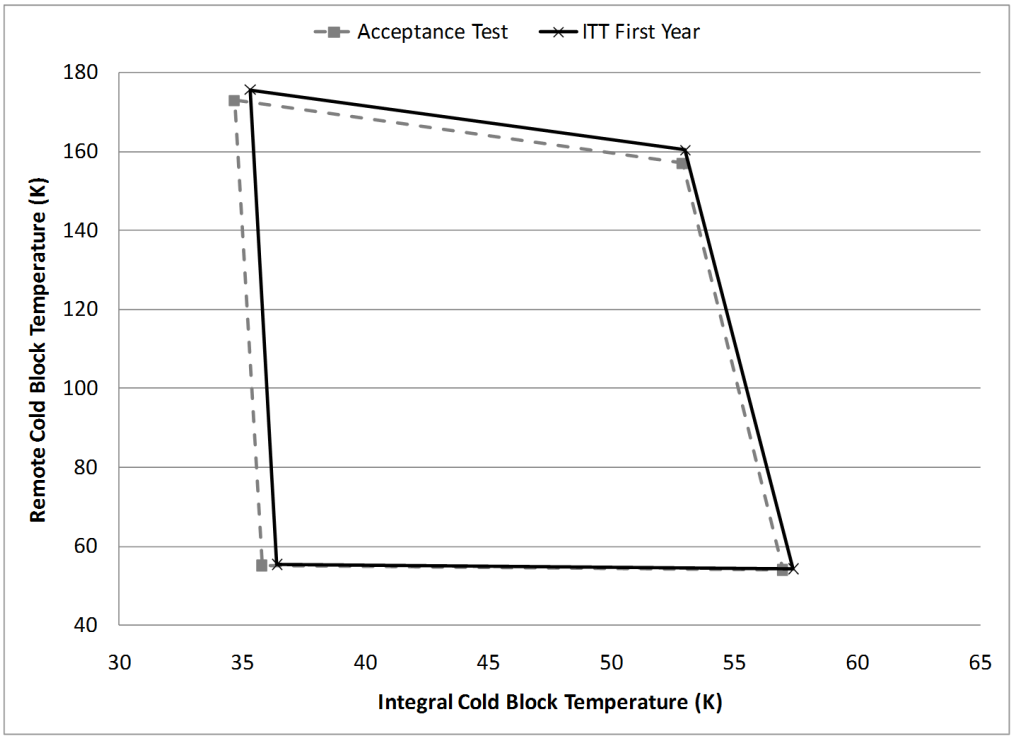

Figure 2: Window Pane Plot from Acceptance Test and One Year Check. Total Compressor Power Approximately 123 W.

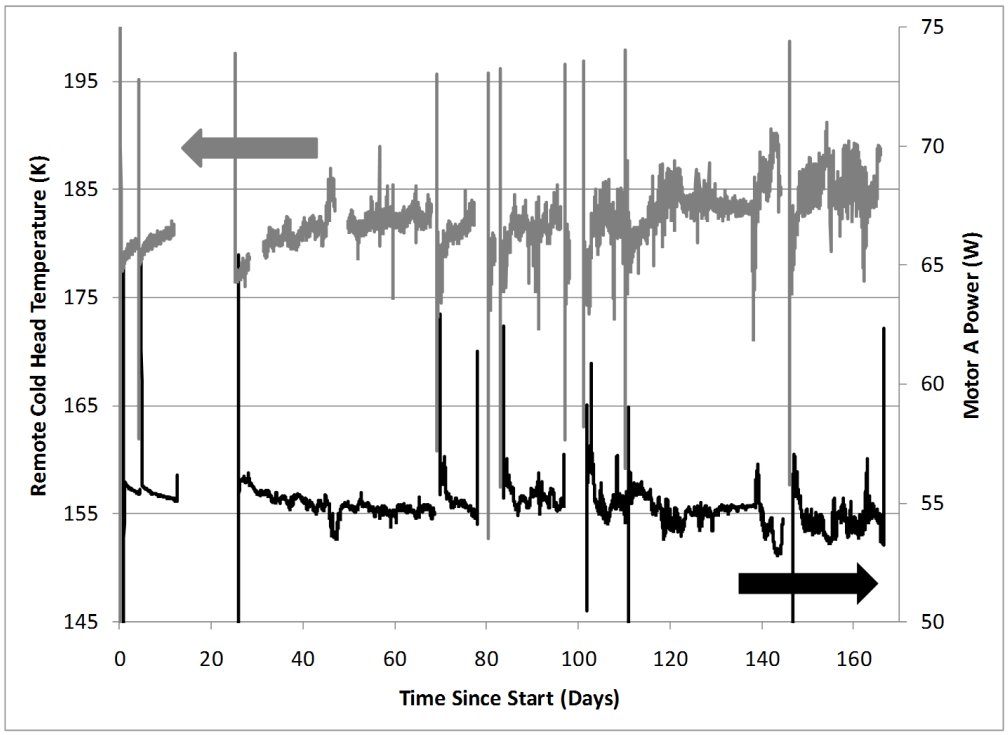

Figure 3: Side A Motor Power and Remote Cold Head Temperature Show Generally Stable Operation After Initial Increases. Power is Upper Series, Cold Head Temperature is Lower.

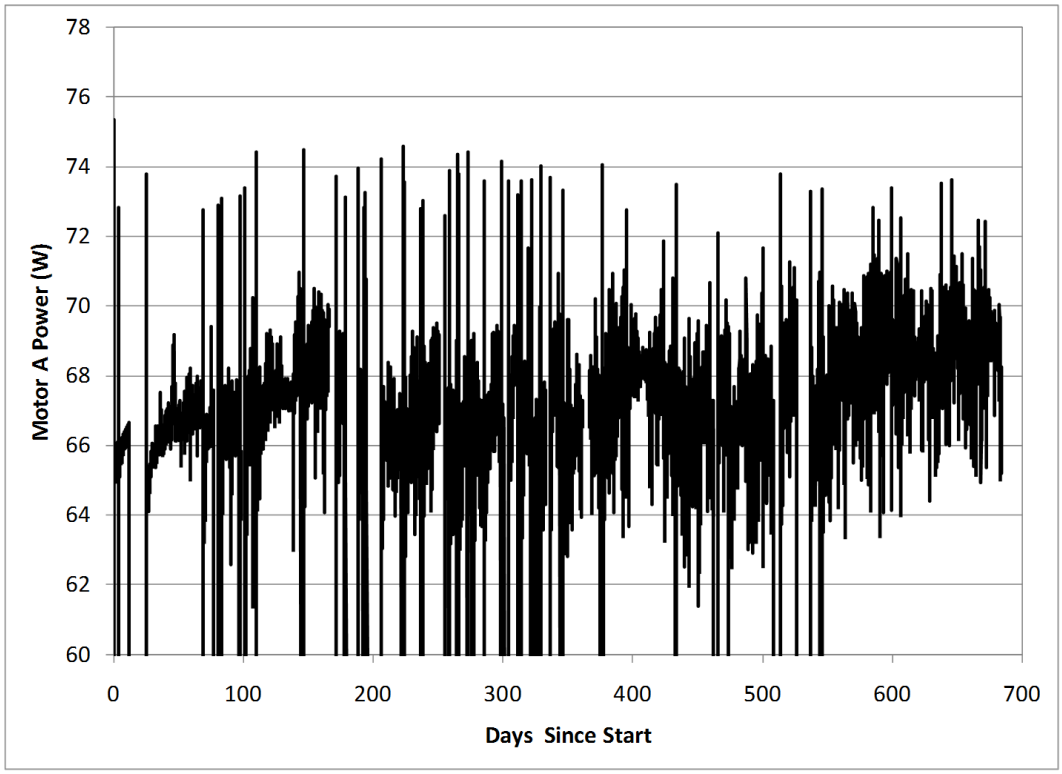

Figure 4: Motor A Power, First 700 Days of Testing

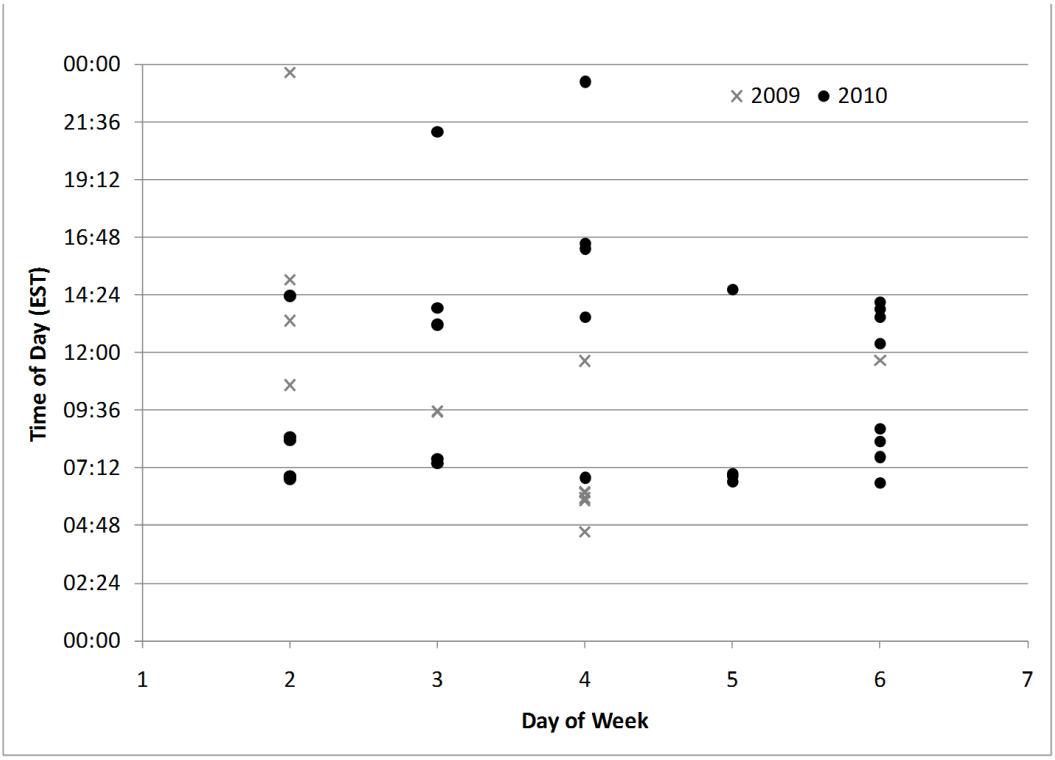

Figure 5 - System Trips as a Function of Day of Week and Time of Day (1=Sunday, 7=Saturday)

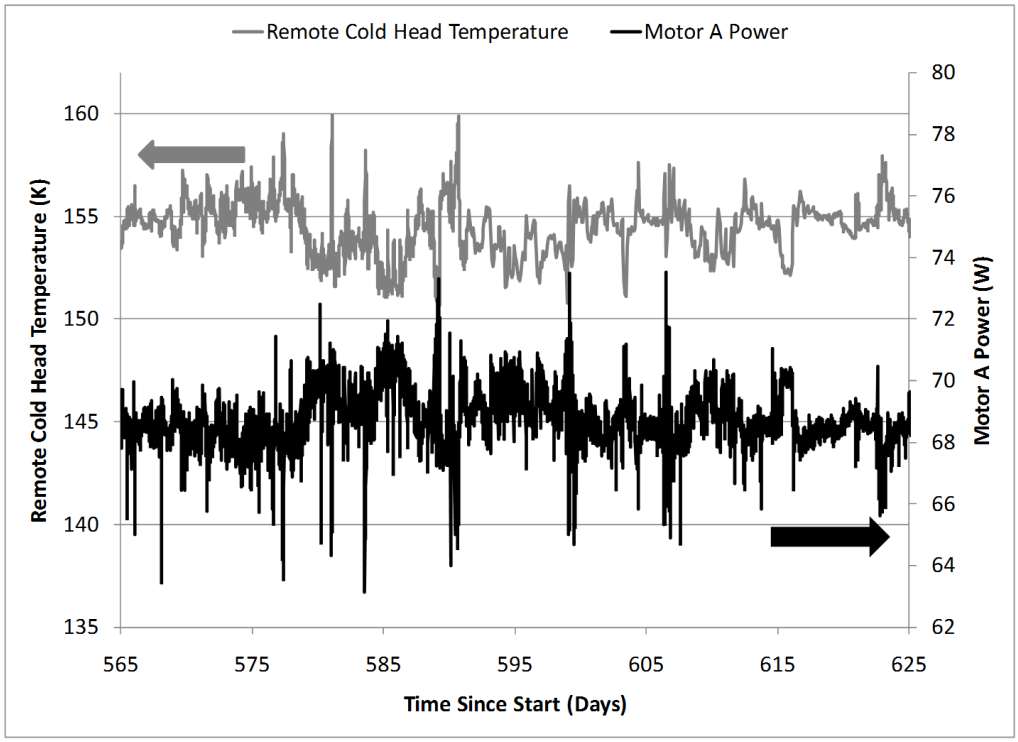

Figure 6 - Motor A Power Fluctuations Early 2011

Table 1. Temperature telemetry and location

Sensor	Location
PRT-1	Integral cold block (primary)
PRT-2	Integral cold block (redundant)
PRT-3	Remote cold block (primary)
PRT-4	Remote cold block (redundant)
PRT-5	Compressor heat rejection surface
PRT-6	Remote heat rejection surface
PRT-7	Integral cold head orifice block
PRT-8	Cold plate (primary)
PRT-9	Cold plate (redundant)

Table 2. Summary of Load Line Performance Tests to Date

Test	Integral Load (W)	Remote Load (W)	Integral Temp (K)	Remote Temp (K)	Motor Power (W)	Reject Temp (K)
NGST Pre-Ship	0	0	35.79	55.15	123.90	299.8
	2.275	5.25	52.90	157.03	124.30	299.9
Pre-Vibe (2009)	0	0	36.30	54.50	123.10	299.5
	2.27	5.24	53.00	156.52	124.04	300.3
Pre-Cycling (2009)	0	0	35.47	55.03	115.38	299.0
	2.27	5.24	53.00	172.00	115.81	299.5
Initial Start (2009)	0	0	36.04	55.06	121.66	299.4
	2.27	5.24	53.01	157.79	122.31	300.2
Annual Check (2010)	0	0	36.41	55.44	122.11	301.0
	2.27	5.24	53.00	160.31	122.60	301.7

High-Capacity 60 K Single-Stage Coaxial Pulse Tube Cryocoolers

Haizheng Dang

Shanghai Institute of Technical Physics, Chinese Academy of Sciences,
500 Yutian Road, 200083, Shanghai, P.R. China
Tel.: +86-21-25051191
Fax: +86-21-65441819
Email: haizheng.dang@mail.sitp.ac.cn

Abstract

A high-capacity single-stage coaxial pulse tube cryocooler (PTC) operating at around 60 K have been developed. The typical cooling capacity of 4.06 W at 60 K has been achieved with an electric input power of 180 W at 300 K reject. Over 4.7 W can also been achieved when the input power increases to 200 W. Over 9.0% of Carnot at 60 K has been realized. The application background and system design are described, and the performance characteristics are presented. Tests indicate that they are promising candidates for cooling the developing next-generation very large-scale long wave infrared focal plane arrays.

Key words: High-capacity; 60 K; single stage; coaxial; E. pulse tube cryocooler

Highlights

> The high-capacity single-stage coaxial pulse tube cryocooler operating at around 60 K have been developed to provide appropriate cooling for the developing next-generation very large-scale FPAs. > The cooler is a scale-up model of the mature 2W/60K-class coolers. The geometrical and operating parameters have been optimized based on the new dimensions and the results verify the design approaches. > The typical cooling capacity of 4.06W at 60K has been achieved with an electric input power of 180 W at 300 K reject temperature. Over 9.0% of Carnot at 60 K has been realized. The 4.72 W can also been achieved when the input power increases to 200 W. > The larger pulse tube diameter is used and the evident orientation sensitivity is observed, which is one of the important characteristics different from those of the developed 2W/60K-class coolers.

1. Introduction

Around 60 K, or to speak more exactly, 50-65 K, is a relatively important temperature range, since at which specific HgCdTe-based infrared detectors with longer response wavelengths (normally longer than 10 μm) can work effectively with the required identification and discrimination capability. On the other hand, with the rapid advances of space-based infrared remote sensing technology (such as in weather monitoring, Earth observation system, etc.), the detector systems have developed quickly from single element to focal plane array (FPA), and then to large-scale FPAs. Correspondingly, the cooling requirements increase sharply, from the initial hundreds of milliwatts to 1-2 W class, and now up to much higher. The developing next-generation very large-scale FPAs are expecting the cooling requirement up to 4 W. Naturally, there is an urgent need for the cryocoolers operating at this temperature range with the required high capacity.

The development of space-qualified cryocoolers operating at around 60 K temperature range has a relatively long history. The flight models of the 65 K single stage reverse Brayton machine [1] and single-stage 60/65 K Stirling cryocoolers [2] had become feasible even in mid 1990's. However, in 1996, TRW made the marked breakthrough in 60 K PTC technology, when the efficiency of its TRW 6020 version PTC exceeded those of the Stirling coolers at 60 K yet reported [3]. Especially, in view of that the additional attractive advantages of the PTC such as simplicity and reliability brought by the absence of the moving cold component, the 60 K PTC quickly became the research focus, and then almost the first choice for the related applications. The practical applications of the 60 K PTCs in space were then reduced to practice time and again. For instance, MTI [4] employed a slight variant of the TRW 6020 (the nominal operating point was adjusted to 2.25W at 65K); AIRS [5] and TES [6] used the TRW's PTCs with the similar structures and the nominal capacities were set as 1.63 W at 55 K and 1 W at 57 K, respectively. In the late 1990's, Lockheed Martin also developed its 2 W-class 60 K PTC christened Mark III with the comparable thermodynamic efficiency to those of TRW's [7].

It should be mentioned here that all of the abovementioned 60 K PTCs developed by TRW and Lockheed Martin chose the in-line arrangement, which is also regarded as one of the main reasons why the noteworthy efficiencies have been achieved. In recent years, 60 K coaxial PTCs have also achieved noticeable advances. For example, Air Liquide [8] developed its space-oriented coaxial PTC (LPTC version) operating at around 50 K, and Sunpower [9] successfully worked out its commercial 2W/60K-class coaxial PTC, which also achieved considerable thermodynamic efficiencies, respectively.

In the author's group, the study on the 60 K high frequency PTCs has been one of the research focuses, and the successful development of the 2.0W-class coaxial-type ones have been achieved recently [10-12]. The typical performance is to provide 2.2 W at 60 K with 100 W of electric input power at 300 K reject temperature, and the typical 8.8% of Carnot at 60 K has been achieved. One of the disadvantages of the developed 2.0W-class coolers is that they can not achieve much higher cooling power. For the maximum cooling capacity of 2.5-2.7 W, the compressor piston attains its 95-97% stroke. Therefore, in response to the need of the 4 W or higher cooling capacities, a compressor with a much larger swept volume has to be employed, and the intrinsic physical mechanism will be

investigated further.

2. Development goals and design considerations

Table 1 gives the key development goals of the high capacity single-stage 60 K PTC. The coaxial arrangement is still adopted to ease the complexity of system integration and to minimize the cost of the dewar system. It is required to provide at least 4.0 W of net cooling power at 60 K with an electric input power of less than 180 W at 300 K reject temperature. The above cooling requirements mean the coolers should achieve at least the similar refrigeration efficiency to the developed 2W-class ones. According to our past design experiences, the goal is feasible since, for two similar structures with the comparable sizes, the proportion of the irreversible losses to the gross refrigeration power will decrease as the latter increases. The overall weight including cooler control electronics should be kept below 10 kg. Parameters like ambient temperature adaptability, temperature stability, vibration output of the cold head, and expected lifetime are especially important to future practical applications and will be laid special emphasis on for the engineering model development.

The cryocooler design combines our relevant experience in pulse tube modeling and linear compressor optimization. The physical model is based on a finite difference method to solve the mass, energy, and momentum conservation equations, and some empirical coefficients have been added considering the multi-dimensional effects in practical pulse tubes. Since the specific applications often prescribes the definite dimensions of the cold finger diameter, for the developing coaxial PTC where the pulse tube is concentrically inserted into the regenerator, the left key dimensional parameters to be decided are regenerator length, pulse tube length and diameter. Reference [13] gives the design principles and the specific examples about these parameters about our large capacity high frequency coaxial PTCs. The optimization goal is to maximize the COP and the cooling capacity at the same time, and the geometrical and operating parameters are optimized simultaneously in the optimization process. It should also be pointed out that, during the optimization, the primary concern is to maximize the cooler's efficiency at 60 K, while the no-load temperature and the capability working over wide temperature ranges are not the main targets.

3. Cooler description and performance characteristics

3.1 Cooler descriptions

The cooler described here is a scale-up model of the mature 2W/60K-class coaxial PTCs [12]. Except for size, the new cooler is in large identical in configuration to the 2W-cooler. However, the structures of the slit-type exchangers have been optimized further to achieve higher heat-exchanging efficiency. The slits are cut with finer gaps, with the typical value of 0.15 mm. The swept volume of the used compressor is enlarged to 9.5 cc to enhance the input power potential. The connecting tube between the

compressor and cold finger is 30 cm long with a larger inner diameter of 5.5 mm. The double-segmented inertance tube has been optimized again based on the new cooler dimensions, together with a larger gas reservoir of 380 cc to achieve the desired phase-shift. The charge pressure is heightened to 3.4 MPa, and the operating frequency is increased to as high as 57 Hz to enhance the energy density in the limited volume.

3.2 Cooling performance

Figure 1 shows the typical experimental refrigeration performances in terms of the electric input powers of 180 W and 200 W, respectively. The experimental data are measured with the cold head in the horizontal orientation relative to the gravitational field. The typical experimental performance is to provide 4.06 W of cooling power at 60 K with a 180 W of electric input power at 300 K reject temperature. A 4.72 W of cooling capacity at 60K can also be achieved while the input power increases to 200 W. Over 9.0% of Carnot at 60 K has been achieved, which is considerably better than the 8.8% in case of 2W-class coolers. This is the expected result that the efficiency increases with the increasing capacity.

The simulated performances based on the model are also given for comparisons in figure 1. The general trends between the model and experiments confirm each other, which verify the design and optimization method to a large extent. Still, the irreversible losses in the system are somehow underestimated in the model. However, the situation is better compared with the case of 2W-class coolers [12], which benefits from some improved empirical coefficients for modifying the model.

3.3 Orientation sensitivity

As discussed by Radebaugh [14, 15], one of the well-known disadvantages of PTCs is the potential for gravitationally induced convective instabilities inside the pulse tube, and the effect may be particularly pronounced while the pulse tubes with the greater diameters are used or the coolers operate at lower frequencies. Swift [16] has observed and theoretically analyzed the phenomena that high frequency PTCs could be tipped without obvious performance variation. Based on his explanation, at a high enough frequency, natural convection is suppressed by sufficiently fast velocity oscillations, via a nonlinear hydrodynamic effect that tends to align the density gradients in the pulse tube parallel to the oscillation direction.

In our previous experiments in terms of the developed coaxial PTCs, when the medium pulse tube diameters (larger than 11 mm but still smaller than 13 mm) and moderate high frequencies (from 55 Hz to 60 Hz) are used, we still measured an ignorable angular dependence relative to gravity (typically less than 0.1 W with around 100 W of input electric power) [12, 13]. However, when the pulse tube diameter continues to increase, such as the case of 4 W-class PTCs with a diameter of around 14.2 mm, the evident orientation sensitivity is observed.

Figure 2 and 3 show the variations of refrigeration performance with the inclination angle of the cold finger. Here 0° means the cold finger is horizontal, and 90° and -90° refers to vertically up and down, respectively. Two typical situations have been investigated and either is measured with the reject temperature of 300 K. For the first

situation, as shown in figure 2, the input electric power and the heat load are kept to constant 180 W and 4.06 W, respectively, a 3.8 K of temperature change is measured for the 180° inclination angle variation. For the second situation, as shown in figure 3, the input electric power and the cold head temperature are kept constant at 180 W and 60 K, respectively, for the 180° angle variation, a 0.82 W of heat lift change is measured.

As shown in figure 2 and 3, the most favorable orientation is to put the cold finger vertically down, and a possible explanation is that the working gas in the pulse tube becomes stably stratified and limits the free convection inside. However, when the cold finger is gradually rotated to vertically up, the convection effect gradually becomes more and more obvious, until large enough to bring evident influence to the cooler performance. The evident orientation sensitivity of refrigeration performance is a new important phenomenon and is being investigated further.

3.4 Reject temperature dependence

The dependence of the cooler performance on the reject temperatures has been investigated under two specific circumstances. One is to keep constant input power, and the other is to keep constant applied heat lift.

Figure 4 shows the variations of heat lift with the reject temperatures when the constant 180 W of input electric power is applied at 60 K of cold head temperature. As shown in the figure, the cooling capacity decreases from 4.5 W to 3.6 W when the reject temperature increases from 283 K to 313 K. The slope is bout 0.25W/10K.

Figure 5 shows the variations of input electric power with the reject temperatures when the constant 4.06 W of heat lift is applied at 60 K of cold head temperature. As shown in the figure, the input electric power increases from 141 W to 210 W when the reject temperature increases from 283 K to 313 K. The slope is bout 23W/10K.

4. Discussions and conclusions

A high-capacity single-stage coaxial pulse tube cryocooler (PTC) operating at around 60 K have been developed to provide appropriate cooling for the developing next-generation very large-scale FPAs. The application background and system design are described. The cooler prototype with the aimed cooling capacity of over 4 W is a scale-up model of the mature 2W/60K-class coolers developed in the same group. The geometrical and operating parameters have been optimized based on the new dimensions and the results verify the design approaches.

The cooler performance characteristics are presented. At present, the typical cooling capacity of 4.06W at 60K has been achieved with an electric input power of 180 W at 300 K reject temperature. The 4.72 W can also been achieved when the input power increases to 200 W. Over 9.0% of Carnot at 60 K has been realized.

The effects of the orientation and reject temperature on the cooler performance have been investigated in detail. The larger pulse tube diameter is used and the evident orientation sensitivity is observed, which is one of the important characteristics different from those of the developed 2W/60K-class coolers. The obvious reject temperature

dependence has also been measured. Further optimizations are underway to provide an appropriate cooler candidate having better environment adaptability.

Acknowledgements

The work is financially supported by The Chinese Academy of Sciences and also partly sponsored by Shanghai Pujiang Program (No. 10PJ1410800).

References

[1] Swift WL. Single stage reverse Brayton cryocooler: performance of the engineering model. Cryocoolers 1995; 8:499-506.
[2] Crawford LD, Kalivoda CM, Glaister Ds. An overview of Air Force Phillips Laboratory cryocooler programs. Cryocoolers 1997; 9:1-9.
[3] Burt WW and Chan CK. New mid-size high efficiency pulse tube coolers. Cryocoolers 1997; 9:173-82.
[4] Tomlinson BJ, Davidson D, Lanes C, et al. Multispectral Thermal Imager (MTI) space cryocooler development, integration, and test, Cryocoolers 1999; 10:129-38.
[5] Chan CK, Carlson C, Colbert R, et al. Performance of the AIRS pulse-tube engineering model cryocooler. Cryocoolers 1997; 9:195-202.
[6] Raab J, Abedzadeh S, Colbert R, et al. TES FPC Flight Pulse Tube Cooler System. Cryocoolers 2001; 11:131-8.
[7] Kotsubo V, Olson JR, Nast TC. Development of a 2 W at 60 K pulse tube cryocooler for spaceborne operation, Cryocoolers 1999; 10:157-61.
[8] Trollier T, Tanchon J, Buquet J, et al. Status of Air Liquide space pulse tube cryocoolers. Cryocoolers 2009; 15:115-22.
[9] Wilson KB, Fralick CC, Gedeon DR, et al. Sunpower's CPT60 pulse tube cryocooler, Cryocoolers 2007; 15:123-32.
[10] Dang HZ. High frequency coaxial pulse tube cryocoolers for cooling infrared focal plane arrays. In: Proceedings of SPIE 7854, 2010.
[11] Dang HZ, Wang LB, Wu YN, et al. Development of a 2.0W at 60K single-stage coaxial pulse tube cryocooler for long-wave infrared focal plane array applications. In: Proceedings of SPIE 7660, 2010.
[12] Dang HZ, Wang LB, Wu YN, et al. Performance investigation on SITP's 60 K high frequency single-stage coaxial pulse tube cryocoolers. Cryocoolers 2011; 16:149-56.
[13] Dang HZ, Wang LB, Wu YN, et al. Development of SITP's large capacity high frequency coaxial pulse tube cryocoolers. Cryocoolers 2011; 16:167-73.
[14] Radebaugh R. Development of the pulse tube refrigerator as an efficient and reliable cryocooler. In Proceedings of Institute of Refrigeration (London) 1999-2000, 2000
[15] Radebaugh R. Pulse tube cryocoolers for cooling infrared sensors. In Proceedings of SPIE 4130, 2000
[16] Swift GW, Backhaus S. Why high-frequency pulse tubes can be tipped. Cryocoolers 2011; 16:183-92.

Table list

Figure list

Table 1. Key development goals of the high-capacity single-stage 60 K PTC.

Parameters	Design goal
Geometrical arrangement	Coaxial
Cooling capacity (at 300K reject temperature)	≥ 4.0W/60K
Power consumption (electric input power)	≤ 180 W
No-load temperature	≤ 40 K
Mass (including cooler control electronics)	≤ 10 kg
Ambient temperature adaptability	243 K ~ 323 K
Temperature stability	± 0.1 K
Vibration output of the cold head	≤ 0.1 Nrms
Expected lifetime	≥ 55,000 hours

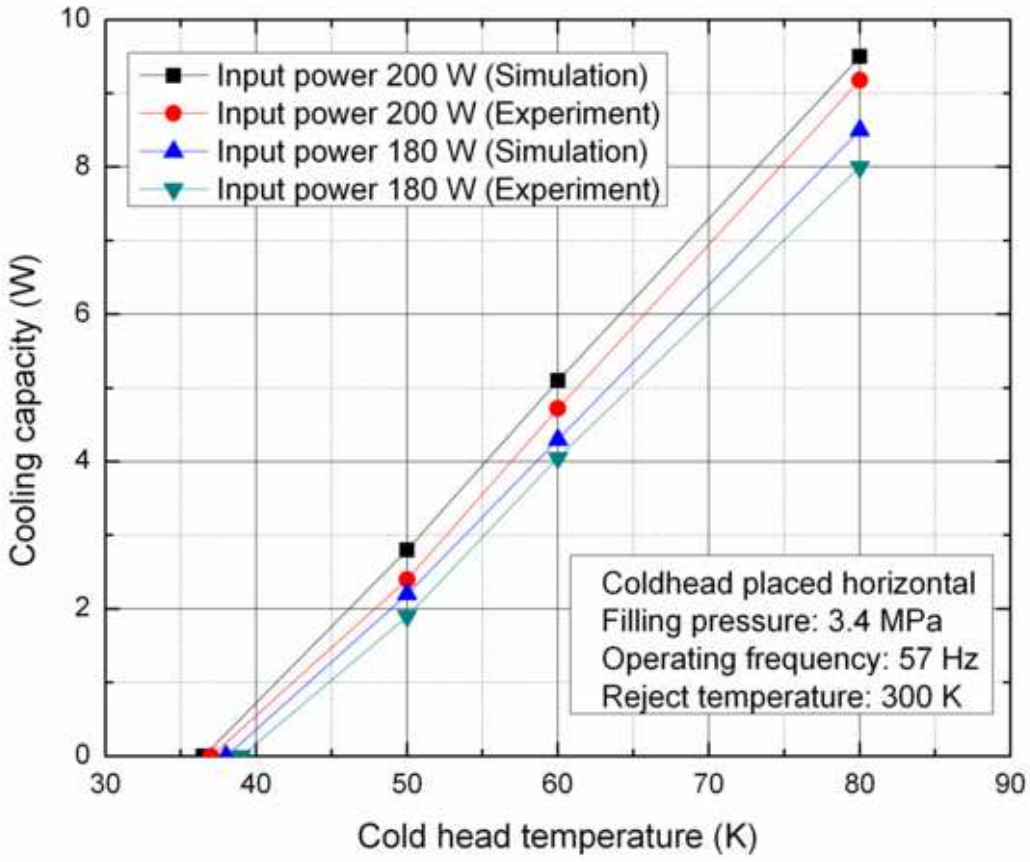

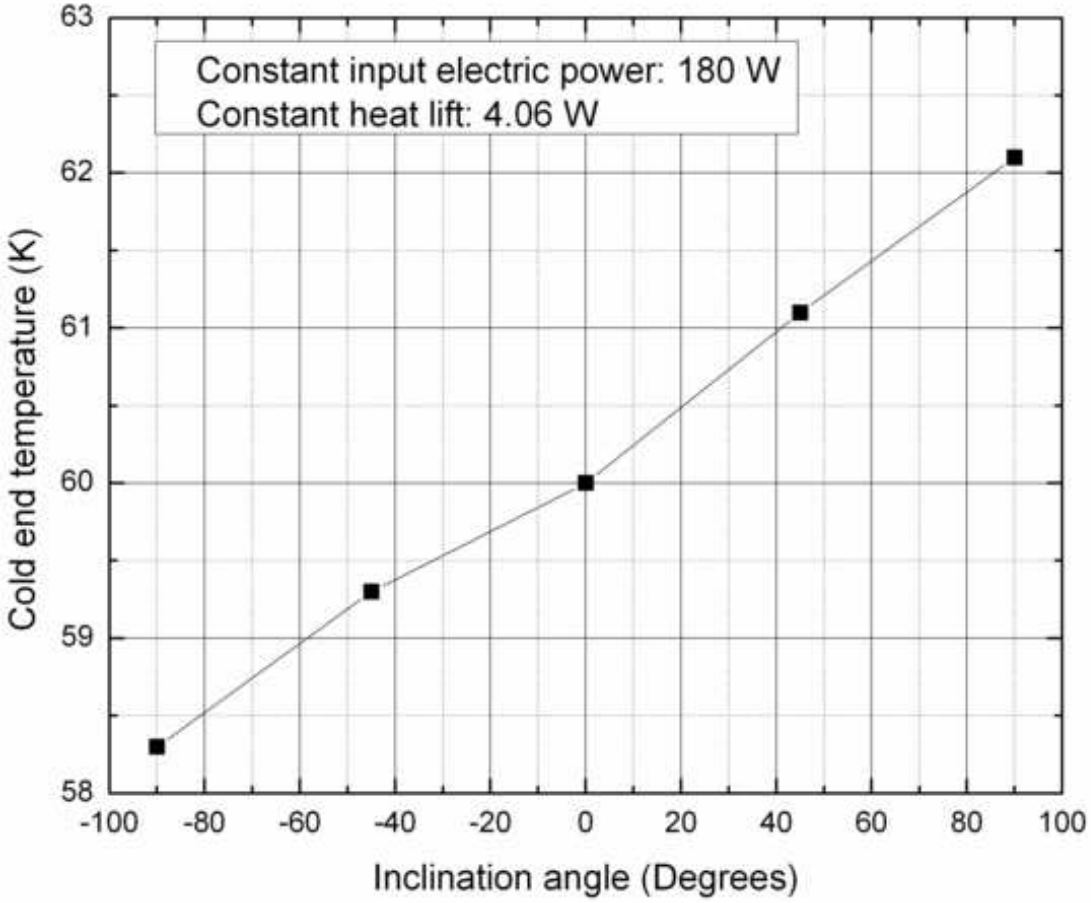
Constant input electric power: 180 W
Constant heat lift: 4.06 W
Cold end temperature (K)
Inclination angle (Degrees)
63
62
61
60
59
58
-100
-80
-60
-40
-20
0
20
40
60
80
100

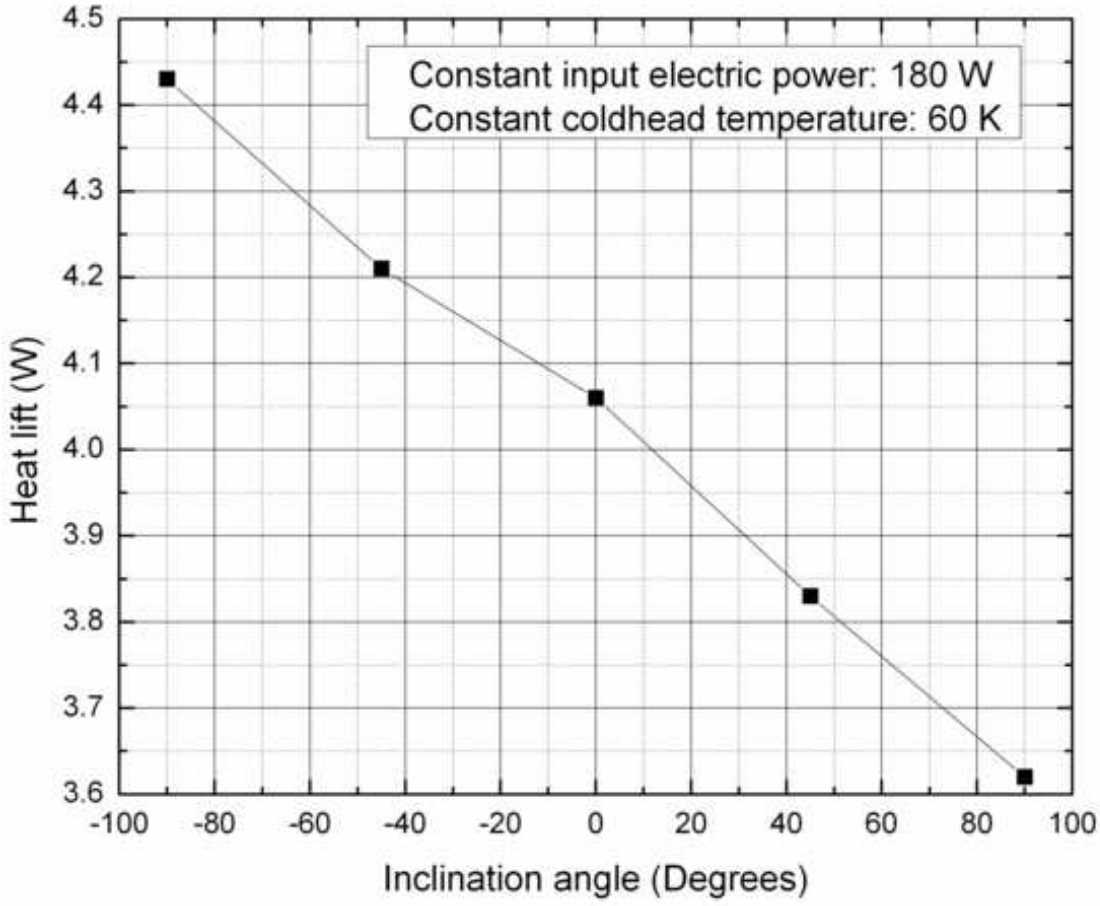
Constant input electric power: 180 W
Constant coldhead temperature: 60 K
Heat lift (W)
4.5
4.4
4.3
4.2
4.1
4.0
3.9
3.8
3.7
3.6
-100
-80
-60
-40
-20
0
20
40
60
80
100
Inclination angle (Degrees)

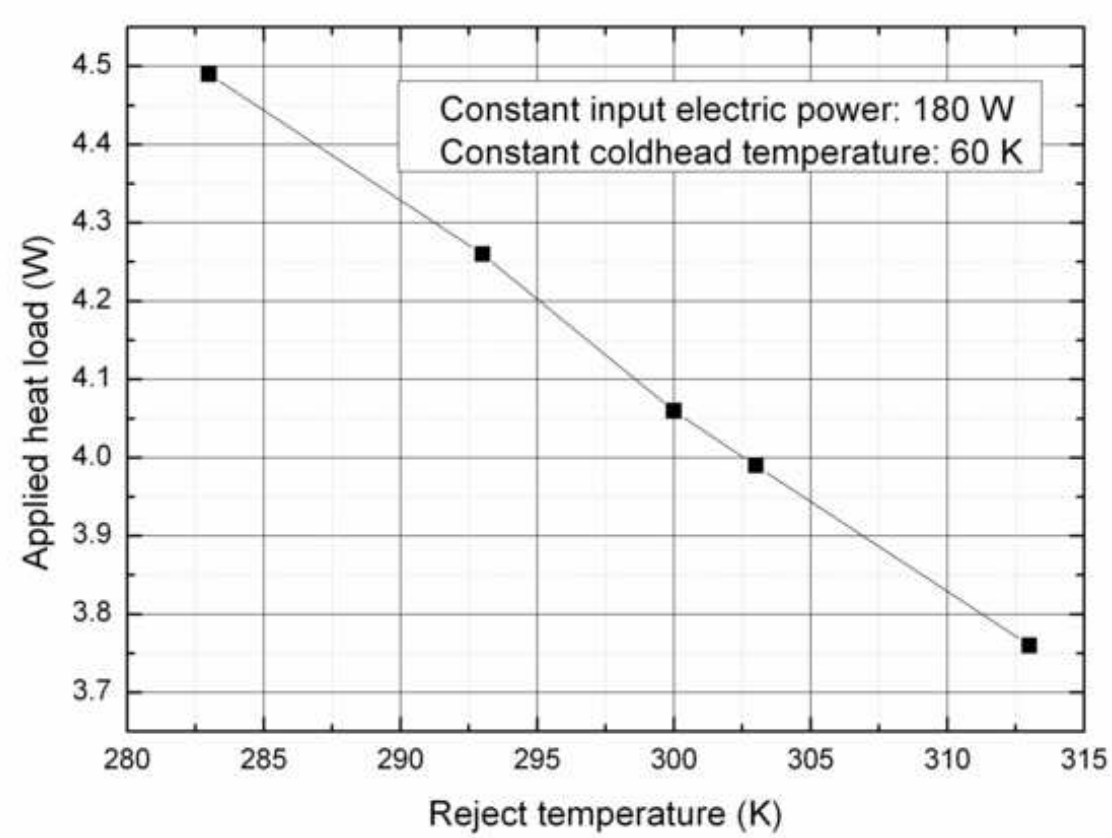
Constant input electric power: 180 W
Constant coldhead temperature: 60 K
Applied heat load (W)
Reject temperature (K)
4.5
4.4
4.3
4.2
4.1
4.0
3.9
3.8
3.7
280
285
290
295
300
305
310
315

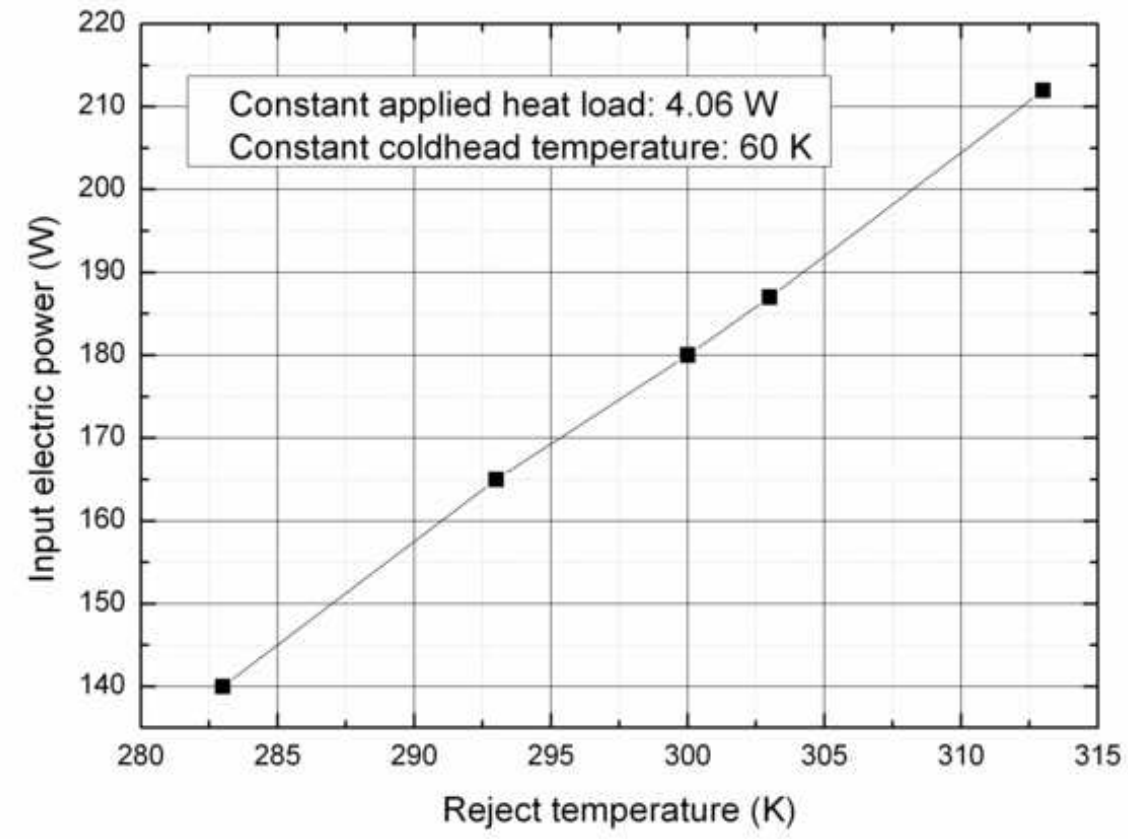
Constant applied heat load: 4.06 W
Constant coldhead temperature: 60 K
Input electric power (W)
Reject temperature (K)
220
210
200
190
180
170
160
150
140
280
285
290
295
300
305
310
315

Mathematical Model and Experimental Results for Cryogenic Densification and Sub-cooling Using a Submerged Cooling Source

J.K. Partridge[1], J.W. Tuttle[2], W.U. Notardonato[1], W.L. Johnson[1]

[1]*Cryogenics Test Laboratory, Kennedy Space Center*
[2]*ASRC Aerospace, Kennedy Space Center*

ABSTRACT

Among the many factors that determine overall rocket performance, propellant density is important because it affects the size of the rocket. Thus, in order to decrease the size of a rocket, it may be desirable to increase the density of propellants. This study analyzes the concept of increasing the propellant density by employing a cooling source submerged in the liquid propellant. A simple, mathematical model was developed to predict the rate of densification and the propellant temperature profile. The mathematical model is generic and applicable to multiple propellants. The densification rate was determined experimentally by submerging a cooling source in liquid oxygen at constant, positive pressure, and measuring the time rate of change in temperature with respect to vertical position. The results from the mathematical model provided a reasonable fit when compared to experimental results.

1. Introduction

In an attempt to lower the inert mass of a launch vehicle, propellant densification is viewed as a method to reduce the propellant tank volume and a means to reduce the mass of the propellant tank and, therefore, increase payload mass. Many have conducted studies for propellant densification (Fazah, 1994) (Haberbusch, et al., 2002) (Lak, et al., 1996). Most of the studies suggest to place the densification operation between the ground storage tank and launch vehicle (Greene, et al., 1998) (Tomsik, 1997) (Lak, et al., 2002). This paper investigates placement of the densification operation within the ground storage tank. Also, this paper predicts the rate of propellant densification using a cooling source within the liquid propellant and compares the prediction to experimental results. This work is similar to the Integrated Refrigeration and Storage method proposed by Notardonato (Notardonato, et al., 2009) (Notardonato, et al., 2009).

2. Material and methods

2.1 Test Article

The main test article is comprised of a 400L dewar with a 0.254 m neck opening that accepts a male bayonet. Eden Cryogenics constructed the dewar using 304 stainless steel with an inside diameter of 0.76 m and a maximum allowable working pressure of 515 kPa absolute. The male bayonet, also constructed with 304 stainless steel, incorporated two fluid penetrations and two instrumentation cable penetration. A heat exchanger extended below the male bayonet and connected to the male bayonet by 0.013m and 0.025m stainless steel tubing, which insulated with a thickness of 0.076m of polytetrafluoroethylene. The fluid penetrations allowed coolant to enter the heat exchanger through the 0.013m diameter tubing and exit the heat exchanger through the 0.025m tubing. The heat exchanger was 0.013m diameter copper tubing with annular fins totaling 0.36m in length.

Peripheral equipment included a liquid nitrogen source, liquid nitrogen subcooler, and gaseous oxygen source. Liquid nitrogen, in 110L and 180L dewars saturated at 0.21 kPag, provided the cooling fluid for the heat exchanger inside the main test article. The liquid nitrogen flowed through a simple liquid nitrogen subcooler to ensure the liquid nitrogen is subcooled before entering the main test article. The liquid nitrogen subcooler consisted of copper heat exchanger submerged in liquid nitrogen subjected to atmospheric pressure. The gaseous oxygen source, from a 43L k-bottle at ambient temperature and an initial pressure of 16.6 kPag, provided the means to control the pressure within the main test article.

2.2 Instrumentation

A micarta instrumentation rake was attached to the bottom of the neck flange. A total of 28 RTD measured the temperature inside the test dewar. Twenty RTD measured the temperature of position in vertical and the remaining eight RTD measured the horizontal temperature at two vertical positions. One pressure transducer measured the test dewar pressure, while a separate pressure transducer measured the pressure in the coolant system. Two thermocouples measured the temperatures of the coolant entering and exiting the male bayonet. Two mass flow controllers measured and controlled the quantity of coolant flowing through the heat exchanger and the quantity of gaseous oxygen flowing into the test dewar. The specifications for the nitrogen and oxygen were MIL-PRF-27401F Grade B and MIL-PRF-25508G Grade F, respectively.

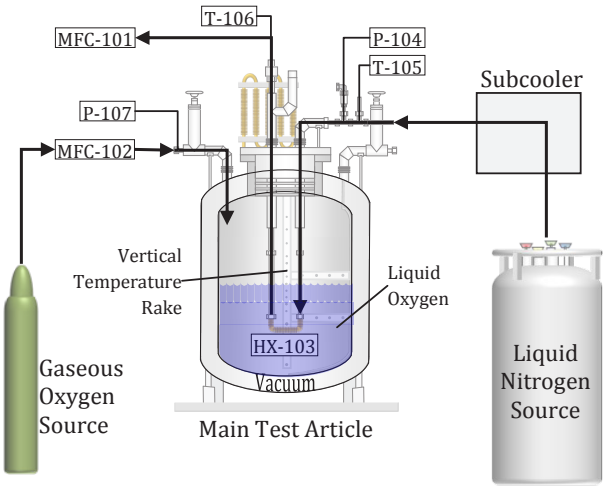

MFC-101	Coolant Mass Flow Controller
MFC-102	Main Test Article Pressure Controller
HX-103	Internal Heat Exchanger (Submerged)
P-104	Coolant Pressure Transducer
T-105	Coolant Inlet Temperature Sensor
T-106	Coolant Exit Temperature Sensor
P-107	Main Test Article Pressure Transducer
T1 – T20	RTD along Vertical Temperature Rake
T21 – T28	RTD along Horizontal Temperature Rakes

Figure 1: Mechanical and Instrument Schematic of Test Materials

2.3 Operation

The test dewar was filled with 200L of liquid oxygen, so that the liquid height above and below the heat exchanger is 0.152m and 0.305m, respectively. Liquid nitrogen is used as the coolant and flowed from the liquid nitrogen dewar through the heat exchanger inside the test dewar and to the nitrogen mass flow controller. The nitrogen mass flow controller was set at its maximum value of 100 standard liters per minute. The gaseous oxygen source maintained constant pressure within the test dewar, by flowing through the oxygen mass flow controller. The gaseous oxygen mass flow controller was controlled using a PID controller within Labview referencing the main test article pressure, P-107. Three tests were run at a constant pressure of 3 psig, 5 psig, and 7 psig.

3. Mathematical Model

Prior to activating the internal heat exchanger, the steady-state condition of the main test dewar begins with a thermally stratified ullage with respect to vertical position and a uniform temperature throughout the liquid. The temperature of the liquid is saturated temperature at the main test dewar storage pressure. Once the internal heat exchanger is activated, the liquid is divided into two zones depending on whether the liquid is above or below the internal heat exchanger. A mathematical model is provided for both zones.

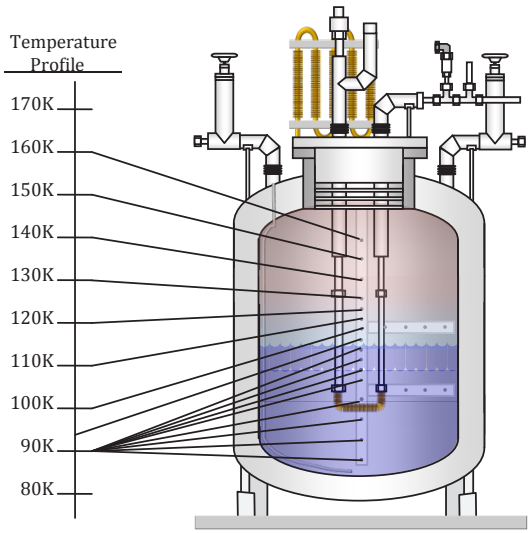

Figure 2: Main Test Article at Steady-State, Initial Condition

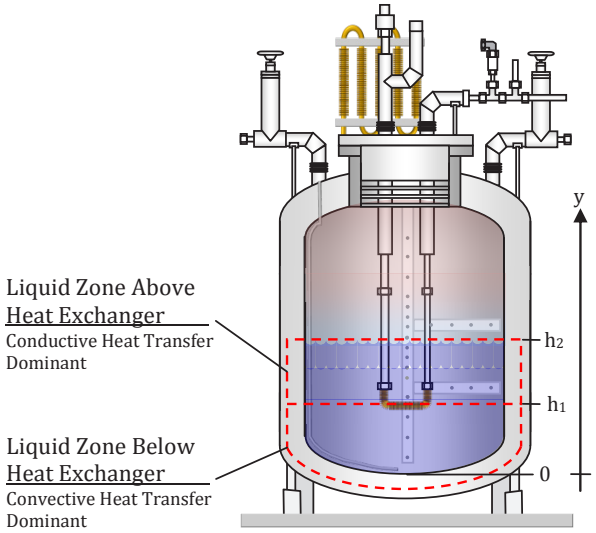

Figure 3: Main Test Article During Heat Exchanger Operation

3.1 Liquid Zone Above Heat Exchanger

The liquid zone above the heat exchanger is modeled using the heat equation with constant temperature boundary conditions at both, the top condition and bottom condition. The top boundary is the vapor-liquid interface, which is always at the saturated temperature at the system pressure. Because the main test dewar is operated at constant pressure, the temperature at the top boundary remains constant. The temperature at the bottom boundary is given by the temperature of the internal heat exchanger. The heat equation (1) is solved using the boundary and initial conditions (2), (3), and (4) to arrive at the modeled temperature change rate for the liquid zone above the heat exchanger (5).

Governing Equation:

$$\alpha \frac{\partial^2 T(y,t)}{\partial y^2} + r = \frac{\partial T(y,t)}{\partial t} \qquad (1)$$

Boundary Conditions:

$$T(h_2,t) = T_{sat} \qquad (2)$$

$$T(h_1,t) = T_s \qquad (3)$$

Initial Condition:

$$T(y,0) = T_i = T_{sat} \tag{4}$$

$$\begin{aligned} &T(y,t) \\ &= \frac{(T_{sat} - T_s)}{(h_2 - h_1)}(y - h_1) \\ &+ \sum_{n=1}^{\infty} \frac{2(T_{sat} - T_s)}{n\pi} \sin\left(\frac{n\pi(y - h_1)}{h_2 - h_1}\right) e^{-\alpha\left(\frac{n\pi}{h_2 - h_1}\right)^2 t} + T_s \end{aligned} \tag{5}$$

3.2 Liquid Zone Below Heat Exchanger

The liquid zone below the heat exchanger is modeled using the heat equation averaged across the entire zone height to estimate the convective heat transfer. The upper boundary condition, modeled as a constant temperature boundary, is given by the temperature of the internal heat exchanger. The lower boundary condition is taken to be insulated. The liquid is initially uniform in temperature with respect to vertical height. The heat equation (6) is solved using the boundary and initial conditions (7), (8), and (9). The solution is provided by (10).

Governing Equation:

$$\alpha \frac{\partial^2 T(y,t)}{\partial y^2} = \frac{\partial T(y,t)}{\partial t} \tag{6}$$

Boundary Conditions:

$$T(h_1, t) = T_s \tag{7}$$

$$\left.\frac{\partial T}{\partial y}\right|_{y=0} = 0 \tag{8}$$

Initial Condition:

$$T(y,0) = T_{sat} \tag{9}$$

$$\begin{aligned} &T(y,t) \\ &= \sum_{n=1}^{\infty} \frac{4(T_{sat} - T_s)}{(2n-1)\pi} \sin\left(\frac{(2n-1)\pi\, y}{2\, h_1}\right) e^{-\alpha\left[\left(\frac{2n-1}{2}\right)\frac{\pi}{h_1}\right]^2 t} \\ &+ T_s \end{aligned} \tag{10}$$

Because the temperature of the heat exchanger is always cooler than or equal to the temperature of the liquid oxygen below the heat exchanger, natural convection occurs in the liquid zone beneath the heat exchanger. The natural convection provides a uniform temperature with respect to height at all times. Thus, the temperature profile, (10), is averaged over the entire height of the liquid zone beneath the heat exchanger to arrive at the modeled temperature change (11).

$$T(t) = \sum_{n=1}^{\infty} \frac{8(T_{sat} - T_s)}{[(2n-1)\pi]^2} e^{-\alpha\left[\left(\frac{2n-1}{2}\right)\frac{\pi}{h_1}\right]^2 t} + T_s \tag{11}$$

4. Results

4.1 Test Results for Liquid Zone Above Heat Exchanger

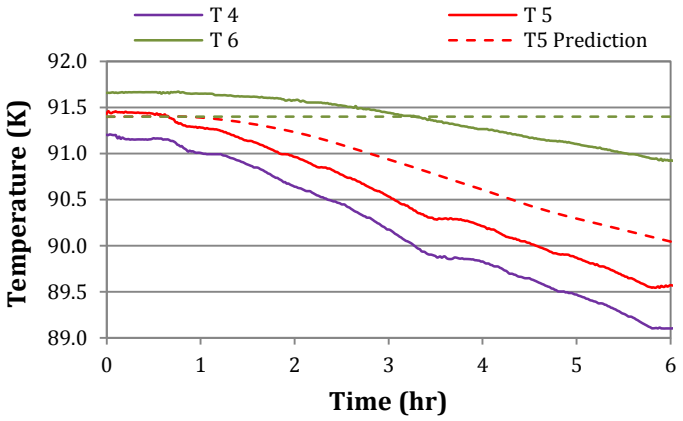

Figure 4: Test Results for Liquid Zone Above the Heat Exchanger (3 psig)

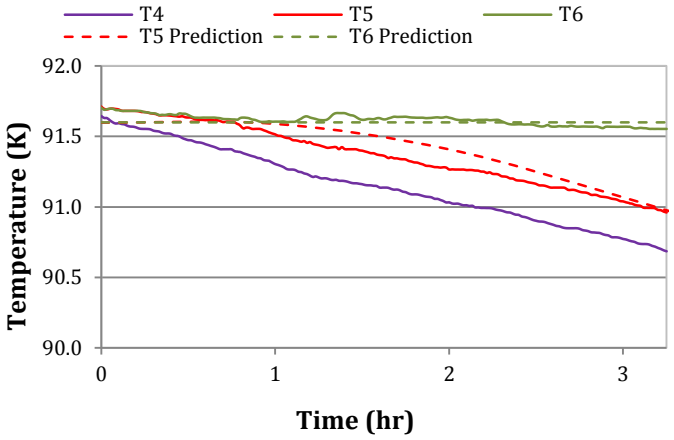

Figure 5: Test Results for Liquid Zone Above the Heat Exchanger (5psig)

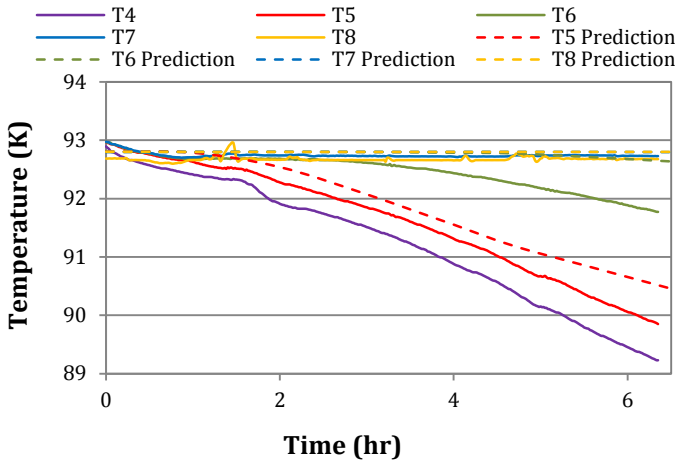

Figure 6: Test Results for Liquid Zone Above the Heat Exchanger (7psig)

4.2 Test Results for Liquid Zone Below Heat Exchanger

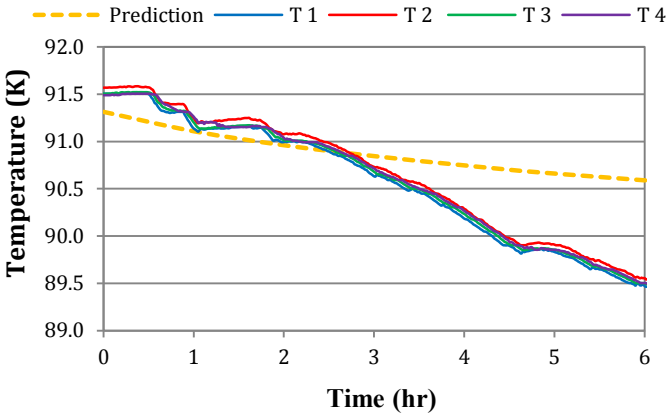

Figure 7: Test Results for Liquid Zone Below the Heat Exchanger (3psig)

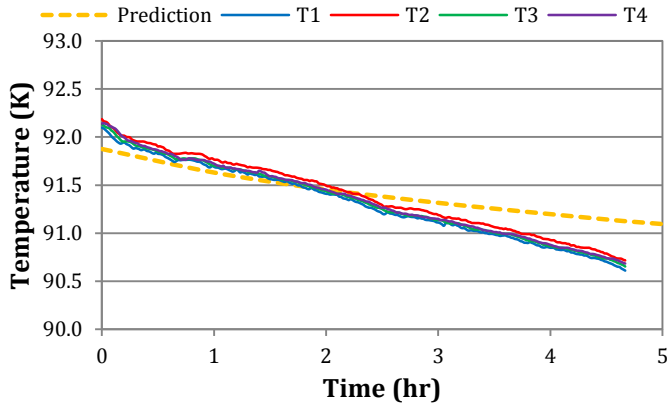

Figure 8: Test Results for Liquid Zone Below the Heat Exchanger (5psig)

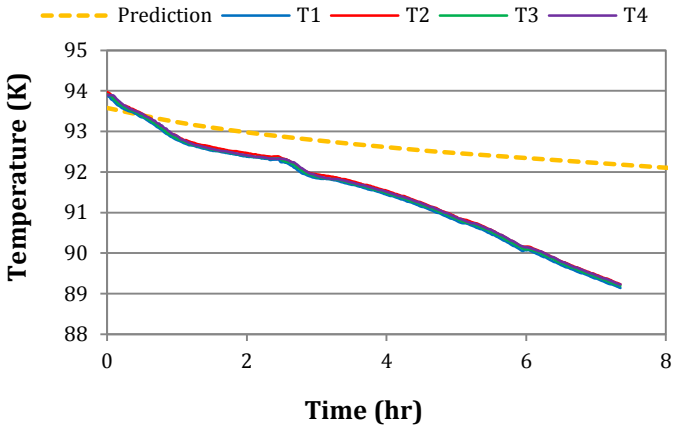

Figure 9: Test Results for Liquid Zone Below the Heat Exchanger (7psig)

5. Discussion

The results from Figure 4, 5 and 6 show that the liquid zone above the heat exchanger experiences conductive heat transfer. Minimal convection occurs within the liquid zone above the heat exchanger as shown by the stratification that grows throughout the heat exchanger operation. The mathematical model, Equation (5), predicts the temperature change rate at the T5 position with a slight lag. However, with exception of the results in Figure 4, the lag increases for the T6 position prediction in temperature change rate.

The results from Figure 7, Figure 8, and Figure 9 show the liquid zone below the heat exchanger experiences convective heat transfer. All four position temperature sensors, T1 through T4, maintain the same temperature throughout the heat exchanger operation, which implies a fluid well mixed by convection currents. The mathematical model, Equation (11), predicts a temperature change that is less than the experimental results. The reason for the temperature change rate lag could be that Equation (11), is an average for a conduction model and does not model the convection currents, which increases the heat transfer from the upper boundary at the internal heat exchanger.

The mathematical models presented neglect the heat flux that enters the dewar from the sides in Equation (5), and the heat flux that enters the dewar from the sides and bottom in Equation (11). Thus, Equation (5) and Equation (11) produce models that are one-dimensional. However, from the horizontal temperature sensors, T21 through T24, showed no gradient in the radial direction and was the same temperature as the centerline temperature at the same vertical height. Therefore, the one-dimensional mathematical models are reasonable.

Because the mathematical model for the liquid zone beneath the heat exchanger is an average temperature throughout the liquid zone, the temperature at the upper boundary does not equal temperature of the heat exchanger. Thus, a temperature discontinuity exists between the two models, Equation (5) and Equation (11), at the heat exchanger, and the possibility exists for colder fluid positioned above warmer fluid. In reality, natural convection occurs when a colder, more dense fluid is above a warmer, less dense fluid. Therefore, the temperature of the liquid above the heat exchanger can never be less than the temperature below the heat exchanger. Thus, the discontinuity between (5) and (11) can be corrected by mandating that temperature of the liquid above the heat exchanger be the maximum of either Equation (5) or Equation (11). Equation (12) and Equation (13) provide the unified temperature model.

$$T(y,t) = \max \begin{cases} \text{Equation (5)} \\ \text{Equation } (\mathbf{11}) \end{cases} \text{ for } h_1 \leq y \leq h_2 \qquad (12)$$

$$T(y,t) = \text{Equation } (\mathbf{11}) \text{ for } 0 \leq y < h_1 \qquad (13)$$

Figure 10 shows the predicted vertical temperature profile, during heat exchanger operation. The vertical temperatures are represented by T1-T12, which are located vertically in the main test dewar. The vapor-liquid interface is at the T8 and the heat exchanger is located at the T4. The left portion of Figure 10 shows the temperature discontinuity between the mathematical models, (5) and (11). The right portion of Figure 10 shows the unified temperature models from Equation (12) and Equation (13). Figure 11 shows the combined experimental data of Figure 6 and Figure 9 for comparison with Figure 10.

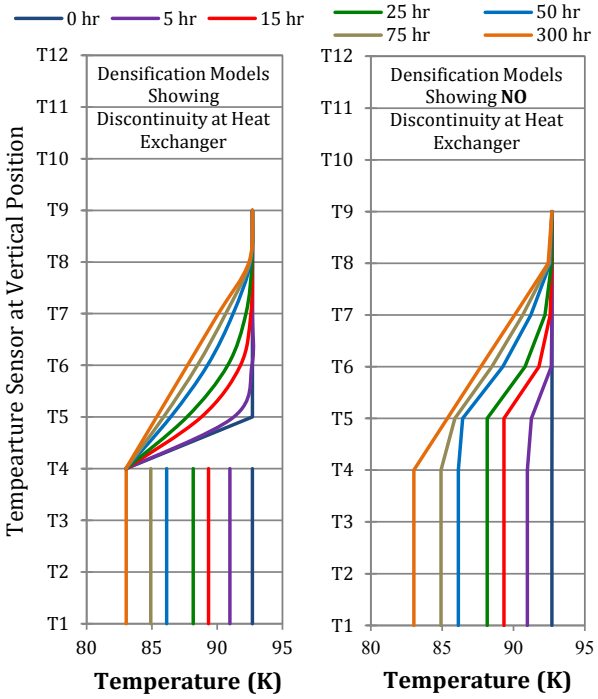

Figure 10: Exposure and Correction of the Discontinuity Between Both Mathematical Models

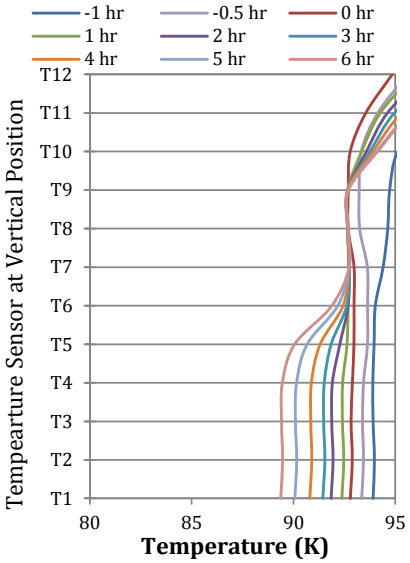

Figure 11: Test Results for the Liquid (7psig) Shown as the Temperature Profile for the Vertical Position.

The coolant removed about 330W from the main test article. However, not all of the heat removed was used to cool the liquid oxygen. The heat transfer from the ambient was approximately 20W, according to the experimental normal evaporation rate. Also, a portion of the gaseous oxygen that flows into the ullage is cooled and liquefied, accounting for 180W. Therefore, 130W of heat was removed from the liquid oxygen.

The major benefit for densification within the storage tank under positive pressure allows the use of a low power cooling source that densifies the propellant over time while inhibiting atmospheric intrusion. Same species pressurization also assures that propellant purity will be maintained throughout the densification process. However, as shown above, the liquid below the heat exchanger can be fully densified, while the liquid above the heat exchanger is partially densified. Also, cooling the pressurant gas required about 55% of the cooling available from the heat exchanger, decreasing the densification rate of the liquid.

6. Conclusions

The use of a submerged cooling source is a viable method to obtain densified and sub-cooled propellants. Also, same species pressurant can be used to maintain positive pressure of a storage tank during the densification operation. This study confirmed that conduction heat transfer dominates the fluid above the heat exchanger, while convection heat transfer dominates the fluid below the heat exchanger.

7. References

Fazah M. M. STS Propellant Densification Feasibility Study Data Book [Report] : NASA Technical Memorandum 108467. - Marshall Space Flight Center, AL : NASA, 1994.

Greene William D. and Vaughn David A. Simulation and Testing of In-Tank Propellant Densification For Launch Vehicles [Journal] // AIAA. - 1998. - p. 3688.

Haberbusch M.S. [et al.] Modeling the RL10 with Densified Liquid Hydrogen and Oxygen Propellants [Journal] // AIAA. - 2002. - p. 3597.

Lak T., Lozano M. and Tomsik T. Advancement in Cryogenic Propulsion System Performance Through Propellant Densification [Journal] // AIAA. - 1996. - p. 3123.

Lak T.I., Lozano M.E. and Neary D.A. Propellant Densification Without Use of Rotating Machinery [Journal] // AIAA. - 2002. - pp. 3599-3608.

Notardonato William U. [et al.] Experimental Results of Integrated Refrigeration and Storage System Testing [Conference] // Advances in Cryogenic Engineering. - Melville, NY : American Institute of Physics, 2009. - pp. 1369-1376.

Notardonato William U. [et al.] Integrated Refrigeration and Storage System - Heat Exchanger Characterization [Report] : Final Report. - Kennedy Space Center : NASA, 2009.

Tomsik Thomas M. Performance Tests of a Liquid Hydrogen Propellant Densification Ground Support System for the X33/RLV [Journal] // AIAA. - 1997. - pp. 2976-2992.

8. Variables

n	integer used for summation ( )
h	height (m)
t	time (s)
T	temperature (K)
r	non-homogeneous component of heat equation
y	vertical component of coordinate system (m)
α	thermal diffusivity (m^2/s)

Subscripts

1	vertical height at heat exchanger
2	vertical height at vapor liquid interface
sat	saturated temperature
s	heat exchanger surface temperature

Concept for On Orbit Liquid Hydrogen Test bed

D. Frank, T. Nast and J. Mix
Lockheed Martin Space Systems Company
Advanced Technology Center
3251 Hanover St.
O/A015S
Palo Alto, CA 94304 USA

Abstract:

There is growing interest in the utilization of cryogenic propellants for future space missions. The utilization of these propellants for long duration in space presents substantial challenges in fluid management in the low g environment. Lockheed Martin (LM) is developing the concept for a space borne system for demonstration of long term storage, various fluid management tests involving control of tank pressure, location and identification of vapor and liquid phases, venting in low g, mass gauging, and extension of life with cryocoolers and location of liquid for transfer. In addition the concept includes autonomous coupling and hydrogen transfer from tank to tank. The concept is based on a flight qualified flight proven hydrogen Dewar design from a previous program The concept for this system is described.

Keywords:

Cryogenic Fluid Management, Liquid hydrogen, long-term space storage

Introduction:

With the completion of construction on the ISS and the retirement of the Space Shuttle, human space flight is in the position to explore more distant and ambitious destinations. Arguably the most interesting path is following the trajectories of robotic missions to asteroids, the Moon, Mars, and beyond. Cryogenic propulsion provides the necessary performance for Earth departure, and it would facilitate Mars returns and other difficult deep space missions. Presently the use of cryogenic propellants is limited due to high boil-off rates and lack of maturity for low gravity fluid management. Moreover, experience with transfer of cryogenic propellants is limited, impacting the technical feasibility of future propellant depots, for enabling deep space missions.

A Cryogenic Fluid Management (CFM) demonstration system will pave the way for full-scale propellant storage systems, providing utility to diverse organizations including the National Aeronautics and Space Administration (NASA), the Department of Defense, commercial satellite providers, and international partners. NASA, along with its international partners for potential future human and robotic exploration mission collaborations, stands to gain significant mission capabilities from in-space cryogenic storage and transfer.

Lockheed Martin (LM) is developing a test bed for demonstration of CFM technologies. The approach taken is an architecture with a low-risk platform for the cryogenic payload. The cryogenic payload incorporates LM's Dewar thermal protection technology and heritage designs in order to permit a long-term, low-risk test bed in space. This payload represents many of the technologies needed for the very large tanks of the mission scenarios.

Relevant Technology Base at ATC:

Cryogenic propellant storage and fluid management technology at LM was active in the 1960's and 1970's, but was largely discontinued until recent renewed interest in space exploration. Long term orbital storage of cryogens at the Advanced Technology Center (ATC) has been demonstrated in the interim on instrument cooling systems, which include cryogens such as hydrogen, methane, ammonia, and helium for orbital missions in excess of five years.

Cryogenic propellant systems employed to date have very short storage requirements, typically days. Aspects of both long term instrument cooling and present short term propellant systems must be melded together to achieve an optimum system for long term propellant storage which includes thermal efficiency, cost, weight and reliability.

Lockheed Martin has developed twenty systems for orbital operation, which include hydrogen, methane, ammonia, carbon dioxide, and superfluid helium. These systems circumvent the issue of venting the sub critical fluid without liquid loss, by operating the cryogens in the solid condition so that the gas could be directly vented by sublimation. The only exception was the operation with superfluid helium, which utilized its unique properties by venting through a porous plug. A summary of systems developed for instrument cooling at ATC in space is shown in Fig. 1.

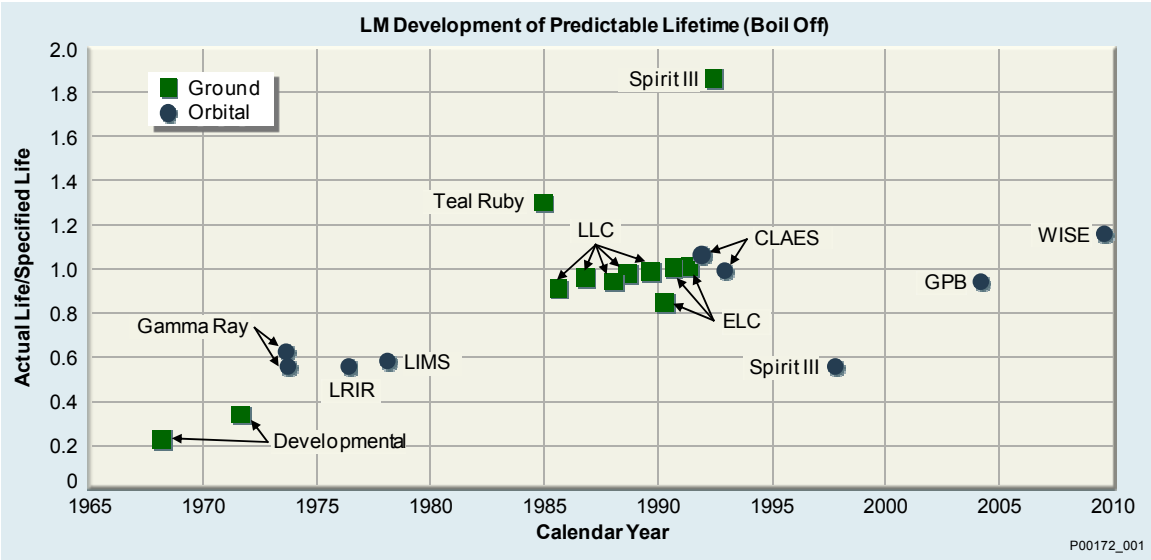

Figure 1: LM Development of Predictable Lifetime (Boil-Off). Good performance predictability took two decades to achieve.

All of these systems utilized conductive shields cooled by vented vapor, composite support tubes, composite plumbing lines and a hard vacuum shell. The insulation systems utilized double aluminized Mylar with silk net spacers. Because of the dominant importance of good multi-layer insulation (MLI) performance, the layers were applied one at a time with joints taped for the Mylar and sewn for the spacers. This technique consistently resulted in excellent performance approximately 50% above the ideal flat plate performance. The evolution of the systems to reliable and predictable performance required approximately two decades as shown in Fig. 1 with substantial support from LM independent research. It should be noted that the actual in-flight instrument duty cycle or environments usually turn out different then that used for ground testing, which results in different ground and orbital lifetimes as can be seen by the data in Fig.1 for Spatial Infrared Imaging Telescope (SPIRIT III). A system recently operated in orbit is the Wide-Field Infrared Survey Explorer (WISE) instrument, which was cooled by a two stage solid hydrogen system developed by LM. Its configuration is shown in Fig. 2 in which the advanced thermal isolation technology is shown.

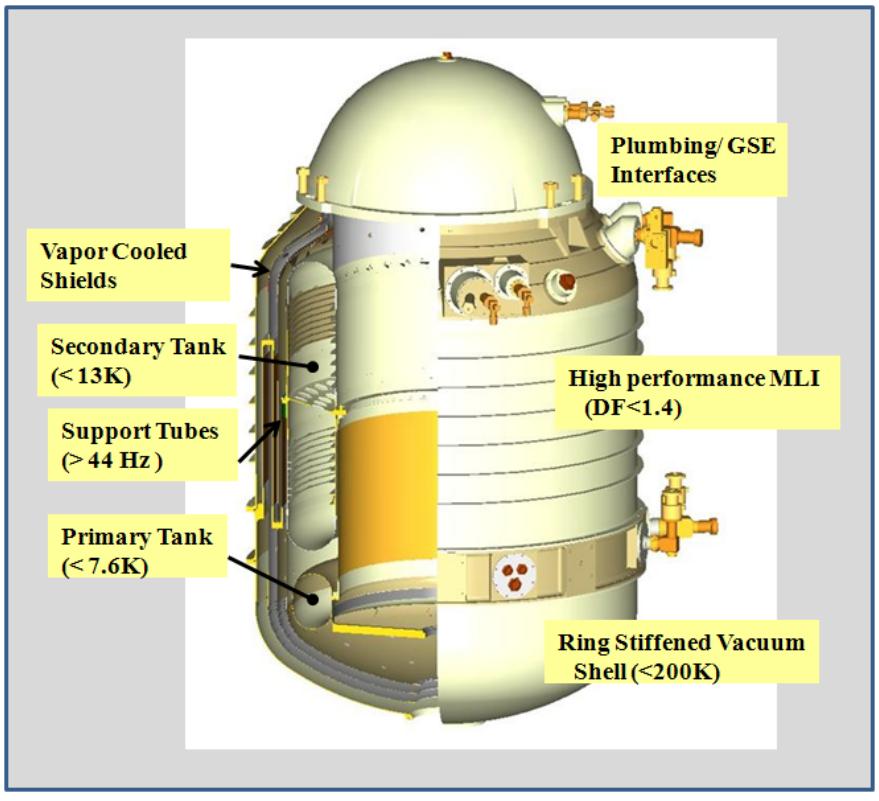

Figure 2: Characteristics of recent instrument cryostat (WISE) at LM. This technology along with other LM hydrogen Dewars forms the basis for the CFM demonstrator test bed.

This system implemented extensive advanced thermal isolation technology and utilized a vacuum shell, which was cooled to 200K in orbit. The hydrogen was frozen by circulation of LHe through cooling lines on the tanks, which utilized the aluminum tank shell as the extended heat exchanger.

These examples of long-term cryogenic storage prove the capability to extend these technologies to long life cryogenic propellant storage. A summary of approaches to reduce cryogenic propellant boil-off is discussed in reference 1.

Ground Demos vs. Space Demo:

Many of the technologies required for long duration cryogenic propellant storage could be matured by ground demonstrations at a fraction of the cost of the space demonstration. Most of these ground demonstrations relate to thermal isolation of the tanks from the external thermal environments. The unique storage technologies that have not been demonstrated on large propellant tanks to date include the following: 1) Large tank multi layer insulation application and performance data; Excellent performance has been demonstrated on tank sizes up to about 2500 Liters, but data on larger tanks has yielded poor results 2) Plumbing lines for higher pressures; ATC has utilized convoluted Teflon for various plumbing lines, however pressure capabilities may be too low for some of the propellant plumbing lines. Low heat leak lines using low heat leak composites will be required. 3) Integration and demonstration of cryocooler cooling over large shield areas; although cryocoolers are available which provide most of the required cooling, distribution of cooling over large surfaces and the shield construction have not been completely demonstrated.

The technologies that are required for long term orbital demonstration are shown in Fig. 3.

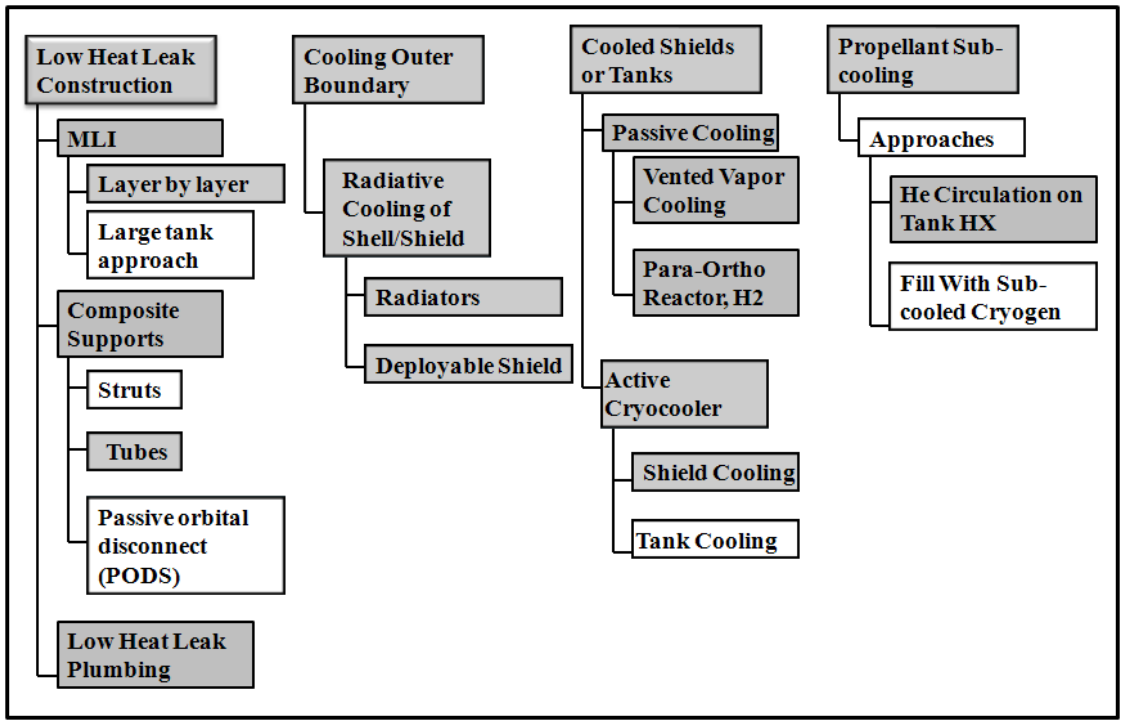

Figure 3: Required Thermal Storage Technologies for Long Duration Cryogenic Propellant storage. Items shaded in grey have been selected for the LM CFM approach.

Although space operation is not required for demonstration of these technologies they are required in order to provide sufficient orbital test time to provide the micro-g technology demonstrations. The items shown in grey are included in our proposed orbital demonstration.

The technologies that are gravity dependent and must be matured and demonstrated in space are shown in Fig. 4. The categories shown in grey have been selected for orbital demonstration.

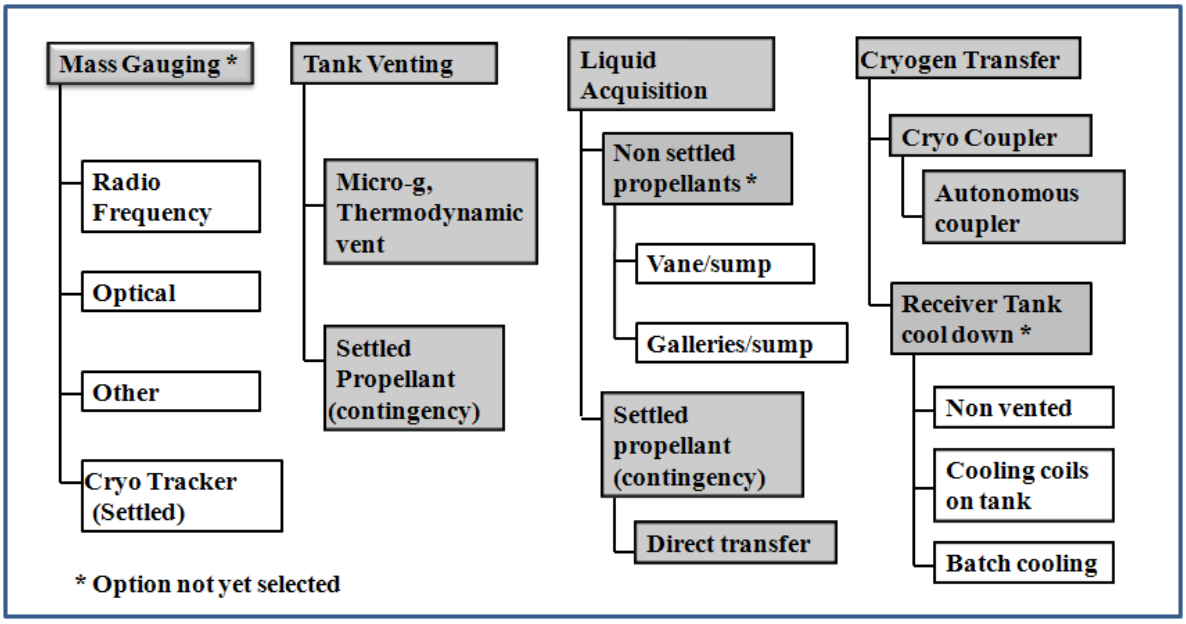

Figure 4: Technologies that require orbital validation. Items shaded in grey have been selected for the LM CFM approach.

Many of these technologies have been under development at various NASA centers but will require additional maturation in ground tests prior to implementation into an orbital experiment.

CFM Demonstration Approach:

The cryogenic payload provides a long-duration test bed for CFM hardware and supports model correlations and validations for in space storage and transfer of propellants. Fluid management addresses approaches for pressurization and pressure control. Fluid acquisition and transfer characteristics represent large tankage applications. The tanks and their thermal protection and support system are based on systems developed by LM for providing long-term storage of cryogenic fluids for instrument cooling. The LH_2 storage utilizes the space qualified and flown SPIRIT III hydrogen system, with adaptations to support CFM hardware demonstrations.

The 940-liter hydrogen system shown in Fig. 5 is a high thermally protected tank providing the desired environments for the CFM hardware. The thermal protection insulation around the tank contains a shield that is vapor-cooled and contains interfaces for an active-cooling system. The support system is a folded composite tube design, previously flown on numerous cryogenic tanks. The use of a vacuum shell provides for much simpler ground and launch processing but is not necessarily the architecture for a full-scale system. The tank is filled prior to spacecraft integration with the launch vehicle. Servicing at the launch pad is limited to periodic, simple re-cool operations with liquid helium and permits subcooling of the hydrogen, increasing ground hold time and longer storage in orbit. The system may also incorporate a para-to-ortho catalytic converter, which was previously developed. This methodology assures an operational system as soon as it is placed in orbit, with higher-risk fluid transfers taking place near the end of mission.

The addition of the CFM hardware will result in an increase in the heat load to the tank and an alternation of the thermal distribution through the insulation.

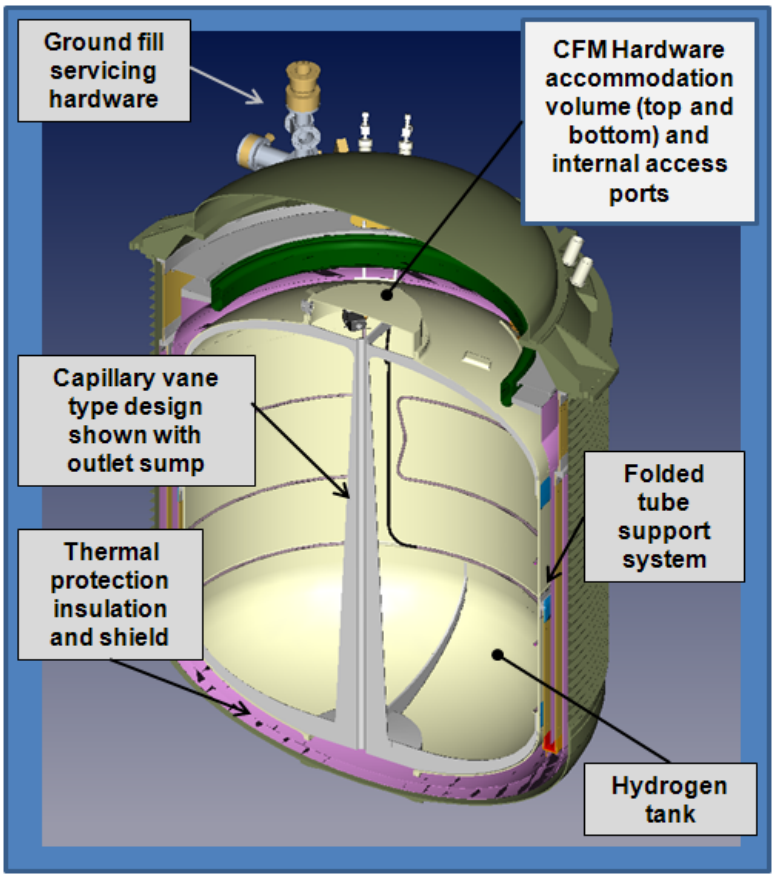

Figure 5: Cryogenic Fluid Management system liquid hydrogen storage system. This heritage design provides the required environments and lifetime for CFM hardware testing.

The interfaces between the CFM hardware and the tank thermal protection system can result in serious degradation in heat rates if not designed properly. Fig. 6 shows the effect of insulation degradations on the lifetime of the system with a 300K outer boundary. A Degradation Factor (DF) of 1.6 is typical for our insulations with a value of three for well-degraded systems. It can be seen that the resultant heat load to the tank from the CFM hardware must be limited to just over a half watt in order to store the cryogen for close to a year. However, the transfer operations need to be performed with the supply tanks having a residual on the order of 40%, which leads to a mission lifetime of just over six months. The mission time can be substantially increased by utilization of a cryocooler for shield cooling.

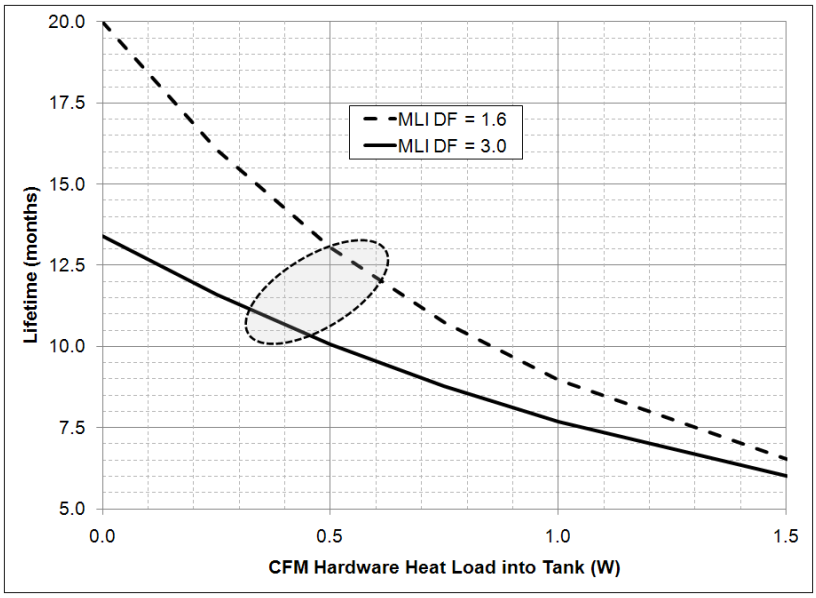

Figure 6: Effect of insulation degradations on the lifetime of the hydrogen subsystem due to CFM hardware penetrations with a warm boundary of 300K.

Instrumentation is a key component of the system. It is divided into two categories: 1) instrumentation needed to provide and record the environment for the CFM hardware under test and 2) the read-out capability for the instrumentation being provided with the CFM hardware. The system instrumentation includes sets of heaters on and in the tanks that are used to provide a wide range of test conditions for hardware and model correlations. These are conditions such as stratification and gradients within the fluids and thermal loading from the tank walls. Note that this tank surface area to volume ratio is two to three times higher than large depot size tanks which makes the attainment of long mission times for the larger tanks easier in this respect.

The cooling requirement for reducing (reduced boil-off) the temperature of the shield in the insulation space for the hydrogen system is shown in Fig. 7. The figure shows the cooling required to lower the shield temperature. This shows that for a range of MLI degradation of 1.3 to 3.0 that with 100W of cooler input power (not including the control electronics) the shield temperature is lowered from around 110K to around 70K. For 200W the shield can be lowered to around 50K and so forth. The cryocooler data in the plot is actual measured data with a Lockheed Martin cryocooler. The predicted response of the shield to cooling is based on no heat dissipation at the tank temperature. This reasonable range of cooling and power needs opens a number of options to be evaluated. This would be one of the primary power needs along with the payload processor (65W). This size cryocooler can be used to remove all the heat in an oxygen tank leaving it with the ability to be stored non-vented (zero boil-off).

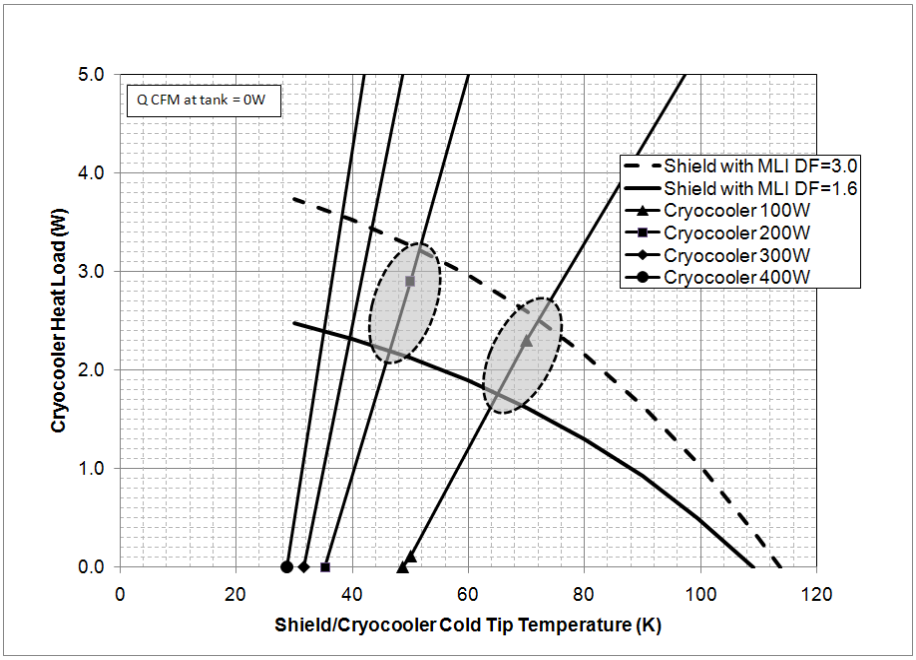

Figure 7: Cooling requirement for reducing the shield in the insulation space for the hydrogen system. The graph, based on actual cryocooler measured data, shows a reasonable range of cooling power needs.

The result of the effect of reducing the shield temperature on the lifetime with the cryocooler is shown in Fig. 8. The figure shows the two insulation degradations used in Fig. 7. It can be seen that the 100W to the cryocooler, which reduced the shield to 70K with 2W of cooling, increased the lifetime of the cryogen substantially. In the case where the CFM hardware results in a watt at the hydrogen tank, the effect of active cooling on the insulation shield has much less benefit. This can occur if the CFM hardware going through the thermal protection system is not properly thermally grounded at the shield.

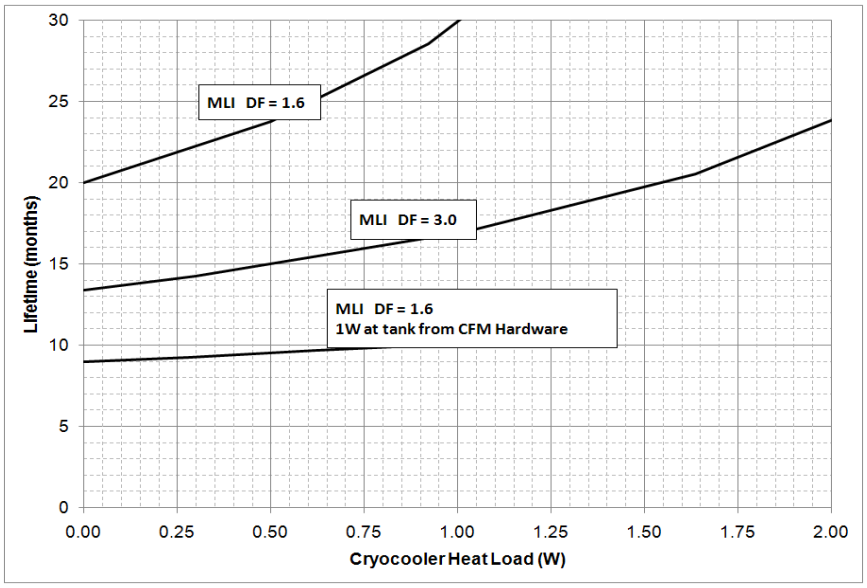

Figure 8: Effect of Active Cooling on Lifetime. Benefit from active cooling of the shield is much less pronounced when the CFFM hardware is not properly thermally anchored and results in high heat to tank.

Fluid transfer parameters, such as fluid acquisition and withdrawal rates, during this mission have not been selected and must address the needs of the large tank applications and their operating conditions. A typical vane type fluid acquisition vane device is shown in Fig. 5. It is expected that the final selection will be a mix of vane/gallery/sump designs. Another key feature of transfer, incorporated in the system, is an autonomous cryogenic coupler. The objective is to have one coupler perform a de-mate and mate prior to the last tank-to-tank transfer.

Conclusion:

A test bed for in-space demonstration of cryogenic propellant storage and transfer fluid management technologies in a space qualified long life hydrogen tank is under development. The test bed is based on heritage LM designs for long-tern storage of cryogens, which will keep its development cost and schedule within acceptable levels.

Acknowledgements:

We would like to acknowledge the support by Lockheed Martin in numerous in house funded research projects, which has led to the development of long-term storage of cryogens.

References:

1. Nast, T.C. et al, Cryogenic Propellant Boil-Off Reduction Approaches, January 2011, AIAA Paper 2011-806

Cryogenic Orbital Testbed (CRYOTE) Development Status

M. Gravlee [1], B. Kutter[2], and C. McLean[3], J. Marquardt[4]

[1]Advanced Programs, United Launch Alliance
[2]Advanced Programs, United Launch Alliance
[3]Principal Engineer, Ball Aerospace
[4]Principal Engineer, Ball Aerospace

The Cryogenic Orbital Testbed (CRYOTE) is a project that brings together several NASA centers, several industry partners, and ULA toward a common goal – the advancement of Cryogenic Fluid Management (CFM) technologies. The testbed provides an in-space environment in which the fluid transfer, handling, and storage of liquid hydrogen (LH2) and/or liquid oxygen (LO2) can be demonstrated.

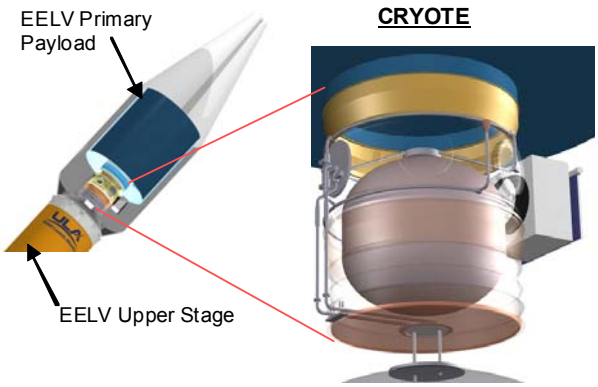

Figure 1 – CRYOTE is affordable because it launches as an EELV secondary payload and utilizes residual upper stage propellant for the technology demonstration

Using extensive trades and discussions with experts from across ULA, NASA, and industry, the CRYOTE detailed concept provides a cost effective, flexible, and extensible method for flight demonstrating CFM technologies and integrated cryogenic systems. Results from CRYOTE can be used to anchor analytic models and applied directly to the design of cryogenic propulsion stages (CPS) and cryogenic depots.

CRYOTE avoids the high costs of a dedicated launch vehicle by flying as a secondary payload on an Atlas V (Figure 1). CRYOTE is launched with empty tanks and is filled on-orbit from residual LH2 and LO2 in the Centaur tank following primary payload delivery. The transfer of LH2 and LO2 residual propellants from Centaur to CRYOTE demonstrates transfer out of an actual CPS (Centaur) into CRYOTE's tanks. Launching empty, CRYOTE demonstrates how future CPSs and propellant depots can be made ultra light weight with very low structural tank heating, enhancing the ability to support long duration missions.

With empty, ambient temperature tanks and dormant avionics, CRYOTE represents minimal risk to the primary payload, simplifying acceptance by the primary payload community. The primary payload community may have serious issues flying with a cryogenic secondary payload, especially if this cryogenic payload drives launch day requirements such as loading, venting, and recycle turn around duration. The CRYOTE approach of on-orbit cryogenic loading may be mandatory to gaining broad primary mission acceptance to flying a cryogenic secondary payload. Centaur's avionics bring CRYOTE to life after the primary payload is separated.

There are three distinct versions of CRYOTE designed to flexibly satisfy a broad range of mission objectives (Table 1):

- **CRYOTE Lite** – To save cost and schedule, CRYOTE Lite utilizes the existing Centaur avionics for power and control. Reliance on Centaur batteries limits the primary mission duration to <24 hours. CRYOTE Lite provides on-orbit demonstration with either LH2 or LO2 of system chilldown, liquid transfer, tank fill, transient boil-off, mass gauging, propellant management device, thermodynamic vent system and vapor cooling. With the addition of an independent battery-powered telemetry system, CRYOTE Lite can transmit limited cryogenic system performance (temperature, pressure) for a period of months.

- **CRYOTE Pup** – Expands CRYOTE Lite's capabilities with the addition of dedicated mission avionics including a flight computer, solar power, two-way communications and guidance enabling multi-month mission duration. CRYOTE Pup increases mission capability over CRYOTE Lite by incorporating closed loop control, multi-month mission, increased sensor count, active cooling, long term stratification, cryogenic fluid couplings, and integrated GH_2 propulsion attitude control.

- **CRYOTE Grande** – Enhances CRYOTE Pup by enabling both LH2 and LO2 in a single mission thanks to additional plumbing and extra tanks. This additional hardware provides the capability to perform numerous LH2 and LO2 transfers (settled and unsettled), demonstrate H_2/O_2 propulsion, zero LO2 boil-off storage, low and zero LH2 boil-off storage, and multiple tank designs, propellant management devices, and liquid acquisition devices on a single mission.

Table 1 CRYOTE's Three Configurations are Designed to Flexibly Satisfy a Broad Range of Mission Objectives Enabling Testing of NASA, Academia and Industry Defined Experiments.

	Lite	Pup	Grande
Duration on-orbit	<24 Hours	>6 Months	>6 Months
Lead Time to ILC	2 Years	2+ Years	2+ Years
Flight Computer	Centaur	CRYOTE Avionics	CRYOTE Avionics
System Control	Open Loop	Closed Loop	Closed Loop
Power	Centaur Batteries	Solar Arrays	Solar Arrays
Attitude Control	Centaur Hydrazine	Cold Gas Thrusters Using Vented H_2	Cold Gas & H_2/O_2 Thrusters
Telemetry	Centaur	CRYOTE Antennas	CRYOTE Antennas
Upper Stage Launch Vehicle Separation	Remains Attached to Centaur	Remains Attached to Centaur	Remains Attached to Centaur
Cryogen	Centaur Residual LH2 or LO2	Centaur Residual LH2 or LO2	Centaur Residual LH2 & LO2
Tank size	1 * 1000L 1.2 m (48 in) diameter	1 * 1000L 1.2 m (48 in) diameter	1 * 1000L; 1.2 m dia 3 * 400L; 0.9 m (36") dia

CRYOTE Core: The subsystem for all CRYOTE mission variants is called the CRYOTE Core and is shown in Figure 2. CRYOTE Core employs a custom, 1,000L LH2/LO2 compatible tank. Solenoid latching valves are employed to facilitate propellant transfer and control of multiple experiments, which are under development by Ball Aerospace and United Launch Alliance (ULA). CRYOTE core resides in an ESPA ring. Support of the tank is provided by low conductivity, Ball Aerospace flight heritage cryogenic struts, mounted in a hexapod arrangement. For initial missions, Ball Aerospace high performance cryogenic multi-layer insulation (MLI), integrated MLI (IMLI), or a combination of the two will be used to provide tank acreage insulation.

The tank design is based on Ball Aerospace heritage design and manufacturing processes. The tank can accommodate multiple internal experiments, and has external mounting provisions for experimental hardware. Provisions to the tank design have been included for the incorporation of multiple propellant management device (PMD) technologies as well as zero-g mass gauging sensors such as the NASA Glenn Research Center (GRC) radio frequency technologies and the Sierra Lobo CryoTracker.

Cryogenic Propellant Transfer: At a minimum, any CRYOTE configuration demonstrates cryogenic propellant transfer: LH2 only, LO2 only, or both LH2 and LO2. This description will include both propellants.

Figure 2 – CRYOTE Core provides a flexible testbed for short and long term on-orbit cryogenic propellant storage and transfer experiments.

Following launch and safe delivery of the primary payload, Centaur will perform a standard Collision Contamination and Avoidance Maneuver (CCAM) to ensure adequate separation from the primary payload and that Centaur is in an appropriate disposal orbit. During CCAM the initial chilldown of the CRYOTE plumbing and tanks commences. This is accomplished by flowing Centaur's cold hydrogen ullage gas through CRYOTE's LH2 tank and then venting the GH_2 overboard through a balanced vent system. During this venting Centaur's is settled to ensure acquisition and transfer of gaseous, not liquid, hydrogen.

A settling sequence including reverse settling and a Centaur transverse spin chills the system and prepares the Centaur upper stage for filling the CRYOTE tanks (Figure 3). A similar pulse/vent chilldown process has been demonstrated on past Centaur flights using both LH2 and LO2 to chill Centaur's feedlines and RL-10 pump housing.

Once the transfer lines and CRYOTE tanks have been chilled the transfer of Centaur residual LH2 and LO2 can commence. The LH2 and LO2 transfers are pressure fed. Centaur tank pressures ensure that the LH2 and LO2 will be sub-cooled. This sub-cooled LH2 and LO2 will enter their respective CRYOTE tanks, quenching the vapor and sucking in additional liquid. This "zero vent fill" transfer process is indifferent to the liquid-gas location inside the CRYOTE tanks, avoiding inadvertently venting liquid overboard which would represent wasted performance. This zero vent fill process has been ground-demonstrated to be very effective, attaining nearly 100% fill. This entire chill-and-fill process is designed to be accomplished in less than 30 minutes. 30 minutes represents the available time before Centaur's hydrogen tank pressure starts to approach structural limits forcing the LH2 to be resettled aft allowing for Centaur tank venting.

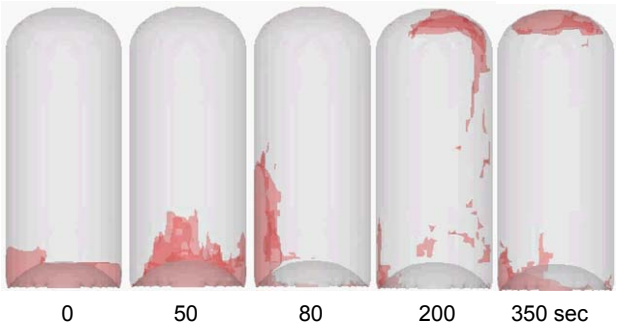

Figure 3 The Use of Reverse Settling and Transverse Spin Will Reorient the LH2 to the Forward End of Centaur's LH2 Tank Enabling Bubble Free Liquid Acquisition.

Following completion of the LH2 and LO2 transfer, Centaur's tanks are vented to vacuum, evacuating the majority of residual propellants, safing Centaur. Centaur's systems will then be turned off leaving CRYOTE avionics in control.

Thermal modeling: In order to evaluate the transfer and storage performance of the CRYOTE Core[i] subsystem, detailed thermal/fluidics models were developed that allowed parametric evaluation of the system level design. These models were developed to allow extensibility to other cryogenic propellant storage and delivery systems. A model was developed to predict the performance of the CRYOTE Ground Test Article[ii] to not only predict the performance of this experiment, but also to validate the CRYOTE Core model predictions with actual data.

As can be seen in the analysis in Figure 4, all aspects of the mechanical, thermal, and pneumatic design must be accounted for to optimize the results of a successful CRYOTE transfer. For the CRYOTE platform, propellant transfer is pressure fed based on a significant residual gas volume and subcooling of the liquid hydrogen within the Centaur hydrogen tank.

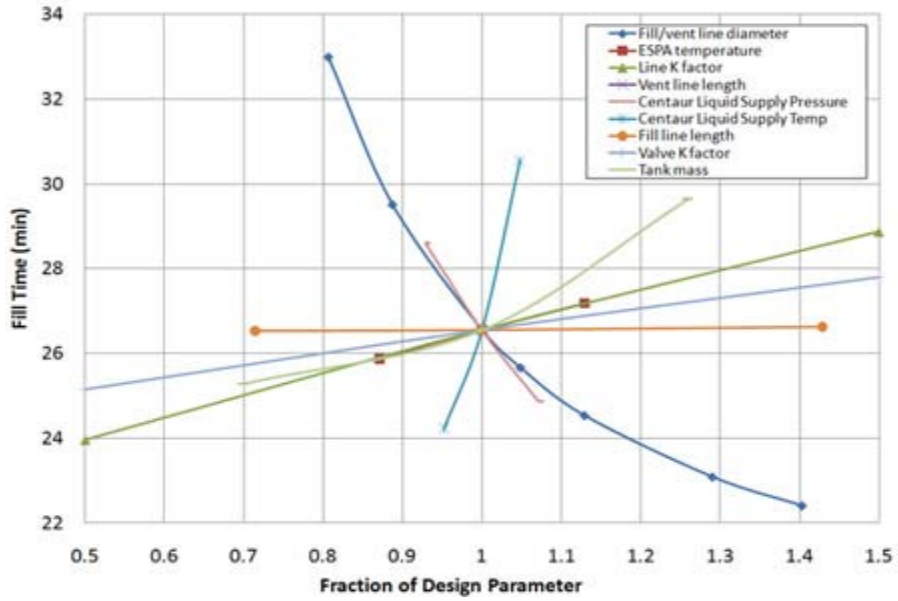

Figure 4 - Parametric analysis of CRYOTE tank cool down and fill design parameters

Orbital Analysis: Another systems level goal of the CRYOTE Lite/Pup was the ability to provide attitude control though the use of hydrogen boil-off in lieu of a hydrazine based attitude control system. Various operational orbits were analyzed, and optimization of attitude control requirements was performed (Figure 5).

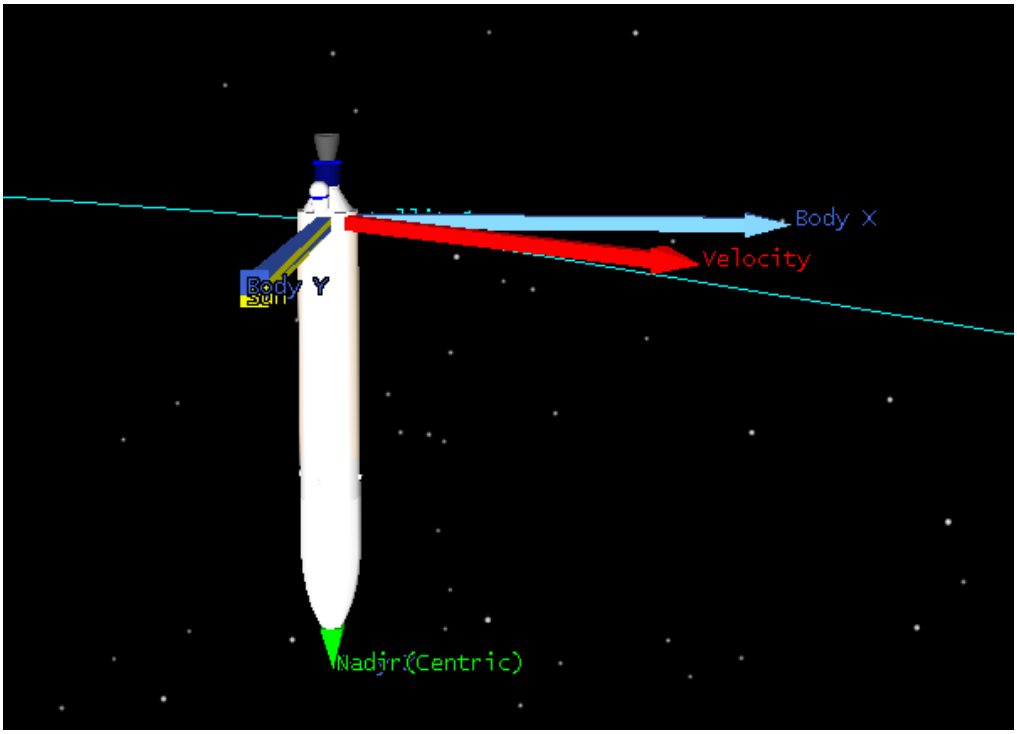

Figure 5 - CRYOTE Lite/Pup orbital analysis was used to optimize the mission attitude control requirements

This analysis not only validated the ability to employ cold gas hydrogen thrusters for attitude control, but also evaluated the quantities of propellant required for various mission scenarios.

Thermodynamic Venting System (TVS): The system level thermal analysis shown in Figure 4 incorporated both a TVS and a Vapor Cooled Shield (VCS) to maximize the passive storage duration for CRYOTE Core. A TVS can be used to provide significant cooling to stored, subcritical two-phase cryogenic propellants. Expansion and pressure drop of liquid (or two-phase fluid) propellant across a Joule Thompson (JT) orifice provides cooling that can be used to intercept system heat leaks, or cool the bulk gaseous or liquid stored in the propellant tank. The heat exchange process with the stored fluid can take place within the tank utilizing an internal heat exchanger within the tank, or by using fluid lines coupled to the tank wall.

For CRYOTE Core, the TVS is used primarily to intercept parasitic heat leaks from structural and plumbing penetrations though the Integrated Multi-Layer Insulation (IMLI) and into the tank. The TVS on the CRYOTE Lite/Pup programs was optimized to provide the maximum amount of cooling using duty cycled TVS operation, or TVS flow rates matched to the system level boil-off.

Vapor Cooled Shield (VCS): Also included in the Figure 4 analysis was a VCS, imbedded in the IMLI, to intercept the broad area heat leak into the stored hydrogen. The analysis indicated that a significant increase in the LH2 storage life was achievable by the incorporation of the VCS. For the CRYOTE Core, the VCS is embodied as an aluminum shield embedded in the IMLI blanket. This shield is cooled by the gas exiting the TVS. The technology used to support this design is identical to that used on the Ball Aerospace Near Infrared Camera and Multi-Object Spectrometer (NICMOS) program for the Hubble Space Telescope, as well as on every Space Shuttle Power Reactant and Storage Distribution (PRSD) tank. Inclusion of the VCS layer within the IMLI further increases Micro-Meteoroid and Orbital Debris (MMOD) protection.

Structural Heat Load: For cryogenic in-space stages such as the Saturn IVB, Centaur, and DCSS, structural supports account for a large fraction of the total heat load. This support structure heating is even more critical for long duration cryogenic stages where incorporation of high performance IMLI and integrated VCS substantially reduces the surface area heating. Substantially reducing the structural load path requires a combination of minimizing the load (e.g., launching tank empty when possible) and providing a structural interface designed for minimum heat transfer (e.g., struts). Ball cryogenic dewar strut technology (Figure 6***)*** is readily extensible to large propulsion stage architectures. Key elements include leveraging Ball flight heritage strut designs, as well as vapor cooling leveraged from flight programs such as Spitzer.

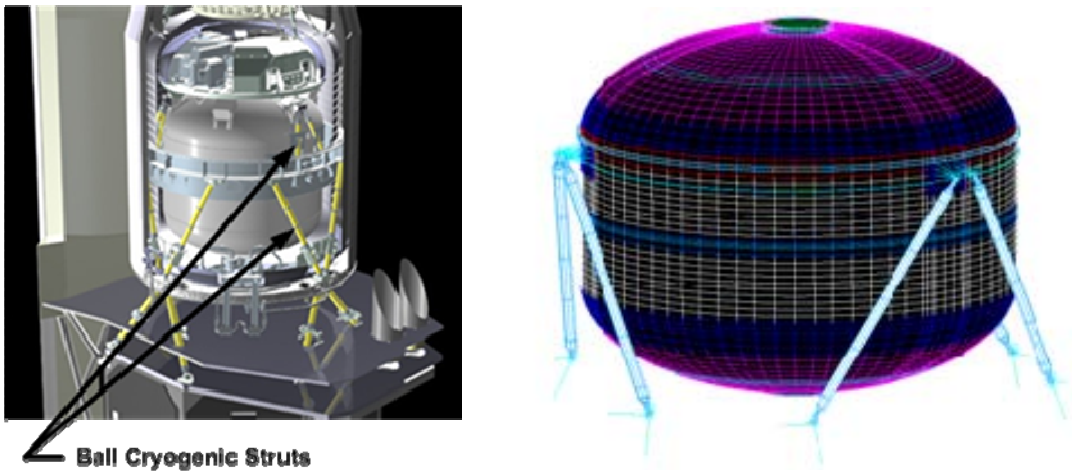

Figure 6 - Ball Aerospace flight heritage cryogenic strut technology has been optimized to meet the structural and thermal requirements of the CRYOTE missions

This hexapod strut technology has been tailored specifically for the CRYOTE Lite/Pup[iii] mission as shown in Figure 6. The hexapod arrangement is also based on flight heritage designs, and was examined in detail in the Cryogenic Propellant Storage and Delivery contract performed by Ball Aerospace for NASA GRC[iv]. This design was optimized to provide the best design solution for the CRYOTE mission by evaluating the structural, thermal, and coupled loads requirements for the mission.

Integrated Multi-Layer Insulation (IMLI) for CRYOTE Ground Test Article: NASA, Quest, and Ball Aerospace have been developing advanced, cryogenic IMLI to enhance on-orbit storage of cryogenic propellants[v]. The cryogenic propellant storage and experimental tanks are shrouded in IMLI, incorporating radiation barriers and Micrometeoroid Orbital Debris (MMOD) protection. The various IMLI layers are separated by micro-molded polymer structures (Figure 7)**.** The polymer substructures promise to improve IMLI thermal and MMOD performance by providing precise, engineered layer spacing.

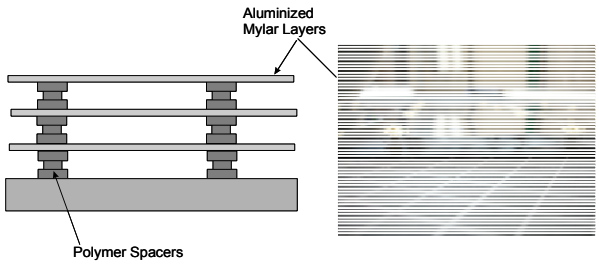

Figure 7 - Integrated MLI provides enhanced thermal and MMOD protection

A NASA-led study is currently underway to optimize the lay-up of IMLI for the CRYOTE Ground Test article, with extensibility to the flight application. An example of an optimized layup for this ground test is shown in Figure 8. This study is looking to optimize the application of IMLI technologies to various tank geometries.

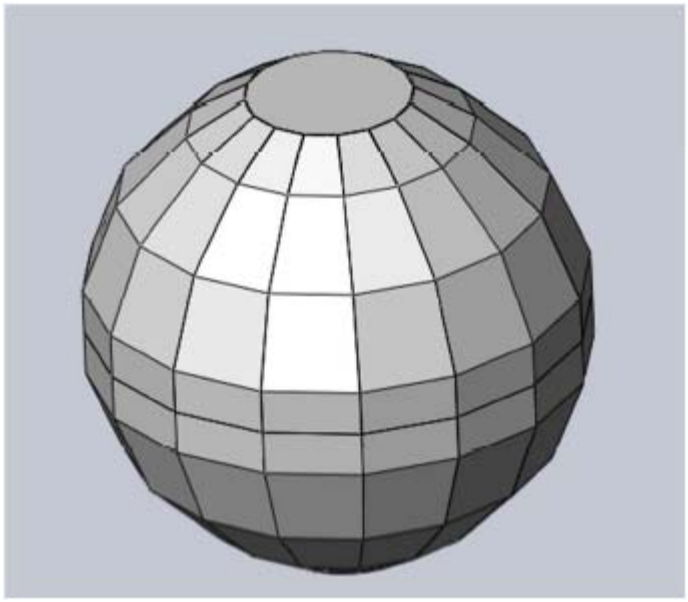

Figure 8 - Optimization of CRYOTE IMLI layup (Credit: Quest)

Active Broad Area Cooling (BAC): As the CRYOTE Core concept matured, the experimental platform has also been designed to incorporate multiple NASA based technology demonstrations. One key goal of the current NASA technology roadmaps is the demonstration of zero boil off (ZBO) LO2 and LH2 propellant storage systems, which requires the use of active cooling. Active BAC on a cryogenic propellant tank simulator was demonstrated in a laboratory environment by NASA and Ball Aerospace (Figure 9)[vi]. For this testing, the BAC was embodied as a helium cooled shield imbedded within cryogenic Multi-Layer Insulation (MLI).

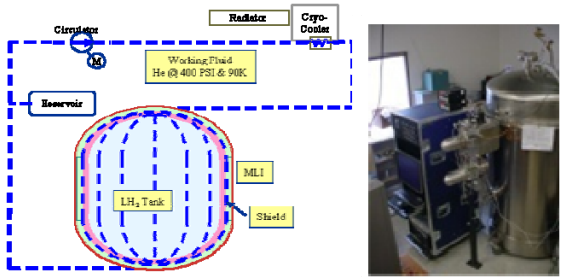

Figure 9 - NASA/Ball Aerospace Broad Area Cooling test program

For this program, a pumped helium circulation loop was employed to transfer heat from a 500 liter LN2 dewar shield to a cryocooler. Ball Aerospace built a novel system that uses the Stirling refrigerator's compressor to drive the circulating flow by means of valves in its transfer line, eliminating the need for a separate circulation pump. This technology demonstration is identical to that which could be employed on the CRYOTE Core to demonstrate ZBO.

Flying cryocooler technology on the CRYOTE Lite/Pup missions will validate the capability of cryocooler technology to extend the life of stored cryogenic propellants. With sufficient power and intelligent system design, ZBO for any cryogenic propellant is achievable. Ball Aerospace has designed, built, and delivered two flight cryocoolers, with one reaching seven years on-orbit

with no performance degradation. Ball's current cryocooler focus is on higher capacity Stirling coolers with approximately 2 W at 35 K. In addition, circulation loops have been added to these Stirling coolers to produce very low temperatures and remote cooling.

Conclusion

Demonstrated CFM technologies become even more important as we venture beyond the Moon to explore NEOs, Mars, and beyond. CRYOTE is a customizable laboratory for demonstration a variety of CFM technologies, shown with multiple tanks and a long-duration avionics system in Figure 10. CRYOTE Lite provides an affordable first step toward enhanced CFM, providing the risk reduction flight test for more costly and demanding technology demonstration missions such as CRYOTE Pup and CRYOTE Grande.

Results from CRYOTE can provide the critical in-space CFM demonstration to allow selection of mission architectures that utilize on-orbit fueling, long duration cryo storage and development of cryo propulsion stages truly designed for in-space use that have higher mass fractions and reduced boil-off compared to current designs.

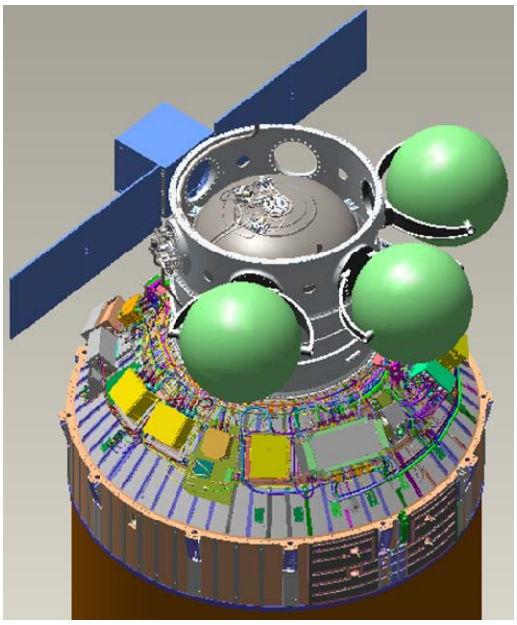

Figure 10 CRYOTE Provides a Cost Effective Laboratory for Orbital Testing of CFM Technologies.

---

i Gravlee, M., Vera, C., Wollen, M., McLean, C., and Walls, L.; "Micro-gravity Cryogenic Experiment Opportunity," AIAA 2010-8838, AIAA Space 2010 Conference & Exposition, Anaheim, CA, 30 August – 2 September 2010

ii Wollen, M. A., Gravlee, M., Johnson, W.L.; 'CRYOTE (Cryogenic Orbital Testbed) – Goals, Progress, and Potential', 2009 JANNAF Conference, Colorado Springs

iii McLean, C.H., et al.; Simple, Robust Cryogenic Propellant Depot for near Term Applications", IEEE 2011-1044 IEEE Aerospace Conference, Big Sky, MT, January 2011

iv McLean, C., Mills, G., Riesco, M., Meyer, M., Plachta, D., Hurlbert, E.; "Long Term Space Storage and Delivery of Cryogenic Propellants for Exploration", Joint Propulsion Conference, AIAA-2008-4853, Hartford, CT, July 2008

v Dye, S.A., Kopelove, A.B., Mills, G.L.; "Integrated and Load Responsive Multilayer Insulation", Advances in Cryogenic Engineering. AIP Conference Proceedings, Volume 1218, pp. 946-953, 2010

vi Feller, J.R., Plachta, D.W., Mills, G., and McLean, C.; "Demonstration of a Cryogenic Boil-Off Reduction System Employing an Actively Cooled Thermal Radiation Shield," in Cryocoolers 16, edited by S.D. Miller and R.G. Ross, Jr., International Cryocooler Conference, Inc., Boulder, CO, 2011, pp. 601-609

Active Control of Cryogenic Propellants in Space

W.U. Notardonato[1]

[1]*Cryogenics Test Laboratory, Kennedy Space Center*

ABSTRACT

A new era of space exploration is being planned. Exploration architectures under consideration require the long term storage of cryogenic propellants in space. This requires development of active control systems to mitigate the effect of heat leak. This work summarizes current state of the art, proposes operational design strategies and presents options for future architectures. Scaling and integration of active systems will be estimated. Ideal long range spacecraft systems will be proposed with Exploration architecture benefits considered.

1. INTRODUCTION

With the retirement of the Space Shuttle fleet and the cancellation of the Constellation program, a new era or human space exploration in the Unites States is dawning. But there is much uncertainty regarding the future direction of space exploration in the United States. This uncertainty is extensive and includes the role of the commercial enterprises in manned launches to low earth orbit (LEO), the near term destination of manned exploration, and the type and size the future space launch systems. However, it is certain that near-term human exploration beyond low earth orbit will require the use of cryogenic propellants, and that in-space cryogenic propellant storage durations will exceed our current capabilities by two or more orders of magnitude. This will require development and validation of a new suite of technologies, from large scale insulation systems to microgravity fluid control to active thermal control of cryogens for extended duration zero boil off. Cryogenic fluid management technology may enable deployment of orbital propellant depots, and these propellant depots may dramatically lower the cost of human exploration beyond LEO. This work will consider the current state of the art in cryogenic operation in space and will propose operational design principles to use as a guideline for developing space exploration architectures. These principles will be used to develop a reference propellant depot architecture. This is not an approved mission architecture that has been vetted by NASA and should be considered to be for discussion purpose only.

2. CRYOGENIC DEPOT DESIGN PRINCIPLES

The advantages of cryogenic propellant depots in space have been discussed since early in the space program (ref). Werhner Von Braun used in space refueling as a components of his famous human exploration of space articles in Colliers magazines in the 1950's. Most early concepts called for large orbiting complexes requiring multiple launches to assemble the depot in orbit, followed by multiple resupply missions to transport large quantities of cryogens to the orbital storage complex. Depot customers then rendezvous with the station and purchase propellants in whatever quantities needed. This architecture is analogous to a terrestrial gas station, where semi-permanent facilities are built to provide a range of refueling capabilities. The scale and complexity of these types of depots will probably prohibit their deployment for the near future, until launch costs are decreased significantly. Other smaller depot studies have been performed over the years. More recently, Kutter et al have been proposing a simpler depot concept that uses a single launch to provide refueling capability to a single dedicated mission.ref). The Augustine committee report (ref) identified in space refueling as a "significant potential benefit to the in-space transportation system beyond low-Earth orbit", and considers both models of depots as feasible. However, perceived complexity and launch costs have helped limited the development of propellant depots, and critical technology demonstrations for microgravity handling of cryogens must be achieved before these concepts will gain acceptance by NASA mission planners. NASA is currently planning a technology demonstration mission that will prove many of the systems needed for long duration cryogenic storage in LEO, including active and passive thermal control, propellant acquisition and gauging, and cryogenic transfer between storage vessels. This work is an attempt to look at an in-space consumable depot from a perspective of operability Key principles to consider during design are maintaining simplicity, commonality and reliability in the system, and maximum reusability of hardware when possible. Active control of the propellant so there are no consumable losses are achievable

2.1 Commonality

To keep spacecraft more simple and to reduce resupply requirements for long term, sustainable human exploration, future architectures should minimize the different number of fluids on board the spacecraft. Minimizing the number of different commodities, especially hazardous commodities, has been identified as a top priority for operability for spacecraft systems (ref). Using common fluids reduces the overall parts count of the spacecraft fluid systems, reducing mass and complexity. Fluid needs include propulsion, power and life support. Almost all consumable needs can be met by delivery of one single fluid, water. Water, plus its individual components of hydrogen and oxygen, can meet all the requirements of human exploration consumable supplies.

Propulsion - Liquid hydrogen and liquid oxygen are already in use for primary in space propulsion applications, and exhibit the highest performance of any practical chemical propellant combination. LOX/LH2 engines such as the RL-10 and J2-X are considered the likely choices for future exploration propulsion needs. Future advanced primary propulsion needs can also be met using hydrogen, as hydrogen can be used for nuclear thermal and solar electric propulsion as well. Additionally, spacecraft designers need to consider hydrogen and oxygen as ideal candidates for secondary propulsion as well. Hypergols are currently the first choice of designers due to their storability, reliability, and long history of successful use. But advances in active and passive thermal control will enable long

duration cryogenic storage, making these propellants essentially as "storable" in space as hypergols (which often requires heating as an active thermal control scheme for many mission profiles). Work is also ongoing at several companies to prove reliability of GOX/GH2 thrusters, and some units have demonstrated 10,000 successful ignition cycles. Use of common fluids for all propulsion needs will greatly simplify spacecraft design and operations.

Power – hydrogen and oxygen have been used as power reactants in fuel cell systems since the Gemini program. Fuel cell power will be needed to supplement solar power for future exploration missions, and regenerative fuel cell power is needed during nighttime at lunar bases. Fuel cells have a higher power density that batteries and will also be needed on rovers and other remote equipment. Until nuclear power and improved battery power is available, fuel cells will be part of the exploration architecture, and hydrogen and oxygen will be the necessary reactants. With the use of Proton Exchange Membrane fuel cells, ultra-high purity oxygen will not be needed, and propellant grade LOX and LH2 is sufficient.

Life support – Life support consumables include potable water for drinking, water for cleaning and bathing, cooling water for thermal control loops, and oxygen for atmospheric revitalization. In addition, water and oxygen are also needed in portable life support systems for extravehicular activities for heat rejection and breathing. Some gaseous nitrogen will be needed for atmospheric pressure control. Until fully closed loop life support systems can be developed, there will be a need for resupply of these critical commodities. Some estimates for total quantities of these consumables for lunar bases are substantial (ref) and an orbital consumable depots that supplies these consumables is needed.

Pressurization – Currently, gaseous helium is used as a pressurant for spacecraft propulsion tanks as well as pneumatics for various actuations. On the ground however, typical cryogenic operations use autogenous pressurization via vaporizers to provide necessary pressure for fluid transfer. Autogenous pressurization is used for pressurization of hydrogen tanks during operation, but helium is used for liquid oxygen tanks. However helium pressurization adds complexity, especially in reusable systems where multi-species mixtures may not be desirable.

2.2 Reusability

Another key operability principal is maximum reusability of assets in space. This will help minimize overall mission mass. A simple example of this concept is reusability of the upper stage propulsion system as an earth departure stage (EDS) after reservicing by in-space consumable stations. While there are still benefits to using an upper stage to deploy an empty EDS on orbit, and then filling the EDS using a consumable depot after the upper stage has been discarded, there is a considerably higher benefit to reusing the upper stage as an EDS after refueling. This allows for elimination of the dry mass of the EDS from the payload mass of the upper stage and maximizes the true payload mass to be delivered. This also simplifies the servicing of the cryogenic tanks, as reservicing a cold tank does not require chill down of large quantities of mass to cold temperatures like servicing a warm talk would.

Taking this concept to the limits of practicality, mass should be distributed in the system to the location where it can utilize the concept of reusability to its maximum extent. This means all systems necessary for operation of a depot should reside on the depot where practical. Active components of docking systems should be placed on the depot side of the interface so the spacecraft docking plates can be made simpler and less massive. If possible, active thermal control systems should remain with the depot as well, unless it is absolutely necessary to include them on the spacecraft.

2.3 Design for the Environment

Current cryogenic propulsion stages are loaded using fluid stored at or near the normal boiling point (NBP) on the ground. Prior to use, the fluid is subcooled by pressurizing with gaseous helium. This subcooling is necessary for operation of the engine turbomachinery, but does little to increase the storage density of the fluid. Over the years, there have been numerous proposals to use densified propellants, or propellants that are cooled to below their NBP temperature. The decrease in temperature is accompanied by an increase in fluid density, allowing for greater mass of propellant to be stored in a given volume. While densification will help increase the payload mass fraction, there are operational impacts associated with use on earth and there have been no known vehicles that have used both densified hydrogen and oxygen as propellants. However, in space propulsion stages experience different surroundings than Earth based stages, specifically the presence of vacuum. This begs the question, what is the normal boiling point of fluids in space? With no atmospheric backpressure to limit the venting, cryogens can be stored well below their "NBP" and storage at the triple point or below is achieveable. However there are engineering challenges associated with slush cryogens and the preferred state of normal storage is assumed to be saturated liquid at 16K for hydrogen and 65 K for oxygen. This storage condition increases the density of LH2 by 6% over NBP hydrogen, and 10% over the NBP of liquid oxygen. Vehicles that are intended to operate exclusively in space should be designed to take advantage of the unique space boundary conditions, and lowering the storage temperature to increase fluid density is a feasible method of minimizing spacecraft volumes and masses.

The surroundings of a cryogenic system in space is very different than on Earth.. The main difference is the presence of high vacuum, eliminating the need for a vacuum jacket. This also has an effect on the effective surroundings of the thermodynamic system. On earth, the surroundings generally are assumed to form a warm boundary temperature of 300K. However, proper design of outer insulation layers and their material properties have demonstrated that warm boundary temperatures of 220K are achievable in LEO (ref). This affects the cryogenic system in two ways. First, heat leak will be reduced as the temperature gradient across the insulation will be smaller. Second, the coefficient of performance of the refrigerator system will be increased. The corresponding decrease in cryocooler power will decrease the mass of the system, but the penalty is increased mass of the radiator due to the lower temperature. Table XX shows the effect of lowering the heat sink temperature on the COP of an ideal refrigeration system that has a source temperature of 20 K or 15 K. The secondary y-axis shows the mass trade.

2.4 Active Control of Propellants

The potential key to cryogenic fluid management in space is to maintain active control of the propellant. Active control means control of both the state of the cryogen (active thermal control) as well as the position of the fluid in the tank (active fluid control). In this work, the word control is taken to mean; "to exercise directing influence over, to have power over". Used in this context there is no such thing as passive thermal control and concepts for "reduced boil off" (RBO) using active thermal control is a misnomer. There is no effective control if all one can do is minimize the effect of heat leak, because the state of the propellant is being controlled by external forces, not the active or passive systems in the spacecraft. To have true control, one must be able to regulate or govern the state of the propellant, including decreasing the bulk fluid temperature or system pressure when desired. To have true active thermal control in these cases, the ratio of the provided refrigeration power to the vessel heat leak must be greater than 1.

$$\frac{Q_{ref}}{Q_{HL}} > 1$$

Active thermal control has been the topic of many thermal analysis exercises recently. In these cases, active thermal control is typically restricted near the point of zero boil off (ZBO), where refrigeration is provided to maintain the cryogen at steady state. Current NASA plans for in space cryogenic demonstrations with liquid oxygen are considering refrigeration ratios slightly higher than 1, to account for transient heating during ascent and to maintain some level of pressure control. Plans for LH2 are reduced boil off, where the refrigerator intercepts around 80% of the heat leak using a shield at an intermediate temperature. However, more than just zero boil off is possible with a focused effort to develop larger capacity staged refrigeration systems like the Claude cycles used in hydrogen liquefiers on Earth.

Active fluid control means the spacecraft has the ability to control the position of the fluid in the tank. Used in this context Propellant settling maneuvers is considered active fluid control. But a better example is a tank mixing pump with a spray bar, although it depends on a passive liquid acquisition device to provide liquid to the pump inlet. The pump with the discharge nozzles are capable of directing liquid to a desired location in order to achieve isothermal conditions desired for better thermal and pressure control. But with proper design, the pump mass flow can be used to help maintain liquid position as well. For example, a tangential velocity relative to the tank wall can create centrifugal forces to hold the liquid to the outer wall while vapor concentrates down the axis. Or diffusers can inject the liquid axially down the tank to accumulate at the liquid acquisition device. Active fluid control can use a mechanical phase separator system, especially in a liquefier system. Turbulators built into injectors may be able to separate the liquid or centrifugal pumps like the space shuttle humidity separators can be use. Finally, magnetic forces can be used, especially for LOX, to actively control the position of the fluid.

3. PROPOSED DEPOT ARCHITECTURE

Using the principles outlined above, a proposed depot architecture will now be presented. The depot is based on the concept of simplifying launch operations by launching water on an as needed basis to facility that can electrolyze the water and liquefy hydrogen and oxygen product for storage in the customers spacecraft propellant tanks. The facility also has the capability to supply pressurized oxygen and hydrogen gas as well as water to the customer. An Excel based model of the system thermodynamics has been developed and a schematic of the proposed system is shown in Figure 1.

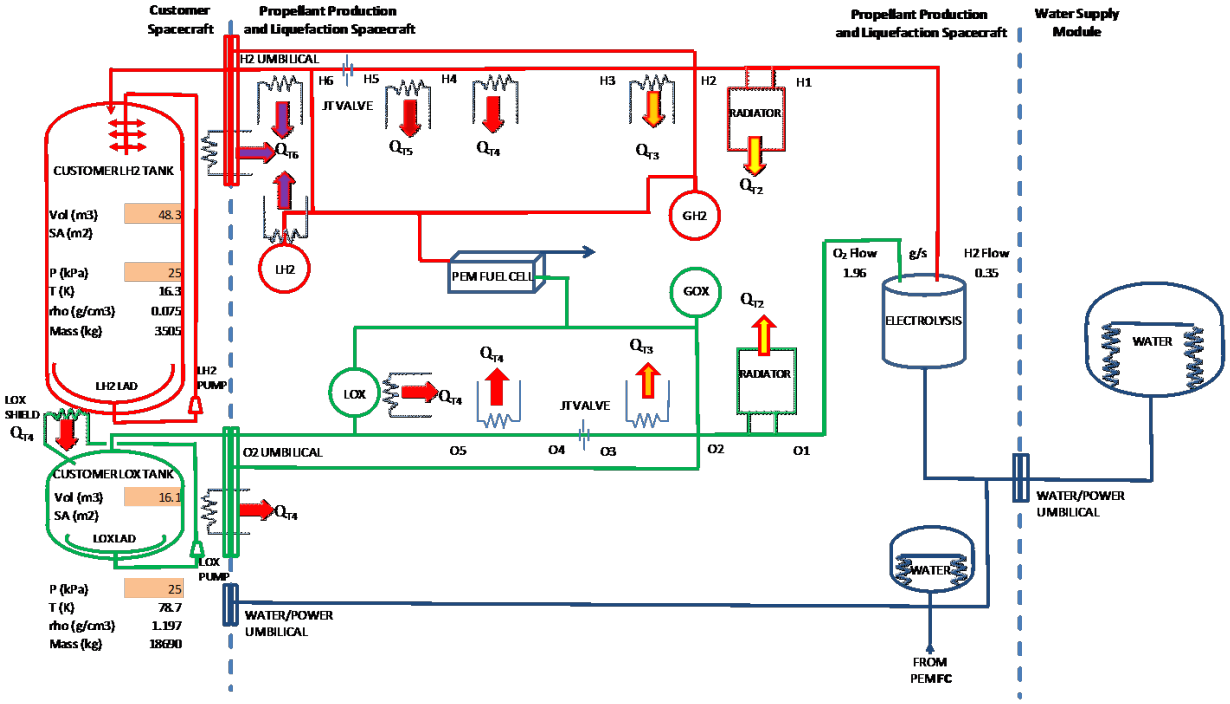

Figure 1. Fluid schematic of depot architecture

3.1 Water supply modules

The depot facility is only supplied with the feedstock of high purity water. This offers many advantages. Water storage is simple compared to a LOX and LH2. Water launch does not need a vacuum jacket or efficient insulation systems. Water is easier to store near thermal equilibrium, especially during ground and launch phases of operations. Water is a volumetrically efficient method of storing hydrogen and oxygen. INSERT QUANTIFIED DATA HERE. These factors lead to a much higher payload mass fraction for the resupply portions of the operations. This helps minimize the repetitive launch costs that form a large fraction of the depot cost structure, making the depot more attractive from a commercial standpoint. Launchs site will not require LH2 ground support equipment, and water is a simple payload to process.

The water supply modules should be as simple as possible. They can be mass produced for economy of scale. In order to maximize reusability and minimize single-use systems, all the active components for rendezvous and docking should reside on the depot side. The water supply module should have minimum capability for attitude control, communication, and power supply.

3.2 Depot Spacecraft

The depot spacecraft is the key component of the system. It is a multifunctional spacecraft that includes all command and control systems, propulsion for orbital maneuvering, attitude control, and docking operations, a remote manipulator system, power supply and distribution network, and thermal control systems. The depot spacecraft's primary purpose is to receive water from the WSM, electrolyze it at high pressure, and liquefy the oxygen and hydrogen output streams. The LOX and LH2 is then transferred to fill the empty storage tanks on the customer spacecraft. The depot has the capability to transfer liquid water, gaseous hydrogen and oxygen, and liquid hydrogen and oxygen. The depot also provides refrigeration to the customer spacecraft while they are docked. Further explanations of the key payload systems are provided next.

Water Electrolysis – Water is split into hydrogen and oxygen via the electrolysis process. The electrolysis system consists of the electrolysis stack, probably a proton exchange membrane system, the gaseous purification process to ensure the product is ready for liquefaction, and the associated fluids and electrical controls components. The process is well understood and the engineering is mature. There is an electrolyzer of the International Space Station (ISS) and has displayed good reliability. It is capable of producing x g/s of hydrogen and x g/s of oxygen and the specific power is roughly xx j/g. While this unit is too small for the depot purpose, the US Navy has extensive experience using larger electrolysis units for submarines. Several companies manufacture the units including Treadwell, Hamilton Sunstrand, and Giner with oxygen flow capacity greater than 2 g/s. Specific power ranges from 50 to 60 j/g. Another advantage of the US Navy electrolysis development is high output pressures can be achieved for minimal power increase. Oxygen pressures up to 20 MPa and hydrogen pressure up to 5.2 MPa have been demonstrated. This minimizes the liquefication energy required. However water electrolysis is still a very energy intensive process and drives the size of the spacecraft power systems. The system model that was created uses electrolysis efficiencies, flow capacity, and outlet pressures as input variables.

Power Generation - While future depot spacecraft will leverage off development of space based nuclear power, the initial models will need to rely on solar power. Due to the large amount of energy required by the electrolysis and liquefaction/refrigeration system, very large solar arrays will be needed. The model estimates maximum power required by considering total LH2 and LO2 produced and liquefied over a range of possible time durations. The estimated solar array area and mass are calculated using parametric relations (ref). The power generation system includes the main solar arrays and solar tracking components, power conditioning and distribution units, and a regenerative fuel cell that provides backup power during periods of eclipse or other off nominal operations. Similar to the ISS solar array wings, needs multiple arms each of the depot solar arms are 34 m long by 12 m wide, and are capable of generating nearly 32.8 kW of DC power. Total System mass is 4400 kg.

Active Thermal Control - Refrigerator – There are many possible cycles that can be used to liquefy the gaseous product from the electrolyzer. The spacecraft model considers two main alternatives to liquefaction. The first is a closed cycle Brayton refrigeration system that is designed to remove heat from the product stream in a series of stages, finalizing in a cold stage temperature a few degrees colder than the desired storage temperature. This is the type of system shown in Figure 1. Following the hydrogen product stream out of the electrolysis unit, the hydrogen is first precooled in a radiator passively to a desired temperature. Next, a series of heat exchangers further pre-cools the gas using a multi-stage Brayton refrigerator. This refrigerator also cools the oxygen stream using the same temperature expansion stages. After the hydrogen is cooled to below 40K, a Joule-Thompson (JT) valve expands the gas isenthalpically into a two phase fluid. The refrigerator then provides the additional cooling necessary to liquefy the remaining saturated vapor prior to being delivered to the customer spacecraft in an expanded metal foam condensing heat exchanger. The depot provides refrigeration to the spacecraft customer for full propellant conditioning for the duration the two are docked. This allows all the necessary refrigeration equipment to remain on the depot to be continuously reused, and no cryocoolers will be necessary for individual customer spacecraft.

The system model uses input variables for mass flow rate, inlet pressure, and refrigeration efficiency. Thermodynamic state variables are calculated for a series of processes. Optimum radiator temperatures are calculated based on mass trades against the refrigerator power mass. The heat exchangers are modeled as an isobaric process with ideal heat exchanger. This gives the refrigeration capacity required at each stage. An isenthalpic expansion reduces the propellant pressure to just above the desired storage pressure. The refrigeration required to remove the remaining latent heat is added to the refrigeration required to remove all system parasitic to find the final capacity at the storage temperature. Once all the refrigeration heat sources are added together, taking into account each stages coefficient of performance and the overall cycle efficiency, a required input power can be estimated. Individual stage temperatures are then optimized for minimum input power for given hydrogen storage temperature, radiator

temperature, and gas pressure. The temperature of the fourth thermal station (around LOX temperatures) is then set by this refrigeration efficiency analysis, which dictates the LOX storage temperature. Figure 2 below displays the system model output for a representative mission.

	T	P	rho	h	s	Qliq	Qhl	CoP	Power
	K	kPa	g/cm3	J/g	J/g-K	W	W		W
O1	300	5050	0.07	261.0	5.365				
O2	240	5050	0.09	199.2	5.134	65			
O3	138.4	5050	0.86	-42.3	3.699	253		0.86	1073
O4	78.7	25	0.00	-42.3	5.552				
O5	78.7	25	1.20	-152.6	5.552	115	144	0.36	2654
								O2 TOTAL	3727
H1	300	5050	0.004	4226	48.566				
H2	240	5050	0.005	3366	45.368	161			
H3	138.4	5050	0.009	1950	37.738	264		0.86	1123
H4	78.7	5050	0.016	1038	29.003	170		0.36	1742
H5	36.5	5050	0.058	13	9.849	191		0.14	5025
H6	16.3	25	0.075	13	0.374				
H7	16.3	25	0.075	-316	0.374	62	38	0.06	6284
	H2 flow	0.19	g/s			efficiency	0.275	H2 TOTAL	14174
	O2 flow	1.05	g/s					TOTAL	17901

Figure 2) Refrigeration Capacity at Temperature and Required Input Power

Active thermal control - Liquefier – Instead of using a closed-cycle refrigeration system to liquefy the gas, a more conventiaonal open cycle liquefier can be employed Figure xx shows a rough schematic of one such system. In this case, product gas is provided from the electrolyzer ate high pressure as a make-up gas to the cycle. The oxygen is liquefied using a relatively simple Linde-Hampson cycle, pre-cooled by the radiator to below 250K. After the final expansion stage, two phase fluid is sent to the storage tank, either on board the depot or on the customer spacecraft. For liquid oxygen, phase separation is achieved using a magnetic settling system, and the return vapor is sent to the liquefier compressor to complete the cycle. The liquid hydrogen follows a similar cycle, being precooled first by a radiator and then by the oxygen cycle, prior to several stages of expansion itself. Again, the two phase fluid is separated in the storage tank, this time using either liquid acquisition devices or an active centrifugal separator. A recuperative heat exchanger is used to recover any latent heat of vaporization present in the return vapor stream in the event some small amount of liquid enters the return line.

Storage and distribution – The storage and distribution system includes all the components necessary to control the position of the fluid in the system, including lines, valves, instrumentation, and storage. The primary storage tanks are the customers tanks, still cold from the orbital insertion phase of their mission but drained to their residual point. When A customer is not docked at the depot, there is secondary storage on board the depot to allow the refrigeration system to maintain operations, to provide for H2/Os2 storage for depot systems such as OMS/RCS, and to provide energy storage for the fuel cells. The depot has both GH2/GO2 and LH2/LO2 storage, as well as water.

Umbilicals- The active components of the docking systems reside on the depot sides of the interfaces. The depot has a simple umbilical interface with the WSM, with water and power disconnects only. Heaters serve as active thermal control to keep the water above freezing. The mating capture and alignment is performed by a remote manipualor arm on the depot, while actuation force for the umbilical plate is supplied by the active mechanism on the depot side.

Propulsion – The depot has the capability for orbital maneuvering and reaction control. The customer spacecraft will have the responsibility to attain a nearby orbit and the depot will have the responsibility to perform the necessary maneuvers to bring the three spacecraft together. Both the OMS engines and the RCS thrusters use hydrogen and oxygen as propellants. The OMS engines may use liquid similar to a scaled version of the RL-10 and the RCS thrusters will probably use gas.

Thermal Insulation systems – The depot spacecraft will use an integrated thermal insulation system designed to minimize parasitic loads on the refrigerator. The depot will use a heat stationing approach where warm components are located together at one end of the spacecraft and the progressively colder stages are positioned to take maximum advantage of the shielding (and active cooling) of the higher temperature stations. All penetrations between stations will use low conductivity supports and feedthrus where possible. Deployed solar shields may be used to protect against radiation, or the large solar arrays can be designed to fill that role. Since the depot is launched dry and refrigeration is not activated until orbital insertion, there is no need for hybrid insulation to protect systems during ground processing or ascent phases of the mission. The spacecraft design should be optimized for use only at its intended location, in LEO. Since the capacity of the active thermal control system is many times larger than the typical parasitic heat leak of the depot stage, there are no attitude constraints on the spacecraft thermal system when the depot is not in liquefaction mode.

3.3 Customer Spacecraft

A number of different customers could use such a depot. A typical customer is a refueling of an upper stage to serve as an earth departure stage for lunar or planetary missions. In this case, the upper stage arrives with propellant tanks near empty but still cold. The depot initiates the docking and connection of umbilicals and then starts filling the customer tanks. All customers will be required to have standard umbilical interfaces for water, gaseous oxygen and gaseous hydrogen, and liquid oxygen and liquid hydrogen transfer

The exact umbilical connection will change depending on the type of liquefier used in the depot. Refrigeration is provided in a separate umbilical if that thermal control scheme is used. The customer will have to integrate refueling specific hardware in its systems, such as spray bars, mixing pumps, enhanced insulation, and thermal shields. The depot controls the attitude of the system while docked to maintain maximum solar power.
The functions of these individual spacecraft and their associated systems will now be demonstrated in a consideration of a typical mission concept of operations.

4. CONCEPT OF OPERATIONS

To demonstrate the capability of this depot architecture, a representative concept of operations will be presented. This will include the initial depot launch and activation, a nominal water resupply, and servicing of a projected customer. A centaur refueling for an interplanetary science mission is the customer.

First, the depot spacecraft will be launched to the designated orbit by a launch vehicle. The depot is a payload that is launched with minimal consumable mass on board, just enough to pass a functional checkout and enter stable operational mode on orbit. The depot water tank is filled to 10% with water. The depot water tanks are pressurized with gaseous nitrogen using a bellows like bladder similar to the space shuttle water tanks. The depot GOX and GH2 tanks are pressurized to maximum allowable working pressure to provide propellant for the OMS/RCS systems, as well as back-up power reactants to the regenerative fuel cell system. The LH2 and LOX tanks are filled to a minimal level necessary to start the system on orbit. The spacecraft is launched powered down, and is activated upon being delivered to the intended orbit. Once in orbit, the spacecraft is powered up by starting the PEM fuel cell, with the product water being sent to the depot water tank. The depot then establishes communication and control with the ground stations and the OMS/RCS system is checked out. Next, the solar arrays are deployed to the correct orientation. After full power is available the propellant production and liquefaction system can be activated.

To activate the PPLS, The refrigerator is started and allowed to chill down. Chill down of the H2 and O2 transfer system can be helped by liquid in the storage tanks. Water from the depot water tank is then sent to the electrolyzer, and the electrolysis system produces hydrogen and oxygen at a pressure of 5000 kPa. This charges the high pressure line and the cold, high pressure gas is expanded and liquefied in the condensing heat exchanger. The system is now in stable operational mode with power produced by the fuel cell used to run the electrolyzer. The solar arrays provide the power for refrigeration for liquefaction plus maintaining thermal equilibrium, as well as make up power for the electrolysis/fuel cell cycle and spacecraft operations. The depot is now ready to receive water.

The concept of operations is simple for the water launch. A water supply module is launched using an expandable launch vehicle and sent to an orbit near the depot. The WSM processing is very simple and payload is very mass and volumetrically efficient. The WSM has the capability for 1 week in orbit prior to rendezvous with the depot. One the depot acquires the WSM, the water umbilical is mated and large scale propellant production and liquefaction is ready to start.

The customer spacecraft then arrives. A range of possible refueling options exist but consider the upper stage arrives near empty but cold. The customer is required to rendezvous within xx delta V of the depot and then the depot actively mates with the customer spacecraft. In the event of refrigerator active thermal control the cooling service is connected and chilled down. Then the spacecraft mixing pump is activated, establishing steady operation with the refrigerator. The liquid supply ports are then opened, routing the propellant from the depot cycle to the customer tanks. The two spacecraft remain together until the desired amount of propellants is transferred. This is period could last six months or more, depending on the depot power level and the customer tank size.

	LH2		LOX
Vehicle volume	10210.4	gal	3411.2
	38.7	m3	12.9
Bulk Storage temp	-430.9	F	-342.7
	16	K	65
Storage Pressure	3.5	psi	3.5
	24	kPa	24
Storage Density	0.075119	g/cm3	1.259715
	75.12	kg/m3	1259.72
Storage Mass	2903	kg	16266
	0.151	%	0.849
Liquefaction time	180	days	180
Liquefaction rate	57	GPD	19
	16	kg/day	90
	0.186688	g/s	1.045939
Ideal energy of Liq	12019	kJ/kg	635.6
Efficiency	0.275		0.275
Liquefaction power	11.2	kW	2.4
Refrigeration power	14	kW	4
Electrolysis energy	50	kW-hr/kg	
Electrolysis power	34	kW	
Total Power Input	52		

5. SUMMARY

A summary of operability principles is used to develop a reference concept architecture for a propellant depot in low earth orbit. The architecture is based on large scale active control of the propellants similar to hydrogen production and liquefaction plants on earth. Components include water supply modules, a depot spacecraft with solar power, a electrolysis and fuel cell cycle, refrigeration/liquefaction system, and storage and transfer systems, and a variety of customer spacecraft including earth departure stages, orbital transfer vehicles, and manned spacecraft. First order system size and mass estimates for the depot are analyzed. A concept of operations is included.

4 REFERENCES

[1] William U. Notardonato, Wesley L. Johnson, et al., Experimental Results of Integrated Refrigeration and Storage System Testing, in: Advances in Cryogenic Engineering, American Institute of Physics, Melville, NY, 2009, pp. 1369-1376.

[2] William U. Notardonato, Wesley L. Johnson, et al.,Integrated Refrigeration and Storage System - Heat Exchanger Characterization, Final Report, NASA, Kennedy Space

"Spread Your Wings, It is Time to Fly". NASA. July 26, 2006. http://www.nasa.gov/mission_pages/station/behindscenes/truss_segment.html. Retrieved September 21, 2006

^ a b HSF Final Report: Seeking a Human Spaceflight Program Worthy of a Great Nation, October 2009, *Review of U.S. Human Spaceflight Plans Committee*, p. 65-66.

The evolution of oxygen generation in US Navy Summarines; Breifing by Rich Hagar; NAVSEA Technical authority

Application of Cryogenic H2 storage to low-altitude electric powered VTOL-PAV

L.J. Skriba[1]
[1]Gigmedia Consulting,(1) L.J. Skriba owner

ABSTRACT:

Fundamental properties of cryogenic materials and system's performance developed for unique deep space exploration have direct application to 21st century electric powered aircraft. Key to both are: reliability, ultra-light-weight, low power consumption, and solar energy input. For "inner-space" we can add the generation, storage and use of refrigerated H2 as an essential energy carrier. H2's low gravimetric density makes it a perfect energy source for potentially massive numbers of ultra-light electric powered personal vehicles (PAVs). As has been the case for all H2 applications, gas storage has been the central challenge. Given a new mission, a new/radical aircraft architecture, potential high production volumes and recent breakthroughs in material science, hydrogen and Cryogenics will be found in wide spread consumer use this century. We here define the broad and unique architecture of a total aircraft system likely to evolve due to a world-wide energy and transportation crisis forecast for this century. Initial experimental focus by aviation pioneers has been on solar photo-voltaic energy conversion mounted on the wings of ultra-light experimental craft and high temperature super-conducting materials for possible commercial "jet" aircraft electric motor/generators. Rather, we here define the system parameters of a VTOL flight regime that can be practical and popular within 20 years. Major research needs are defined in terms of materials, construction methods, and the unprecedented level of system integration that will be needed. Specific attention is given to the Cryo technique for a closed nitrogen refrigeration circuit that safely stores 2 to 10 gigajoules of H2.

Louis J. Skriba
188 E. Bluewater Ln.
Vernon Hills, Illinois, 60061-1220
director@gigmedia.com
224-772-7559

KEYWORDS:
hydrogen, VTOL, fuel-cell, Cryo-refrigeration, electric-powered-flight.

1.1 INTRODUCTION

1.1.1 Under ideal conditions, major scientific breakthroughs lead to publications that permit engineers to identify practical applications with identifiable markets. We are no longer living under ideal conditions for major innovations for space cryogenics. Public/political priorities, that certainly should be supportive, are now obviously internationalized and widely diverse, if not out-rightly antagonistic. R&D objectives, beyond our long standing: (man-in-space) space station, and (deep-space science) planetary exploration, are not yet well established or securely funded. It is time for a new approach, perhaps to bring advanced "space" Cryo engineering technologies back down closer to earth.

1.2 RESEARCH OBJECTIVES

1.2.1 We here define an entirely new research objective for "inner space" (within the atmosphere and below commercial air traffic) so demanding that only the most advanced Space-Cryogenic refrigeration and gas storage technologies are candidates for a potential successful outcome. With the help of NASA researchers, DOE scientists, major corporate engineers, and university educators, we have been able to define a new aircraft paradigm that is based on hydrogen as the essential energy carrier. Politically, our craft is to do what the DOE's "freedom car" has failed to do: To liberate the world's needs for "transportation" from its history of near absolute dependence on the productivity and total system efficiencies of petroleum based fuels. Scientifically, we have identified a new field of application oriented research, namely: "ULTRA-LIGHT CRYOGENICS"

1.2.2 It is practical to assume that for the intermediate future of inter-city and inter-continental passenger travel, as well as FedEx type air-freight traffic, the best approach will continue to be: large, high-speed, petroleum-fueled, jet-powered commercial aircraft built using well established Airbus and Boeing type designs. However, given the increasing scarcity of petroleum at cheap prices, the world's relentless population growth in previously non-technical nations, and the economic/financial uncertainties of the international credit markets, the long range future of this approach to "flight" is no longer attractive.

1.2.3 Certainly, out of the history of Cryo-engineered superconductivity, radically light designs of electric generators and motors might permit the development of electric powered jet engines powerful enough for these heavy commercial craft, sometime this century. However, if hydrogen were to be the fuel in such aircraft, the problem of its unbelievable low density creates insurmountable problems for storage of great volumetric amounts of fuel. Hence, Gigmedia Consulting postulates that, if hydrogen is to fly in anything other than uniquely massive deep-space launch vehicles, the craft has to be pre-emptively designed using unique structures centered first on viable hydrogen storage over any other criteria. It is this hydrogen fuel storage centricity that has led us to propose the following new craft and its even newer mission.

2.1 VEHICLE MISSION STATEMENT:
TO LIFT OFF VERTICALLY ON ELECTRICITY GENERATED FROM HYDROGEN

2.1.1 "Flight" may finally have an opportunity to be redefined as a serious option for small, slow, low-altitude craft powered by electric motors. In that window of opportunity, the most exciting option would be a craft that is simultaneously: ultra-light, super quiet, and capable of vertical take-off. The best example of that has been the recent work of Dr. Mark D. Moore (2), NASA (Langley) and his approach to Personal Aircraft Vehicles (PAVs) powered by ultra-light electric motors for single passenger flight. His approach's success, however, depends on powerful, small, light, and inexpensive batteries. There is hope for his success, since such batteries are needed if we are to have electric powered automobiles.

2.1.2 However, the major result of DOE's massive research, on the storage subsystems for fuel-cells running on hydrogen, is their documentation that the core problem is the combination of size, weight, cost, reliability and safety of the storage tank options thus far proposed. Worse was their identifying the massive costs needed to make and distribute industrially supplied hydrogen safely to "gas-stations." The same would also apply to conventionally designed aircraft fueled by hydrogen, (this was also concluded by Lockheed Martin's brilliant designer Kelly Johnson; aka "skunk works," trying to build CIA's cold war supersonic spy planes).

2.1.3 A graphical representation of Gigmedia Consulting's proposed VTOL craft is presented here to help as a visual reference for the remaining discussions. Comprehensive description of the vehicle's features is beyond the scope of this article. Currently this work-in-progress draft image is identified as "Holy Grail v0.2".

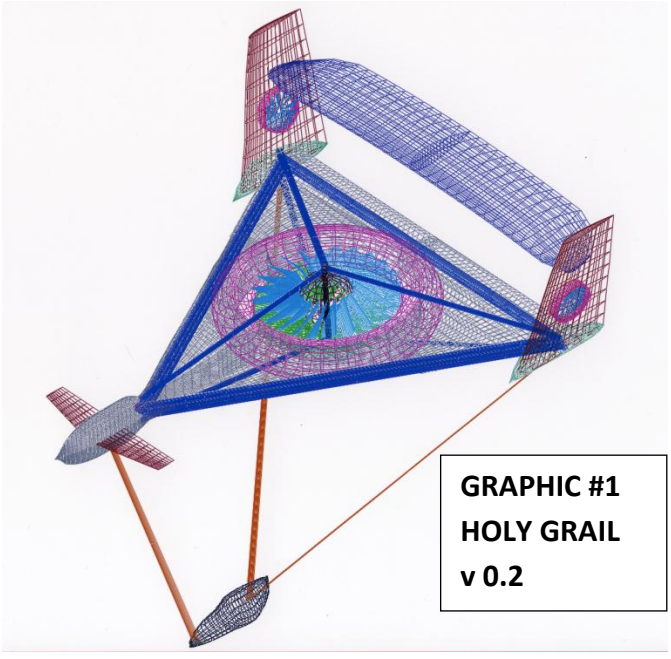

3.1 HYDROGEN STORAGE METHODS

3.1.1 Our preliminary feasibility study (limitedly available upon request) has determined that hydrogen-fueled, electric-powered VTOLs do NOT have to be small, but ALL components must be ultra-light including Cryo-refrigerators, heat-exchangers, insulation materials, etc. Unobvious is the idea that the hydrogen does NOT have to be supplied and stored as a -20K liquid, and that the gas can rather be stored at liquid nitrogen temperatures, under modest pressures, by using absorber materials similar to activated carbon. This work was proposed and patented by Dr. J. A. Schwartz (3) at Syracuse University in 1988 during our first "petroleum" energy crisis due to international politics rather than climate changes.

3.1.2 However, it is further unobvious to those skilled in the Cryo-arts, even using Dr. Schwartz's "metal assisted" principles, that, for our unique VTOL craft, the costs of supplying hydrogen have to ALSO be integrally solved. The most efficient and economical approach is to use the very specialized aerodynamic structures that are used to provide highly efficient VTOL lift to ALSO be the very means to intercept "free" (wind) energy to power hydrogen generating electrolyzers, compressors and Cryo-coolers.

3.1.3 This innovative approach in turn demands a studious effort at integrating various functions into single devices and various separate devices into a single ultra-light structure. This "outside the box" approach requires a "start from scratch" blank-page for the design of the aircraft's mechanical structures (and common materials) which can be both: generators and motors; electrolyzers and fuel cells; airframe structures and storage tanks; chemical process controls and aerodynamic flight controls. It is only by this absolutely essential effort at extremely integrated design that this craft can be built as a VTOL vehicle light enough to be powered electrically. The overall challenge of this earth bound craft is certainly equal to the design of a lunar habitat for astronauts. Indeed, NASA's previous Cryo fuel research for THAT mission can contribute handsomely to that which is necessary for an ultra-light (400 kilogram) aircraft to fly at 1,000 meter altitudes and 100 Kmph speeds, piloted by brilliant autonomous computer control.

3.2 UNCONVENTIONAL ENERGY STORAGE THEORY AND DESIGN PHILOSOPHY

3.2.1 Specifically, previously proposed moon based energy systems, using fuel cells for heat and electricity, created the demand for reversible catalytic chemical pathways that permit solar energy input to electrolyze locally discovered water, and subsequently permit consumption of generated/stored hydrogen and oxygen to again provide on-demand electrical power (in the absence of strong sunlight) and conserve the resulting water and oxygen for human biological needs. Properly selected catalysts (apparently originally proposed as variations of noble metal amalgams) were researched by NASA for an electrolyzer/fuel-cell unit that could be compatible with the ultra-low weight structural requirements needed to be supplied from the earth by rocket. Given the logic that not many moon based units would be required, that the highest "efficiencies" of every electro-chemical step is an absolute necessity, and that the costs of development could be expensed without limitations, such previous work might need to be re-evaluated. Our proposed craft, on the other hand, someday will be made in the millions of units/year, necessarily at materials and labor costs competitive to automobile manufacture, and used by untalented owners who would be expected to supply regular maintenance as we now do with tires, oil filters, and windshield wipers.

4.1 APPROACH TO SYSTEM RELIABILITY: CHEAP TO REPLACE FREQUENTLY

4.1.1 Specifically, the needed electro-chemical catalysts (and their supporting PEMs/conductors) cannot be based exclusively on precious metals for reasons of their safety and long range higher efficiencies. In our case, efficiency (in most system performances) is not the overwhelming important driving criteria. The key feature must be, in ALL cases, the lowest conceivable cost. As an example, we are considering variations of catalysts that could be made via electroplated/chemical-vapor-depositions of nickel/chrome type amalgams. Even more cost effective could be the fabrication of the PEM electrolyte membranes in situ rather than as a Nafion membrane separately purchased from conventional suppliers. All this should be attractive from the point of view of manufacturing costs, even if obviously or slightly less efficient electrochemically.

4.1.2 Totally unacceptable for a moon base, but essential to our design of an "inner"-spacecraft is our approach that makes the fuel-cell structure an easily removable/serviceable component. Those skilled in the electrochemical arts, working on fuel cells for vehicles, understand fully the difficult MTBF limitations due to catalyst migrations, poisonings, membrane short circuits, etc. 10,000hr MTBF may have been the Holy Grail for the "Freedom Car". In our case, given the proper design of this essential sub-system as an inexpensive replaceable element, we have the freedom to use materials and techniques previously researched and rejected from deep space travel consideration. It is time to do some NASA and DOE/NREL data-mining.

4.1.3 The same approach to "integration" must be directed at the needed electric motors/generators. Electric powered human flight has very recently become a reality as an outgrowth of brushless DC electric motors designed to be light enough for model aircraft hobbies. With Lithium battery designs resulting from the growth of consumer markets for cell phones and laptop computers, a few minutes of General Aviation flight time are now possible by intermittently powering an aircraft designed much like a sailplane. Our feasibility study suggests that batteries will never be the final solution for electric flight.

4.1.4 The reliability of existing brushless DC motors capable of continuous 1 to 5 horsepower per pound, is certainly not up to NASA deep space performance criteria, but their failure modes are most likely related to thermal management design issues. Hence, a motor-generator that is appropriate for manned VTOL power levels cannot be a separate, point-load device, remotely manufactured by a supplier and installed. Rather, for what are essentially thermal management reasons, the magnets, wires, and their locations, must be designed by appropriate aerospace engineers who are more concerned about total trust and aerodynamic drag at almost zero weight. As Burt Rutan was once heard to say, regarding the design of winning ultra-light craft, "if you throw it (construction material candidate) up into the air, and it comes back down, it's too heavy!"

5.1 DISCUSSION OF THE DESIGN APPROACH AND DISCOVERIES

5.1.1 To move energy to/from the fuel-cells/electrolyzers (multiple, for reasons of failure avoidance) and motors/generators, long lengths of large diameter copper cables are not an option. Nor are multiple AC/DC to DC/AC power conditioning devices to deal with variable device load demands and efficient distribution. New structural materials for such components, chosen for their ultra-light weight per gigajoule must be an integral part of airframe design. An aircraft is a wind machine, and hence all "process" cooling issues must be made in the context of where the air is and how fast it is passing a hot component. For our design, we believe that the only possible solution has been to propose a ducted fan turbine that has an integrated generator/electrolyzer-AKA-fuel-cell/motor built into the fan's aerodynamic blade structures. Such a device has never before been needed. It is essential for successful hydrogen fueled VTOLs.

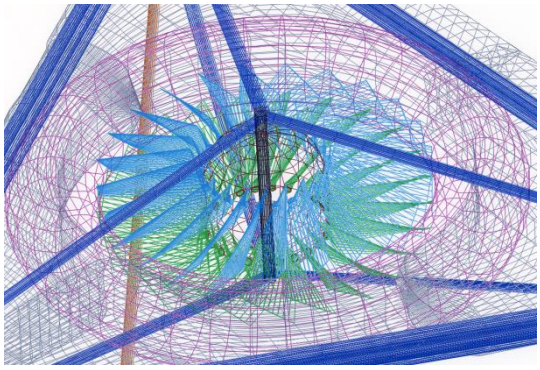

GRAPHIC # 2
INTEGRATED
DUCTED LIFT FAN

5.1.2 An ultra-light electrochemical process to do what fuel cells did for space-applications and potential terrestrial transportation would be impossible for VTOL flight if all the classical support plumbing and gas/water flow controls of existing technology are employed for reasons of their added weight. Rather, a totally integrated design must avoid the building of high pressure multi-layered fuel cell stacks that generate high voltages. Worse would be to again recondition high voltages in yet other motor speed control supporting devices. In our case, control of motor speed must be done via digital electronic control of gas flows (ultimately from storage), using miniature computer sub-processors communicating to a network of similar processors. All this must be done to replace pounds of weight with "bits" of RF signals. That is, this craft must exploit the massive processing power per microgram of devices the size of cellphones to automatically/programmatically deal with hydrogen and its generation, storage and use.

5.1.3 As for our novel approach to hydrogen storage, past DOE research has focused on the "weight percent" performance criteria of storage tanks. This originally flowed from the use of metal hydrides that simply weighted too much to store a few kilos/gigajoules of hydrogen for a passenger car. Most DOE solutions tried to develop ultra-light "nanocarbon" materials that could temporarily absorb hydrogen. But their total volumes were considered too big to be the petroleum gas-tank replacement. Other research focused on using graphite fiber composite pressure tanks, with metal (aluminum) liners, to hold the gas at

10,000 PSI. Even though the volumes of such tanks were almost acceptable, the weight, cost and shape of such tanking were not attractive to automobile designers. Hence the "weight-percent" issue asked: "what percent of the 'tank's' total weight is to be that of usable hydrogen?" The typical answer from this DOE history of excellent research has always been: "not enough." The right answer will cost more in future R&D.

5.2 MULTIFUNCTIONAL TANKING, THE SOLUTION TO "HYDROGEN WEIGHT PERCENT"

5.2.1 We have solved that "weight percent" problem simply by a design approach that could never be used in terrestrial vehicles but is common in aircraft design. The wing of a 747 is NOT just a lifting-force appendage, but it is also the housing for weighty fuel that is close to the consuming jet engines as well as close to critical aerodynamic lifting structures (flaps) for fully loaded take-off conditions. "Wings" must also be strong enough to carry and survive landing gear operation. Such total system design integration issues, controlled by the aerodynamicists, have long been part of NASA spacecraft development history.

5.2.2 Our approach to a VTOL craft's design assumes that the major structural components needed to withstand air pressures created by 100 Kmph flight must also be designed to contain from 1 to 10 gigajoules of hydrogen on a very large surface area of a cooled-absorber material. Even more demanding, the flow control of hydrogen to/from storage, in our unique case, is asymmetric… The hydrogen is slowly generated and cooled to liquid nitrogen temperatures, but, upon use, to power a VTOL launch, flow rates to the fuel cells have to be rather high for short periods of time. The "Freedom Car" had the opposite problem. Their tanks had to be filled in minutes at a "gas-filling-station" and the gas had to be stored and/or used for MANY days between refills. This is the challenge we believe can be easily resolved. How the hydrogen is to be cooled to practical physi-sorption temperatures, is dramatically different than the methods used to feed the gas into fuel-cell driven electric motors. Little of this seems to be obvious.

6.1 CONCLUSIONS FOR CRYO-HYDROGEN ENGINEERING DESIGN OBJECTIVES

6.1.1 For those skilled in the art of Cryo refrigeration at liquid nitrogen temperatures, the challenges to cool up to 10 gigajoules of H2 are serious if total system weight must be near zero. We address this aspect as an issue for the aircraft's design rather than as sub-component electrical efficiency optimization. Since we generate hydrogen via the collection of "FREE ENERGY", environmental energy (wind/solar), store it ONLY on this very same craft, and use it primarily for occasional, and brief vertical flight, we therefore potentially have an excess of hydrogen at our disposal.

6.1.2 First, we use hydrogen also to fill lifting bladders to reduce the craft's weight that a lift-fan thruster must deal with. The upper airfoil of this two-body craft has ever-so-slight positive buoyancy due to available and inevitable H2 boil-off from its cold storage condition. Also, it can be assumed that hydrogen can be used as an in-craft, super-light-weight energy "carrier" (vs. heavy copper conductive wires) to supply the energy for the pumping forces that could drive pulse tube refrigeration techniques. We have to deal only with a closed system to re-liquefy nitrogen at a rather slow cool down rate once the entire system is brought up to pressure and down to operating temperatures before launch. Exactly how this is best done is certainly an opportunity for future research. Today, we believe we already have viable approaches.

6.1.3 With all of the above as background, we have identified many opportunities for research, innovation and invention. The required application background (re this VTOL craft's needs for H2 storage) is:

1) Upper body delta-shaped airfoil Blended-Wing-Body span ranges: from 10 to 20 meters.
2) Upper body airfoil total dry weight: maximum 200 kilos (which includes storage tank structures)
3) Upper body located ducted turbine-generator power range: from 50 to 100 kilowatts
   (weight of the integrated motor/generator unit: 20 kilos…included in total upper body weight)
4) Turbine fan blades (with integrated PEM membranes) weight: 30 kilos (included in upper total)
5) Long term hydrogen storage capacity: 5 to 10 gigajoules. (Initially 1-3 gigajoules acceptable)
6) Cost: initial demo= $10-50 million, First production unit= $1 million, future= under $100K.

6.1.4 Other specifications regarding the craft's design are to be published by Gigmedia Consulting in the 2011 Spokane conference proceedings of the CEC.

6.1.5 Examples of needed research opportunities are:
1) composite aircraft structural methods/materials for Cryo-cooled pressure tanks used for H2 storage
2) ultra-light weight methods to power an electric VTOL aircraft
3) methods to generate hydrogen using inexpensive catalysts
4) micro-miniature computerized methods to wirelessly control all aircraft electrochemical subsystems
5) methods to rapidly extract hydrogen from cold storage (in the liquid nitrogen range…70K-100K)
6) extremely-light PEM electrolyzer/fuel-cell structures
7) techniques to control and eliminate hydrogen gas leakage
8) ultra-light "motors" for pulse-tube Cryo-re-refrigeration of nitrogen
(more opportunities available upon request)

REFERENCES

(1) www.Gigmedia.com

(2) Mark Moore PAV http://www.nasa.gov/topics/technology/features/puffin.html

(3) J.A. Schwartz US Patent # 4716736, 1988

Dielectric Studies of a Novel High Pressure Helium Gas Cooled DC Power Cable

H. Rodrigo[1], F. Salmhofer[1], D.S. Kwag[1], S. Pamidi[1], L. Graber[1], D.G. Crook[1], S.L. Ranner[1], S.J. Dale[1], and D. Knoll[2]

Corresponding Author:
Dr. Horatio Rodrigo[1],
Phone: (850)645-1714
Fax: (850)644-7456
Email: Rodrigo@caps.fsu.edu

[1]Center for Advanced Power Systems, Florida State University
2000 Levy Avenue, Tallahassee, Florida 32310

[2]Southwire Company
One Southwire Drive, Carrollton, Georgia 30119

Abstract:

High-temperature superconductors (HTS) allow power cables of substantially higher current density than conventional copper or aluminum cables. This is important for applications where a low mass and a low volume are critical such as naval, aeronautical and space applications. The novel type of cable under consideration is cooled by gaseous Helium at elevated pressure. Helium is known for having poor electric breakdown strength; therefore the dielectric capabilities of this type of cable must be tested under conditions similar to the envisaged operation. In order to study the dielectric performance we have designed and built a novel high pressure cryostat rated at 2.17 MPa which has been used for testing model cables of lengths of up to 1 m. The cryostat is an open system where the gas is not re-circulated. This allows maintaining a high purity of the gas. The target temperature range is between 40 K and 70 K. This substantially increases the critical current density of the HTS compared to 77 K, which is the typical temperature of cables cooled by liquid Nitrogen. The cryostat presented allows for adjusting the temperature and keeping it constant for the time necessary to run a complete dielectric characterization test. We give a detailed description of the cryostat. Measurements of partial discharge inception voltages as well as the temperature distribution along the model cables as a function of time are presented.

Cryogenics, Superconductor, Medium Voltage, Helium, Dielectrics

1 Introduction

Terrestrial systems for transmission and distribution of electrical power are dominated by conductors made of copper or aluminum. Such conductors have limited capabilities regarding maximum current density, typically around 0.5 A/mm^2 to 10 A/mm^2. The current density is limited not only by the conductor itself but also by the capabilities of the power system to remove heat due to ohmic losses in the conductor. High power applications therefore are required to have conductors of large cross-sectional areas together with high system voltage levels. The latter requires substantial amounts of insulation material. This is unfavorable for naval, aeronautical and space applications where high power density by volume and mass are of utmost importance. High-temperature superconductors (HTS) are considered an option [1] as they would allow power cables of substantially higher current density. According to Haugan et al., a reduction of mass of approximately 80 kg per meter length and a reduction of volume by a factor

of ten can be achieved by replacing a 270 V / 20 kA copper cable by an HTS cable of equivalent rating [1].

The standard method of cooling for HTS power cables is based on liquid Nitrogen, which limits the operating temperature to between 63 K and 77 K. The critical current of HTS materials increases significantly as they are cooled to lower temperatures, which further increases the power density. Gaseous Helium allows operating temperatures below 63 K with additional benefits, such as omission of phase changes, lower risk of asphyxiation if operated in confined spaces and wider operating temperature range. Fitzpatrick et al. [2] and Kephart et al. [3] have described a Helium gas cooled HTS degaussing system for Navy shipboard application. The optimum operation temperature for this application was reported to be 55 K.

Among the disadvantages of gaseous Helium is the low dielectric strength compared to liquid Nitrogen, even when operated at elevated pressure levels. This needs a conservative design regarding maximum electric field and careful dielectric characterization by laboratory tests. The Helium serves both as the coolant and forms an important integral part of the dielectric system of the cable together with several layers of polymeric tape. It is critically important to ensure high dielectric integrity of such a cable. Therefore, the primary aim in this project is to study the dielectric characteristics of the insulation system. The project deals with a superconducting cable operating under DC voltage capable of carrying high power. The aim of the project is to manufacture a 30 m monopole DC cable rated at 1 kV, 3 kA operating at between 40 K and 70 K at a maximum pressure of 2.17 MPa, in a Helium gas environment.

An essential apparatus for the study of dielectrics at cryogenic temperatures is a well-designed and fabricated cryostat. The conditions under which the dielectric studies are to be conducted is determined by the final application, hence it dictates the final form of the cryostat. Previous studies in Helium [4] had utilized a high pressure vessel containing the electrodes which was immersed in a cryostat that contained a pool of liquid Helium at the bottom. In the present work we have designed and built a cryostat that can be pressurized up to 2.17 MPa where the medium is purely gaseous Helium and we are able to achieve temperatures of between 40 K and 77 K at various pressure levels.

We define a figure of merit for the cryostat based on the following parameters: Consumption of liquid Helium, rate of rise of temperature on the test object (in this case it is the model cable) and the inception voltage level of partial discharge of the high voltage bushing which forms part of the cryostat.

2 Experimental Setup

2.1 High Pressure Cryostat

Figure 1 shows a single line diagram of the high pressure cryostat (manufactured by Technifab Products of Indiana) that has been used for all experiments reported in the present work. The innermost enclosure of the pressure vessel (1) is rated at 2.17 MPa. Its inner dimensions are, diameter 265 mm and height 1.5 m. The pressure vessel is surrounded by a vacuum jacket (3) which contains a liquid Nitrogen jacket (2) for radiation shielding. The vacuum jacket was maintained at around 100 μPa. The lid of the cryostat (4) is dome shaped and double walled with a vacuum space between the walls. This vacuum space was also maintained at a similar pressure level to the other one. The lid carries seven ports, six of which are 69.85 mm flanges (2.75 Inch ConFlat) and one is 152.4 mm (6 Inch ConFlat). The largest of the ports on the lid is situated centrally and carries the high voltage bushing (5). The others are spaced evenly around the central port. They were utilized for pumping, exhausting, liquid Helium admittance, pressurized gas input and instrumentation. The lid and the cryostat are joined through a large flange. Figure 2 shows a picture of the cryostat.

2.2 The HTS Model Cable

The test object was a 1 m long model cable rated at 1 kV DC. It consists of a stainless steel former on which are wound a number of copper conductors of the same dimensions as HTS conductors, which will be used for the final design. Here, the emphasis was on the dielectric properties of the cable, therefore no expensive HTS tape was used. The insulation was in tape form, which was spiral wound. All winding gaps were filled by the cooling medium, which was Helium. An aluminum ground shield was wound over the insulating layers and connected to ground potential. Each end of the cable carried a stress cone in order to reduce the electric field at the termination points.

2.3 Partial Discharge Measurement Method

Partial discharge (PD) has a detrimental effect on the dielectric and therefore is an important parameter in the operation of any type of cable. The inception voltage of PD has to be well above the maximum operating voltage of the cable. Even though the demonstration cable under consideration will operate under DC voltage, we consider PD characterization an important design criterion. In order to do such measurements, only AC voltages can be used. Tests under DC voltages will follow.

The partial discharge measurement system consists of a 100 kV (RMS[*]), 5 kVA transformer connected via an inline filter and a capacitive voltage divider to a power coupling filter rated at 100 kV, 1 nF and a calibration injection capacitor rated at 100 kV, 100 pF. The output was taken from the injection capacitor and connected to the object under test. In this case it was the model cable, which was 1 m in length. The model cable was connected to the high voltage bushing and was suspended vertically with the lower end being terminated in a sphere of diameter 50 mm. All the above described equipment was housed within a Faraday enclosure. The partial discharge measurement system, instrumentation and the control console for the equipment in the Faraday enclosure was supplied by Haefely of Switzerland.

Initially, a ceramic feed through for liquid Nitrogen applications was utilized as high voltage bushing. However, its hollow design exposing the bare conductor to gaseous Helium at room temperature led to low PD inception voltage (PDIV). This could not be tolerated for the anticipated purpose of the cryostat, which includes PD measurements on the model cables. Therefore, the cavity was filled with a suitable epoxy resin and extended along the conductor. This eliminates the high-field region in gaseous Helium and increases the creepage distance at the same time. A second PD test of the modified bushing revealed a PDIV of around 16 kV (peak), which is good enough for characterization of model cables.

2.4 Temperature Measurement System

Temperature sensors were attached to the surface of the model cable along its axis, one was at the top where the high voltage bushing connected to the model cable, one at the midpoint of the model cable and the third was at the end of the model cable. Sensor types used were E-type thermocouples and 100 Ω Platinum resistance temperature detectors (RTDs), supplied by Lakeshore Cryogenics. For the measurement with thermocouples, a National Instruments card was used. For the RTDs we used a Lakeshore Temperature Monitor. Our RTD instrumentation has a higher accuracy than our thermocouple instrumentation; therefore the RTDs were used to calibrate the thermocouple measurement. Thermocouples on the other hand have benefits in robustness against electromagnetic radiation during electrical breakdown tests. They are also comparatively inexpensive.

[*] All voltage values are expressed as RMS values except where specified otherwise

3 Experimental Method

3.1 Dielectrical Characterization

The pressure vessel in the cryostat was first pumped down to a vacuum of around 100 μPa. The model cable with the spherical termination was then connected onto the electrical feed through. Temperature sensors were fixed onto the model cable along its length. The model cable has a ground shield, which was connected to the inside of the lid. All fixtures were cleaned before installation with isopropyl alcohol. A gasket made of Teflon was placed on the flange of the bottom part of the cryostat and the lid was put in place. The cryostat was grounded to the same point as the transformer inside the Faraday enclosure. Two gas inlet ports of the cryostat were connected through two position valves to regulated gas cylinders of Nitrogen and Helium. The Helium input had a 10 mm stainless steel tube, which extended all the way down to near the bottom of the cryostat. The pumping port was connected to a turbo-molecular pump. The exhaust port was connected to a ball valve and the liquid Helium inlet port was connected to a fixture that clamped onto a KF fitting; it has a vacuum jacket and carries a high pressure valve, the open end was a female bayonet, which mates with a male bayonet termination from the Helium transfer line.

The two gas cylinders were connected to the inner pressure vessel through a heat exchanger, which was held inside an open cryostat. This arrangement was first evacuated with an oil fore pump, then flushed alternatingly with Nitrogen and Helium a few times. Finally it was evacuated using a turbo molecular pump over a period of about two days until the pressure was down to about 10 μPa. The pump was then disconnected from the vessel and the vessel was filled with Helium to a pressure level of just above atmospheric pressure. The liquid Nitrogen jacket and the open cryostat containing the heat exchanger were filled with liquid Nitrogen twelve hours before starting the experiments. This procedure of filling the liquid Nitrogen jacket helps to reduce the amount of liquid Helium needed for the subsequent cooling since it pre-cools the inner walls of the pressure vessel and the model cable. The temperature sensors on the cable read below 180 K prior to the transfer of liquid Helium in preparation for the electrical measurements.

A quantity of 53 L of liquid Helium was then admitted into the pressure vessel using a transfer line with the ball valve in the open position. This was continued until the temperature sensors placed at both the top and bottom of the cable read below 14 K. The ball valve was closed and the admittance of liquid Helium was stopped. Subsequently Helium from the gas cylinder was admitted into the vessel until the absolute pressure reached 2.17 MPa. The temperature rose to about 60 K. The experiment was allowed to stand for approximately four hours, after which time the temperature had reached about 75 K. The gaseous Helium was then exhausted out of the vessel and about 30 L of liquid Helium were again admitted into the pressure vessel until the temperature reached below 14 K. The vessel was pressurized with gaseous Helium through the heat exchanger and the temperature stabilized at around 50 K.

The output from the partial discharge measurement system was connected to the experiment through the high voltage bushing. The voltage was gradually increased in steps of about 500 V, at each level of voltage the PD was recorded. As the voltage crossed a threshold, corona activity started in the gaseous Helium as it was weaker than the tape insulation. This corona activity was manifested as PD in our measurements. The voltage was increased until the indicated apparent charge of the PD activity reached a value of about 50 pC. At this point the voltage was reduced gradually in a similar manner and at each level of voltage the PD level was recorded.

The pressure in the vessel was reduced in steps of about 340 kPa by exhausting Helium. At each such pressure the PD measurements were carried out as described above. The lowest pressure at which the experiments were done was 446 kPa.

Once all the PD measurements were completed, the cable was cooled a second time with liquid Helium, after which the pressure was increased again by adding gaseous Helium until the pressure reached 2.17 MPa. The temperature at this point was again about 50 K. The transformer was connected directly to the cable through the electrical bushing and the voltage was ramped at the rate of 0.5 kVs^{-1} until a breakdown was recorded. We have made measurements on three model cable samples, reported here.

Figure 5 shows a typical result of the level of apparent charge as a function of applied voltage level of a model cable, at a pressure of 2.17 MPa and a temperature of 50 K. Open circuit PD activity was at around 1 to 2 pC, which can be interpreted as background noise. It gradually increases with increasing applied voltage. It has to be pointed out that at voltages higher than 16 kV (peak) the contribution to PD was not only from the cable but also from the high voltage bushing. An earlier measurement of PD involving only the high voltage bushing showed that the PDIV for the bushing was 16 kV (peak). We define PDIV as the voltage where the apparent charge exceeds 10 pC. The PDIV of the model cables is about 7.4 kV (peak) at 2.17 MPa as shown in Figure 5. The PDIV is pressure dependent.

3.2 Thermal Characterization

In order to ensure that the temperature variations along and across the model cable were within reasonable levels, a dummy cable was fabricated with similar thermal properties as the model cable. We utilized seven E-type thermocouples to measure the temperature distribution along the cable length and diameter. At the midpoint of this model we attached three thermocouples. One was attached to the inside of the stainless steel tube core, the second was embedded in the tape insulation halfway between the innermost layer and the outermost layer of the insulation. The third was fixed onto the earth shield, which was made of Aluminum tape. The other sensors were placed on the upper and lower ends of the cable, as well as on the conductor from the high voltage bushing. Figure 1 shows the distribution of all thermocouples.

The results of the temperature variations are shown in Figure 3. It is evident that the temperature variation across the mid-section is marginal under these operating conditions of the model cables.

The experiment to determine the temperature distribution was carried out in the same way as we had done with the model cables, as described in the previous section. The temperature at the lower end of the cable rose by approximately 1 K during the 40 min test (Figure 4). During the same period of time, the temperature at the top part of the cable rose by 8 K. We regard this as an acceptable performance. Therefore, it can be concluded that the thermal insulation characteristics of this cryostat are good enough for tests of up to 1 hour duration.

4 Results and Discussion

The results presented here are twofold: Firstly, it is the utility of the high pressure cryostat that has been built to carry out the necessary dielectric studies for a variety of materials, and secondly, the studies that have been conducted so far on three model cables.

With reference to the figure of merit defined in the introduction, the maximum measured rate of rise of temperature was around 12 K per hour. The consumption of liquid Helium to reach a temperature of approximately 60 K at 2.17 MPa was 53 L. By repeated injection of liquid Helium lower temperature levels can be achieved. The cryostat is free of PD up to a peak AC value of 16 kV, which is the PDIV of the bushing currently in place. These values are well within our design requirements.

It has been demonstrated in these experiments that the dielectric performance of the tested Helium gas cooled model cables exhibit promising dielectric characteristics. A more comprehensive treatment of the dielectric performance is given in a companion paper [5].

Acknowledgments

The authors would like to thank the Office of Naval Research, USA for financial support under Grant N00014-02-1-0623.

References

[1] T.J. Haugan, et al., "Design of Compact, Lightweight Power Transmission Devices for Specialized High Power Applications", SAE Int. J. Aerosp. 1(1), 1088-1094, 2008.
[2] B.K. Fitzpatrick, et al., "Characterization of Gaseous Helium Flow Cryogen in a Flexible Cryostat for Naval Applications of High Temperature Superconductors", IEEE Trans. on Applied Superconductivity, Vol. 17, No. 2, 1752-1755, 2007.
[3] J.T. Kephart, et al., „High Temperature Superconducting Degaussing From Feasibility Study to Fleet Adoption", accepted for publication in IEEE Trans. on Applied Superconductivity.
[4] R.J. Meats – "Pressurized Helium Breakdown at a Very Low Temperature", Proc. IEEE 1972, Vol. 119(6), 760-766
[5] L. Graber, et al., "Experimental Determination of Dielectric Properties of Cryoflex in High Pressure Cold Helium Gas", submitted to be published at the International Symposium on High Voltage Engineering ISH 2011, Hannover, August 22-26, 2011.

Figures

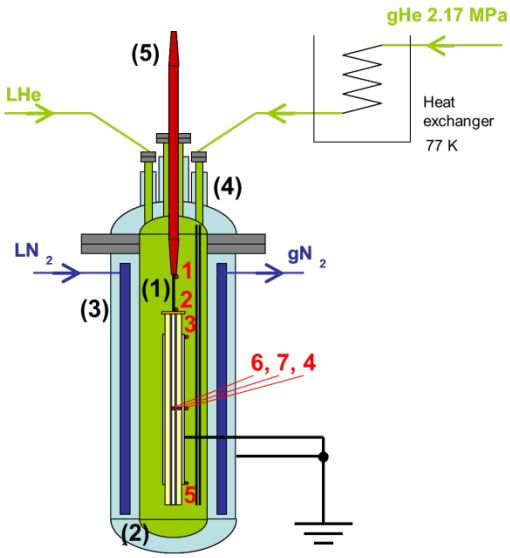

Figure 1: Schematic illustration of the cryostat design and temperature sensor locations

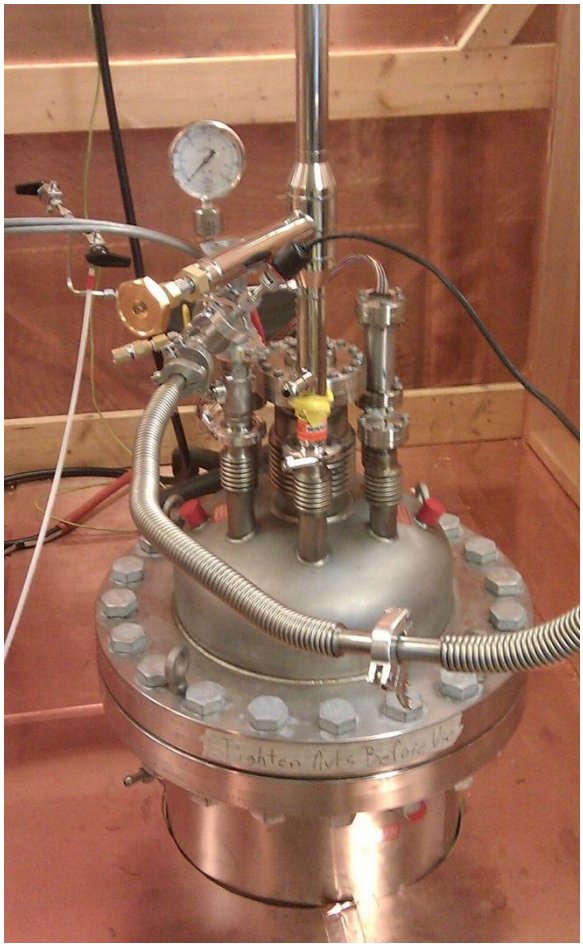

Figure 2: Photograph of Cryostat

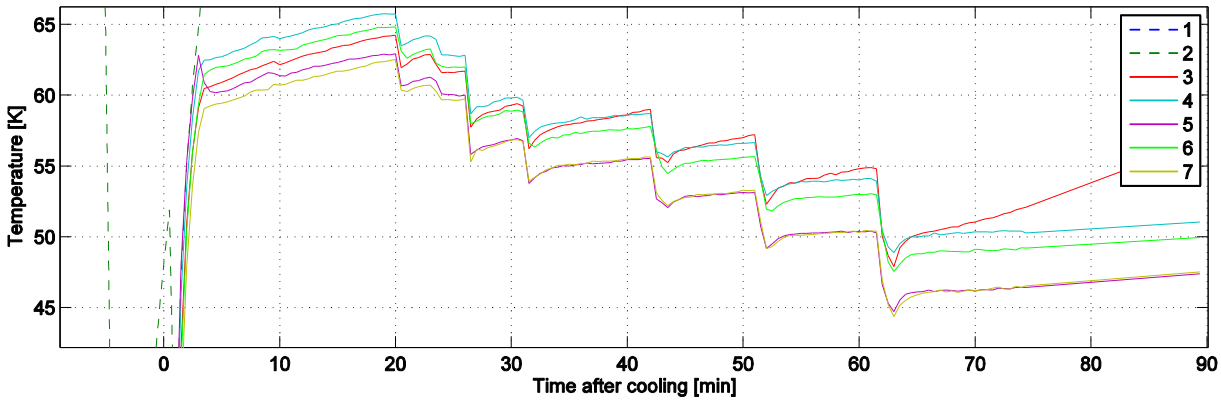

Figure 3: Temperature data over time along dummy cable diameter and length. Numbers correspond to positions given in Figure 1.

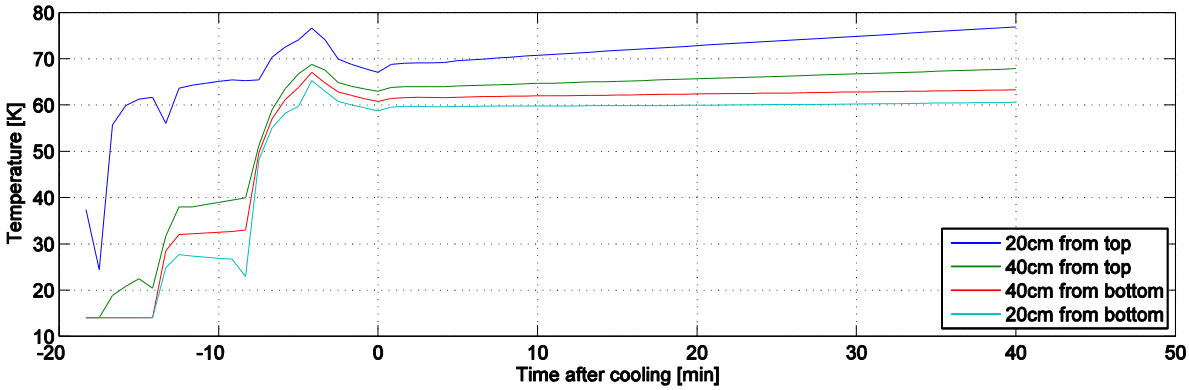

Figure 4: Temperature development along model cable length over warming period.

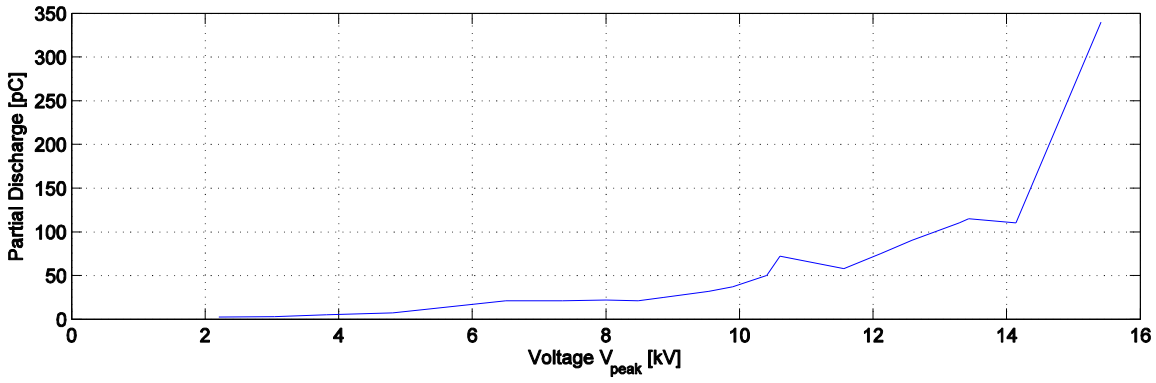

Figure 5: Partial discharge measurement of model cable

REPORT DOCUMENTATION PAGE

Form Approved
OMB No. 0704-0188

1. REPORT DATE *(DD-MM-YYYY)*	2. REPORT TYPE	3. DATES COVERED *(From - To)*
01–03–2013	Conference Publication	

4. TITLE AND SUBTITLE

2011 Space Croygenics Workshop
"Poised for the Future, Reflecting on the Past"

5a. CONTRACT NUMBER

5b. GRANT NUMBER

5c. PROGRAM ELEMENT NUMBER

6. AUTHOR(S)

W.L. Johnson,* Co-Chair, A.R. Schnell, Co-Chair, and L. Huget, Executive Director**

5d. PROJECT NUMBER

5e. TASK NUMBER

5f. WORK UNIT NUMBER

7. PERFORMING ORGANIZATION NAME(S) AND ADDRESS(ES)

Kennedy Space Center, Orlando, FL 32899
George C. Marshall Space Flight Center, Huntsville, AL 35812

8. PERFORMING ORGANIZATION REPORT NUMBER

M–1355

9. SPONSORING/MONITORING AGENCY NAME(S) AND ADDRESS(ES)

National Aeronautics and Space Administration
Washington, DC 20546–0001

10. SPONSORING/MONITOR'S ACRONYM(S)

11. SPONSORING/MONITORING REPORT NUMBER

NASA/CP—2013–217479

12. DISTRIBUTION/AVAILABILITY STATEMENT

Unclassified-Unlimited
Subject Category 31
Availability: NASA CASI (443–757–5802)

13. SUPPLEMENTARY NOTES

Prepared for the Propulsion Systems Department, Engineering Directorate
*Kennedy Space Center, Orlando, FL **Cryogenic Society of America, Inc., Oak Park, IL

14. ABSTRACT

The 24th Space Cryogenics Workshop was held at the Best Western Coeur d'Alene Inn and Conference Center, Coeur d'Alene, Idaho, June 8–10, 2011. The workshop was organized and sponsored by NASA Kennedy Space Center and NASA Marshall Space Flight Center, with a theme of "Poised for the Future, Reflecting on the Past." Over 100 scientists and engineers from around the world came together to discuss space applications for cryogenics, renew old acquaintances, and meet new practitioners in the field of space cryogenics.

15. SUBJECT TERMS

cryogenics, cryocoolers, insulation, thermal analysis, refrigeration

16. SECURITY CLASSIFICATION OF:			17. LIMITATION OF ABSTRACT	18. NUMBER OF PAGES	19a. NAME OF RESPONSIBLE PERSON
a. REPORT	b. ABSTRACT	c. THIS PAGE			STI Help Desk at email: help@sti.nasa.gov
U	U	U	UU	428	19b. TELEPHONE NUMBER *(Include area code)* STI Help Desk at: 443–757–5802

National Aeronautics and
Space Administration
IS20
George C. Marshall Space Flight Center
Huntsville, Alabama 35812